Sweep and clean

A laboratory investigation on fine-sediment erosion in immobile coarse-grained beds

Zur Erlangung des akademischen Grades eines

DOKTOR-INGENIEURS

von der Fakultät für
Bauingenieur-, Geo- und Umweltwissenschaften
des Karlsruher Instituts für Technologie (KIT)

genehmigte

DISSERTATION

von

M.Sc. Michele Trevisson

aus Bozen, Italien

Tag der mündlichen Prüfung: 15.12.2021

Referent: Prof. Dr. Olivier Eiff
Korreferent: Prof. Dubravka Pokrajac

Karlsruhe (2022)

Abstract

In river systems characterized by sediment-supply limited conditions, such as mountain streams or river-reaches below damns, fine-sediments are transported over a coarse bed of cobble or gravel, immobile for most of the flow conditions. The prediction of sediment transport is particularly challenging, under these conditions, as it is strongly correlated to the level of protrusion of the immobile grains. The aim of this work is to investigate the influence of immobile grains on the fine-sediment erosion at the bedform- and grain-scale on the basis of an experimental approach in a laboratory flume. The immobile gravel bed was modelled with a staggered pattern of spheres (2 cm in diameter) with different roughness densities. Two types of fine sediments were used. Experiments were performed for varying Shields parameter, aspect ratio and relative submergence. The bed topography and the sediment transport were measured during the whole duration of the experiment (until a stable bed elevation was reached), while simultaneous stereo-PIV measurements were performed at selected staged of the bed development. A novel approach is developed to extend the stereo-PIV measurements to obtain data deep in between the roughness elements down to the level of the fine-sediments. The morphodynamic measurements at the reach scale showed the development of ridges with a lateral inter-ridge spacing of 1.3 times the water depth, which defines the characteristic ridge wavelength. The number of ridges is given by the integer number of wavelengths which fit into the effective width of the channel. It is shown that the reason for faster erosion over the troughs than over the ridges is connected to the local downflow that pushes the sweeps towards the bed.

Both over the ridges and over the troughs, the analysis shows that the erosive behaviour changes with the protrusion level of the spheres P. Four stages take place: reduced erosion for $P < 0.2$, enhanced erosion rates for $0.2 < P < 0.4$, decreased erosion rates $0.4 < P < 0.7$ and complete sheltering for $P > 0.7$. The first transition at $P_{c1} = 0.2$ is connected to the development of a shear layer at the top of the spheres which induces enhanced fine-sediment shear stresses through generation of sweep events. The second transition transition for $P_{c2} = 0.4$ is connected to the dominance of strong upflow conditions in the lee side of the spheres which locally prevent the shear layer to reach the fine sediments, damping the shear stress. The flow there is characterized by isotropic turbulent conditions. In the stoss side of the spheres, the shear layer is still able to reach the fine-sediment bed. Here the flow is characterized by the predominance of sweeps which effectively originate in the shear layer. The interaction between the shear layer and the sphere downstream suggests wake-interference regimes. The third transition for $P_{c3} = 0.7$ is characterised by the switch to skimming flow conditions, as the upflow extends up to the top of the spheres pushing the shear layer out of the bed interstices. At the level of the bed critical conditions of motion are observed. In the lee side of the spheres, inward interactions are predominant, while in the stoss side isotropic turbulence is observed. The influence of the roughness density, Shields parameter, sediment size and relative submergence on the fine-sediment erosion were also investigated. For a generic rough bed, the second and third transitions can be identified by the protrusion levels for which the planar density of the roughness elements reach 0.3 and 0.5. The first

transition is expected when the protrusion level corresponds to the angle of attack of approximately 20° for which the shear layer starts to develops.

Kurzfassung

In Flusssystemen, die durch ein begrenztes Sedimentangebot gekennzeichnet sind, wie z. B. Gebirgsbäche oder Flussabschnitte unterhalb von Staudämmen, werden Feinsedimente über ein grobes Bett aus Geröll oder Kies transportiert, das für den größten Teil der Strömungsbedingungen unbeweglich ist. Die Vorhersage des Sedimenttransports ist unter diesen Bedingungen besonders schwierig, da er stark mit dem Ausbreitungsgrad der unbeweglichen Körner zusammenhängt. Ziel dieser Arbeit ist es, den Einfluss immobiler Körner auf die Feinsedimenterosion auf der Bettform- und Kornskala auf der Grundlage eines experimentellen Ansatzes in einer Laborrinne zu untersuchen. Das unbewegliche Kiesbett wurde mit einem gestaffelten Muster von Kugeln (2 cm Durchmesser) mit unterschiedlichen Rauhigkeitsdichten modelliert. Es wurden zwei Arten von Feinsedimenten verwendet. Die Topographie des Bettes und der Sedimenttransport wurden während der gesamten Versuchsdauer (bis zum Erreichen einer stabilen Betthöhe) gemessen, während gleichzeitig Stereo-PIV-Messungen in ausgewählten Stadien der Bettentwicklung durchgeführt wurden. Es wurde ein neuartiger Ansatz entwickelt, um die Stereo-PIV-Messungen so zu erweitern, dass Daten tief zwischen den Rauhigkeit-selementen bis hinunter auf die Ebene der Feinsedimente gewonnen werden können.

Die morphodynamischen Messungen auf der Bettformskala zeigten die Entwicklung von Rippen mit einem seitlichen Abstand zwischen den "Ridges" (parallel zur Strömungsrichtung verlaufende Sedimentstrukturen) von 1.3 mal der Wassertiefe, was die charakteristische Wellenlänge der "Ridges" definiert. Die Anzahl der "Ridges" ist durch die ganzzahlige Anzahl der Wellenlängen gegeben, die in die effektive Breite des Gerinnes passen. Es wird gezeigt, dass der Grund für die schnellere Erosion über den "Troughs" (Regionen des Bettest zwichen den Ridges) als über den "Ridges" mit der lokalen Abwärtsströmung zusammenhängt, die die Sweeps in Richtung Sohle drückt.

Sowohl über den "Ridges" als auch über den "Troughs" zeigt die Analyse, dass sich das Erosionsverhalten mit der Höhe des Vorsprungs der Kugeln P ändert. Es finden vier Phasen statt: verringerte Erosion für $P < 0.2$, erhöhte Erosionsraten für $0.2 < P < 0.4$, verringerte Erosionsraten $0.4 < P < 0.7$ und vollständige Abschirmung für $P > 0.7$. Der erste Übergang bei $P_{c1} = 0{,}2$ steht im Zusammenhang mit der Entwicklung einer Scherschicht an der Kronenoberkante der Kugeln, die durch die Erzeugung von Sweep-Ereignissen er-höhte Feinsediment-Schubspannungen induziert. Der zweite Übergang für P_{c2} ist mit der Dominanz starker Aufströmungsbedingungen im Lee der Kugeln verbunden, die lokal verhindern, dass die Scherschicht die Feinsedimente erreicht, wodurch die Scherspannung gedämpft wird. Die Strömung dort ist durch isotrope turbulente Bedingungen gekennzeichnet. Vor den Kugeln kann die Scherschicht immer noch das Feinsedi-mentbett erreichen. Hier ist die Strömung durch das Vorherrschen von Sweeps gekennzeichnet, die tatsächlich in der Scherschicht entstehen. Die Wechselwirkung zwischen der Scherschicht und der stromabwärts gele-genen Kugel deutet auf Nachlauf-Interferenz-Regime hin. Der dritte Übergang für $P_{c3} = 0.7$ ist durch den Wechsel zu Skimming-Strömungsbedingungen gekennzeichnet, da sich die Aufwärtsströmung bis zur Ober-seite der Kugeln ausdehnt und die Scherschicht aus der Kappe verdrängt. Auf der Höhe des Bettes werden kritische Bewegungsbedingungen beobachtet. Auf der Leeseite der Kugeln herrschen nach innen gerichtete

Wechselwirkungen vor, während auf der Stoss-Seite isotrope Turbulenz herrscht. Untersucht wurden auch Änderungen der Rauhigkeitsdichte, des Shields-Parameters, der Sedimentgröße und der relativen Überflutung. Für ein allgemeines raues Bett können der zweite und dritte Übergang durch die Vorsprungsniveaus identifiziert werden, für die die Flächendichte der Rauhigkeitselemente 0,3 und 0,5 erreicht. Der erste Übergang wird erwartet, wenn der Überstandsgrad dem Anstellwinkel von etwa 20° entspricht, bei dem sich die Scherschicht zu entwickeln beginnt.

Aknowledgements

First of all, I would like to express my gratitude and special appreciation to my supervisor Prof. Eiff. I thank Olivier for his precious and constant academic support over the last six years, started during my master-thesis and continued during the PhD. He first introduced me to the fascinating world of experimental hydraulics and I thank him for having been such a dedicated mentor. I will always remember with great pleasure the many stimulating scientific discussion we had, which helped me to shed new light on my findings and open new challenging questions.

I want to express also my gratitude to all the members of the Environmental fluid mechanics group for being always a source of good advice and support.

A big thanks goes to the technicians Michael Ziegler, Jürgen Ulrich and Dieter Gross for helping me to build the experimental set-up and to solve any technical difficulty I encountered. Without their precious help the experiments wouldn't have been possible.

I would like to thank all HiWis who have aided me in the preparation and calibration of the experiments. They have been of an invaluable help.

A special thanks goes to the secretaries Heidi Lauinger and Angelika Fels for helping me always out with any administrative issues but most of all for brightening up my mornings with our daily chats.

I would like to express my heartfelt and deep gratitude to my colleague and dearest friend Yulia Akutina, who has been a pillar of support during my whole PhD, always caring for me and cheering me up during my ups and downs. I thank Yulia for having spent with me many many hours of stimulating scientific discussions, which helped me to improve considerably my work, and for the many hours spent in the lab helping me. I wouldn't have really managed it without your help!

A special thanks goes also to my dear friend, Wendy Gonzalez, who started the PhD at the same time as me, for being a trustworthy friend and sharing with me the pains and joys of a PhD student. It was an invaluable support.

To my housemate, dear and special friend Ramiz a particular thanks for having been always on my side in the last two years, continuously encouraging me to go on. Thank you for your love and care.

Last but not least, I want to express my eternal gratitude to my wonderful parents and my amazing grandmas for always holding my back over the years and believing in me. I want to thank them for all the ways they managed to support me, even from afar, listening to me, encouraging me day by day and visiting me expectedly and unexpectedly.

List of Publications

The content of this thesis is based in part on the following works published by the author during the PhD.

Peer-reviewed publications

Trevisson, M., Eiff, O. (2022). Fine-sediment erosion and sediment-ribbon morphodynamics in coarse-grained immobile beds. *Water Resources Research*.

Conference contributions

Trevisson, M. and Eiff, O. (2018). Static equilibrium over rough beds with bedload transport. In *5th IAHR Europe Congress: New challenges in hydraulic research and engineering*.

Trevisson, M. and Eiff, O. (2018). Erosion of fine sediments from a rough bed. In *River Flow 2018: Proceedings of the 9th International Conference on Fluvial Hydraulics*, volume 40 of *E3S Web of Conferences*. EDP Sciences.

Trevisson, M., Eiff, O., and Akutina, Y. (2020). Experimental investigation of the morpho- and hydrodynamics of fine sediment erosion over a fixed coarse-grain bed. In *River Flow 2020: Proceedings of the 10th Conference on Fluvial Hydraulics*, London. Taylor & Francis Group.

Contents

Nomenclature

Latin symbols

a_j, b_j	parameters of the affine transformation with j = [0,1,2]
A	aspect ratio
A_e	effective aspect ratio
A_f	frontal area of the protruding spheres
$A_{f,fs}$	frontal area of the bed-forms within the reference pattern
A_p	planar area of the protruding spheres
A_r	total planar area of the reference pattern of spheres
A_ϕ	roughness geometric function
c	concentration of fine sediments as suspended- or bed-load
C	solidity of the fine sediments
C^*	concentration of suspended sediments
$C_{d,R}$	drag coefficient for an isolated roughness element
$C_{d,S}$	drag coefficient of the fine-sediment surface in the absence of protruding roughness elements
C_{P0}	aerial concentration of displaced sediments over a uniform fine-sediment bed
C_s	aerial concentration of displaced sediments
$C_{s,ci}$	critical aerial concentration of displaced sediments at the ith-transition in bed behaviour
D	diameter of the spheres
D_*	non-dimensional particle diameter
D_{i,H_s}	duration of the ith turbulent event at the level of the fine-sediment roughness sublayer
D_s	corrected spatial dispersion of a flow statistic
D_t	spatial dispersion of a flow statistic
d_{50}	mean diameter of the fine sediments
d_i	fine sediments' diameter for which the percentage i of the grains is smaller

d_0	distance between the laser sheet and the lens
d_c	distance between the stereo-PIV cameras
d_M, d_m	major and minor axis of the seeding particles
E	erosion rates so as if the bed was uniform
E_{ci}	critical erosion rate at the ith-transition in bed behaviour
E_{P0}	reference erosion rates measured over a uniform fine-sediment bed
E_t	total erosion rates including the influence of the protruding spheres
Fr	Froude number
F	image frequency
f	camera focal length
f_{i,H_s}	frequency of the ith turbulent event at the level of the fine-sediment roughness sublayer
f_p	pressure drag
f_v	viscous drag
g	gravitational acceleration
G	gravitational term
h_{rs}	roughness sublayer of the protruding spheres
h_{rs}^s	roughness sublayer of the fine-sediment bed
H	reference water depth defined from the top of the spheres to the water surface
H_c	height of the cameras above the bed
H_e	effective water depth
H_r	height of a ridge
H_s	hole size
H_w	total water depth
i	slope of the channel
I_{i,H_s}	indicator function for the quadrant analysis
I_{i,H_s}^*	indicator function for the quadrant analysis defined on the basis of u_*
I_x, I_y	inclination index in the streamwise and transverse direction
k	exposed height of a protruding sphere
k_r	radial distortion parameter

k_s	equivalent sand roughness
k_s^+	sand-roughness Reynolds number
k_t	tangential distortion parameter
K	pressure drop coefficient through a grid
K_j	camera matrix
K_ϵ	constant for the estimate of the TKE dissipation
K_u	kurtosis of the bed elevations
l_x, l_y	streamwise and spanwise dimensions of the reference pattern of spheres
L	length of the boat
L_{BL}	boundary-layer development length
L_x	streamwise integral length scale
L_t	integral time scale
m	roughness-density reduction parameter for the definition of the maximum surface shear stress in the Raupach et al. (1993) model
m_s	sediment mass
M	magnification factor
$M_{i,j}$	third-order moments
N	nodal point
N'	half node
N_c	size of the camera sensor
N_Λ	number of wavelengths which fit into the effective width
$N_{r,e}$	number of expected ridges
$N_{r,o}$	number of observed ridges
N_s	number of grains displaced
OA	obtuse angles
p_D	pressure diffusion
P	level of protrusion of an immobile sphere above the mobile sediment bed
P_{ci}	critical protrusion level for the ith-transition in bed behaviour
P_s	shear production
P_m	wake production due to the work of the spatial fluctuations against the double averaged shear

P_w	wake production due to the work of the spatial fluctuations against the bed-induced shear
Q	flow rate
q_s	sediment transport rate
r_{eq}	equivalent radius of the planar projection of a protruding sphere
r_0, r_1	radiometric parameters
R	radius of the spheres
R_j	rotation matrix from the world coordinate system to the reference system of camera j
R_H^c	hydraulic radius with side-wall correction
Re	bulk Reynolds number
$Re*$	particle Reynolds number
RS	relative submergence
S	saddle point
S'	half saddle
Sk	skewness of the bed elevations
S_r	relative submergence
S_{i,H_s}	relative contribution of the ith quadrant turbulent event to the turbulent shear stress
S_{i,H_s}^*	relative contribution of the ith quadrant turbulent event defined on the basis of the shear velocity u_*
s	spacing between spheres centre to centre
s_r	side-slope of a ridge
t	time variable
t'	time with the time-periods characterized by depositional patterns removed
t_0	time at which a sphere starts to protrude without being covered again
T	distance between the stereo-photogrammetric cameras
T_e	duration of the experiment
T_{i,H_s}	time fraction of the ith-turbulent event
T_j	translation vector from the world coordinate system to the reference system of camera j
T_k	turbulent kinetic energy transport
T_θ	transport stage parameter
T_v	viscous diffusion

xvi

u, v, w streamwise, spanwise and vertical velocity component

u_* shear velocity obtained from the extrapolation of the total shear stress to the top of the spheres

u_{*H} shear velocity based on the water depth

u_{*P0} reference shear velocity measured over a uniform fine-sediment bed

u_{*R} shear velocity based on the hydraulic radius

u_{*R^c} shear velocity based on the hydraulic radius with side-wall correction

U bulk velocity

U_δ time-averaged streamwise velocity at the edge of the boundary layer

U_e effective bulk velocity

$\overline{u'w'}_{i,H_s}$ contribution to the turbulent shear stress of the ith-turbulent event

w_{nu} vertical velocity induced by a streamwise flow non-uniformity

W width of the channel

W_e effective width of the channel

W_r width of a ridge

V_c control volume for the definition of the continuity of mass

V_g volume of a sediment particle

x, y, z streamwise, spanwise and vertical axis of the coordinate system of the flume

x'_j, y'_j reference system attached to the camera sensor j

X, Y, Z   world coordinate system of the stereo-PIV system

$\Delta x'$, $\Delta z'$ projected particle displacement on the camera sensor

x_{fd} longitudinal position for the full-development of the boundary layer

x_{PIV} longitudinal position of the planar PIV system

$x_{topo,u}$, $x_{topo,d}$

       longitudinal position of the upstream sn downstream topographic measurement system

y_r transverse position of a ridge

z_b fine sediment bed level

z_c reconstructed elevation of the calibration dots via the stereo-photogrammetric system

z_{cd} clean-out depth

z_d zero-plane position

z_0 roughness length

z_{ts} reconstructed elevation of the crest of the spheres via the stereo-photogrammetric system

Greek symbols

α_a angle of attack of a sphere

α_x, α_y bed inclination angles in streamwise and transverse direction

α_s level of significance of the test of Pearson

β non-uniformity parameter

β_c half-angle of view of a camera

β_R ratio of element to surface drag coefficients

γ stereo-PIV camera angle

δ boundary layer thickness

δ^* displacement thickness

Δ relative density of the fine sediments

ΔH increase in water level due to the boat

ΔS_* residual shear stress contribution

Δt bulk time unit

Δu increase in streamwise velocity induced by the boundary layer developing along the boat

Δx virtual origin of the boundary layer developing along the boat

ϵ turbulent kinetic energy dissipation

ϵ_P error on the protrusion level

ϵ_x^q, ϵ_y^q, ϵ_z^q quantization error in the longitudinal, transverse and vertical direction

$\epsilon_{r_{eq}}$ error on the equivalent radius

$\epsilon_{\overline{\phi_v}}$ time-convergence error of a flow variable

ϵ_{Deltax} peak-locking error in the streamwise direction

ϵ_{Deltaz} peak-locking error in the out-of plane direction

ζ vertical viewing angle of the stereo-PIV cameras

η Kolmogorov length scale

θ Shields parameter

θ_c critical Shields parameter for permanent motion

θ'_c — critical Shields parameter for the onset of motion

$\theta'_{c,\alpha}$ — critical Shields parameter for the onset of motion with bed-slope correction

θ_{P0} — reference Shields parameter for a uniform fine-sediment bed defined on the basis of τ_{P0}

θ_S^x, θ_S^y — local Shields parameter acting on the fine-sediments defined on the basis of τ_s^x and τ_s^y

κ — von Karman constant

λ_f — frontal density of the protruding spheres

λ_p — planar density of the protruding spheres

λ_t — Taylor miscroscale

Λ_l, Λ_c, Λ_r — left-wall, central and right-wall ridge spacings

Λ_{Col} — theoretical ridge-wavelength by Colombini and Parker (1995)

μ — area coverage of the fine sediments

ν — cinematic viscosity

ξ — corrected time frame

ξ_{ci} — critical time for the i$^{\text{th}}$-transition in bed behaviour

ρ_s — density of the fine sediments

ρ_p — density of the seeding particles

σ — ratio between planar and frontal density

σ_g — geometric standard deviation of the grain size distribution

σ_u — streamwise turbulent intensity

σ_z — standard deviation of bed elevations

τ — Kolmogorov time-scale

τ_p — relaxation time of the seeding particles

τ_b — bed shear stress

$\tau_{c,i}$ — critical shear stress of the grain fraction i

$\tau_{c,d_{50}}$ — critical shear stress of the mean size fraction

τ_f — form-induced shear stress

τ_{P0} — reference bed shear stress acting on an uniform fine-sediment bed

τ_s^x, τ_s^y — shear stress acting on the fine sediments in the longitudinal and transverse direction

$\tau_{s,i}$ — shear intensity of the ith turbulent event acting on the fine-sediments

$\tau_{s,max}$	maximum shear stress acting on the fine sediments
τ_{uw}	Reynolds shear stress in the longitudinal direction
τ_{vis}	viscous shear stress
τ_{vw}	Reynolds shear stress in the transverse direction
τ_{vis}	viscous shear stress
τ_{xz}	total shear stress in the longitudinal direction
$\tau_{xz}\vert_{local}$	local fluid shear stress
τ_{yz}	total shear stress in the transverse direction
χ_a	Euler characteristic of a surface given a priori
χ_e	Euler characteristic of a surface
ϕ	porosity of the bed
ϕ_f	friction angle of the fine sediments
ϕ_v	flow variable
ϕ_s	porosity of the fine sediments

Mathematical symbols and operators

$\overline{*}$	time average of a quantity $*$
$*'$	time fluctuation of a quantity $*$ compared to its average in time $\overline{*}$
$\tilde{*}$	spatial fluctuation of a quantity $*$ compared to its spatial average $\langle * \rangle$
$\langle * \rangle$	spatial average of a morphological variable $*$ within the reference pattern
$\langle * \rangle_x$	spatial average of a quantity $*$ in the streamwise direction
$\langle * \rangle_y$	spatial average of a quantity $*$ in the transverse direction

Abbreviations

DEM	digital elevation model
IBL	internal boundary layer
$JPDF$	joint probability density function
OA	obtuse angle
OBL	outer boundary layer

TKE turbulent kinetic energy

1   Introduction

Many river systems, such as mountain streams or river reaches downstream of dams, are characterized by coarse grained beds, where the dominant grain sizes are gravel or cobbles as the result of streamwise grain sorting (Powell, 1998; Ferguson et al., 1989). Gravel beds represent important aquatic habitats, providing suitable spawing sites for salmonid species Kondolf and Wolman (1993), housing a variety of macroinvertebrates Gibins et al. (2007b) and connecting surface waters with the groundwater through fluxes of dissolved substances (Pretty and Hildrew, 2006). Unfortunately, these habitats can be greatly endangered by the increased supply of fine sediments into the river, as a consequence of natural events such as landslides or bank collapses (Tuijnder and Ribberink, 2012; Bathurst, 1985), of changes in land use practices like increased deforestation, logging and tilled agriculture (Davies and Nelson, 1993; Collins et al., 1997; Mohta et al., 2003), and of reservoir flushing, dam removal or construction (Wren and Kuhnle, 2014; Grant, 2012). Dams have in fact a significant impact on the fine sediment balance of streams: dams block the sediment supply to downstream reaches, so that sediments deposit upstream of dams, causing river aggradation (Kondolf and Wilcock, 1996; Parker, 2008; Grant, 2012). At the same time, the reduction of discharges for flood mitigation leads to a reduced sediment transport capacity downstream of dams, so that the river is not able any more to flush, during flood events, the fine sediments deposited by downstream tributaries (Wilcock et al., 996b; Andrews, 1984). Increased ingress of fine sediments in the riverbed leads to substantial changes in the riverbed structure with potential degradation of fish, benthic and macrophyte habitats (Wharton et al., 2017), associated, for example, to a reduction of spawning sites (Nelson et al., 1989), to higher embryo mortality (Buffington et al., 2004) or to a reduction in macroinvertebrates communities due to reduced hiding spots against predators and floods Lancaster et al. (1991). The restoration of aquatic habitats in dam regulated rivers can be performed through flushing operations to remove superficial and interstitial fine sediments from the gravel (Kondolf and Wilcock, 1996). These operations have to be carefully planned in order to avoid invertebrate drift (Gibins et al., 2007a) and high fish mortality (Crosa et al., 2010). For this purpose, accurate modelling and prediction of fine sediment transport over coarse gravel beds is needed, in order to predict the clean out depth of fine sediments and the time to achieve it, without entraining the gravel (Kuhnle et al., 2016).

Fine sediments infilling the gravel induce a substantial change in the riverbed grain size distribution, which tends to become bimodal. For this reason, classical sediment transport models developed for uniform grain size distributions, such as Meyer-Peter and Müller (1948); Engelund and Hansen (1967); Yang (1984) are of difficult applicability for mixed sediment mixtures. As a result, mixed sediment mixtures have been the subject of various studies (Parker et al., 1982; Parker and Klingeman, 1982; Ashworth and Ferguson, 1989; Wilcock and McArdell, 1993; Wilcock et al., 2001; Hassan and Reid, 1990) focusing on the relative mobility of single grain sizes in the mixture. In a mixture, the mobility of a certain sediment fraction depends both on its absolute and relative grain size (Parker and Klingeman, 1982; Wilcock and Kenworthy, 2002). On the one hand, the absolute grain size effect dictates that larger grains are more difficult to move than smaller grains, so that the critical shear stress is a function of the grain diameter and size selective entrainment takes place

(Powell, 1998; Shields, 1936). On the other hand, the relative size effect in a sediment mixture results in a reduced mobility of finer grains and, at the same time, an increased mobility of larger grains as compared to a uniform bed matrix (Einstein, 1950; Egiazarov, 1956; Parker and Klingeman, 1982; Parker et al., 1982). Finer particles tend in fact to be hidden in the interstices between larger grains (Wittenberg, 2002; Parker and Klingeman, 1982), while larger grains are more exposed to the flow due to the presence of fine sediments (Ferguson et al., 1989; Wilcock et al., 2001). The relative size effect tends, therefore, to equalize the mobility of all grain fractions in a mixture. If the relative size effect dominates, then the critical shear stress for grain motion is independent of grain diameter and all size fractions are entrained at the same shear stress: equal mobility conditions are thus achieved (Parker, 1991; Parker and Toro-Escobar, 2002). The relative mobility of grain fractions is classically taken into account in sediment transport formulas through a hiding factor (Parker et al., 1982), which expresses the critical shear stress of a grain fraction i, $\tau_{c,i}$, as a function of the critical shear stress of the mean size fraction D_{50}, $\tau_{c,d_{50}}$, and the representative diameter D_i of grain fraction i:

$$\frac{\tau_{c,i}}{\tau_{c,d_{50}}} = \left(\frac{d_i}{d_{50}}\right)^{b-1} \tag{1.1}$$

For $b = 0$ size dependent entrainment dominates, while for $b = 1$ equal mobility conditions are given. These two conditions represent the two limiting cases of a plethora of flow conditions in which size dependent and size independent sediment entrainment interact (Ferguson et al., 1989). Equal mobility conditions of the whole bed have been found to be present only for high transport rates, characterized by shear stress 3-4 times higher than the critical shear stress (Wilcock and McArdell, 1993, 1997; Kuhnle, 2012) corresponding generally to bankfull discharges (Ryan et al., 2002). For low transport rates only finer grain fractions are under equal mobility conditions while larger particles are rarely set in motion so that only a small part of the surface is active, a condition termed partial transport (Wilcock and McArdell, 1997). As a result, larger grains are immobile for most of the flow conditions (Ashworth and Ferguson, 1989; Vericat et al., 2008). Under these conditions most sediment transport models based on equation 1.1 or two fraction routing models like the Wilcock and Kenworthy (2002) model, tend to overpredict sediment transport by various orders of magnitude (Rickenmann, 2001; Schneider et al., 2015), as they do not take into account the influence of the immobile grains on local flow conditions (Yager et al., 2007).

Large immobile grains influence flow resistance (Rickenmann and Recking, 2011), induce local flow separation (Smith and McLean, 1977), modify turbulent structures reaching the bed (Wren et al., 2011), but their impact on the transport of fine sediments is still not well understood. Kuhnle et al. (2013) and Wren and Kuhnle (2014), studying the sand transport over immobile gravel and cobble, observe that the sand transport rates decrease with decreasing sand bed content, even though the total bed shear stress increases. The experimental study by Grams and Wilcock (2007) on the entrainment of sand into suspension over bed composed of gravel-sized fixed hemispheres, shows that for high sand bed levels close to the top of the immobile grains, the entrainment rates of sand into suspension are enhanced as compared to a full sand bed. However, with decreasing sand bed level, the entrainment rates decrease. In a similar manner, in the field of aeolian sediment transport, Nickling and McKenna Neumann (1995); McKenna Neuman and Nickling (1995) observe that the sand flux induced by wind erosion over a bed of immobile spheres increases as soon as the spheres start to protrude from the bed, eventually reducing to zero for higher protrusion levels. Ghilardi et al. (2014a) analysing the influence of immobile boulders on fine sediment transport observes that boulders promote hysterical cycles of deposition and mobilization dependant on the protrusion levels of the boulders. To

this regard, Ghilardi et al. (2014b) and McKie et al. (2021) highlight that the sediment transport rates depend not only on the protrusion levels of the boulders, but also on their planar density with decreasing sediment transport capacity the closer the boulders are positioned. Overall, these experimental observations suggest that immobile grains exert two competing effects on the mobile sediment, sheltering them or enhancing the sediment transport rates.

The local enhancement of sediment transport has been explained in various studies by the increased spatial variability of the flow field and of the local shear stresses in the presence of immobile grains, both isolated or in a bed matrix (Sambrook Smith and Nicholas, 2005; Strom and Papanicolaou, 2007; Papanicolaou et al., 2011; Fang et al., 2017; Raus et al., 2019). Investigations on isolated immobile obstacles, such as boulders, (Euler and Herget, 2012; Dixen et al., 2013) or on groups of obstacles (McKenna Neuman et al., 2013; Liu et al., 2017; Fang et al., 2017) have observed the formation of horseshoe vortices around immobile grains causing local peaks in shear stress, potentially enhancing sediment transport. At the same time, flow separation in the lee side of the immobile grains leads to the development of a strong mixing layer at the top of the immobile grains which can cause enhanced shear stresses at the level of fine sediment bed if the protrusion level of the immobile grains is small, as shown by Raus et al. (2019) who studied the effect of the protrusion level of a square pattern of spheres on a rough rigid bed.

As for grain sheltering, it was observed that the flow separation in the lee side of immobile grains generates a recirculation region near the bed characterized by lower shear stress conditions (Raus et al., 2019; Dey et al., 2011a; Papanicolaou et al., 2011). The morphological signature of these recirculation regions was identified in sediment shadows in the lee side of immobile grains (Nickling and McKenna Neumann, 1995; Dixen et al., 2013) or by the formation of sediment patches behind boulders (Papanicolaou et al., 2012). (Raus et al., 2019) highlighted a possible connection between sheltering and a decrease in sweep events reaching the bed for low protrusion levels. Furthermore, part of the momentum is extracted in the bed interstices from the flow by the immobile grains in the form of form and viscous drag (Raupach and Shaw, 1982; Nikora et al., 2001), locally reducing the fluid shear stress available to set the mobile sediments in motion.

Even though evidence of shear stress enhancement and grain sheltering are numerous in the literature, their mechanisms and competing effects are clearly not well understood yet. Few studies have, in fact, analysed the evolution over time of the sediment levels over an immobile bed, as measurements in between roughness elements are generally impeded due to optical access limitations. To the knowledge of the author, only two works by Kuhnle et al. (2016) and Stradiotti et al. (2020) have addressed this issue, both experimental works showing that the clear out depth of sand from a gravel bed increases with the shear stress applied at the top of the immobile roughness. The work of Stradiotti et al. (2020) analyses furthermore the evolution over time of the erosion rates showing that they tend asymptotically towards zero.

The influence of an immobile rough bed is not limited to a local scale but extends also to the reach scale in terms of bed-forms. The immobile gravel influences in fact the availability of fine sediments, since the area covered by sediments reduces as the fine sediments are eroded, (Grams and Wilcock, 2007). As such, the fine sediments tend to gather into a variety of low-relief bed forms larger than the grain roughness scale, typical of sediment supply limited conditions, i.e. barchans and ridges (Kleinhans et al., 2002). Barchans are crescent-shaped transverse bed-forms. Ridges are instead sediment ribbons developing parallel to the flow due to the presence of secondary currents (McLean, 1981; Nezu et al., 1988). The presence of these bed-forms influences the local hydrodynamics at a larger scale than the grain one. As observed by Nezu

and Nakagawa (1993), upflow develops over the sand ridges while downflow over coarse gravel stripes. Furthermore, over smooth sand stripes, the shear stress is lower than over coarser sediment stripes leading to differential erosion of the sediment bed (McLelland et al., 1999; Nezu and Nakagawa, 1989). Studies over artificial ridges have observed furthermore that the ridges' height, width and spacing influence the strength of the secondary currents (Nezu and Nakagawa, 1984; Wang et al., 1993; Willingham et al., 2014; Medjnoun et al., 2020). The local erosion rates are as such influenced by the morphodynamics of the ridge. To the knowledge of the author, there are no studies which have analyzed the temporal evolution of ridges over a rough immobile bed, conditions which have been observed to take place quite often in nature in ephemeral rivers (Culbertson, 1967; Karcz, 1973).

Aim and overview of the thesis

This work focuses on the experimental investigation of the hydro- and morphodynamic processes governing fine-sediment transport in immobile coarse-grained beds. From the literature review, it is apparent that the presence of immobile grains protruding from a fine-sediment bed has significant implications on the bed morphodynamics both at the grain and at the bed-form scale. At the grain scale, the immobile grains are capable of reducing or enhancing the fine-sediment transport rates, leading to a bed stabilization or destabilization, respectively. The interaction between these two competing effects and their connection to the near-bed hydrodynamics are still not clear, though. At the bedform scale, the reduction in sediment availability induced by the protruding immobile grains leads to the formation of ridges, whose morphological evolution has not yet been described. This work tries, as such, to answer the following main research questions:

- At the grain-scale: How does the change in protrusion levels of immobile grains over a fine-sediment bed influence the erosion and transport rates of the mobile fine sediments? Which are the near-bed hydrodynamic processes responsible for these alterations?

- At the bedform-scale: How do the ridge morphology and the correlated secondary flow field evolve over time?

To tackle these main research questions, flume experiments are performed to analyse the erosion of an initially uniform fine-sediment bed covering an immobile coarse bed of regularly-arranged spheres, used to model coarse immobile grains. A top-down approach is employed to study first the hydro- and morphodynamics at the bedform-scale and second at the grain-scale. The structure of the thesis, subdivided in two parts, follows this logic.

Part I of the thesis, corresponding to Chapter 2, describes the results of a first-series of experiments aimed at analysing primarily the bed morphodynamics at the bedform scale, focussing on the morphological evolution of ridges. The erosion of coarse-sand-like sediments from a dense configuration of spheres is investigated for different shear stress and water depth conditions. A non-intrusive topographic technique able to reconstruct the average protrusion level of each sphere, is used to track and describe the temporal evolution of the geometrical features of ridges, such as height, side-slope, width and lateral position. A way to predict the number of possible ridges developing in the presence of protruding immobile grains given the imposed flow conditions is presented. Planar PIV measurements of the bulk flow above the top of the spheres are also performed over the ridges and the troughs in order to analyse how changes in the geometrical features of the

ridges affect the secondary currents. Part I of the thesis focuses, secondarily, on the analysis of the evolution of the protrusion levels of the spheres at the grain-scale both over the ridges and the troughs. The aim is to identify possible critical protrusion levels for which the erosion rates of the fine-sediments are suppressed or enhanced and define accordingly erosive regimes as a function of the protrusion level of the spheres.

Part II of the thesis, comprising Chapters 3, 4, 5 and 6, focuses on a second series of experiments for the analysis of the bed-hydrodynamics at the grain-scale, aimed at explaining the changes in fine-sediment erosion with the sphere's protrusion observed in Part I . The experiments do not only investigate changes in the hydrodynamic forcing of the system as in Part I, but also changes in the configuration of the spheres and in the fine-sediment grain size.

For this second series of experiments a new experimental setup is developed capable of simultaneously resolving the flow field in between the protruding spheres, reconstructing the bed topography at fine-sediment grain scale and measuring sediment transport. Chapter 3 describes this experimental setup, composed of a stereo PIV system and a stereo-phogrammetric system, along with the flow conditions to be analysed. A validation of the stero-PIV system is presented in Appendix H.

In Chapter 4 the hydro- and morphodynamics of a uniform fine-sediment bed in the absence of protruding spheres are analysed. The aim is to define reference conditions for the bed shear stress, erosion rates and sediment transport in the presence of a sole fine-sediment bed for the further comparison of the same quantities in the presence of protruding spheres.

Chapter 5 aims at analysing how the protrusion level of the spheres alters the hydrodynamic conditions near the fine-sediment bed, in order to explain the erosive regimes identified in Part I from a hydrodynamic point of view. The analysis focuses on the erosion of fine sediments, similar to coarse sand, within one pattern of spheres for just one reference flow condition. The analysis of the flow patterns within the bed interstices is presented as the protrusion level of the spheres increases. The focus is set on how the shear stress conditions acting directly at the level of the fine-sediments are altered by the presence of the protruding spheres. Particular emphasis is given to the analysis of the coherent structures reaching the fine-sediment bed as the protrusion level of the spheres changes.

Chapter 6 presents a parametric study of the influence of various flow parameters and geometric characteristics of the bed on the fine-sediment erosion. The aim is to generalize the hydro-and morphodynamic results obtained in Part I and Chapter 5, assessing whether the same erosive regimes and hydrodynamic processes can be identified for different flow conditions and sphere configurations. The analysis focuses first on changes in the flow conditions, such as the bed shear stress or the relative submergence, by maintaining the same geometric configuration of spheres and fine-sediments. Second, the effects of the change in the density of the spheres and in the fine-sediment size are presented by holding the flow conditions constant.

Part I

Ridge morphodynamics and fine-sediment erosion in coarse-grained immobile beds: a grain-scale resolved analysis

2 Morphodynamic processes at the bedform scale with a focus on local fine-sediment erosion induced by protruding spheres

2.1 Introduction

The aim of this first experimental campaign is to analyse the behavior of a sand-gravel bed system under sediment-supply limited conditions in terms of the bed morphodynamics at the reach-scale and of the local erosive behaviour of the bed at the roughness scale. A series of experiments are conducted in a tilting flume with a layer of plastic spheres glued at the bottom to simulate an immobile gravel bed and small plastic particles to simulate the sand. There is no sediment supply and the bed freely evolves under the action of the water flow, allowing the spheres to protrude after a few hours of experiments. The sediment bed evolution is captured by means of a non-intrusive topographic measurement technique in order to analyse both the large-scale morphodynamics, characterized by the presence of ridges and the erosive behaviour of the bed at a local scale. The results give further insights on the characteristic spacing of ridges and on the evolution of their geometrical features over time. The local analysis of bed levels allows to determine the bed levels at which the erosion rates are enhanced and when sheltering takes over. Complementary to the topographic measurements, the local flow field at different instants of the experiments is also investigated using planar particle image velocimetry (PIV) measurements, in order to describe the temporal evolution and the spatial distribution of the bed shear stress, in connection with the bedforms.

2.2 Experimental setup and methodology

2.2.1 Experimental facility

The experiments were conducted at the Institute of Hydromechanics (KIT) in a water recirculating, tilting flume 9.2 m long, 30 cm wide and 32 cm high with a weir positioned at the outlet to adjust water levels (Figure 2.1). A horizontal convex grid installed in the entrance tank and followed by a contraction ensured low turbulence and quasi-uniform flow conditions at the inlet. The water discharge Q was measured with a calibrated venturi meter and water levels were measured through a point gauge with a precision of 0.1 mm. The point gauge was attached to a movable carriage to sample the water levels at different positions along the flume to ensure uniform flow conditions. The flume was run under sediment-supply-limited conditions, i.e. with no sediment feed from upstream. The sediments were collected in an underlying settling tank.

The coordinate system was chosen as follows: x = streamwise direction with origin at the beginning of the sediment bed, i.e., 80 cm downstream of the inlet at the end of a 1.7° inclined ramp, y = spanwise direction

with origin in the middle of the flume, z = vertical direction with origin at the top of the spheres constituting the immobile rough bed (Figure 2.1).
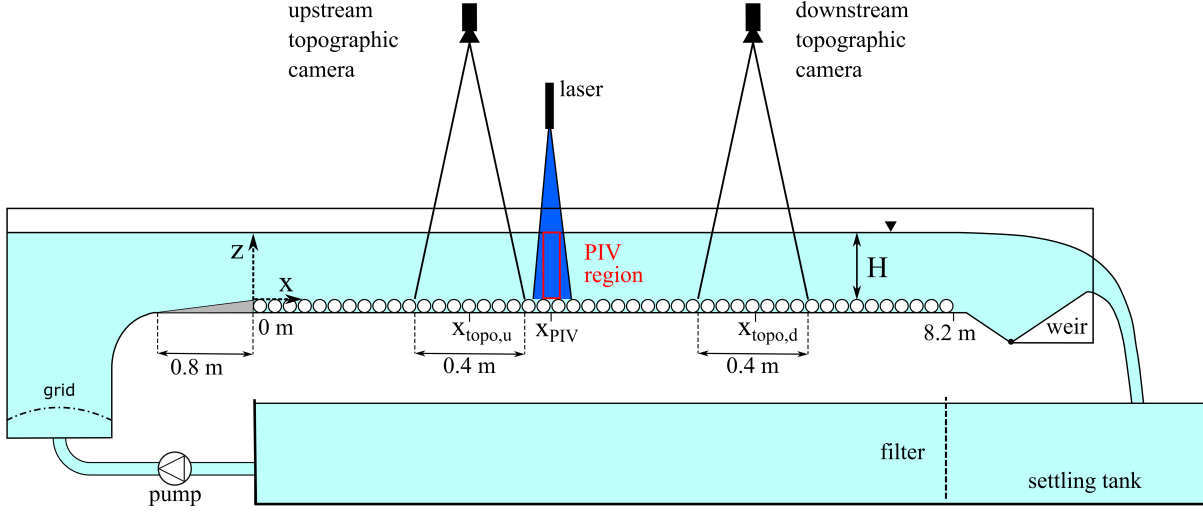
Figure 2.1: Experimental setup. See Table 2.3 for values of the position of the measurement systems.

2.2.2 Bed and sediment properties

The bed of the experiments was designed to analyse the effect of large immobile roughness elements on the erosion of fine sediments. Field studies on various gravel-bedded streams have reported that the ratio between the immobile grain fraction, represented by the d_{90} of the bed, to the d_{50} of the transported bedload is of the order of 4-100 (Ferguson et al., 1989; Lisle, 1995; Lenzi, 2004). Accordingly, the sediments were selected to obtain a size ratio between immobile roughness elements and fine mobile sediments equal to 11.6. The immobile roughness elements were made of white polyurethane spheres with a diameter $D = 2R = 2$ cm. In order to realize a regular, well-defined and reproducible immobile rough bed, the spheres were glued in a staggered symmetric pattern (Figure 2.2a) over the whole length of the flume (Figure 2.1). The reference pattern in Figure 2.2a, with a length $l_x = 4.54$ cm and a width $l_y = 2.62$ cm, was characterized by a total bed porosity in the absence of fine sediments $\phi = 0.65$, similar to the one characterizing the upper layer of static armoured gravel beds (Aberle et al., 2008). A diagonal sphere-spacing to diameter ratio of $s/D = 1.31$, higher than 1 (characteristic of the highest sphere packing) was chosen to avoid any influence of fine sediment bed-clogging on the erosion process. The size ratio between spheres and fine sediments of 11.6, used in this study, was slightly higher than the threshold of 10.6 for fine sediment clogging of a closely-packed bed (Gibson et al., 2009). This pattern of spheres was chosen, furthermore, to guarantee that the bed could reach skimming flow conditions, i.e. high interaction between the wakes shed by the spheres, for low fine sediment levels, as it is the case for natural densely-packed gravel beds (Montgomery and Buffington, 1993). The planar density of the pattern $\lambda_p = A_p/A_r = 0.53$ (where A_p is the planar area of the spheres in the reference pattern and $A_r = l_x l_y$ the total area of the pattern) defines skimming flow conditions (Grimmond and Oke, 1999).

The fine sediments were made of plastic granulate consisting of urea, melamine and phenol with a specific weight $\rho_s = 1.49$ g/cm^3 and a porosity $\phi_s = 0.45$. The grain size distribution was determined by measuring
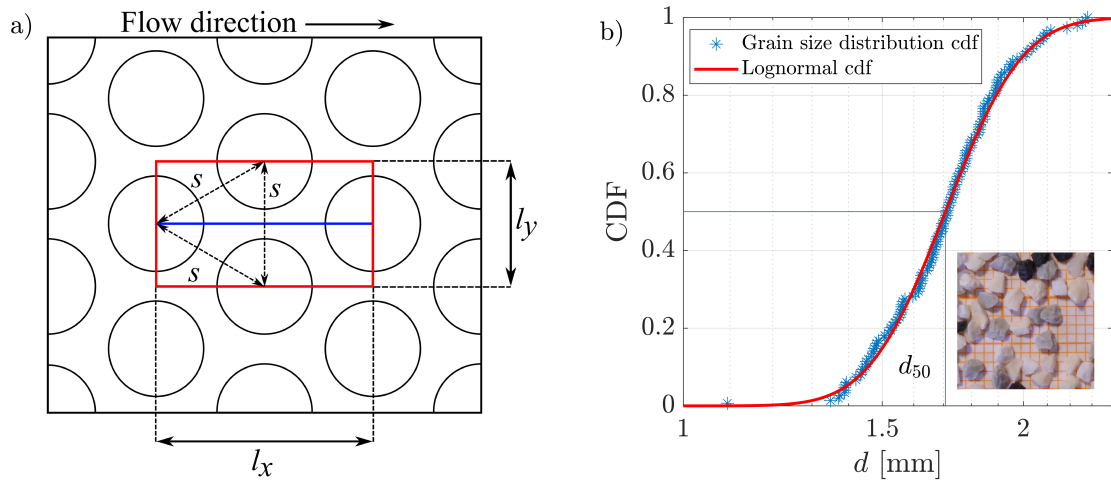
Figure 2.2: (a) Staggered pattern of spheres with reference pattern highlighted in red with its characteristic dimensions in longitudinal $l_x = 4.54$ cm and vertical direction $l_y = 2.62$ cm equal to the spacing s between the spheres. The blue line identifies the position of the laser sheet in the pattern; (b) Grain size distribution and fitted lognormal cumulative density function of the plastic granulate; in the lower right corner a sample of the plastic grains scattered over graph paper with 1 mm mesh size.

the intermediate principle b-axis of the grains, as done in the analysis of river sediments (Church et al., 1987). The b-axis was measured by image sampling a large amount of grains scattered over a black background, after verifying that no overlap between grains was present. The b-axis was determined on the basis of the minor axis of the ellipse, which best fits each grain, as it represents the best estimate of the b-axis (Graham et al., 2005). It was then ascertained that the grain size distribution of the plastic granulate followed a lognormal probability density function (Figure 2.2b), as for natural fine sediments (Dey and Das, 2012), by applying the test of Pearson with a level of significance $\alpha = 0.5$ (Bendat and Piersol, 1986). The grain size distribution was characterized by a median diameter $d_{50} = 1.72$ mm and by a geometric standard deviation $\sigma_g = (d_{84.1}/d_{15.9})^{0.5} = 1.13$. Since $\sigma_g < 1.4$, the plastic granulate was classified as well-graded and uniform (Dey, 2014). In this manner, the bimodal behaviour of the bed arised only from the interaction between the spheres and the fine sediments, given their large size ratio.

The bed configuration at the start of the experiments was defined so as to reproduce river bed conditions encountered after extreme flood events with fine sediment patches deposited on the immobile gravel bed (Yager et al., 2012). Before each experiment, the spheres were completely covered, over the whole length of the flume, by a layer of plastic granulate 3 cm thick, i.e. 1 cm over the top of the spheres (see below). The bed was then mechanically screeded to a uniform, flat surface to ensure reproducible initial experimental conditions and to reduce roughness anisotropies. Since the erosion process can be potentially influenced by the screeding of the bed, as it creates a randomly organized bed less complex than a natural water worked one (Cooper and Tait, 2009), the fine sediment level was not flush with the top of the spheres, but was set 1 cm higher, in order to allow a complete reworking of the first layer of the fine sediments by the flow.

Prior to the start of the experiments, the bed was filled with water to push air out of the system. The flow rate was then carefully increased to the final working conditions in order to avoid an abrupt flushing of the fine sediments. Furthermore, in order to avoid increased erosion at the beginning of the sediment bed due to

a jump of the incoming flow from the flume bed level to the sediment bed level, the aforementioned 80 cm long ramp, inclined by 1.7°, was installed at the channel entrance with the downstream end flush with the top of the spheres (Figure 2.1). The surface of the ramp was glued with a layer of the fine sediments in order to trigger an early development of the rough boundary layer.

2.2.3 Flow conditions

The flow conditions of the experiments were designed with two main objectives, first, to induce erosion of the fine sediments under bedload conditions without entrainment of the grains into suspension and second, to analyse the dependency of longitudinal bedforms on the flow depth. With this in mind, a total of seven experiments were performed under uniform flow conditions by varying two parameters: the total shear stress, expressed in terms of the Shields parameter $\theta = u_{*R^c}^2/(g\Delta d_{50})$ and the water depth, expressed in terms of the flow aspect ratio $A = W/H$, see Table 2.1. Here, Δ is the relative density of the fine sediments, W is the width of the channel and H is a reference water depth with respect to the spheres' top (z = 0 cm plane - see Figure 2.1). In order to avoid lengthy adjustments with the mobile bed while stetting the desired flow conditions for each experiment, the shear (friction) velocity u_{*H} and channel slope i were first estimated for a uniform fine-sediment bed at the level of the top of the spheres ($z = 0$) with water depth H and flow rate Q by using the standard logarithmic friction law with an equivalent sand-roughness equal to the d_{50} of the granulate. Then, pre-experiments for each configuration with a mobile fine-sediment bed were performed to fine-tune the flow rate Q and water depth H via the weir position. The final shear velocity u_{*R^c} in Table 2.1 is obtained from the integral momentum balance for a uniform flow with $u_{*R^c} = \sqrt{gR_H^c i}$, where R_H^c is the hydraulic radius based on H with side-wall correction by Chiew and Parker (1994). u_{*R^c} therefore represents the mean bed shear stress of the uniform fine sediment at the level of the spheres' top. It further represents the shear stress acting at the top of the spheres when they protrude from the fine sediments during the experiments. It should be noted that the water level, measured with the point gauge at regular time intervals along the whole length of the flume, remained constant during each experiment.

The erosive conditions of the bed were defined by imposing values of the Shields parameter θ about 3-4 times the critical Shields parameter of the fine sediments, $\theta_{cr} = 0.033$ (defined on the basis of the Shields diagram (Shields, 1936) by the means of the explicit relationship by Wu and Wang (1999), which relates θ_{cr} to the particle parameter $D_* = d_{50}\Delta g/\nu^2$). These values corresponded to flow conditions encountered in natural gravel-bed rivers, for which selective sediment transport takes place with the coarsest sediment fractions remaining mostly immobile (Powell et al., 2001). The shear stress conditions for all experiments were such that sediment transport took place in the form of bed-load.

Table 2.2 illustrates the parametric concept of the experiments where three Shields parameters and three aspect ratios of low, medium and high magnitudes were investigated. Considering Exp. 1a as the reference with a medium aspect ratio and low Shields parameter, the flow conditions of the other experiments were defined by either holding the aspect ratio A of the reference experiment constant and modifying the Shields parameter θ or vice-versa. In Table 2.1 the experiments were given acronyms with θ and A referring to the Shields parameter and the aspect ratio, respectively, while the relative magnitude is noted by l (low), m (medium) or h (high). As seen in Table 2.2, Exp. 1a/b (θlAm), Exp. 2 (θmAm) and Exp. 3 (θhAm) were performed with the same medium aspect ratio and with increasing Shields parameter to analyse how the erosion depth was affected by increasing bed shear stress. Exp. 1a/b (θlAm), Exp. 4 (θlAl) and Exp.

5a/b (θlAh) were performed, instead, with the same low Shields parameter and with varying aspect ratio to study the influence of secondary currents on the bed morphodynamics. Exp. 1b and Exp. 5b were performed under the same conditions as Exp. 1a and Exp. 5a, respectively, to assess, whether the experiments were reproducible and to perform measurements of the velocity field (see Section 2.2.4.2). The experiments lasted between two days and four days depending on the velocity at which the bed reached a constant erosion depth.

Exp.		θ	A	Q	i	H	R_H^c	u_{*R^c}	u_{*H}	U	Re^*	Re	Fr	T_e
		[-]	[-]	[l/s]	[%]	[cm]	[cm]	[cm/s]	[cm/s]	[cm/s]	[-]	[-]	[-]	[h]
1a	θlAm	0.11	4.6	5.0	0.16	6.50	5.8	3.0	3.2	26	51	16600	0.32	71
1b	θlAm	0.11	4.7	5.0	0.16	6.43	5.8	3.0	3.2	26	51	16600	0.33	92
2	θmAm	0.15	4.4	6.1	0.20	6.85	6.1	3.5	3.7	30	59	20300	0.36	44
3	θhAm	0.18	4.4	7.4	0.25	6.84	6.1	3.8	4.0	36	66	24600	0.44	70
4	θlAh	0.12	6.5	3.0	0.23	4.59	4.3	3.1	3.2	22	53	10000	0.32	67
5a	θlAl	0.12	2.9	9.4	0.12	10.26	8.6	3.2	3.5	31	54	31300	0.30	66
5b	θlAl	0.12	2.9	9.4	0.12	10.35	8.6	3.2	3.5	30	54	31300	0.30	43
		±0.01	±0.1	±0.5	±0.01	±0.05	±0.1	±0.1	±0.1	±2				

Table 2.1: Flow parameters of the seven experiments: Shields parameter $\theta = u_{*R^c}^2/(g\Delta d_{50})$, aspect ratio A = W/H, flow rate Q, slope i, water depth H, hydraulic radius with side-wall correction R_h^c, shear velocity $u_{*R^c} = \sqrt{gR_h^c i}$ based on the hydraulic radius R_h^c, , shear velocity $u_{*H} = \sqrt{gHi}$ based on the water depth H, bulk velocity $U = Q/(WH)$, particle Reynolds number $Re^* = u_{*R^c}d_{50}/\nu$, bulk Reynolds number $Re = HU/\nu$, Froude number $Fr = U/\sqrt{gH}$, time duration of the experiment T_e.

			A	
		l	m	h
	l	5a/b	1a/b	4
θ	m		2	
	h		3	

Table 2.2: Parametric concept for the definition of the experimental conditions based on the Shields parameter θ and the aspect ratio A: the experiments listed on the rows share the same Shields parameter, while the experiments listed on the columns share the same aspect ratio.

2.2.4 Measurement configurations

The temporal evolution of the bed topography and of the flow field above the spheres were measured via a topographic system as in Nickling and McKenna Neumann (1995) and Raus (2019) and a 2D planar PIV system, respectively. While the topographic measurements were performed continuously over the entire duration of all experiments, the PIV measurements were performed, for efficiency, only during Exp. 1b and 5b and only at three selected times during the experiments.

The measurement systems were located at a distance downstream of the inlet sufficient for the full development of the boundary layer. The boundary layer development length L_{BL} was estimated on the basis of the semi-empirical relationship proposed by Monin and Yaglom (1975) and valid for boundary layer growth both

in smooth and rough conditions (Nikora et al., 1998): $L_{BL} = HU/(0.33u_{*R^c})$. In Table 2.3 the boundary layer development lengths and the position of the topographic and PIV systems are listed. During Exp. 1b and Exp. 5b the topographic system was installed 2.7 m and at 5.8 m downstream of the inlet, while the PIV system was positioned at 3.7 m (Figure 2.1). When the PIV system was not present, the topographic system upstream was positioned at 3.35 m. Overall, the results obtained from the topographic measurements and the PIV measurements confirmed the full development of the boundary layer at all measurement locations, since the topographic patterns were similar at the upstream and downstream measurement location and the velocity measurements did not present signs of a developing boundary layer.

Exp.		1a	1b	2	3	4	5a	5b
L_{BL}	[m]	1.70	1.70	1.80	1.90	1.00	2.90	2.90
$x_{topo,u}$	[m]	3.35	2.70	3.35	3.35	3.35	3.35	2.70
$x_{topo,d}$	[m]	5.80	5.80	5.80	5.80	5.80	5.80	5.80
x_{PIV}	[m]		3.70					3.70

Table 2.3: Development length L_{BL} of the boundary layer based on the Monin and Yaglom (1975) formula and location of the upstream and downstream topographic system and of the PIV system. The indices u and d refer to upstream and downstream positions, respectively.

2.2.4.1 Topographic measurements

The mean protrusion k around each sphere (see Figure 2.3a) was determined by measuring the exposed planar area of the protruding spheres. The bed was periodically imaged from above with two Prosilica GE 1650 cameras with a resolution of 1600x1200 pixels, equipped with Sigma 24mm f1.8 EX DG macro lenses. The cameras were installed at a height of 2.10 m above the bed perpendicularly to the bottom of the flume (Figure 2.1). At each measurement location a 40 cm long area of the bed was analysed. The images with a resolution of 17.14 px/cm were recorded every 40 s. Since the Froude number was well below 1 for all experiments, surface perturbations were negligible and recordings through the water surface were possible. Figure 2.3b shows a raw bed-image with the protruding spheres appearing as uniform grayish regions over the
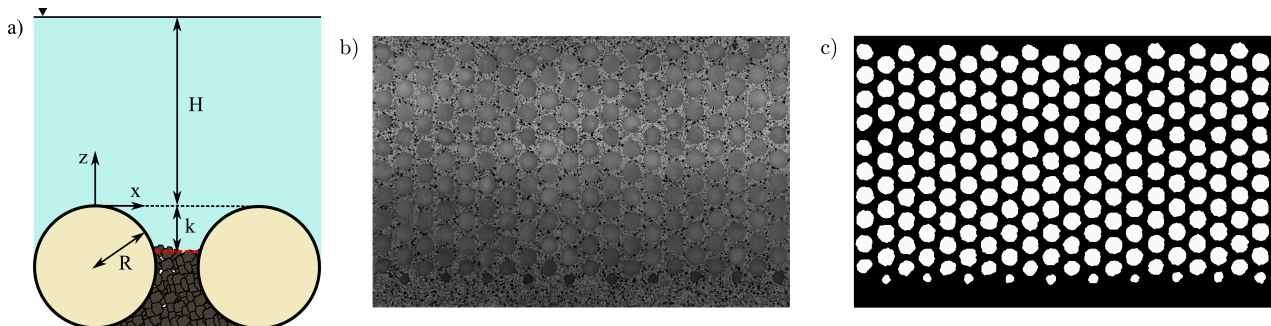

Figure 2.3: (a) Protrusion height k defining the normalized protrusion $P = k/R$; (b) example of a raw bed-image; (c) example of a processed binarized bed-image for the identification of the protruding spheres (highlighted in white).

non-uniform black and white background of fine-sediments. In order to identify the spheres, the raw images were first sharpened to highlight the edge of the spheres with an unsharp masking technique which subtracts a blurred, unsharp version of the raw image from itself. At each pixel location, the standard deviation of the intensity levels within a square area of 5x5 pixels was then computed. The spheres were identified by extracting the regions with the smallest standard deviation compared to their surroundings. A morphological closing filter (Jähne, 2012) was then applied to close holes erroneously detected as sediments within the area of the spheres. Figure 2.3c shows the processed binarized image with the protruding spheres highlighted. On the basis of the planar area of a protruding sphere A_p extracted from Figure 2.3c, two main parameters were defined for each sphere: the planar density λ_p and the mean level of protrusion P. λ_p was estimated for each sphere, as the ratio between A_p and half of the reference-pattern's area $A_r/2 = l_x l_y/2$. P was defined on the basis of the equivalent radius $r_{eq} = \sqrt{A_p/(4\pi)}$ as follows:

$$P = \frac{k}{R} = 1 - \frac{\sqrt{R^2 - r_{eq}^2}}{R} \tag{2.1}$$

where k is the exposed height of the sphere over the sediment bed. $P = 0$ and $\lambda_p = 0$ when the spheres are covered and they reach a maximum value of 1 and of 0.53, respectively, when the spheres are fully visible down to the equator, corresponding to the limit of the measurements. The error ϵ_P in determining the protrusion P increases with P, since the surface slope of a sphere tends to infinity at the equator. In order to estimate ϵ_P, the protrusion P measured with a point gauge in the stoss and lee side of a sample of 5 spheres at different bed levels was compared with the image based protrusion for the same sample. The resulting mean relative protrusion error is shown in Figure 2.4. A curve fit of the errors based on the theoretical relationship between ϵ_P and the error of the equivalent radius $\epsilon_{r_{eq}}$ ($\epsilon_P = \epsilon_{r_{eq}} r_{eq}/(\sqrt{R^2 - r_{eq}^2})$ with $\epsilon_{r_{eq}} = 0.02$ cm obtained from the best fit) is also shown (red line). It can be seen that for $P = 0.05$ and $P = 0.8$, the relative error reaches about 10%. The values were taken as cutoff for the applicability of equation

Figure 2.4: Mean relative protrusion error ϵ_P/P

2.1. The corresponding cutoff limits for the planar density were equal to $\lambda_p = 0.05$ and $\lambda_p = 0.51$. Since the main bedforms developing on the bed were ridges, which induce the highest spatial dispersion in the transverse direction, the topographic data were line averaged in the longitudinal direction along the total field of view, i.e. 40 cm, so that for each timestep a transverse protrusion and planar density profile, $P(t,y)$ and $\lambda_p(t,y)$, respectively, were obtained.

2.2.4.2 PIV setup

The PIV measurements were performed in streamwise vertical planes during Exp. 1b and Exp. 5b, yielding the vertical and streamwise velocity components. To account for the variability of the flow in the spanwise direction, the measurements were performed both in the middle plane (m) at $y/W = 0$ and in the quarter plane (q) at $y/W = -0.22$, as shown in Figure 2.5. During the PIV measurements, the bed and the flow were considered stationary
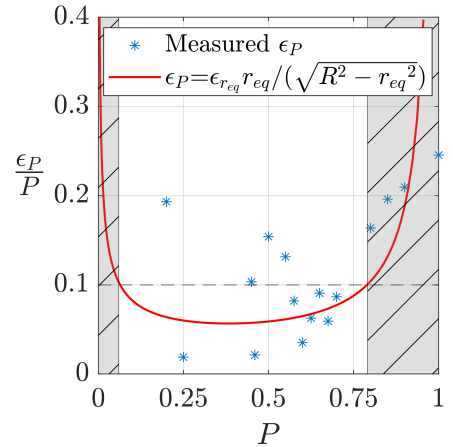
A 2000 mW blue diode continuous laser was used to generate the laser sheet. The laser beam was expanded through a cylindrical diverging lens to a sheet with a thickness of 3 mm in the spanwise direction and a width of 10 cm in streamwise direction. Since the PIV system was based on a continuous laser, a high frequency camera was used to attain small enough time intervals between PIV images. A UI-3060CP-M-GL Rev.2 iDS 8-bit high frequency camera, with a resolution of 1936x1216 and equipped with an AF DC-Nikkor 105mm f/2 D lens, was installed perpendicularly to the laser sheet at a distance of 3 m from the flume glass wall. The field of view spanned over one pattern of spheres from crest to crest, i.e. one l_x wide, and covered the entire water depth from the top of the spheres to the water surface. Due to presence of the spheres it was not possible to resolve the flow in between the spheres. The flow was seeded with 10 μm micro-glass spheres with a specific weight of 1.1 g/cm^3.

A total of three PIV runs were performed at three different times during the evolution of Exp. 1b and Exp. 5b in order to capture the flow at different erosive stages of the bed. For each of these runs at t = [21.2, 45.3, 69.3]h for Exp. 1b and t = [4.8, 18.6, 42.9]h for Exp. 5b, both the flow fields in the middle and quarter plane were acquired. During each PIV measurement over one plane, 1000 bursts were recorded at a burst frequency of $1.1Hz$, a frequency low enough to obtain statistically independent samples as the measured auto-correlation function dropped to zero at the corresponding time lag. Two images per burst were recorded at a frequency of $274Hz$. The bursts were processed with the Davis-PIV software version 8.4.0 based on a multipass iterative PIV algorithm with universal outlier detection by Westerweel and Scarano (2005). The final correlation box size for all PIV measurements was equal to 12x12 pixels with a 50% overlap, resulting in a grid resolution of 1.1x1.1 mm^2.

Figure 2.5: Cross-sectional plane with the PIV setup

Since the flow in the roughness sublayer is spatially heterogeneous, double averaging (Nikora et al., 2001) was performed in the longitudinal direction to determine the 1D profiles of the mean and turbulent flow statistics. Owing to the symmetry of the pattern, even though the measurements were performed only over its centre (see Figure 2.2a), this double averaging was equivalent to averaging three planes in the transverse direction.

2.3 Results

2.3.1 Visual observations of bed morphodynamics at early times

At the start of the experiments, transverse bedforms, in the form of dunes or barchanoids, developed simultaneously along the entire length of the channel. The development of dunes is expected for high sediment availability, which was given here by the initial sediment layer 1 cm thick over the spheres (Kleinhans et al., 2002; Tuijnder and Ribberink, 2009; Grams and Wilcock, 2007). In Exp. 1a/b (θlAm) and Exp. 4 (θlAl) with a low Shields number, clearly defined channel-spanning two-dimensional dunes were observed, gliding over a layer of non-moving fine sediments with no spheres appearing in the bed depressions in between the dunes' crests. The height of the dunes was equal or lower than the initial sediment layer thickness above the top of the spheres. Thus, it can be surmised that enough sediments were present on the bed to guarantee a

full development of the dunes. However, in Exp. 2 ($\theta m Am$), Exp. 3 ($\theta h Am$) and Exp. 5a/b ($\theta l Ah$) with medium or high shear or with low shear and high aspect ratio, the bed was characterized by a sequence of barchanoids (transitional bedforms between dunes and barchans with an almost crescent shape (Kleinhans et al., 2002)), spanning over half of the channel in checkerboard or pair-like patterns and characterized by the presence of regions of protruding spheres in their tail, as seen in Figure 2.6. Thus, the entire initial sediment layer above the top of the spheres was mobilized in the barchanoids, possibly limiting the sediment availability for the full development of the bedforms. As shown by Tuijnder and Ribberink (2009), sediment-supply limited conditions for the development of dunes (or barchanoids) over immobile gravel beds persist when the height of the dunes is larger than the average thickness of the sediments above the coarse immobile layer, as in the case just discussed. As in the present experiment, they also observed the presence of exposed regions of immobile gravel in between developing sand dunes with limited sediment supply.

The depletion of the first layer of sediments above the top of the spheres and no sediment feed from upstream led to the disappearance of the last traveling dunes after about 2 h in Exp. 2a/b ($\theta m Am$) and 1 h in Exp. 3 ($\theta h Am$) with medium and high shear stress, respectively, and after about 3.5 h to 6 h in Exp. 1a/b ($\theta l Am$), Exp. 4 ($\theta l Al$) and Exp. 5a/b ($\theta l Ah$) with low shear stress.
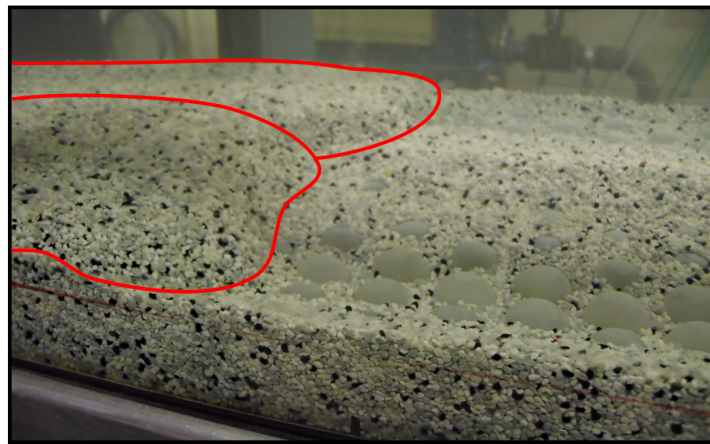
Figure 2.6: Barchanoid dunes (on the left side of the picture and contoured in red) at the beginning of Exp. 5b with protruding spheres in the tail of the barchanoid downstream which is not present in the picture. The flow is from left to right.

2.3.2 Long-term evolution of the bed

With the disappearance of the dunes and barchans, the spheres start to protrude permanently from the sediment bed. The evolution of the bed can now be quantified by determining how the longitudinally averaged protrusion level P(y,t). P(y,t) is plotted in Hovmöller (1949) diagrams, shown in Figures 2.7a-l. The diagrams are presented for both the upstream and downstream measurement locations, when available.

In all experiments shown in Figures 2.7a-l, after an initial period with low protrusion levels $P \leq 0.05$ when measurements are not possible, i.e. in the presence of the dunes, the bed development is characterized in all experiments by increasing protrusion levels, implying that the sediments are being washed out. The bed is not eroded homogeneously though. The bed topography is characterized by high transverse heterogeneity due to the development of longitudinal low protrusion stripes, i.e. fine sediment ridges, as seen for example in

Figures 2.7j and 2.7k for Exp. 5b. Figure 2.8a shows a physical image of such a ridge for Exp. 5b. In Figures 2.7a-l, the bed displays for all experiments regions of higher sediment levels, i.e. low P, identifying ridges in the centre of the channel as well as side-wall accumulations, alternated with regions of higher sediment erosion, i.e. troughs, thereby creating a lateral pattern of smooth and coarse roughness stripes, respectively. Similar variations in lateral bed roughness were also observed by Nezu et al. (1988) and McLean (1981) while studying the formation of sand ridges over a uniform fine gravel bed, and by McLelland et al. (1999), as the result of lateral sorting of bimodal sediment mixtures, with the difference that in the latter case the coarse sediment sizes were also mobilized.

It should be noted, that the ridges do not develop abruptly. Indeed, they were already visually observed to form before the dunes disappeared. In Figure 2.6, the two bed depressions in the tail of the barchanoids are, in fact, separated by a longitudinal sediment stripe, which continues to develop into a reach-spanning ridge after the dunes have disappeared. The superimposition between longitudinal and transverse bedforms was particularly evident with decreasing sediment availability, as the ridges became more pronounced.

Figures 2.7a-l also show that the ridges develop at different lateral positions, producing symmetric or asymmetric bed topographies. The beds of Exp. 1a/b, Exp. 2 and Exp. 3 (Figures 2.7a-g) are characterized by one asymmetric ridge developing on the left hand side of the channel (y > 0). An asymmetry is also given by the presence of left and right side-wall deposits of different transverse extension, particularly evident in Exp. 1a/b (Figures 2.7a-c). A single ridge develops also during Exp. 5a and 5b, but exactly in the middle of the channel leading to a symmetric bed topography. Both of these observations are reproducible, as can be seen by comparing Exp. 1a with Exp. 1b and Exp. 5a with Exp. 5b, which were run for the same flow conditions, respectively. Comparing the left (upstream) and the right (downstream) plots of Figure 2.7a-l, for Exp. 1a, Exp. 2, Exp. 3 and Exp. 5a, the ridge evolution and positions do not change between the upstream and downstream measurement locations, and can, therefore, be considered stable over the entire length of the flume. In Exp. 4, the development of two ridges is observed both at the upstream and downstream measurement location (Figures 2.7i-j), but at different times and different transverse locations. The reason for this discrepancy will be further investigated in Section 2.3.3.

From the results presented in Figures 2.7a-l it is apparent, that the ridges persist for a longer time than the dunes. This is true for all experiments, including Exp. 2 and Exp. 3 where the entire bed erodes beyond P = 0.8 within 10 h, much faster than all the others. Nevertheless, the ridges in all experiments decay more slowly in amplitude than the troughs. In all experiments, the troughs reach P levels of about 0.6 in 1-2 hours after the dunes. While they continue to erode in Exp. 2 and Exp. 3, the trough levels stay roughly constant in all other experiments. In some experiments, i.e. Exp. 1b, Exp. 4 (up, down) and Exp. 5a (up), the ridges can be seen to flatten down eventually, establishing a uniform bed with no significant transverse variations in bed levels. In Exp. 2 and Exp. 3, the same uniform bed was observed for $P > 0.8$. In the other experiments, the measurements were too short to observe this. Nevertheless, comparison of repeated Exp. 1a, Exp. 1b upstream and Exp. 5a/b upstream strongly suggest that the experiments are reproducible and that uniform bed conditions are also reached even when the measurement times are too short.

To summarize, at the end of the experiments two different behaviours of the bed are observed. In Exp. 1a/b ($\theta l Am$), Exp. 4 ($\theta l Ah$) and Exp. 5a/b ($\theta l Al$), the bed reaches a stable condition with an almost constant protrusion level, as can be seen in Figures 2.7a-c, 2.7h-i and 2.7j-l and in Figure 2.8b. This is in agreement with the observation that sediment transport rates are characterized at the end by rare and sporadic movements of individual grains. Clearly, threshold conditions of motion have been reached due to grain sheltering induced
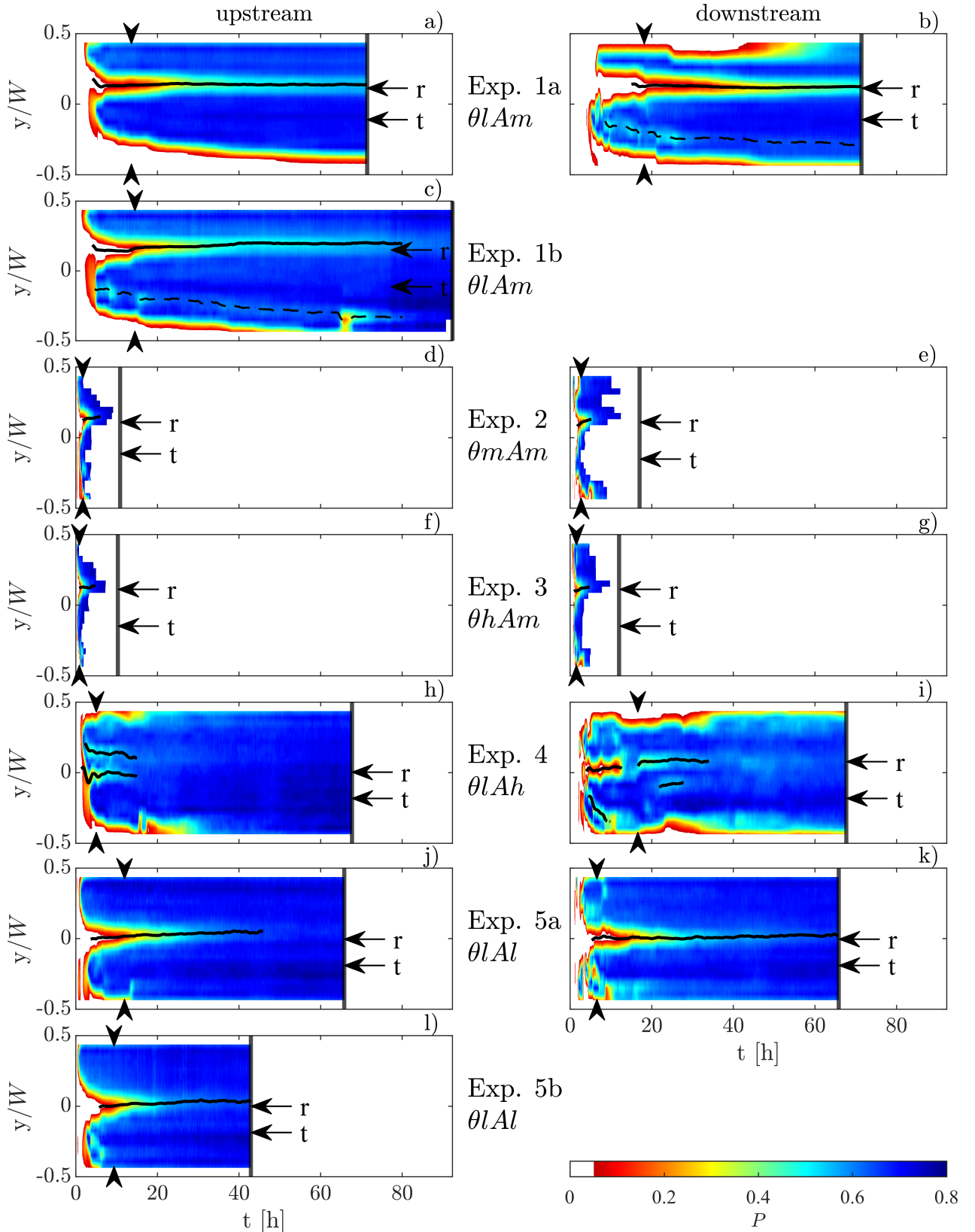
Figure 2.7: Hovmöller diagrams of the line averaged protrusion P as a function of t and y/W; the continuous black lines identify the position of the peak of the ridges; the arrows identify the ridge and trough over which the local analysis in Section 2.3.4 is performed; the vertical arrows identify the time for which the position and the width of the ridges have reached stationarity; the dashed lines in Figures b and c identify secondary ridges; the vertical black lines identify the end of the experiments.

by the spheres. In Exp. 2 ($\theta m Am$) and Exp. 3 ($\theta h Am$) with medium and high global shear stress conditions, the bed is observed to erode completely down to the glass plates. A final stable protrusion level is not reached, likely due to the fact that the grains can slide easily on glass, when $P = 2$ is approached. Nevertheless, it can be expected that a stable and uniform fine sediment bed would be reached if the bed consisted of more levels of spheres filled with sediments.

In conclusion, the bed evolves from three-dimensional dunes/barchanoids to two-dimensional ridges and finally to a uniform coarse bed with no bedforms and negligible sediment motion. Previous studies on fine sediment erosion from a rough bed under sediment supply limitation (Grams and Wilcock, 2014) and (McLean, 1981) have also reported a transition from three-dimensional to two-dimensional longitudinal bedforms as the availability of sediments reduces. In a gravel-sand transition of a river with sediment supply the inverse bedform sequence has been observed by Venditti et al. (2019). The present results support the conceptual model by Kleinhans et al. (2002) for which the type of bedform depends on the thickness of the mobile sediment layer with ridges present in sediment starved environment and dunes present in sediment rich environments (see Figure 2.8c).
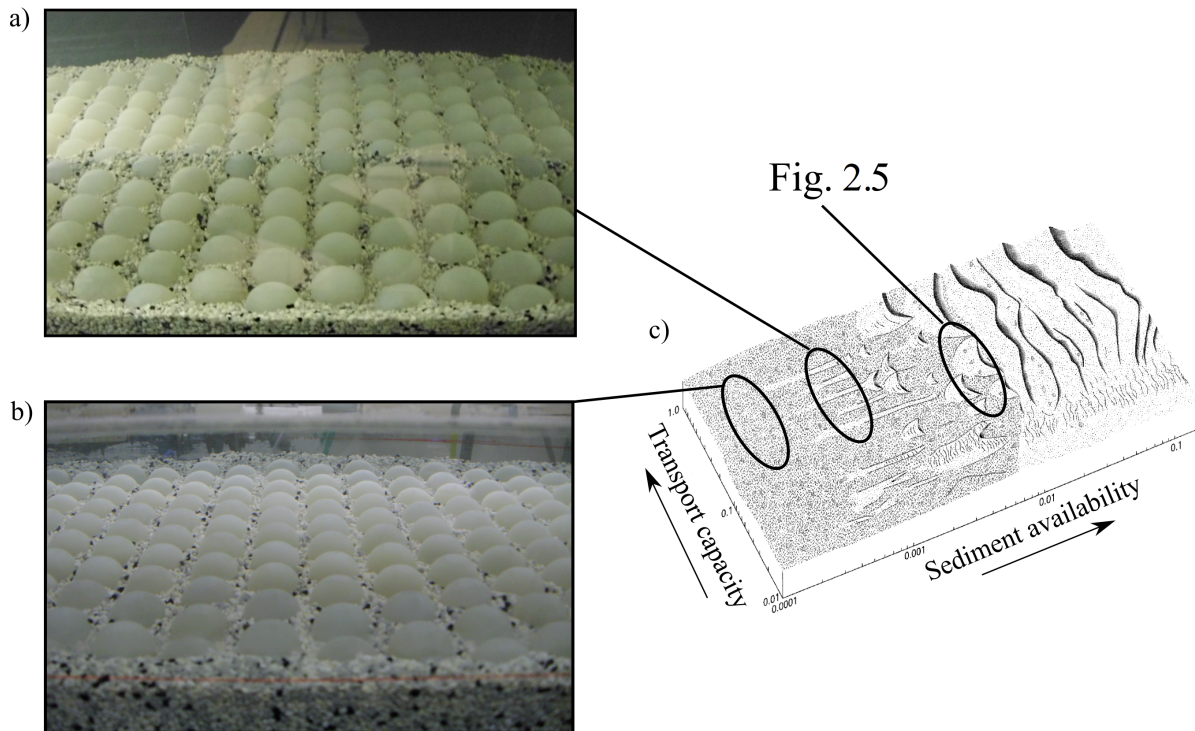
Figure 2.8: (a) Longitudinal ridge in the middle of the flume at t = 13h during Exp. 5b; (b) stable sediment bed reached at the end of Exp. 5b; (c) conceptual model of bed-form development over coarse immobile beds. Modified from Kleinhans et al. (2002).

2.3.3 Ridge analysis

As discussed in the last Section, the ridges decrease in height over time as a result of the absence of sediment supply. Even though various experimental studies under sediment supply limitation have observed ridges

(McLean, 1981; Nezu et al., 1988; Nezu and Nakagawa, 1989; McLelland et al., 1999), the temporal development of the ridge geometry (position, height, width and slope) has not been investigated to the knowledge of the author. The geometrical features of the ridges are determined as follows: first, to determine the position of the peak of the ridges (y_r) with sub-pattern precision, the transverse profile of the longitudinally averaged bed elevations is interpolated at each time step through a smoothing spline procedure. The transverse bed level profile is subdivided into troughs, ridges or side wall accumulations on the basis of its inflection points. The height of a ridge H_r is defined as the difference between the bed-level at the ridge peak and the bed-level averaged between the troughs to the left and to the right of the ridge. Since the ridges decrease in height during the experiments, a ridge is considered significant, if its height is larger than two times the standard deviation of the troughs' bed level variation, which represents a robust statistical measure of the roughness height of the troughs (Coleman et al., 2011). The width of a ridge W_r is defined as the distance between the position of the inflection points on both sides of the ridge. The average slope of the ridge flanks s_r is determined as the mean value of the slope of the bed level profile evaluated at the inflection points on the sides of the ridge. The side-wall accumulation's regions are defined as the region comprised between the side wall and the nearest inflection point of the bed to the side wall. If no inflection point is present in the vicinity of the wall, the inner edge of the side wall accumulation is considered to be the first protruding sphere near the side-wall.

In Figures 2.9a-h the temporal evolution of the position y_r/W, height H_r/d_{50}, width W_r/d_{50} and slope s_r of the ridges determined for Exp. 1a/b ($\theta l Am$) and Exp. 4 ($\theta l Ah$) at the up- and downstream locations is presented. These experiments with medium and high aspect ratio were chosen to analyse the behaviour of the bed in the presence of one or two ridges, respectively. As can be observed in Figures 2.9a and 2.9b, the transverse position of the ridges y_r/W is characterized by an initial phase of adjustment of 2-5 hours, stabilizing afterwards to an almost constant transverse position. For Exp. 1a (Figure 2.9a), the position of the ridge for the upstream and downstream measurement locations of match very well. The position of the ridge of the repeated Exp. 1b (only measured upstream) is also very close.

In Exp. 4, the ridges at the upstream measurement location (blue profiles in Figure 2.9b) develop parallel to each other on the left side of the channel, while at the downstream location (green profiles in Figure 2.9b) two pairs of ridges develop one after the other. The first pair of ridges at the downstream location develops during the first 10 hours. It is characterized by a stable ridge in the centre of the channel and a second ridge which drifts with time towards the right side of the channel, merging, in the end, with the side wall accumulations. On the basis of visual observation of the sequence of bed images, the central ridge dies quickly out at about 15 hours, so that the development of the following pair of ridges (downstream) is disconnected from the preceding downstream one. The fact that the central ridge dies out and the second ridge drifts considerably to the side, shows that the first bed configuration is not stable. The second pair of downstream ridges, instead, produces a symmetric topographic pattern. The distance between these two ridges is similar to the distance between the ridges upstream (blue profiles). It is therefore surmised that the second ridge pair at the downstream location is, in fact, the pair of ridges first observed upstream, which have travelled downstream. Figures 2.9c and 2.9d, for Exp. 1a/b and Exp. 4, respectively, show that the non-dimensional ridge height h_r/d_{50} is characterized by three stages: a rapid increase, a plateau and finally a decrease. The initial rapid increase in height can be related to the secondary currents enforced by the strong lateral roughness anisotropy induced by the appearance of the spheres in the troughs. As shown by Willingham et al. (2014) on the basis of LES simulations over an immobile bed characterized by alternated stripes of high and low roughness,
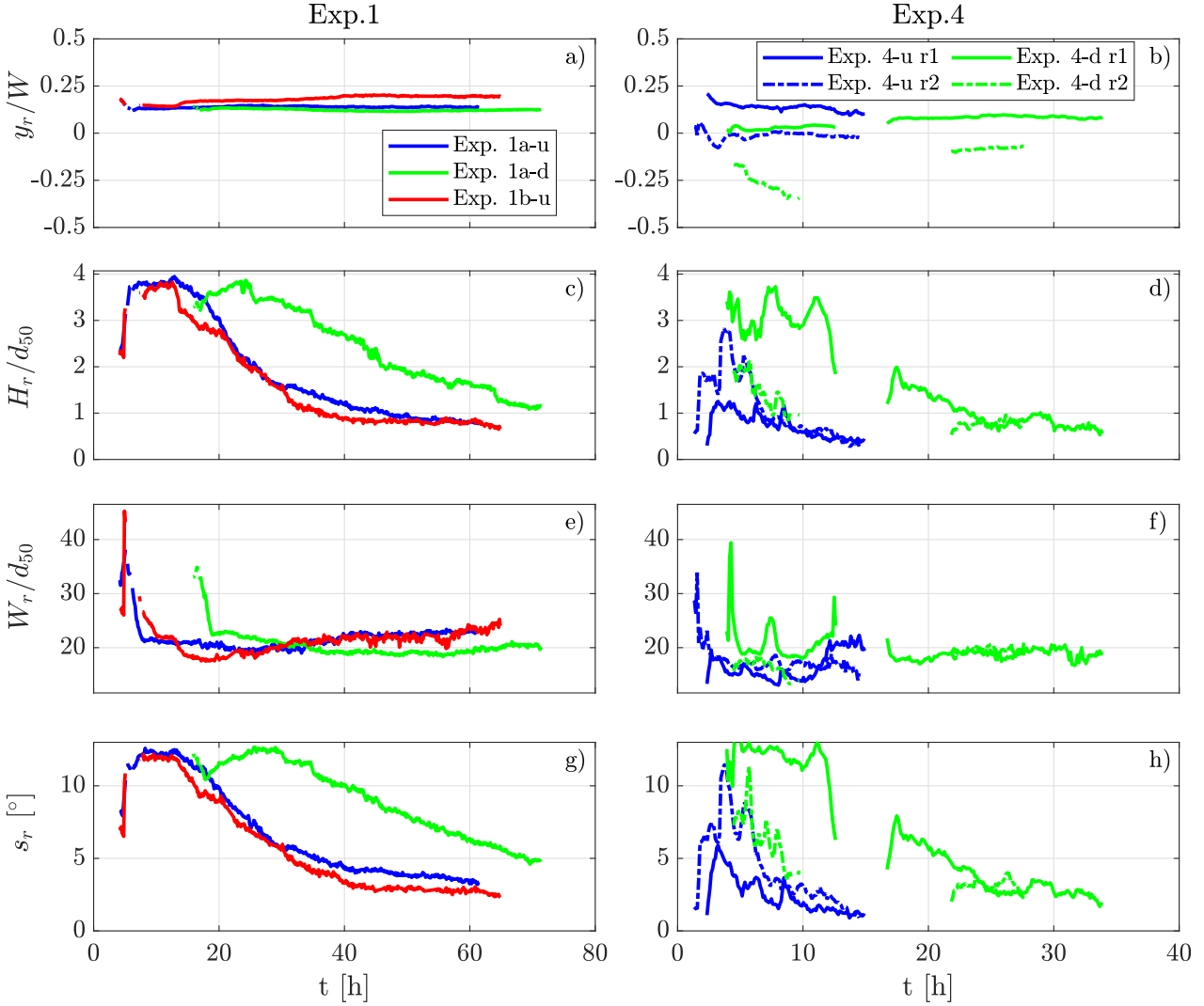
Figure 2.9: Transverse position y_r, height H_r, width W_r and slope s_r of the longitudinal ridges as a function of time; on the left column plots of Exp. 1a at the upstream (u) and downstream (d) measurement location and of Exp. 1b upstream; on the right column plots of Exp. 4 upstream and downstream with specification of the first (r1) and second ridge (r2).

the strength of the secondary currents increases when the ratio between the roughness lengths of adjacent stripes increases. This is likely to be the cause, in the case of a mobile bed, of a self-enhancing mechanism whereby the strengthened secondary currents in turn increase the sediment erosion in the troughs leading to higher roughness anisotropy. The ensuing plateau suggests that similar erosion conditions are present over the troughs and over the ridges, since both troughs and ridges are eroding at the same rate when H_r is constant. It is surmised that higher sediment sheltering by the higher protruding spheres in the troughs leads to a temporary equalization of the sediment transport rates between troughs and ridges. The ensuing decrease in ridge height H_r can be explained by the observation that the sediment bed in the troughs reaches a constant level (with no further erosion due to grain sheltering) and erosion takes place only over the ridges.

The evolution of the width of the ridges W_r/d_{50} is shown in Figures 2.9e and 2.9f. It can be seen that the width of the ridges decreases in the initial growth phase, quickly reaching a constant and stable value. The initial reduction of the width of the ridges is also in accordance with an increased intensity of the secondary
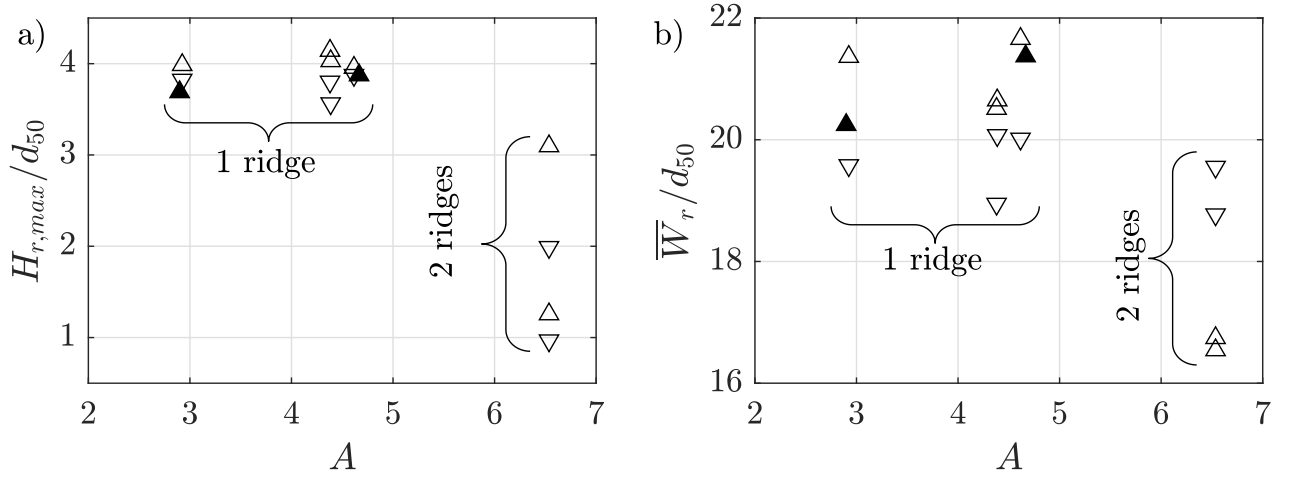
Figure 2.10: (a) Maximum height of the ridges $H_{r,max}$ normalised by the grain diameter d_{50} as a function of the aspect ratio; (b) time-averaged width of the ridges $\overline{W}_r$ normalised by the reference pattern width l_y as a function of the aspect ratio; ($\triangle$) upstream location, ($\triangledown$) downstream location and ($\blacktriangle$) for repeated experiments.

currents. Studies on the influence of the width of artificial ridges on secondary currents (Hwang and Lee, 2018; Willingham et al., 2014; Wang and Cheng, 2006), show that the strength of the secondary currents increases with decreasing width of the ridges. The shape of the ridge also contributes to the destabilization of the bed: as seen in Figures 2.9g and 2.9h, the transverse slope s_r of the ridges first increases and then decreases with similar trends as the height. The initial reduction in width and the increase in slope leads to a triangular cross section, which is shown by Medjnoun et al. (2020) and Wang and Cheng (2006) to concentrate and enhance the upflow region in the case of artificial ridges.

In Figures 2.10a-b the normalized maximum ridge height $H_{r,max}/d_{50}$ and the time-averaged ridge width $\overline{W}_r/l_y$ are plotted, respectively, as a function of the aspect ratio for all experiments (the time-averages are computed when the width reaches a stable value - see Figures 2.9g-h). Figure 2.10b shows that all ridge widths are relatively close being comprised between 16-22 d_{50}, although ridge pairs at higher aspect ratio are generally lower. The normalized heights (Figure 2.10a) vary much more though. While for experiments presenting only one ridge, the maximum height is close to 4 d_{50} for both aspect ratios ($A = $[3,4.5]), H_{r_max} is comprised between 1-3 d_{50} for $A = 6.5$ with 2 ridges. Since the ridges develop when the initial sediment layer on top of the spheres is almost depleted, the lower maximum ridge heights detected in the case of pairs of ridges is likely related to the limited sediment availability partitioned in two instead of only one ridge. Since the ridges share almost the same width, the total sediment volume is about the same for one or two ridges.

To analyse the formation of symmetric and asymmetric bed topographies observed in Section 2.3, the spacing between ridges is quantified. The ridge spacing is defined at the time t_s for which the position and the width of the ridges has reached stationarity. In particular, t_s is defined as the earliest time instant for which the ridge position at all later times does not exceed one standard deviation around the globally time-averaged ridge position (the vertical arrows in Figures 2.7a-h identify t_s). In the case of one ridge, the left- and right-wall ridge spacings, Λ_l and Λ_r, are defined as the distance between the position of the ridge and the inner edges of the side-wall accumulations, as shown in Figure 2.11a. In the presence of two ridges, a central ridge spacing Λ_c is included (see Figure 2.11b). The effective width of the channel W_e, representative for the development of the ridges, is defined, consequently, as the distance between the inner edges of the side-wall accumulations
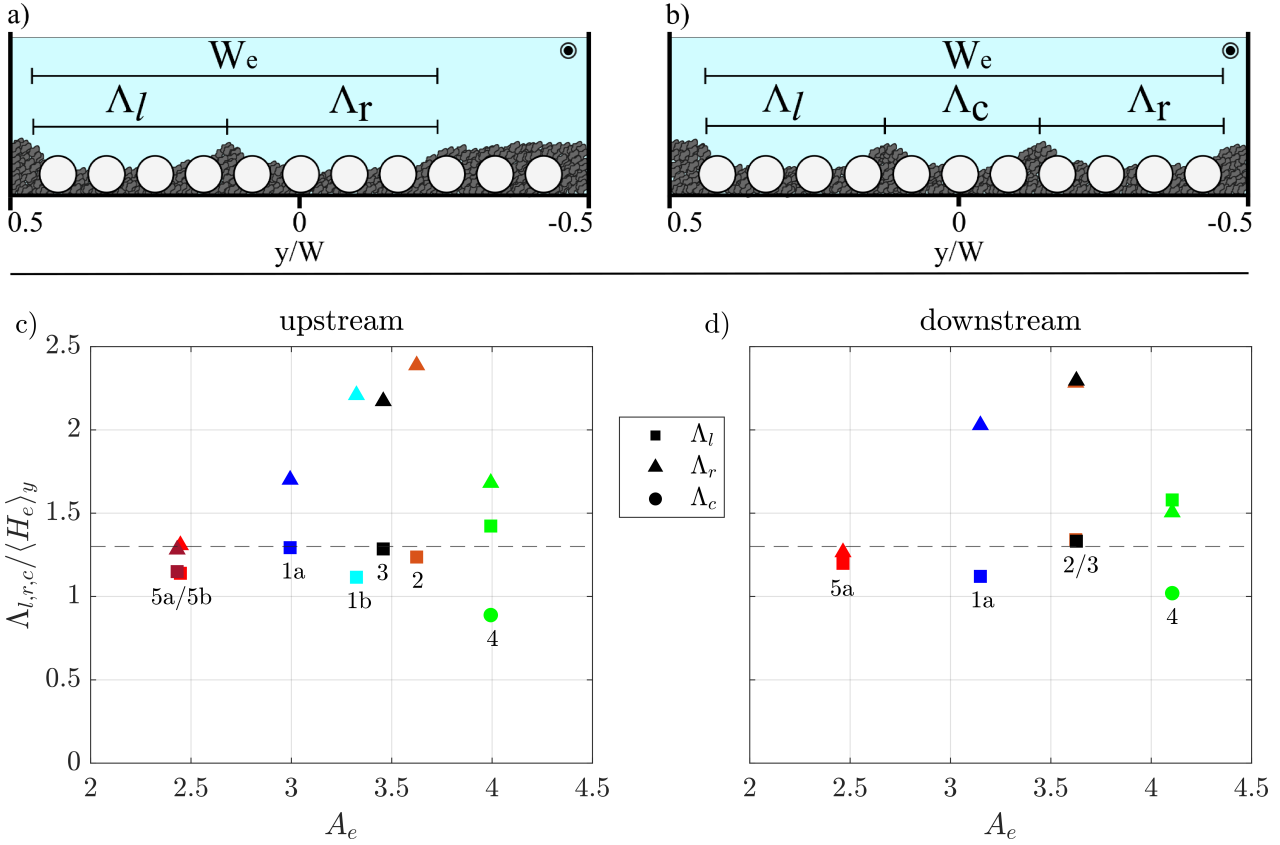
Figure 2.11: (a) Definition of the left-wall Λ_l and right-wall Λ_r spacings for one ridge; (b) definition of left-wall, right-wall and central spacings Λ_c for two ridges; (c-d) left-, right-wall and centre ridge spacings Λ_l, Λ_r and Λ_c normalized by the spatially-averaged effective water depth $\langle H_e \rangle_y$ as a function of the effective aspect ratio $A_e = W_e / \langle H_e \rangle_y$ for the upstream and downstream measurement location, respectively. The horizontal dashed line represents the theoretical ridge spacing derived by Colombini and Parker (1995).

(see Figures 2.11a-b) and yields the effective aspect ratio $A_e = W_e / \langle H_e \rangle_y$, where $\langle H_e \rangle_y$ is the effective water depth[1] averaged along the effective width W_e at time t_s. The ridge spacings Λ_l, Λ_r and Λ_c, all normalized by the effective water depth $\langle H_e \rangle_y$, are shown in Figures 2.11c-d for the upstream and downstream measurement locations, respectively. Since two consecutive ridge pairs develop during Exp. 4 at the downstream location, only the ridge spacings for the second ridge pair are plotted in Figure 2.11d.

Figures 2.11c-d (up- and downstream, respectively) both show that for Exp. 5a and 5b ($\theta l A l$), characterized by one single ridge up- and downstream, both the left wall and right wall spacings are close to 1.3 $\langle H_e \rangle_y$. For Exp. 1a/b ($\theta l A m$), 2 ($\theta m A m$) and 3 ($\theta h A m$), also all with a single ridge, the left wall spacings are close to 1.3 $\langle H_e \rangle_y$, while the right wall spacings vary between 1.7 and 2.4 $\langle H_e \rangle_y$. For Exp. 4 ($\theta l A h$), with two ridges, the left wall and the right wall spacings vary between 1.4 and 1.7 $\langle H_e \rangle_y$, while the spacing between ridges Λ_c is about 1 $\langle H_e \rangle_y$. In previous studies on longitudinal ridges in natural rivers or laboratory flumes with both uniform and bimodal sediment bed mixtures, the observed ridge-spacing to water-depth ratios were in

---

[1] The effective water depth $H_e(y,t_s) = H + \langle \phi[k(x,y,t_s)]k(x,y,t_s) \rangle_x$ accounts for the volumetric displacement induced by the spheres with ϕ the porosity of the bed given by $\phi = \int_{-k}^{0}[1-\lambda_p(z)]dz$ and $\lambda_p = 2A_p(z)/A_r$ the planar density of a protruding sphere, as in Akutina et al. (2019).

the range of 1-4 $\langle H_e \rangle_y$ (Wolman and Brush (1961); Ikeda (1981); Nezu et al. (1988) and (Culbertson, 1967; McLean, 1981; McLelland et al., 1999), for rivers and flumes, respectively). Yet, figures 2.11c-d could suggest that the ridge spacing tends to be around 1.3 $\langle H_e \rangle_y$, ignoring the right wall outliers for the moment. This spacing would agree with the linear stability analysis of an infinitely large river bed with bimodal sediments by Colombini and Parker (1995), who found, on the basis of linear stability analysis, a wavelength of 1.3 H (= Λ_{Col}) for maximum amplification of the system. McLelland et al. (1999) also observed experimentally the development of ridges with a wavelength of 1.25 H in a bimodal sand mixture, where both the coarse and fine sediment fractions were mobile.

On the basis of the characteristic wavelength Λ_{Col}, it is possible to explain the bed observed topographies,

Exp.		1a		1b	2		3		4		5a		5b
		u	d	u	u	d	u	d	u	d	u	d	u
$\langle H_e \rangle_y$ [cm]	6.9	6.9	6.8	7.2	7.2	7.2	7.2	5.0	5.0	10.7	10.6	10.8
W_e [cm]	20.7	21.9	22.7	26.2	26.2	24.9	26.2	20.1	20.7	26.2	26.2	26.2
A_e [-]	3.0	3.2	3.3	3.6	3.6	3.5	3.6	4.0	4.1	2.4	2.5	2.4
N_Λ [-]	2.3	2.5	2.6	2.8	2.8	2.7	2.8	3.1	3.2	1.9	1.9	1.9
$N_{r,e}$ [-]	1	1	1	1	1	1	1	2	2	1	1	1
$N_{r,o}$ [-]	1	1	1	1	1	1	1	2	2	1	1	1

Table 2.4: Effective water depth $\langle H_e \rangle_y$, effective width W_e, effective aspect ratio A_e, number of wavelengths fitting in the effective width $N_\Lambda = A_e/1.3$, number of *expected* ridges $N_{r,e} = int(A_e/1.3 - 1)$, and number of *observed* ridges $N_{r,o}$ for all experiments both at the upstream and downstream measurement location.

including the ones with larger spacings. For Exp. 5a/b, characterized by a symmetric bed topography, Λ_l and Λ_r are both close to Λ_{Col}, so that the available lateral spacings are enough for the development of one ridge in the middle of the channel. In the case of Exp. 1a/b, Exp. 2 and Exp. 3, characterized by an asymmetric bed topography with only one side ridge, Λ_l is close to Λ_{Col}, while Λ_r is in the range of 1.3-1.8 Λ_{Col}. Since two complete Λ_{Col}-wavelengths do not fit into Λ_r, the development of an additional ridge towards the right side-wall accumulation is evidently suppressed or highly attenuated. Figures 2.7b-c show, in fact, that for Exp. 1a downstream and 1b upstream, both characterised by Λ_r closer to 2 Λ_{Col}, a shallow secondary ridge develops near the right side-wall accumulation with a distance of Λ_{Col} from the primary ridge at time t_s. This secondary ridge is unstable though and shifts over time towards the side-wall accumulation and disappears. In the case of Exp. 4, the sum of Λ_l, Λ_c and Λ_r corresponds to 3 Λ_{Col}, so that two ridges manage to develop. In conclusion, it appears that the number of ridges which can develop depends on the integer number of Λ_{Col}-wavelengths which fit into the effective width of the channel, $N_\Lambda = W_e/(1.3H_e)$. In terms of the effective aspect ratio, the number of ridges N_r is then given by the integer part of $A_e/1.3-1$ (= N_Λ-1). In Table 2.4 the effective water depth $\langle H_e \rangle_y$, the effective width W_e, the effective aspect ratio A_e, the number of wavelengths N_Λ, the number of expected ridges $N_{r,e}$ and the number of observed ridges $N_{r,o}$ are listed. As can be seen, $N_{r,e}$ corresponds to the number of observed ridges $N_{r,o}$ for all cases. For example, in the case of Exp. 5a/b, the effective aspect ratio is equal to 2.4, which corresponds to about 2 wavelengths, i.e. one expected ridge, consistent with the central ridge observed in Figure 2.7a. In the case of Exp. 1a/b, Exp. 2 and Exp. 3, the number of wavelengths presents intermediate values between 2 and 3, so that only one stable ridge is expected, as the effective width is not wide enough to guarantee three full Λ_{Col}-wavelengths. The

good agreement between $N_{r,e}$ and $N_{r,o}$ suggests that in addition to Λ_{Col} being the natural wavelength, the lateral side-wall accumulations, defining the effective width of the channel, adequately help to determine the number of ridges which can develop. Since preferential upflow is expected to take place over the up-sloping inner edge of the side-wall accumulations, it is surmised that the side-wall accumulations act as virtual walls, laterally bounding the development of the secondary-currents' cells responsible for the ridge formation. As such, the side wall accumulations can be interpreted as half-ridges.

2.3.4 Local analysis of the evolution of the bed

In this section, the temporal evolution of the protrusion level P over ridges and troughs is analysed. The positions of the ridges and the troughs are identified through arrows in Figure 2.7 for all experiments. Figure 2.12 shows in blue an example of the measured evolution of P averaged around a single sphere over the trough in Exp. 5b (denoted as raw data). Two main features can be noted. Firstly, a time t_0 can be defined, after which P remains positive and the sphere is not covered anymore. Before this time, after a short erosion period ($P > 0$), the sphere is covered again by dunes ($P = 0$). t_0 is a function of the longitudinal and transverse position of the spheres within the measurement area, increasing in longitudinal direction due to the advection of bedforms and displaying higher values over the ridges than over the troughs. Secondly, after t_0, the protrusion profile displays periods of local decrease in P, i.e. deposition, likely due to the appearance of sediment sheets traveling under the top of the spheres, temporarily causing increased bed levels. These depositional periods are identified in only 2% of the ridges' and troughs' profiles analysed, while in all other profiles a purely monotonic increase of the protrusion levels is observed (the small fluctuations are measurement noise). Moreover, the depositional periods do not modify evidently the erosive behaviour of the bed, as the variation of P in time is similar before and after the depositional pattern. Therefore, in order to compare effectively the different profiles and analyse only the erosive behaviour of the bed, the P-signal is offset by t_0 and the depositional periods are removed. The new time frame $\xi = t'-t_0$ is defined where t' is the time with the removed depositional patterns[2]. These are defined between a local minimum and the point with the same protrusion level as the local minimum before the preceding local maximum (see Figure 2.12). To this end, the protrusion profile is interpolated with a smoothing spline (red profile in Figure 2.12). The green profile in Figure 2.12 illustrates the result as a function of ξ. Once the raw data are processed, the local protrusion levels on the ridges and on the troughs, $P(\xi, x)$, are spatially averaged in the longitudinal direction (over 9 spheres) at each time step and denoted by $P(\xi)$.

Figures 2.13a-b show the temporal evolution of the longitudinally averaged protrusion levels $P(\xi)$ at the upstream measurement location over the troughs and the ridges, respectively. The temporal evolution of P at the downstream measurement location is very similar and is not displayed. It can be seen that Exp. 2 and Exp. 3, which are characterized by medium and high θ, respecively, display the fastest evolution in protrusion levels for both the trough and the ridge positions, while Exp. 1a/b, Exp. 4 and Exp. 5a/b with low θ, evolve slower, as might be expected. Within the fast group though, Exp. 2 (θmAm) evolves faster than Exp. 3 (θhAm). Also, as seen in Figures 2.7d-g, for Exp. 2 and Exp. 3, the bed erodes beyond $P = 0.8$, i.e, beyond

---

[2] By identifying all N local minima P_i, $t' = t-\sum_{i=1}^{N}(t_i\text{-}t_i^*)$ is defined on the basis of the time $t_i = t(P = P_i)$ at which the ith local minimum P_i is reached and of the time $t_i^* = t(P = P_i \wedge t < t_i)$ immediately preceding t_i and characterized by the same protrusion level as the local minimum P_i
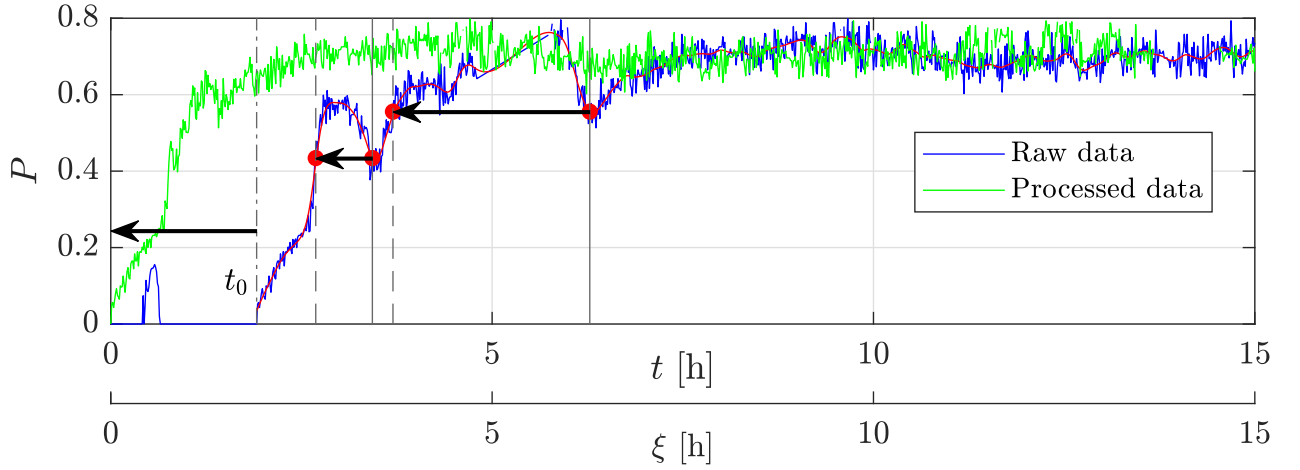
Figure 2.12: Example of data treatment of the temporal evolution of the protrusion levels of a sphere at the trough position of Exp. 5b. In blue the raw signal (in red the interpolation via a cubic smoothing spline) and in green the processed data obtained by: i) shifting the raw signal by t_0, i.e. the time instant, when the spheres start to protrude, and ii) removing local maxima to where the protrusion level returns to its earlier level, to obtain a monotonic and comparable profile.
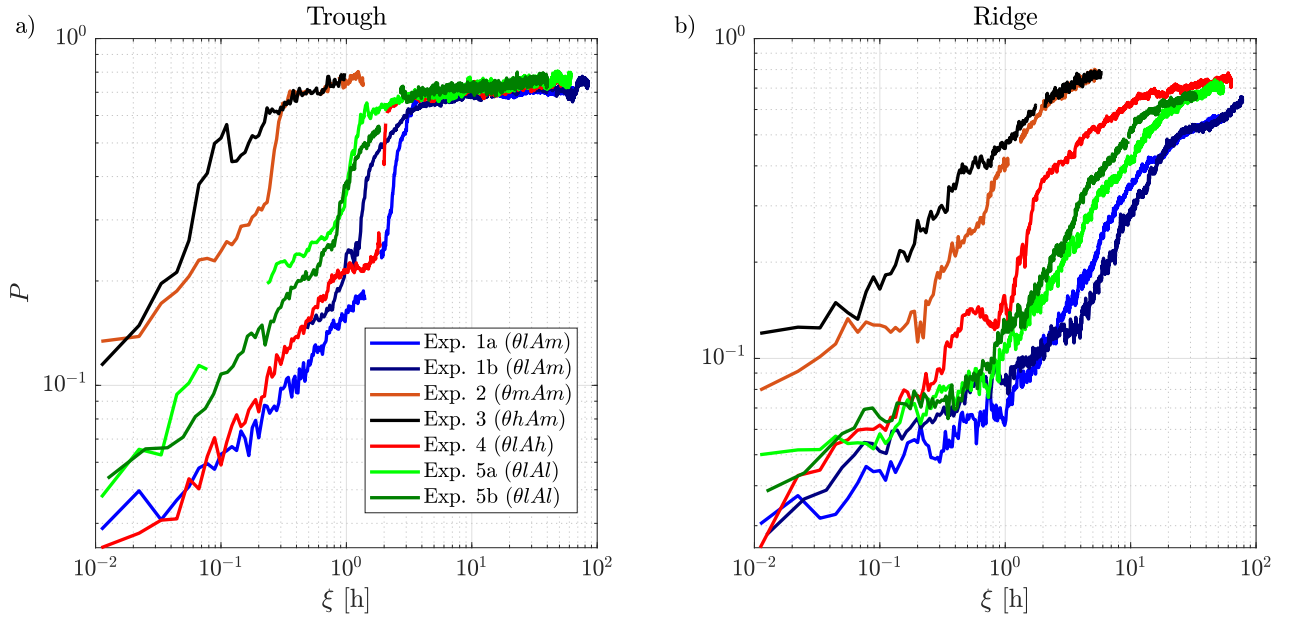
Figure 2.13: Protrusion levels as function of $\xi = t'-t_0$: (a) trough, (b) ridge, at y-positions indicated with arrows in Figure 2.7 at the upstream measurement location for all experiments.

the measurement range, so that only the initial bed development is displayed.

Over the troughs (Figure 2.13a), the protrusion levels of the spheres increase quickly from $P = 0$ to $P \simeq 0.7$ within the first 0.5-3 h. Thereafter, a strong reduction in the evolution of the bed is observed. While Exp. 2 and Exp. 3 suggest a trend for further erosion of the bed (confirmed by an ultimate complete erosion of the bed, as observed visually), Exp. 1a-b, Exp. 4 and Exp. 5a-b reach an almost constant bed level. The remaining but very slow erosion is consistent with visual observations of very intermittent movements of individual grains, once this plateau is reached.

Over the ridges (Figure 2.13b), the spheres reach protrusion levels as high as in the troughs but with much

delay: after an additional 3 h for Exp. 2 and Exp. 3 and after an additional 30-40 h for Exp. 1a/b, Exp. 4 and Exp. 5a/b. As for the troughs, there is a significant slowdown in the evolution of the bed for high protrusion levels. Yet, while the troughs for Exp. 1a/b, Exp. 4 and Exp. 5a/b reach a quasi-plateau, the ridges do not reach quite such a stable bed level, even after several days.

The time rate of change of the protrusion level can be used to estimate the local erosion rate. In the presence of large immobile roughness elements, the Exner equation can be written as

$$\frac{\partial q_s}{\partial x} = E_t \tag{2.2}$$

by applying the conservation of mass of the mobile sediment fraction over a control volume excluding the immobile roughness elements (see Appendix A). This equation provides the balance between the the longitudinal variation in sediment transport rates q_s and the total erosion rates E_t of the fine sediments from an immobile gravel bed, given by

$$E_t = \mu E = (1 - \lambda_p) C R \frac{\partial P}{\partial t} \tag{2.3}$$

where $\mu = 1\text{-}\lambda_p$ is the longitudinally-averaged area coverage of the fine sediments with λ_p the planar density of the protruding spheres and $E = CR\partial_t P$ the longitudinally-averaged erosion rate of a uniform bed in the absence of immobile roughness elements with $C = 1 - \phi_s$ (= 0.55) the fine sediment concentration (solidity). In order to calculate E_t as a function of time, P (blue stars in Figures 2.14a-b) and $1\text{-}\lambda_p$ (green stars in Figures 2.14a-b) are interpolated with a smoothing spline (red curves in Figures 2.14a-b). $\partial_t P$ is, then, estimated by the means of a second-order central-finite-difference scheme.

Figures 2.14c-d show typical temporal evolutions of E_t and E over troughs and ridges, respectively, for Exp. 5a upstream. First, it can be observed that E and E_t follow similar trends. The highest erosion rates, E or E_t, are observed just when the spheres start to protrude from the bed, but are higher over the trough than over the ridge. The erosion rates then globally decrease, eventually tending towards zero but preceded by a local maximum. As seen in Equation 2.3, E_t does not give a direct estimate of the sediment transport rate, but rather of the spatial variability in the sediment fluxes in the longitudinal direction. This means, that as long as E_t is positive, the bed is not in equilibrium as more grains are eroded than deposited in the measurement section. A state characterized by zero erosion rate, is either a consequence of equal sediment transport rates between upstream and downstream (resulting in a dynamic equilibrium) or a consequence of the cessation of sediment transport, i.e. $q_s = 0$ (resulting in a static equilibrium). Visual observations in the case of Exp. 1a/b, 4 and 5 show that, at the end of the experiments, the sediment transport is highly intermittent, i.e. close to zero, suggesting that the bed tends to a static equilibrium.

The local maxima seen in both E_t and E and over troughs and ridges in Figures 2.14c-d occurs at $\xi \simeq 1$ hour. This enhancement in erosion rates is much more significant over the troughs than over the ridges though. Comparing Figures 2.14a,c and 2.14b,d, the contribution to the total erosion rates E_t which is a product of the area coverage $\mu = 1 - P$ and the erosion rates E, it is observed that the peak in the total erosion rates E_t derives from a steep increase in P, i.e. from E, while the area coverage only acts as a damper of the erosion rates E, as it monotonically decreases over time. The temporary increase in the erosion rates marks a change in the local flow dynamics. In the following, the analysis on changes in bed behaviour is performed on the basis of the erosion rate E to avoid the small influence of the area coverage.

The temporal evolution just discussed can be separated into four different regions, the transition points being marked by black dots in Figures 2.14c-d: the first region is characterized by a fast and monotonic decrease in
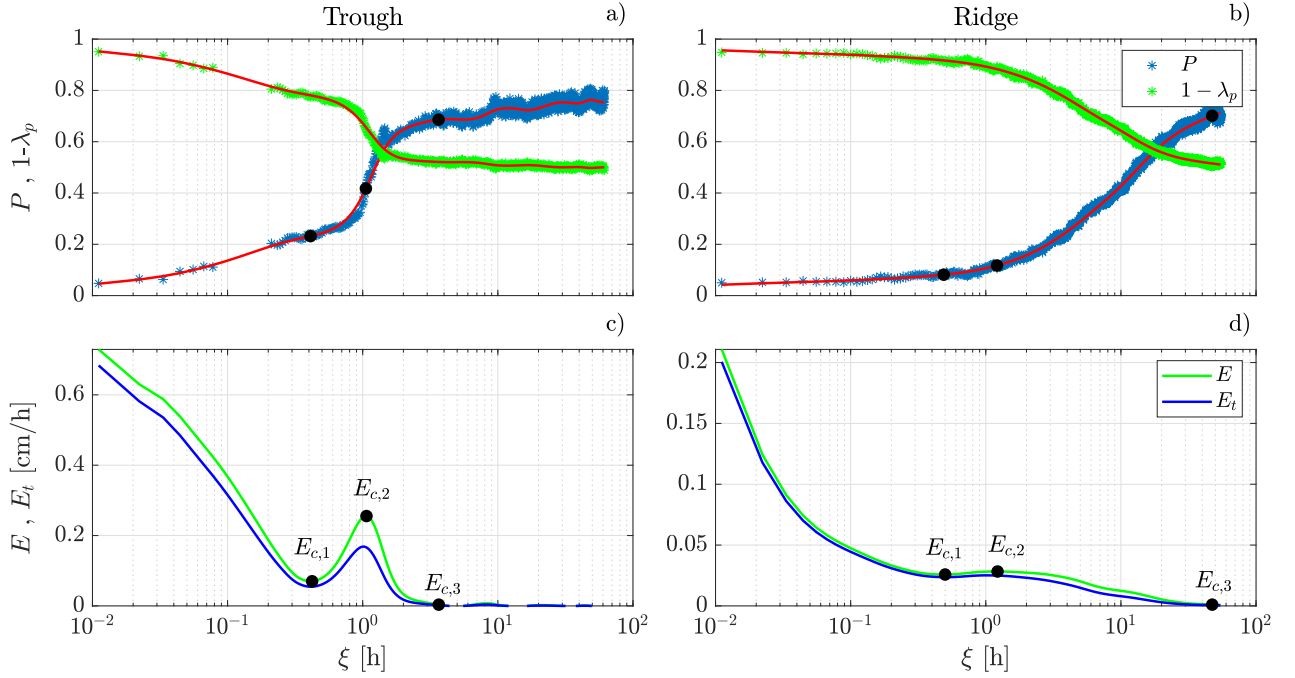
Figure 2.14: (a-b) Temporal evolution of the protrusion levels P and of the surface area coverage $1 - \lambda_p$ (the red lines are the interpolated profiles with a smoothing spline); (c-d) Temporal evolution of the erosion rates $E = CR\partial_t P$ and of the total erosion rates $E_t = (1 - \lambda_p)E$. The data are of Exp. 5a at the upstream measurement location. The left column are trough data while the right column ridge data.

the erosion rate, the second one by a growing erosion rate, the third one by a decrease again, and the fourth by a negligible erosion rate. The critical protrusion levels, labelled P_{ci} with $i = 1,2,3$ corresponding to the three marked transitions are defined at the times ξ when the erosion rates E reaches the local minimum (E_{c1}), the local maximum (E_{c2}) and 0.5% of the erosion rate E_0 at time $\xi = 0$ (E_{c3}). These three critical levels P_{ci} are plotted as a function of the Shields number in Figures 2.15a-b for the troughs and ridges, respectively. P_{c1}, P_{c2} and P_{c3} are connected by continuous, dashed and dot-dashed lines, respectively. For the troughs, Figure 2.15a shows that the three critical protrusion levels do not depend on the Shields number θ, i.e. on the shear stress acting on the bed, since each critical point takes place at almost the same protrusion levels for all experiments: $P_{c1} \simeq 0.2$, $P_{c2} \simeq 0.4$ and $P_{c3} \simeq 0.7$. A dependency on the aspect ratio A is thereby excluded, as the experiments are characterised by different A. It should be noted that in the case of Exp. 2 downstream and Exp. 3, the first two transitions are not observed, since the measurements are probably not time-resolved enough to capture them. In the case of the ridges, Figure 2.15b shows that the first two transitions take place for lower protrusion levels compared to the troughs and are not quite as constant. The first transition is observed for $P_{c1} \simeq 0.1$-0.2 and the second transition for $P_{c2} \simeq 0.2$-0.4. The third transition displays, instead, similar protrusion levels as over the trough ($P_{c3} \simeq 0.7$).

While the transitions in bed behaviour take place at an almost constant bed level, the time instants at which the transitions occur, defined as ξ_{ci}, decrease with increasing θ, as shown, for example, in Figures 2.15c-d for the time instant relative to the second transition ξ_{c2}. In Figures 2.15e-f, the erosion rates E_{c2} at the second transition show also a dependency on θ: the higher θ, the higher the peak erosion rates E_{c2}. A similar trend is also observed for E_{c1}, E_{c3} and E_0 (not shown here). The relative increase in the local peak erosion rate,

29

E_{c2}/E_{c1} shown in Figures 2.15g-h, shows that over the troughs, $E_{c2}/E_{c1} \simeq 2 - 3.5$, and over the ridges, $E_{c2}/E_{c1} \simeq 1 - 2$. The peak increase in erosion rates is evidently much less pronounced over the ridges than over the troughs. Among the different experiments, Exp. 4 shows higher E_{c2}/E_{c1} ratios both over the troughs and the ridges, possibly due to the higher aspect ratio corresponding to a lower relative submergence (ratio between the water depth and the protrusion level of the spheres). Compared to the erosion rate E_0 at ξ = 0 when the spheres start to protrude, Figure 2.15i shows that over the troughs $E_{c2}/E_0 \simeq 0.4 - 1$ for low θ, while for high θ it can be higher than one, a clear case of shear-stress enhancement rather than sheltering. Over the ridges, Figure 2.15l shows that with increasing θ, E_{c2}/E_0 increases and can reach values as high as 1.

Since the three transitions in erosion rates over the troughs and the ridges occur at essentially the same protrusion levels P_{ci} independently of the global flow parameters θ and A, the change in erosion regimes must be due to changes in the local flow dynamics around the protruding spheres. In the first region of decaying erosion rate before P reaches the first transition, the caps are relatively shallow with small angles of attack. The decaying erosion rate is evidently a sheltering effect due to the increasing drag exerted on the spheres as P increases. Yet, it is surmised that the angle of attack of the protruding caps is too shallow to form horseshoe vortices. The first regime for $P < P_{c1}$ can therefore be described as a drag sheltering regime.

Studies on submerged and fully-exposed isolated obstacles, such as boulders, have shown that the flow separates around the obstacles due to the surface pressure distribution, leading to the development of horseshoe vortices in the front and side regions and of arch-shaped shear layers detaching in the lee and reattaching some distance downstream while enclosing a recirculation region (Shamloo et al., 2001; Pattenden et al., 2005; Sutton and McKenna Neuman, 2008a; Dey et al., 2011c; Lacey and Rennie, 2012; Dixen et al., 2013; Euler et al., 2017). Below the horseshoe vortex, increased shear stresses are observed (Dey and Raikar, 2007; Dixen et al., 2013; Fang et al., 2017), potentially causing increased erosion with the formation of a scour hole in the front of the obstacle, if critical conditions of motion are overcome (Karcz, 1973; Shamloo et al., 2001; Sutton and McKenna Neuman, 2008a; McKenna Neuman et al., 2013; Euler et al., 2017). Accordingly, the first transition in erosion rate, observed for a protrusion level $P_{c1} \simeq 0.2$, could be explained by the development of a horseshoe vortex around the sphere. Experimental studies on cylinders with varying inclination (Euler et al., 2014), on cones with varying side slopes (Okamoto et al., 1977) and on spherical caps with different protrusion levels (Raus, 2019), on mobile-sediment, with smooth and rough immobile beds, respectively, have observed the development of horseshoe vortices for angle of attacks of the impinging flow greater than 25-30°. This would be consistent with the critical protrusion level P_{c1} observed herein when defining the angle of attack for a protruding sphere (comparable to a spherical cap) by the ratio between the protruding height and the planar radius measured at half height, as done in the case of hills (Ferreira et al., 1995). One could therefore reasonably surmise that the increase in erosion rates observed for $P > 0.2$ is due to an increasing intensity of the horseshoe, as the scour hole induced by the developing horseshoe vortex deepens down. Such an increase in intensity of the horseshoe vortex with increased bed shear stress levels was observed in developing scour holes around vertical cylinders by Muzzammil and Gangadhariah (2003) and Dey and Raikar (2007). Yet, the increase in erosion rates for $P > 0.2$ can be also promoted by the development of a shear-layer in the lee side of the spheres. Raus et al. (2019), albeit for a square pattern of spherical caps over an immobile flat rough bed, showed that for $P = 0.2$ the shear-layer developing at the top of the spheres can reach the underlying bed causing locally enhanced shear stresses, potentially increasing the erosion rates. The ensuing increase of the erosion rate for $P > 0.2$ in the second regime towards E_{c2},
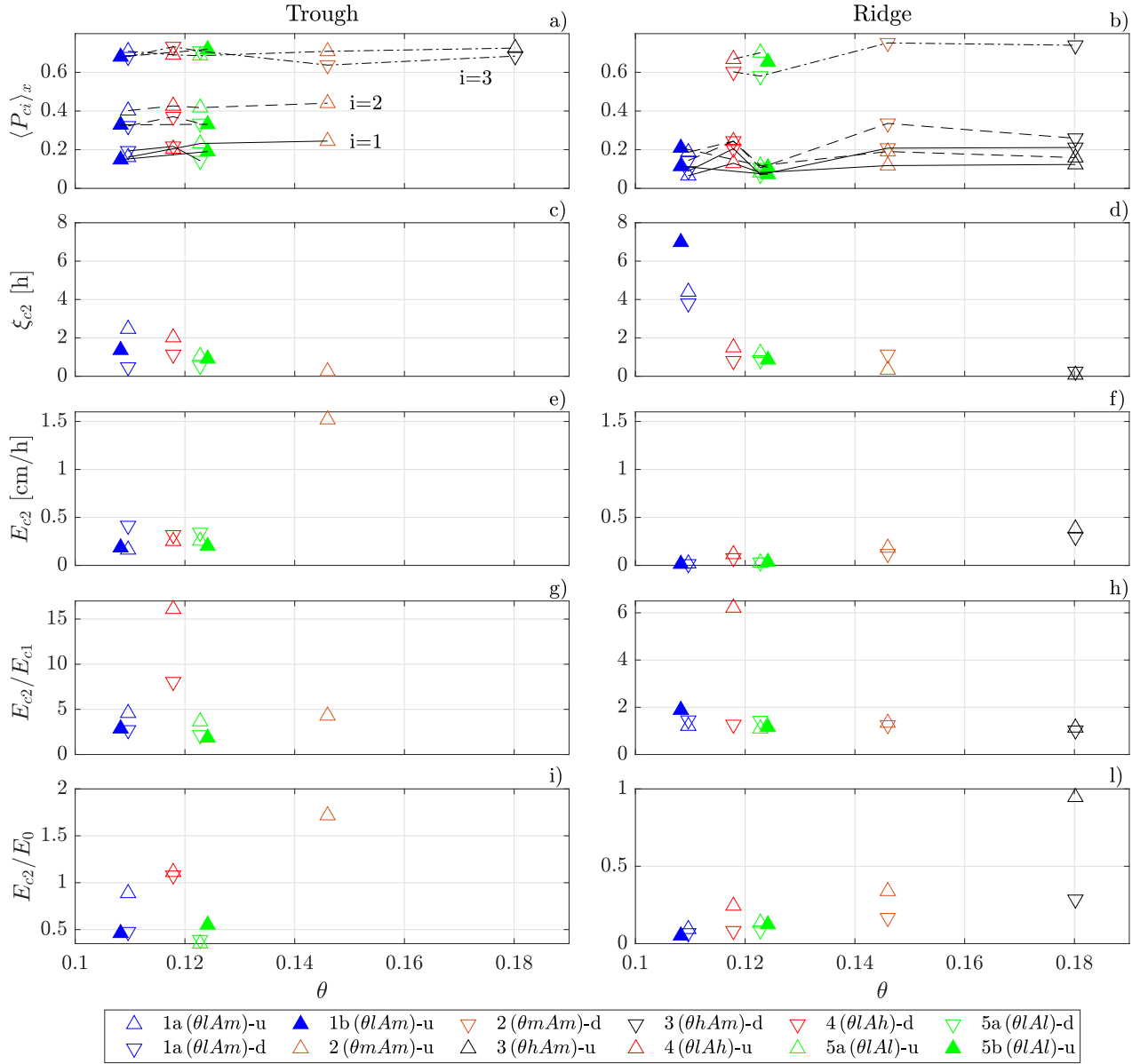
Figure 2.15: Critical values as a function of the Shields parameter θ for the trough (left column) and the ridge (right column): (a-b) Critical protrusion levels P_{ci}; (c-d) critical time at the second transition ξ_{c2}; (e-f) erosion rate at the second transition E_{c2}; g-h) ratio between E_{c2} and the erosion rate at the first transition E_{c1}; (i-l) ratio between E_{c2} and the erosion rate at $\xi=0$, E_0. For diagrams a-b the continuous line identifies the critical points for the first transition, the dashed line for the second transition and the dot-dashed line for the third transition. ($\triangledown$) upstream, ($\triangle$) downstream measurement location and ($\blacktriangle$) repeated experiments.

can therefore be explained by increased shear stresses induced by the development of a horseshoe vortex and/or by the development of a strong interfacial shear layer. The increased shear stresses can even lead to $E_{c2}/E_0 > 1$, i.e. erosion rates at the local maximum higher than when the spheres start to protrude, as seen in Figure 2.15i over troughs for high θ. The second regime for $P_{c1} < P < P_{c2}$ can therefore be described as a turbulence-enhancement regime.

The second transition in erosion rate E_{c2}, followed by a reduction in erosion rate, is observed for $P_{c2} \simeq 0.4$,

which corresponds to a planar density $\lambda_p \simeq 0.3$. This value of the planar density is identified by Grimmond and Oke (1999) as the threshold condition for the transition from isolated to wake-interference flow conditions in the bed interstices. According to the definition of Morris (1955), the flow in between roughness elements can be considered isolated as long as the wake of a roughness element dissipates before the next one. As soon as the wake interacts with the downstream roughness element, wake-interference conditions are given. As shown by Raus et al. (2019) for a pattern of hemispheres or by Liu et al. (2019) and Ferreira et al. (1995) for hills, the size of the recirculation region in the lee side of obstacles, increases with increasing height of the obstacles. As such it is surmised that the second regime for $P < P_{c2}$ is an isolated wake regime and that with increasing protrusion of the spheres, the reattachment point of the recirculation region moves downstream, eventually reaching the downstream sphere for $P = P_{c2} \simeq 0.4$. Then, in the third regime for $P > P_{c2}$, the flow becomes a wake-interference regime with a recirculation region characterized by increasingly reduced bed shear-stress conditions, i.e. sheltering. This would be in agreement with Dey et al. (2011c) and Papanicolaou et al. (2012) who observed that recirculations are associated with reduced shear stresses. The third regime for $P_{c2} < P < P_{c3}$ can therefore be described as a wake-interference sheltering regime.

Over the ridges, the first and second transition take place at lower protrusion levels than the troughs. This difference could be related to different topographic features between ridges and troughs: while the sediment levels are quite homogeneous around spheres located in the trough, the spheres at the ridge protrude in an asymmetric manner, with higher bed levels observed towards the ridge crest due to the transverse up-sloping bed. This asymmetry might cause non-uniform flow conditions at the level of the spheres which erode faster on one side showing lower protrusion levels for the first transition. Further studies are necessary to confirm this difference.

The third transition in erosion rate E_{c3} at which the erosion rates reach zero, is observed both on the troughs and the ridges for protrusion levels $P_{c3} \simeq 0.7$, corresponding to a planar density $\langle \lambda_p \rangle_x \simeq 0.5$. This planar density in turn corresponds closely to the transition between a wake-interference and a skimming flow regime (Grimmond and Oke, 1999). The skimming flow regime is characterized by the persistence of stable vortices filling completely the interstitial region between roughness elements thereby disconnecting the flow in between the roughness elements from the outer flow Leonardi et al. (2003); Coleman et al. (2007). Experimental and numerical studies (Raupach et al., 1980; Leonardi, 2010; Placidi and Ganapathisubramani, 2015; MacDonald et al., 2016) have shown that the transition between wake-interference and skimming flow is characterized by a peak in drag acting on the bed. As a result, the shear stress acting on the fine sediments, resulting from the difference between the total shear stress and the drag in a shear stress partitioning framework Raupach (1992); Yager et al. (2007), reaches a minimum. The fourth regime for $P > P_{c3}$ can therefore be described as a skimming-flow sheltering regime. For Exp. 1a/b, Exp. 4 and Exp. 5, all characterized by a final quasi-stable bed, the reduction in shear stress acting on the fine sediments is evidently enough to reach sub-critical conditions of motion. For Exp. 2 and 3, with medium and high shear stress, the reduction in shear stress is not enough to reach sub-critical conditions of motion before the bed fully erodes.

2.4 Local flow field

The analysis of the bed morphodynamics has shown that the erosive behaviour of the bed changes in space, leading to the development of longitudinal ridges, and in time, leading to changes in the protrusion level of the spheres, i.e. in roughness. These topographic and roughness-factors influence the local shear stress conditions. Both stripe-type surfaces, characterized by lateral variation of roughness, and ridge-type surface with variations in the transverse bed elevations have been shown to lead to secondary flow patterns and the redistribution of momentum in the cross section (Nezu, 2005; McLelland, 2013; Wang and Cheng, 2006; Medjnoun et al., 2020; Stroh et al., 2020). These effects have been considered only separately and in stationary conditions, though. PIV measurements were therefore performed here to characterize the development of the secondary flows with simultaneous changes in bed topography and roughness and to determine the shear stress conditions acting on the troughs and ridges. The measurements were performed during Exp. 1b ($\theta l Am$) and Exp. 5b ($\theta l Al$) with asymmetric and symmetric bed topographies, respectively. Figures 2.16a-b display the temporal evolution of uncorrected P measured upstream of the PIV system at the same transverse location of the two PIV planes in the middle (noted m for y/W=0) and in the quarter plane (noted q for y/W=-0.22) of the channel. The vertical lines highlight the times t_1, t_2, t_3 around which the PIV measurements were performed. In Figures 2.16c-d the transverse profile of P, measured immediately before each PIV run, is displayed. Figure 2.16c shows that during Exp. 1b the m- and q-planes are located over the trough region

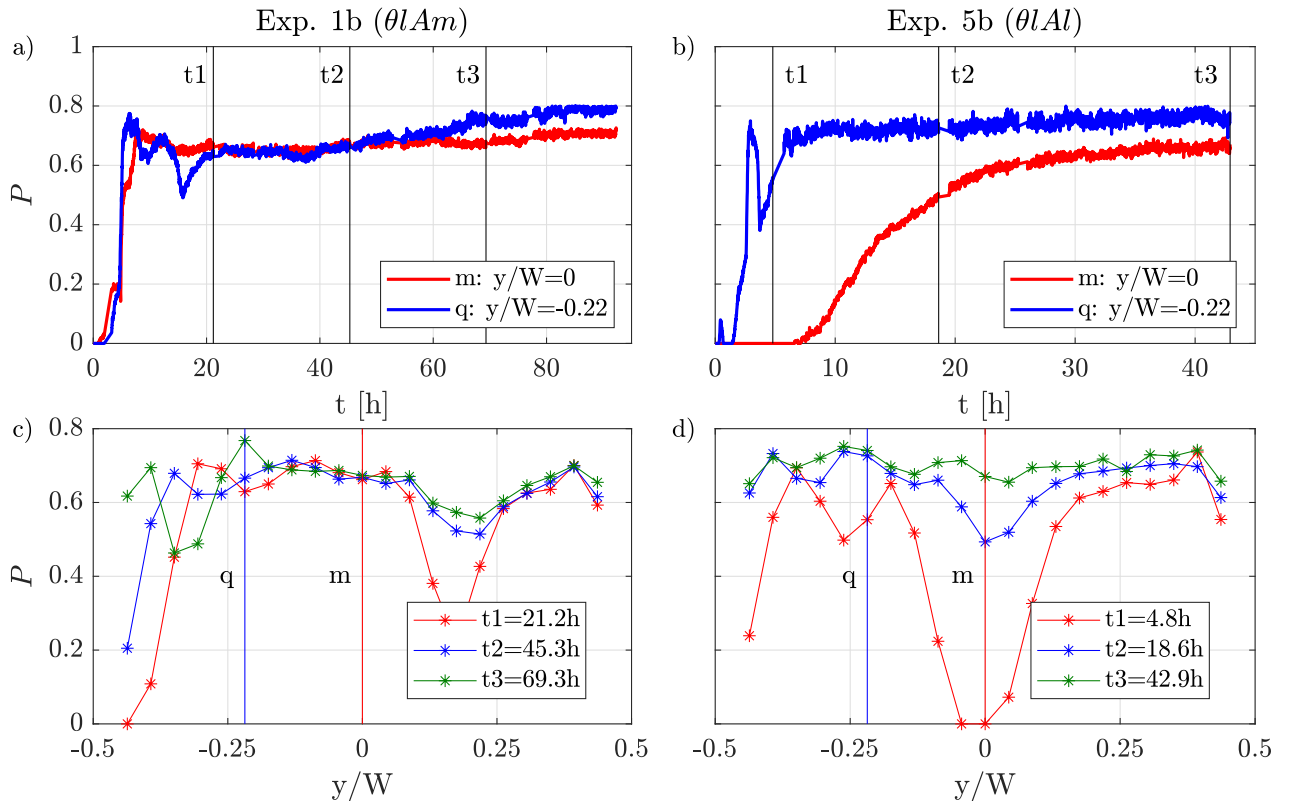**Figure 2.16:** (a-b) Protrusion level profiles as a function of time at the middle (m: y/B = 0) and quarter plane (mq: y/B = -0.22) during Exp. 1b and 5b (the vertical lines identify the time instants at which the PIV runs were performed); (c-d) Tranverse profiles of the protrusion level P just before the PIV runs for Exp. 1b and 5b (the vertical lines identify the PIV planes).

(maximum P values). For Exp. 1b, Figures 2.16a & c show, furthermore, that for all three PIV measurements, the bed level in the trough region has reached a quasi-stable level, corresponding to the complete sheltering region identified in Section 2.3.4 ($P \geq P_{c3}$). However, the ridge in Exp. 1b, situated at y/W=0.22, is still evolving, as seen in Figure 2.16c. In the case of Exp. 5b (Figure 2.16b,d) the PIV planes are located over the ridge in the m-plane and over the trough in the q-plane. As for Exp. 1b, the bed is still evolving in the m-plane (ridge) while it has reached a stable bed level in the q-plane (trough) at t_2 and t_3.

In Figures 2.17a-f, the vertical profiles of the longitudinally and time-averaged streamwise and vertical velocities ($\langle \overline{u} \rangle_x$ and $\langle \overline{w} \rangle_x$) as well as the longitudinally-averaged profiles of the Reynolds shear-stresses ($\langle \tau_{uw} \rangle_x$ = -$\rho \langle \overline{u'w'} \rangle_x$) are plotted (recall that the z/H = 0 level corresponds to the top of the spheres). The horizontal dashed lines in Figures 2.17b,d & f for Exp. 5b represents the fine-sediment bed level during the first PIV run in the m-plane which was higher than the top of the spheres. This level was extracted from the PIV images.

Figure 2.17b (Exp. 5b) shows that while the streamwise velocity profile over the ridge (m-plane) displays the maximum velocity at the water surface, the velocity profile over the trough (q-plane) is characterized by a velocity dip. This is consistent with the observation in Figure 2.17d, that over the ridge upflow takes place and over the trough downflow. Similar patterns in streamwise and vertical velocity were observed to develop on ridges and troughs, both artificial and natural, as the result of counter-rotating secondary flows (Nezu and Nakagawa, 1984, 1989; McLelland et al., 1999; Vanderwel and Ganapathisubramani, 2015). In Figure 2.17d, the vertical location of the velocity dip is observed at about 70% of the water depth for all three PIV runs. The position of the velocity dip remains constant throughout the PIV runs as the downflow over the troughs does not change. On the other hand, the maximum velocity observed at the water surface over the ridge increases with time, since the vertical velocity decreases. It has been observed by studies over fixed ridges (Nezu and Nakagawa, 1984; Willingham et al., 2014; Vanderwel et al., 2017) that the upflow advects low momentum budgets to the water surface, reducing locally the velocity and vice versa.

Figure 2.17d also reveals that the upflow over the ridge is stronger than the downflow over the trough. In agreement with this, it can be seen in the transverse bed topography profile (Figure 2.16d), that the width of the trough is wider than the one of the ridge, so that per continuity the downflow needs to be less strong than the upflow. While the downflow reaches a maximum value equal to 2% of the maximum streamwise velocity, the upflow is observed to reach values as high as 6% during t_1, i.e. three times stronger than the downflow. This upflow value is much higher than the ones observed for secondary flows developing in a rectangular open-channel over a smooth bed (Nezu and Rodi, 1985) or in the case of ridges developing over uniform or weakly bimodal sediment (Nezu and Nakagawa, 1989; McLelland et al., 1999), where maximum values of 1.5-3% were observed. Here,evidently, the secondary flows are not only driven by the bed topography, but also by the associated lateral roughness heterogeneity though the lateral variation in P, which was also found to influence the intensity of secondary currents in the case of longitudinal stripes of different roughness (Naot, 1984; Willingham et al., 2014).

The signature of secondary currents can be also observed in the case of Exp. 1b. Figure 2.17a shows that the dip phenomenon takes place both in the m- and q-plane, consistent with the downflow taking place over both planes positioned over the trough (see Figure 2.17c). In the m-plane, the double-averaged streamwise-velocity profiles increase over time as the result of the reduction in downflow observed in Figure 2.17c. Figure 2.16c shows that, even though locally the bed level does not change over the trough, the ridge positioned at y/W = 0.2 decreases over time. As seen for Exp. 5b, a decrease in the ridge height is associated with a decrease of the intensity of the secondary currents. Considering that the interridge spacing was found to scale with 1.3
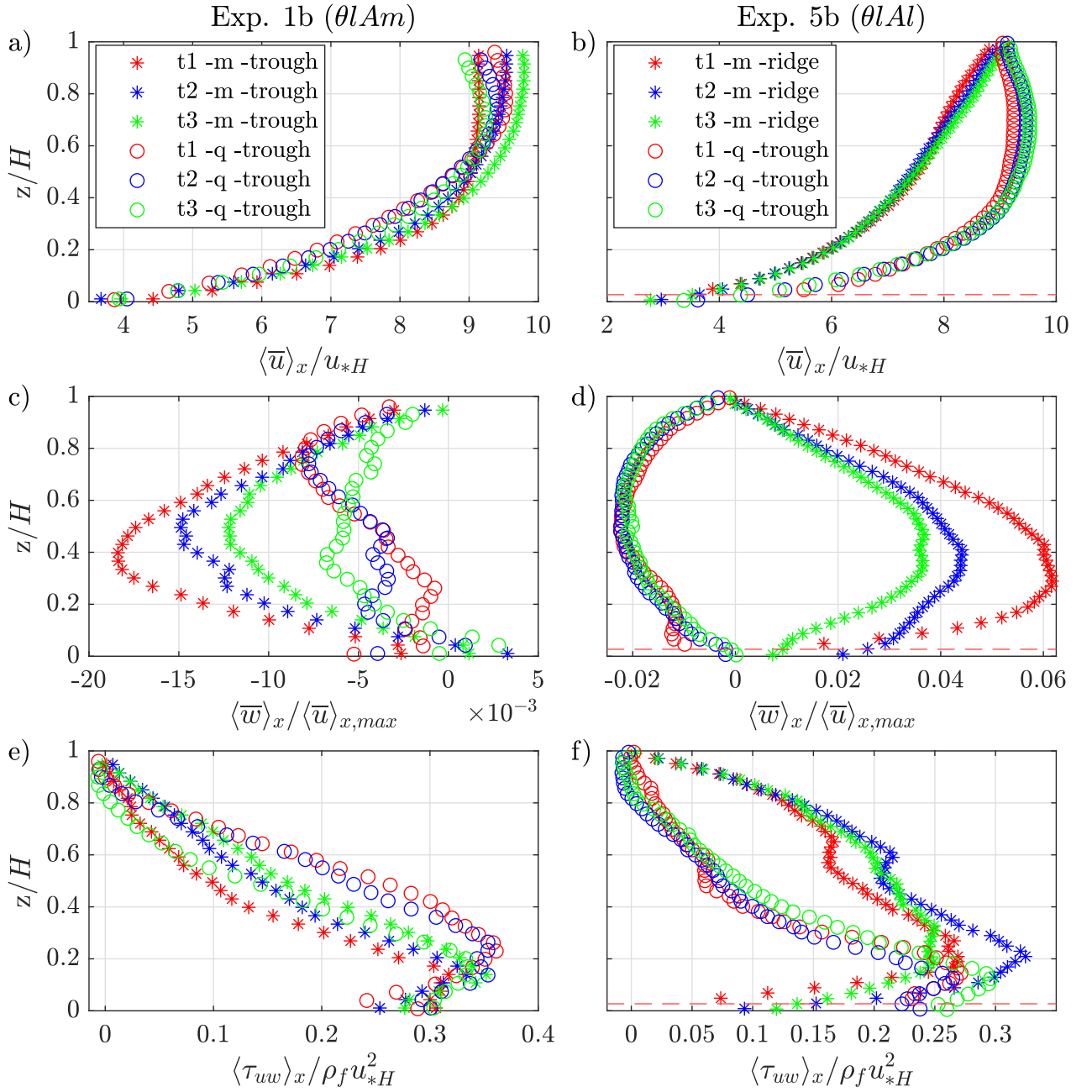
Figure 2.17: Vertical profiles of the double-averaged streamwise velocity $\langle\overline{u}\rangle_x$ (a-b) and vertical velocity $\langle\overline{w}\rangle_x$ (c-d) and of the longitudinally-averaged Reynolds shear stresses $\langle\tau_{uw}\rangle_x$ for Exp. 1b and 5b for both the middle and the quarter plane. $\langle\overline{u}\rangle_x$ and $\langle\tau_{uw}\rangle_x$ are normalized by the shear velocity obtained from the slope-water-depth product u_{*H} and $\langle\overline{w}\rangle_x$ by the maximum double-averaged streamwise velocity $\langle\overline{u}\rangle_{x,max}$. The dashed red line in the plots of Exp. 5b represents the fine sediment bed level during the first PIV run at the middle plane.

H_e, which in the case of Exp. 1b corresponds roughly to $0.2\,W$, the distance between the middle plane and the ridge corresponds exactly to half this length, i.e. to the size of the secondary current cell influenced by the ridge. It is therefore highly likely, that the decrease in downflow over the middle plane for Exp. 1b is related only to the decreasing ridge height.

The normalized longitudinally-averaged Reynolds shear-stress profiles, shown in Figures 2.17e-f, are not linear as in uniform and steady 2D open-channel flows. In the case of Exp. 5b (Figure 2.17f) the Reynolds shear-stress profile is convex in the q-plane where downflow takes place and concave where upflow takes place (Figure 2.17h), in accordance with previous studies on fixed ridges (Nezu and Nakagawa, 1984; Wang and Cheng, 2005). The peak in shear stress is not observed at the level of the roughness crests, but it is displaced upwards. Over the ridge, the upflow induces an upward shift of the peak of the shear stress profile at a level equal to 20% of the water depth, while over the trough the peak is pushed towards the level of the roughness crests by the downflow. While previous studies over smooth fixed ridges (Nezu and Nakagawa, 1984; Wang and Cheng, 2005) have not observed the presence of a peak in the shear stress profiles above the bed, this has been attested in the case of secondary flows developing over rough beds with high aspect ratio (Albayrak and Lemmin, 2011). The work of Albayrak and Lemmin (2011) shows the presence of a peak at 20% of the water depth for both the upflow and downflow locations. The difference in peak location between upflow and downflow observed in here could be related to a higher intensity of the secondary currents compared to the work of Albayrak and Lemmin (2011).

In the case of Exp. 1b, the Reynolds shear-stress distribution profiles are measured only over the trough. In the m-plane, they display typical convex shapes (Figure 2.17e), associated with the downflow. The convexity is less pronounced and limited to $z/H > 0.6$ for the Reynolds shear-stress profiles measured in the q-plane, where the downflow is weaker compared to the m-plane.

Near the roughness elements for $z/H \lesssim 0.1$, the Reynolds shear-stress is influenced by the bed roughness with, accordingly, higher turbulent shear stress values over the trough than over the ridge, as seen in Figure 2.17f for Exp. 5b when both ridges and troughs are measured. Since P is lower for a ridge than for a trough, it is indeed smoother than a trough. The differences in shear stress between the ridge and the trough are also in good agreement with the higher erosion rates observed over the ridges than over the troughs in Section 2.3.4.

The local shear velocity u_* acting at the spheres' top is determined on the basis of the total fluid shear stress τ_{xz} (i.e. the sum of the double-averaged viscous shear stress, of the spatially-averaged turbulent shear stress and of the form-induced stress (e.g. Nikora et al., 2001)) at the top of the roughness, $u_* = \sqrt{\tau_{xz}/\rho_f}$. Figures 2.18a and b show the evolution of the shear velocity, normalized by the shear velocity obtained from the water depth u_{*H}, as a function of P in the m- and q-plane for Exp. 1b and Exp. 5b, respectively. Reflecting the observations made with the Reynolds stress profiles, the shear velocites are higher for troughs than for ridges. It can also be observed that u_* is just 30-50% of u_{*H}, which represents the total momentum exchanged by the flow at the top of the spheres. This reduction can be explained by considering that in the presence of secondary flows, the gravitational force is not only balanced by the total fluid shear stress, but also by the convective and the transverse shear stresses (Nezu et al., 1993). As such, the total fluid shear stress measured at the spheres' top in the presence of secondary currents does not match the total shear stress u_{*H}, as also observed by Coleman et al. (2007) for secondary flows developing over transverse bars.

In the case of Exp. 5b, Figure 2.18b shows furthermore that with increasing protrusion level, the local shear stress u_*/u_{*H} increases both over the ridge and the trough. The same behaviour is observed in the case of Exp. 1b (Figure 2.18a) with u_*/u_{*H} increasing with increasing P over the q-plane and slight changes of u_*/u_{*H} over the m-plane where P does not change.

These changes in local shear stress can help to further explain the changes in vertical velocities observed earlier for Exp. 5b and connect them to changes in the lateral roughness gradient. Figure 2.18b shows that
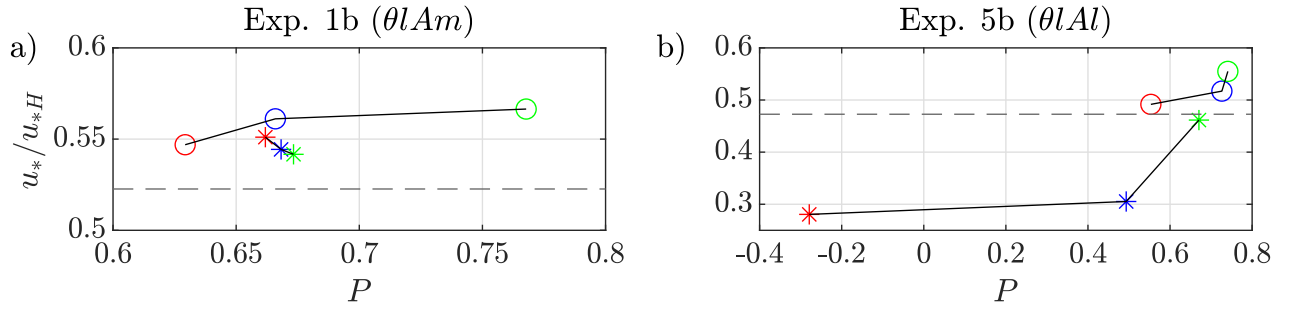
Figure 2.18: (a-b) Shear velocity acting at the top of the roughness u_* normalized by the shear velocity obtained from the slope u_{*H} as a function of the local protrusion level P. The colors and symbols are equivalent to the ones used in Figure 2.17 ($\star$ are ridges, $\circ$ troughs). The horizontal dashed line represents the threshold of motion for the mobile sediments.

in Exp. 5b over the ridge (m-plane) the shear velocity is constant between t_1 (red star) and t_2 (blue star), while the protrusion level increases (i.e. the ridge decreases in height). Therefore, the reduction in the upflow over the ridge, observed in Figure 2.17d, can be initially ascribed to a change in the shape of the ridge. Then, between t_2 (blue star) and t_3 (green star) there is a significant increase in the shear velocity over the ridge with only a mild increase in P, so that the further reduction in upflow between t_2 (blue star) and t_3 (green star) in Figure 2.17d can be ascribed to the decreased lateral roughness variability seen in Figure 2.16d. Indeed, at t_3 the shear velocity of the trough and of the ridge are similar, so that the upflow and downflow are of the same order (see Figure 2.17d). Over the trough, the shear velocities and protrusion levels are quite constant (Figures 2.18b and 2.16d, respectively), so that the downflow does not change. In summary, the shear velocities show that the intensity of the secondary currents over ridges are influenced primarily by variations in the ridge height (i.e. in their aspect ratio, since their width is constant - see section 2.3.3), which persist also when the ridges are embedded within the roughness, and second by lateral variations in roughness.

The expected normalized critical shear stress for the onset of motion given by the Shields diagram for uniform beds is included in Figures 2.18a-b by a dashed line. For Exp. 1 (Figure 2.18a), it is observed that the local shear stress above the troughs is above the threshold of motion for t_1, t_2 and t_3 even though the bed has reached a quasi-constant protrusion level (Figure 2.17a). The same can be observed in Figure 2.18b for the troughs in Exp. 5b. This reveals the sheltering effect of the protruding spheres, as the spheres extract momentum from the flow, they reduce the shear stress acting on the fine sediments (Raupach, 1992; Yager et al., 2007; Papanicolaou et al., 2012; Raus et al., 2019).

For the ridge in Exp. 5b (Figure 2.18b), on the other hand, at times t_1 and t_2 in particular, the Reynolds shear-stress at the spheres' top is below the threshold, i.e. no erosion would be expected. Yet, the ridge is eroding, as seen in Figure 2.16b. At t_1 though, P is negative over the ridge, i.e. the spheres are covered by grains, so that the measured shear stress acts directly on the fine sediment. Since there is no possible shear enhancement in this case as within the canopy, the erosion is likely connected to strong turbulent events impacting the bed, whose contribution in the time-averaging of the Reynolds shear stress is averaged out. To pursue this conjecture, a quadrant analysis is performed in the next Section.

2.4.1 Quadrant Analysis over the Ridges and the Troughs

A quadrant analysis is performed for Exp. 5b both in the middle and in the quarter plane for the time instants t_1 and t_3. Quadrant analysis decomposes the Reynolds shear stress in the contributions from different turbulent events, identified in the u'-w' plane (Lu and Willmarth, 1973; Raupach, 1981). Each quadrant in the u'-w' plane is associated with an event: Q1-outward interaction ($u' > 0$, $w' > 0$), Q2 - ejections ($u' < 0$, $w' > 0$), Q3-inward interactions ($u' < 0$, $w' < 0$) and Q4-sweep ($u' > 0$, $w' < 0$). The time fraction of the ith-quadrant event and its contribution to the Reynolds shear stress at a single point in space is given by:

$$T_{i,H_s} = \frac{1}{T} \int_0^T I_{i,H_s} dt \tag{2.4}$$

$$\overline{u'w'}_{i,H_s} = \frac{1}{T} \int_0^T u'w'(x,z,t) I_{i,H_s} dt \tag{2.5}$$

where T is the sampling duration and I_{i,H_s} the indicator function. Consistent with a double-averaged framework, the indicator function is defined on the basis of the double-averaged shear stress $\langle \overline{u'w'} \rangle_x(z)$, as in (Mignot et al., 2009b):

$$I_{i,H_s} = \begin{cases} 1, \text{ if } (u',w') \text{ is in quadrant } i \text{ and } u'w'(x,z,t) > H_s \langle \overline{u'w'} \rangle_x(z) \\ 0, \text{ otherwise} \end{cases} \tag{2.6}$$

where H_s is the hole size, which represents a threshold level for the identification of the turbulent events. Here, $H_s = 0$ is chosen, in order to consider all turbulent events. The analysis will mainly focus on the sweep events which have been suggested to be effectively responsible for sediment bed-transport (e.g. Nelson et al., 1995; Sechet and Guennec, 2000; Hofland et al., 2005).

Figures 2.19a-b illustrate the double-averaged profiles of the intensity of the Reynolds shear stress components $\langle \overline{u'w'}_{i,0} \rangle_x / T_{i,0}$ over the ridges and troughs, respectively. Figure 2.19a shows that at time t_1, the intensity of the sweeps over the ridge is higher than the intensity of the ejections for z/H < 0.25, while the opposite is true for z/H > 0.25. At the time t_3, the extension of the region dominated by sweeps reduces to a height z/$H \simeq 0.15$, likely as the result of the reduction in the upflow (see Figure 2.17d). At both times, the vertical extent of the region dominated by sweeps is much higher than the one observed over flat rough beds, presumably without secondary currents, which extends at most up to 5% of H (Raupach, 1981; Mignot et al., 2009b; Dey and Das, 2012; Sarkar et al., 2016).

Figure 2.19a further shows that over the ridge, the contribution of sweeps and ejections to the total Reynolds shear stress follows the same vertical trend: the sweep and ejection profiles increase up to z/$H \simeq 0.2$-0.3 and then decrease. This is in contrast with the results over a flat gravel bed by Mignot et al. (2009b) and Dey et al. (2012), where the contribution of sweeps and ejections peaks near the top of the roughness. The displacement of the peak in sweep intensity can be attributed to the upflow conditions dominating over the ridges. As a result, the near bed-region is characterized by more quiescent sweeps, with an intensity slightly higher than the critical shear stress conditions defined by the Shields diagram for permanent grain movement, indicated by a vertical dashed line in Figure 2.19a. As such, at t_1, when the ridge is higher than the top of the spheres (Figure 2.16b), intermittent sediment transport is possible, even though the average shear stress $\langle \tau_{uw} \rangle_x$ is below the threshold of movement (Figure 2.17f). At t_3, the intensity of the sweeps near the bed slightly
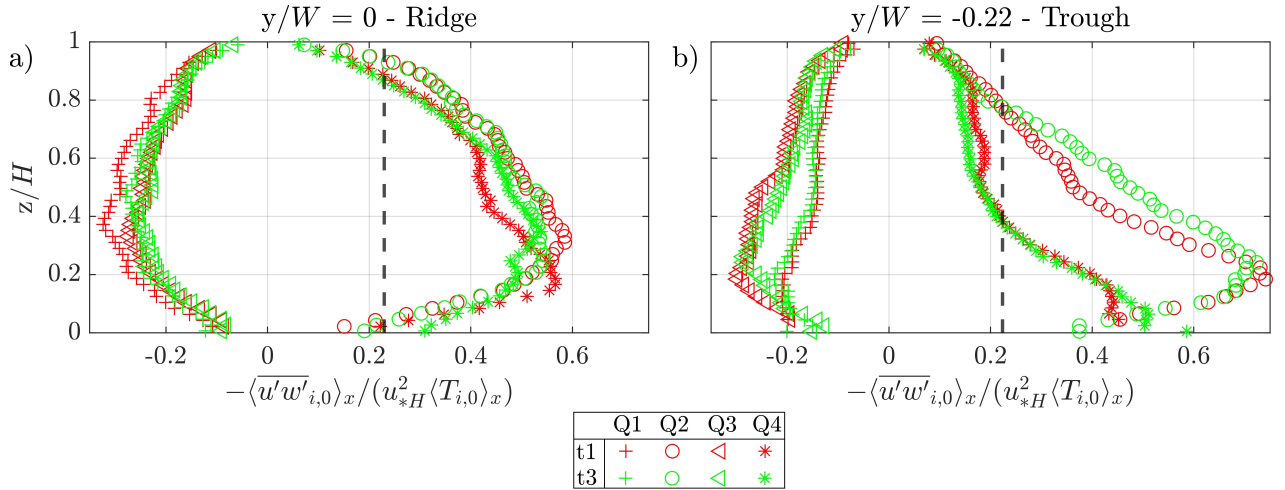
Figure 2.19: Longitudinally-averaged profiles of the intensities of the shear stress contributions $\langle\overline{u'w'}_{i,0}\rangle_x/\langle\overline{T}_{i,0}\rangle_x$ of the turbulent events for Exp. 5b over the ridge (a) and the trough (b). The vertical dashed line represents the critical conditions of motion.

increases, due to the protruding spheres, but the erosion is suppressed as the protrusion levels $P_{c2} < P < P_{c3}$ correspond to the wake-interference sheltering regime.

Over the troughs, Figure 2.19b shows that the sweeps dominate the shear stress production over a narrow region near the top of the spheres for $z/H < 0.05$. Since the intensity of the downflow does not change between the time instants t_1 and t_3 (Figure 2.17d), the sweeps and ejections profiles are similar and the transition takes place at the same height. Compared to the ridge, the downflow causes the region dominated by sweeps to vertically reduce. The turbulent structure near the bed is, as such, similar to the one observed over flat rough beds (Mignot et al., 2009b; Dey and Das, 2012; Sarkar et al., 2016).

Figure 2.19b further shows that the contribution of the sweep events presents a peak near the bed, while the contribution of the ejections reaches a maximum at $z/H = 0.2$. Compared to the ridge, which shows a peak in sweep intensity of similar magnitude higher above the bed (Figure 2.19a), the downflow over the troughs displaces the peak near the bed, causing higher erosion rates compared to the ridge. The intensity of the sweeps over the troughs is indeed consistently higher than the critical condition of motion (Figure 2.19b). However, the fine sediments in the troughs at t_2 and t_3 are essentially not eroding anymore, highlighting again the strong sheltering effect of the protruding spheres in the skimming flow regime ($P > P_{c3}$ at t_2 and t_3 over the trough).

2.5 Conclusion

The erosion of an initially uniform fine-sediment bed covering a rough bed composed of immobile spheres under sediment-supply limited conditions has been analysed by topographic and PIV measurements to assess the influence of the immobile roughness on the erosion rates and morphodynamics of ridges expected in sediment-supply-limited systems. The results show that, as the fine-sediment bed levels decrease, after exposing the spheres with a consequent reduction of the area covered by fine-sediments, a transition between three-dimensional reach-spanning dunes to two-dimensional longitudinal ridges takes place as observed by Kleinhans et al. (2002). However, the transition does not take place abruptly, rather, a superimposition of the

two types of bed-forms is observed, with ridge-like sediment structures developing in the tails of the dunes. While the dunes are quickly washed out, the ridges shape the bed topography over longer periods of time, including after the sediment bed erodes below the spheres' top. Once the dunes disappear, the sediments are preferentially winnowed from the bed troughs. Then, the erosion in the troughs reduces significantly within a few hours, much faster than the ridges so that the ridges become the main sediment source. The ridges persist for days before eventually disappearing, reaching the same stable bed level as the troughs, thus leading to a uniform bed level and roughness. For the broader purpose of fine-sediment decolmation from a clogged gravel bed, this study suggests that the presence of ridges can locally slow down the process, but eventually the fine-sediments are eroded to a uniform sediment bed.

In their initial development phase after the dunes disappear, the ridges meander in the transverse direction. This meandering can be associated with the ridge-formation process identified by Scherer et al. (2022) for a uniform fine-sediment bed in an infinitely wide-channel, by which the alternation of meandering large-scale high- and low-velocity streaks induce regions of high- and low shear stress. While Scherer et al. (2022) observed a continuous rearrangement of the ridges over time, here, the ridges stabilize after a few hours at a given lateral position. Evidently, the presence of side-walls helps to stabilize the ridges, consistent with the observations of Nezu et al. (1988); McLelland (2013); McLean et al. (1999).

The lateral position of the ridges is shown to correspond to an inter-ridge spacing of 1.3 effective water depths (H_e), which corresponds to the theoretically derived transverse ridge wavelength (Λ_{Col}) by Colombini and Parker (1995), resulting from the interaction with the secondary currents induced by an initial bed perturbation. It is shown that the number of Λ_{Col} wavelengths (N_Λ) which fit into the effective width of the channel (W_e), determines the final number of ridges equal to $N_\Lambda - 1$. The effective width in turn, results from the reduction of the actual width of the channel caused by the side-wall accumulations. For the cases with a remaining fractional part higher than $0.5\Lambda_{Col}$, the development of secondary ridges is observed, but these are highly unstable and disappear over time. For a remaining fractional part less than $0.5\Lambda_{Col}$, no additional ridges are observed. Given that the studies of McLelland et al. (1999) and Scherer et al. (2022) without roughness find similar ridge spacings, it can be inferred that the presence of immobile roughness does not influence the lateral spacing of the ridges.

The ridge spacing can be associated to a maximum intensity of the secondary currents as well as to a maximum friction factor. With regard to the maximum intensity, recent experimental and numerical studies by Vanderwel and Ganapathisubramani (2015) and by Hwang and Lee (2018) observed that by varying the lateral spacing of immobile artificial ridges, the strongest secondary flows developed for a ridge spacing equal to 1.18 boundary layer thickness δ (with no other spacings tested between 1.18 and 1.76 δ). In a similar manner, an experimental wind tunnel study by Wangsawijaya et al. (2020) over heterogeneous roughness stripes, identified the strongest secondary flow for spacings of 1.24δ. These spacings are close to the ones observed here. With regard to the maximum friction factor, Zampiron et al. (2020a) observed that by varying the width and the height of fixed ridges, the peak in friction factor occurs for ridge spacings comprised between 1.1 and 1.6 water depths. In this sense, the naturally-developing lateral wavelength of 1.3 H observed herein, corresponds to a ridge spacing for the maximization of both the intensity of the secondary currents and of the energy dissipation of the system. As hypothesized by Davies and Sutherland (1983), channels have a tendency to self-adjust their geometry to achieve the maximum friction factor.

The morphological evolution of the ridges is characterized by an initial rapid increase of the ridge's height

and side-slopes and by a decrease of the ridge's width. These three factors lead to increased lateral roughness heterogeneity (see P levels, Figure 2.7) and to a triangular cross-section (see Figure 2.9). This, in turn, leads to increased strengths of the secondary currents as studies on artificial ridges and roughness stripes have shown (Willingham et al., 2014; Hwang and Lee, 2018; Wang and Cheng, 2006; Medjnoun et al., 2020). Thus, it can be deduced that a self-enhancing mechanism exists in which the increased secondary currents induce higher shear stresses over the troughs leading to higher ridge heights and increased lateral roughness variation - enhancing in turn the secondary currents. Eventually, though, the height and the slope values of the ridge reach a plateau, implying that both ridges and troughs erode at the same rate. After this plateau, once a stable bed level is reached in the troughs, the ridges' height and side slope continue to decrease. The width of the ridges is found, instead, to reach a constant value after its initial decrease.

The secondary flows are affected by the ridges not only when they are elevated compared to the surrounding immobile roughness, but also when they are recessed. With embedded roughness elements, the ridges influence the secondary flows via both topographical and roughness variations. For low protrusion levels of the spheres over the ridges ($-0.2 < P < 0.4$), changes in the intensity of the secondary flow are mainly related to changes in the ridge height while the local roughness remains unaltered. On the contrary, for high protrusion levels ($P > 0.4$) the secondary flow is affected mainly by changes in the lateral roughness heterogeneity. The decrease in the ridge height for low P and the decrease in the lateral roughness heterogeneity for high P induce a reduction of the upflow over the ridge and an increase in the streamwise velocity at the water surface.

At the roughness scale, higher erosion rates are observed over the troughs than over the ridges. This difference in erosion rates is due to increased and decreased sweep events at the top of the canopy. The trends in erosion rates are similar though. The erosion rates are dominated by changes in the protrusion levels of the spheres, rather than changes in the area covered by fine-sediments, whose effect is just to dampen the erosion rates without modifying the trends. Both for the ridges and the troughs, four erosive regimes were identified for increasing protrusion levels of the spheres, with an alternation of erosion reducing (sheltering) and enhancing conditions. An initial drag sheltering regime is identified when the spheres start to protrude, characterized by decreasing erosion rates resulting from the increased drag of the protruding spheres. A second turbulence enhancement regime, characterized by increasing erosion rates, is identified for protrusion levels for which a horseshoe vortex or a shear layer are surmised to develop, in accordance with literature results on the necessary geometric conditions for the formation of horseshoe vortices and shear layers. A subsequent reduction in erosion rates is observed and identified as a wake-interference sheltering regime. The final regime, characterized by negligible erosion rates, was identified as a skimming-flow sheltering regime. Over the troughs, the critical protrusion levels for the transition in erosive regimes are found to be independent of the Shields parameter and correspond to $P_{c1} \simeq 0.2$ (drag-sheltering $\rightarrow$ turbulence-enhancement regime), $P_{c2} \simeq 0.4$ (turbulence-enhancement $\rightarrow$ wake-interference sheltering regime) and $P_{c3} \simeq 0.7$ (wake-interference sheltering regime $\rightarrow$ skimming-flow sheltering regime). The critical protrusion levels can be associated with the geometry of the roughness elements. Specifically, P_{c1} corresponds to the angle of attack of the flow of 20° for which horseshoe vortices develop (Okamoto et al., 1977; Euler et al., 2014), P_{c2} to a planar density $\lambda_p \simeq 0.3$, for which the transition between isolated and wake-interference flow is observed and P_{c3} to a planar density $\lambda_p \simeq 0.5$, for which the transition between wake-interference and skimming flow occurs (Grimmond and Oke, 1999). Over the ridges, the first and second critical protrusion levels are observed for lower protrusion levels, probably due to the asymmetry of protrusion levels around the spheres at the ridge location.

While other experimental studies on fine-sediment erosion from a rough immobile bed deduce an increase in erosion rates when the immobile roughness elements start to protrude from the fine-sediment bed (Grams and Wilcock, 2007; Nickling and McKenna Neumann, 1995), this study clearly shows that the enhancement in erosion does not take place immediately after the spheres start to protrude, but only after the critical pro-trusion level P_{c1} is surpassed. This implies that if the shear stress conditions are low enough, the initial drag sheltering can lead to critical conditions of motion before P_{c1} is reached so that no further erosion of the bed is possible. On the other hand, if the shear conditions are high enough for the erosion to reach P_{c1}, the development of the horseshoe vortex or of the shear layer will guarantee that the erosion continues until the grains are sheltered again when the wake-interference regime kicks in (for $P = P_{c2}$). A minimum clean-out depth can be therefore defined by the level for which the flow changes its behaviour from isolated to wake interference at $P = P_{c2}$. The maximum clean-out depth is reached once $P > P_{c3}$ under skimming flow conditions. Raupach et al. (1980); Leonardi (2010); Placidi and Ganapathisubramani (2015) show that the transition from wake-interference to skimming flow condition for $P = P_{c3}$ is associated with the highest drag production, so that the average shear stress acting on the fine-sediments reaches a minimum. However, this does not guarantee that critical conditions of motion at the level of the fine-sediment bed are reached, once skimming flow conditions are reached, as seen for Exp. 2 and 3 with higher shear stress conditions where the bed continued to erode. Regardless of the driving shear stress, the skimming flow conditions for $P > P_{c3}$ imply a significantly reduced erosion rate. In other words, skimming flow conditions are a necessary but not sufficient condition for the bed to reach a stable sediment level.

Part II

Hydro- and morphodynamic interactions at the fine-sediment scale within an immobile coarse bed

3 Experimental methods

3.1 Introduction

The experimental methods applied in the first part of this work have allowed to connect the bed morphodynamics and the flow field at a macroscale level, highlighting differences in local erosive behaviour due to transverse changes in bulk flow statistics, measured above the roughness. Both the topographic system and the PIV system used, fail though to resolve the physical processes acting at the level of the fine sediment bed, both in terms of the microtopography developing around the immobile roughness elements (spheres) and of the near-bed shear stress conditions. Even though the topographic system used in Part I resolves the bed topography on a local scale, it allows only the measurement of a mean bed level around each sphere, so that the differences in bed levels, visually observed to develop in the stoss and the lee side of the spheres, cannot be resolved. In a similar manner, the planar PIV system is not able to resolve the flow field in the bed interstices due to restricted optical access.

In order to overcome these limitations, a new experimental setup is developed herein to reconstruct both the three-dimensional bed topography at a grain-scale level through stereo photogrammetry and the flow field in the bed interstices through stereo-PIV measurements. In the following the new experimental concept and apparatus is presented along with the validation of the experimental techniques applied.

3.2 Experimental concept

In the following experimental investigation, the impact of immobile roughness elements on the erosion of fine sediments on a local pattern scale is investigated not only by modifying the hydrodynamic forcings of the system (as done in Part I of this work), but also by changing the geometric characteristics of the immobile bed and of the sediments. The set of parameters investigated in Part I, which has focused mainly on the influence of the aspect ratio and of the Shields parameter on the development of ridges and on the local erosive behaviour of the fine sediment bed, respectively, is expanded to take also into account variations in the roughness density of the immobile bed and of the grain size of the mobile sediments. The focus is set, in the following, on the analysis of the influence of these flow and geometric parameters on the hydro- and morphodynamics at the pattern scale and not anymore on the flow and topographic patterns at the reach scale. As such, variations in the flow depth, which derived, in Part I, from variations in the aspect ratio for secondary-flow analysis purposes, will be associated to changes in relative submergence S_r of the immobile roughness elements (defined as the ratio of the water depth to a characteristic vertical size of the roughness elements). Changes in relative submergence have been shown to influence the intensity and the topology of the coherent structures shed by isolated roughness elements and, as a result, the obstacle mark geometry (Shamloo et al., 2001; Schlömer et al., 2020). Moreover, over rough beds, the relative submergence influences the boundary

layer structure (Jiménez, 2004; Nikora et al., 2004; Manes et al., 2007; Rouzes et al., 2019). It is still not clear, though, how variations in relative submergence influence the fine-sediment erosion and ultimately the clean out depth, when the immobile roughness elements act not as isolated elements but as part of a bed matrix. The roughness density of the immobile spheres is also varied, in order to analyse different flow conditions at the level of the bed, i.e. the isolated, the wake-interference and the skimming flow regimes. It has been shown, in fact, that the flow separation behind roughness elements and the coherent structures shed into the outer flow or towards the bed are deeply influenced by the spacing and the density of roughness elements (Hardy et al., 2010; Sutton and McKenna Neuman, 2008b; Papanicolaou et al., 2012; Fang et al., 2017). At the same time, the roughness density of the immobile roughness elements influences the resistance of the bed in terms of form drag exerted by roughness elements on the flow, influencing the grade of sheltering of the fine sediments (Raupach, 1992; Yager et al., 2007; Rickenmann and Recking, 2011; Papanicolaou et al., 2012; Placidi and Ganapathisubramani, 2015). Finally, the size of the fine mobile sediments is varied, in order to examine different flow conditions at the level of the fine sediments from transitional to quasi-laminar.

3.2.1 Bed and sediment properties

An immobile gravel bed is modelled in a similar manner as in the first series of experiments in Part I of this work, by using plastic spheres 2 cm in diameter (see Section 2.2.2). In Part I, the spheres were arranged only over one layer, which led to the complete erosion of the fine sediments for two flow conditions, due to the sediments gliding on the exposed flume bed. Furthermore, the volume of fluid potentially interacting with the surface flow is limited for a one-layered bed of spheres, rendering it similar to an almost impermeable bed compared to a bed composed of multiple layers of spheres (Manes et al., 2009). In order to create a permeable bed matrix closer to a natural gravel bed, the spheres are arranged, in this case, over two layers with a total thickness of 3.3 cm. The bottom layer of spheres is characterized by the same staggered symmetric pattern of
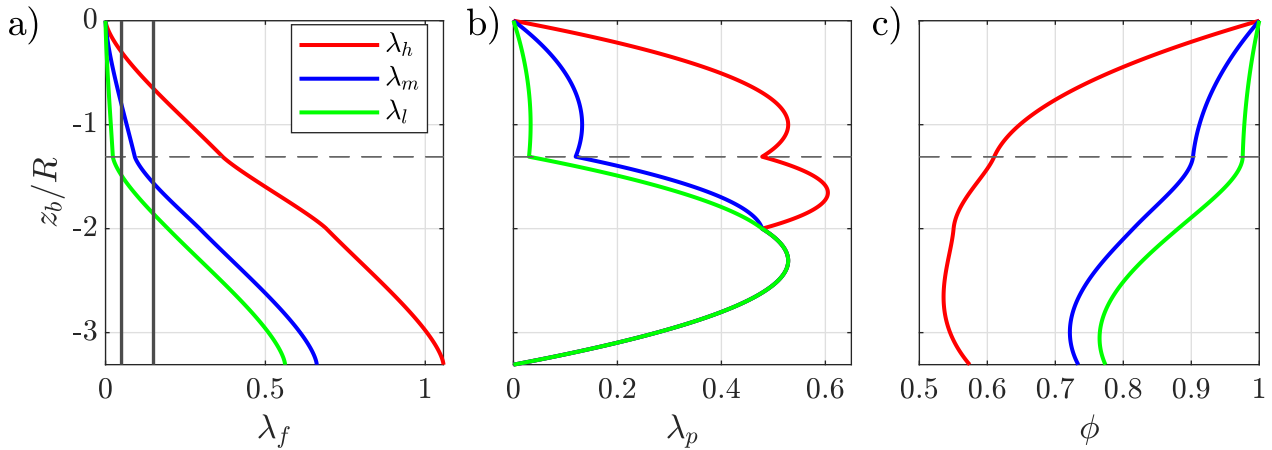
Figure 3.1: (a) Frontal density λ_f, (b) planar density λ_p and (c) bed porosity ϕ (= $\int_{-z_b}^{0}(1 - \lambda_p)dz$) for the three different bed configurations of spheres, so as if they were protruding above a flat fine-sediment bed at the elevation z_b. The horizontal dashed line identifies the top of the bottom layer of spheres; the vertical lines in Figure a identify the threshold values for the transition between the isolated and the wake-interference regime and between the wake-interference and the skimming flow regime, according to Raupach et al. (1991) and Hanna and Britter (2002)
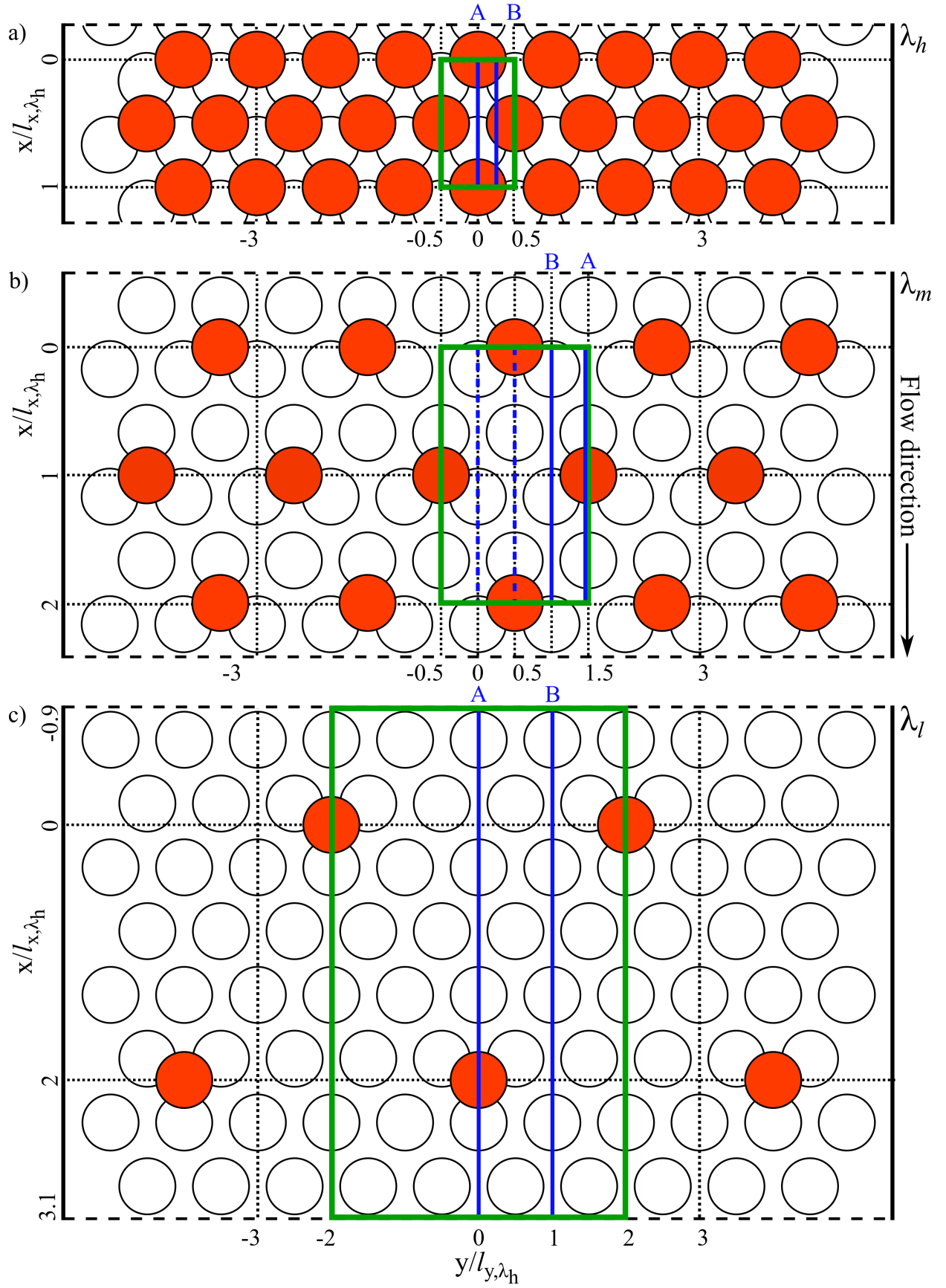
Figure 3.2

Figure 3.2 (*previous page*): Planar view of the bed configuration with the highest λ_h (a), intermediate λ_m (b) and low λ_l (c) roughness density of the top layer of spheres. The reference pattern over which the stereo photogrammetric and stereo-PIV measurements are performed, is highlighted in green and the PIV laser planes in blue. The dashed blue lines highlight additional PIV planes not analysed in this work. The x and y coordinates are normalized by the longitudinal l_{x,λ_h} and transverse dimensions l_{y,λ_h} of the reference pattern with the highest roughness density λ_h.

the the first series of experiments with a planar density of $\lambda_p = 0.528$ (calculated at the equator of the spheres) and is kept unaltered between experiments. The top layer of spheres is arranged, instead, in three different configurations with decreasing planar density (see Figure 3.2). The densest spheres' configuration λ_h, shown in figure 3.2a, is a replica of the spheres' configuration of the bottom layer, characterized by a reference pattern with a length l_x = 4.54 cm and a width l_y = 2.62 cm. The spheres' configuration with intermediate and low density, λ_m and λ_l (see Figures 3.2b and 3.2c), are characterized by a reference pattern twice and four times as big as the densest bed configuration λ_h, corresponding to planar densities λ_p = [0.13, 0.03], respectively. The reference frontal density λ_f (ratio of the frontal area A_f of the spheres exposed to the flow to the total reference pattern area A_r) of the upper layer of spheres for the three bed configurations λ_h, λ_m, λ_l, defined without considering the contribution of the second layer of sphere, is equal to λ_f = [0.53, 0.13, 0.03], respectively.

In order to fully characterize the three bed configurations, the vertical profiles of frontal density λ_f, of planar density λ_p and of bed porosity ϕ (= $\int_{z_b}^{0}(1 - \lambda_p)dz$) are presented in Figures 3.1a-c so as if the spheres were protruding from a fine sediment bed level position at an elevation z_b below the top of the spheres. The frontal density λ_f is the ratio of the frontal area of the protruding part of the spheres and of the total planar area of the pattern. The three bed configurations allow to reach skimming, wake-interference and isolated flow conditions in between the spheres at different sediment levels. Given that the transition between the isolated and the wake-interference regime and between the latter and the skimming flow regime is defined for values of frontal density λ_f = 0.05 and λ_f = 0.1-0.2 (Raupach et al., 1991; Hanna and Britter, 2002; Placidi and Ganapathisubramani, 2015), Figure 3.1a shows that, for the densest bed configuration λ_h, skimming flow conditions can be reached already within the top layer of spheres. For the bed configuration with intermediate density λ_m, the bed reaches transitional flow conditions between wake interference and skimming flow regime, when the top layer of spheres is fully exposed. For the

Figure 3.3: Grain size distribution and fitted lognormal cumulative density function of the sand; in the lower right corner a sample of the sand grains scattered over graph paper with 1 mm mesh size.

low density case λ_l, the top layer of spheres is always characterized by isolated flow conditions. The bed configuration with the lowest density is, in fact, characterized by a planar density $\lambda_p \simeq 5\%$ in the top layer of
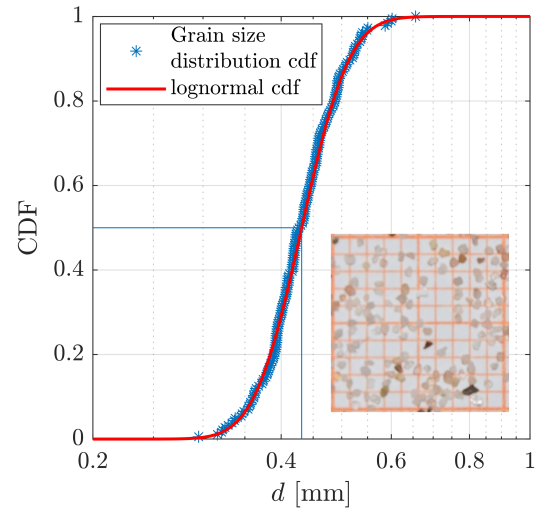
spheres, which can be found in nature in the case of isolated boulders.

Two different types of mobile sediments are used: plastic granulate and fine sand. The plastic granulate, already used in the first series of experiments in Part I, is characterized by a mean diameter of 1.72 mm and a specific weight of ρ_s = 1.49 g/cm^3 (see Section 3.2.1 for further details). The friction angle of the plastic granulate is also determined through a fixed funnel method yielding $\phi_f \simeq 35°$. The sand is characterized by a specific weight of ρ_s = 2.65 g/cm^3, by a mean diameter of 0.43 mm (determined on the basis of the inter-mediate principle axis of the grains obtained through image sampling, as done for the plastic granulate - see Section 3.2.1). The sand can be considered uniform, since the geometric standard deviation $\sigma_g = d_{84.1}/d_{15.9}$ = 1.15 is smaller than 1.4 (Dey, 2014). As done for the plastic granulate, it is ascertained through a test of Pearson that also the grain size distribution of the sand follows a lognormal cumulative density function (see figure 3.3). The friction angle of the sand is estimated to be $\phi_f \simeq 34°$.

3.2.2 Flow conditions

A total of 10 experiments are performed, in order to analyse the influence of 4 parameters, i.e. the Shields parameter θ, the roughness density of the bed λ_f, the relative submergence S_r [1] and the size of the fine sediments d_{50}, on the erosion of the fine sediments from the immobile bed of spheres. The flow parameters in Table 3.1 are defined by taking, as a reference condition, a uniform fine sediment bed with same thickness as the bed of spheres, as done in Part I (see Section 2.2.3). Accordingly, the reference water depth H is defined as the difference between the water surface and the top of the spheres (z = 0 cm plane). The reference shear stress conditions are defined on the basis of the integral momentum balance for a uniform flow and by applying the side-wall correction by Chiew and Parker (1994), yielding the average bed shear stress $u_{*R^c} = \sqrt{gR_h^c i}$ (where R_H^c is the hydraulic radius with side-wall correction). The shear velocities obtained by assuming an infinitely wide channel, i.e. $u_{*H} = \sqrt{gHi}$, and by assuming that the side walls are characterized by the same roughness as the bed $u_{*R} = \sqrt{gR_H i}$ (with R_H the hydraulic radius of the cross section), are also reported in Table 3.1, as they represent the lower and upper limit of the actual shear stress acting on the bed (Manes et al., 2007).

The flow conditions of the present set of experiments are defined on the basis of the flow conditions of the first series of experiments. The reference conditions represented by Exp. 1a in Table 2.1 are modified, in this case, as it was observed that these flow conditions applied to a two layered bed of spheres led to a higher erosion depth of the plastic granulate. In order to reach a comparable erosion depth as in Exp. 1a in Part I, a lower Shields parameter is adopted for the reference case of this set of new experiments, represented by Exp. 1 in Table 3.1. The experimental conditions of the other experiments are defined, then, by modifying each time one of the three reference parameters (θ, λ_f, RS or d_{50}) of Exp. 1. The name of the experiments in Table 3.1 highlights which parameter is modified each time (λ-, S_r- or θ-) with the corresponding magnitude (h-high, m-medium and l-low); R identifies experiments with shear stress conditions equal to the reference experiment 1 and G or S the type of sediments used, i.e. granulate or sand. Four groups of experiments are defined:

---

[1] The relative submergence is defined as the ratio between the water depth H and the diameter of the spheres $S_r = H/D$. Please note that it represents a reference conditions, as the protrusion level of the spheres increases during the experiments.

- **Exp. 1-3** (sediments used: granulate) characterized by decreasing roughness density λ_f of the top layer of spheres and by the same flow parameters as Exp. 1;

- **Exp. 4** (sediments used: granulate) characterized by a higher relative submergence S_r compared to Exp. 1 but similar shear stress conditions;

- **Exp. 5-7** (sediments used: granulate) characterized by values of the Shields parameter θ either tending to critical conditions of motion (Exp. 5 $G\theta l$ and 6 $G\theta m$) or to higher erosive conditions (Exp. 7 $G\theta h$) compared to the reference Exp. 1. The Shields parameter of experiment 7 corresponds to the Shields parameter of Exp. 1a in Part I;

- **Exp. 8-10** (sediments used: sand) characterized by the use of sand with varying shear stress conditions from almost critical ones (Exp. 8 $S\theta l$) to highly erosive ones (Exp. 10 $S\theta h$); the shear stress conditions for Exp. 8, 9 and 10 are defined so as to obtain the same non-dimentional sediment transport parameter θ - θ_{cr} (for the definition of the critical Shields parameter see Section 3.2.2.1), used in Exp. 5, 1 and 7 for the plastic granulate, respectively.

All experiments are performed under uniform flow conditions. The duration of the experiments is approximately 70 hours, long enough to reach a stable bed level. In Figure 3.4 the experimental conditions defined in Table 3.1 are located in the Shields diagram. The experiments 1-3 overlap as they are characterized by the same flow conditions. The experimental flow conditions for the plastic granulate are localized in the transitional regime ($10 < Re^* < 70$), while the ones for sand are in the quasi-laminar regime ($Re^* \simeq 10$).
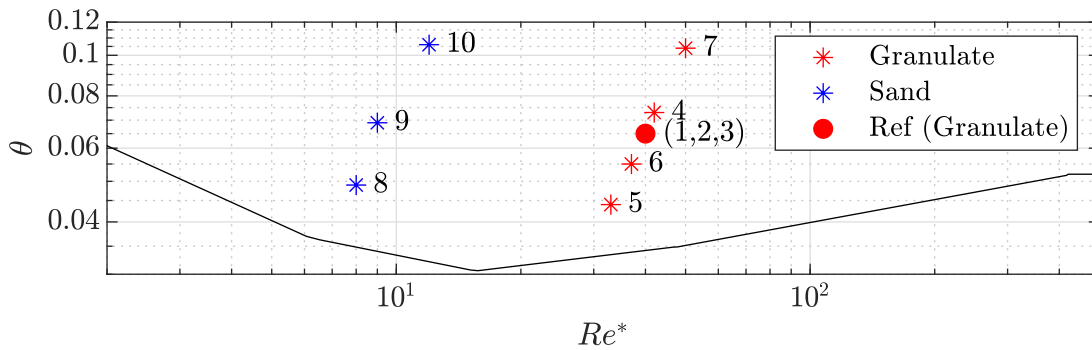

Figure 3.4: Shields diagram with the location of the experimental conditions listed in Table 3.1

Exp.		θ	λ_f	S_r	d_{50}	Q	i	H	U	R_h	u_{*R}	u_{*R^c}	u_{*H}	Re^*	Re	T_e
		[-]	[-]	[-]	[mm]	[l/s]	[%]	[cm]	[cm/s]	[cm]	[cm/s]	[cm/s]	[cm/s]	[-]	[-]	[h]
1	$R\text{-}G\lambda h$	0.065	0.53	2.9	1.72	4.5	0.11	5.8	26	4.18	2.1	2.3	2.5	40	15000	67
2	$R\text{-}G\lambda m$	0.065	0.13	2.9	1.72	4.5	0.11	5.8	26	4.18	2.1	2.3	2.5	40	15000	71
3	$R\text{-}G\lambda l$	0.065	0.003	2.9	1.72	4.5	0.11	5.8	26	4.18	2.1	2.3	2.5	40	15000	71
4	$R\text{-}GS_r h$	0.073	0.53	5.4	1.72	9.2	0.07	10.8	28	6.28	2.1	2.5	2.8	42	30600	70
5	$G\theta l$	0.044	0.53	2.9	1.72	3.8	0.08	5.8	22	4.18	1.8	1.9	2.1	33	12600	71
6	$G\theta m$	0.055	0.53	2.9	1.72	4.2	0.09	5.8	24	4.18	2	2.1	2.3	37	14000	70
7	$G\theta h$	0.104	0.53	2.9	1.72	5	0.17	5.8	29	4.18	2.6	2.9	3.1	50	16600	77
8	$S\theta l$	0.049	0.53	2.9	0.43	3.65	0.07	5.8	21	4.18	1.7	1.8	2	8	12200	88
9	$S\theta m$	0.069	0.53	2.9	0.43	4.4	0.1	5.8	25	4.18	2	2.2	2.4	9	14600	216
10	$S\theta h$	0.106	0.53	2.9	0.43	5.4	0.15	5.8	31	4.18	2.5	2.7	2.9	12	18000	68
		±0.008			±0.1	±0.5	±0.01	±0.05	±3	±0.1	±0.2	±0.2	±0.2			

Table 3.1: Hydraulic parameters of the experiments: Shields parameter $\theta = u_{*R^c}^2/(g\Delta d_{50})$, roughness density of the first layer of immobile spheres λ_f, relative submergence $S_r = H/D$, mean diameter of the mobile sediments d_{50}, flow rate Q, slope i, water depth H, bulk velocity $U = Q/(WH)$, hydraulic radius R_h, shear velocity based on the hydraulic radius $u_{*R} = \sqrt{gR_h s}$, shear velocity based on the hydraulic radius with side-wall correction $u_{*R^c} = \sqrt{gR_h^c i}$, shear velocity based on the water depth $u_{*H} = \sqrt{gHi}$, particle Reynolds number $Re^* = u_{*R^c}d_{50}/\nu$, bulk Reynolds number $Re = UH/\nu$, time duration of the experiments T_e.

3.2.2.1 Definition of the critical shear stress conditions for grain motion

The critical conditions for sediment motion are usually defined on the basis of the Shields diagram (Shields, 1936). However, the Shields diagram defines threshold conditions for which permanent particle movement is witnessed at all locations on a uniform bed (Rijn, 1993). This result stems from the fact that this critical condition was determined by Shields (1936) by back extrapolating the transport rates to zero sediment transport. Visual observations of transport rates by Graf and Pazis (1977) have shown, though, that grains move also below the critical conditions of motion defined by Shields in an isolated, localized manner as the result of localized turbulent events (Vanoni, 1964). In this sense, the critical shear stress by Shields defines an upper limit for the critical conditions of motion and is best taken as a reference for the definition of the sediment transport conditions (such as bed-load). The critical Shields parameter for the definition of the flow conditions in Table 3.1 was defined by the means of the explicit relationship by Wu and Wang (1999), which defines θ_c as a function of the particle parameter $D_* = d_{50}\Delta g/\nu^2$. The critical Shields parameters for the sand and the granulate are $\theta_{c,g} = 0.033$ and $\theta_{c,s} = 0.036$, respectively.

As shown in Part I of this work, the presence of protruding roughness elements on the fine sediment bed, lead to low intermittent movement of grains, so that the critical Shields parameter, just defined, does not represent a proper reference for the identification of shear stress conditions leading to the cessation of sediment transport. As such, a critical Shields parameter for the onset of motion $\theta_c{}'$ was determined by performing an experiment in the flume described in Section 3.3 with a flat uniform fine-sediment bed and visually assessing under which shear stress conditions occasional grain movement is observed. The threshold conditions for the onset of sediment movement were determined by incorporating in the fine sediment matrix also the bed of spheres with the highest density λh, since the flow conditions near the bed are also influenced by the hyporheic flow (Manes et al., 2009; Voermans et al., 2017), which depends significantly on the sediment matrix.

The bed was filled initially with sediments until a uniform layer of 2 sediment grains covers the top of the spheres. By maintaining a constant uniform flow with a water depth equal to 5.8 cm, the flow rate and the slope were increased until sporadic localized sediment movement was detected. The critical conditions were identified with a camera filming a bed area of $A = 20 \times 30$ cm^2, when the threshold non-dimensional number of moving particles per unit area and time $n = 10^{-5}$ (with $n = N d_{50}^3/(A t u_*)$), defined by Neill and Yalin (1969) as the condition for the onset of particle movement, was reached. 2D planar PIV measurements over a vertical plane in the center of the channel were performed, to determine the critical shear stress acting on the sediments by linear extrapolation of the Reynolds shear stress $-\rho_f \overline{u'w'}$ to the level of the fine sediments. The experiments were repeated for each sediment type three times to ensure reproducibility. The critical Shields parameter for the onset of motion for the plastic granulate and the sand were determined, in this manner, to be $\theta'_{c,g} = 0.021$ and $\theta'_{c,s} = 0.023$, corresponding to a critical shear velocity for the onset of motion $u'_{*c,g} = 1.33$ cm/s and $u'_{*c,s} = 1.27$ cm/s, respectively. These values are lower than the ones defined on the basis of the Shields diagram by about 30%.

3.3 Flume facility

The experiments are performed at the Institute of Hydromechanics in the water recirculating tilting flume 9 m long and 30 cm wide, used also in the first series of experiments in Part I (see Section 2.2.1). The inlet conditions are modified by adding a set of two vertical grids with an open area of 64% and a distance of 5cm (see figure 3.5) to reduce turbulence anisotropy and dampen large scale structures. The grids are designed on the basis of grid theory ensuring a total pressure drop coefficient K of 3.2 (Hancock and Johnson, 1997), yielding a water level drop less than 4 mm for the flow conditions analysed. Horizontal planar PIV measurements, performed at the beginning of the bed of spheres under the flow conditions of Exp. 1 (R-Gλh), show that low free stream turbulence levels less than 2.5% and homogeneous over the whole cross-section, effectively reach the rough bed (for further details see Appendix B). The transverse streamwise velocity profile shows a slight asymmetry, though, with a local velocity minimum in the centre of the channel slightly shifted by 5% of the channel width towards the right side-wall in streamwise direction. The velocity minimum suggests the presence of secondary currents already developing at the beginning of the channel.

In order to trigger an early development of the boundary layer an 80 cm long ramp inclined by 2.5° and covered with glued fine sediments is installed just before the immobile bed of spheres (see figure 3.5). The downstream end of the ramp is not flush with the top of the spheres, as in Part I of this work, but it is 3 mm below the top, in order to break up the shear layer developing at the edge of the ramp through the presence of the spheres and reduce the localized erosion. Vertical PIV measurements, performed at the transition between the ramp and the bed of spheres with no fine sediments present, show that the ramp triggers the development of an outer boundary layer with a thickness of 0.2 H at the end of the ramp, while an internal boundary layer develops over the spheres (for further details see Appendix C). The internal boundary layer, even though not yet fully developed at the beginning of the bed, is characterized by a roughness sublayer displaying shear stress conditions comparable to the fully developed flow already three reference patterns lengths (l_{x,λ_h}) downstream of the leading edge of the ramp. A uniform erosive behaviour is, as such, expected over the whole length of the flume. Extrapolation of the outer and inner boundary layer depths to the water surface, predict that the flow reaches full development 3 m downstream of the ramp. For this reason, the measurement

location is set 5 m downstream of the ramp (see Figure 3.5).

The reference system is located 5.7 m downstream of the inlet on top of the spheres: the origin of the streamwise x-axis is located one pattern length l_{x,λ_h} downstream of the leading edge of the boat used for the stereo-PIV measurements (see Section 3.4.1.2), the transverse y-axis is centred in the middle of the channel and oriented according to the right-hand rule and the vertical z-axis originates on top of the layer of spheres (see Figure 3.5).
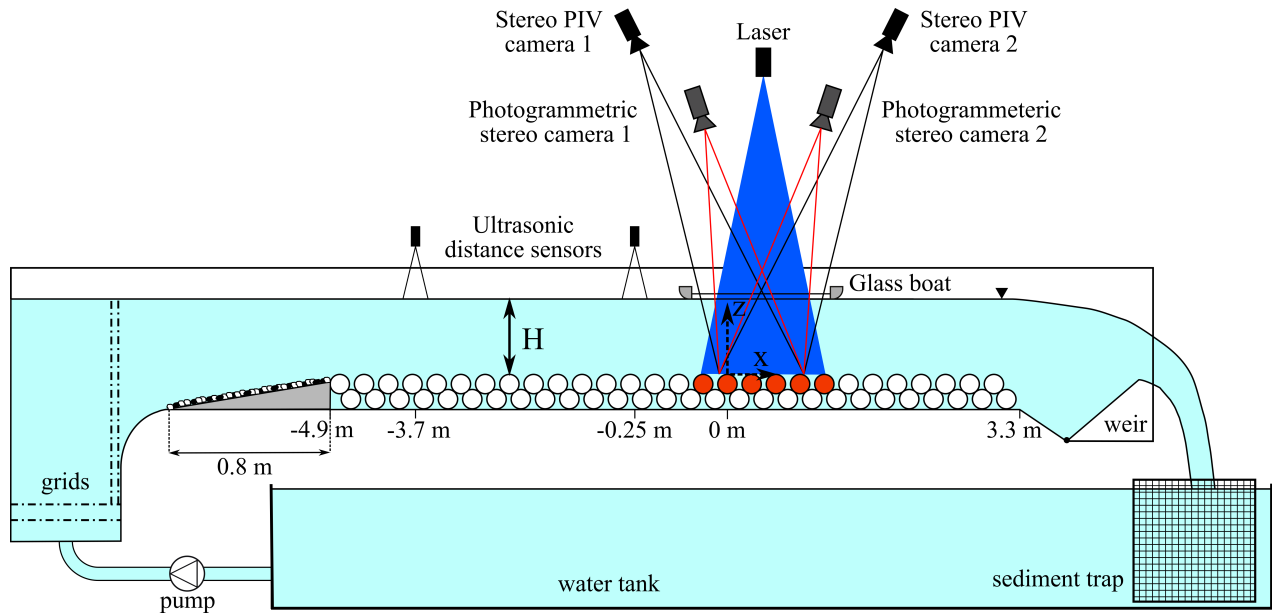
Figure 3.5: Experimental setup

3.3.1 Experimental protocol

The initial bed conditions, common for all experiments, are created by first filling the immobile bed of spheres with water up to 1 cm above the top of the spheres. The fine sediments are, then, slowly poured into the water-filled immobile-bed matrix, in order to create a fully saturated fine sediment layer with no air inclusions with a thickness of 4.3 cm, i.e. 1 cm above the top of the spheres (as done in the first series of experiments - see Section 2.2.2). The bed is mechanically screeded with a plastic plate to define reproducible initial conditions and reduce roughness anisotropies. At the beginning of the experiments the flume is first filled with water to reach the desired water surface elevation. The flow rate is then carefully increased to the working conditions, in order to avoid an abrupt flushing of the sediments.

The flume is run under sediment supply limited conditions, so that the fine sediments are gradually evacuated from the flume during the experiment. The sediments are collected in an underlying sediment trap, installed in the water tank (see figure 3.5).

During the experiments two ultrasonic distance sensors with a vertical resolution of 0.5 mm, installed 1.2 m and 4.65 m downstream of the inlet ramp (see figure 3.5), monitor the water levels with a frequency of 1 Hz, in order to ensure uniform flow conditions and guarantee that the water surface is always in contact with the glass plate needed for the PIV and topographic measurements through the water surface (see Section 3.4.1.2).

Since the roughness of the bed increases over time, while the spheres protrude from the fine sediment bed, the water levels remain almost constant throughout the experiment, so that slight corrections of the water surface elevation are needed in the range of $\pm$ 0.5 mm.

3.4 Measurement techniques

The tight coupling between the highly heterogeneous flow field in the roughness-elemnt region and the local morphodynamics of the fine sediment bed, gives rise to the challenging need of investigating the flow field and the bed morphology simultaneously and at the same location. To this end, a stereo-PIV system and a stereo photogrammetric system are collocated at the measurement section 5.8 m downstream of the inlet (see Figure 3.5). The experimental setup developed is one of a kind, as it tackles the challenge of resolving the flow field in between roughness elements, which still represents a constraint for most measurement techniques (such as ADV, LDA and PIV), while simultaneously measuring the bed topography and the sediment transport. In the following, the experimental setups, the calibration procedures of both measurement techniques are presented.

3.4.1 Stereo particle image velocimetry

Particle image velocimetry (PIV) has been increasingly used in the last decade to study open-channel flows over smooth and rough beds in the laboratory, as it is a non-intrusive technique, offering spatially and temporally resolved measurements of the turbulent flow. Over rough beds, 2D planar and 2D3C stereo-PIV systems have been successfully applied to measure the flow above the bed (e.g. Manes et al. (2007); Mohajeri et al. (2015) and Akutina et al. (2019); Rouzes et al. (2019), respectively). However, impaired optical access and laser reflections on the bed hamper the investigation of the flow in the interstices between the roughness elements. Solutions to overcome these shortcomings have been found for relatively simple bed configuration composed of cubes: Florens et al. (2013) used a planar PIV system with "spy cubes" with embedded mirrors to visualize the flow in the obscured bed interstices, while Chagot et al. (2020) used a telecentric optical arrangement with transparent cubes. Unfortunately, this type of approaches is not feasible, when the immobile bed matrix is filled with sediments, as in the present case. To measure the flow field in the two-layered bed of spheres with the presence of eroding grains, horizontal PIV imaging approaches would necessitate of refractive index matching (RIM) of the bed elements and the fluid (e.g. Voermans et al. (2017); Kim et al. (2020); Rousseau and Ancey (2020)). RIM is hampered, though, by complexity, costs and inadequate flow scaling. In order to avoid this, the flow is imaged herein from above, requiring (i) a stereoscopic PIV approach to assess the strong out-of-plane velocity component, (ii) a method to reduce strong laser reflections at the bed, (iii) a window on the free surface to eliminate distortions due to water surface irregularities. These three aspects are discussed in the following.

3.4.1.1 Principles of stereo-PIV

Stereo particle image velocimetry is based on the same working principle as 2D2C planar PIV, which consists in measuring the flow field in a plane by recording the displacement of neutrally buoyant suspended tracer-particles over a short time interval. The main difference in the two measuring systems is represented by

the number of views visualizing the flow. Conventional 2D2C planar PIV arrangements make use of only one camera positioned perpendicularly to the measuring plane. This single view approach is not able to resolve the out-of-plane velocity component (typically present in 3D flows such as turbulent ones), which is projected onto the measurement plane, resulting in an irremediable perspective error (Raffel et al., 2018). As pointed out by Prasad (2000), a planar PIV system provides, in fact, only two resolving equations for the three unknowns of the particle displacement. By combining two (or more) different views of the same measuring plane, stereo-PIV is able to resolve the full 3D velocity field. Conventional stereo-PIV arrangements foresee two cameras recording the same flow field from two different viewing angles, obtained either by a lateral translation of the two cameras maintaining their axes parallel to each other (translation system - Figure 3.6a) or by a rotation of the camera axes intersecting the measurement plane (rotational system - Figure 3.6b).

With reference to the translational setup in Figure 3.6a, let us consider the displacement of a particle $\Delta r = [\Delta x, \Delta y, \Delta z]$ in the laser sheet, approximating, with negligible error, the PIV procedure of volume averaging of the particle-displacements within the measurement volume, defined by the laser sheet thickness and the interrogation area (Prasad, 2000). For each camera, the projected particle displacement on the camera sensor $[\Delta x', \Delta z']$ can be defined on the basis of the physical particle displacement Δr (Raffel et al., 2018):

$$\Delta x_i' = M(\Delta x + \Delta y \frac{x_i'}{f_i}) \tag{3.1}$$

$$\Delta z_i' = M(\Delta z + \Delta y \frac{z_i'}{f_i}) \tag{3.2}$$

where $M = f_i/d_0$ is the magnification factor with d_0 the distance between the laser sheet and the lens, f_i the focal length of the camera-lens and $[x_i', z_i']$ the final position of the displaced particle on the image plane. Equations 3.1 and 3.2 show that for one camera the projected image displacement depends on the out-of-plane component Δy. By combining the set of equations 3.1 and 3.2 for both cameras, Prasad (2000) obtained the following geometric relationships of the physical particle displacement:

$$\Delta x = \frac{\Delta x_1'(x - d_c/2) - \Delta x_2'(x - d_c/2)}{M d_c - (\Delta x_1' - \Delta x_2')} \tag{3.3}$$

$$\Delta z = \frac{-z\Delta y}{d_0} + \frac{\Delta z_1' + \Delta z_2'}{2M}\left(\frac{\Delta y}{d_0} - 1\right) \tag{3.4}$$

$$\Delta y = \frac{-d_0(\Delta x_1' - \Delta x_2')}{M d_c - (\Delta x_1' - \Delta x_2')} \tag{3.5}$$

where d_c is the distance between the two cameras. A similar set of equation can be derived also for the rotational system (Lawson and Wu, 1997a). For a translation system the out-of-plane error scales with d_0/d_c (Lawson and Wu, 1997a). Maximizing the camera distance d_c to reduce the out-of-plane error, results, unfortunately, in a reduction of the measurement area and of the performance of the lenses (Prasad, 2000). In this sense, the rotational system represents a more flexible option as there is no restriction on the camera angle γ. In order to accommodate for the limited depth of field of the lenses and ensure a uniform focus over the whole measurement plane, the image plane has to be tilted according to the Scheimpflug criterion so that it intersects the lense plane and the measurement plane in a line (see Figure 3.4.1.2b). This results in a relevant perspective distortion and a non-uniform magnification factor, which can be accounted for by calibrating the
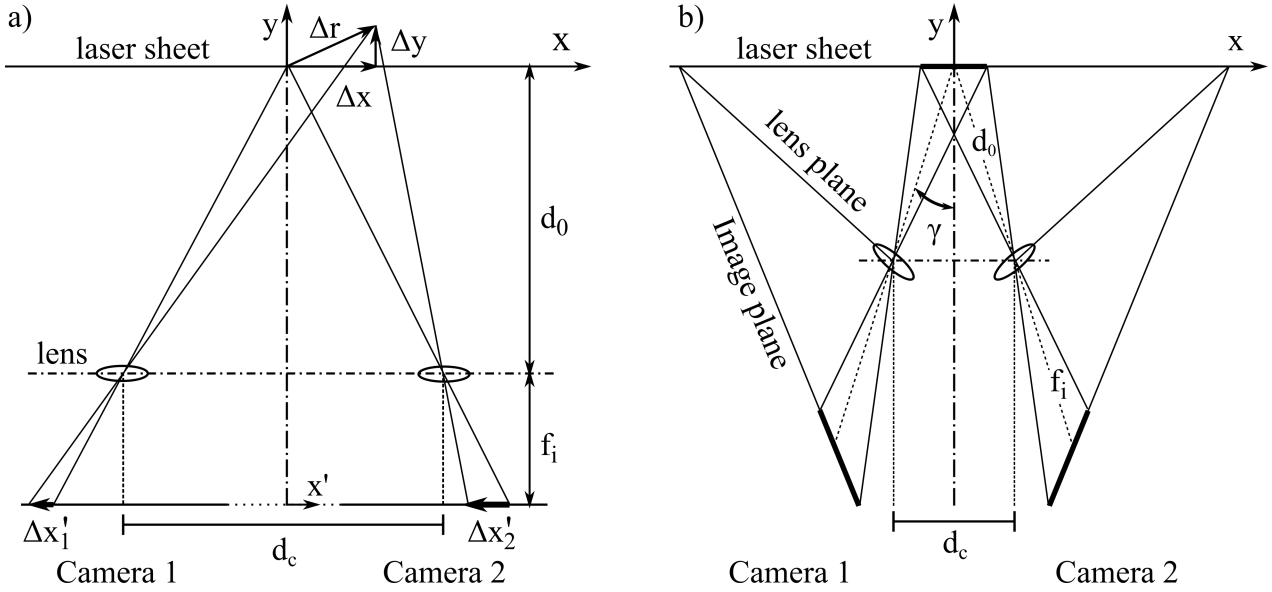
Figure 3.6: Stereo-PIV translation system (a) and angular-displacement system (b). The figures are adapted from Prasad (2000) and Raffel et al. (2018).

cameras. Camera calibration maps the image plane of each camera to the world coordinate system defined by the measurement plane, defining in this manner the relative position and the viewing directions of the cameras to solve the system of equations 3.3-3.5 (for further details see Section 3.4.1.5).

3.4.1.2 Measurement setup

The flow measurements are performed with a rotational stereo-PIV system composed of two high-speed UI-3060CP-M-GL Rev.2 iDS cameras with a resolution of 1936x1216 pixels and of a 4W continuous blue laser with a nominal wavelength of 445 nm. The cameras and the laser are mounted on a rigid, movable frame which allows to fix their relative position and, at the same time, translate them in the transverse direction to investigate the flow at different transverse positions (see Figure E.1 in Appendix E). The laser is installed at a height of 105 cm from the top of the spheres and is oriented parallel to the streamwise direction perpendicularly to the bottom of the flume (see Figure 3.7). The laser beam is expanded through a cylindrical diverging lens to a laser sheet with a thickness of 1 mm in the spanwise direction and 20 cm in the streamwise direction, in order to cover all three patterns of spheres over their whole length.

The cameras, equipped with AF DC-Nikkor 105mm f/2 D lenses and LaVision Mount Version 3 Scheimpflug adapters, are installed 1.30 m above the top of the spheres 50 cm apart from the laser on its right hand-side in streamwise direction, as shown in Figure 3.7. A horizontal stereo angle γ of 26° is chosen (see Figure 3.6b) according to the optimal stereo angle range of 20°-30° recommended by Lawson and Wu (1997b) to reduce the error in the out-of plane velocity component and, at the same time, avoid an excessive increase of the error in the streamwise component. In the vertical direction, the cameras look down on the spheres from the side with an angle ζ of 20° (see Figure 3.7), in order to resolve the flow in between the spheres. As this steep vertical viewing angle causes significant vertical distortions of the the PIV images, the stereo-PIV system is validated with a 2D planar PIV system. The validation is presented in Appendix H.

To avoid laser reflections at the level of the bed, the flow is seeded with in-house produced fluorescent particles (for further details see Section 3.4.1.4). The fluorescent particles are characterized by a different emission spectrum than the absorption spectrum, so that by equipping the cameras with longpass filters with a cut-off wavelength of 475nm, laser reflections near the bed in the blue spectral region are filtered out, while the particle-signal, emitted in the yellow-red spectral region, is retained.

Since the stereo-PIV measurements are preformed through the water surface, a glass plate (hereafter boat) 25cm long and 29.5 cm wide, held through a plastic frame rounded at the leading edge, is installed at the water surface, in order to avoid surface waves (see Figures 3.5 and 3.7; a technical drawing is illustrated in Figure D.3 in Appendix D). The boat can be shifted vertically through 4 vertical rods connected to the railing of the flume, to adjust its height at the beginning of the experiments to be flush with the water surface within ± 0.5 mm. Details on the influence of the glass plate on the flow are presented in Appendix H.3.
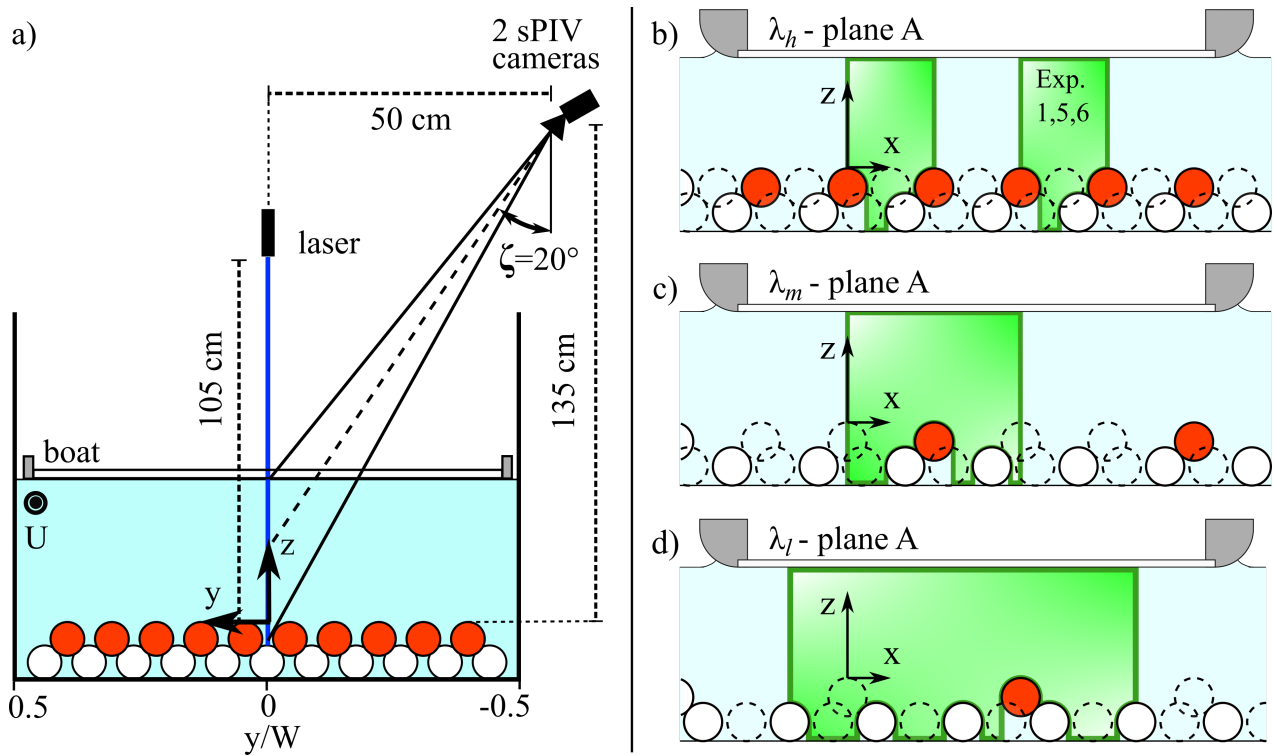
Figure 3.7: Cross-sectional view of the stereo-PIV s (a) and stereo-PIV measurement regions in the measurement plane A for the bed configurations λ_h (b), λ_m (c), λ_l (d)

3.4.1.3 Data acquisition

The PIV measurements are performed for all bed configurations over two reference planes positioned over a pattern of spheres in the centre of the channel, as shown in Figure 3.2: plane A spans along the crest of the spheres, while plane B is shifted by one quarter of the pattern width. For the bed configuration λ_m, planes A and B are not located in the centre of the pattern as in the other two bed configuration, but are located towards the outer edge of the pattern in the positive transverse direction due to an asymmetric fine-sediment bed topography (for further details see Section 6.2.1). The measurement area spans over the whole water depth

and its longitudinal extension is adjusted to the length of the pattern of spheres investigated. Figures 3.7b-d illustrate the measurement areas for the bed configurations λ_h, λ_m and λ_l, respectively, in the measurement plane A. The areas are located approximately one pattern length l_{x,λ_h} downstream of the leading edge of the boat to restrict the influence of the boundary layer developing along the surface boat to less than 10% of the water depth and guarantee that the velocity profiles are self-similar, as discussed in Section H.3. Just for experiments 1, 5 and 6 over the densest bed configuration (Figure 3.7b) the measurement area is located over the fourth pattern of spheres from the leading edge .

During the experiments, a total of four PIV runs are performed at different times in order to analyse the evolution of the flow field, while the bed is eroding. During each PIV run, PIV measurements are performed over all measurement planes just described. During each PIV measurement, a total number of bursts equivalent to 4500 bulk time units ($\Delta t = H/U$) is recorded, in order to guarantee statistically independent samples and time-convergence of the mean flow statistics (for further details see Appendix F). Two images per burst are recorded at a frequency F high enough to obtain an average image particle displacement of 10 pixels. For each PIV measurement, it is checked a posteriori that stationary conditions of the bed morphology are given. If this is not the case, the PIV measurement is subsampled to analyse flow fields for which the bed can be considered temporarily stable. In Table 3.2 the bulk time units and the image frequency for all experiments is reported.

During the PIV measurements, images of the bed surface are also recorded by the photogrammetric system with the same sampling period Δt of the PIV bursts with a negligible time delay less than 1 ms (for further details on the data acquisition of the topographic system see Section 3.4.2.2).

Exp.		1	2	3	4	5	6	7	8	9	10
Δt	[s]	0.20	0.22	0.22	0.42	0.20	0.24	0.20	0.28	0.23	0.20
F	[Hz]	377	377	377	362	345	364	400	345	385	400

Table 3.2: Bulk time units Δt, defining the burst sampling period, and image frequencies F of the PIV runs for all experiments.

3.4.1.4 Fluorescent PIV particles

The use of commercial fluorescent seeding-particles for large scale flume experiments is hampered by their prohibitive cost. As such, a simple method for producing in-house PIV particles is developed herein by using plastic masterbatches made of fluorescent pigments. A masterbatch is a mixture of pigments concentrated through a heat process into a carrier plastic resin, which is then shaped into pellets in the size of 2-4 mm. To suit as seeding particles, the density of the pellets needs to be close to the density of water and their size reduced to the micrometer scale, to guarantee almost neutrally buoyant conditions when floating.

A masterbatch made of an ABS plastic carrier and fluorescent yellow pigments with a density $\rho_p = 1.09$ g/cm^3 is selected. The fluorescent pigment is characterized by an absorption spectrum in the blue wavelength range, characteristic of the laser, and a broadband emission spectrum ranging from yellow into deep red with a peak at yellow wavelengths. The pellets are mechanically grounded to a characteristic seeding particle size of 10-100 μm. The particle are characterized, before use, by a median major axis d_M of 16 μm with

20% of the particles having sizes bigger than 40 μm (see Figure 3.8a) and aspect ratios d_M/d_m (where d_m is the minor axis) higher than 2 for more than 30% of the particles (see Figure 3.8b). 3.8d show, in fact, that the seeding particles display before use the presence of filaments, which might cause inhomogeneous light scattering. Sampling of the seeding particles after use shows the absence of filaments (see Figure 3.8d), which were probably mechanically cut down passing through the flume pump. Figure 3.8a and b show that the used seeding particles are characterized by a d_M of 10 μm with a median aspect ratio of 1.4 with only 10% of the particles with aspect ratios larger than 2. A homogeneous light scatter is observed in the PIV images, displaying rounded particles with an image size of 2-3 pixels (see Figure 3.8c).

In order to asses whether the PIV seeding particles effectively follow the flow, the relaxation time τ_p of the
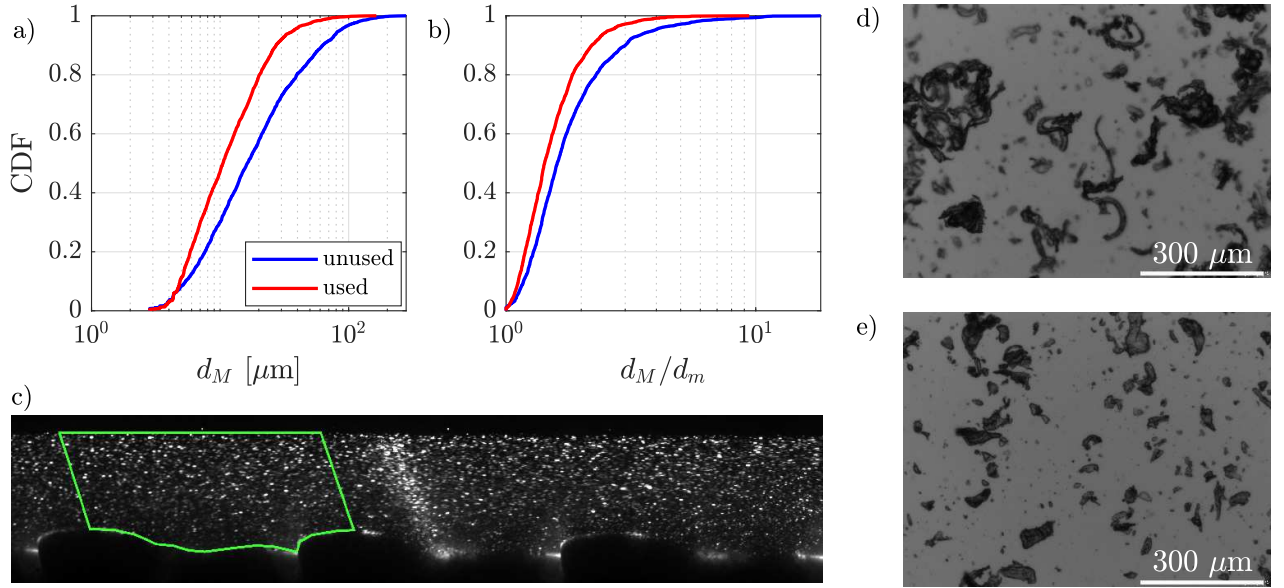
Figure 3.8: (a) Cumulative distribution function of the major axis d_M of the fluorescent seeding particles; (b) Cumulative distribution function of the aspect ratio d_M/d_m of the fluorescent seeding particles; (c) PIV image of the PIV camera downstream recorded during Exp. 4 (the region highlighted in green represents the measurement area for the bed configuration λ_h); (d-e) Fluorescent seeding particles before and after the use, respectively.

particles to adjust to the flow conditions of the ambient fluid needs to be smaller than the characteristic time scale of the flow, given by the Kolmogorov time scale $\tau = (\nu/\epsilon)^{0.5}$ (where the turbulent energy dissipation ϵ is estimated with the approximate relationship by Nezu et al. (1993), $\epsilon \simeq (\overline{u'^2})^{3/2}/L_x$ with $L_x \simeq H$ the longitudinal integral length scale). By evaluating the turbulent intensity at the level of the spheres where the highest turbulent production takes place, values of τ comprised between 0.02-0.04 s are obtained for the experiments in Table 3.1. Given that for small particles the viscous drag dominates, the relaxation time is given by $\tau_p = \frac{\rho_p d_M^2}{18\mu}$ (Raffel et al., 2018). A ratio τ_p/τ (i.e. a Stokes number S_k) less than 0.1 guarantees a tracing accuracy below 1% (Tropea et al., 2007). The lowest and highest shear stress conditions investigated are effectively characterized by values of the Stokes number of about 0.02-0.04.

3.4.1.5 Calibration procedure

For the accurate reconstruction of the 3D velocity field from a pair of stereo-PIV images, the three-dimensional world coordinate system has to be mapped to the bi-dimensional image space through camera calibration. More specifically, the position and orientation of the camera planes relative to the measurement plane has to be determined on the basis of a set of points with known world coordinates. The image-world mapping model adopted is based on the camera pinhole model by Tsai (1986) implemented in the Davis-PIV software version 8.4.0. The camera pinhole model assumes that all light rays directed from the measurement plane to the camera sensor pass through one single point (Raffel et al., 2018). The model is based on 11 independent parameters, which need to be estimated for each camera: 6 external camera parameters which account for a translation and a rotation to define the position and orientation of the camera, 3 internal camera parameters defining the image plane (the focal length and the coordinates of the optical centre) and 2 additional parameters to account for radial distortions of the lens (for additional details on the camera pinhole model see Section 3.4.2.3). The calibration procedure consists in taking a set of two images (one for each camera) of a calibration plate with a two-levelled dot pattern of known geometry aligned with the measurement plane. By matching the image coordinates of the dots with their world coordinates, the 11 parameters are optimized by least-square matching.

Two two-sided calibration plates with a two-level dot marking are used in this work with a height of 5.6 and 10.6 cm, respectively, to cover both water depths investigated. The calibration plates are machined from alluminum plates anodized with black dye carved with 2 mm deep equispaced vertical grooves for the second level of dots. The dots 2mm in diameter are drilled 0.3 mm deep into the surface at a spacing of 10 mm with a 0.02 mm precision (see the technical drawings in Appendix D for more details). The dots are filled with white silicone, making sure that the surface is flat with a razor blade to eliminate excess material, as done in Akutina (2015).

The calibration of the cameras is performed at the end of each experiment. The calibration plate, held from the side by a rigid frame, is submerged vertically under the glass boat with the lower edge flush with the top of the spheres (see Figure E.1 in Appendix E). In this manner, the reference plane for the vertical coordinate is uniquely defined. The calibration plate is then aligned with the laser sheet making sure that the upper dot plane is coplanar with the centre of the laser sheet. A pair of images of the calibration plate is recorded simultaneously by the two stereo-PIV cameras.

The accuracy of the reconstructed flow field is very sensitive to misalignments between the laser sheet and the calibration plates. Self calibration is performed in the aftermath to correct the position of the calibration plate relative to the laser sheet for possible misalignments. Based on the algorithm by Wieneke (2005), a cross-correlation is performed on a set of 100 dewarped PIV image pairs from the first and the second stereo camera. The image particle patterns should ideally match, if the calibration plate and the laser sheet were coplanar. The camera parameters are iteratively corrected for any disparity in the particle position of the dewarped camera images, until an average residual disparity of less than 0.4 pixels is reached. A final resolution of 140 px/cm is achieved on the dewarped images.

3.4.1.6 PIV processing and data treatment

The PIV images are first pre-processed, in order to enhance the quality of the signal. Localized laser reflections at the level of the bed due to the occasional presence of fluorescent particles settled on the surface, are removed by subdividing the image series in subsets of 50 images from which the minimum intensity value at each pixel location, determined from the whole subset, is subtracted. The intensity of the particles is then adjusted to increase the contrast between the particles and the background and, consequently, the signal to noise ratio.

The stereo-PIV image bursts are processed with the DAVIS-PIV software version 8.4.0. The 3D velocity vector field computation is based on the approach presented by Wieneke (2005). The PIV images are first dewarped to reconstruct the 2D2C vector field for both cameras in the real world coordinates system. In this manner, a common interrogation grid for vector calculation can be used for both cameras. An iterative multi-pass correlation method with a decreasing interrogation window size, based on a standard cyclic FFT algorithm with no zero-patting, is applied to determine at each grid point the particle displacement with the highest correlation peak. At each computational pass, the velocity information from the previous pass is used to adapt the shape of the interrogation window to account for particle-pattern deformation due to shearing (Fincham and Delerce, 2000; Wieneke and Pfeiffer, 2010). Image dewarping and deformation are performed simultaneously on the basis of a bicubic spline interpolation. A 3D reconstruction is performed at each pass to filter out 2C velocity vectors with a reconstruction error higher than 0.5 pixels. Spurious vectors are also identified on the basis of the universal outlier detection algorithm by Westerweel and Scarano (2005). Vectors characterized by a correlation coefficient of the particles-displacement less than 0.4 for the intermediate passes and 0.3 for the last pass are rejected. For all experiments, the initial correlation window is equal to 64x64 pixels, while the final correlation window is equal to 36x36 pixels^2 with a 50% overlap, resulting in a grid spacing of 1.1x1.1 mm^2. Appendix G shows that this measurement resolution is enough to resolve the Taylor microscale (i.e. cover the inertial subrange) and partially resolve the dissipation length scales down to 10-20 times the Kolmogorov length scale.

Velocity-vector field post-processing is performed in order to filter out remaining outliers in the near-bed regions. For this purpose, the spatial outlier detection algorithm by Fincham and Spedding (1997), is applied to each instantaneous vector field. Furthermore, a time-filter, i.e. the multivariate detection algorithm by Griffin et al. (2010) based on the adjusted outlyingness algorithm by Hubert and Vandervieren (2008), is applied at each grid-point to the whole time series of velocity vectors. The algorithm analyses the complete probability density function of the three-variate velocity signal (u,v,w), assessing for all possible univariate projections of the signal the maximum probability of each observation to be an outlier. The advantage of the algorithm is that it is insensitive to influences of spatial neighbours and is not bound to pre-defined thresholds on the turbulence level. The result of the combined temporal and spatial outlier detection algorithms show that only 1% to 3% of the vectors in the near-bed region are spurious.

Further data treatment is performed during some experiments for specific issues related to the laser. The laser is characterized by a defect causing a narrow vertical region of increased particle intensity (see Figure 3.8c), not larger than 5 mm positioned 10 cm downstream of the leading edge of the boat. For Exp. 2 and 3, characterized by the largest measurements fields needed to analyse the bed configurations λ_m and λ_l, this region cannot be avoided, as in the case of all other experiments with the bed configuration λ_h. Given that

the particles in this area are over-saturated, causing as such a non-uniformity in particle intensities and potentially leading to outliers, the area is masked out during the PIV processing. The flow statistics in this vertical region are reconstructed in the post-processing through cubic spline interpolation just for the time-averaged flow statistics. The instantaneous turbulent velocity signal is not reconstructed, though.

During the PIV measurements over plane A in Exp. [1,2,4,5,6,7], the laser sheet rotates over time in the transverse positive direction due to the laser warming up (with a maximum transverse translation of 1mm at the level of the top of the spheres by the end of the PIV measurement). In this case, the self calibration is still performed only over the first 100 images, as described in Section 3.4.1.5, without reiterating the self-calibration along the measurement to follow the movement of the laser sheet. It was assessed that the the two procedures yield similar results. To account anyway for the shift, a rotation around the x-axis is applied to the velocity vector field assuming a linear dependency of the rotation over time. For the measurements performed over the other planes B-D, the laser sheet is stable over time in the shifted position and only a static rotation corresponding to 1 mm over 1 m is applied to all vector fields. It was assessed, that the potential error committed by rotating the vector field is comparable to the peak locking-error.

3.4.2 Stereo photogrammetric measurements

During the erosion of fine sediments from the interstices of a rough immobile bed, the sediment transport rates and the bed topography can change significantly both in time and in space. Therefore, a topographic measurement technique able to resolve the morphological time and spatial scales is needed. Topographic techniques used in previous experimental studies were able to resolve adequately just one of the two scales. Ecosounders and graduated scales have been used for example to measure the bed evolution continuously in time at a few selected locations, like in the studies by Euler et al. (2017), Dixen et al. (2013) and Dey and Raikar (2007) on the scour hole evolution around submerged obstacles. Laser scanning techniques and stereo photogrammetric systems have been used, instead, to obtain spatially resolved digital elevation models of gravel beds with restricted time resolution (Smart et al., 2004; Euler and Herget, 2012; Curran and Waters, 2014; Powell et al., 2016; Schlömer et al., 2020). The experimental protocol of all these studies required, in fact, the complete drainage of the flume, to avoid errors deriving from the refraction of the laser or of the optical rays through the water surface. The drainage of the flume can cause, however, disturbances of the bed topography. For these reasons, Bertin and Friedrich (2019) performed stereo topographic measurements of an armouring gravel bed through the water surface, after having stopped the flow to avoid surface waves and by correcting the water surface refraction through camera calibration. Bouratsis et al. (2013) applied instead a different approach, by recording the evolution of the scour around a bridge pier through a submerged stereo-photogrammetric system. The limitation in this case is represented by possible sediment bed scouring induced by the submerged cameras. In the present work, a similar approach to Bertin and Friedrich (2019) is implemented through a stereo photogrammetric system recording the bed evolution through the PIV boat, without the need to suspend the flow. In this manner, high resolved topographic measurements are obtained both in space and in time.

3.4.2.1 Principles of stereo photogrammetry

Stereo photogrammetry allows to reconstruct the position and shape of an object on the basis of images recorded by a pair of cameras. The technique is based on the triangulation principle. Once the position of the cameras is known in a world reference frame (such as the laboratory), the 3D position of any point P in space imaged by both cameras can be determined from the intersection of the two lines of sight connecting the point P with its projections onto the two image planes. In this manner, the spatial information lost in the imaging process, from the 3D world geometry to the 2D image plane, is recovered.

The mathematical model commonly used for the camera optical system is the pinhole model (Luhnmann
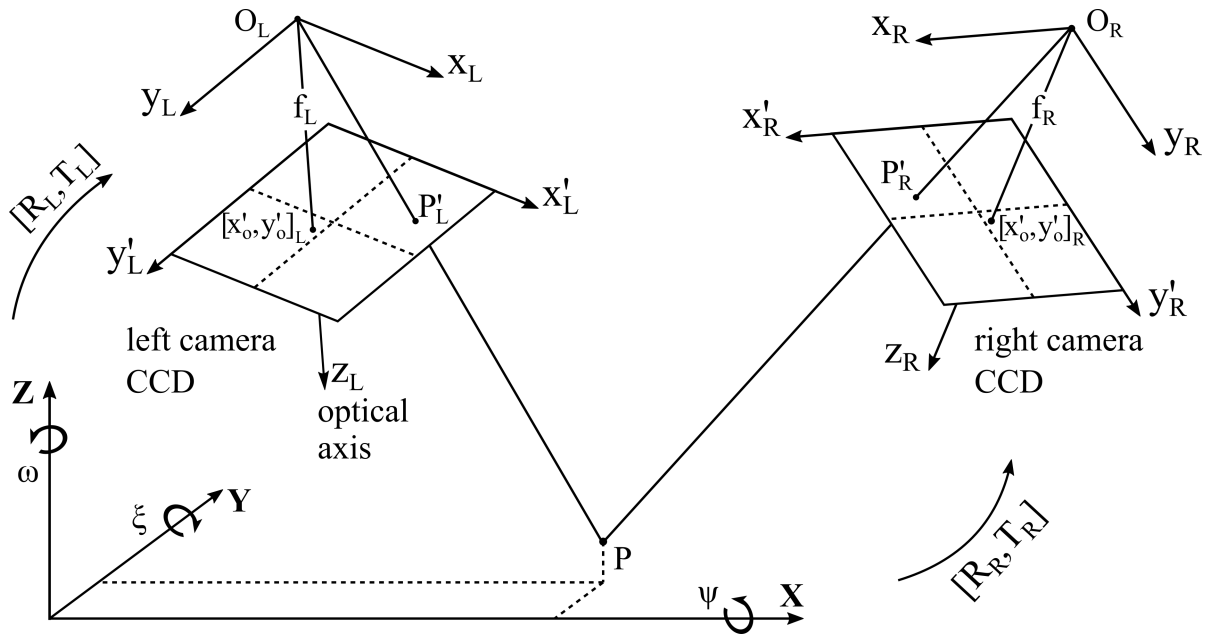
Figure 3.9: Stereo photogrammetric setup with two cameras (left and right) represented through the camera pinhole model; for each camera the point P in the world coordinate frame $[\mathbf{X}, \mathbf{Y}, \mathbf{Z}]$ is related to its image projection P'_j in the image reference frame $[x'_j, y'_j, z'_j]$ through the focal length f_j, the principal point $[x'_{o,j}, y'_{o,j}]$ and the rigid body transformation $[R_j, T_j]$. Picture adapted from Benetazzo (2006).

et al., 2014). The model assumes that the camera lens can be represented by a point in space, the so called focal point, through which all optical rays, connecting the object with the camera plane, pass (see Figure 3.9). With reference to Figure 3.9, a camera reference system $[x_j, y_j, z_j]$ (with j denoting the L-left or R-right camera) centred in the focal point O_j, is defined with the z_j axis coincident with the optical axis and the x_j and y_j axis parallel to the image reference frame $[x'_j, x'_j]$ attached to the CCD camera sensor. The origin of the image coordinate system is a corner of the image plane and the coordinates are given in pixels. The relation between the camera and the image reference system is uniquely defined by the internal camera parameter, i.e. the focal length f_j, the principal point $[x'_{o,j}, y'_{o,j}]$ (projection of the focal point onto the image plane) and the size of the pixels (taken into account through direction dependent scaling factors $k_{x'_j}$ and $k_{y'_j}$). The mapping

of a point $P_j = [x_j, y_j, z_j]$ in the camera reference frame onto its image projection $P'_j = [x'_j, y'_j]$ is given by simple geometrical considerations based on the law of similar triangles:

$$
\begin{bmatrix} x'_j - x'_{o,j} \\ y'_j - y'_{o,j} \end{bmatrix} = \begin{bmatrix} f_{x,j}\frac{x_j}{z_j} \\ f_{y,j}\frac{y_j}{z_j} \end{bmatrix}
\tag{3.6}
$$

where the focal length and the scaling factors are merged in a single parameter $f_{x,j} = f_j k_{x'_j}$ and $f_{y,j} = f_j k_{y'_j}$, as they cannot be dissociated during the calibration procedure if they are both unknown (Heikkilä and Silvén, 1997; Bouget, 2010). The orientation and position of the cameras in the world reference frame $[\mathbf{X}, \mathbf{Y}, \mathbf{Z}]$ is defined through six external camera parameters consisting of three rotation angles $[\psi, \xi, \omega]$ around the world reference frame and three translations along the axes. The transformation between world coordinates and camera coordinates is given by a rigid body motion $[x_j, y_j, z_j] = [R_j T_j][\mathbf{X}, \mathbf{Y}, \mathbf{Z}]^t$, where R_j is the rotation matrix and T_j is the translation vector. In this manner, equation 3.6 can be recast in homogenous coordinates as a transformation from the world coordinate system to the image plane:

$$
z_j \begin{bmatrix} x'_j \\ y'_j \\ 1 \end{bmatrix} = \underbrace{\begin{bmatrix} f_{x,j} & 0 & x'_{o,j} & 0 \\ 0 & f_{y,j} & y'_{o,j} & 0 \\ 0 & 0 & 1 & 0 \end{bmatrix}}_{K_j} \begin{bmatrix} R_j & T_j \\ 0_{1\times3} & 1 \end{bmatrix} \begin{bmatrix} \mathbf{X} \\ \mathbf{Y} \\ \mathbf{Z} \\ 1 \end{bmatrix}
\tag{3.7}
$$

where K_j is the camera matrix. Given the image coordinates $[x'_j, y'_j]$ of the unknown point P in both cameras, the triangulation process consists in solving the overdetermined system 3.7 of 4 equations in the 3 unknown world point coordinates $[\mathbf{X}, \mathbf{Y}, \mathbf{Z}]$ by the least square method (Benetazzo, 2006).

Since the camera pinhole model is a simplification of the physical lens system, additional parameters need to be introduced to account for image distortions. Imperfections in the curvature of the lens can cause, in fact, radial distortion, while tangential distortions arise from the image plane and the lens not being parallel to each other. The radial model by Brown (1971) and the tangential model by Heikkilä and Silvén (1997) are applied to equation 3.6 to correct the image coordinates for both radial and tangential distortions:

$$
\begin{bmatrix} x'_j - x'_{o,j} \\ y'_j - y'_{o,j} \end{bmatrix} = \begin{bmatrix} f_{x,j}\left(\frac{x_j}{z_j} + \delta x_{r,j} + \delta x_{t,j}\right) \\ f_{y,j}\left(\frac{y_j}{z_j} + \delta y_{r,j} + \delta y_{t,j}\right) \end{bmatrix} =
$$
$$
\begin{bmatrix} f_{x,j}\frac{x_j}{z_j} \\ f_{y,j}\frac{y_j}{z_j} \end{bmatrix} + \begin{bmatrix} f_{x,j} \\ f_{y,j} \end{bmatrix} \begin{bmatrix} \frac{x_j}{z_j}(k_{r1}r^2 + k_{r2}r^4 + k_{r3}r^6) \\ \frac{y_j}{z_j}(k_{r1}r^2 + k_{r2}r^4 + k_{r3}r^6) \end{bmatrix} + \begin{bmatrix} f_{x,j} \\ f_{y,j} \end{bmatrix} \begin{bmatrix} 2k_{t1}\frac{x_j y_j}{z_j^2} + k_{t2}\left(r^2 + 2\frac{x_j^2}{z_j^2}\right) \\ k_{t1}\left(r^2 + 2\frac{y_j^2}{z_j^2}\right) + 2k_{t2}\frac{x_j y_j}{z_j^2} \end{bmatrix}
\tag{3.8}
$$

where $r = \sqrt{(x_j/z_j)^2 + (y_j/z_j)^2}$ and k_r and k_t are the radial and tangential distortion parameters, respectively. For the proper modelling of the camera system the internal and external camera parameters along with the radial and tangential distortion parameters need to be estimated for each camera through camera calibration before the actual measurements can be performed (see Section 3.4.2.3).

3.4.2.2 Measurement setup and data acquisition

The measurements of the sediment bed topography are per-formed with a stereo photogrammetric system composed of two iDS high-frequency cameras (UI-3180CP Rev. 2.1 model with a resolution of 2592 x 2048 pixels) equipped with 50 mm/f1.2 Nikkor lenses. The cameras are mounted on a rigid frame dis-connected from the flume, to avoid vibrations. The two cameras are installed at a height of 130 cm above the top of the spheres in the centre of the channel (y = 0 m), one upstream and one downstream of the measurement area, symmetrically facing each other at a distance of 85cm (see Figure 3.10). The cameras look over the measurement area with an angle of 18° to the ver-tical direction, which corresponds to the cameras' stereo angle γ. The presence of the glass boat, installed to allow stereo-PIV measurements through the water surface, avoids optical distor-tions induced by surface waves. An LED flash light, which can be operated continuously or triggered with a specific frequency during the PIV measurements, is installed above the measure-ment area to guarantee uniform lighting. For an overview of the setup see Appendix E.
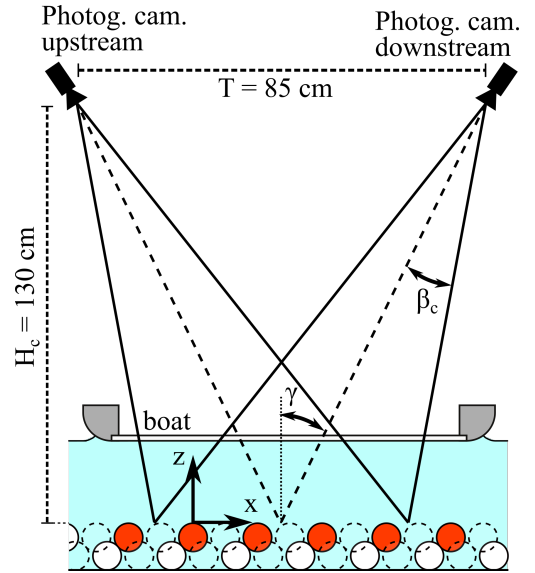

Figure 3.10: Setup of the stereo-photogrammetric system

The field of view of the cameras is 28.5 cm wide in the spanwise direction, spanning over the entire width of the flume with a narrow area near the glass walls being covered by the frame of the glass boat, and 18 cm long in the streamwise direction to cover the entire length of the pattern of spheres with the lowest density λ_l. The cameras are triggered simultaneously and they record each a burst of 9 images every 1.5 minutes for the entire duration of the experiments. Only the first image of the burst is used for the reconstruction of the bed topography, while the others are used for sediment transport measurements (for more details see Sec-tion 3.4.3). The time resolution of the measurements is considered appropriate to resolve the morphological changes of the sediment bed on the basis of the morphological results obtained in Part I.

During the stereo-PIV measurements the burst acquisition of the photogrammetric system is triggered at a higher frequency in phase with the PIV bursts with a negligible time delay (for further details on the PIV burst sampling frequencies see Section 3.4.1.3). Due to time constraint, the photogrammetric cameras record, in this case, a burst of three images. The LED lamp is triggered simultaneously with the photogrammetric cameras, in order to not interfere with the PIV image acquisition performed in the dark. In order to filter out reflections of the laser sheet, while acquiring the bed images, the lenses are equipped with filters with a cut-off wavelength of 590 nm.

3.4.2.3 Calibration procedure

The calibration procedure consists in estimating the internal and external camera parameters on the basis of a set of stereo images of known world coordinates. A global stereo calibration of the cameras is performed through the camera calibration toolbox by Bouget (2010), implementing the calibration method by Zhang

(1999) with internal camera model by Heikkilä and Silvén (1997) (similar to the one presented in Section 3.4.2.1). The method optimizes the camera parameters to minimize the pixel reprojection error of the imaged set of points of known world coordinates, i.e. the distance between their measured image location and their projection onto the image plane derived from equation 3.7.

Since the photogrammetric reconstruction of the sediment bed is performed through the water surface, the calibration procedure is performed in the water, in order to account for optical distortions induced by the refraction of the optical rays. Bertin et al. (2013) and Bruno et al. (2011) successfully applied this technique to reconstruct submerged surfaces by correcting the refraction through the radial and tangential distortion parameters already implemented in the camera pinhole model. In the present case, the use of a second order radial distortion model (i.e. with $k_{r3} = 0$ in equation 3.8) and of a full tangential distortion model (with both k_{t1} and k_{t2} estimated) leads to reprojection errors lower than 0.1 pixels.

The calibration is performed with a flat ceramic plate ($160 \times 160 \times 1$ mm^3) with a regular 7×7 black dot pattern printed on a white background (dot size: 9.5 mm, dot spacing: 18.75 mm - see Figure 3.11a). The cameras are calibrated at the end of each experiment by recording with both cameras the calibration plate submerged under the boat in 30 different positions and orientations (see Figures 3.11a-d), as this number of stereo calibration images was found to minimize the projection error by Bertin et al. (2015). Particular care is taken in the process to cover uniformly the whole field of view with calibration dots.

The image location of the calibration dots is extracted from the pairs of stereo calibration images by applying the pattern recognition technique developed first by Ferré and Giralt (1989) for eddy-detection and successively adapted by Astruc et al. (2012) for dot-detection. The method consists in the construction of a correlation map of the calibration image with a dot-template, whose size is iteratively modified to match the average imaged calibration-dot size. The initial size of the dot template is a circle with a radius similar to the one of the imaged calibration dots ($\simeq 100$ pixels in radius). At each iteration the approximate location of the image dots is identified through the correlation map maxima and a new dot-template is defined as average of the detected image-dots. The new template is then used to calculate a new correlation map. A subpixel gaussian interpolation of the correlation peaks is implemented, leading to an accuracy of 0.03-0.05 pixels (Astruc et al., 2012) .

For the calibration, a local world reference system is attached to the plane defined by the imaged calibration plate, with the **X** and **Y** axis parallel to the edges of the dot pattern (see Figures 3.11a-d). The geometry of the dot pattern defines, in this manner, the world coordinates of the dots.

A global stereovision calibration is performed, where the cameras are first calibrated independently and the resulting internal and external camera parameters are further optimized by deriving the rigid body transformation of one camera with respect to the reference system of the other camera, as in (Astruc et al., 2012). The method has been proved to result in a better estimation of the camera parameters Garcia et al. (2000). Given the image and world coordinates of the calibration dots, the camera parameters are estimated by minimizing, in the least square sense, the reprojection error of the calibration dots through the gradient descent method. The cost function to be minimized independently for each camera is given by the difference between the measured image dot location $P'_{j,d}$ in camera j and equation 3.7 (Astruc et al., 2012):

$$C_f^1 = \sum_{i=1}^{30} \sum_{d=1}^{49} (P'_{j,d} - K_j \mathbf{T}_{j,i} P_d)^2 \qquad (3.9)$$
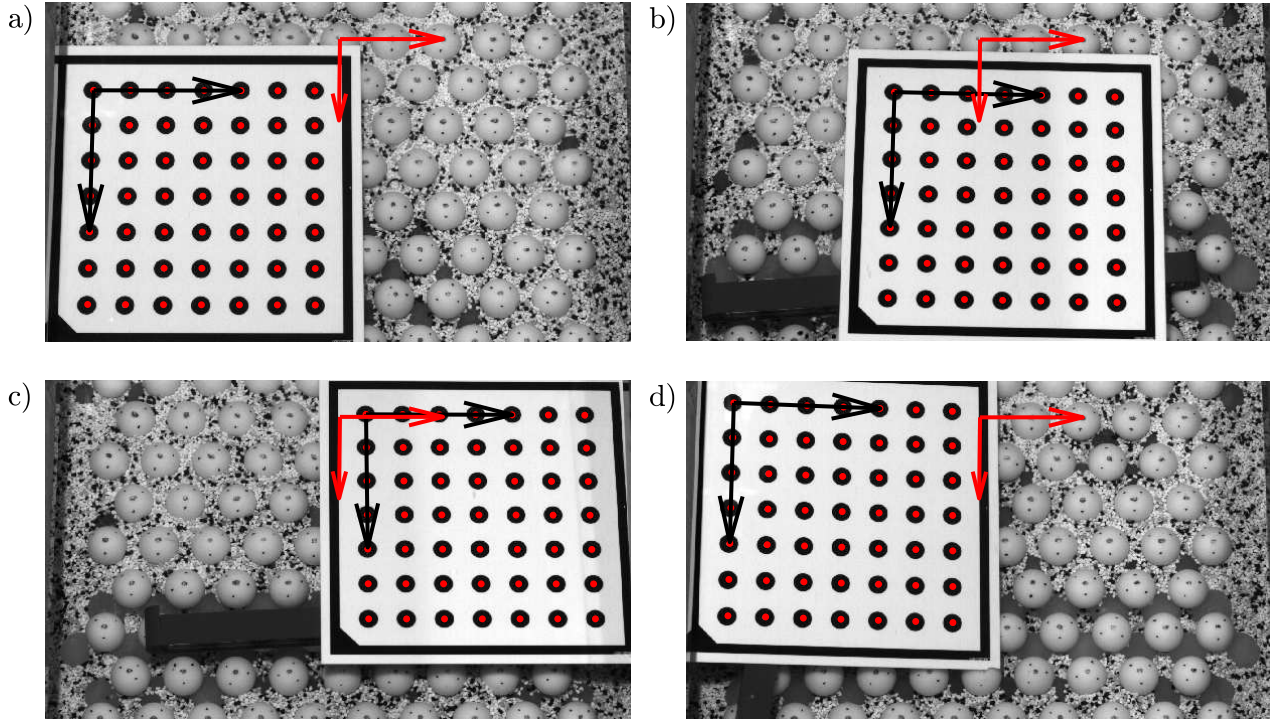
Figure 3.11: (a-d) Four different positions of the calibration plate imaged by the photogrammetric camera downstream for the global calibration procedure. The red points represent the detected calibration dots. The calibration plate in Figure a is the reference plate to fix the position and orientation of the camera downstream. The black arrows identify the local world reference system [**X**,**Y**] and the red arrows the reference system of the flume [x,y]. The flow direction is from top to bottom.

where the sums are performed over the number of orientations of the calibration plate i and the number of calibration dots d. For the initialisation procedure, the principal point is set at the centre of the image and the focal length is estimated on the basis of the extension of the field of view and the camera sensor size. The estimated internal camera parameters are used then to initialize the second step of the global stereovision calibration technique, which minimizes the following cost function (Astruc et al., 2012):

$$C_f^2 = \sum_{i=1}^{30} \sum_{d=1}^{49} (P'_{R,d,i} - K_R \mathbf{T}_R P_d)^2 + (P'_{L,d,i} - K_L \mathbf{T}_{LR} \mathbf{T}_R P_d)^2 \tag{3.10}$$

where $\mathbf{T}_{LR}$ is the rigid body transformation between the left and right camera (with the left camera being the camera upstream and the right one the camera downstream in figure 3.10). The rigid body rotation T_R, which defines the position and orientation of the right camera, is the only view-dependent parameter and can be fixed by defining a reference plane with known orientation and position. The reference plane is identified by the calibration plate in Figure 3.11a, positioned on top of the spheres with the **X** axis parallel to the side-walls, i.e. to the streamwise direction, the **Y** axis perpendicular to the side-wall and parallel to the y-direction and the origin of the vertical **Z** axis displaced 1 mm above the top of the spheres (corresponding to the thickness of the calibration plate). It is ensured beforehand that the top of the spheres lies on a plane parallel to the flume bed, by measuring the orientation of a flat metal plate positioned on top of spheres and covering the whole field of view with a digital level with a precision of less than 0.1°. The world reference system attached

to the reference calibration plate is shifted through a simple translation to the reference system of the flume (see the red arrows in Figure 3.11a) after the topographic reconstruction.

The results of the calibration procedure for the different experiments show estimated values of the focal length of 60 mm (with relative errors less than 1%). This apparent higher value compared to the nominal focal length of the lens of 50 mm, is a result of the object magnification induced by the refraction.

3.4.2.4 Image matching and reconstruction of the bed topography

For the stereo reconstruction of the bed topography, homologous points in each pair of stereo images need to be matched. Given a point on the sediment surface, its projection onto the left camera image plane has to be matched with the corresponding image projection onto the right camera image plane. The correspondence between the two image planes can be performed on the basis of epipolar geometry (Ma et al., 2004). With reference to Figure 3.12a, a point in the world coordinate frame P and its projections onto the image planes (P'_L and P'_R) lie on the, so called, epipolar plane. The intersection of the epipolar plane with the camera planes, corresponding to the projection of the line of sight of one camera (e.g. $O_L P'_L P$ or $O_R P'_R P$) onto the image plane of the opposite camera, defines the epipolar lines e'_L and e'_R. Even if the precise location of the image projection P'_j is not known, it is bound to lie on an epipolar line, such that the search for corresponding points in the two image planes can be restricted to the epipolar lines.

For the image correspondence, a pattern based correlation method is applied exploiting the principles of epipolar geometry and a least-square image matching technique for sub-pixel interpolation. In a first step, a reference square pattern centred on the image-projected surface point of interest is defined in the image plane of the camera downstream (see Figure 3.12b). The epipolar line, corresponding to the point of interest, is constructed in the image plane of the camera upstream by applying the algorithm by Bouget (2010) (green line in Figure 3.12c), based on a manipulation of the system of equations 3.7. The square pattern in the right image plane with the highest correlation with the reference pattern is identified along the epipolar line (green square in Figure 3.12c). In this manner, a first correspondence at a pixel level between homologous image points is established.

This pattern recognition procedure is affected, though, by some limitations, which can deteriorate the correlation between patterns. First, the two cameras are characterized by different view angles, so that a sediment surface pattern projected onto the image planes is affected by different perspective distortions, leading to differences in the shape of the image pattern between the two cameras. Second, the camera sensors are affected by noise, which results in local difference in pixel intensity at the pattern scale between the two camera. Third, the position of the epipolar line is affected by some uncertainty deriving from the calibration procedure, so that the actual conjugate point might lie outside of the epipolar line. An area-based matching refining method, i.e. the least square image matching technique (hereafter LSM), is, therefore, applied to account for radiometric and geometrical differences between homologous patterns. If $f(x'_R, y'_R)$ is the reference pattern in the right camera image plane and $g(x'_L, y'_L)$ is the search pattern in the left camera image plane, the LSM adjusts the position and shape of g to minimize the intensity level difference between the two patterns. The geometric relationship between the two patterns is locally approximated with an affine transformation

(while, strictly speaking, the camera induces a perspective distortion of the patterns) and the intensity level adjustment is performed through a linear radiometric transformation (Ackermann, 1984):

$$f(x'_R, y'_R) = r_0 + r_1 g(x'_L, y'_L) \tag{3.11}$$

$$\begin{cases} x'_L = a_0 + a_1 x'_R + a_2 y'_R \\ y'_L = b_0 + b_1 x'_R + b_2 y'_R \end{cases} \tag{3.12}$$

where $[r_0, r_1]$ are the radiometric parameters and $[a_j, b_j]$ the parameters of the affine transformation. The eight unknown parameters are estimated by minimizing in the least square sense the difference between the reference and the adjusted search pattern. Since equation 3.11 is a non linear function, the cost function v to be minimized is linearised through a Taylor expansion:

$$v = f(x'_R, y'_R) - r_0 - r_1 g(x'_L, y'_L) = dr_0 + g dr_1 + r_1 \frac{\partial g}{\partial x'_L} da_0 + r_1 x'_L \frac{\partial g}{\partial x'_L} da_1 + r_1 y'_L \frac{\partial g}{\partial x'_L} da_2 +$$
$$r_1 \frac{\partial g}{\partial y'_L} db_0 + r_1 x'_L \frac{\partial g}{\partial y'_L} db_1 + r_1 y'_L \frac{\partial g}{\partial y'_L} db_2 \tag{3.13}$$

The number of equations defined in the linear system 3.13 depends on the number of pixel locations in the reference pattern. Since the system is solved iteratively, accurate initial guesses of the parameters are needed to avoid diverging solutions Remondino et al. (2013). The parameters a_0 and b_0, defining the position of the search pattern, are initialized with the difference in image coordinates between the centre of the pattern identified along the epipolar line in the left image plane and the centre of the reference pattern in the right image plane. The other parameters are initialized in the following way: $[r_0, r_1] = [0,0]$ and $[a_1, a_2, b_1, b_2]$ = [1,0,1,0]. The iteration process is terminated, as soon as the parameters a_0 and b_0 converge to a constant value. In figure 3.12c the final search pattern in red, matching the reference pattern in Figure 3.12b, is presented along with the position of the edges determined during each iteration step. A threshold on the correlation value between the matched search pattern and the reference pattern equal to 0.4 is set, in order to discard potential outliers.

The convergence and accuracy of the LSM depends on the size and the texture of the pattern (Bethmann and Luhmann, 2011). Several sizes of the pattern are tested in order to maximize the correlation between the reference and the search pattern. The tests are performed at various locations of the imaged sediment bed, since the texture of the sediment surface is spatially non-homogeneous. For the plastic granulate characterized by a pronounced texture due to the presence of black and white grains in a proportion of 1 to 3, an optimal pattern size of 50×50 pixels is selected. Smaller pattern sizes would lead, in fact, to a more homogeneous texture, given that the average grain size is 10 pixels. For the experiments with sand, a bigger pattern size of 80×80 pixels is selected, in order to compensate for the low sediment texture. Given an accurate first estimate of the position of the search box and a good pattern texture, the subpixel accuracy reached by the LSM method is of the order of 0.02 pixels (Gruen, 1985; Remondino et al., 2013).

For the construction of the DEM of the sediment surface, a regular grid of points is superimposed onto the left camera image. Within the reference pattern of spheres (see Figures 3.2a-c) where the PIV measurements are also performed, a fine mesh grid size of 10×10 pixels is employed, corresponding to a resolution of $\simeq 1$ mm after surface reconstruction. For the plastic granulate bed, this mesh size corresponds to four measurement points per sediment grain. A resolution of half a grain diameter or lower is, in fact, necessary to resolve
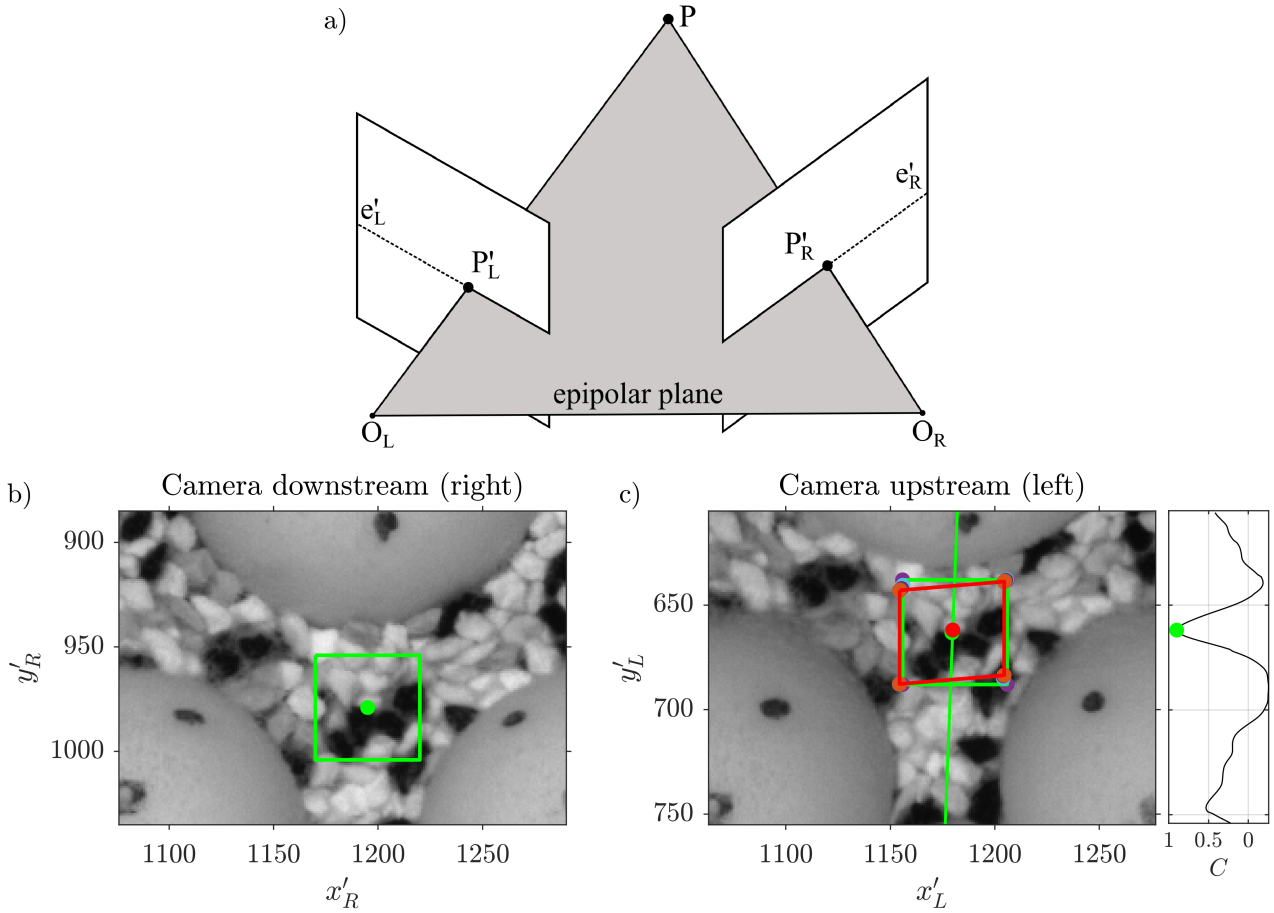
Figure 3.12: (a) Epipolar geometry; (b) Reference pattern in the image plane of the camera downstream; (c) Matched pattern in the image plane of the camera upstream corresponding to the reference pattern in image a; the green pattern represents the first match in the image plane of the camera upstream identified by the correlation peak along the epipolar line; the red pattern is the final match obtained through the least square image matching method.

also the grain roughness and not only the large-scale roughness (Groom et al., 2018). For the sand bed, characterized by a grain size 5 times smaller than the plastic granulate, the mesh size is not adjusted to comply with this criterium as the processing times for image matching would be not feasible. Outside of the reference pattern of spheres, a coarser mesh size of $30{\times}30$ pixels is chosen to resolve only the large-scale roughness features (such as bed-forms).

Since the spheres do not possess any kind of surface texture (apart from some painted markings applied to distinguish different pattern of spheres), the image matching technique would fail to deliver accurate results of the topography of the spheres. The spheres are characterized by evolving protrusion levels during the course of one experiment, so that an adaptive masking technique, based on the sphere's recognition method developed in the Part I (see Section 2.2.4.1), is applied to each stereo image pair to detect the spheres and delete grid points falling over them. The topography of the spheres is reconstructed analytically in a second step after the construction of the DEM of the sediment surface.

The DEM of the sediment surface is reconstructed by first matching the grid points extracted from the right camera image plane with the homologous points in the left camera image plane with the matching technique just described. The position in the world coordinate frame of the matched surface image points is determined

by the triangulation method described in Section 3.4.2.1.

As a result of the reconstruction, the cloud of surface points is not arranged any more in a regular pattern. The data are therefore re-interpolated on a regular grid with a spacing of 1×1 mm^2 in the reference pattern of spheres and 3×3 mm^2 outside. Outliers are then filtered out by identifying points whose elevation is higher or lower than the average bed elevation of the surrounding points over an area 9×9 mm^2 by two standard deviations. Since the bed topography is relatively homogeneous in longitudinal direction given the development of ridges, a global filter is also applied row by row in the longitudinal direction to filter out points with elevation exceeding two times the standard deviation of the streamwise line-averaged bed-level. Finally, a filter based on the deviation of the average bed level gradient in all possible directions over a 3×3 grid-point window centred on the grid-point analysed from the average bed level gradient obtained on a larger 5×5 window without considering the grid-point analysed, is applied (Barzaghi et al., 2001). All outliers are then replaced by bicubic spline interpolation.

3.4.2.5 Error analysis of the stereo photogrammetric technique

An intrinsic source of error in the stereo reconstruction process is the resolution or quantization error. The error arises from the discretization of the continuous world by the discrete pixel size of the CCD camera sensor. With reference to Figure 3.10, Benetazzo (2006) provides an analytical estimation of the maximum quantization error:

$$\epsilon_x^q = \frac{H_c}{2N_c} \frac{\sin 2\beta_c}{\cos^2(\gamma + \beta_c)} \tag{3.14}$$

$$\epsilon_y^q = \frac{H_c}{2N_c} \frac{\sin 2\beta_c}{\cos^2(\beta_c)} \tag{3.15}$$

$$\epsilon_z^q = \frac{H_c^2}{2TN_c} \frac{\sin 2\beta_c}{\cos^2(\gamma + \beta_c)} \tag{3.16}$$

where H_c is the height of the cameras above the surface, T the distance between the cameras, N_c the size of the sensor in pixels, $2\beta_c$ the angle of view of the cameras and γ the angle between the line of sight of the cameras. In the present case, the maximum quantization errors are estimated to be $\epsilon_x^q \simeq 75$ μm, $\epsilon_y^q \simeq 60$ μm and $\epsilon_z^q \simeq 110$ μm (with $H_c = 130$ cm, $T = 85$ cm, $N = 2048$, $\beta_c = 5.6°$ and $\gamma = 18°$).

In practice, de Vries et al. (2011) and Benetazzo et al. (2012) observe that the actual quantization error is smaller than the predicted one when applying sub-pixel interpolation algorithms for image matching. Furthermore, in the present case the refraction through the water surface magnifies the sediment surface, resulting in an apparent reduction of the distance between cameras and sediment surface. Therefore, the predictions of the quantization error by Benetazzo (2006) overestimate the actual quantization error.

The accuracy of the stereo technique can be also estimated by reconstructing the position of the calibration dots on the calibration plane (Astruc et al., 2012). The reconstruction of four calibration plates oriented with their edges parallel to the x and y axis and positioned flush with the top of the spheres leads to a mean dot distance of $\Delta x = 18.764$ mm and $\Delta y = 18.769$ mm. The bias error of the dot distance is as such equal to 14 μm and 19 μm. The rms error of the dot distances provides, instead, a measure of the precision of the measurement, which is estimated to be less than 10 μm.

In order to estimate the accuracy along the vertical direction, six calibration plates covering the whole field of view and positioned flush with the top of the spheres are reconstructed. The calibration dots should ideally lie on a plane displaced 1 mm above the top of the spheres (corresponding to the thickness of the calibration plate). Figure 3.13a shows that the field of the vertical elevations of the calibration dots z_c is characterized by a slight concavity. The elevation values increase, in fact, towards the edges of the field of view. The concavity is probably related to a non planarity of the calibration plate. Nevertheless, the central region of the field of view, where the reference patterns of spheres are located (identified by the three rectangles in figure 3.13a), is characterized by random deviations from the reference plane of the order of 100 μm, so that high accuracy is guaranteed in the regions of interest.

The accuracy in the vertical direction can be also estimated by measuring the distance between the reconstructed position of the calibration dots z_c and the reconstructed vertices of the spheres z_{ts}, which should be equal to 1 mm. Figure 3.13b shows that the distance between these two planes randomly deviates from 1 mm. The deviations are of the order of 100-200 μm over the whole field of view, such that the two planes are effectively reconstructed parallel to each other.

The precision of the stereo reconstruction method applied to the sediment surface is tested by reconstructing the same sediment surface for several successive images (more than 100). The rms error of the position of the surface points is equal to 9 μm, 2 μm and 35 μm for the x, y and z component, respectively. Overall, the accuracy of the stereo reconstruction is estimated, on the safe side, to be of the order of 50 μm in the x and y directions and 100 μm in the vertical direction.
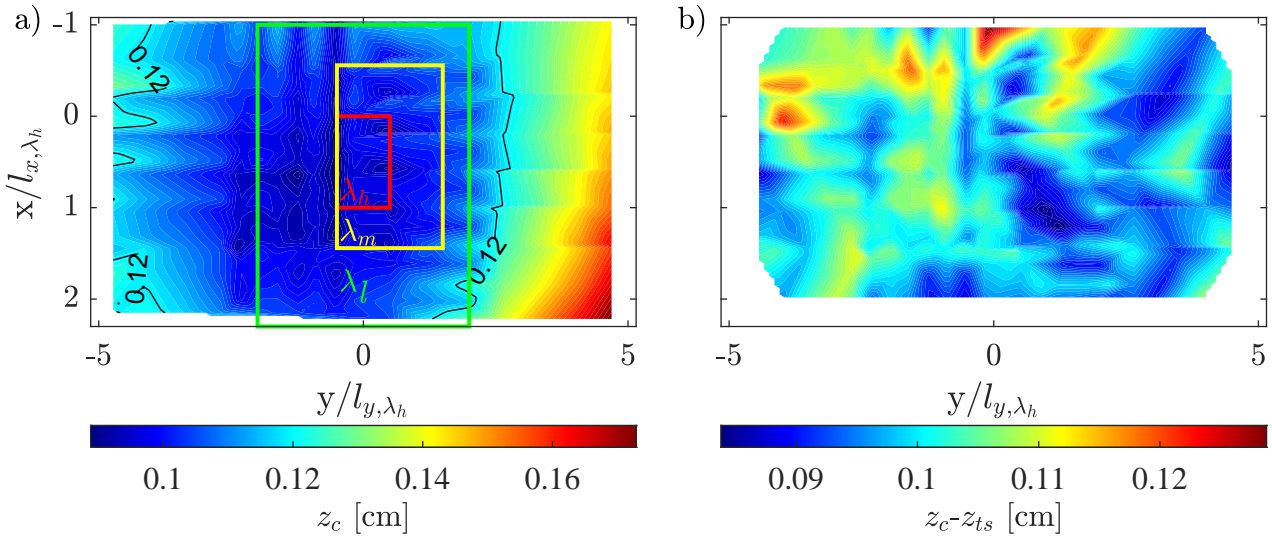
Figure 3.13: (a) Reconstructed vertical elevation of the calibration dots z_c pertaining to six calibration plates positioned on top of the spheres; (b) Distance between the reconstructed elevation of the calibration dots z_c and the reconstructed elevation of the top of the spheres z_{ts}.

3.4.3 Sediment transport measurements

Imaging techniques have been increasingly used in laboratory application for the measurement of bedload transport (Radice et al., 2006; Lajeunesse et al., 2010; Yager and Schmeeckle, 2013; Terwisscha van

Scheltinga et al., 2018) since they are non intrusive and provide both integrated and spatially resolved measurements as compared to sediment traps, impact sensors or hydrophones (Aberle et al., 2017). These techniques, which usually foresee a camera recording the sediment bed from above, are particularly suited for bed-load measurements with the active upper sediment layer. In this case, the grain-movement takes place in contact with the bed with the grains rolling or sliding intermittently in response to the random forcing induced by the turbulent events (Dey, 2014). As such, the bed surface is characterized by the presence of immobile and mobile grains. By applying image processing techniques, the concentration of displaced grains C_s and the average particle velocities v_s can be detected to yield a spatially averaged sediment transport rate $q_s = C_s v_s d_{50}$ (Radice et al., 2006; Yager and Schmeeckle, 2013). Given these premises, the stereo topographic system, described in Section 3.4.2, is used to measure the sediment transport through an image subtraction technique similar to the one used by Radice et al. (2006). Since the sediment transport is primarily modulated by the sediment concentration and only in second instance by the grain velocity (Lajeunesse et al., 2010), C_s is chosen as a proxi of the sediment transport rate and will be solely measured.

3.4.3.1 Measurement principle

The measurement technique is based on the subtraction of successive images of the bed to determine the number of particles displaced. On this basis, the aerial concentration of displaced sediments is defined as (Radice et al., 2006):

$$C_s = \frac{N_s V_g}{\Delta x \Delta y} \tag{3.17}$$

where N_s is the number of grains displaced, $V_g = \pi d_{50}^3/6$ the volume of a sediment particle and $\Delta x \Delta y$ the spatial extent of the measurement area. Since the number of displaced particles N_s depends on the time lag between image frames, equation 3.17 defines a concentration averaged both in time and in space.

The image resulting from the subtraction of two consecutive frames (image difference in the following) shows, in the absence of noise, zero intensity values where no sediments have moved, while positive or negative values where grains have moved. For the technique to work, a sufficient intensity contrast between the background and the displaced grains is needed. Figure 3.14b shows an example of image difference
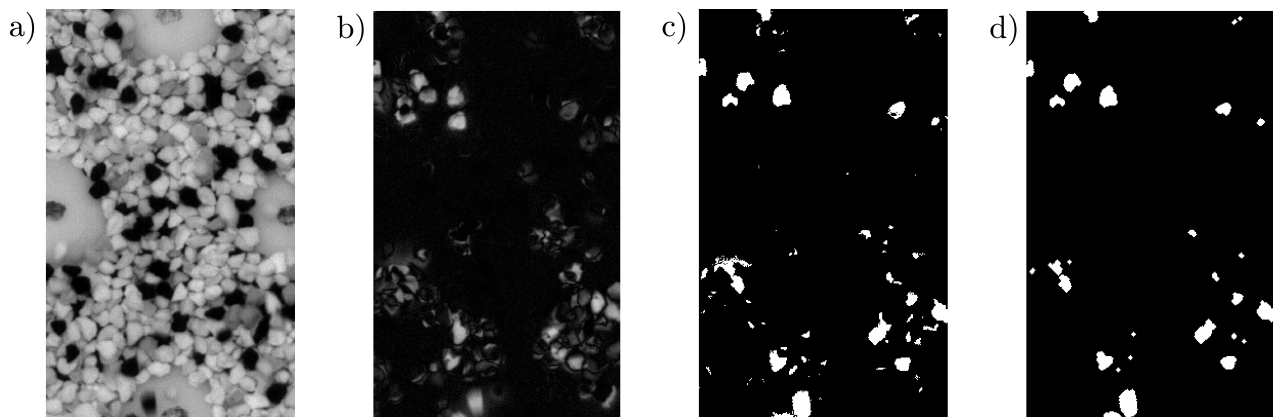

Figure 3.14: (a) Original frame; (b) Difference image obtained from the subtraction of the two frames; (c) Binarized positive part of the difference image; (d) Filtered binarized positive part of the difference image.

obtained with a plastic granulate bed during Exp. 1 (see 3.14a). Since the difference image displays both the initial and final position of the displaced grains, only its positive part is retained. The difference image is then binarized on the basis of the automatic object detection method by Otsu (1979), obtaining a pattern of white blobs over a black background (see Figure 3.14c). Due to image noise, blobs with a small diameter, which do not represent significant displacements, are present. These are filtered out by applying a morphological erosion filter based on a circular structural element with a diameter of 3 pixels (Jähne, 2012), followed by a dilation filter with the same size to restore the size of the remaining particles. As in Radice et al. (2006), the particles with a size smaller than 20% of the average particle size are then removed. The final image is presented in Figure 3.14d.

3.4.3.2 Data acquisition

The sediment transport measurements are performed with the camera of the stereo photogrammetric system positioned downstream of the measurement region, as described in Section 3.4.2.2. Given that the images are distorted due to the oblique orientation of the camera compared to the sediment bed, they are first stereo rectified on the basis of the calibration parameters determined in Section 3.4.2.3. In this manner, the concentration of displaced sediments is determined within the reference area defined by reference pattern of spheres over which the PIV measurements are performed (see Figures 3.2a-c).

The concentration of displaced sediments is measured only during Exp. 1-7 as the plastic granulate, composed of black and white particles in a proportion of 20 to 80, guarantees enough background contrast to distinguish moving particles. During Exp. 8-10 sediment transport measurements are not performed, as the sand used is characterized by a homogenous texture.

For the measurement of the number of grains displaced, a burst of 9 images is recorded every 1.5 minutes during the whole duration of the experiments (please recall that the first image is used for the topographic reconstruction of the bed - see Section 3.4.2.2). During the PIV measurements only bursts of three images are recorded due to time constraints. The image frequency is defined as high as possible in order to constrain the particle motion to the local and intermediate range, i.e. to trajectories not overstepping two resting periods of a particle (Nikora et al., 2002a). In this manner, the concentrations defined by equation 3.17 can be considered instantaneous with a negligible error (Radice et al., 2006). Given that the highest particle velocity observed is equal to 2 cm/s, the image frequency is set to 32 Hz in order to guarantee a minimum particle displacement of 0.3 d_{50}, necessary for a robust detection of the particles. Each burst provides 8 samples of C_s, which are averaged to increase the measurement accuracy.

By comparing the number of displaced sediments obtained from the image processing and from visual counting, it is observed that the technique tends to underestimate the actual concentration of displaced sediments by 1% when the bed is uniformly covered by sediments, i.e. in the presence of diffuse sediment transport. The measured and observed N_s tend, instead, to converge when the spheres protrude and the sediment transport reduces.

3.5 Definitions and operators

In this Section, an overview of the relevant morphological, sediment transport and flow parameters derived from the stereo-PIV and topographic measurements is presented along with the temporal and spatial averaging operators used in the rest of the work. To define the common relevant geometrical properties of the measurements, Figure 3.15 illustrates, as an example, a longitudinal flume section below the boat along the measurement plane A for the spheres' configuration with the highest roughness density λ_h (see Figure 3.2a) filled with an idealized fine-sediment bed. The geometrical properties defined hereafter are also valid for the spheres' configuration with medium and low roughness density, λ_m and λ_h. The origin of the coordinate system is common to all spheres' configurations and is located one pattern length l_{x,λ_h} downstream of the leading edge of the boat, in the centre of the channel and at the top of the second layer of spheres. The x-axis is oriented in the streamwise direction, the z-axis in the vertical direction and the y-axis follows the right-hand rule. Since all experiments are performed under uniform flow conditions, the slope of the flume i coincides with the slope of the free surface or equivalently with the slope of the boat installed at the free surface (see Figure 3.15). The water depth H is defined as the distance between the top of the spheres and the water surface.
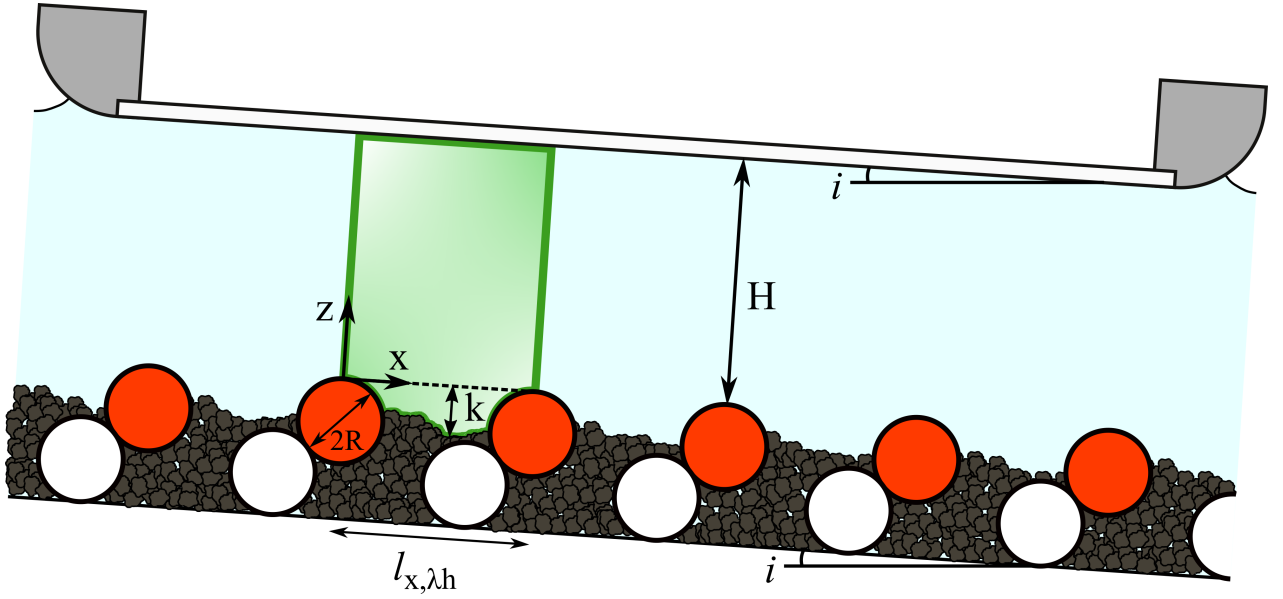
Figure 3.15: Sketch of the geometrical properties and of the measurement region for the bed configuration λ_h along the measurement plane A for an idealized fine-sediment bed. The origin of the coordinate system is located at the top of the second layer of spheres at the beginning of the second pattern (the location of the coordinate system is the same also for the bed configurations λ_m and λ_l). The flume bed and the boat installed at the water surface share the same slope i. The protrusion height $k(x,y)$ is defined as the distance between the local fine-sediment bed level and the top of the spheres. The green region represents the measurement region of the stereo PIV. Its length, equal to one pattern length l_{x,λ_h}, corresponds to the longitudinal extension of the topographic measurement region.

3.5.1 Morphological and sediment transport parameters

The definition of the morphological parameters is based on the digital elevation model of the bed topography obtained with the stereo photogrammetric technique described in Section 3.4.2. The digital elevation model describes the two-dimensional field of bed elevations z_b(x,y) within the topographic measurement area which covers the whole width of the channel in the transverse direction and the whole length of the reference pattern of spheres in the longitudinal direction (see Figure 3.15). The length of the measurement area varies according to the length of the reference pattern which depends on the configuration of spheres (see Figure 3.2). Figure 3.16a shows an example of a digital elevation model extracted during Exp. 1 at t = 3.56 h. The protruding spheres can be clearly identified on the basis of the circular isocontour lines.

The main morphological parameter is the <u>protrusion level</u> of the spheres $\underline{P} = k/R$ where k is the local protrusion height. The protrusion height k is defined as the distance between the local fine-sediment bed level and the top of the spheres, as illustrated in Figure 3.15. Given the digital elevation model extracted at a certain time during the experiments, the protrusion level map P(x,y) is given by $P = k(x,y)/R = -z_b(z_b \in$ fine-sediment bed$)/R$. Figure 3.15b shows an example of a protrusion map obtained from the DEM in Figure 3.15a. The holes represent the regions where the spheres are protruding. Note that the definition of P is similar to the one given in Part I of this work (see Section 2.2.4.1), even though the present definition differs in as much as the protrusion level P, here defined, does not represent an average protrusion around a sphere, but a point measurement. Compared to Part I, P can assume, in this case, also negative values when the fine sediments cover the spheres (see Figure 3.15b).

For the analysis of the bed-forms, such as ridges, the protrusion level map is spatially averaged in the longitudinal direction, yielding a transverse profile of <u>longitudinally-averaged protrusion levels</u> $\langle P \rangle_x$(y). Figure 3.15c shows an example of a transverse profile of $\langle P \rangle_x$ obtained from the protrusion level map in Figure 3.15a.

For the analysis of the bed morphodynamics at the pattern scale, i.e. within the reference pattern of spheres highlighted in Figures 3.2a-c and in red in Figures 3.16a-b, the following morphological variables are defined:

- <u>pattern-averaged protrusion level</u> $\langle P \rangle$, obtained by spatially averaging the protrusion levels within the reference pattern;

- <u>standard deviation</u> of the bed elevation: $\underline{\sigma_z} = \sum_{i=1}^{N}(z_{b,i} - \langle z_b \rangle)^2/N$, where N is the number of sampling points within the reference pattern and $\langle z_b \rangle$ the pattern-averaged bed-level;

- <u>skewness</u> of the bed elevations: $\underline{S_k} = \sum_{i=1}^{N}(z_{b,i} - \langle z_b \rangle)^3/(N\sigma_z^3)$;

- <u>kurtosis</u> of the bed elevations: $\underline{K_u} = \sum_{i=1}^{N}(z_{b,i} - \langle z_b \rangle)^4/(N\sigma_z^4) - 3$;

- <u>inclination index in the x-longitudinal or y-transverse direction</u> $I_{x/y} = (i_b^+ - i_b^-)/N_i$, where i_b^+ and i_b^- are the number of positive and negative bed slopes specified by increasing and decreasing bed elevations, respectively, in longitudinal or transverse direction and N_i is the total number of bed slope within the pattern;

- <u>frontal density</u> of the pattern $\lambda_f = (A_f + A_{f,fs})/A_r$ where A_f is the frontal area of the protruding spheres within the pattern, $A_{f,fs}$ the frontal area of the topographic features of the fine-sediment bed within the pattern and A_r the planar area of the pattern. Given a wall-normal vector to the bed surface
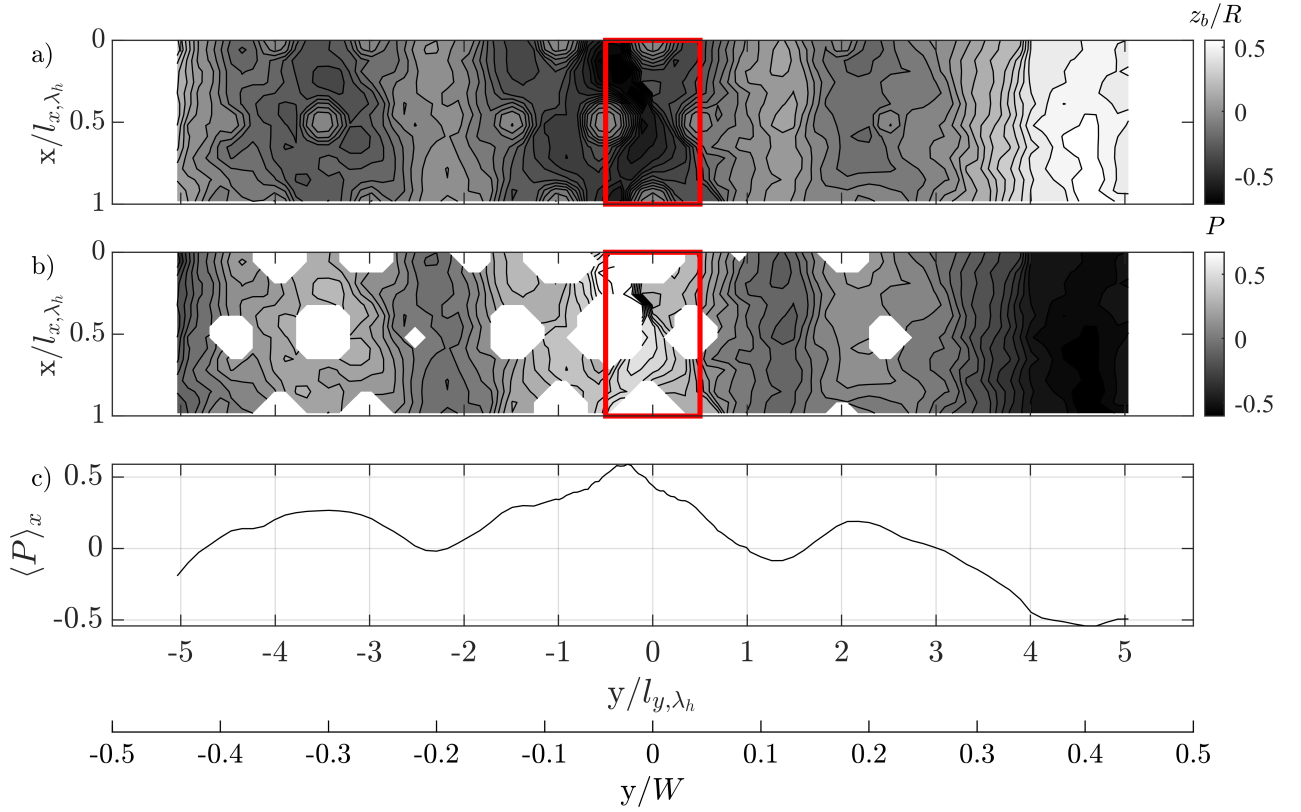
Figure 3.16: (a) Example of digital elevation model of the bed elevations $z_b(x,y)$ (the data are extracted from Exp. 1 at t = 3.56 h); (b) 2D-field of the protrusion levels of the spheres $P = k/R$ obtained from the digital elevation model in Figure (a); (c) Transverse profile of the longitudinally averaged protrusion levels $\langle P \rangle_x$ (the vertical scale is magnified three times compared to the transverse scale). The region contoured in red in Figures (a) and (b) identify the reference pattern of spheres, where the PIV measurements are also performed.

with components $[n_x, n_y, n_z]$ and an elemental area of the bed surface dA, the total frontal area of the pattern is given by $A_f + A_{f,fs} = \int_{n_x<0}(-n_x)dA = \int_{n_x<0}(-\partial_x z_b)dA_r$;

- <u>planar density</u> of the spheres $\underline{\lambda_p} = A_p/A_r$ where A_p is the planar area of the protruding spheres.

- <u>angle of attack of the spheres</u> α_a defined by the ratio between the pattern-averaged protrusion height of the spheres $\langle k \rangle$ and the planar radius of a sphere obtained at half the pattern-averaged protrusion height, as done in the case of hills (Ferreira et al., 1995).

- <u>erosion rates</u> $\underline{E} = CR\partial_t\langle P \rangle$, where $C = 1 - \phi_s$ is the solidity of the fine-sediments; E is equivalent to the erosion rate of a uniform bed in the absence of protruding spheres;

- <u>total erosion rates</u> $\underline{E_t} = (1 - \lambda_p)CR\partial_t\langle P \rangle$; E_t describes the actual volume of fine-sediments eroded over time in the presence of the protruding spheres;

As for the sediment transport variables, the <u>concentration of displaced sediments</u> $\underline{C_s}$ is measured within the reference pattern area according to equation 3.17.

3.5.2 Flow parameters

The flow parameters are calculated on the basis of the flow field measurements performed over plane A and plane B within the reference pattern of spheres (see Figures 3.2a-c and Figures 3.7a-c). The stereo PIV measurement yield the velocity vector fields both above and within the bed interstices as exemplary shown in Figure 3.15a. Three velocity components components are provided: the streamwise velocity component u (x-direction), the transverse velocity component v (y-direction) and the vertical velocity component w (z-direction). Instantaneously, the viscous shear stress is also defined as $\tau_{vis} = \rho_f \nu \partial_z u$.

In a time-averaged framework, the flow variables are averaged in time within the measurement plane, yielding a two-dimensional vector field. The time-averaged velocity components are denoted as $\overline{u}$, $\overline{v}$ and $\overline{w}$ and the time-fluctuations of the velocity components are defined as $u' = u - \overline{u}$, $v' = v - \overline{v}$ and $v' = v - \overline{v}$. The following shear stresses are defined according to the time-averaged Reynolds equations:

- time-averaged viscous shear stress $\overline{\tau}_{vis} = \rho_f \nu \partial_z \overline{u}$

- Reynolds shear stress in the longitudinal direction $\tau_{uw} = - \rho_f \overline{u'w'}$

- Reynolds shear stress in the transverse direction $\tau_{vw} = - \rho_f \overline{v'w'}$

- local fluid shear stress $\tau_{xz}|_{local} = \overline{\tau}_{vis} + \tau_{uw}$

The local fluid shear stress and the Reynolds shear stress in the transverse direction are used to define the local forcing acting on the fine sediments. By sampling $\tau_{xz}|_{local}$ and τ_{vw} at the top of the roughness sublayer of the fine-sediments h_{rs}^s (see Section 5.4 for further details), the local shear stress in the streamwise and transverse directions are defined:

- $\tau_s^x = \tau_{xz}|_{local}\Big|_{z'=h_{rs}^s}$

- $\tau_s^y = \tau_{uw}\Big|_{z'=h_{rs}^s}$

The local sediment transport conditions are then defined on the basis of the local Shields parameters in the streamwise and transverse directions, $\theta_S^x = |\tau_s^x|/(\rho_f \Delta g d_{50})$ and $\theta_S^y = |\tau_s^y|/(\rho_f \Delta g d_{50})$, respectively.

In a double-averaged framework, the flow variables are averaged in the longitudinal direction within the stereo-PIV measurement plane (A or B), once time-averaging is performed. The spatial average within the bed interstices is performed along lines parallel to the x-direction only over the regions occupied by fluid (intrinsic spatial averaging). The double-averaged velocity components are denoted as $\langle \overline{u} \rangle_x$, $\langle \overline{v} \rangle_x$ and $\langle \overline{w} \rangle_x$ with the spatial fluctuations defined as $\tilde{u} = \overline{u} - \langle \overline{u} \rangle_x$, $\tilde{v} = \overline{v} - \langle \overline{v} \rangle_x$ and $\tilde{w} = \overline{w} - \langle \overline{w} \rangle_x$. According to the double-averaged momentum equation (Nikora et al., 2001), the following shear stresses are defined:

- double-averaged viscous shear stress $\langle \overline{\tau}_{vis} \rangle_x = \rho_f \nu \partial_z \langle \overline{u} \rangle_x$

- spatially-averaged Reynolds shear stress in the longitudinal direction $\langle \tau_{uw} \rangle_x = - \rho_f \langle \overline{u'w'} \rangle_x$

- spatially-averaged Reynolds shear stress in the transverse direction $\langle \tau_{vw} \rangle_x = - \rho_f \langle \overline{v'w'} \rangle_x$

- form-induced shear stress $\tau_f = - \rho_f \langle \tilde{u}\tilde{w} \rangle_x$

- total shear stress $\tau_{xz} = \langle \overline{\tau}_{vis} \rangle_x + \langle \tau_{uw} \rangle_x + \tau_f$

The total shear stress τ_{xz} is used to define the local shear velocity u_* by linearly extrapolating the τ_{xz}-profile to the top of the spheres.

4 Erosion of a uniform fine-sediment bed

4.1 Introduction

The aim of this chapter is to investigate the flow and the erosive conditions characterizing a uniform fine-sediment bed without the presence of protruding spheres. As discussed in Part I (see Chapter 2), the spheres can enhance or reduce the erosion rate of the mobile sediments depending on their protrusion level. The analysis was performed, though, in absolute terms. The shear stress and erosive conditions of a uniform fine-sediment bed serve, therefore, as reference conditions, in the next chapters, to effectively quantify the influence of the protruding spheres on the local shear stress and on the transport of the fine mobile sediments as compared to a uniform fine-sediment bed.

The erosion of sediments from a uniform bed, intended as volume of sediments removed per unit area and per unit time, has been investigated by various authors who developed stochastic (Einstein, 1950; de Ruiter, 1983) and empirical (Fernandez-Luque, 1974; Nakagawa and Tsujimoto, 1980; van Rijn, 1984a; Dey and Debnath, 2001) predictive approaches. These approaches are based on the assumption that the erosion rates scale with the Shields parameter θ. For example, van Rijn (1984a) developed the following empirical formula:

$$\frac{E}{\sqrt{g\Delta d_{50}}} = \alpha_E D_*^{0.3} T_\theta^{1.5} \tag{4.1}$$

where $\alpha_E = 0.0003$ is an empirical proportionality factor, D_* the non-dimensional particle parameter (see Section 2.2.2) and $T_\theta = (\theta - \theta_c)/\theta_c$ the normalized transport stage parameter. The applicability of these approaches for this case of study is limited by three factors, though. First, they were determined by measuring the amount of sediments being removed from a localized sediment-injecting system installed in an otherwise immobile bed, neglecting as such the influence of the sediment transport type (such as irregular bed-load or generalized sheet flow or suspended) on the erosion process. Second, they are applicable only within the range of sediment sizes, for which they were developed, usually not ranging over 1.5 mm (van Rijn, 1984a; Dey and Debnath, 2001). As such, these formulas can be barely applied for the plastic granulate used herein. Third, they require the knowledge of the shear stress acting on the sediments, which is not trivial to determine a priori for mobile bed conditions, as the momentum transmitted to the bed is partially dissipated to overcome the inter-granular contact resistance (Dey et al., 2012).

For these reasons, the erosion rates, the aerial concentration of transported sediments and the shear stress conditions representative of an uniform sediment bed are determined, in the following, on the basis of an experimental approach measuring simultaneously the flow, the bed topography and the sediment transport for the flow conditions of the reference Exp. 1 (see Table 3.1). The turbulent structures near the bed, responsible for the sediment transport, are also investigated to clarify, in the next chapters, how the protruding spheres modify the turbulence at the level of the fine sediments. The reference sediment-transport and shear-stress

conditions for a uniform sediment bed for the other flow conditions investigated in Table 3.1 are derived via scaling arguments.

4.2 Flow conditions and experimental setup

The experiment was designed to monitor the erosion of a uniform flat bed made of plastic granulate with a thickness 3 grain diameters higher than the top of the immobile bed of spheres. The fixed bed of spheres with the highest roughness density λ_h was left in the fine sediments in order to guarantee hyporheic flow conditions similar to a natural gravel bed. This bed configuration corresponds to the reference bed condition used to define the flow conditions of the experiments in Table 3.1, i.e. with the fine sediment bed flush with the top of the spheres. Table 4.1 illustrates the experimental flow conditions, similar to the reference Exp. 1 in Table 3.1.

The experimental apparatus is composed of the stereo PIV system and the stereo-photogrammetric system

θ	H	d_{50}	Q	i	U	R_h	u_{*R}	u_{*R^c}	u_{*H}	Re^*	Re
[-]	[cm]	[mm]	[l/s]	[%]	[cm/s]	[cm]	[cm/s]	[cm/s]	[cm/s]	[-]	[-]
0.063	5.6	1.72	4.5	0.11	27	4.1	2.1	2.3	2.5	39	15000
±0.008	±0.05		±0.5	±0.01	±0.05	±0.1	±0.2	±0.2	± 0.2		

Table 4.1: Parameters of the uniform sediment bed experiment: Shields parameter $\theta = u_{*R^c}^2/(g\Delta d_{50})$, water depth H, grain diameter d_{50}, flow rate Q, slope i, bulk velocity $U = Q/(WH_w)$, hydraulic radius R_h, shear velocity based on the hydraulic radius $u_{*R} = \sqrt{gR_h s}$, shear velocity based on the hydraulic radius with side-wall correction $u_{*R^c} = \sqrt{gR_h^c i}$, shear velocity based on the water depth $u_{*H} = \sqrt{gHi}$, particle Reynolds number $Re^* = u_{*R^c}d_{50}/\nu$, bulk Reynolds number $Re = UH/\nu$.

described in Sections 3.4.1.2 and 3.4.2.2, respectively. The laser sheet of the stereo PIV system is positioned in the centre of the channel. The stereo-PIV measurement region corresponds to the one shown in Figure 3.7b over the second pattern of spheres below the boat, vertically spanning from the fine sediment bed to the water surface. The topographic measurement region is located at the same position below the boat with the same longitudinal extension as the PIV measurement region and covering the whole cross Section.

The stereo PIV system and the topographic system are operated simultaneously with the same number of images per burst and the same image frequencies f as described in Sections 3.4.1.3 and 3.4.2.2. The duration of the measurements is limited to 2 minutes, in order to avoid that the spheres protrude from the fine sediment bed and that dunes develop. Given the limited duration of the measurements, an image burst period of 0.12 s, equal to half a bulk time unit, is selected for an amount of 1000 roughly independent samples. At each time step, the 2D3C-vector velocity field with a resolution of 1.1×1.1 mm^2, a digital elevation model with a resolution of 1 mm over the whole measurement field and the aerial concentration of displaced sediments are all reconstructed as described in Sections 3.4.1.6, 3.4.2.4 and 3.4.3, respectively.

The experimental protocol consists in filling the bed of spheres with fine sediments in submerged conditions to avoid water inclusions. The fine sediment bed is then screeded to 3 grain diameters higher than the top of the spheres. The flow rate is then slowly increased to the desired flow conditions. The measurements are started then after 5 minutes to allow the bed to adjust to the flow conditions.

4.3 Erosion and sediment transport rates

In this Section, the temporal evolution of the uniform bed of sediments is analysed in order to determine the erosion and sediment-transport rates. Figure 4.1a shows the transverse profiles of the bed elevations $\langle z_b \rangle_x$, obtained from longitudinal average of the DEM, at the beginning (black line) and at the end of the measurement time (red line). Please note that the vertical scale is magnified ten times compared to transverse scale. The profiles show the presence of a ridge near the centre of the channel, pointing out to the presence of secondary currents. The transverse variation in bed elevations induced by the presence of the ridge is below one grain diameter and the lateral slopes do not exceed 2°, so that the bed can be considered almost flat. A ridge is also observed to develop in the same position during the experiments for the characterization of the influence of protruding spheres (see chapters 5 and 6), so that these measurements effectively serve as reference condition. Comparing the $\langle z_b \rangle_x$-profiles for $t = 0$s and $t = 120$ s, erosion of the bed is clearly observed to the left and to the right of the ridge peak, i.e. in the regions centred in the centre of the channel (for y/W = 0) and in the quarter plane (for y/W = -0.25). As such, the measurement region located in the centre of the channel for the definition of the reference shear stress conditions (see Section 4.5.1) and of the sediment transport rates, effectively characterizes the highest erosive conditions for a uniform fine sediment bed in the presence of mild lateral changes in bed elevations.

As discussed in Appendix A and in Section 2.3.4, the longitudinally averaged erosion rates for a uniform fine sediment bed can be expressed as $E = -C\partial_t \langle z_b \rangle_x$ (where C is the solidity of the plastic granulate). Figure 4.1b shows the temporal evolution of $\langle z_b \rangle_x$ below the laser sheet at y/W = 0. It can be observed that the bed level fluctuates over time, as the result of the spatially heterogeneous nature of sediment transport with pockets of
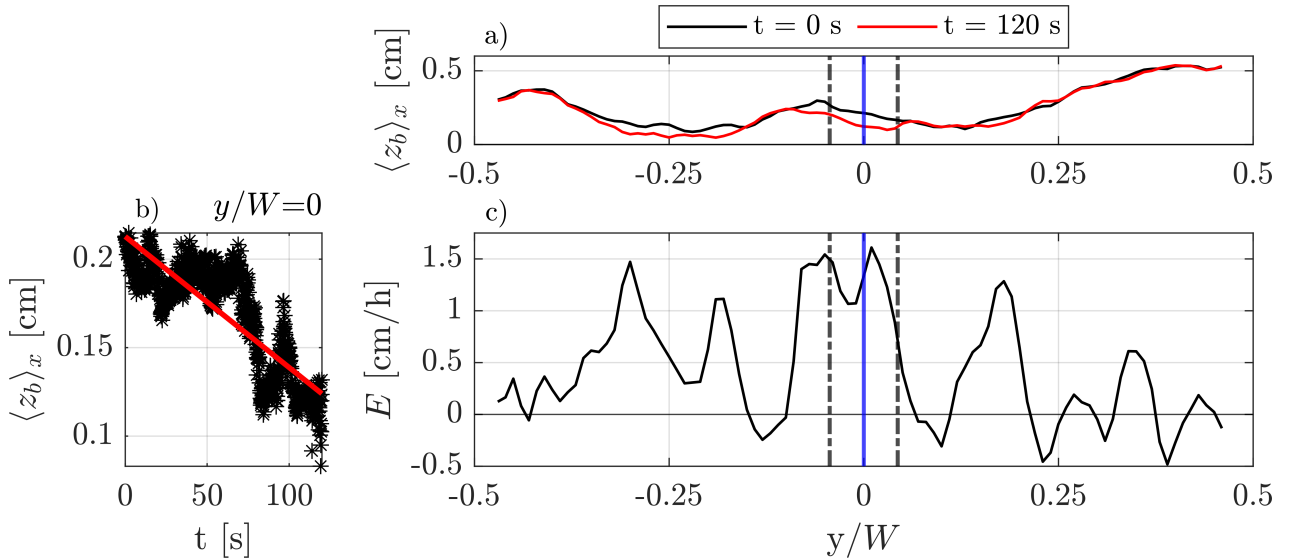
Figure 4.1: (a) Transverse profile of the longitudinally averaged bed elevations $\langle z_b \rangle_x$ at the beginning and at the end of the measurement (the vertical scale is magnified 10 times compared to the transverse scale). (b) Temporal evolution of the fine sediment bed level at y/W = 0; the red line is the linear fit for the definition of the erosion rate. (c) Transverse profile of the erosion rates. In Figures (a) and (c), the vertical blue line identifies the position of the laser sheet and the dashed-dot lines the lateral extension of the reference area for the definition of the concentration of displaced sediment particles.

sediments being locally washed out downstream or locally deposited from upstream. Nevertheless, a clear decreasing trend is apparent. The local erosion rate at each transverse position is, therefore, determined by linearly interpolating the temporal profile of $\langle z_b \rangle_x$, as shown in Figure 4.1b (red line). $\partial_t \langle z_b \rangle_x$ is estimated on the basis of the slope of the linear best fit. Figure 4.1c shows the transverse profile of the erosion rates. E varies in the transverse direction, with the highest erosion rates observed on the sides of the ridge and quasi equilibrium conditions ($E \simeq 0$) over the ridge. Visual observations of the bed during the experiment confirm that the sediment transport was not uniform over the cross section with consistent reductions in the ridge regions and near the side-walls where almost no erosion takes place. The region in the centre of the channel is characterized by spatially homogeneous erosion rates, representative of the maximum erosive conditions, so that the reference erosion rate for a uniform sediment bed $E_{P0} = 1.5$ cm/h is defined (the subscript $P0$ stands for zero protrusion of the spheres). For comparison, the predictive formula 4.1 by van Rijn (1984a) yields on the basis of the measured shear stress (see Section 4.5.1), a predicted erosion rate of 3.6 cm/h with a similar order of magnitude, but more than double the measured value. The use of the a priori determined shear stress u_{*H} would have resulted in a predicted value of 40 cm/h, showing furthermore that for an accurate prediction of the erosion rates the measure of the actual shear stresses is necessary.

The aerial concentration of displaced sediments C_s representative of the sediment transport conditions, is defined over the reference area with the same size of a pattern of spheres $l_{x,\lambda_h} \times l_{y,\lambda_h}$ centred below the laser sheet (see the vertical dot-dashed lines in Figure 4.1). For each time, the number of sediment particles N_p displaced over this reference area are determined. On this basis, the time-averaged reference aerial concentration of displaced sediments for a uniform fine sediment bed $C_{P0} = 2\%$ is determined.

4.4 Characterization of the roughness scales

The physical roughness of the fine-sediment bed can be analysed at a global scale (considering both the influence of the bedforms and of the grains), at a meso-scale (considering only the bedform induced roughness) and at a grain-scale. To isolate the meso- and grain-scale, a moving window technique is applied to the DEM following the procedure suggested by Smart et al. (2002). The DEM is first downscaled to a grid size of 1.25 d_{50}. The elevation of each grid point is obtained by averaging the elevations of the neighbouring grid points in the original DEM within a radius of 2.5 d_{50}. The mesoscale DEM is then obtained by interpolating this surface to the original grid size of 1 mm through bicubic spline interpolation. The grain scale DEM is determined by subtracting the mesoscale DEM from the measured DEM. Figures 4.2a-c show an example of the DEM at the global-, meso- and grain-scale, respectively.

The three DEM are analysed by calculating the standard deviation $\sigma_z = \sum_{i=1}^{N}(z_{b,i} - \langle z_b \rangle)^2/N$, skewness $S_k = \sum_{i=1}^{N}(z_{b,i} - \langle z_b \rangle)^3/(N\sigma_z^3)$ and kurtosis $K_u = \sum_{i=1}^{N}(z_{b,i} - \langle z_b \rangle)^4/(N\sigma_z^4)$-3 of the bed elevations, where N is the number of grid points. σ_z, S_k and K_u are considered characteristic measures of the vertical roughness scale, of the bed-surface packing and of bed regularity, respectively (Nikora et al., 1998; Coleman et al., 2011; Perret et al., 2020). Positive skewness is characterisitc of a bed elevation pdf with an elongated tail towards extreme infrequent bed elevations higher than the mean bed level. $S_k > 0$ is generally observed for smooth surfaces such as armored gravel beds filled with fine sediments (Coleman et al., 2011; Perret et al., 2020). A negative skewness suggests, instead, to the presence of holes and bumps on the bed surface. The kurtosis characterizes the flatness of the bed elevation pdf, with $K_u > 0$ for pdfs narrower than a Gaussian
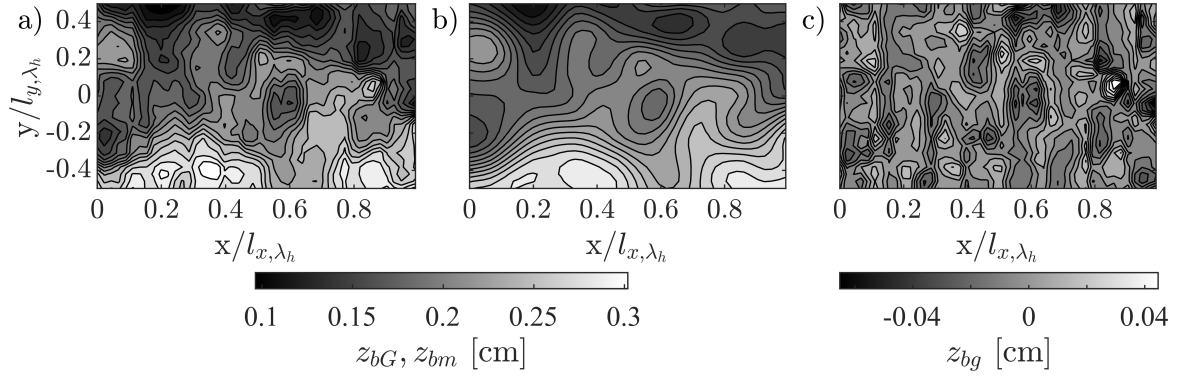
Figure 4.2: (a) Global-scale DEM, (b) meso-scale DEM and (c) grain-scale DEM of the reference pattern below the laser sheet at the end of the experimental run.

distribution. $K_u > 0$ is observed in the case regular surfaces with sporadic changes in bed elevations, such as widely spaced sand dunes Coleman et al. (2011). The opposite is true for $K_u < 0$.

The analysis of the DEMs is restricted to a region below the laser sheet with the same size as the pattern of spheres, already chosen for the analysis of the sediment transport in the previous Section. The size of this region, equal to $26 \times 15\ d_{50}^2$ is large enough to robustly measure the roughness parameters at all scales. As shown by Bertin et al. (2017), a widow size of 12-18 d_{50} in both horizontal and transverse directions is necessary to capture the spatial variability of the grain-scale topography.

Table 4.2 lists the time-averaged roughness parameters obtained for the global- (G), meso- (m) and grain-scale (g) DEMs. It is observed that the standard deviation of the global and meso-scale, $\sigma_{z,G}$ and $\sigma_{z,m}$, are similar and consistently higher than the grain-scale standard deviation $\sigma_{z,g}$. This means that the roughness at the patch scale is predominantly influenced by the bed structures larger than the grains. Furthermore, $\sigma_{z,G}$ is not the result of the sum of $\sigma_{z,m}$ and $\sigma_{z,g}$, showing that the meso- and grain-scale roughness are statistically correlated. This confirms the observation by Bertin et al. (2017), who also studied the separation between roughness scales on a gravel bed, that the grain and bed-form scales interact.

Comparing now the statistical bed roughness with the geometrical bed roughness, identified by the mean grain diameter d_{50}, the ratio $d_{50}/\sigma_{zG} = 4$ is consistent with previous studies on mobile uniform sand by Coleman et al. (2011).

The time-averaged skewness and kurtosis are negative for both the global- and meso-scale DEMs. This is consistent with the irregular bed topography, characterized by holes and bumbs, as shown in Figures 4.2a-b. The relatively large local deviations in bed elevations can be ascribed to the spatially heterogeneous sediment transport conditions. Visual observations of the bed have shown, that the bed load does not constitute a spatially homogenous sediment transport layer, but pockets of sediments are moved intermittently over an otherwise immobile bed, creating small bumbs. This is consistent with transitional regime characterizing the flow (as later shown in Section 4.5.2), for which, as discussed by Gyr and Müller (1996), the turbulent sweep events move patches of grains intermittently and at random locations, which eventually settle down due to the viscous energy loss.

In the case of the grain-scale DEM, both the skewness and the kurtosis are positive. This means that the grains are regularly arranged and well packed. As shown in Figure 4.2c the grain elevations are homogeneous over the whole reference pattern. As shown by Perret et al. (2020) and Penna et al. (2021) comparing screeded and water-worked immobile gravel beds, positive values of kurtosis and skewness are observed at the grain-scale

for water worked beds. This shows that, even though the present bed was initially screeded, the bed quickly rearranges to display a grain-scale structure similar to natural water worked beds. This is in agreement with the work by Powell et al. (2016), who found that screeded beds subjected to armoring quickly develop a natural bed structure.

DEM	$\overline{\sigma}_z$	$\overline{S_k}$	$\overline{K_u}$
	[cm]	[-]	[-]
Global scale	0.042	-0.06	-0.4
Meso scale	0.038	-0.07	-0.5
Grain scale	0.012	0.09	0.6

Table 4.2: Time-averaged roughness parameters for the patch-, meso- and grain-scale DEMs.

4.5 Flow statistics

For the analysis of the flow statistics a reference bed level is defined at each time step by averaging the bed elevations measured below the laser sheet at y/W = 0. Since the sediment bed level lowers over time, the time average of the flow statistics is performed over horizontal layers with the same relative distance z/δ from the fine sediment bed (where δ is the thickness of the boundary layer developing over the fine-sediment bed identified by the zero iso-stress line, as defined in Appendix H.3.3). In order to do so, it is assumed that the vertical profiles of the flow statistics remain self-similar.

4.5.1 Bed shear stress

Figure 4.3a shows the turbulent shear stress field $\tau_{uw} = -\rho_f \overline{u'w'}$. The highest shear stresses are observed near the bed. They display a relatively non-homogeneous behaviour in the longitudinal direction, probably related to the roughness heterogeneity associated with the bumps and holes observed on the bed surface in Section 4.4. Given the limited duration of the PIV measurements, though, time-convergence issues might also play a role.

Figure 4.3b shows the vertical profiles of the total fluid shear stress τ_{xz} and of its components, i.e. of the longitudinally-averaged turbulent stress $-\rho_f \langle \overline{u'w'} \rangle_x$, of the double-averaged viscous stress $\rho_f \nu \partial_z \langle \overline{u} \rangle_x$ and of the form-induced stress $-\rho_f \langle \tilde{u}\tilde{w} \rangle_x$ (Nikora et al., 2001). The turbulent shear stress dominates the momentum exchange over the whole water depth, as expected. The contribution of the viscous and form-induced stresses increases near the bed, with the viscous shear stresses dominating over the form-induced stresses. This feature is consistent with the transitional flow conditions of the bed (as disussed later in Section 4.5.2) for which the roughness height is of the same order of magnitude as the viscous sublayer, so that the flow heterogeneities induced by the grain roughness are partially suppressed by viscosity.

The total fluid shear stress profile τ_{xz} shows a linear distribution below the boundary layer developing along the boat, showing that the secondary currents are quite weak. Therefore, the reference bed shear stress acting on the fine-sediments in the absence of spheres, τ_{P0} = 0.34 Pa, is determined by linearly extrapolating the

τ_{xz}-profile to the average fine-sediment bed. The corresponding reference bed shear velocity u_{*P0} = 1.84 cm/s is 25% lower than the shear velocity obtained from the water depth and slope u_{*H} (see Table 4.1), which is representative of the shear stress conditions for an immobile bed but not for a mobile bed (Dey et al., 2012). As shown by Dey et al. (2012) comparing an immobile and mobile fine-sediment bed under the same flow conditions, this shear stress deficit can be associated to the fluid momentum extracted to overcome the frictional force acting on the moving particles. The difference between the total shear stress $\rho_f u_{*H}^2$ and the turbulent shear stress $\rho_f u_{*P0}^2$ is compensated by the particle friction $\tau_f = tan(\phi_f)(\Delta - 1)\rho_f g(\pi d_{50}^3/6)Cn$ (Dey et al., 2012), where n ($= C_s/(\pi d_{50}^2/4)$) is the total number of particles per unit area and ϕ_f the friction angle (see Section 3.2.1). Equating $\tau_f = \rho_f u_{*H}^2$-$\rho_f u_{*P0}^2$, a concentration of displaced particles C_s = 5% can be determined, consistent with the concentration C_{P0} obtained in Section 4.3 through direct sediment transport measurements.
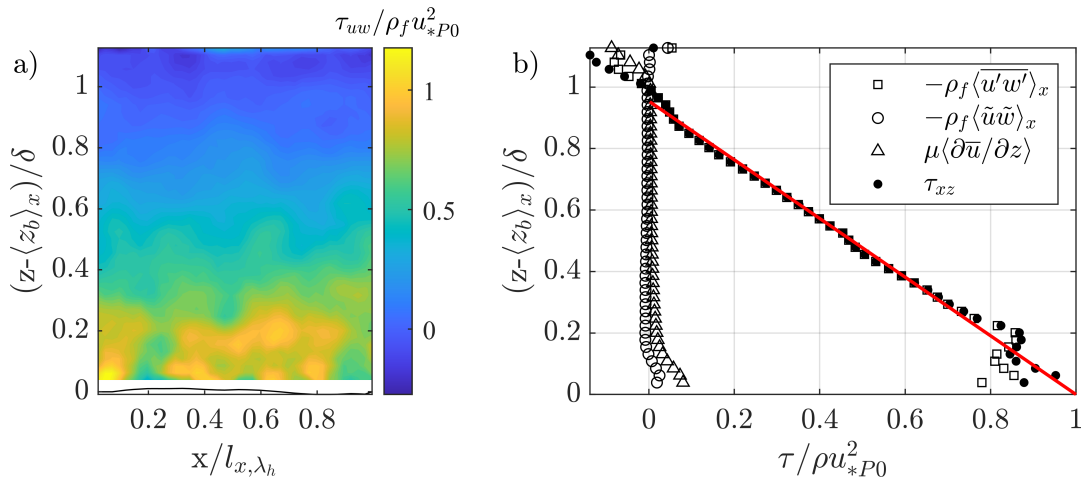

Figure 4.3: (a) 2D-field of the turbulent shear stress $\tau_{uw} = -\rho_f \overline{u'w'}$. (b) Vertical profiles of the longitudinally-averaged turbulent stress $-\rho_f\langle\overline{u'w'}\rangle_x$, of the form-induced stress $-\rho_f\langle\tilde{u}\tilde{w}\rangle_x$, of the double-averaged viscous stress $\rho_f \nu \partial_z \langle\overline{u}\rangle_x$ and of the total shear stress τ_{xz}. The 2D-field and the vertical profiles are normalized by the reference bed shear velocity u_{*P0}, obtained from the linear extrapolation of the τ_{xz} profile down to the bed, as highlighted by the red line in figure b.

4.5.2 Streamwise velocity and log law

Figure 4.4a shows the time-averaged streamwise velocity field $\overline{u}$. It is observed that the $\overline{u}$-field is uniform in the streamwise direction and that the influence of the boundary layer developing along the boat is restricted to a narrow region near the water surface.

Figure 4.4b illustrates the double-averaged streamwise velocity profile $\langle\overline{u}\rangle_x$, which can be usually described by the log law:

$$\frac{\langle\overline{u}\rangle_x}{u_*} = \frac{1}{\kappa} \ln\left(\frac{z - z_d}{z_0}\right) = \frac{1}{\kappa} \ln\left(\frac{z - z_d}{k_s}\right) + B_r \tag{4.2}$$

where κ = 0.41 is the von Karman constant, z_d the zero-plane position, z_0 the roughness length and k_s the equivalent-sand roughness, as defined by Nikuradse (1933). The relationship between z_0 and k_s is given by $k_s/z_0 = \exp(\kappa B_r)$, where B_r = 8.48 only for fully rough flow conditions, i.e. for a roughness Reynolds
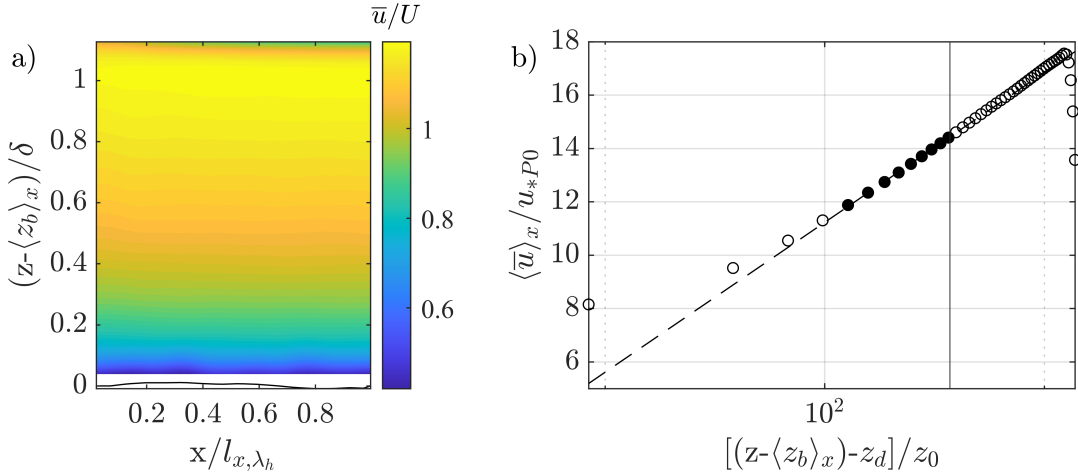
Figure 4.4: (a) Time-averaged streamwise velocity field $\overline{u}$ normalized by the bulk velocity U. (b) Vertical double-averaged profile of the streamwise velocity $\langle\overline{u}\rangle_x$ normalized by u_{*P0}. The dashed line represents the log law and the filled black dots the region where the best fit is found. The vertical line corresponds to the elevation z/δ = 0.3.

number $z_0^+ = z_0 u_{*P0}/\nu > 2$ or equivalently for $k_s^+ = k_s u_{*P0}/\nu > 70$ (Raupach et al., 1991). z_d and z_0 are determined by fitting equation 4.2 to the longitudinal velocity profile by a linear interpolation in the parameter space $[z, \exp\left(\langle\overline{u}\rangle_x \kappa/u_{*P0}\right)]$, as done by Rouzes et al. (2019). The lower and upper boundaries of the log law (z_m and z_M) are adjusted to minimize the error on the slope in the range between z = 0 and z = H. A minimum of 5 points with an error on the slope less than 5% are required to define the log law. k_s is then derived, checking that fully rough flow conditions are given. If this is not the case, since the ratio z_0/k_s becomes a function of k_s^+, k_s is determined by iteratively solving the equation given by García (2008) which expresses B_r as a function of k_s^+ for both smooth and rough flows, obtained on the basis of the experimental data by Nikuradse (1933):

$$B_r = 8.43 + (2.5 \ln k_s^+ - 3) \exp[-0.121(\ln^{2.42} k_s^+)] \tag{4.3}$$

Table 4.3 lists the interpolated log-law parameters for the uniform fine-sediment bed . The start and end elevation of the best-fit range, z_m and z_M, show that the log law is valid between 0.13δ (i.e. outside of the roughness sublayer which reaches up to 7% δ) and 0.3δ, as expected (Jiménez, 2004; Nezu and Nakagawa, 1993). Figure 4.4 shows furthermore that the double averaged velocity profile $\langle\overline{u}\rangle_x$ is characterized by a positive wake in the outer layer (below the boundary layer developing along the boat), as generally observed in 2D open-channel flows (Nezu and Nakagawa, 1993; Pope, 2000). In Table 4.3, the roughness Reynolds number $z_0^+ = z_0 u *_{P0}/\nu$, being higher than 0.14 and lower than 2, shows that the flow is in the transitional regime (Raupach et al., 1991). The value of B_r obtained from equation 4.3 differs, in fact, from the rough-bed value and is equal to 9. If the representative vertical roughness scale is assumed to be equal to $2\sigma_{zG}$, as in Perret et al. (2020), Table 4.3 shows that k_s is approximately equal to two times $2\sigma_{zG}$.

The zero-plane position z_d is above the mean fine sediment bed level, but still within the sediment transport layer estimated to be about $2\,\sigma_{zG}$ above the average bed elevation. As mentioned in Section 4.3, the sediment transport is highly irregular, so that the average sediment bed level represents the immobile bed surface, above

which the sediments intermittently roll. These results are consistent with the studies by Dey et al. (2012) and Ferreira et al. (2012), who also found z_d to be about 80% of the sediment transport layer.

$\langle\delta\rangle_x$	u_{*P0}	z_0	z_0^+	$k_s/2\sigma_{zG}$	k_s^+	B_r	z_d	z_m/δ	z_M/δ
[cm]	[cm/s]	[cm]	[-]	[-]	[-]	[-]	[cm]	[-]	[-]
4.8	1.84	0.0038	0.7	1.97	28	9	0.07	0.13	0.29
	±0.01	±0.0001		±0.02			±0.01		

Table 4.3: Log-law parameters: boundary layer thickness $\langle\delta\rangle_x$, shear velocity u_{*P0}, roughness length z_0, roughness Reynolds number $z_0^+ = z_0 u_{*P0}/\nu$, equivalent sand roughness k_s, sand-roughness Reynolds number $k_s^* = k_s u_{*P0}/\nu$, constant B_r, zero-plane position z_d, z_m and z_M start and end elevation of the best-fit range of the log-law.

4.5.3 Quadrant analysis

In this Section, the structure of turbulence in the near bed region is analysed, in order to determine the turbulent events responsible for the sediment transport over a uniform-sediment bed. Quadrant analysis is performed along a bed-parallel line at an elevation z = $2d_{50}$, in order to determine the turbulent events reaching the fine sediments. With reference to Section 2.4.1, the shear stress fraction of the turbulent events is defined in the following way:

$$\overline{S}_{i,H_s} = \frac{1}{\overline{u'w'}} \frac{1}{T} \int_0^T u'w'(x, z = 2d_{50}, t) I_{i,H_s} dt \tag{4.4}$$

where T is the sampling duration and I_{i,H_s} the indicator function identifying the turbulent events stronger than the ones contained in the hyperbolic hole region $H_s \overline{u'w'}(x, z = 2d_{50})$ (Please note that the hyberbolic hole region is defined on the basis of the local turbulent shear stress $\overline{u'w'}$ and not on the basis of the longitudinally-averaged turbulent shear stress as in Section 2.4.1). Figure 4.5a shows the spatially-averaged quadrant shear-stress fractions $\langle S_{i,0}\rangle_x(z = 2d_{50})$ for increasing Hole-sizes. It is observed that the contribution of sweeps (Q4) and ejections (Q2) dominate over the contributions of inward (Q3) and outward (Q1) interactions for all Hole sizes. For H_s the contribution of the sweep events is 10% higher than the contribution of the ejection events, as also observed by Dey et al. (2012) in the near bed region of a flat mobile fine sediment bed. The near-bed region is, as such, dominated by strong inrush of fluid induced by the sweep events, which have been shown to be responsible for the sediment transport (Nelson et al., 1995; Niño and Garcia, 1996; Dwivedi et al., 2012; Radice et al., 2013).

The vertical distribution of the longitudinally-averaged residual shear stress, defined as the difference between the contribution of the ejections and of the sweeps $\langle\Delta S^*\rangle_x = (|\langle\overline{u'w'}_{2,0}\rangle_x| - |\langle\overline{u'w'}_{4,0}\rangle_x|)/u_{*P0}^2$ (Raupach, 1981) is presented in Figure 4.5b. It is observed, that the sweep events clearly dominate the momentum transfer in the lowest 10% of the boundary layer with a contribution 20% higher than that of ejections to the total bed shear stress (u_{*P0}). For z/δ > 0.10 the ejections dominate over the sweeps. This vertical turbulent structure is consistent with the one observed both over rough and mobile beds (Raupach et al., 1991; Grass et al., 1991; Mignot et al., 2009b; Dey et al., 2012, 2011c).
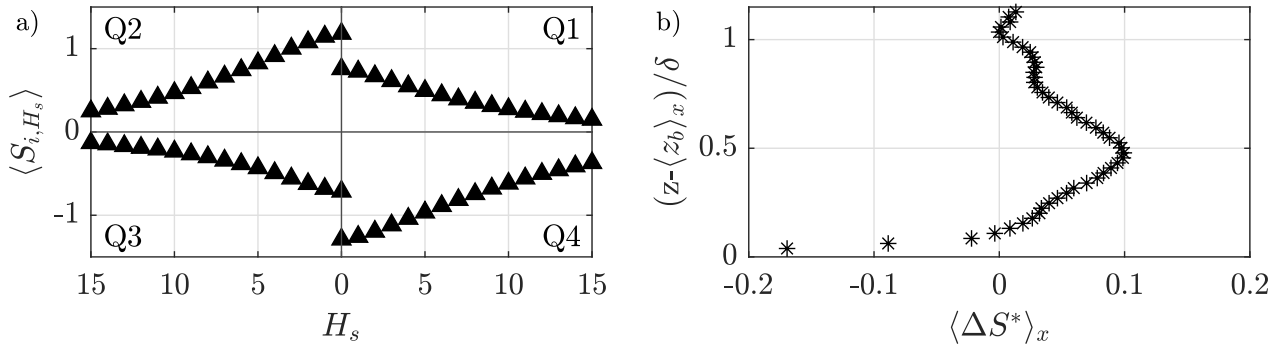
Figure 4.5: (a) Longitudinally-averaged quadrant shear-stress fractions $\langle S^*_{i,H_s} \rangle_x$ defined at z = $2d_{50}$ as a function of the hole size H_s; (b) Vertical profile of the longitudinally-averaged residual shear stress $\langle \Delta S^* \rangle_x$.

4.6 Reference bed conditions

In this Section, the reference flow and sediment transport conditions for a uniform sediment bed are derived for the other flow conditions investigated in Table 3.1 by the means of scaling arguments on the basis of the reference parameters just derived for Exp. 1 in Sections 4.3 and 4.5.1.

The reference shear stress u_{*P0} is scaled by taking into account that the shear stress in the presence of mobile sediments is reduced compared to the theoretical value of u_{*H} (see Section 4.3). The reduction Δu_* = $(u_{*H} - u_{*P0})/u_{*H}$ is proportional to the concentration of sediments displaced C, which is expected to depend on the shear stress applied. As such, Δu_* is scaled on the basis of the excess Shields parameter $\Delta\theta$ = $\theta - \theta_c$, i.e. $\Delta u_{*i} = \Delta u_{*1} \Delta\theta_i / \Delta\theta_1$ (where $\Delta\theta_i$ is the excess Shields parameter based on $u_{*H,i}$ for the flow condition of the i-th experiment and $\Delta u_{*1} = 25\%$ - see Section 4.5.1). The reference shear stress for the ith-experiment is then determined as $u_{*PO,i} = u_{*H,i}\Delta u_{*,i}$.

The concentration of sediments displaced was shown by Dey and Ali (2018) to scale with the ratio $\Delta\theta/d_{50}^2$. The concentration of the displaced sediments for the i-th experiment is therefore given by $C_{P0,i} = C_{P0,1}(\Delta\theta_i/\Delta\theta_1)(d_{50,1}^2/d_{50,i}^2)$, where $\Delta\theta_i$ is defined on the basis of $u_{*P0,i}$.

Exp.		1	2	3	4	5	6	7	8	9	10
u_{*P0}	[cm/s]	1.84	1.84	1.84	1.9	1.7	1.8	2.1	1.6	1.8	1.9
τ_{P0}	[cm/s]	0.34	0.34	0.34	0.36	0.29	0.32	0.44	0.26	0.32	0.36
E_{P0}	[cm/h]	1.5	1.5	1.5	1.6	0.3	0.9	2.7	0.3	1.4	2.2
C_{P0}	[%]	2	2	2	2	0.7	1.5	3			

Table 4.4: Shear velocity u_{*P0}, bed shear stress τ_{P0}, erosion rate E_{P0} and concentration of displaced sediments C_{P0} for a uniform fine sediment bed for all experimental flow conditions. Exp. 1 represents the reference on the basis of which the other values were determined.

The erosion rates for the other flow conditions are estimated on the basis of the scaling law given by equation 4.1 by van Rijn (1984a), which has provided an erosion rate estimate close to the one measured (see Section 4.3). Even though equation 4.1 was derived experimentally, the erosion rates follow a "3/2" scaling law with

the transport parameter $T_\theta = \Delta\theta/\theta_c$, which is consistent with the theoretically derived scaling law for sediment transport (Dey and Ali, 2018). In order to increase the predictive accuracy of equation 4.1 for the grain types investigated, a new proportionality factor $\alpha_E = 1.4{\times}10^{-4}$ is defined on the basis of the erosion rate E_{P0} and the bed shear stress u_{*P0} measured in Sections 4.3 and 4.5.1. The sediment transport parameter is defined on the basis of the reference shear stress $u_{*P0,i}$ for each experimental flow condition.

Table 4.4 lists the reference shear velocities, erosion rates and concentrations of displaced sediments for a uniform sediment bed for all experimental conditions. For Exp. 8-10 no reference concentrations are given, as it was not possible to determine the sediment transport for these flow conditions (see Section 3.4.3).

5 Hydro- and morphodynamics at the roughness scale (Exp. R-Gλh)

5.1 Introduction

In this Chapter, the bed morphodynamics and hydrodynamics are analysed at a roughness scale during the reference Exp. 1 R-$G\lambda h$. The focus is set on the analysis of the shear stress conditions at the level of the fine-sediments. To the knowledge of the author, few studies managed to analyse the shear stress conditions at the level of the bed. For example, Raus et al. (2019) analysed the flow field over a flat immobile bed of fine sediments for different protrusions of a squared pattern of spheres. He found out that for low protrusion levels the shear layer impacts the bed potentially causing enhanced sediment transport, while for higher protrusion levels he found that the recirculation region in the lee side of the spheres shelters the bed. No measurements with a mobile bed were yet done. The work of Neuman and Bédard (2015) comparing the wake development between an isolated obstacle over a mobile and an immobile bed, shows that the wake characteristics are significantly different due to the interactions between the mobile bed and the local flow field. This suggests that also for a packed bed interacting with a mobile fine-sediment surface, the local hydrodynamics will differ from those observed over an immobile fine-sediment surface.

5.2 Bed morphodynammics

In this Section, the temporal evolution of the bed topography during the reference Exp. 1 R-$G\lambda h$ is analysed. First, the bed morphodynamics at the reach scale are investigated, in order to identify the presence of large scale bed-forms and their position in relation to the reference pattern of spheres selected for the local analysis of the erosion processes (see Figure 3.2a in Section 3.2.1). Second, the analysis is focused on the bed morphodynamics at the pattern scale to elucidate how the spheres influence the local bed topography, the erosion rates and the sediment transport. The analysis is based on the digital elevation model and the sediment transport measurements obtained through the stereo topographic system, described in Sections 3.4.2 and 3.4.3. The bed topography is analysed on the basis of the protrusion level of the spheres which is locally defined as $P = -z_b/R$, where the bed elevation obtained from the digital elevation model z_b is evaluated only in the areas covered by fine-sediments (see Section 3.5.1). This definition is similar to the one given in Part I in Section 2.2.4.1, even though the present definition differs in as much as the protrusion level P, given here, does not represent an average protrusion around a sphere, but a point measurement. Compared to Part I, P can assume, in this case, also negative values when the fine sediments cover the spheres. For the analysis of the bed evolution at the pattern scale performed in Section 5.2.2, the planar density of the protruding spheres λ_p is determined on the basis of the digital elevation model as the ratio between the area not covered by

fine sediments and the total planar area of the pattern. The frontal density of the pattern λ_f is determined as the ratio between the frontal areas of the protruding spheres summed with the frontal area of all topographic features of the fine-sediment bed within the pattern and the total planar area of the pattern (see also Section 3.5.1).

5.2.1 Reach-scale analysis

The temporal evolution of the bed topography at the reach scale is analysed by averaging in the longitudinal direction the protrusion level of the spheres P over one reference pattern length l_{x,λ_h}. Figure 5.1 shows $\langle P \rangle_x$(y,t) in a Hovmöller (1949) diagram. Figure 5.1 shows that dunes with an amplitude of about 5 mm develop at the beginning of Exp. 1 (R-$G\lambda h$) for t $\lesssim$ 3 hours as the result of the high sediment availability (recall that the initial fine sediment layer above the spheres is about 1 cm thick). A similar behaviour was also observed at the beginning of the experiments analysed in Part I (see Section 2.3.1). Figure 5.1 clearly shows that two train of dunes develop parallel to each other in longitudinal direction separated by a region of higher sediment bed levels at y/W = -0.08. This higher sediment region develops ultimately in a longitudinal ridge, showing a superimposition of longitudinal and transverse bed-form for early times, as also visually observed in the first series of experiments in Part I (see Figure 2.6). The ridge drifts between t = 2 h and t = 3 h towards the right side-wall (negative y), eventually stabilizing at y/W = -0.15. The position of the ridge is symmetrical to the position of the ridge observed during Exp. 1a/b ($\theta l Am$) in Part I, characterized by a similar aspect ratio as Exp. 1 (R-$G\lambda h$) equal to $\simeq$ 5. In this case, the presence of a wider left-side wall accumulation compared to the right one, suggests that also in this case the side-wall accumulations reduce the effective width of the channel influencing the position and number of the ridges (for more details see Section 2.3.3). No reason is apparent, though, for this change in bed symmetry compared to the experiment analysed in Part I, which might be related to the change in the immobile sphere matrix composed of two layer instead of one or in the inlet conditions where a set of grids was added.

Overall, after the dunes disappear, the protrusion levels increase fast and reach in less than one hour values as high as 1 in the troughs. Figure 5.1 shows that the troughs are characterized by periodic oscillations of the protrusion levels in the transverse direction. This lateral periodicity is equal to half the width of the pattern of spheres, with the lowest $\langle P \rangle_x$ observed behind the spheres along their symmetry plane and higher $\langle P \rangle_x$ in between. This shows that the spheres create sediment shadows, which remain stable over time.

In the long term, the bed reaches a constant bed level in the troughs, characterized by highly sporadic sediment transport, as also observed for the end-state of Exp. 1a/b, Exp. 4 and Exp. 5a/b in Part I (see Section 2.3.2). Noteworthy is the fact that, even though the Exp. 1a/b, 4 and 5a/b in Part I are characterized by a higher global shear velocity compared to Exp. 1 (R-$G\lambda h$), they stabilized, in the troughs, at a lower protrusion level equal to 0.8. This discrepancy might be related to the different number of spheres composing the immobile bed, i.e. one layer in the first series of experiments in Part I and two layers in this case. The inter-sphere volume available for the flow exchange between the surface and the subsurface is higher for a multi-layered sphere bed compared to a one-layered one, which can be considered therefore more impermeable (Manes et al., 2009). Cooper et al. (2017) showed furthermore that a permeable porous bed is characterized by a higher vertical momentum exchange into the bed compared to an impermeable bed, resulting in higher shear stresses near the bed. As such, the hyporeic flow conditions between a two-layered and a one-layered sphere bed are different and might play a significant role in defining the final erosion level.

Considering the central pattern of spheres, where the analysis is focused in the following Sections, Figure 5.1 shows that it is located in the trough region, so that the erosive behaviour can be ascribed to the highest shear stress conditions observable.
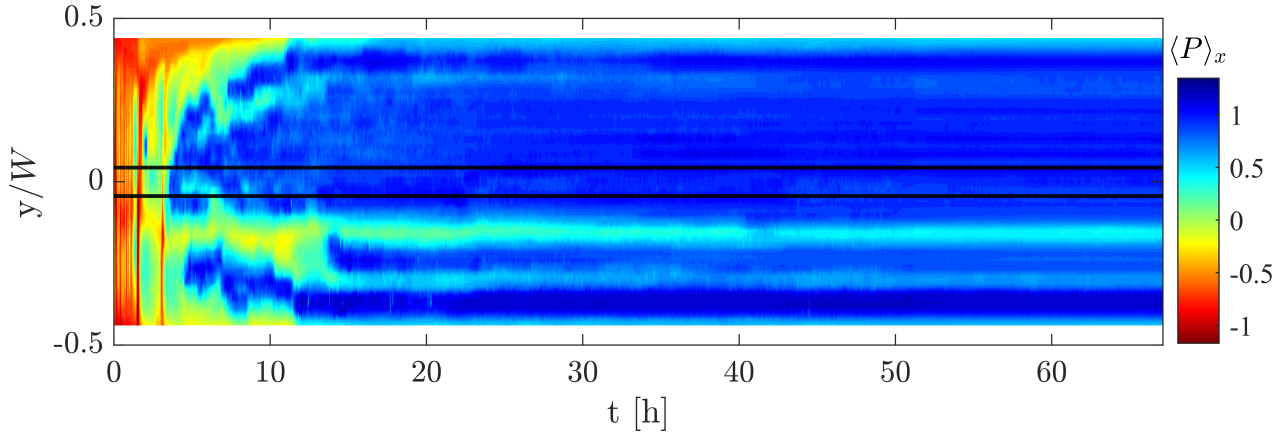

Figure 5.1: Hovmöller diagram of the longitudinally-averaged protrusion level $\langle P \rangle_x$ during Exp. 1 (R-$G\lambda h$) as a function of t and y/W. The two horizontal lines in the centre of the channel identify the lateral extension of the reference pattern of spheres.

5.2.2 Pattern-scale analysis

In this Section, the bed morphodynamics is investigated at the pattern scale within the reference pattern of spheres in the centre of the channel (see Figures 3.2a and 3.7b) by analysing the temporal evolution of the spatially-averaged protrusion levels $\langle P \rangle$, of the total erosion rates E_t and of the concentration of displaced sediments C_s. The protrusion levels $\langle P \rangle$ are spatially averaged over the reference pattern. As such, they are comparable to the protrusion levels investigated in Section 2.3.4 in Part I, which were based on the measure of an average bed level around a sphere. The following analysis is similar to the one conducted in Part I in Section 2.3.4 to analyse the bed evolution over a trough.

The temporal evolution of $\langle P \rangle$ is shown in Figure 5.2a. In the first three hours $\langle P \rangle$ oscillates over time due to the passage of dunes. The local minima of $\langle P \rangle$ for t < 3 h coincide with the dune's fronts, which are characterized by higher sediment bed levels, completely covering the spheres (negative values of $\langle P \rangle$). The maxima correspond, instead to the tail of the dunes, which can be characterized by the presence of protruding spheres (see for example the time instants t = [1.4,2,4] h with $\langle P \rangle > 0$). For t $\gtrsim$ 3.2 h the spheres start to protrude in the tail of the last dune without being covered again, as the first layer of fine sediments above the top of the spheres is completely depleted.

For t $\gtrsim$ 3.2 h the bed experience a rapid evolution reaching, within 20 minutes, protrusion levels as high as 0.8-0.9 (peak in $\langle P \rangle$ at t $\simeq$ 4 hours). A reduction in protrusion levels is then observed, caused by a temporary enlargement of the ridge between 4 and 7 hours, as seen in Figure 5.1. During this period, it is observed, that the rate of variation of $\langle P \rangle$ is reduced compared to similar protrusion levels observed before the peak for t < 4 h, consistent with reduced erosion rates generally observed over ridges. For t ≥ 8 hours, the influence of the ridge is negligible again and the protrusion levels increase at a rate similar to the one observed at the peak at t $\simeq$ 4 hours. The protrusion levels reach then at t = 11 hours an almost constant value of $\langle P \rangle \simeq$ 1, i.e. the

level of the equator of the first layer of spheres. The oscillations for $\langle P \rangle > 11$ hours are within the vertical measurement accuracy of 0.1 mm, so that the bed can be considered stable from this point on.

The total erosion rates are defined in a similar way as in Section 2.3.4: $E_t = (1 - \lambda_p)E = (1 - \lambda_p)CR\partial_t\langle P \rangle$, where λ_p is the planar density of the spheres protruding within the reference pattern. Please recall that E defines the variation in bed elevation over time and it is equivalent to the erosion rate of a uniform bed if no spheres protruded, while E_t defines the actual volume of fine sediments eroded over time resulting from the reduction of the area covered by fine sediments due to the presence of protruding spheres. To obtain a more robust estimate of the erosion rates free of spurious gradients due to noise, the protrusion curve is first smoothed with a smoothing spline (see blue dashed line in Figure 5.2a).

Figure 5.2b shows the temporal evolution of E and E_t normalized by the reference erosion rates E_{P0} over a uniform fine sediment bed (see Section 4.3). For t<3.2 hours E and E_t are characterized by strong oscillations from negative to positive values due to the passage of the dunes. The highest erosion rates are observed in the tails of the dunes corresponding to the rising limbs of the $\langle P \rangle$-profile. The peak in erosion rates are higher than the erosion rates for a uniform bed, consistent with accelerated flow conditions observed in the stoss side of dunes (Best, 2005; Sarkar and Dey, 2020). The insert in Figure 5.2b shows that a peak in erosion rates takes place just before the spheres protrude from the bed at t $\simeq$ 3.2 hours, as the result of the last dune passing by. As soon as the spheres protrude from the bed (identified by a vertical continuous line), a clear reduction of both E and E_t below the erosive conditions for a uniform fine sediment bed, is observed. The erosion rates reach a local minimum at t = 3.36 hours (vertical dashed line) with a reduction of almost 50% compared to uniform bed conditions. The erosion rates are soon after enhanced, reaching a local maximum at t = 3.5 hours (vertical dot-dashed line). This erosive behaviour is consistent with the one described in part I in Section 2.3.4. It is observed, furthermore, that the peak value of E is higher than E_{P0} by almost 50%, meaning that the actual sediment bed level is eroded faster than in the case of a uniform fine sediment bed. The peak value of the total erosion rates E_t is, instead, slightly lower than E_{P0}, showing that the effective volume of fine sediments being instantaneously eroded is of the same order of magnitude of the one eroded from a uniform fine sediment bed.

The protrusion levels corresponding to the first and second transition in erosive behaviour (as defined in Section 2.3.4) are equal to: $\langle P_{c1} \rangle = 0.15$ and $\langle P_{c2} \rangle = 0.43$. These values are consistent with the ones observed in Part I in Section 2.3.4. As a reminder, the first critical point was hypothesized in Section 2.3.4 to be related to the development of a horseshoe vortex or of a shear layer in the lee side of the spheres, leading to enhanced erosion rates. The second one, instead, was hypothesized to be related to the transition from isolated to wake-interference regime, leading to a reduction in erosion rates. The planar density at the second transition in bed behaviour (see table 5.1) is in conformity with the threshold of 0.3 defined by Grimmond and Oke (1999) for this transition. Confirmation of these hypothesis will be given on the basis of the flow measurements in the bed interstices presented further on.

Figure 5.2b shows that for t > 4.5 hours the erosion rates decreases significantly, as the result of the enlargement of the ridge, as discussed before. For t > 8 hours, when the ridge does not influence the bed evolution any more, the erosion rates become eventually negligible, consistent with the final stable bed level. This region of highly attenuated erosion rates was also identified in Part I. The protrusion level corresponding to the transition to negligible erosion rates $\langle P_{c3} \rangle$ is defined here as the protrusion level for which E reaches
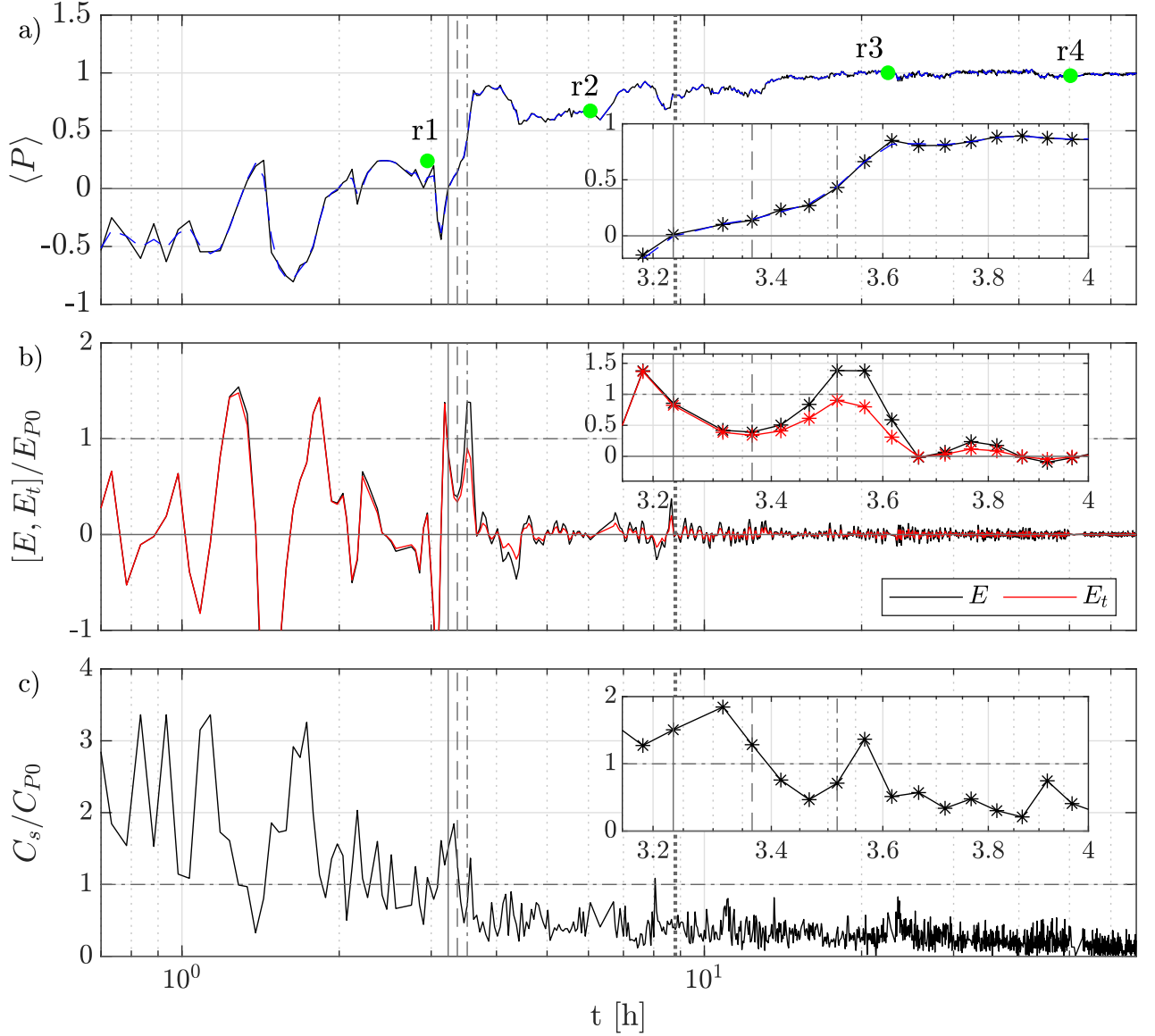
Figure 5.2: Temporal evolution of: (a) spatially-averaged protrusion level $\langle P \rangle$, (b) erosion rates $E = CR\partial_t \langle P \rangle$ and total erosion rates $E_t = (1 - \lambda_p)E$ and (c) concentration of displaced sediments C_s. $[E, E_t]$ and C_s are normalized by the erosion rates and the concentration of displaced sediments for a uniform fine-sediment bed. The vertical lines identify the time at which the spheres protrude without being covered again (continuous) and the time of the first (dashed), second (dot-dashed) and third (dotted) transition in erosive behaviour. The green dots in Figure (a) identify the four PIV runs. The protrusion level of the first PIV run $r1$ is higher than the $\langle P \rangle$-profile, since the PIV measurements were performed in planes C/D (see Figure 3.2a).

	$c1$	$c2$	$c3$
$\langle P \rangle$	0.14	0.43	0.8
λ_p	0.13	0.34	0.49
λ_f	0.06	0.13	0.23

Table 5.1: Geometric features of the bed topography at the critical transition points in erosive behaviour: pattern averaged protrusion level $\langle P \rangle$, planar density λ_p and frontal density λ_f.

0.5% of the erosion rate over a uniform fine sediment bed [1]. The $\langle P_{c3} \rangle$ determined for the present data, is equal to 0.8 (see the vertical dotted line in Figures 5.2a-c). This value is within the measurement error of the critical protrusion level $\langle P_{c3} \rangle_x$ observed in Part I in Section 2.3.4 and approximately equal to 0.7. The $\langle P_{c3} \rangle_x$, observed here, is associated with a similar planar density of about 0.49 (see Table 5.1), consistent with the transition from wake-interference to skimming flow defined by (Grimmond and Oke, 1999).

The concentration of displaced sediments C_s is defined by determining the number of displaced sediments over the reference pattern as described in Section 3.4.3. Figure 5.2c shows the evolution of C_s normalized by the reference concentration of displaced sediments for a uniform fine-sediment bed C_{P0} (see Section 4.4). For t < 3.2 hours C_s oscillates as the result of the dunes passing by. The magnitude of C_s is 2 to 3 times higher than a uniform sediment bed, as it is expected from the flow accelerated over the stoss side of the dunes. When the dunes disappear at t $\simeq$ 3.2 hours, the insert in Figure 5.2c, shows that the concentration of displaced sediments peaks after the spheres have uncovered. There is, therefore, a lag between the peak in erosion rates and the peak in sediment transport [2] likely due to a hysteresis effect, by which the sediment transport takes more time to adjust to the new flow conditions induced by the protruding spheres. C_s reduces then reaching a local minimum at t $\simeq$ 3.46 hours followed by a local maximum, both lagged compared to the local minimum and maximum of the erosion rates (identified by the vertical dashed and dot-dashed lines, respectively). The peak in sediment transport rate at t = 3.57 hours is 1.4 times higher than the sediment transport rate on a uniform sediment bed. C_s reduces then over time, reaching low sediment transport rates consistent with the sporadic grain movement characterizing the bed at the end of the experiment.

The analysis has focussed till now on morphometric quantities spatially-averaged over the pattern of spheres. The bed topography within the pattern is not homogeneous, though, as can be seen, for example, in the DEM displayed in Figure 5.3a at t = 3.52 hours (corresponding to the second transition in erosion rates). As such, a punctual analysis of the evolution of the bed levels along the central plane of the pattern is performed to highlight differences in bed elevation between the lee (L), the stoss (S) side of the spheres and the centre (C) of the pattern, as identified in Figure 5.3a. The positions of the sampling points L and S follow the evolution of the bed topography being always positioned at the edge of the spheres. The protrusion levels are locally averaged over a small area of 3×3 mm^2 centred in the sampling points. Figures 5.3b and 5.3c are complementary and show the temporal evolution of the bed profile along the centre of the pattern for 3.18 < t < 3.82 hours (i.e. the period characterized by the fastest bed evolution) and of the protrusion levels sampled at the

---

[1]   In Section 5.2 of Part I a slightly different definition of $\langle P_{c3} \rangle$ was given as the protrusion level for which E equals 0.5 % of the erosion rate observed when the spheres start to protrude E_0, as E_{P0} was not available. It is observed in Figure 5.2b, that E_0 can be considered effectively equivalent to the erosion rates over a uniform fine-sediment bed, as the value of E at t $\simeq$ 3.3 hours shows.

[2]   Recall that the erosion rates are equal to the longitudinal variation in sediment transport rates (see Appendix A), so that a lag between the erosion and sediment transport peaks is possible

locations L, C and S for the whole duration of the experiment, respectively.

The insert in Figure 5.3c shows that when the spheres start to protrude from the fine sediment bed, the pro-
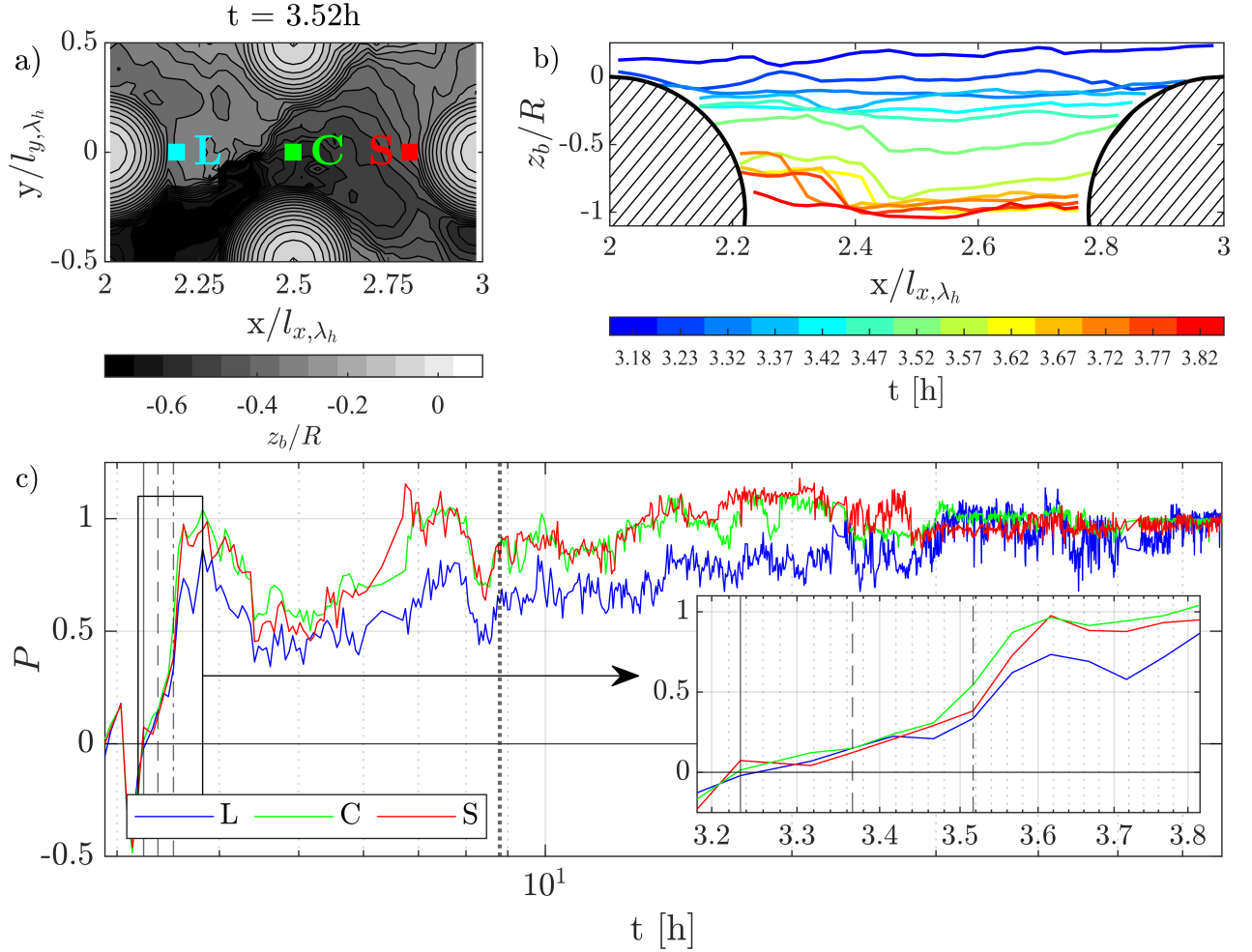

Figure 5.3: (a) Bed topography at t = 3.52 hours with definition of the local sampling points in the sphere's L-lee, S-stoss side and in the C-centre of the pattern; (b) Longitudinal profiles of bed elevations z_b at $y/W = 0$ for $3.18 < t < 3.82$ hours; (c) Temporal evolution of the protrusion levels at the sampling points. The vertical lines identify the time at which the spheres protrude without being covered again (continuous) and the time of the first (dashed), second (dot-dashed) and third (dotted) transition in erosive behaviour.

trusion levels in the lee and stoss side of the spheres as well as in the centre of the pattern are similar. Almost horizontal bed level profiles are, in fact observed for $t \leq 3.42$ hours in Figure 5.3b. For low level of protrusions of the spheres, the bed fluctuations due to protruding grains are of the same order of magnitude of the protrusion of the spheres (see the central bed elevation profile for t = 3.23 h in Figure 5.3b), so that the spheres are almost undistinguishable for the flow from the fine sediment roughness. Once the first transition in erosive behaviour is reached at t = 3.36 h (i.e. the local minimum in erosion), Figure 5.3b shows that the protrusion levels at the three sampling points start to diverge, with the lee side of the sphere presenting the lowest P, the centre the highest and the stoss side intermediate values. Figure 5.3b shows that the bed profiles present for t > 3.36 hours higher bed levels in the lee of the sphere for $x/l_{x,\lambda_h} < 2.45$ (defining as

such a sediment shadow), while for $x/l_{x,\lambda_h} > 2.45$ the bed elevations are significantly lower. This topographic pattern is similar to the scour pattern observed during the development of horseshoe vortices around isolated obstacle Dey and Raikar (2007); McKenna Neuman et al. (2013); Dixen et al. (2013); Euler et al. (2017), characterized by sheltered region behind the obstacles with higher sediment accumulation and scours in the front and lateral sides, as can be exemplarily observed in the DEM in Figure 5.3a. The lower bed levels observed in the centre of the pattern can be also ascribed to flow accelerations taking place in between the two central spheres, which represent effectively a contraction for the flow the higher the spheres protrude.

As for the long-term bed evolution, Figure 5.3c shows that the protrusion levels in the central region of the pattern and in the stoss side of the spheres level out. Lower protrusion levels are consistently observed, instead, in the lee side of the spheres for t < 12 hours, showing that the spheres are effective in sheltering the sediments which remain trapped in their lee side for a longer time. For t > 12 hours the protrusion levels in the lee side of the spheres are almost equivalent to the ones observed in the centre and stoss side. It is observed that fluctuations in protrusion levels in the lee side are higher than the ones in the centre and in the stoss side, showing that there is an exchange of grains being intermittently trapped in the lee side of the spheres. In summary, as long as the fine sediment bed is active with a consistent sediment transport, the sediment shadows are continuously fed with new sediments being temporarily trapped. Over time, as the grain are sheltered, the sediment transport becomes more and more intermittent, reducing the supply of sediments to the sediment shadows which are slowly depleted of sediments. Nevertheless, randomly dislodged grains at the end of the experiment, while critical conditions of motion are present, can still get trapped in the lee side of the spheres temporarily enhancing the bed level.

5.2.3 Analysis of the bed structure

In this Section, the evolution of the bed structure is analysed in terms of morphometric variables, to characterize the roughness length scale, the bed regularity and the grade of imbrication following the changes in sphere's protrusion. The DEM of the reference pattern of spheres is separated at each time in a meso-scale and grain-scale DEM, following the procedure already presented in Section 4.4. If protruding spheres are present in the DEM, they are not taken into account during the averaging and fitting procedures applied to extract the meso-scale and grain-scale DEMs. The meso-scale and grain-scale DEMs present as such only features pertaining to the fine-sediment bed without any influence of the spheres. The morphometric variables used to analyse the DEMs are the standard deviation σ_z, the skewness S_k, the kurtosis K_u of the bed elevations (as defined in Section 4.4) and the inclination index $I = (i_b^+ - i_b^-)/N_i$ (i_b^+ and i_b^- are the number of positive and negative bed slopes, specified by increasing and decreasing bed elevations in longitudinal or transverse direction, respectively, and N_i is the total number of bed slopes). I is a measure of the preferential surface inclination and bed-form shape for the meso-scale DEM (Bertin et al., 2017) and of the grain imbrication for the grain-scale DEM (Smart et al., 2004; Perret et al., 2020).

Figures 5.4a,b,c show the temporal evolution of the vertical roughness scale, equal to $2\sigma_z$, of the skewness and kurtosis for the global, meso-and grain scale DEMs. Figure 5.4 a shows that for t < 3.2 hours (vertical black continuous line), while the bed is covered with dunes, the roughness scale of the grain-scale DEM $2\sigma_{z,g}$ is quite constant and similar to the one obtained for a uniform fine sediment bed (see table 4.2 in Section 4.4). The meso-scale and global roughness scales, $\sigma_{z,m}$ and $\sigma_{z,G}$, oscillate as the result of the passage of dunes. Furthermore, $\sigma_{z,m}$ is of same order of magnitude of $\sigma_{z,G}$, showing that the global bed roughness is
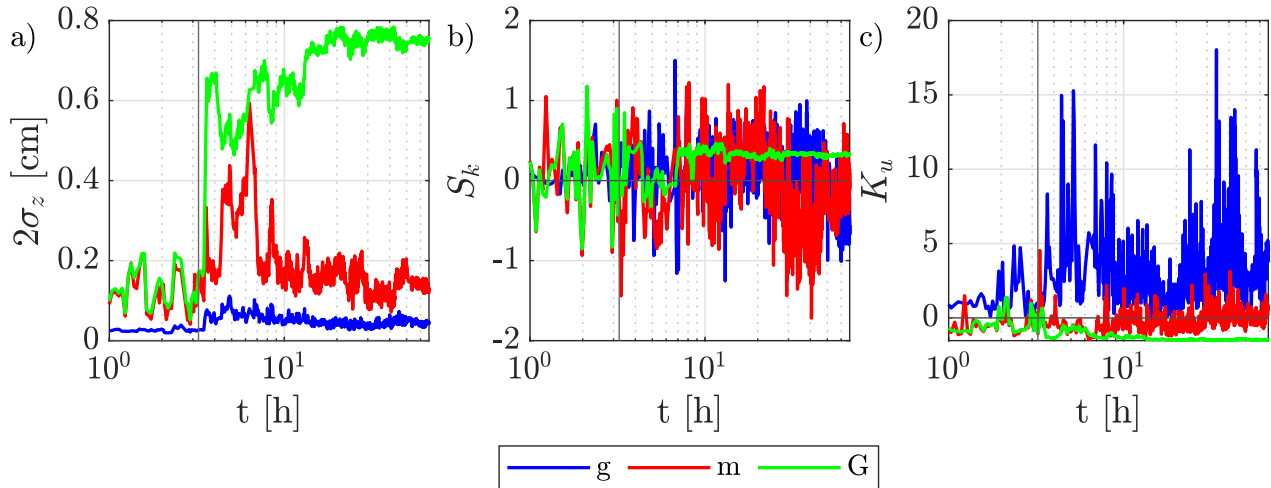
Figure 5.4: Temporal evolution of the standard deviation σ_z (a), the skewness S_k (b) and the kurtosis K_u (c) of the bed elevation for the G-global, m-meso and g-grain scale DEMs. The vertical continuous line identifies the time at which the spheres protrude from the bed.

mainly defined by the dunes topography. The values of $2\sigma_{z,m}$ and $2\sigma_{z,G}$ are below 2 mm, since the analysis is performed over the reference pattern of spheres at a scale significantly smaller than the longitudinal and transverse scales of the dunes.

As soon as the spheres protrude from the fine sediment bed, Figure 5.4a shows a rapid increase in the global bed roughness $\sigma_{z,G}$, which follows exactly the same trend as the protrusion levels $\langle P \rangle$ in Figure 5.2a. The ratio between the vertical global roughness scale $\sigma_{z,G}$ and the protrusion level $\langle P \rangle$ is found to be constant over time and equal to 0.76. As such, a clear linear dependency between $\sigma_{z,G}$ and P is given. The global roughness $\sigma_{z,G}$ is observed to be higher than $\sigma_{z,m}$ and $\sigma_{z,g}$ when the spheres protrude from the bed, showing that the bed roughness is mainly dominated by the protruding spheres.

The meso-scale roughness $2\sigma_{z,m}$ is observed to first increase, reaching a broad peak between 4.3 and 7 hours and then decrease again. This peak in meso-scale roughness is coincident with the temporary enlargement of the ridge, already observed in Section 5.2.2. As can be seen in Figure 5.1, the patter is characterized by significant transverse gradients in protrusion levels over the pattern for this period and, as a result, the topographic roughness increases. The contribution of the meso-scale roughness to the global scale roughness $\sigma_{z,G}$ dominates, in fact, between 4.3 and 7 hours over the contribution given by the protruding spheres. The reduction over time of $\sigma_{z,m}$ can be related to a homogenization of the bed elevation of the fine sediment bed. As shown in Figure 5.3c, the difference in bed elevation between the lee, the stoss side of the sphere and the centre of the pattern decrease over time, reducing as such the meso-scale roughness heterogeneity.

The grain-scale roughness $\sigma_{z,g}$ does not increase directly when the spheres start to protrude, as observed for $\sigma_{z,G}$ and $\sigma_{z,m}$, but when the erosion rates start to increase. As shown in Section 5.2.2, this is associated with the formation of sediment shadows in the lee of the spheres and eroded regions in their stoss sides, whose grain roughness is rearranged in different manners as the result of lower and higher local sediment transport rates, respectively. As shown by Perret et al. (2020) analysing the response of a gravel bed to varying flow conditions, a decrease in flow power (as it is expected in the lee side of the spheres) increases the grain roughness. As such, the grain roughness is overall increased due to the high spatial heterogeneity in shear stress conditions. $\sigma_{z,g}$ decreases then over time, as the sediment transport conditions homogenize over the pattern.

The values remain though higher than the ones observed over the dunes, due to the flow sheltering induced by the spheres which causes intermittent sediment transport conditions.

Figure 5.4b shows that the skewness at the global scale $S_{k,G}$ oscillates between positive and negative values as the dunes pass by. This is expected due to the small size of the reference pattern compared to the dune's size, so that relatively regular surfaces in the dune's tails or highly irregular surfaces at the dunes crest are detected. When the spheres protrude from the bed, $S_{k,G}$ becomes positive consistent with a bed topography characterized by fine particles infilling the bed depressions in between the spheres and resulting in bed elevation in average below the mean bed elevation. Quasi-zero $S_{k,G}$ is observed for 4.3 < t < 7 hours as the result of the temporary increase in bed levels which normalized the bed elevations. Overall, the bed presents similar characteristics to natural armoured gravel bed, which are also characterized by positive skewness values (Nikora et al., 1998; Aberle and Nikora, 2006; Coleman et al., 2011). The negative kurtosis values $K_{u,G}$ in Figure 5.4c highlight the intermittency in bed surface elevations. The values close to -1.5 are higher than the ones usually observed for natural armoured gravel beds usually close to -0.2 (Coleman et al., 2011), as the result of the regular pattern of spheres.

As for the skewness values for the meso-scale and grain-scale DEMs, $S_{k,m}$ and $S_{k,g}$, Figure 5.4b shows that both positive and negative values are observed as the spheres protrude from the bed. At the meso-scale, negative skewness values can be related to holes and bumps on the surface induced by the presence of sediment shadows and eroded areas. Positive values, on the other hand, to a more regular surface, the result probably of temporary erosion of the sediment shadows. At the grain scale, the presence of negative skewness values is likely the result of the heterogeneous and intermittent sediment transport which causes temporary agglomerations of grains. Overall, the results show that both at the meso-scale and at the grain scale the surface structure is highly dynamic.

Complementary to these observations, Figure 5.4c shows that the kurtsosis at the meso-scale $K_{u,m}$ is positive for t < 3.46 hours (i.e. before the increase in erosion rates), consistent with the regular and uniform bed profiles observed in Section 5.2.2. For t > 3.46 hours $K_{u,m}$ becomes negative, consistent with the formation of the sediment shadows, i.e. an irregular bed configuration. For t > 10 hours $K_{u,m}$ oscillates around zero consistent with the observations of Section 5.2.2 that the sediment shadows decrease over time and are intermittently formed and eroded by the end of the experiments. As for the grain scale, the kurtosis values $K_{u,g}$ are always positive, indicating a regular grain structure.

Figures 5.5a,b show the streamwise and transverse inclination indices. $I_{x,G}$ for the global DEM shows negative values while the dunes pass by. This is consistent with the dunes shape with prevalent negative bed inclinations. As the spheres protrude, $I_{x,g}$ oscillates around zero, following the same trend as the meso-scale inclination index $I_{x,m}$. The meso-scale $I_{x,m}$ is preferentially negative, meaning that the fine-sediment bed surface is characterized by downstream oriented slopes, connected to the sand deposits in the lee side of the spheres and potentially leading to local bed instabilities. Negative streamwise inclination indices were also observed by Bertin and Friedrich (2019) during the sand infilling of an armoured bed. This potential meso-scale instability is counteracted by the positive values of $I_{x,g}$ at the grain scale. This means that the grains lean onto each other with their faces looking upstream, increasing the bed imbrication. The transverse inclination indices for the grain scale $I_{y,g}$ in Figure 5.5b oscillate around zero, so that the grain can be considered aligned with the flow direction. The global and meso-scale the transverse inclination indices, $I_{y,G}$ and $I_{y,m}$, are negative while the dunes are present, as the pattern is always located on a transverse down-sliding side of the dunes. As the spheres appear, the inclination indices oscillate around zero showing the variability in bed
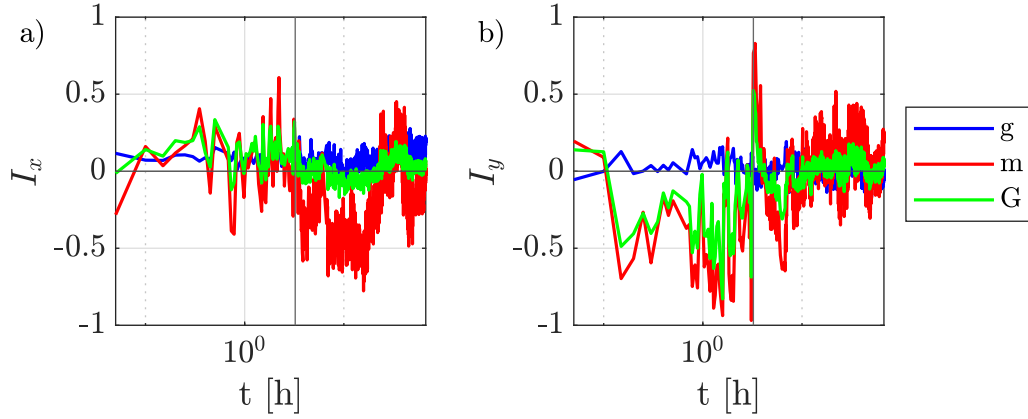
Figure 5.5: Temporal evolution of the inclination index in the streamwise I_x (a) and transverse I_y direction (b) for the global, meso- and grain-scale DEMs. The vertical continuous line identifies the time at which the spheres protrude from the bed.

topography at the level of the fine-sediments. The negative peak at t $\simeq$ 7 hours is related to the increase in bed elevation due to the temporary enlargement of the ridge, with is characterized by a down-sloping side in the positive y-direction.

5.3 Flow structure analysis

During Exp. 1 (G-$R\lambda h$) a total of four PIV runs were performed over the reference pattern of spheres, in order to analyse the flow field in the bed interstices, as the bed topography evolves. The four PIV runs were performed at t = [3, 6.1, 22.5, 50.2] hours. The times and the corresponding protrusion levels of the PIV runs are identified as green dots in Figure 5.2a. During each PIV run, two flow measurements of 4500 bulk time units each were performed one over plane A and one over plane B in the reference pattern in the centre of the channel (see Figure 3.2a). The stereo PIV system and the data acquisition parameters are thoroughly described in sections 3.4.1.2 and 3.4.1.3. During the first PIV run, characterized by a fast evolving bed topography, the number of bulk time units acquired during each PIV measurement was reduced compared to the other PIV runs, in order to guarantee stationary conditions of the bed topography during the flow measurements. For the first PIV run[3], the duration of the PIV measurement over plane A was equal to 700 bulk time units, while over plane B to 500 bulk time units. For plane A, it was ascertained that the number of samples is enough to obtain time-convergence for all statistics, while for plane B, it was assessed that the second order moments are not fully time-converged. In the following the PIV measurements were given acronyms with r- referring to the PIV run (1 to 4) and p- referring to the measurement plane (A or B). For the analysis of the temporal evolution of the local bed hydrodynamics, the time difference between two PIV measurements performed one after the other during the same PIV run with a time delay of five minutes, can

---

[3]   Due to the fact, that in the centre of the channel the bed was not stationary enough during the PIV measurements to obtain time-converged statistics, another set of data is used not mentioned in this thesis and obtained from PIV measurements performed at y/W = 0.22 and y/W = 0.24, over the crest of the spheres as plane A and in between the spheres as plane B, respectively. This is the reason why the point identifying run 1 in Figure 5.2a is slightly off. Since these PIV measurements performed in the channel quarter plane are also located in the bed-troughs as the ones performed in the centre of the channel, the shear stress conditions at the level of the bed are comparable and as such the erosive processes, too.

be considered negligible, as the bed topographies at the pattern scale do not change significantly. For this reason the PIV measurements, performed during the same PIV run, will be identified by the same time.

Since the bed evolution is not known a priori before the start of an experiment, the first two PIV runs fell outside of the region of the fastest bed evolution, as shown in Figure 3.2a. The first PIV run ($r1$) was performed before the last dune passed by and the second one ($r2$) during the ridge enlargement (see Section 5.2.2). Since this Section is devoted to the analysis of the flow field in the bed interstices, which is mainly dominated by the flow structures shed by the spheres, the first two PIV runs can be used, nevertheless, to connect the shear stress conditions in the bed interstices with the changes in erosive behaviour identified in Section 5.2.2. More specifically, the first PIV run is characterized by a protrusion level of the spheres $\langle P \rangle$ $\simeq 0.25$ higher than the protrusion level for the first transition in erosive behaviour $\langle P \rangle_{c1}$, so that the flow conditions for enhanced erosion can be analysed. The protrusion levels during the second PIV run $\langle P \rangle \simeq 0.6$ are characteristic of the sheltering behaviour observed after the second transition in erosive behaviour. The last two PIV runs were performed when the bed reached a stable bed level and as such, are representative of flow conditions where the bed is fully sheltered.

5.3.1 Bed topography during the PIV measurements

This Section presents a short overview of the bed topographies measured during the PIV measurements both at the reach and at the pattern scale. Figure 5.6 shows the transverse profiles of the longitudinally averaged bed levels $\langle z_b \rangle_x$ measured during the PIV measurements. During the first PIV run, a significant increase in bed levels is observed for y/W < -0.1 between the first ($r1pA$) and the second ($r1pB$) PIV measurement due to an incoming dune. The bed levels do not change, though, for y/W > -0.1, so that the bed topography can be considered stationary below the PIV measurement planes A and B. During the second PIV run, the bed topography changes significantly for -0.15 < y/W < 0 between the first ($r2pA$) and the second ($r2pB$) PIV measurement as the result of a temporary enlargement of the ridge. Changes in the bed levels are also observed for 0.15 < y/W < 0.3. The bed levels below the PIV planes A and B do not change significantly. In the case of the third ($r3$) and fourth ($r4$) PIV runs, no significant changes in bed levels are observed in between the PIV measurements. Comparing the bed profiles for the third and fourth PIV run, it is observed that while the bed levels in the trough remain almost unaltered, the ridge decreases in height. Overall, the bed topographies shows that the bed elevations at the reach scale change in between PIV measurement for the first and second PIV run. These changes in reach scale topography alter the flow patterns in the bulk flow (as seen for example in chapter 2 with ridges), so that for the further analyses no spatial averaging in the transverse direction will be performed on the flow fields obtained during the same PIV run.

Figures 5.7a-h show the DEMs measured during the PIV measurements. Figures 5.7a-b show that the bed topography during the first PIV run is characterized by sediment shadows in the lee side of the spheres and by a region of higher erosion in the centre of the pattern, i.e. on the sides of the central spheres. The sediment shadows appear to be rather symmetric compared to the centre of the pattern. This bed topography is consistent with the one observed in Section 5.2.2 for similar protrusion levels of the spheres ($P \simeq 0.2$) while the erosion rates increase after the first transition in erosive behaviour. This suggests, that, even though the first PIV run is performed while dunes are still present on the bed, the local erosive conditions are dominated by the protruding spheres. Figures 5.2.2c-d show that during the second PIV run, the bed topography of the reference pattern is rather asymmetric compared to the channel centre line, as for y/W < 0 the bed levels
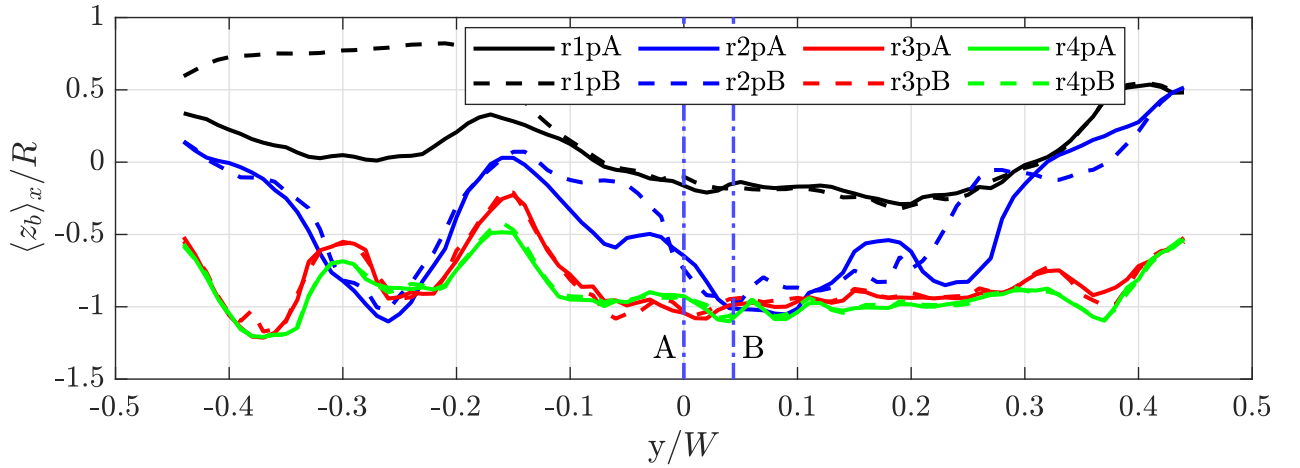
Figure 5.6: Transverse profile of bed elevations $\langle z_b \rangle_x$ measured during the PIV measurements.

increase due to the ridge-enlargement while for $y/W > 0$ the bed is eroded down almost to the equator of the spheres. Nevertheless, it can be noticed, especially in Figure 5.2.2c, that sediment shadows are still present in the lee side of the spheres. In the case of the third PIV run, Figures 5.2.2e-f show the presence of sediment shadows in the lee side of the spheres located asymmetrically to the centre-line of the pattern. Comparison between the DEMs of the PIV measurements $r3pA$ (Figure 5.2.2e) and $r3pB$ (Figure 5.2.2f) shows slight changes in the local morphological patterns resulting from the movement of single grains. Similar bed topographies are observed for the last PIV run in Figures 5.2.2g-h. In this case, though, the sediment shadows are symmetrically located compared to the pattern central line, showing that the shape of the sediment shadows can change over time.

Table 5.2 summarizes the principal morphometric parameters of the bed topographies measured during the PIV measurements. It is distinguished between a pattern-averaged protrusion level $\langle P \rangle$ and a line-averaged protrusion level $\langle P \rangle_x$ over the PIV measurement plane, which is used, in the following, to identify the local bed conditions in the PIV plane. Overall, $\langle P \rangle$ and $\langle P \rangle_x$ are comparable as the bed topographies are quite homogeneous except for run 2, where $\langle P \rangle_x$ in plane B is significantly higher than the average protrusion level due to the significant lateral variations in bed elevations described before.
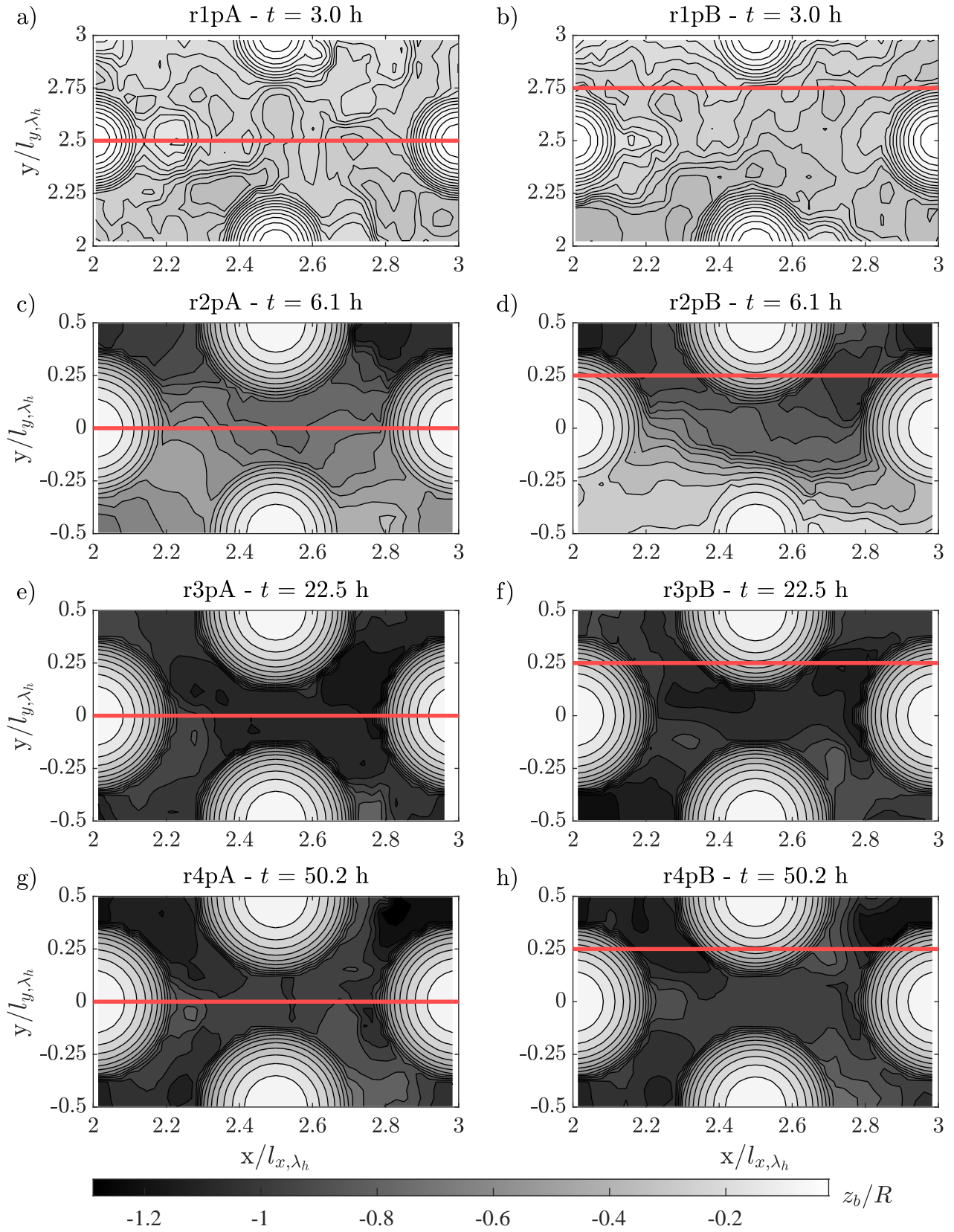
Figure 5.7: Bed topographies at the pattern scale measured during the PIV measurements in plane A (left column) and B (right column). The red lines identify the position of the PIV planes.

	t	$\langle P \rangle$	$\langle P \rangle_x$	$\sigma_{z,G}$	$\sigma_{z,m}$	$\sigma_{z,g}$	λ_p	λ_f	$I_{x,G}$	$I_{y,G}$
	[h]	[cm]	[cm]	[cm]	[cm]	[cm]	[-]	[-]	[-]	[-]
r1pA	3.0	0.24	0.23	0.08	0.04	0.02	0.21	0.07	0.04	0.14
r1pB	3.0	0.27	0.24	0.09	0.05	0.02	0.20	0.06	0.01	0.30
r2pA	6.1	0.68	0.65	0.28	0.16	0.03	0.45	0.20	0.13	−0.26
r2pB	6.1	0.61	0.93	0.31	0.27	0.03	0.41	0.19	0.01	−0.39
r3pA	22.5	1.02	1.04	0.39	0.06	0.03	0.51	0.3	−0.05	0.07
r3pB	22.5	1.00	1.04	0.38	0.07	0.03	0.52	0.29	0.01	0.01
r4pA	50.2	0.98	0.93	0.37	0.09	0.04	0.51	0.3	0.03	−0.03
r4pB	50.2	0.98	1.00	0.37	0.08	0.03	0.51	0.29	−0.02	−0.03

Table 5.2: Morphometric parameters measured during the PIV measurements: protrusion level at the pattern scale $\langle P \rangle$, streamwise averaged protrusion level along the PIV plane $\langle P \rangle_x$, standard deviation at the global $\sigma_{z,G}$, meso- $\sigma_{z,m}$ and grain-scale $\sigma_{z,g}$, planar density of the spheres λ_p, pattern integrated frontal density λ_f, inclination index in the streamwise and transverse direction at the global pattern scale, $I_{x,G}$ and $I_{y,G}$.

5.3.2 Time-averaged velocity fields

In this Section, changes in the time-averaged flow fields of the streamwise, vertical and transverse velocities as the result of the increasing protrusion level of the spheres are analysed. Figures 5.8 and 5.9 show the time-averaged fields of the streamwise and vertical velocities, $\overline{u}$ and $\overline{w}$, in plane A and plane B, respectively, as the bed evolves. Figures 5.8a-d and 5.9a-d show that, both in plane A and in plane B, the protruding spheres cause flow deceleration in the bed interstices compared to the undisturbed flow above the top of the spheres. In plane A (Figures 5.8a-d), the region of strongest streamwise flow deceleration is observed for low plane-averaged protrusion levels $\langle P \rangle_x \simeq 0.2$ in the centre of the pattern, while for $\langle P \rangle_x > 0.6$ it is observed in the lee and the stoss side of the spheres, as the result of flow separation and stagnation, respectively. For $\langle P \rangle_x > 0.6$, the region of flow retardation in the sphere's lee side is characterized by negative streamwise velocities above the fine sediment deposit. In the centre of the pattern a flow recovery is observed with $\overline{u}$ reaching a local maximum. This flow recovery can be ascribed to two factors. On the one hand, the influence of the sphere's wake reduces with increasing distance from the sphere (Dey et al., 2011b; Papanicolaou et al., 2012; Liu et al., 2017). On the other hand, the staggered configuration of sphere induces a flow contraction in the centre of the channel due to the central pair of spheres, resulting in a local flow acceleration. The maximum streamwise velocity values reached near the bed decrease, though, with increasing protrusion levels. While for $\langle P \rangle_x \simeq 0.2$, $\overline{u}$ reaches maximum values of 60-70% of the bulk velocity U near the fine-sediment bed, for $\langle P \rangle_x \simeq 0.6$ and $\langle P \rangle_x \simeq 1$, $\overline{u}$ does not exceed 40% and 20% of U, respectively. The decrease in the maximum streamwise velocity with increasing protrusion of the spheres shows that the fine sediments are increasingly sheltered from the outer flow as the region of flow separation in the lee side of the sphere's increasingly dominates the flow dynamics in between the spheres.

Compared to the streamwise velocities, the temporal variability of the vertical velocities $\overline{w}$ in the bed interstices in plane A is much higher, as Figures 5.9e-f show. Figure 5.8e shows that for low levels of protrusion $\langle P \rangle_x \simeq 0.2$ the bed interstices are dominated by negative $\overline{w}$, while a region of positive $\overline{w}$ develops above

Figure 5.8: Time-averaged fields of the streamwise $\overline{u}$ (a-d) and vertical $\overline{w}$ velocity (e-h) in plane A at different stages of the bed development. The red isocontours identify the isovelocity lines for which $\overline{u} = 0$ or $\overline{w} = 0$.
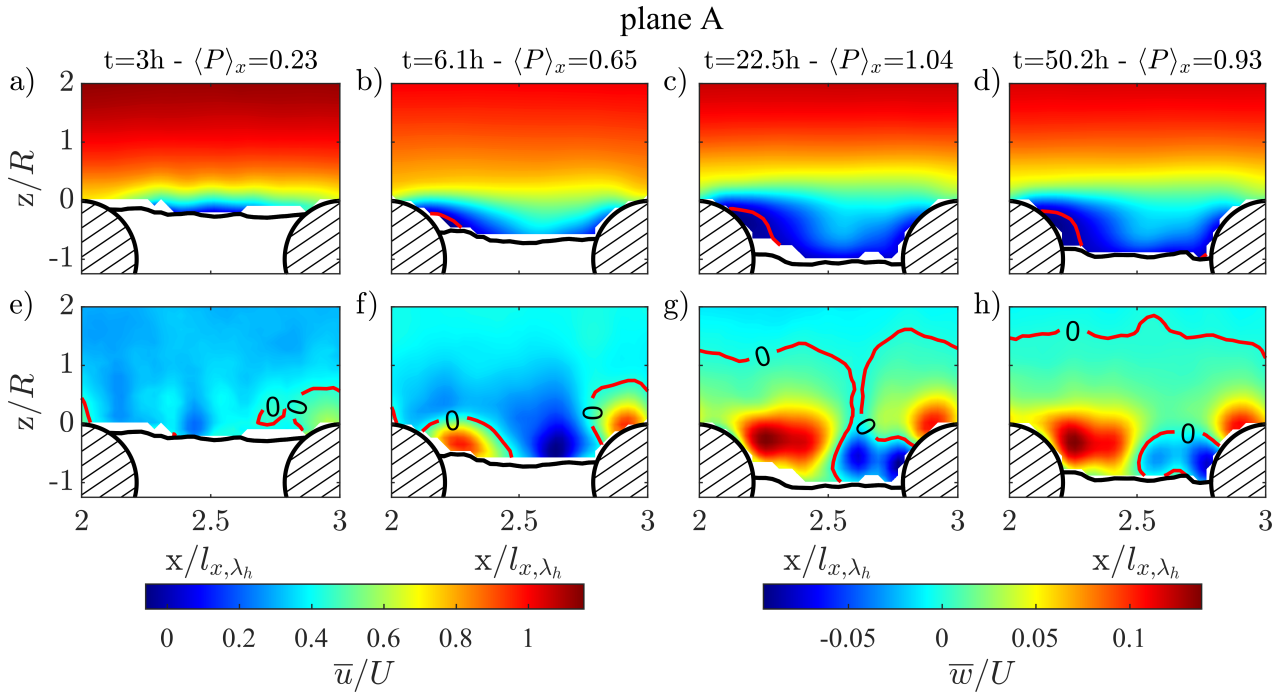

Figure 5.9: Time-averaged fields of the streamwise $\overline{u}$ (a-d) and vertical $\overline{w}$ velocity (e-h) in plane B at different stages of the bed development. The red isocontours identify the isovelocity lines for which $\overline{u} = 0$ or $\overline{w} = 0$.
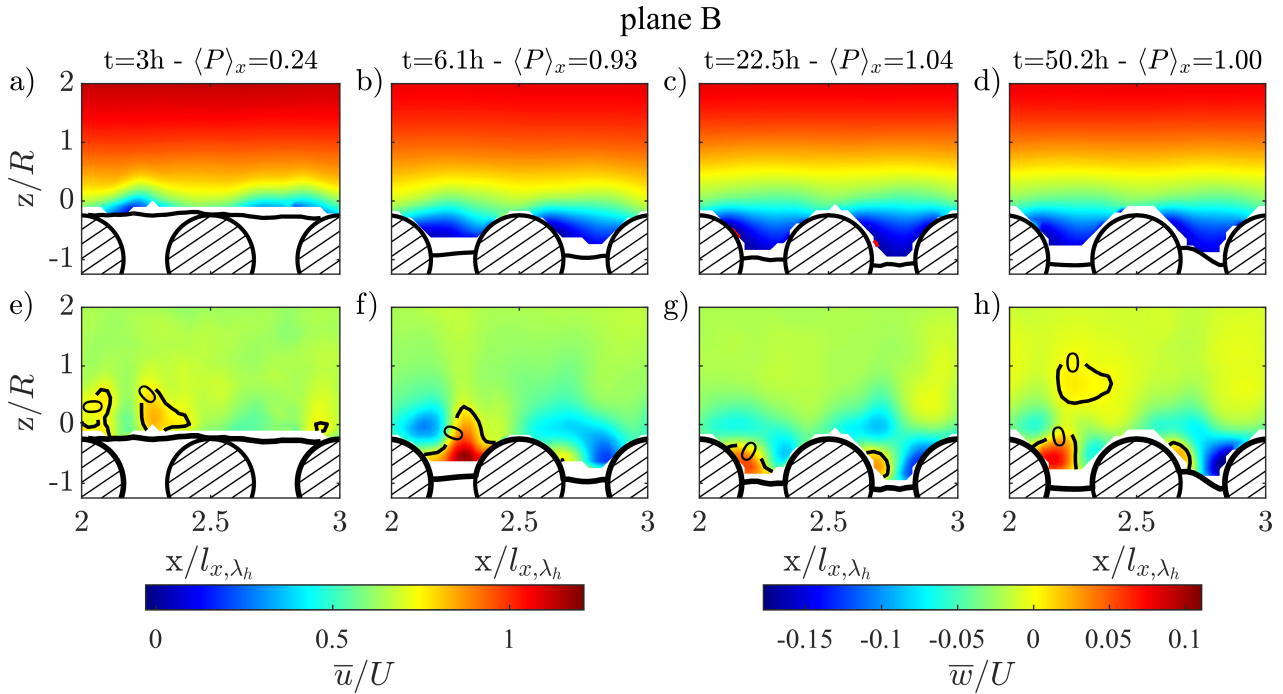
the spheres in their stoss side. At t = 6.1 hours, Figure 5.9f shows that a region of positive vertical velocity develops in the lee side of the spheres above the sediment deposit. This upflow region is embedded in a region of downflow taking place over the sphere. The development of this upflow region intensifies the downflow in the stoss side of the spheres compared to lower protrusion levels. For high protrusion levels $\langle P \rangle_x \simeq 1$, Figures 5.8g,h show a significant change in the vertical velocity pattern with a positive vertical velocity region extending continuously from the lee side of the spheres up to one R above the top of the spheres. The region of downflow is being restricted, instead, to the stoss side of the spheres.

In plane B, Figures 5.9e-h show that the vertical velocities are negative above the top of the spheres at all times. Within the bed interstices for $\langle P \rangle_x > 0.6$, Figures 5.9f-h show an alternation of positive and negative vertical velocities, with positive $\overline{w}$ usually observed in the lee side of the spheres and negative in the stoss side.

Figures 5.10a-h show the time-averaged fields of the transverse velocity $\overline{v}$ superimposed with the vector plot of the time-averaged velocity field in the x-z plane, as the bed develops. At t = 3 hours, Figures 5.10a,b show that the transverse velocity $\overline{v}$ in plane A is below 1% of U, while, in plane B, the magnitude of $\overline{v}$ is about 2-3% of U. The approximately zero transverse velocities observed in plane A are consistent with the symmetric bed topography observed in Figure 5.7a, for which no transverse momentum exchange in the central plane is expected. In plane B, $\overline{v}$ is negative in the first half of the pattern for x/$\lambda_{x,h} < 0.5$ while positive in the second half for x/$\lambda_{x,h} > 0.5$. This velocity pattern suggests that the flow is being deflected around the protruding sphere in the centre of the pattern at y/W = 3 in Figure 5.7b. At t = 6.1 hours, Figures 5.10c,d show that the transverse velocities strengthen in magnitude both in plane A and B. Negative transverse velocities of about 10% of U are observed in plane A (see Figure 5.10c). They can be related to the non-symmetric bed topography, as observed in Figure 5.7c. The pattern is characterized by a downsloping bed in the transverse direction due to the presence of the ridge. Since local flow upwelling is expected above the ridge, negative transverse flow velocities develop in plane A per continuity. In plane B, characterized by a higher protrusion level $\langle P \rangle_x$ compared to plane A, Figure 5.10d shows negative $\overline{v}$ in the stoss side of the central sphere and positive $\overline{v}$ in its lee, showing that locally the flow deflection induced by the protruding central sphere dominates over the large-scale flow patterns induced by the ridge. The magnitude of the transverse velocities is about 15-20% of U similar to the magnitude of the streamwise velocity component observed in Figure 5.9b. Similar transverse velocity patterns are observed in plane B at t = 22.5 hours and t = 50.2 hours in Figures 5.10f and 5.10g. At the same times, Figures 5.10e and 5.10g show that the transverse velocities in plane A are much lower than in plane B, being just 1-2% of U. The transverse velocities in plane A can be related to slight asymmetries in the position of the sediment deposits and of the eroded regions compared to the pattern central plane, as it can be observed in the bed topographies in Figures 5.7e,g. Overall, it is observed that in plane B the transverse flow exchange is much more significant than in plane A.

The transverse velocity patterns analysed and the overall symmetry of the fine-sediment bed topographies suggest that the flow in the bed interstices has a meandering behaviour, as exemplary sketched in Figure 5.11a for the bed topography at t = 50.2 hours. The flow, deriving from the sides of the sphere positioned at the upstream end of the pattern, converges in its lee side over the fine-sediment deposit, where it is diverted upwards. The vector plots in Figures 5.10a,c,e,g show, in fact, that in plane A a region of upwash is present

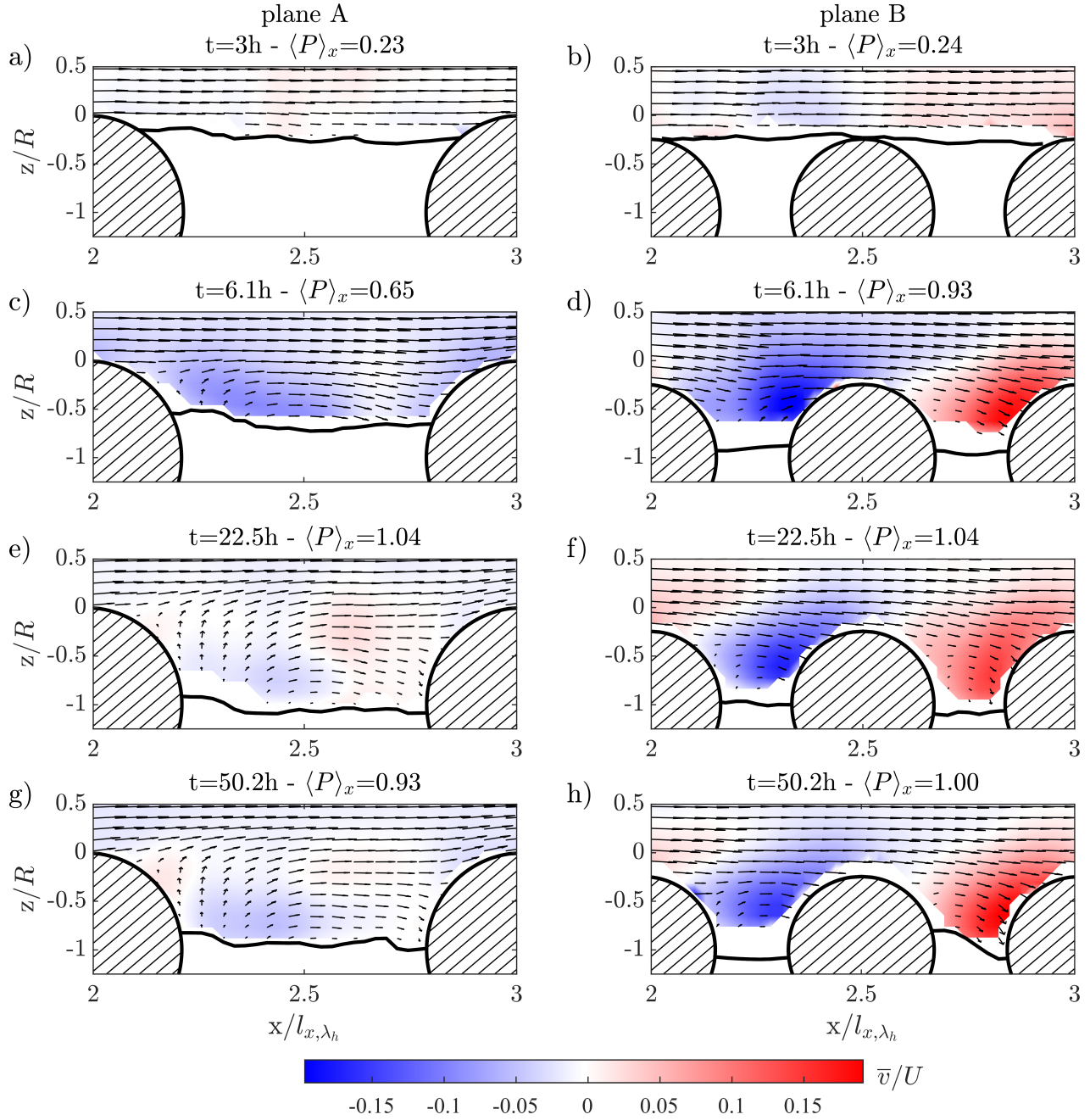**Figure 5.10:** Vector plots of the time-averaged velocity field in the x-z plane superimposed to the time-averaged transverse velocity field $\overline{v}$ in plane A (left column) and B (right column) at different stages of the bed development.
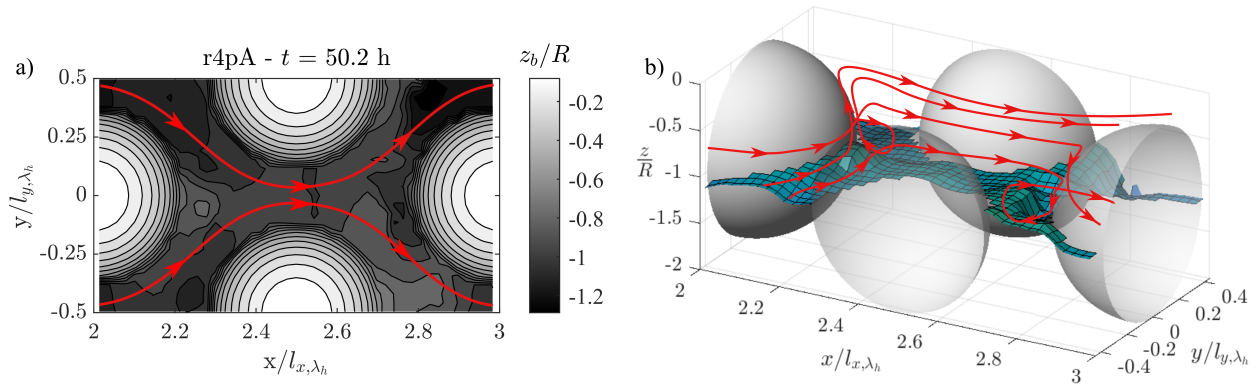
Figure 5.11: (a) Planar view of the probable meandering flow pattern in the bed interstices and (b) 3D sketch of the probable streamline configuration, both superimposed to the bed topography measured at t = 50.2 hours.

in the lee side of the spheres at all protrusion levels [4]. The sediment deposit in the lee side of the spheres acts as such as flow convergence zone where the flow surges upwards (potentially also from the porous bed). With reference still to Figures 5.10a,c,e,g, the velocity vectors are directed then preferentially in the stream-wise direction in the central part of the pattern. Near the sphere positioned downstream, the vectors are then slightly diverted upwards over the sphere and downwards towards the fine-sediment bed (particularly evident in Figures 5.10e,g), where the flow is likely to infiltrate in the porous bed or to be diverted around the sphere towards plane B given the low but non-negligible transverse velocities. In Figure 5.11b a possible sketch of the streamlines within the bed interstices is presented, according to the flow topology just described.

The flow patterns in the wake of the spheres, just described, present the peculiarity of the absence of a recirculation region. Experimental studies on the flow separation behind spheres or hemispheres protruding from immobile rough beds both as part of patterns (Papanicolaou et al., 2012; Liu et al., 2017; Fang et al., 2017; Raus et al., 2019) or isolated (Shamloo et al., 2001; Dey et al., 2011b; Hajimirzaie et al., 2014) have usually observed the development of recirculation region in the lee side of the spheres, as the result of the downwash over the spheres. In this case, though, the bed is not immobile, but mobile and characterized by the presence of obstacle marks (upstream and side scours and sediment deposit in the lee side) resulting from a dynamic interaction between the flow and the sediment bed (Karcz, 1973; Neuman and Bédard, 2015). It is surmised that the upwash taking place over the sediment deposits in the lee side of the spheres, as the result of flow convergences, annihilates the vorticity production induced by the otherwise dominating downwash over the spheres. Regions of flow convergence are known, in fact, to annihilate vorticity (Hunt and Eames, 2002). Sau et al. (2003) shows, for example, how the disappearance of the near-wake (i.e. the recirculation region) at some distance behind a cylinder is the result of the flow contraction of the streamlines in the far-wake due to a transverse pressure difference between the near- and far-wake. A similar absence of a recirculation region, as the one observed herein, has been highlighted by Neuman and Bédard (2015) and Euler et al. (2017) studying the development of obstacle marks around an isolated cylinder and an isolated sphere, respectively. They both observed increased erosion in the front and on the sides of the obstacles, as the result of flow downwelling

---

[4]   The region of upwash is strictly speaking not observed for $\langle P \rangle_x \simeq 0.2$ due to the lack of flow measurements in the lee side of the spheres directly above the sediment deposit. It is expected, though, that the flow pattern in the lee side of the sphere for $\langle P \rangle_x \simeq 0.2$ is similar to the flow patterns observed for the other protrusion levels, since the bed topography is similar (see Figures 5.7a,c,d,e).

in the front of the obstacles and the consequent development of horseshoe vortices, and sediment deposits in the lee side associated with flow upwelling. Neuman and Bédard (2015) suggests, in this case, that the legs of the horseshoe vortices exiting the lateral scour in the lee of the obstacle counteract the recirculation region with vorticity of opposite sign. In the present case, though, the time-averaged fields in Figures 5.10a,c,e,g do not show signs of the development of a horseshoe vortex in the stoss side of the spheres. For high protrusion levels, the absence of a horseshoe vortex might be related to the interaction with the wake of the sphere upstream which dominates the whole region below the spheres's top. For low protrusion levels, it is plausible that the spatial resolution of the measurements is not enough to visualize the horseshoe vortex.

5.3.3 Shear-stress fields

In order to analyse the influence of the protruding spheres on the bed shear stress conditions within the bed interstices as compared to a uniform fine sediment bed, the local fluid shear stress $\tau_{xz}|_{local} = \overline{\tau}_{vis} + \tau_{uw}$ is investigated, where $\overline{\tau}_{vis} = \rho_f \nu \partial_z \overline{u}$ is the time-averaged viscous shear stress and $\tau_{uw} = -\rho_f \overline{u'w'}$ the turbulent shear stress. Figures 5.12a-h show the spatial distribution of $\tau_{xz}|_{local}$ in plane A and in plane B, normalized by the reference bed shear stress acting on a uniform fine sediment bed τ_{P0}, as defined in Chapter 4. They show the development of a shear layer near the top of the spheres, as they protrude from the fine sediment bed. Within the shear layer $\tau_{xz}|_{local} > \tau_{P0}$, i.e. increased shear stress conditions are observed compared to a uniform fine-sediment bed. At t = 3 h, Figure 5.12a shows that the shear layer impacts the fine-sediment bed in plane A. A region of higher shear stress conditions, apparently detached from the shear layer, is observed in the stoss of the sphere downstream, where a lower fine-sediment bed level is present. The scour patterns extending from the stoss to the side of the spheres in Figure 5.7a along with the just observed shear stress peak in the sphere's stoss side, suggest the development of a horseshoe vortex simultaneously with the development of the shear layer. Unfortunately the spatial resolution is not enough to resolve it. At the same time, Figure 5.12e shows high spatial variability in the shear stress conditions in plane B, probably due to the spatial heterogeneity induced by the fine sediment bed. The limited time-convergence characterizing the shear stress for this PIV measurement might actually be the cause.

As the protrusion level of the spheres increases over time, the shear stresses within the shear layer increase, as it is observed both in plane A and in plane B in Figures 5.12a-d and 5.12f-h, respectively. Maximum $\tau_{xz}|_{local}$ values of 1.5 τ_{P0} are observed at t = 3 hours ($\langle P \rangle_x = 0.23$), while $\tau_{xz}|_{local}$ reaches values as high as 1.8 τ_{P0} and 2.5 τ_{P0} at t = 6.1 hours ($\langle P \rangle_x = 0.65$) and t = [22.47, 50.22] hours ($\langle P \rangle_x \simeq 1$), respectively. With increasing protrusion levels, a reduction of the shear stresses near the fine-sediment bed is observed in plane A, first restricted to the spheres' lee side at t = 6.1 hours (Figure 5.12b) and then occupying the whole near-bed region at t = 22.5 hours and t = 50.2 hours (Figure 5.12c-d). Noteworthy is a region of negative $\tau_{xz}|_{local}$ in the lee side of the spheres above the sediment deposit, which is first observed for $\langle P \rangle_x = 0.65$ (Figure 5.12b), but persists also at higher protrusion levels $\langle P \rangle_x \simeq 1$ (Figure 5.12c-d). This region of negative shear stress in the near bed region is limited to plane A while plane B is characterized by a reduction in shear stresses near the bed for high protrusion levels (Figures 5.12f-h).

The vertical extent of the shear layer varies with increasing protrusion level. Figures 5.12a-b show that in plane A at t = 3 hours, the shear layer occupies the whole region in between the spheres, while at t = 6.1 hours, the shear layer extends down towards the fine sediment bed only in the stoss side of the spheres. It is likely that the upflow, developing in the lee side of the spheres (see Figure 5.8b), prevents the shear layer
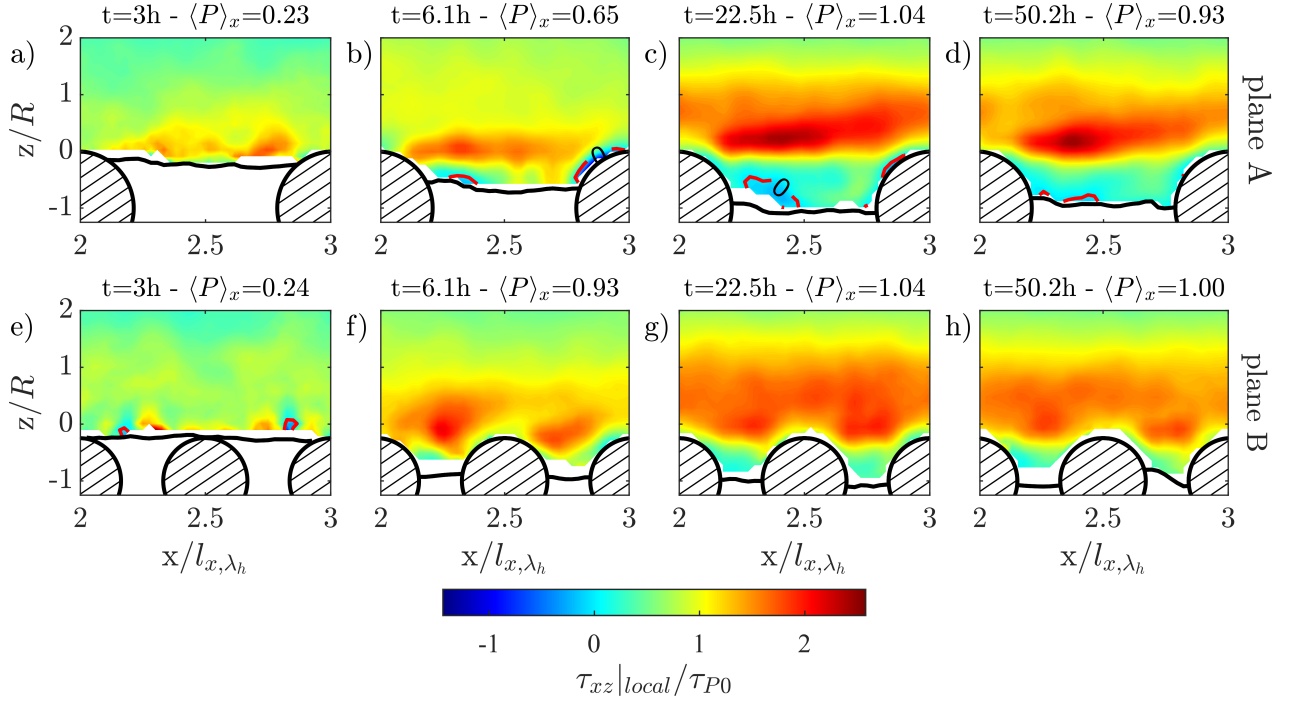
Figure 5.12: Streamwise local fluid shear stress fields $\tau_{xz}|_{local}$ normalized by the reference bed shear stress for a uniform fine sediment bed τ_{P0} in plane A (a-d) and B (e-h) at different stages of the bed development. The red isocontour lines define the isostress lines $\tau_{xz}|_{local} = 0$.

from reaching the fine sediment bed in the sphere's lee side. The shear layer interacts, though, with the sphere downstream, suggesting that wake interference flow conditions are present. The planar density of the pattern at t = 6.1 hours, equal to approximately 0.4 (see Table 5.2), supports this hypothesis, as within the range of planar densities $0.3 < \lambda_p < 0.5$, defined by Grimmond and Oke (1999) for the dominance of wake-interference conditions.

At t = 22.5 hours and t = 50.22 hours ($\langle P \rangle_x \simeq 1$), Figures 5.12c,d show that in plane A, the shear layer does not reach the fine-sediment bed any more, so that a higher degree of sheltering is achieved. The shear layer at $\langle P \rangle_x \simeq 1$ appears to be bound to a region close to the top of the spheres and negatively inclined in the streamwise direction, while it is clearly horizontal for lower protrusion levels (see Figure 5.12a-b). It is likely, that the upflow region dominating the bed interstices for protrusion levels $\langle P \rangle_x \simeq 1$ (see Figures 5.8g-h) forces the shear layer over the next roughness element. As a result, the shear layers merge above the top of the spheres to create a continuous region of higher shear stresses 1-1.5 R thick, as observed in Figures 5.12c,d. The net separation between the shear stress conditions in the near-bed region and in the shear layer along with the dominance of upflow conditions in the near-bed region at t = 22.5 hours and t = 50.2 hours suggests that in plane A, the bed interstices are decoupled from the outer flow, resulting in the flow skimming over the roughness elements for protrusion level $\langle P \rangle_x \simeq 1$. In the original definition by Morris (1955), skimming flow conditions are characterized by the presence of stable recirculating vortices in the bed interstices, which are not observed herein. MacDonald et al. (2016) showed, though, that the definition of skimming flow conditions on the basis of the flow patterns is not adequate, as similar flow patterns can result in different flow regimes. Table 5.2 shows that the planar densities associated with the protrusion levels $\langle P \rangle$ $\simeq 1$ for the last two PIV runs are equal 0.5, which represents the threshold for the onset of skimming flow
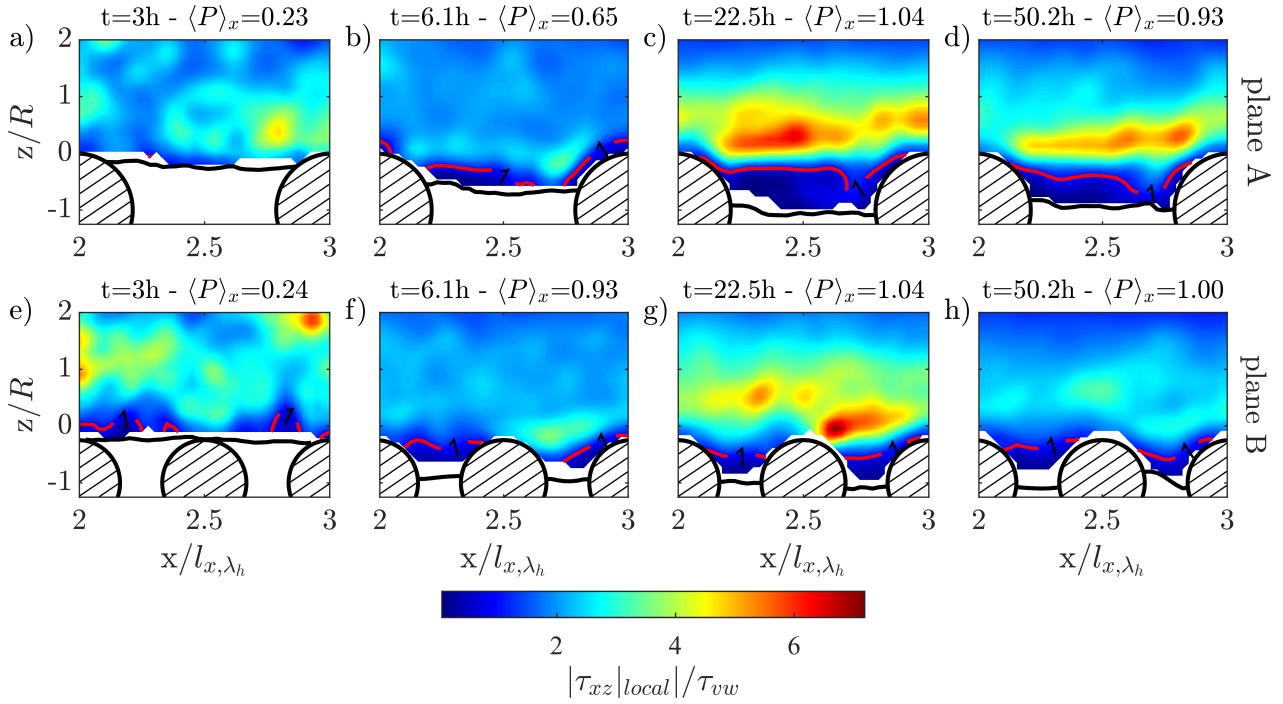
Figure 5.13: 2D-fields of the ratio between the absolute value of the streamwise local fluid shear stress $|\tau_{xz}|_{local}|$ and the transverse $\overline{\tau}_{vw}$ turbulent shear stresses in plane A (a-d) and B (e-h) at different stages of the bed development. The red isocontour lines define $|\tau_{xz}|_{local}|/\overline{\tau}_{vw} = 1$.

conditions in the flow classification by Grimmond and Oke (1999), corroborating the hypothesis that the flow is effectively skimming in plane A when stable bed conditions are reached at $\langle P \rangle \simeq 1$. In plane B, the shear stress patterns observed at times t = 22.5 hours and t = 50.2 hours in Figures 5.12g-h, show a separation between the shear layers developing at z/R = -0.3 and the near bed region, similar to the one observed in plane A. Furthermore, compared to plane A, a similar region of higher shear stresses extending up to z/R = 1 and associated to the streamwise nesting of shear layers, is observed also in plane B. These shear stress patterns suggest that skimming flow conditions are present also in plane B, even though the near bed region is dominated predominantly by negative vertical velocities (see Figure 5.9g-h).

The analysis of the transverse velocities in Section 5.3.2 has highlighted a meandering flow pattern in the bed interstices, pointing out to a significant momentum exchange in the transverse direction. Figures 5.13a-h show the spatial distribution of the ratio between the absolute value of the streamwise local fluid shear stresses $\tau_{xz}|_{local}$ and the transverse turbulent shear stress τ_{vw} = -$\rho_f \overline{v'w'}$ in plane A and in plane B. At t = 3 hours, the streamwise total shear stresses dominate over the transverse shear stresses both in plane A and in plane B (Figures 5.13a,e). At t = 6.1 hours, Figure 5.13b shows that in plane A, $|\tau_{xz}|_{local}|/\tau_{vw}$ < 1 in the lee side of the spheres in coincidence with the region of reduced $\tau_{xz}|_{local}$ (see Figure 5.12b). $\tau_{xz}|_{local}$ is in this area about 30-40 % of τ_{vw}, suggesting that lateral sediment transport is prevalent (considering also the inclined bed topography in the transverse direction - see Figure 5.7b). In the stoss side of the sphere, $\tau_{xz}|_{local}$ dominates instead over τ_{vw}, as the result of the shear layer impacting the fine-sediment bed (see Figure 5.12b). For high protrusion levels $\langle P \rangle_x \simeq 1$, the transverse shear stresses dominate over the streamwise shear stresses near the fine-sediment bed both in plane A and plane B, as observed in Figures 5.12c,d and in Figures 5.12f-h, respectively.

5.3.4 Analysis of the double-averaged flow field

The double-averaging methodology is applied, in the following, by decomposing the time-averaged flow statistics $\overline{\phi}_v$ in a time- and spatially-averaged component $\langle\overline{\phi}_v\rangle$ and a spatial fluctuation $\tilde{\phi}_v$ (Raupach and Shaw, 1982; Nikora et al., 2001). The spatial averaging is performed just over one pattern of spheres, as the bed topography is periodic in the streamwise direction. Since the bed topography at the reach scale changes in between the PIV measurements performed during the first and the second PIV runs (see for further details Section 5.3.1), the spatial average is performed for all PIV runs only in the streamwise direction over plane A and over plane B. An intrinsic spatial average is performed only over the areas occupied by fluid (Nikora et al., 2007).

5.3.4.1 Double-averaged streamwise velocities

Figures 5.14a-d illustrate the double-averaged vertical profiles of the streamwise velocity $\langle\overline{u}\rangle_x$ in plane A and in plane B, as the bed evolves. $\langle\overline{u}\rangle_x$ is normalized by the bulk velocity U for Exp. 1 R-$G\lambda h$ (see Table 3.1). The level $\langle\overline{u}\rangle_x/U = 1.2$ is identified by a vertical line, in order to compare the velocity profiles at the different time instants. Both in plane A and in plane B, $\langle\overline{u}\rangle_x$ decreases over time above the top of the spheres. The decrease in $\langle\overline{u}\rangle_x$ in the bulk flow region is the result of the increased bed roughness caused by the protruding spheres and of the partial redistribution of the flow discharge within the increasing bed interstices. The depth-averaged velocity decreases from 27 cm/s at t = 3 hours to 22.5 cm/s at t = 50 hours. At the same time, the total water depth increases from $\simeq$ 6 cm to $\simeq$ 6.8 cm, so that the discharge per unit width does not change and remains equal to $\simeq 160 \, \mathrm{cm^2/s}$. Considering the fact that the adjustments of the weir to maintain the water levels in contact with the boat were not higher than 0.05 mm, i.e. considerably less than the total water depth increase of 1 cm, it can be concluded that the system self adjusts to the increased roughness conditions with no changes in the water surface elevation.

In the bed interstices for z/H < 0, Figures 5.14a-d show that $\langle\overline{u}\rangle_x$ is dampened and decreases towards the fine-sediment bed. The peaks in $\partial_z\langle\overline{u}\rangle_x$ observed in Figures 5.14e-f show that in all cases where the PIV measurement plane intersects a protruding sphere (i.e. apart plane B at t = 3 hours) the velocity profiles are characterized by the presence of an inflection point at z/R = 0 in plane A and at z/R $\simeq$ -0.25 in planes B. The inflection point is the result of the flow retardation within the bed interstices. The presence of an inflection point at the top of the spheres is an ubiquitous feature of velocity profiles observed in vegetated flows Raupach et al. (1996); Finnigan (2000); Nezu and Sanjou (2008), over gravel bed rivers (Mignot et al., 2009a; Dey and Das, 2012; Sarkar et al., 2016) but also isolated boulders (Dey et al., 2011b; Papanicolaou et al., 2012). Raupach et al. (1996) showed that the inflection point observed near the top of a vegetation canopy generates Kelvin-Helmholtz instabilities which give rise to coherent eddies characteristic of a mixing layer. The shear layers observed in the time-averaged shear stress fields in Figures 5.12a-f are the result of this shear instability. The fact that the inflection point is observed at a lower height in plane B compared to plane A suggests that the point where the mixing layer separates follows the sphere's curvature. The region of highest shear stress is observed, in fact, below the spheres' top in plane B (see Figures 5.12f-h).

Below the spheres' top, Figures 5.14a-d show, that the shape of the streamwise velocity profile deviates from the log law profile, which is found to hold above the spheres (see Section 5.3.6). The shape of the velocity profile in the bed interstices at t = 3 hours is difficult to determine due to the few number of measurement
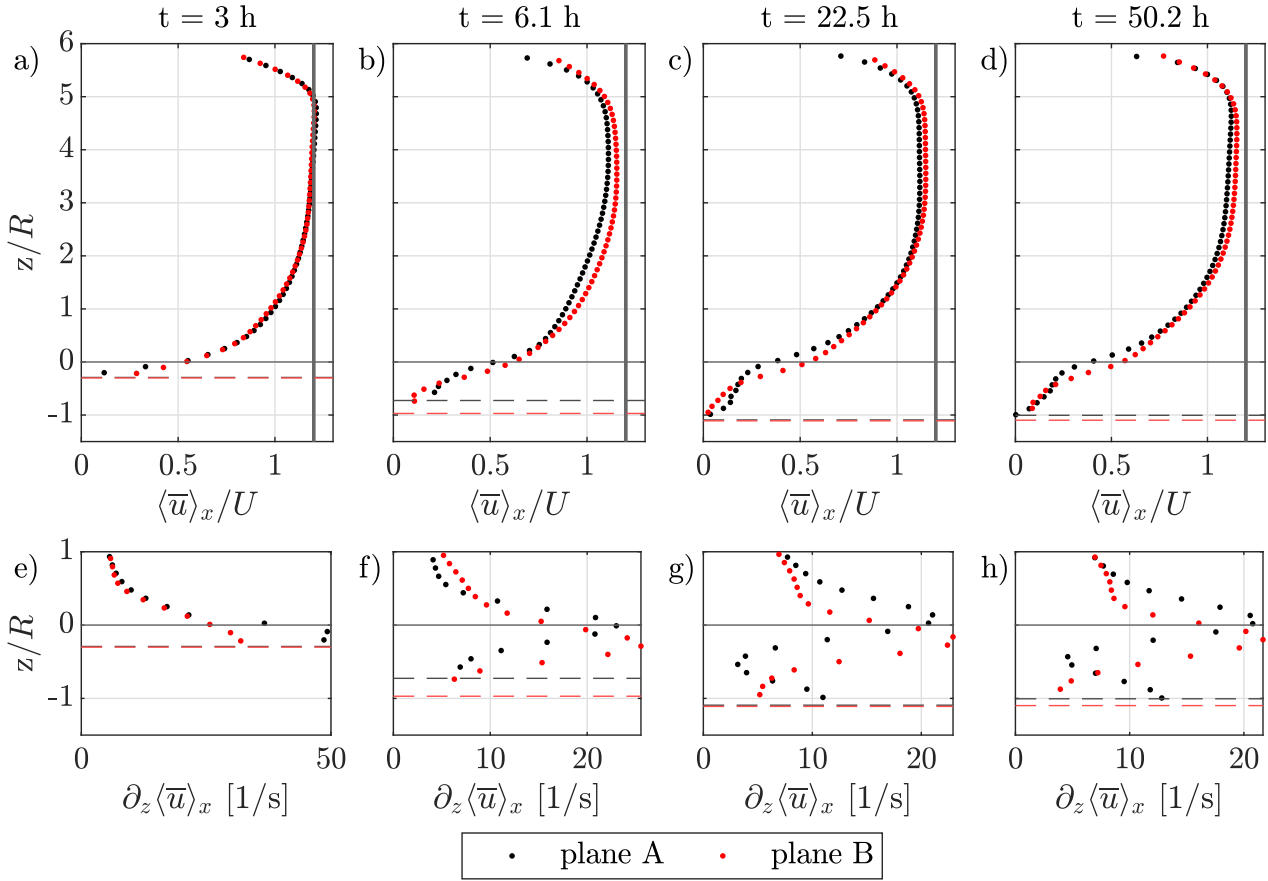
Figure 5.14: (a-d) Double-averaged streamwise velocity profiles $\langle\overline{u}\rangle_x$ and (e-f) profiles of the vertical derivative of the double-averaged streamwise velocity $\partial_z\langle\overline{u}\rangle_x$ in plane A and B at different stages of the bed development. The vertical continuous line in (a-d) corresponds to $\langle\overline{u}\rangle_x/U = 1.2$. The horizontal continuous line represents the top of the spheres and the black and red dashed lines the minimum sediment bed level in plane A and B, respectively.

points (Figures 5.14a,b). At t = 6.1 hours, Figure 5.14b shows that the velocity profiles in plane A and B are concave below the spheres' top and follow roughly an exponential decay, as also observed in vegetated canopies as the result of the developing mixing layer (Raupach and Thom, 1981; Raupach et al., 1991; Finnigan, 2000; Nezu and Sanjou, 2008). As the bed is eroded, Figures 5.14c,d show that in plane A at t = 22.5 hours and t = 50.2 hours, $\langle\overline{u}\rangle_x$ follows an exponential profile near the crest of the sphere, while at z/H $\simeq$ -0.4 the curvature of the velocity profiles becomes convex (as highlighted by the local minimum reached by $\partial_z\langle\overline{u}\rangle_x$ in Figures 5.14g,h). The convex shape of the profile suggests a quasi-logarithmic velocity distribution near the fine-sediment bed [5]. At t = 22.5 hours and t = 50.2 hours, the mixing layers do not penetrate, in fact, into the bed interstices as observed previously in Figures 5.17c,d, so that it is likely that the velocity profile adjusts to the bottom boundary. A similar vertical velocity distribution characterized by an exponential layer at the spheres' top and a quasi-logarithmic layer in the near-bed region has been speculated by Nikora et al. (2004) to be observable in the case of tall roughness elements.

In plane B, the velocity profiles at [22.5,50.2] hours in Figures 5.14c,d appear to be concave all the way down

---

[5] By plotting the velocity profile within the bed interstices in a semi-logarithmic plot, it was ascertained that the velocity distribution is linear in the near-bed region.

to the fine-sediment bed. The absence of the quasi-logarithmic layer in the near-bed region in plane B can be ascribed to the higher penetration depth of the mixing layer, as it separates from the sphere at a lower depth compared to plane A.

5.3.4.2 Spatially-averaged shear stresses and bed resistance

The momentum transfer in the streamwise direction is analysed on the basis of the double-averaged momentum equation proposed by Raupach and Shaw (1982) and Nikora et al. (2001). Since the bed level does not change during the PIV measurements, stationary flow conditions are assumed. Furthermore, uniform flow conditions are hypothesized, as the bed topography over one pattern of spheres is periodic in the streamwise direction and the non-uniformity induced by the boundary layer developing along the boat is negligible, especially in the near bed region, as discussed in Section H.3. The three-dimensionality of the flow cannot be neglected a priori both in the bulk-flow and in the bed-interstices, given the presence of a ridge and the high-spatial heterogeneity of the flow conditions in the bed. On the basis of the assumptions just made (i.e. $\partial_t = \partial_x = 0$), the streamwise component of the time-averaged momentum equation spatially averaged in the streamwise direction reads:

$$\frac{\partial}{\partial z}\left[A_\phi \underbrace{\left(-\rho_f\langle\overline{u'w'}\rangle_x - \rho_f\langle\tilde{u}\tilde{w}\rangle_x + \rho_f\nu\frac{\partial\langle\overline{u}\rangle_x}{\partial z}\right)}_{\tau_{xz}}\right] = -\underbrace{\rho_f g i A_\phi}_{G} + f_p + f_v +$$

$$-\frac{\partial}{\partial y}\left[A_\phi\underbrace{\left(-\rho_f\langle\overline{u'v'}\rangle_x - \rho_f\langle\tilde{u}\tilde{v}\rangle_x + \rho_f\nu\frac{\partial\langle\overline{u}\rangle_x}{\partial y}\right)}_{\tau_{xy}}\right]\underbrace{-\rho_f A_\phi\langle\overline{w}\rangle_x\frac{\partial\langle\overline{u}\rangle_x}{\partial z} - \rho_f A_\phi\langle\overline{v}\rangle_x\frac{\partial\langle\overline{u}\rangle_x}{\partial y}}_{\text{Advection terms}} \quad (5.1)$$

where A_ϕ is the roughness geometry function defined as the ratio between the horizontal area occupied by fluid at a certain elevation above the fine-sediment bed and the total averaging area. $A_\phi = 1$ above the top of the spheres ($z \geq 0$) and $A_\phi < 1$ below. A_ϕ is equivalent to the cumulative probability function of the bed elevations (Nikora et al., 2001; Aberle and Nikora, 2006), determined, in this case, along the PIV measurement plane, since the spatial average is performed only in the streamwise direction. τ_{xz} and τ_{xy} are the total fluid shear stresses resulting from a momentum exchange in the vertical and transverse direction, respectively. They result from the sum of the respective spatially-averaged turbulent [$-\rho_f\langle\overline{u'w'}\rangle_x$, $-\rho_f\langle\overline{u'v'}\rangle_x$], form-induced [$-\rho_f\langle\tilde{u}\tilde{w}\rangle_x$, $-\rho_f\langle\tilde{u}\tilde{w}\rangle_x$] and double-averaged viscous shear stresses [$\rho_f\nu\partial_z\langle\overline{u}\rangle_x$, $\mu\partial_y\langle\overline{u}\rangle_x$]. The form-induced shear stresses are the by-product of the spatial average and represent the momentum exchange induced by the spatial heterogeneities of the time-averaged flow. f_p and f_v represent the pressure and viscous drag arising from the integration of the pressure and viscous forces on the surface of the roughness elements. The momentum advection terms and the transverse variation of τ_{xy} contribute to the momentum exchange only in the presence of secondary currents or strong lateral spatial heterogeneities.

In the absence of secondary currents and transverse spatial heterogeneities, the integration of equation 5.1 yields the total fluid shear stress:

$$\begin{cases} \tau_{xz} = \rho_f gi(H - z) & \text{,if } z \geq 0 \\ \tau_{xz} = \rho_f giH + \rho_f gi \int_z^0 A_\phi dz - \int_z^0 (f_p + f_v)dz & \text{,if } z < 0 \end{cases} \tag{5.2}$$

Over the spheres' crest, τ_{xz} varies linearly, while in the bed interstices τ_{xz} decreases as momentum is removed by the pressure and viscous drag.

Figures 5.15a-h show the vertical profiles of the total fluid shear stress τ_{xz} and of the longitudinally-averaged turbulent shear stress $-\rho_f \langle \overline{u'w'} \rangle_x$, of the form-induced stress $-\rho_f \langle \tilde{u}\tilde{w} \rangle_x$ and of the double-averaged viscous shear stress $\rho_f \nu \partial_z \langle \overline{u} \rangle_x$ measured in plane A and B. It is first noted, that all shear stress profiles are influenced by the boundary layer developing along the boat as negative total fluid shear stresses are observed near the surface. The boundary-layer depth developing along the boat is identified by the elevation at which the total fluid shear stress τ_{xz} is zero, as discussed in Section H.3.3. At t = 3h, Figures 5.15a and 5.15e show that the boundary-layer depth is restricted to the upper 15 %, consistent with the boundary-layer depths observed in Section H.3.3 for similar flow conditions. At later times, the boundary-layer depth increases and covers up to 35 % of the water depth. It is not clear, though, the reason of this increase, as the flow conditions did not change during the Exp. R-$G\lambda h$ and the water surface levels, measured 20 cm upstream of the boat, showed variations in water levels below 0.5 mm. Nevertheless, it was assessed, that the displacement thickness of the boundary layer developing along the boat increases by about 0.01 mm over the pattern, so that the induced flow acceleration on the flow above the sediment bed can be effectively neglected.

The total shear stresses profiles in Figures 5.15a-h clearly show regions where τ_{xz} varies linearly below the boundary layer developing along the boat. Within these linear regions three-dimensional flow effects can be considered negligible. The local shear velocity u_* is obtained, therefore, by linearly extrapolating the total fluid shear stress profile to the top of the spheres with a best linear fit (red curves in Figures 5.15a-h). The shear velocity obtained in this manner represents the universal velocity scale relevant for the scaling of the turbulence above the spheres (Pokrajac et al., 2006). It is used, as such, to scale the shear stress profiles. The values of the local shear velocity u_* are listed in Table 5.3. It is observed that u_* increases as the protrusion level of the spheres increases over time. As a matter of fact the roughness of the pattern increases over time as both the frontal density and the standard deviation of the bed elevations at the global scale increase over time (see Table 5.2).

In the following, the shape of the total fluid shear stress profiles is analysed, in order to define the top of the boundary layer pertaining to the rough bed. Figure 5.15a shows that at t = 3 hours the total shear stress distribution in plane A is characterized by two linear trends, the lower one characterized by a higher slope than the upper one. Since the sphere's patch over which the velocity measurement is performed, is located between two dunes, the lower linear trend can be associated to the internal boundary layer separating at the point of reattachment of the recirculation region behind the incoming dune, as sketched in Figure 5.16. The shear layer developing along the crest of the dune (Best, 2005) does not influence the shear stress profile over the measurement pattern, as the distance between the latter and the dune is over 30 cm, enough for the shear layer to dissipate. Even though the internal boundary layer is still developing, its roughness sublayer can be considered already in equilibrium, as the analysis of the internal boundary layer development after a roughness transition in Appendix C shows. The shear stress conditions within the bed interstices are,
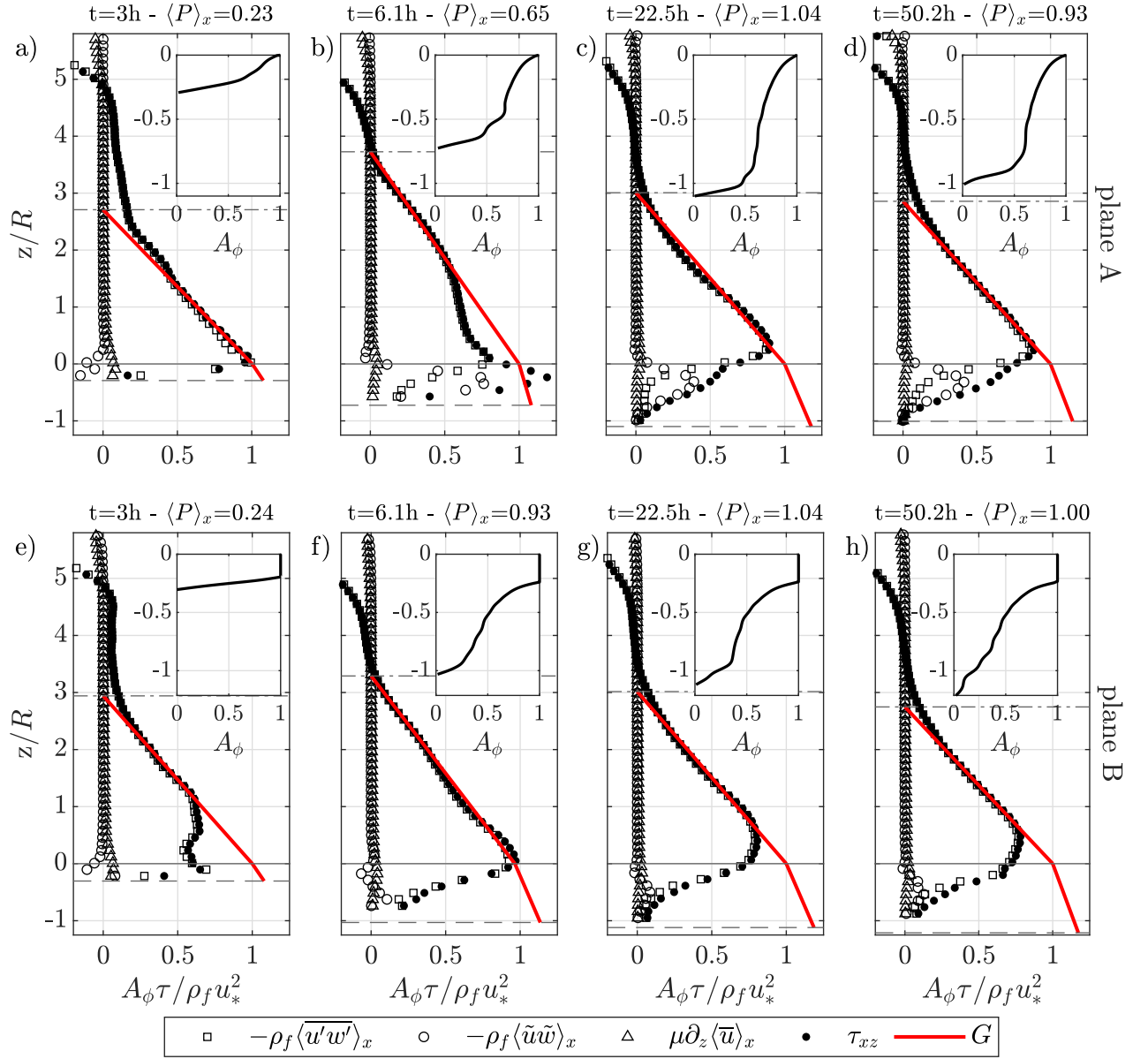
Figure 5.15: Vertical profiles of the longitudinally-averaged turbulent $-\rho_f\langle\overline{u'w'}\rangle_x$ stress, of the form-induced stress $-\rho_f\langle\tilde{u}\tilde{w}\rangle_x$, of the double-averaged viscous stress $\rho_f\nu\partial_z\langle\overline{u}\rangle_x$ and of the total shear stress τ_{xz} in plane A (a-d) and in plane B (e-h) at different stages of the bed development. The stresses are normalized by the shear velocity u_* obtained from the linear extrapolation of τ_{xz} to the top of the spheres, represented by the red line. The red linear profile represents, furthermore, the vertical distribution of the total momentum provided by the gravity to the flow G. The horizontal continuous and dashed lines represent the top of the spheres and the minimum fine-sediment bed level, respectively. The dot-dashed line represents the top of the boundary-layer.

Figure 5.16: Bed topography profile in plane A at t = 3 hours during the PIV measurement $r1pA$ [3]. The incoming dune is located about 30 cm upstream of the PIV measurement region contoured in green.

therefore, representative of a fully developed boundary layer.

The two linear trends observed in Figure 5.15e over plane B at t = 3 hours can be also ascribed to the developing internal boundary layer. The deviation of the τ_{xz}-profile from the linear trend in the near-bed region is related to the fact that the number o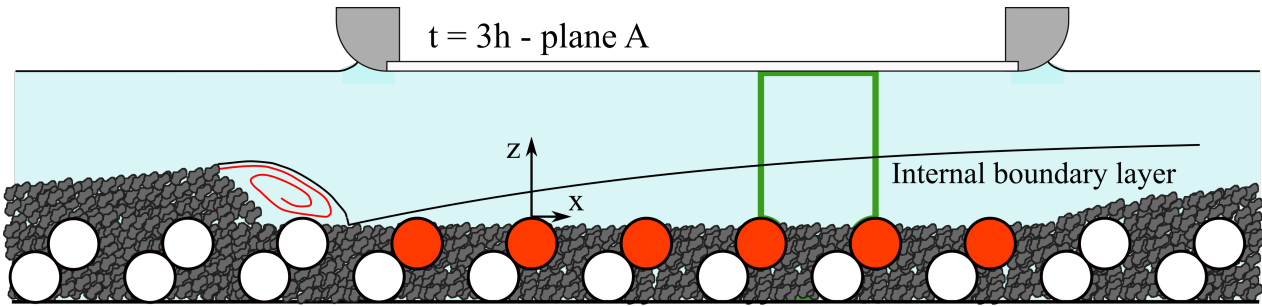f samples is not enough to obtain time-converged turbulent statistics in the near-bed region (as mentioned at the beginning of Section 5.3). The top of the internal boundary layer δ was defined at t = 3 hours by extending the linear fit of the τ_{xz}-profile up to $\tau_{xz} = 0$ both in plane A and in plane B.

At t = 6.1 hours, Figure 5.15b shows that the τ_{xz}-profile increases linearly up to the boundary layer of the boat, while in the near bed region the profile deviates. The deviation can be connected, in this case, to the high spatial heterogeneity of the shear stress conditions observed up to $z/R = 2$ induced by the heterogeneous bed topography with a local upsloping bed (see Figure 5.7c). At t = 6.1 hours, the τ_{xz}-profile in plane B (Figure 5.15f) shows, instead, a neat linear profile up to the boat boundary layer, as locally the bed heterogeneities are less pronounced (see Figure 5.7d). The $\tau_{xz} = 0$ level is also chosen, in these cases, as top of the boundary layer.

At t = 22.5 hours and t = 50.2 hours, the total shear stress profile in plane A (Figures 5.15c-d) and in plane B (Figures 5.15g-d) are characterized by a linear trend on top of which a region of almost zero shear stress develops for $3 < z/R < 5.5$. Compared to the flow conditions at earlier times, the system at t = 22.5 hours and 50.2 hours is characterized by the highest shear velocity (see Table 5.2). In order for the system to adjust to a higher shear stress condition induced by an increased roughness and maintain the water surface at a constant height, the energy slope of the flow has to increase compared to uniform flow conditions (i.e. the slope of the shear stress profile has to increase). It is surmised that for high protrusion levels, the system develops a flow non-uniformity in streamwise direction by adjusting the fine-sediment bed surface. From stereo photogrammetric measurements performed simultaneously 2 m in front of the measurement section during the experiment (not mentioned in this work), the fine sediment bed levels appears 2-3 mm lower than the fine-sediment bed level at the measurement section. Flow acceleration develops in the streamwise direction to guarantee increased shear stress conditions at the bed adjusted to the increased roughness. The top of the boundary layer induced by the developing flow non-uniformity in streamwise direction can be estimated, in first approximation, by linearly extrapolating the τ_{xz}-profile to the elevation for which $\tau_{xz} = 0$. The estimated boundary layer depths δ are listed in Table 5.3. The relative submergence of the protruding spheres, determined on the basis of the pattern-averaged protrusion level ($S_r = (\delta + \langle P \rangle)/\langle P \rangle$), decreases over time.

Figure 5.15a-b and 5.15c-f show that the total fluid shear stresses τ_{xz} reach a maximum at the top of the spheres for t = 3 hours and t = 6.1 hours both in plane A and plane B [6]. Figures 5.15c-d show, instead, that at t = 22.5 hours and t = 50.2 hours, the peak in τ_{xz} is observed above the top of the spheres in plane A. The shift in the location of the maximum total fluid shear stress is the result of the upflow conditions characterizing the near bed region, as shown in Figures 5.8g-h for plane A. The effect is similar to the one produced by secondary currents, just at a local roughness level. In plane B, Figures 5.15g-h show also a shift in the elevation of the total-fluid-shear-stress peak above the spheres, even though no upflow conditions are observed (see Figures 5.9g-h). The upward peak-shift in plane B can be plausibly connected to the fact that for high protrusion levels, the region of high shear stress resulting from the streamwise merging of the shear layers in plane A (see Figure 5.12c-d), expands in the lateral direction superimposing with the shear layer developing in plane B at a lower height, as can be observed in Figures 5.12g-h.

In the bed interstices, Figures 5.15a-h show that the total fluid shear stresses τ_{xz} decrease towards the fine-sediment bed. The momentum deficit between the total fluid shear stress profile and the red gravity line gives an idea of the amount of momentum extracted by the form and viscous drag. It is noteworthy that at t = 6.1 hours in plane A (see Figure 5.15b), the total fluid shear stress reaches a peak higher than the momentum provided by gravity. The peak is ascribed to the contribution of the form-induced shear-stresses, which are 60 % higher than the Reynolds shear stress at the elevation of the total-fluid-shear-stress peak. Given the high transverse heterogeneity in bed elevation characterizing the bed topography at this time (see Figure 5.7b), the transverse variation of the transverse form-induced shear-stresses $\partial_y \langle \tilde{u}\tilde{v} \rangle_x$ (which cannot be estimated) is not negligible. It is surmised, that this transverse momentum exchange induced by the lateral flow heterogeneity would act as a sink in the streamwise momentum budget.

In plane A, Figures 5.12a-d show that at t = 3 hours in the presence of low protrusion levels, the momentum exchange is dominated by the Reynolds shear stresses in the bed interstices, while for later times and higher protrusion levels, the form-induced shear stresses dominate. It is observed that the peak in form-induced stresses can be up to 4 times higher than the Reynolds shear stresses. The dominance of the form-induced shear stresses suggests that spatial variability of the flow within the bed interstices in plane A plays a relevant role in defining the local forcing on the fine-sediments. In plane B, Figures 5.12f-h show, instead, that in the bed interstices, the form-induced shear stresses are negligible compared to the Reynolds shear stresses . The reason of the local difference in form-induced shear stresses between plane A and plane B can be ascribed to the local distance between the spheres. Plane A is characterized by a sparser linear density of the spheres as compared to plane B. Poggi et al. (2004), analysing the dependency of the turbulent statistics on the density of the roughness elements, showed that sparser canopies are characterized by higher form-induced shear stresses than denser ones.

The fact that the form-induced shear stresses in plane A are significantly larger than the Reynolds shear stresses is remarkable, as previous studies on immobile gravel beds have found that the peak in form-induced shear stresses varies between 5 and 70 % of the Reynolds shear stresses with increasing size of the roughness elements (Mignot et al. (2009b); Sarkar and Dey (2010); Nikora et al. (2001); Dey and Das (2012); Sarkar et al. (2016) - the studies are listed by increasing size of the roughness elements used from 2 cm to 5 cm).

The bed shear stress, which represents the total resistance of the bed induced by both the spheres and the fine-sediment grains, can be estimated on the basis of Equation 5.2 by considering that the total fluid shear

---

[6] With the only exception of the total fluid shear stress profile at t = 3h in plane B (Figure 5.15e) due to the non-convergence of the data.
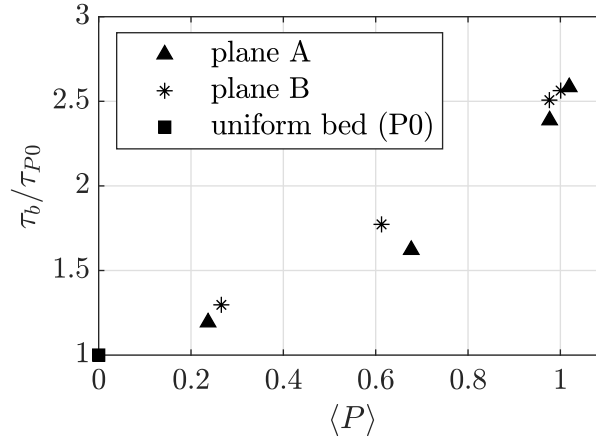
Figure 5.17: Bed shear stress τ_b normalized by the reference bed shear stress for a uniform fine sediment bed τ_{P0} as a function of protrusion level $\langle P \rangle$. The data point at $\langle P \rangle = 0$ refers to the uniform fine sediment bed analysed in Section 4.5.2.

stress becomes negligible at the bed (Pokrajac et al., 2006). Provided that the shear velocity yields the total shear stress at the top of the roughness, the bed shear stress is given by:

$$\tau_b = \rho_f u_*^2 \left(1 + \frac{\int_{min(z_b)}^{0} A_\phi dz}{\delta} \right) \tag{5.3}$$

The τ_b values are listed in Table 5.3. It is noted that at each time, the local bed shear stress in plane A and plane B is comparable within the measurement error. This is also true at t = 6.1 hours when the plane-averaged protrusion level $\langle P \rangle_x$ in plane A is significantly different than in plane B. This means that the bed shear stress is given primarily by the roughness conditions at the pattern scale. For this reason, the pattern protrusion level P is chosen as independent variable to plot, in Figure 5.17, the evolution of the bed shear stress normalized by the reference bed shear stress obtained from a flat uniform fine-sediment bed τ_{P0} (see Section 4.5.1). Figure 5.17 shows that the bed shear stress increases with increasing protrusion level of the spheres. This means, that the contribution of the spheres to the resistance of the bed becomes more significant compared to the grain-resistance with increasing protrusion level. A similar linearly increasing trend of τ_b with the protrusion level of a square pattern of semi-spheres over a flat immobile bed of fine-sediments was also observed by Raus et al. (2019).

	t	$\langle k \rangle$	$\langle P \rangle$	$\langle P \rangle_x$	$\sigma_{z,G}$	δ	S_r	u_*	τ_b	z_0	k_s	$z_d/\langle k \rangle$	z_m/δ	z_M/δ	z_{rs}/δ	$h_{rs}/\langle k \rangle$
	[h]	[cm]	[-]	[-]	[cm]	[cm]	[-]	[cm/s]	[Pa]	[cm]	[cm]	[-]	[-]	[-]	[-]	[-]
r1pA	3.0	0.24	0.24	0.23	0.08	2.7	12.4	1.94	0.40	0.005	0.18	−0.10	0.09	0.34	0.12	2.32
r1pB	3.0	0.27	0.27	0.24	0.09	2.9	12.1	2.01	0.44	0.006	0.23	−0.25	0.07	0.31	0.11	2.18
r2pA	6.1	0.68	0.68	0.65	0.28	3.7	6.5	2.21	0.55	0.020	0.64	−0.60	0.12	0.27	0.06	1.33
r2pB	6.1	0.61	0.61	0.93	0.31	3.3	6.4	2.25	0.60	0.014	0.47	−0.35	0.05	0.29	0.07	1.38
r3pA	22.5	1.02	1.02	1.04	0.39	3.0	4.0	2.66	0.87	0.030	0.97	−0.01	0.08	0.35	0.14	1.41
r3pB	22.5	1.00	1.00	1.04	0.33	3.0	4.0	2.68	0.87	0.028	0.91	−0.01	0.43	0.69	0.08	1.25
r4pA	50.2	0.98	0.98	0.93	0.37	2.9	3.9	2.57	0.81	0.026	0.85	0.00	0.2	0.64	0.13	1.38
r4pB	50.2	0.98	0.98	1.00	0.37	2.7	3.8	2.63	0.85	0.026	0.85	0.00	0.21	0.5	0.06	1.17
								±0.05	±0.03	±0.001	±0.01	±0.01				

Table 5.3: Boundary layer parameters for all PIV measurement in plane A and plane B: pattern-averaged protrusion height of the spheres $\langle k \rangle$, pattern scale protrusion level $\langle P \rangle = \langle k \rangle / R$, streamwise averaged protrusion level in the PIV plane $\langle P \rangle_x$, standard deviation of bed elevations at the pattern scale $\sigma_{z,G}$, boundary layer depth δ, relative submergence of the pattern $S_r = (\delta + \langle P \rangle)/\langle P \rangle$, local shear velocity obtained from the linear extrapolation of the total fluid shear stresses to the top of the spheres u_*, bed shear stress τ_b, roughness length z_0, equivalent sand roughness k_s, roughness displacement height z_d, starting point of the log-law z_m, end-point of the log-law z_M, elevation of the roughness sublayer at 5% dispersion of the streamwise velocities z_{rs}, thickness of the roughness sublayer $h_{rs} = z_{rs} + \langle k \rangle$.

5.3.5 Roughness sublayer

The protruding spheres and the fine-sediments cause spatial heterogeneities of the flow statistics, as seen for the turbulent shear stresses in Figure 5.12. The vertical extent of this region, called the roughness sublayer, can be identified on the basis of the spatial dispersion $D_t(\overline{\phi}_v(z)) = \sqrt{\langle \tilde{\phi}_v^2 \rangle_x}$ of the time-averaged flow statistics $\overline{\phi}_v$ (Florens et al., 2013; Rouzes et al., 2019; Raus et al., 2019), where the spatial fluctuation is defined as $\tilde{\phi}_v = \overline{\phi}_v - \langle \overline{\phi}_v \rangle_x$. Florens et al. (2013) shows, though, that the measured spatial dispersion D_t can be biased by the time-convergence error, so that the actual spatial dispersion D_s is given by:

$$2D_s(\overline{\phi}_v(z)) = 2D_t(\overline{\phi}_v(z)) - \langle \epsilon_{\overline{\phi}_v} \rangle_x \tag{5.4}$$

where $\epsilon_{\overline{\phi}_v}$ is the time-convergence error defined on a 95% confidence interval (estimated as in Appendix F). The vertical elevation of the roughness sublayer above the top of the spheres z_{rs} is defined as the elevation where $D_s(\overline{u})/\langle \overline{u} \rangle_x$ reaches 5% (Florens et al., 2013; Rouzes et al., 2019; Raus et al., 2019). The values of z_{rs} and of the thickness of the roughness sublayer $h_{rs} = z_{rs} + \langle k \rangle$ (where $\langle k \rangle$ is the pattern averaged protrusion height of the spheres) are listed in Table 5.3.

The roughness-sublayer thickness h_{rs} is equal to approximately 2 $\langle k \rangle$ at t = 3 hours, while for later times h_{rs} reduces to values close to 1.3 $\langle k \rangle$. The higher $h_{rs}/\langle k \rangle$ ratio observed for protrusion levels $\langle P \rangle_x \approx 0.25$ can be ascribed to the fact that the concentration of displaced sediments is higher at t = 3 hours than at the later times, as can be observed in Figure 5.2c. The studies on fine-sediment transport on uniform fine-sediment beds by Campbell et al. (2005) and Nikora et al. (2002a) suggested that with increasing sediment transport rates, the roughness sublayer increases. Overall, the roughness sublayer heights observed for higher protrusion levels $\langle P \rangle > 0.6$ of approximately 1.3 $\langle k \rangle$ agree with the roughness sublayer thicknesses observed by Florens et al.
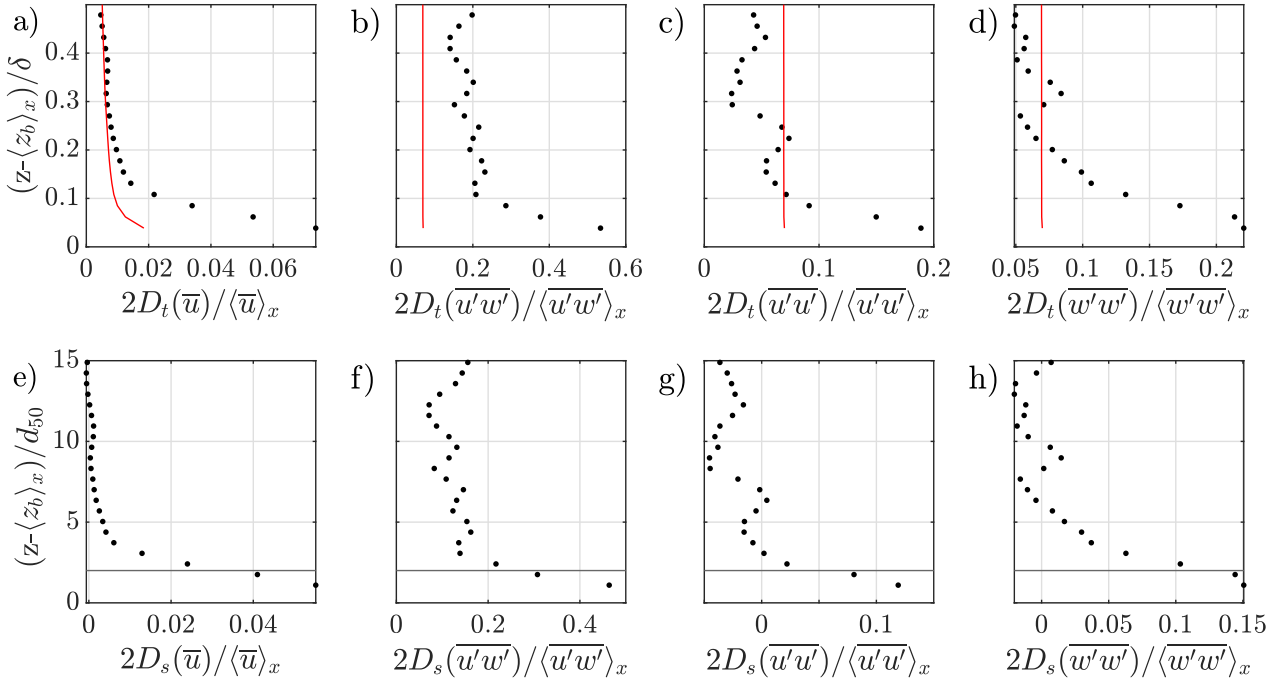
Figure 5.18: (a-d) Normalized total spatial dispersion $2D_t$ (black dots) and double-averaged normalized time-convergence error (red line) for a flat uniform bed (P0). (e-f) Normalized spatial dispersion $2D_s$ for a flat uniform bed (P0). The horizontal black line defines the chosen roughness sublayer height equal to $2d_{50}$.

(2013); Rouzes et al. (2019); Raus et al. (2019) over rough immobile beds.

Noteworthy is the fact that at t = 22.5 hours and t = 50.2 hours, the roughness sublayer height is higher over plane A than over plane B (see Table 5.3). Since at these times, the near bed region in plane A is characterized by strong upflow conditions, it is likely that the roughness sublayer is displaced higher above the top of the spheres.

The roughness sublayer just determined develops at the scale of the protruding spheres. However, in the near bed region, a roughness sublayer develops also at the scale of the fine-sediments. In Section 5.4 the spatial variability of the shear stress conditions induced by the spheres in the near-bed region, will be analysed, so that it is necessary to distinguish them from the ones induced by the fine-sediments. Raus et al. (2019), dealing with a similar issue of determining the local shear stress conditions acting on an immobile fine-sediment bed in the presence of protruding spheres, proposed to estimate the roughness sublayer on the basis of the one induced by a flat uniform bed. Accordingly, the roughness sublayer of the fine sediments is estimated, here, from the data presented in chapter 4 for a uniform flat fine-sediment bed in the presence of sediment transport under equivalent flow conditions as the ones analysed herein. Figures 5.18a-d show the comparison between the normalized total spatial dispersion and the normalized time convergence error for $\langle \overline{u} \rangle_x$, $\langle \overline{u'w'} \rangle_x$, $\langle \overline{u'u'} \rangle_x$ and $\langle \overline{w'w'} \rangle_x$ for the uniform fine-sediment bed. It can be seen that far away from the bed, the spatial dispersion converges to the time convergence error, as observed by Florens et al. (2013). Figures 5.18e-f show that the actual spatial dispersion D_s is the highest near the bed, with values as high as 20-40 % for the second-order moments. The height of the roughness sublayer of the fine-sediments h_{rs}^s based on the 5% threshold on $D_s(\overline{u})/\langle \overline{u} \rangle_x$ is equal to about one grain diameter under mobile bed conditions. For the purpose of remaining outside enough of the fine-sediment roughness sublayer to estimate the spatial variability of the shear stresses

induced by the spheres, a reference roughness sublayer height h_{rs}^s equal to $2d_{50}$ is chosen to guarantee a spatial dispersion of the second-order moments lower than approximately 10% (see horizontal line in Figure 5.18). Compared to the experimental work by Rouzes et al. (2019) where a h_{rs}^s of one d_{50} (associated with the same spatial dispersion level of the second order moments) was observed for a flat immobile fine-sediment bed with a similar grain size, this study shows that the roughness sublayer increases in height in the presence of sediment transport. Since the sediment transport reduces over time during the course of the experiment (see Figure 5.2c), the roughness sublayer of the fine sediments will reduce accordingly. As such, the fine-sediment roughness sublayer height h_{rs}^s will be considered equal to $2d_{50}$ during the first PIV run $r1$ at t = 3 hours where the concentration of displaced sediments C_s is similar to the one characterizing a uniform fine-sediment bed. During the second PIV run at t = 6.1 hours, C_s decreases to about half the transported sediment concentration for a uniform bed, so that h_{rs}^s is estimated equal to 1.5 d_{50}. For the last two PIV runs at t = 22.5 hours and t = 50.2 hours, almost no sediment transport is observed, so that h_{rs}^s is considered equal to d_{50}. Table 5.4 summarizes the roughness sublayer heights for each PIV run.

		$r1$	$r2$	$r3$	$r4$
t	[h]	3	6.1	22.5	50.2
C_s/C_{P0}		1.1	0.6	0.2	0.1
h_{rs}^s	[d_{50}]	2	1.5	1	1

Table 5.4: Concentration of displaced sediment C_s and roughness sublayer heights of the fine-sediment bed h_{rs}^s for each PIV run.

5.3.6 Log-law characterization

The double-averaged streamwise velocity profiles are analysed in order to determine whether they can be described by the log-law above the top of the spheres. A log-law fit is performed on the $\langle \overline{u} \rangle$-profiles, presented in Section 5.3.4.1 and normalized by the local shear velocity u_* obtained from the total fluid shear stresses. The log-law parameters z_d, z_0, as they appear in Equation 4.2, are determined by applying a linear interpolation in the parameter space [z,$\exp\left(\langle \overline{u} \rangle_x \kappa/u_*\right)$] following the procedure described in Section 4.5.2. The equivalent sand roughness k_s (= $z_0 \exp(\kappa B_r)$) is then determined by determining iteratively the value of the constant B_r in the case of transitional flow regimes or assuming a value of $B_r = 8.48$ for the fully rough regime (see Section 4.5.2).

The values of z_0, k_s and z_d are listed in Table 5.3 along with the lower and upper boundary of the log-law. For t = 3 hours and t = 6.1 hours, the log law region is found to be valid up to approximately 0.3 δ, as expected (Raupach et al., 1991; Jiménez, 2004). The lower end penetrates, instead, the roughness sublayer. Even though, in the classical view, the log-law develops above the roughness sublayer (Jiménez, 2004; Nikora et al., 2001), various studies showed that the log-law in a double averaged framework can penetrate the roughness sublayer (Amir and Castro, 2011; Rouzes et al., 2019). At t = 22.5 hours and 50.2 hours, the upper end of the log-law is found to shift higher into the flow up to approximately 0.6 δ. This is likely the result of the low relative submergence, as compared to previous times. Rouzes et al. (2019) found similarly for a rough bed of cubes that with decreasing submergence the vertical extent of the log-law increases.

Figure 5.19a shows the evolution of $k_s^+ = k_s u_*/\nu$ as a function of the protrusion level $\langle P \rangle$. As a reference, k_s^+

for the uniform fine-sediment bed is also plotted (square symbol at $\langle P \rangle = 0$). k_s^+ increases with the protrusion level of the spheres. For $\langle P \rangle \simeq 0.2$ the bed is still in the transitionally flow regime since $5 < k_s^+ < 70$. Over time for the higher protrusion levels, the bed becomes fully rough.

In Figure 5.19b, the equivalent sand roughness k_s normalized by the standard deviation of the bed elevation at the pattern scale $\sigma_{z,G}$ is plotted as a function of the protrusion level. The aim is to assess whether there is a correlation between the equivalent sand roughness and the geometric roughness scale. It is noteworthy that for the uniform fine-sediment bed conditions with the whole bed surface occupied by sediment transport, $k_s/2\sigma_{z,G} \simeq 2$, while for bed conditions for which the spheres protrude from the rough bed, the $k_s/2\sigma_{z,G}$ ratio appears to be independent of $\langle P \rangle$ and approximately equal to 1.

Overall, Table 5.3 shows that k_s, or equivalently z_0, increases with increasing protrusion level of the spheres,
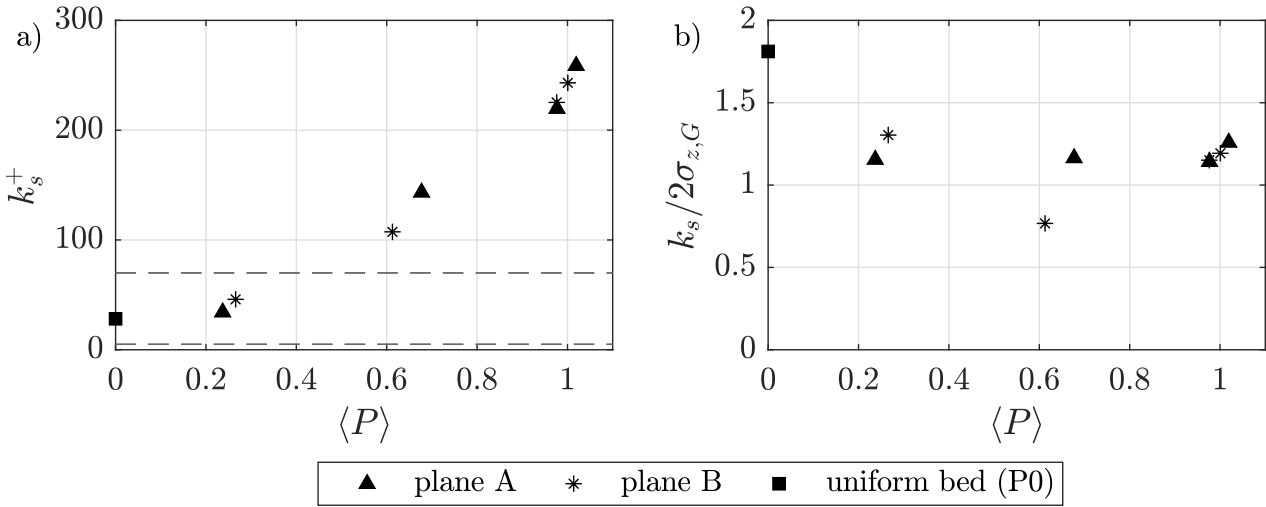

Figure 5.19: (a) Sand roughness Reynolds number k_s^+ and (b) ratio between the equivalent sand-roughness k_s and the standard deviation $\sigma_{z,G}$ as a function of the protrusion level. The data point at $\langle P \rangle = 0$ refers to the uniform fine sediment bed analysed in Section 4.5.2.

pointing out to the fact that the bed roughness increases over time, as the frontal density and the planar density of the spheres increases (see Table 5.2). Previous studies analysing the dependency of the roughness length on the frontal density of cuboid roughness elements (MacDonald et al., 1998; Cheng et al., 2007; Leonardi, 2010; Placidi and Ganapathisubramani, 2015) have shown that z_0 reaches a peak for λ_f comprised between 0.15 and 0.2, when the transition between wake-interference and skimming flow conditions is observed. The frontal density of the spheres at t = 22.5 and t = 50.2, when k_s is the highest, is equal to approximately 0.3 (see Table 5.2), suggesting that the flow patterns in the bed interstices, observed in Section 5.3.3 can be effectively associated to skimming flow conditions. It is noted in Table 5.2, that at t = 6.1 hours when a lower z_0 is observed and the flow patterns in the bed interstices suggest wake-interference conditions, the frontal density of the pattern is close to 0.2, suggesting that the threshold value on the frontal density for the transition from wake-interference to skimming flow conditions is higher for spherical obstacles. As pointed out by Placidi and Ganapathisubramani (2015), the transition is influenced also by the planar density. The transition from wake-interference to skimming flow defined by Grimmond and Oke (1999) on the basis of a planar density $\lambda_p = 0.5$ appears to be more suitable to describe the transition in flow conditions for spherical roughness elements. It is observed, in fact, that at t = 6.1 hours $\lambda_p \simeq 0.45$, while at t = 22.5 hours and t = 50.2 hours λ_p

$\simeq 0.52$.

Analysing now the dependency of the zero-plane position z_d on the protrusion level, Table 5.3 shows that the zero-plane is clearly below the top of the spheres for t = 3 hours and t = 6.1 hours. At t = 22.5 hours and t = 50.2 hours, when the spheres reach the highest protrusion level and the fine-sediment bed is stable, z_d is flush with the top of the spheres. The fact that $z_d = 0$ for $\langle P \rangle \simeq 1$, suggests that the outer flow perceives the top of the spheres as the actually bed, indicating that the flow effectively skims over the spheres. The conditions $z_d = 0$ is, in fact, associated to skimming flow conditions (MacDonald et al., 1998; Leonardi, 2010; Placidi and Ganapathisubramani, 2015). It is noteworthy, that the condition $z_d = 0$ is observed both in plane A and in plane B at t = 22.5 hours and t = 50.2 hours. This fact suggests that, even though the actual flow pattern inducing skimming flow conditions (i.e. the strong upflow in the bed interstices) is observed, strictly speaking, only in plane A (see Section 5.3.2), the outer flow perceives skimming flow conditions over the whole pattern.

A final remark on z_d is due given its behaviour for low protrusion levels. Table 5.3 shows that at t = 3 hours $z_d/\langle k \rangle \simeq$ -0.2, while at t = 6.1 hours it is in the range of [-0.4,-0.6]. This is in apparent disagreement with previous studies on immobile rough beds where the zero-plane position z_d increases with increasing planar density of the roughness elements (Nikora et al., 2002b; MacDonald et al., 1998; Placidi and Ganapathisubramani, 2015). The reason for a higher zero-plane position z_d at t = 3 hours can be connected to the fact that consistent sediment transport is still taking place on the bed. As shown by Dey et al. (2012), the presence of sediment transport on the bed caused z_d to shift upwards. At t = 6.1 hours when the sediment transport is reduced compared to t = 3 hours, z_d lowers accordingly.

5.3.7 Spatially-averaged turbulent kinetic energy budget

The spatially-averaged turbulent kinetic energy (TKE) budget is analysed in order to assess how the way the energy is transferred down to the fine-sediment bed changes as the protrusion level of the spheres increases over time. In the assumption that the flow is stationary and uniform with negligible influence of the secondary currents (as discussed previously), the double averaged TKE equation developed by Mignot and Hurther (2008) can be simplified as follows, as done by Mignot et al. (2009a) for the flow over a gravel bed:

$$\underbrace{-A_\phi \langle \overline{u'w'} \rangle_x \frac{\partial \langle \overline{u} \rangle_x}{\partial z}}_{P_s} \underbrace{-A_\phi \langle \overline{u_i'u_j'} \rangle_x \left\langle \frac{\partial \tilde{u}_i}{\partial x_j} \right\rangle_x}_{P_m} \underbrace{-A_\phi \left\langle \widetilde{u_i'u_j'} \frac{\partial \tilde{u}_i}{\partial x_j} \right\rangle_x}_{P_w} +$$

$$+ \underbrace{A_\phi \langle \epsilon \rangle_x}_{\epsilon} + \frac{\partial}{\partial z} \underbrace{\left[\underbrace{A_\phi \langle \overline{k'w'} \rangle_x}_{F_k} + \underbrace{A_\phi \langle \tilde{k}\tilde{w} \rangle_x}_{F_{fk}} \right]}_{T_k} + \underbrace{\frac{1}{\rho_f} \frac{\partial A_\phi \langle \overline{p'w'} \rangle_x}{\partial z}}_{p_D} - \underbrace{\nu \frac{\partial^2 A_\phi \langle k \rangle_x}{\partial z^2}}_{T_{vis}} = 0 \quad (5.5)$$

where i and j = 1,2,3 in the P_m and P_w terms correspond to the x-, j- and z-directions, respectively, and $k' = (u'u' + v'v' + w'w')/2$, $\tilde{k} = (\tilde{u}\tilde{u} + \tilde{v}\tilde{v} + \tilde{w}\tilde{w})/2$ and $k = \overline{k'}$, i.e. the turbulent kinetic energy. P_s is the shear-turbulence production term resulting from the work performed by the spatially-averaged velocity against the spatially-averaged shear. P_m and P_w are, instead, wake turbulence production terms resulting from the work of the wake-induced spatial velocity fluctuations against the double averaged shear stress and

the bed-induced fluctuations of the shear, respectively (Mignot and Hurther, 2008). ϵ is the TKE dissipation, T_k the TKE transport induced by the vertical TKE flux F_k and by the vertical form-induced energy flux F_{fk}, p_D the pressure diffusion and T_{vis} the viscous diffusion. The TKE equation 5.5 is written in such a way that positive values of the different terms represent an energy gain, while negative ones a loss.

The wake production terms P_m and P_w involve a total of eighteen terms, of which only the twelve involving longitudinal and vertical derivatives can be estimated, given the data available. The remnant terms involving the transverse derivatives can be considered, in first approximation, negligible at least in plane A, as it can be considered a symmetry plane with negligible lateral momentum exchange for times t=[3, 22.5, 50.2] hours, as discussed in Section 5.3.2. The asymmetric bed topography at t = 6.1 hours does not allow do strictly apply this assumption for plane A at this time. As for plane B, the estimated values of P_m and P_w should be taken with care, as the plane is characterized by a consistent lateral momentum exchange (see Section 5.3.2). Overall, the estimated values of P_w are found to be negligible compared to the shear production P_s, consistent with the numerical and experimental studies by Yuan and Piomelli (2014) and Mignot et al. (2009a) on the flow over a rough gravel beds, suggesting that the transverse derivatives can be effectively neglected. In the following, the wake-production term P_w will not be analysed.

The TKE dissipation ϵ is estimated on the basis of the macroscopic approach derived by Batchelor (1953) through dimensional analysis under the hypothesis that the turbulence is in equilibrium (i.e. $\epsilon \simeq P_s$). In open channel flows, this hypothesis can be considered to hold, though, only above the roughness sublayer in the equilibrium layer which roughly corresponds to the region where the log-law holds, as studies both over vegetated canopies (Raupach et al., 1991; Nezu and Sanjou, 2008) and rough beds (Hurther et al., 2007; Yuan and Piomelli, 2014; Sarkar et al., 2016) show. Nevertheless, the macroscopic approach was used by Mignot et al. (2009a) to estimate ϵ for a flow over a gravel, a similar case like the one studies herein. It should anyway kept in mind, that the estimate of the TKE dissipation, given as follows, represents a rough estimate of the true energy dissipation within the roughness sublayer:

$$\epsilon = K_\epsilon \frac{\overline{(u'^2)}^{3/2}}{L_x} \tag{5.6}$$

where K_ϵ is a constant tweaked within the range of admissible values (see Nezu and Nakagawa (1993) p.22) to guarantee an equilibrium layer above the roughness sublayer and L_x the streamwise integral length scale. L_x was estimated on the basis of the integral time scale L_t under Taylor's frozen turbulence hypothesis: $L_x(x, z) = \overline{u}(x, z) L_t(x, z)$ where $L_t(x, z) = \int_0^\infty \frac{\overline{u'(x,z,t+\tau)u'(x,z,t)}}{\overline{u'^2}(x,z)} d\tau$.

The pressure diffusion term p_D is given by the difference between the production terms and the TKE dissipation and transport. The viscous diffusion term T_{vis} is found to be negligible.

Figures 5.20a-h show the vertical profiles of the different TKE-budget terms normalized by u_*^3/δ in plane A and plane B as the bed evolves. It should be first noted, that the double-averaged estimate of the TKE dissipation ϵ at t = 3 h and t = 6.1 h for both plane A and plane B (see Figures 5.20a-b and Figures 5.20e-f, respectively) is probably significantly underestimated within the roughness sublayer. While ϵ balances the shear production above z/R $\simeq$ 0.5, within the roughness sublayer it appears that P_s is balanced mainly by the turbulent diffusion p_D. While a significant contribution of the pressure diffusion cannot be neglected in the energy budget within the roughness sublayer (Raupach et al., 1991), it is unlikely that it dominates over the TKE dissipation. Therefore, for t = 3 h and t = 6.1 h, p_d and ϵ will not be considered in the following analysis. Figures 5.20a-h, show that the shear production P_s reaches a peak near the top of the spheres decreasing both

towards the water surface and towards the fine-sediment bed at all times. Similar vertical trend in P_s were also observed in other studies on flows over vegetated Raupach et al. (1991); Nezu and Sanjou (2008) and gravel beds (Mignot et al., 2009a; Yuan and Piomelli, 2014; Dey and Das, 2012). In plane A, Figures 5.20a-d show that the location of the peak in P_s increases as the protrusion level of the spheres increases over time. More specifically, the peak is initially observed at t = 3.1 hours ($\langle P \rangle_x = 0.23$) below the top of the spheres at z/R = -0.1, at t = 6.1 hours ($\langle P \rangle_x = 0.65$) at the spheres' top and at t = [22.5, 50.2] hours ($\langle P \rangle_x \simeq 1$) above the top of the spheres at z/R = 0.13. The peak appears to follow the position of the inflection point in the streamwise velocity profile observed in Figures 5.14e-h in plane A, suggesting that the main energy production is associated to a Kelvin-Helmholtz instability. The increase in the peak elevation can be related to the change in vertical velocity conditions within the bed interstices being predominantly negative for t = 3 h and t = 6.1 h and positive for t = 22.5 hours and t = 50.2 hours (Figures 5.8e-f). The strong upflow at high protrusion levels, which was associated to skimming flow conditions, pushes the maximum shear production above the top of the spheres along the inclined shear layer observed in Figures 5.12c and 5.12d. In plane B where the vertical velocities remain predominantly negative in the bed interstices at all times (Figures 5.9e-f), the peak in P_s is observed, instead, at z/R = -0.16 at all times (Figures 5.20e-h).

Studies on the flow over immobile gravel beds without the presence of fine sediments (Mignot and Hurther, 2008; Mignot et al., 2009a; Yuan and Piomelli, 2014; Dey and Das, 2012; Sarkar et al., 2016), where also skimming flow conditions are expected to persist given the high packing of the bed, have highlighted that the peak in shear production is usually observed, in a spatially-averaged sense, below the roughness crest. The double-averaging was performed, though, in these studies, over bed areas comprising roughness elements with different degrees of protrusion compared to the average sediment bed level. This study suggests that locally over the crest of the roughness elements, the peak in shear production can be observed above the bed under skimming flow conditions. Performing a spatial average between plane A and plane B at t = 22.5 hours and t = 50.2 hours to get rid of the transverse spatial heterogeneity at the pattern scale would result in an elevation of the peak production below the spheres' top, consistent with the studies just cited.

Considering the distribution of P_s deep within the bed interstices in plane A, Figure 5.20a shows strong energy production near the fine-sediment bed at t = 3 hours for low protrusion levels. At t = 6.1, P_s reaches zero near the fine-sedimet bed at z/R $\simeq$ -0.6. At t = 22.5 hours and t = 50.2 hours ($\langle P \rangle_x \simeq 1$) P_s tends towards zero at a higher vertical elevation, namely at z/R $\simeq$ -0.4. In plane B for similar protrusion levels, i.e. at t = [6.1, 22.5, 50.2] hours, Figures 5.20f-h show instead that P_s tends towards zero deeper in the bed interstices at z/R $\simeq$ -0.6.

Within the bed interstices, the wake production is found to be negligible compared to the shear production at all times apart from t = 6.1 hours. This is in general agreement with the findings over gravel bed, where P_m was found to be at max 5% of P_s as in Mignot and Hurther (2008). At t = 6.1 hours in plane A, Figure 5.20b shows that P_m is of the same order of magnitude as the shear production P_s for z/R < -0.25. This is consistent with the high transverse heterogeneity of the bed elevations at this time instant (see Figure 5.7b), which can cause an increased three-dimensionality of the wake. P_m becomes the dominant contribution to the energy production near the fine-sediment bed. In plane B, Figure 5.20b shows that P_m is negative at the same time. This result is quite surprising as it would mean that the energy is extracted from the wake. Given the strong transverse momentum exchange characterizing this time, it is plausible that the wake energy extracted from plane B is fed to to the wake in plane A resulting in negative and positive P_m, respectively.

Figures 5.20c-d and Figures 5.20g-h show that the TKE dissipation ϵ is characterized by a similar trend as
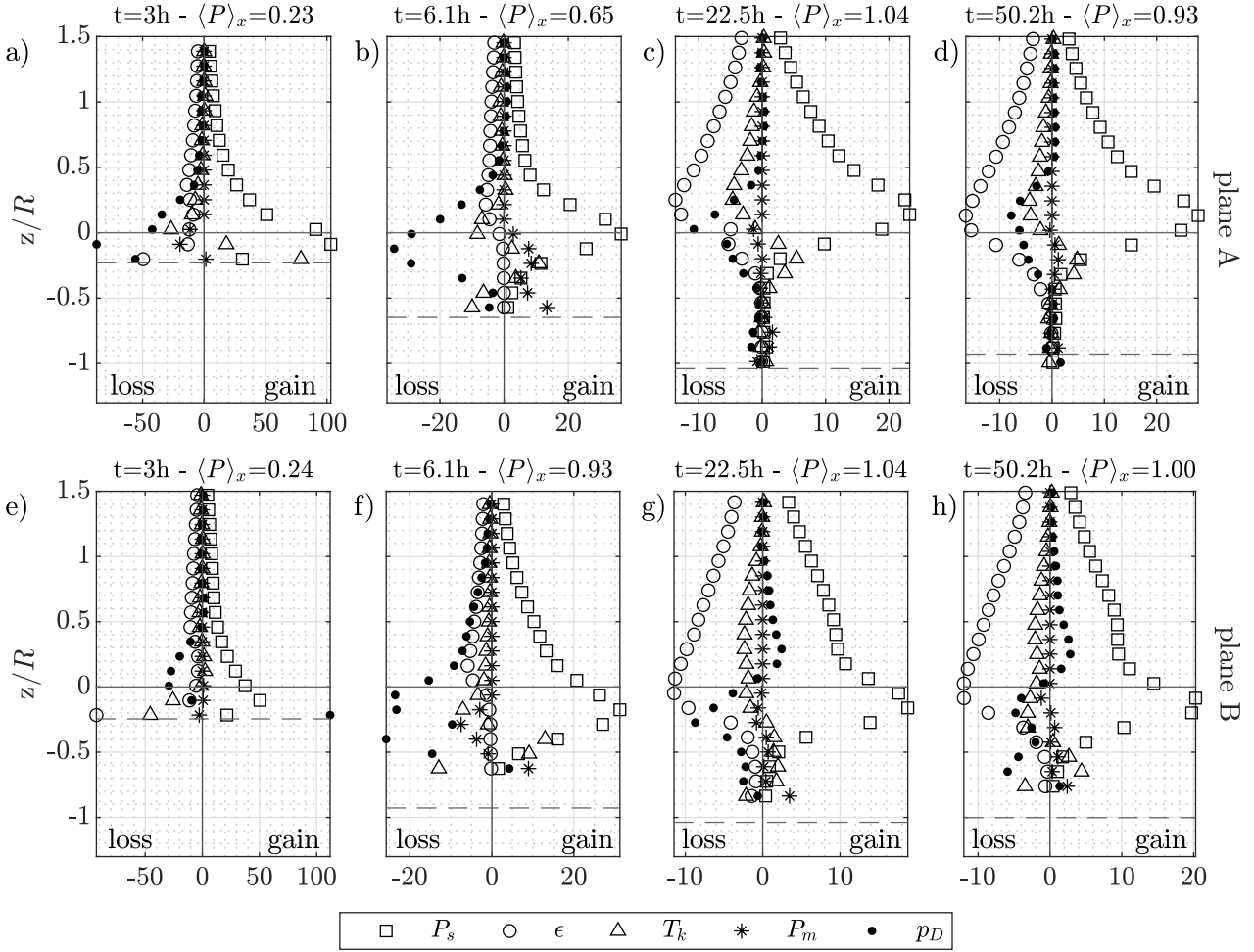
Figure 5.20: Vertical profiles of the spatially-averaged turbulent kinetic energy budget at different stages of the bed development in plane A (a-d) and plane B (e-h). The terms are normalized by u_*^3/δ. The horizontal continuous and dotted lines represent the top of the spheres and the average sediment bed level, respectively.

the shear production P_s both in plane A and in plane B. The peak in TKE dissipation is observed at the same vertical elevation as the peak in shear production. Above the roughness sublayer, ϵ balances the shear production as the other terms in the energy budget tend towards zero. Within the roughness sublayer, the equilibrium state is not satisfied, instead, any more. Within the bed interstices at t = 22.5 hours and t = 50.2 hours, Figures 5.20c-d and Figures 5.20g-h show that ϵ tends towards zero at about the same vertical elevation as P_s, i.e. in the upper part of the bed interstices in plane A and in the lower part of the bed interstices for plane B.

In plane A, Figures 5.20a-d show that the transport term T_k is negative above the top of the roughness. T_k acts for z/R > 0 as a local energy sink diffusing the turbulent kinetic energy towards the bulk flow region and towards the bed interstices. The vertical location of the negative peak in T_d appears to follow the peak in shear production, increasing over time above the top of the spheres. Below the top of the spheres, T_d becomes positive, acting as such as a local energy gain to compensate, along with the shear production P_s, the turbulent dissipation ϵ and the pressure diffusion p_D, as clearly shown in Figures 5.20c and 5.20d. At t = 3 h, Figure 5.20a shows that T_k exceeds locally P_s near the fine sediment bed, showing that the energy generated at the

spheres' top within the shear layer is directly transported down to the level of the fine-sediment bed for low protrusion levels. At t = 6.1 hours ($\langle P \rangle_x$), Figure 5.20b shows that T_k changes again sign deep in between the spheres for $z/R \simeq 0.4$ in order to compensate the wake production term P_m in the near-bed region. For protrusion levels $\langle P \rangle_x \simeq 1$, Figures 5.20c-d shows, instead, that the turbulent transport T_k at $z/R \simeq = -0.4$ tends already towards zero.

In plane B, Figures 5.20e-h show that the region of negative transport T_k stretches down below the spheres' top consistent with the fact that the peak in shear production is observed below the spheres' top. For high protrusion levels $\langle P \rangle_x \simeq 1$, Figures 5.20f-h show that T_k turns positive at $z/R \simeq -0.3$. This region of positive T_k stretches down to $z/R \simeq -0.6$ at t = 6.1 hours (Figure 5.20f) and down to $z/R \simeq -0.8$ at t = 50.2 hours. Below, the data suggest that T_k turns again negative.

Overall, these results clearly show that the amount of energy which reaches the fine-sediment bed decreases over time as the protrusion level of the spheres increases. The TKE budget clearly shows that for $\langle P \rangle_x = 0.23$ and $\langle P \rangle_x = 0.65$, the energy reaches the fine-sediment bed and the sediment transport is active and the bed eroding. The higher amount of energy reaching the fine-sediment bed at $\langle P \rangle_x = 0.23$ compared to the one reaching the fine-sediment bed at $\langle P \rangle_x = 0.61$ is consistent with the higher erosion and sediment transport rates observed at t = 3 hours compared to t = 6.1 hours in Figures 5.2b-c. As the bed reaches protrusion levels $\langle P \rangle_x = 1$, no energy exchange is observed in plane A for $z/R < -0.4$, consistent with the observation that the sediment bed level has reached a stable state with almost no sediment transport (see Figures 5.2a and 5.2c). However, in plane B for similar protrusion levels, there is still residual energy exchange in the near-bed region for $z/R < -0.6$, suggesting that intermittent grain movement is still possible. These results suggest, that skimming flow conditions are effectively reached for protrusion levels close to 1, as the transfer of energy produced in the shear layer to the fine-sediment bed is highly attenuated or annihilated.

5.4 Bed hydrodynamics at the fine-sediment scale

In this Section, the variability of the local shear stress conditions acting on the fine sediments and induced by the protruding spheres is investigated. The local shear stress acting on the fine sediments τ_s, hereafter fine-sediment shear stress, is determined at an elevation above the local bed level $z'(x,y)$ (= z-z_b(x,y)) equal to the fine-sediment roughness sublayer height h_{rs}^s, as sketched in Figure 5.21. As discussed in Section 5.3.5, measuring τ_s at the edge of the fine-sediment roughness sublayer avoids the influence of the spatial hetero- geneity of the flow induced by the fine-sediments. Please recall that the fine-sediment roughness sublayer decreases in time with decreasing sediment transport. The estimated roughness sublayer heights for each PIV run are given in Table 5.4. The fine-sediment shear stresses in the streamwise and transverse directions, τ_s^x and τ_s^y, are derived by evaluating the fluid shear stresses at the elevation of the fine-sediment roughness sublayer above the local fine-sediment bed level, as follows:

$$\tau_s^x = \left(-\rho_f \overline{u'w'} \Big|_{z'=h_{rs}^s} + \nu \frac{\partial \overline{u}}{\partial z} \Big|_{z'=h_{rs}^s} \right) \tag{5.7}$$

$$\tau_s^y = \left(-\rho_f \overline{v'w'} \Big|_{z'=h_{rs}^s} \right) \tag{5.8}$$

Since the bed topography does not present steep slopes at all times, it was not necessary to project the fluid shear stresses in the direction of the local bed topography. The error committed by doing so is estimated to be less than 15 % for the steepest slopes observed.
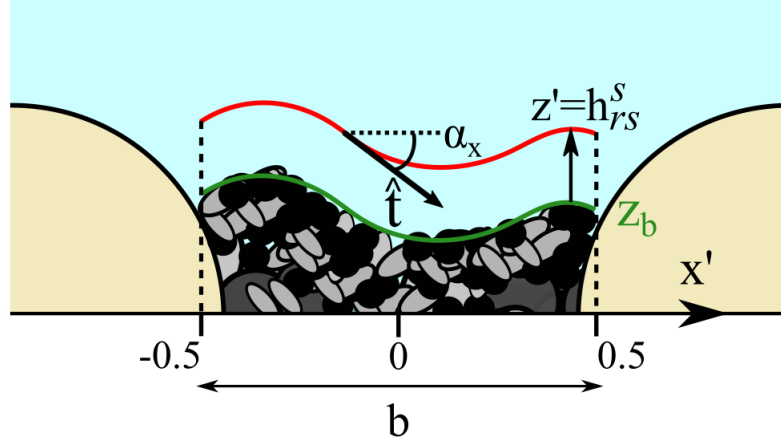

Figure 5.21: Local vertical coordinate system $z'(x,y)$ (= z-$z_b(x,y)$) for the definition of the fine-sediment shear stress at an elevation equal to the fine-sediment roughness sublayer height h_{rs}^s. $\hat{t}$ is a curvilinear coordinate following the fine-sediment bed at $z' = h_{rs}^s$ for the definition of the slope α_x of the local bed topography. $x' = (x - 2.5l_{x,\lambda_h})/b$ is a local reference system centred in the pattern and normalized by the spacing of the protruding spheres b.

5.4.1 Local shear stress distribution acting on the fine sediments

The fine-sediment shear stress conditions are analysed in terms of the local Shields parameter, in order to investigate at the same time the local sediment transport conditions. The local Shields parameters in the streamwise θ_S^x and transverse directions θ_S^y are defined, as follows: $\theta_S^x = |\tau_s^x|/(\rho_f \Delta g d_{50})$ and $\theta_S^y = |\tau_s^y|/(\rho_f \Delta g d_{50})$. In order to assess whether the spheres are able to shelter the grains up to a point that not even localized grain movements take place, the fine-sediment Shields parameter is compared to the critical Shields parameter for the onset of motion θ_c' [7], as experimentally estimated in Section 3.2.2.1. A local critical Shields parameter $\theta_{c,\alpha}'$ is defined as follows, to account for the influence of the streamwise and transverse bed slopes (Dey, 2003):

$$\theta_{c,\alpha}' = \cos(\alpha_x) \left(1 - \frac{\tan\alpha_x}{\tan\phi_f} \right) \left(1 - \frac{\sin^2\alpha_y}{\sin^2\phi_f} \right) \theta_c' \tag{5.9}$$

where ϕ_f is the friction angle of the fine-sediments (see Section 3.2.1) and α_x and α_y are the local slopes in the streamwise and transverse directions, respectively. α_x is positively defined for streamwise downslopig bed areas and negative for streamwise upsloping ones (see Figure 5.21). α_y is always positively defined. The influence of the slope of the flume is considered negligible.

Figures 5.22a-d illustrate the fine-sediment transport parameter in the streamwise and transverse direction,

---

[7] Please recall that θ_c' differs from the critical Shields parameter for permanent sediment transport θ_c given by the Shields parameter.

θ_S^x-$\theta'_{c,\alpha}$ and θ_S^y-$\theta'_{c,\alpha}$, normalized by the streamwise fine-sediment transport parameter for a uniform fine-sediment bed θ_{P0}-θ'_c (where $\theta_{P0} = \tau_{P0}/(\rho_f \Delta g d_{50})$) in plane A and plane B as the bed evolves. A local reference system x' centred on the pattern and normalized by the distance b between the spheres is adopted (see Figure 5.21). The ratio $\frac{\theta_S^{x/y}-\theta'_{c,\alpha}}{\theta_{P0}-\theta'_{c,\alpha}}$ identifies three possible bed states characterizing the influence of the spheres on the local shear stress and sediment transport rates as compared to a uniform fine-sediment bed:

$$
\text{if} \begin{cases}
\frac{\theta_S^{x/y}-\theta'_{c,\alpha}}{\theta_{P0}-\theta'_c} > 1 & \text{, enhanced shear stress and sediment transport,} \\[2em]
0 < \frac{\theta_S^{x/y}-\theta'_{c,\alpha}}{\theta_{P0}-\theta'_c} \leq 1 & \text{, grain sheltering: damped shear stress and sediment transport,} \\[2em]
\frac{\theta_S^{x/y}-\theta'_{c,\alpha}}{\theta_{P0}-\theta'_c} \leq 0 & \text{, complete grain sheltering: damped shear stress and no sediment transport.}
\end{cases}
$$

First the sediment transport parameters in the streamwise direction θ_S^x-$\theta'_{c,\alpha}$ will be analysed over plane A (Figures 5.22a) and plane B (Figure 5.22b). Figure 5.22a shows that in plane A at t = 3 hours ($\langle P \rangle_x = 0.23$), the whole fine-sediment bed is characterized by enhanced shear stress conditions up to 2-2.5 times the ones observed over a uniform fine-sediment bed. The lee side of the spheres is characterized by lower shear stress conditions compared to the stoss side. This difference in shear stress conditions can explain why in the insert of Figure 5.3c the stoss side of the spheres is eroded faster than the lee side for protrusion levels higher than the critical protrusion level for the first transition in erosive behaviour $P_{c1} = 0.15$. The correlated enhanced erosion rates observed in Figure 5.2b after the first transition in bed behaviour for $\langle P \rangle > P_{c1}$ can be explained on the basis of the enhanced shear-stress conditions observed herein at t = 3 hours as the protrusion levels are similar. The separation between the shear stress region in the lee side of the spheres from the one in the stoss side of the spheres by a local reduction in the sediment transport parameter at $x' \simeq 0.1$ in Figure 5.22a, suggests that the enhanced shear stresses in the lee side are the results of the developing shear layer, while the ones in the stoss side are likely connected to a horseshoe vortex.

At t = 6.1 hours ($\langle P \rangle_x = 0.61$), Figure 5.22a shows that in the lee side of the spheres a sheltering region develops, which occupies approximately half of the inter-sphere spacing. In the stoss side of the sphere, the shear stress conditions increase again and are partially enhanced in the near vicinity of the sphere for $0.2 < x'$ < 0.4, where the shear layer impacts the fine-sediment bed (see Figure 5.12b). Even though the bed is partially sheltered in the lee side of the spheres, the bed continues to erode since the shear stress conditions are still above the critical. Since the local sediment transport parameter is in average smaller than the one observed for a uniform fine-sediment bed, the sediment transport rates are damped, consistent with the low C_s/C_{P0} < 1 observed at t = 6.1 hours in Figure 5.2c. At t = 22.5 hours and t = 50.2 hours, the whole fine-sediment bed is under complete sheltering, consistent with the stable bed conditions reached at $\langle P \rangle_x \simeq 1$. At t = 22.5 hours, a region of negative shear stresses is observed in the lee side of the spheres (red-contoured symbols), enforcing even more the bed stability as the particles are stably held in place by a local upstream directed forcing. It is noteworthy, that in the stoss side of the spheres, the shear stress conditions are close to critical, suggesting that in this region, sporadic sediment transport is possible. The local increase of the shear stresses to critical conditions of motion in the stoss side of the spheres suggests that there is still some residual energy penetrating down from the shear layer, as the result of the localised downflow in the stoss side of the spheres visible in Figures 5.8g and 5.8h.
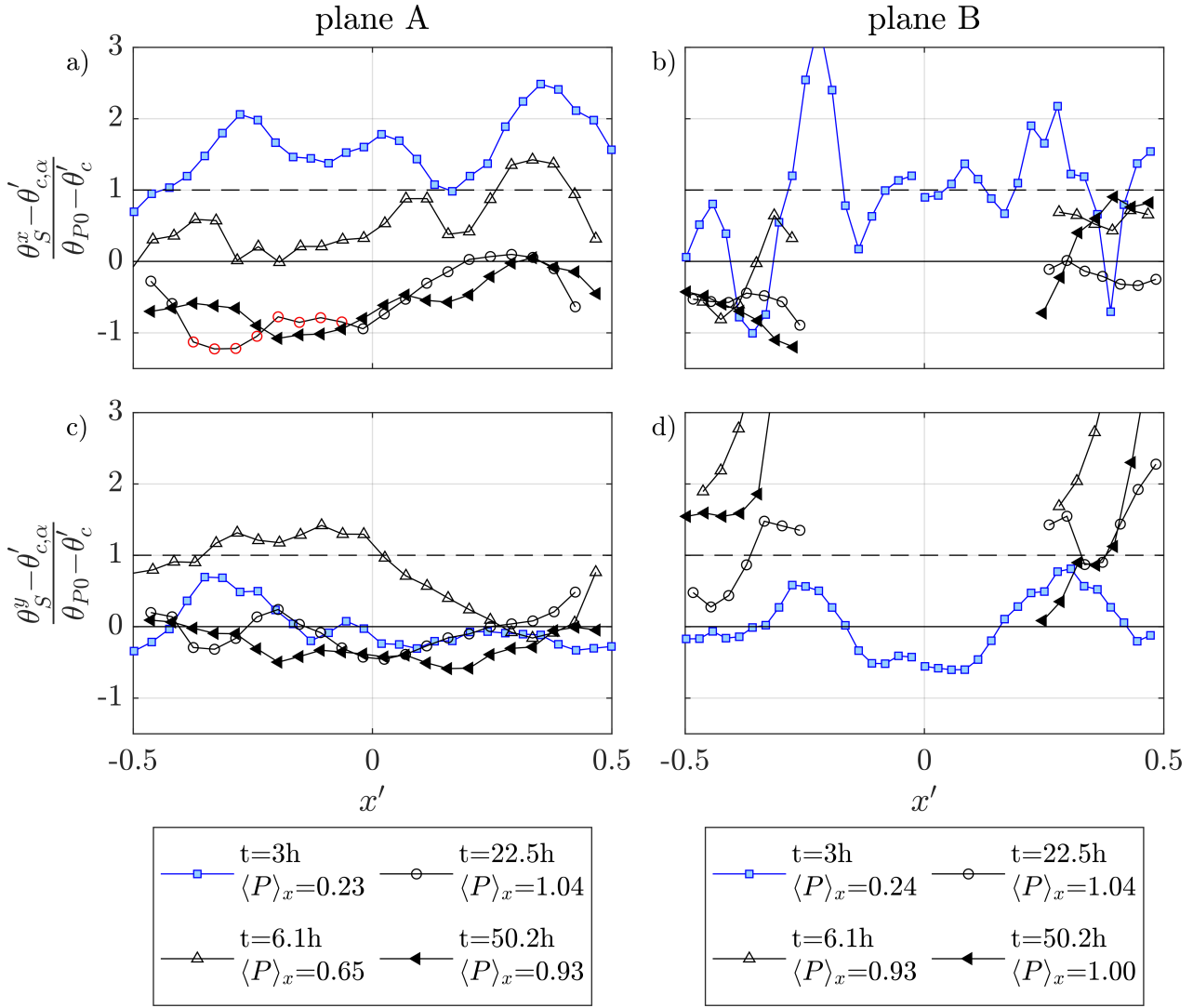
Figure 5.22: Longitudinal profiles of the fine-sediment transport parameter in streamwise direction $\theta_S^x - \theta_c'$ (a-b) and of the fine-sediment transport parameter in transverse direction $\theta_S^y - \theta_c'$ (c-d) normalized by the transport parameter for a uniform bed $\theta_{P0} - \theta_c'$ for different protrusion levels. The symbols contoured in red represent conditions where the shear-stress is negative.

Raus et al. (2019), studying the shear stress conditions over a flat bed of glued fine-sediments for various level of protrusion of a regular pattern of hemispheres[8], observed a similar trend of the sheltering regions. In his case, though, the sheltering was mainly associated to the development of a recirculation region in the bed interstices with negative shear stress value with intensity as high as the one observed for a uniform fine-sediment bed. In this case, no recirculation region is present, instead, and the complete sheltering is the result of a reduction of the shear stresses below critical conditions of motion.

In plane B, Figure 5.22b shows that at t = 3 hours, the sediment transport parameter in streamwise direction is predominantly of the same order of the sediment transport parameter for a uniform bed or locally enhanced. These result should be taken with care as the shear stresses were not fully time-converged. It makes sense,

---

[8]   The ratio between the distance of the centre of the hemispheres and their radius is equal to 2.26 comparable to the one characterizing the configuration of spheres studied herein.

though, that since the protruding spheres do not yet occupy plane B at t = 3 hours (see Figure 5.7b) the shear stress conditions are similar or enhanced compared to a uniform fine-sediment bed. The spikes in sediment transport parameter are likely related to flow separation on the sides of the spheres. Further investigation are needed, though. At t = 6.1 hours $\langle P \rangle_x$ = 0.93, the bed is sheltered and the transport parameters are about half the transport parameters of a uniform bed. This suggests that the shear layer is able to reach still the fine-sediment bed. At t = 22.5 hours and t = 50.2 hours, characterized by a slightly higher protrusion of $\langle P \rangle_x$ = 1 as compared to t = 6.1 hours, the bed is completely sheltered. The only exception is observed at t = 50.2 hours for $0.3 < x' < 0.5$, where the shear conditions are above critical. Indeed, Figure 5.7h shows that the bed topography under plane B behind the central sphere is characterized by a higher sediment bed level. In Figure 5.7g, the bed topography measured during the flow measurement over plane A shows, instead, that this local deposit is absent. It is, therefore, likely that the deposit under plane B behind the central sphere will eventually disappear as the local shear stress conditions are above critical.

The trend in shear stress distributions over plane B strongly deviates from the one observed by Raus et al. (2019) for an equivalent plane positioned also in between spheres. Raus et al. (2019) observed that the shear stress condition remained always enhanced or as high as the ones observed for a uniform bed in the plane positioned in between the spheres. The difference lies in the fact that the array analysed by Raus et al. (2019) is a square pattern, so that the plane positioned in between spheres lies in an ally and as such is not subjected to sheltering. It can be concluded, as such, that the sheltering conditions of the bed depend on the arrangement of the spheres.

Figures 5.22c and 5.22d illustrate the transport parameters in the transverse direction. In plane A, Figure 5.22a shows that at t = 3 hours, the grains are not transported in the transverse direction apart from a region close to the lee side of the spheres. Given the presence of the sediment shadow in the lee side, the grains are positioned closer to the shear layer which is a highly three-dimensional structure, which can trigger later grain movements. At t = 6.1 hours, Figure 5.22c suggests significant lateral sediment transport, comparable in magnitude to the sediment transport over a uniform fine-sediment bed. The significant lateral sediment transport can be connected to the bed topography sloping down in the transverse positive direction (see Figure 5.7c). At t = 22.5 hours and t = 50.2 hours, the transverse shear stress conditions are below or close to the critical, pointing out to sporadic particle grain movement in the transverse direction. The presence of critical conditions of motion in the streamwise direction at $0.2 < x' < 0.3$ (Figure 5.22a) and in the transverse direction at $0.3 < x' < 0.5$ (Figure 5.22c) at t = 22.5 hours and t = 50.2 hours, suggests that the grains sporadically entrained in the streamwise direction between $0.2 < x' < 0.3$, are then pushed out of plane A between $0.3 < x' < 0.5$ in the transverse direction .

In plane B, Figure 5.22d shows, that at t = 3 hours ($\langle P \rangle_x$ = 0.23), transverse shear stress conditions higher than the critical are observed in the lee and the stoss side of the spheres at the same position of the peak in streamwise shear stresses seen in Figure 5.22b. The lateral shear stress peaks support the hypothesis that, even though the protruding spheres do not yet physically occupy plane B, they induce lateral flow separation causing the localized peaks in lateral and streamwise shear stresses. At t = 6.1 hours, Figure 5.22d shows enhanced shear stress conditions in plane B. It appears, that due to the high spatial heterogeneity of the bed topography at t = 6.1 (see Figure 5.7d), significant lateral sediment transport takes place in plane B. At t = 22.5 hours and t = 50.2 hours ($\langle P \rangle_x \simeq 1$), it is observed in Figure 5.22d that the shear stresses are still enhanced compared to a uniform fine-sediment bed, even though the bed has stabilized with almost no sediment transport. It is hypothesized that the significant lateral shear stress does not actively contribute to

the local erosion of the bed, but pushes out of plane B the grains already mobilized in plane A as the result of the longitudinal and lateral mobilization pattern suggested earlier. Further investigations are needed, though, to clarify this aspect.

5.4.2 Influence of the protrusion of the immobile spheres on near-bed turbulent events

In this Section, the connection between the fine-sediment shear stress and the turbulent events which reach the fine-sediments is investigated via quadrant analysis. The attention will be devoted in particular to the turbulent sweep events, as they are considered responsible for the sediment transport (Nelson et al., 1995; Radice et al., 2013). In Figures 5.23 and 5.24 pertaining to plane A and plane B, respectively, the joint probability density functions (JPDFs) of the u'- and w'-fluctuations are investigated at four selected locations within the bed interstices: in the shear layer at the sphere's crest at a distance of $1.5d_{50}$ from the sphere (black contours), at the top of the fine-sediment roughness sublayer h_{rs}^s in the centre of the pattern (blue contours) and in the lee and in the stoss side of the spheres at a distance of $1.5\ d_{50}$ (red and green contours, respectively). In plane A, Figures 5.23e-h show that the JPDFs in the shear layer are characterized at all times by a predominance of sweep events (Q4 - $u' > 0$, $w' < 0$) and ejections (Q2 - $u' < 0$, $w' > 0$), while outward (Q1 - $u' > 0$, $w' > 0$) and inward (Q3 - $u' < 0$, $w' < 0$) interactions are less frequent. In vegetated flows, Zhu et al. (2007) and Nezu and Sanjou (2008) showed that the shear layer is a region of production of sweeps which play a dominant role in the transport of momentum and energy within the bed interstices. The question is how deep the high energetic sweep events produced in the shear layer manage to penetrate into the bed interstices. At t = 3 hours ($\langle P \rangle_x = 0.23$), the ellipses of the JPDFs are predominantly oriented towards the fourth and second quadrant (see Figures 5.23i,m,q), showing that at low protrusion levels, strong sweep events reach the fine-sediments. At t = 6.1 hours ($\langle P \rangle_x = 6.1$ hours), Figure 5.23j shows that in the lee side of the sphere the JPDF is almost circular, meaning that the probability of strong sweep events is consistently reduced. The sheltering region characterized by damped shear stress conditions in the lee side of the spheres observed in the previous Section, is, therefore, the result of reduced streamwise fluctuations. At t = 6.1 hours, Figures 5.23n and 5.23r show that the probability of sweeps events increases moving from the centre of the pattern towards the stoss side of the spheres, where the JPDF is similar to the one observed within the shear layer (see Figure 5.23b). The similar shape of the JPDF in the shear layer and in the stoss side of the sphere at t = 6.1 hours shows that the structures produced in the shear layer manage to reach still the sediment bed, explaining the presence of enhanced shear stress conditions in this region, as observed in the previous Section. At t = 22.5 hours and t = 50.2 hours ($\langle P \rangle_x$), Figures 5.23k and 5.23l show that in the lee side of the spheres the JPDF is vertically stretched, meaning that vertical velocity fluctuations of higher magnitudes compared to the streamwise fluctuations reach the fine sediments resulting in higher lift than drag forces. The significant reduction in streamwise fluctuations compared to lower protrusion levels causes, as a result, a decrease in the drag acting on the particles (Celik et al., 2013; Dwivedi et al., 2010). In the central and quarter planes, Figures 5.23o-p and 5.23s-t show that the shape of the JPDF is almost circular suggesting quasi-isotropic turbulence conditions with a consistent reduction in sweep events, in agreement with the complete sheltering conditions observed in the previous Section at the level of the fine-sediments. Similar conclusions can be drawn also for the JPDFs in plane B (see Figure 5.24).

Figure 5.23: Joint probability density functions of the streamwise and vertical velocity fluctuations, u' and w', sampled within the shear layer at the spheres' top (e-h) and at the top of the fine-sediment roughness sublayer at 1.5 d_{50} downstream of the sphere upstream (i-l), in the centre of the pattern (m-p) and at 1.5 d_{50} upstream of the sphere downstream (m-p) in plane A as the bed evolves. The sampling points are shown with the colours of the corresponding quadrant plots in Figures (a-b) superimposed to the time-averaged turbulent shear stress field.
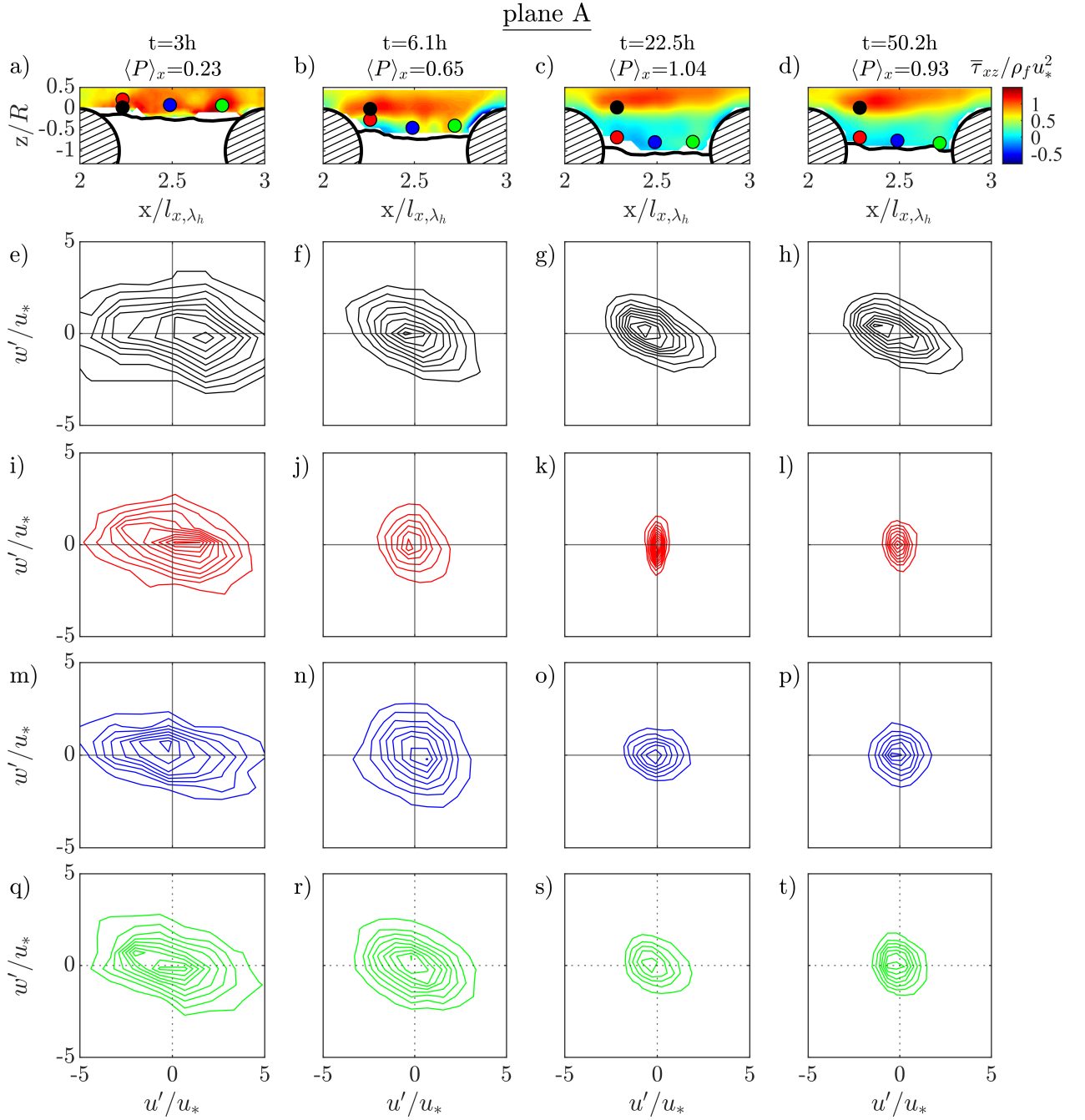
137

Figure 5.24: Joint probability density functions of the streamwise and vertical velocity fluctuations, u' and w', sampled within the shear layer at the spheres' top (e-h) and at the top of the fine-sediment roughness sublayer at $1.5\,d_{50}$ downstream of the sphere upstream (i-l) and at $1.5\,d_{50}$ upstream of the sphere downstream in plane B (m-p) as the bed evolves. The sampling points are shown with the colours of the corresponding quadrant plots in Figures (a-b) superimposed to the time-averaged turbulent shear stress field.
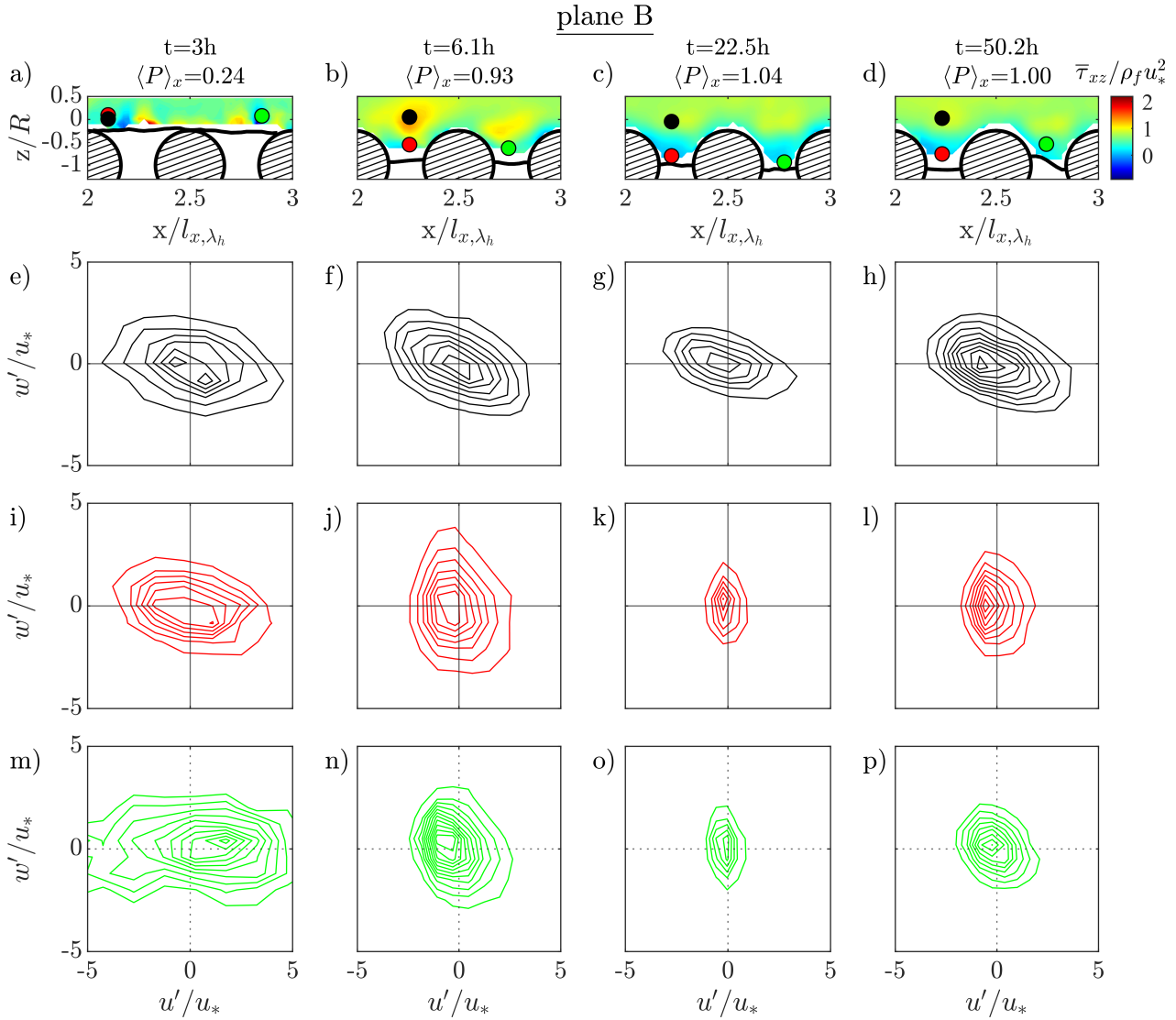
5.4.3 The origin of the turbulent events at the fine-sediment bed

With increasing protrusion level of the spheres, it was observed that the vertical and streamwise velocity fluctuations at the level of the fine-sediments significantly reduce. Since the sediment transport is connected to extreme events resulting from instantaneous turbulent momentum flux stronger than the shear stress, a quadrant hole analysis is performed to assess the origin of the extreme events at the level of the fine sediments and how they are modified by the increasing level of protrusion (see Section 2.4.1 for an overview on the quadrant hole analysis). The analysis is performed at the top of the spheres where the strongest turbulent events are generated, and along the fine-sediment roughness sublayer. Following the procedure suggested by Raus et al. (2019), in order to identify the origin of the turbulent events at the top of the fine-sediment roughness sublayer, the quadrant hole region is not defined on the basis of the local time-averaged shear stress, but rather on the basis of the shear velocity at the top of the spheres. Accordingly, the local shear-stress fraction S^*_{i,H_s} transported by the ith-quadrant event is defined as follows:

$$\overline{S}^*_{i,H_s} = \frac{1}{u^2_*}\frac{1}{T}\int_0^T u'w'I^*_{i,H_s}dt \tag{5.10}$$

where

$$I^*_{i,H_s} = \begin{cases} 1, \text{ for } u'w' > H_s\, u^2_* \\ 0, \text{ otherwise} \end{cases} \tag{5.11}$$

By using a threshold on the friction velocity and by comparing the results of the quadrant analysis performed at the top of the spheres and along the fine-sediment roughness sublayer, it is possible to determine whether the extreme events detected along the fine-sediment roughness sublayer originate from the shear layer. Figures 5.25a-b and 5.25c-d pertaining to plane A and plane B, respectively, illustrate the shear-stress fractions $\langle S^*_{i,H_s}\rangle$ obtained through spatial averaging along the top of the spheres (Figures 5.25a and 5.25c) and along the top of the fine-sediment roughness sublayer (Figures 5.25b and 5.25d). Figure 5.25a shows that at the top of the spheres in plane A the highest shear stress fractions derive from the sweeps (Q4) and ejections (Q2) at all times. The contribution of the outward (Q1) and inward (Q3) interactions is limited and becomes negligible for hole sizes H_s above 5, as observed also by Raupach (1981); Dey and Das (2012); Mignot et al. (2009b) for gravel-beds. It is observed that, while at t = 3.0 hours and t = 6.1 hours the ejections contribute significantly to the total shear stress even for Hole sizes $H_s > 15$, at t = 22.5 hours and t = 50.2 hours, their contribution becomes negligible for Hole sizes $H_s \simeq 12$. It appears that with increasing protrusion of the spheres the dominance of the sweep events within the shear layer increases. In Figure 5.25c, a similar evolution in shear stress fractions is observed for plane B.

If the shear stress fractions measured in the shear layer (Figures 5.25a and 5.25c) are compared to the shear stress fractions measured over a uniform fine-sediment bed in Figure 4.5a [9], it is observed that the shear stress fractions of the sweeps and of the ejections are higher in the presence of protruding spheres. It suggests, that for low protrusion levels, the fine-sediment bed will be occupied by stronger sweep events as compared to a

---

[9] The shear stress fractions over the uniform bed were determined, strictly speaking, on the basis of a hyperbolic hole region considering the local shear stress and not the shear velocity. For a uniform fine-sediment bed, the local shear stress at the bed corresponds, though, to the friction velocity within the error induced by the spatial heterogeneity of the roughness sublayer of the fine-sediments. As such, the shear stress fractions presented for a uniform bed are comparable with the ones presented in this Section.

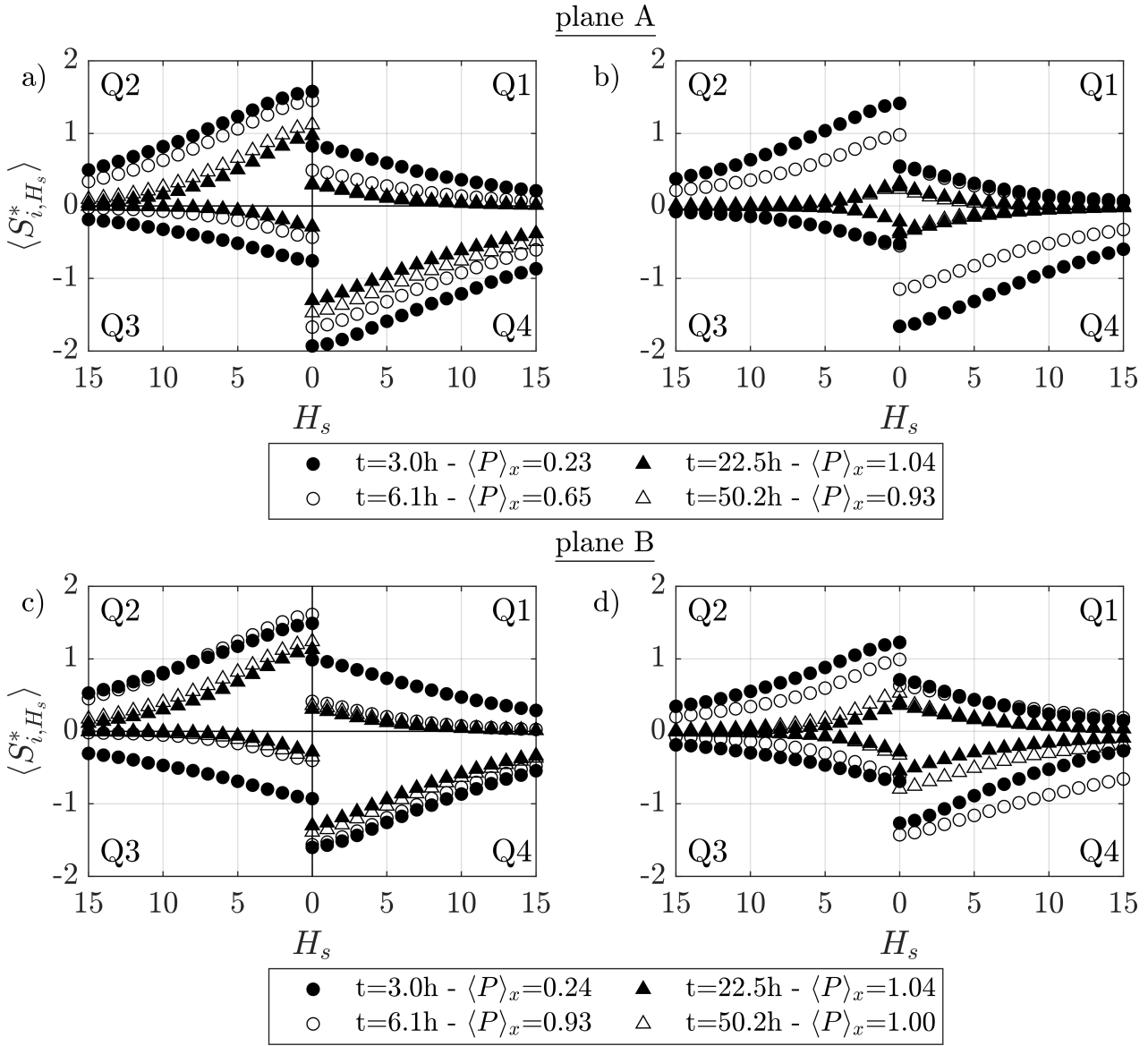**Figure 5.25:** Quadrant shear-stress fraction $\langle S^*_{i,H_s} \rangle$ based on a multiple H_s of the shear velocity u_* at different stages of the bed development and spatially-averaged over a horizontal plane within the shear layer at the top of the spheres (left column) and along the edge of the fine-sediment roughness sublayer (right column) in plane A (a-b) and plane B (c-d).

uniform fine-sediment bed.

At the level of the fine-sediment roughness sublayer in plane A, Figure 5.25b shows that the shear-stress fractions of the quadrant events at t = 3 hours is similar to the one observed at the top of the spheres in Figure 5.25a, suggesting that the fine-sediment bed is occupied by the turbulent events generated in the shear layer. At t = 6.1 hours, the quadrant contributions show similar qualitative trends as the ones observed at the top of the spheres with high contributions of the sweep even for Hole sizes $H_s > 15$. However, the intensities are reduced, showing that only part of the turbulent events generated at the top of the spheres reaches the bed. At t = 22.5 hours and 50.2 hours, a slight dominance of the sweeps over the other turbulent events is observed, suggesting isotropic turbulent conditions. The sweep events vanish, furthermore, at Hole sizes $H_s > 7$.

In plane B, the quadrant shear-stress fractions show a similar qualitative trend over time as in plane A (see Figure 5.25d), with quasi-isotropic turbulence conditions reached for high protrusion levels $\langle P \rangle_x \simeq 1$. In this case, though, the contribution of the sweep events at t = 22.5 hours and t = 50.2 hours, tend towards zero for Hole sizes $H_s \simeq 15$. As such, even though plane A and plane B share similar protrusion levels at t = 22.5 hours and t = 50.2 hours, plane B is occupied by stronger sweeps events than plane A. Therefore, Plane A is characterized by the highest degree of sheltering compared to plane B. The probability of grains being moved at the end of the experiments, when the sediment bed level is stable, is higher over plane B.

Raus et al. (2019) performed a similar analysis on an immobile fine-sediment bed with different levels of protrusion of the spheres. He found also a reduction of the contribution of the sweep events for high protrusions of the spheres with the fraction of sweep events becoming negligible for Hole sizes higher than 10. His analysis was performed, though, by averaging the shear stress fractions over the whole pattern of spheres, considering both contributions from the sheltered area behind the spheres and the non sheltered area in the alleys in between the spheres. As such, possible differences between the two regions are washed out.

5.4.4 Spatial distribution of the intensity, frequency and duration of the turbulent events at the fine-sediment bed

In order to characterize the local forcing induced by the turbulent events on the fine-sediments, the intensity of the contribution of the turbulent events to the fine-sediment shear stress is analysed. The shear intensity of the turbulent events $\tau_{s,i}$ is determined on the basis of the quadrant analysis performed at the edge of the fine-sediment roughness sublayer h_{rs}^s, as also performed when evaluating the fine-sediment shear stress in Section 5.4. The intensity of the turbulent events is given by : $\tau_{s,i} = -\rho_f \overline{u'w'}_{i,H_s}/T_{i,H_s}$, where $-\rho_f \overline{u'w'}_{i,H_s}$ is the quadrant contribution to the fine-sediment shear stress and T_{i,H_s} the time fraction of the quadrant, as defined in Section 2.4.1. When evaluating $\tau_{s,i}$, the velocity fluctuations are evaluated at the elevation of the fine-sediment roughness sublayer without projecting them in the direction of the local bed topography consistent with the evaluation of the fine-sediment shear stresses in Section 5.4. The frequency f_{i,H_s} and the duration D_{i,H_s} of the turbulent events is also determined along the fine-sediment roughness sublayer. f_{i,H_s} is the reciprocal of the average time interval between the single realization of each turbulent event. The relevance of the duration of the turbulent events, lies in the fact, that for a sweep to be effective in moving sediments its duration should be long enough to produce a sufficient impulse to entrain the sediment particles (Diplas et al., 2008; Dwivedi et al., 2010). Sweeps with high intensity but low duration can be less effective than sweeps with less intensity but higher duration in entraining particles (Nelson et al., 1995). Valyrakis et al. (2010) pointed also out that the frequency of the turbulent events is relevant for the entrainment, in as

much as frequent turbulent events with a low energy transfer can be as effective as rarer turbulent events with a higher energy transfer in dislodging the particles.

In Figures 5.26a-h, the shear intensities of the turbulent events determined at the top of the fine-sediment roughness sublayer with a Hole size $H_s = 0$, are compared to the reference bed shear stress over a uniform fine-sediment bed τ_{P0}. The red lines identify the local critical shear stress conditions, determined on the basis of the local critical Shields parameter for the onset of motion defined in Equation 5.9. At t = 3 hours ($P_x = 0.23$), Figure 5.26a shows that in plane A, the shear intensity of the sweeps and of the ejections (round circles) is approximately constant over the fine-sediment bed and approximately 3 times higher than τ_{P0}. Intense sweep events reach the fine-sediments, explaining the enhanced erosion rates observed at these protrusion levels. At t = 6.1 hours, when a sheltering region is observed in the lee side of the spheres and enhanced transport in the stoss side (see Figure 5.22a), Figure 5.26b shows that the shear intensity of both sweeps and ejections decreases in the lee side ($x' < $ -0.4), while it remains as high as the shear intensities observed at t = 3 hours in the stoss side ($x' > 0$). It will be seen further on, that the frequency and duration of the sweep events at t = 6.1 hours is actually reduced compared to t = 3 hours, explaining the overall reduction in sediment transport. At t = 22.5 hours and t = 50.2 hours ($P_x \simeq 1$), when complete sheltering of the fine-sediments is observed (see Figure 5.22a), Figures 5.26c and 5.26d, show that in the lee side of the spheres, the shear intensities of all turbulent events are damped compared to τ_{P0} and below critical conditions of motion. In this region it is observed, that the shear intensity magnitude of sweeps and ejections is similar to the one of inward and outward interactions. In the stoss side of the spheres ($x' > 0$), the shear intensity of the sweeps and of the ejections increases again to values approximately equal to τ_{P0}, suggesting that the sweeps are still able to trigger sediment transport. In plane B, Figures 5.26e-f, show that at t = 3 hours and t = 6.1 hours, the shear intensities of the sweeps remain as high as approximately three times the τ_{P0}, while the bed is still evolving. At t = 22.5 hours and t = 50.2 hours, Figures 5.26g-h show that there is a slight decrees in shear intensity of the sweeps to intensities approximately equal to two times τ_{P0}. The sweeps dominate clearly over the other turbulent events. It appears, that the fine-sediment bed in plane B is characterized by much more intense turbulent events compared to plane A for the same times.

Figures 5.27a-h show the frequencies $f_{i,0}$ of the turbulent events samples along the fine-sediment roughness sublayer in plane A and in plane B, as the bed evolves. Figure 5.27a shows that in plane A at t = 3 hours (P_x = 0.23), the sweeps and ejections events are the most frequent turbulent events with a frequency of 1.5 Hz, as expected. As the bed is eroded, Figure 5.26b shows that the frequency of the sweeps events decreases down to a local minimum of 1 Hz in the lee side of the spheres. The sheltering area is favored not only by decreased shear stress intensities of the sweeps, as seen before, but also by a decrease in their frequency. In the stoss side, the frequency of the sweeps increases again to about 1.25 Hz less than the frequencies observed in the same region at t = 3h. This means, that even though the shear intensity of the sweeps is still high in the stoss side at t = 6.1 hours (as seen in Figure 5.26b), they become less frequent. At t = 22.5 hours and t = 50.2 hours ($P_x \simeq 1$), when the bed is completely sheltered, a further reduction of the frequency of the sweeps below 1 Hz is observed in the lee side of the spheres as compared to the frequencies observed at t = 6.1 hours, while in the stoss side the reduction is not as significant. It is noteworthy that for $P_x \simeq 1$, the frequency of the inward interactions increases significantly up to 2 Hz in the lee side of the spheres, signalising a complete change in the coherent structures reaching the bed. In plane B, Figure 5.26e, shows that at t = 3 hours, the frequency of the turbulent events are comparable to the ones observed in plane A at the same time. Figure 5.27f-h, show that for comparable protrusion levels $\langle P \rangle_x \simeq 1$, the frequencies of the sweep events are consistently damped
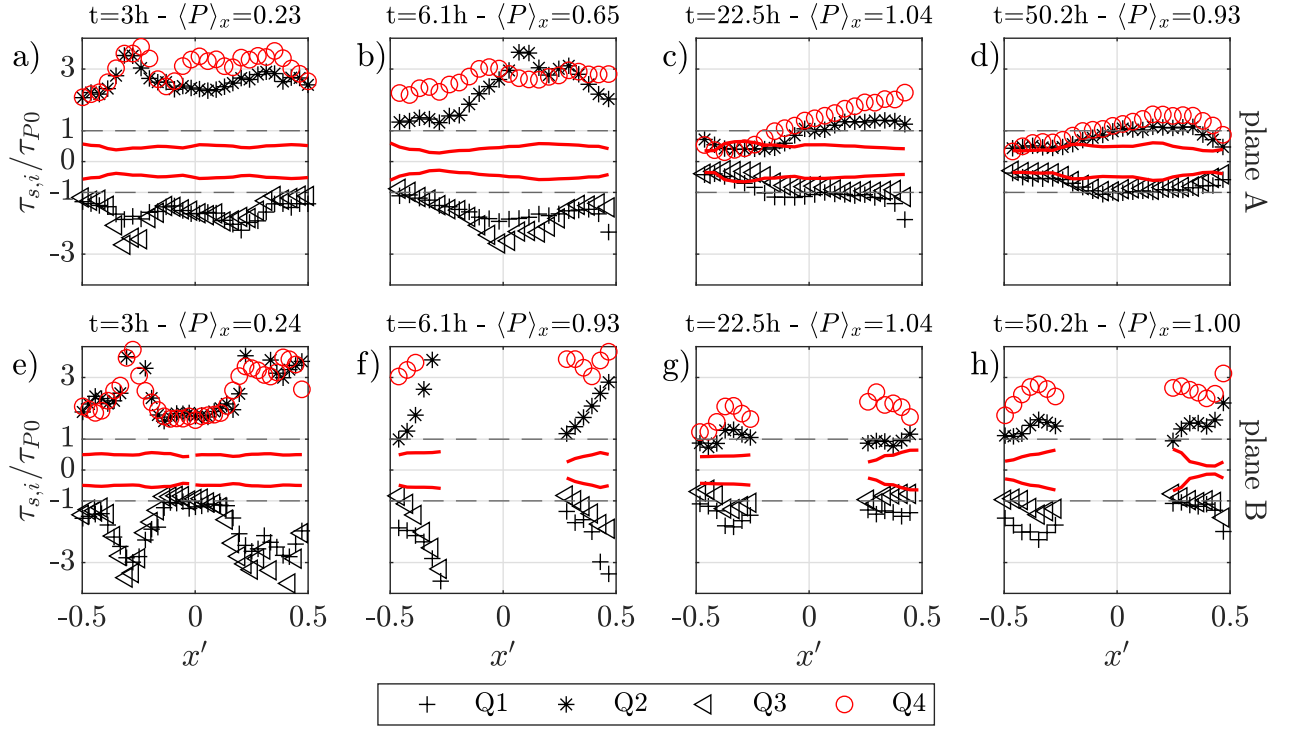
Figure 5.26: Shear intensity of the turbulent events $\tau_{s,i}$ measured with a Hole size $H_s = 0$ at the top of the fine-sediment roughness sublayer h_{rs}^s and normalized by the reference bed shear stress over a uniform fine sediment bed τ_{P0} at different stages of the bed development in plane A (a-d) and plane B (e-h). The horizontal dashed line represents conditions for which $\tau_{s,i}/\tau_{P0} = 1$ and the continuous red lines the critical conditions of motion.

to values close to 1 Hz in average. Even though the shear intensities of the sweep events remain higher than the ones observed in plane A for similar protrusion levels $\langle P \rangle_x \simeq 1$, the sweep events are rarer in plane B, reducing the probability of grain entrainment and stabilizing the bed.

Figures 5.28a-h show the duration of the turbulent events along the fine-sediment roughness sublayer in plane A and plane B as the bed evolves. In plane A, a reduction of the duration of the sweep events is observed in Figures 5.28a-d from approximately 0.32 s for low protrusion levels ($\langle P \rangle_x \simeq 0.2$) to durations of 0.27 s for high protrusion levels ($\langle P \rangle_x \simeq 1$). For protrusion levls $\langle P \rangle_x > 0.6$ lower durations are observed in the lee side of the spheres compared to the stoss sides. The inward interactions dominate in term of duration in the lee side of the spheres for $\langle P \rangle_x \simeq 1$. In plane B (Figures 5.28e-h), the reduction in duration of the sweep events is even higher from 0.3 s at t = 3 hours to approximately 0.25 at ($\langle P \rangle_x \simeq 1$). Overall, the reduction in duration of the sweep events suggests that the increased sheltering conditions are connected to a reduction of the impulse of the sweep events.

Summarizing, it is observed that for low protrusion levels, the enhanced shear stress conditions acting on the fine-sediments are to be associated to sweep events with high shear intensity frequency and duration. As the protrusion level of the spheres increases, the formation of a sheltering region in the lee side of the spheres in plane A is connected to a reduction in the frequency, duration and shear intensity of the sweep events, which reaches critical conditions of motion for high protrusion levels, when the bed is stable. In the stoss side of the spheres in plane A, a reduction of the shear intensity, frequency and duration of the sweep events is also observed, but not as significant as in plane A. In plane B, the shear intensities of the sweeps for high

143
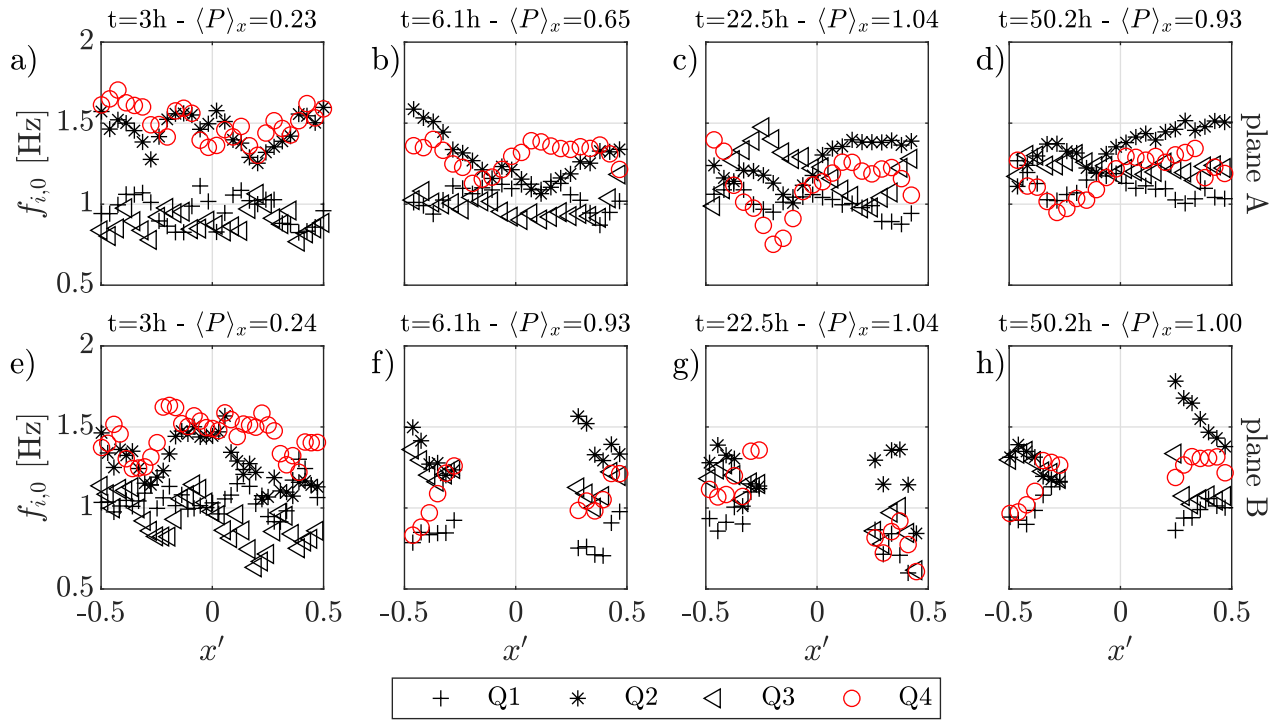
Figure 5.27: Frequencies of the turbulent events $f_{i,0}$ at the top of the fine-sediment roughness sublayer h_{rs}^s and normalized by the frequency of the sweep events for a uniform fine-sediment bed $f_{4,0}^{P0}$ at different stages of the bed development in plane A (a-d) and plane B (e-h).
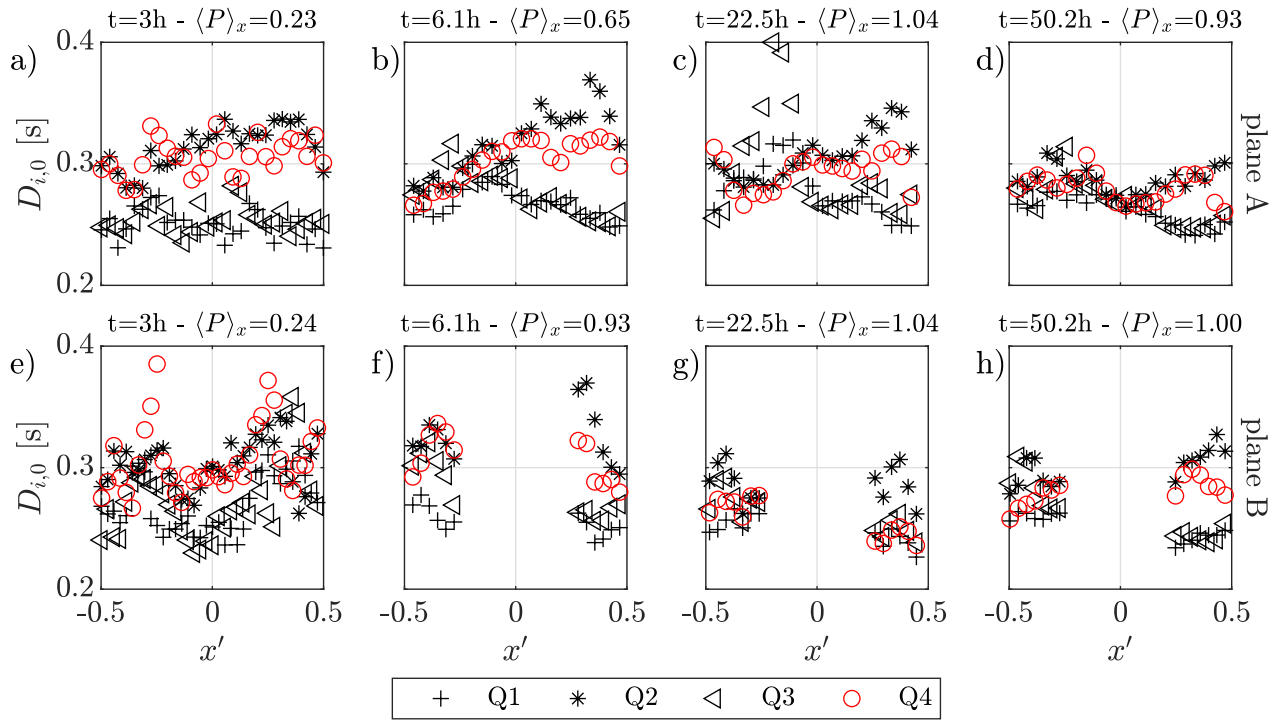

Figure 5.28: Duration of the turbulent events $D_{i,0}$ at the top of the fine-sediment roughness sublayer h_{rs}^s at different stages of the bed development in plane A (a-d) and plane B (e-h).

protrusion levels are similar to shear stress conditions on a uniform bed in the stoss side of the spheres. The frequency and the duration are reduced, though, so that sediment transport is suppressed. For high protrusion levels, plane B is characterized by higher shear intensities as plane A, but lower duration and frequencies. The difference in shear intensities, magnitude and frequencies between plane A and plane B for high protrusion levels can be ascribed to the difference in flow patterns. In plane A, the strong upflow conditions dominating the bed interstices in the lee side of the spheres reduce the frequency, duration and shear intensity of the sweeps. In the stoss side of the spheres, the downflow conditions maintain the frequency and duration of the sweeps higher than the lee side, but the shear intensity is reduced as the shear layer cannot penetrate down. In plane B, where downflow conditions are prevalent, the shear intensity of the sweeps for high protrusion levels remains significant, as the shear layer can penetrate deeper. The frequency and the duration is significantly reduced, though.

5.5 Conclusion

This chapter was devoted to the analysis of the morpho- and hydrodynamics of a fine-sediment bed eroding in a highly packed immobile bed of spheres under the flow conditions defined for the reference Exp. 1 (R-$G\lambda h$). Simultaneous measurements of the flow in the bed interstices, of the bed topography and of the sediment transport rates were performed at a local pattern scale. The analysis of the bed morphodynamics confirms the findings of the first series of experiments in Part I, concerning the presence of four erosive regimes. The bed evolution is characterized by a decrease in erosion rates as soon as the the spheres protrude from the rough bed, confirming an initial sheltering (first erosive regime). Once a critical protrusion level $P_{c1} = 0.15$ is reached, an increase in erosion rates is attested (second erosive regime). At a critical protrusion level $P_{c2} = 0.43$, the erosion rates reach a local peak, 50 % higher than the erosive conditions characterizing a flat-uniform bed. The capacity of the protruding sphere to enhance erosion is confirmed. For higher protrusion levels, the erosion rates decrease again (third erosive regime) until a third critical protrusion level is reached, equal to $P_{c3} = 0.8$, after which the erosion rates tend to zero and the bed to a stable bed level (fourth erosive regime). These three critical protrusion levels are in agreement with the ones identified in Chapter 2 for the transitions in erosive regimes. The sediment transport rates follow a similar trend as the erosion rates, characterized by a peak in enhanced sediment transport rates 40 % higher than the ones observed over a uniform fine-sediment bed. The time at which the sediment transport rates reach this peak is lagged compared to the time at which the erosion rates reach the peak, suggesting that the sediment transport rates take time to adapt to variations in erosion rates.

The analysis of the bed topography at a local scale shows that the erosion is uniform over the whole patter until the first transition in erosive behaviour is reached. At this point, with globally enhanced erosive conditions, increased erosion is observed in the stoss side of the spheres compared to the lee side, leading to the formation of sediment shadows. The sediment shadow persist as stable topographic features for the whole duration of the experiment, decreasing eventually in size. The consistent temporal fluctuations in local bed levels in the lee side of the spheres suggest that the sediment shadows are active zones of sediment exchange, which remain temporarily trapped.

From a hydrodynamic point of view, it was observed that the enhanced erosion rates observed for protrusion levels $P_{c1} < P < P_{c2}$ (second erosive regime) are associated to the development of a shear layer at the top of

the spheres, which causes enhanced shear stress conditions at the level of the fine sediment bed. Lower shear stress conditions observed in the lee side of the spheres compares to the stoss side favour the formation of sediment shadows, as mentioned previously. The higher erosion rates observed in the stoss side of the sphere suggest the presence of a horseshoe vortex, which couldn't be visualized though due to the limited spatial resolution. Nevertheless, the enhanced shear stress conditions are the result of intense sweep events of high frequency and duration, originating in the shear layer and being advected down towards the fine-sediment bed by the predominant downflow conditions in the near-bed region. Analysis of the turbulent kinetic energy budget shows that the bed interstices are characterized by significant turbulent kinetic energy production and transport directed from the spheres' top towards the fine-sediment bed. Thus, the flow measurements confirm that the second erosive regime is associated to an enhancement of the near-bed turbulence, as hypothesized in Chapter 2, and can be evidently identified as turbulence-enhancement regime.

As the protrusion levels of the spheres increase and and the erosion rates decrease for $P_{c2} < P < P_{c3}$ (third erosive regime), it is observed that the sheltering conditions are not associated to the formation of a recirculation region, as it has been suggested by studies on the flow separation behind roughness elements over immobile fine-sediment beds (Raus et al., 2019; Fang et al., 2017; Papanicolaou et al., 2012). Instead, thank to the presence of the sediment shadows, a region of upflow form in the lee side of the sphere causing local vorticity annihilation. As a result, the shear layer is not able to reach the fine-sediment bed in the lee of the sphere. Damped shear stress conditions are observed associated with a local reduction in the frequency and intensity of the sweep events. The shear layer is still able though to reach the fine-sediment bed in the stoss side of the sphere where downflow conditions still persist. In the stoss side, the fine-sediment bed is still characterized by the development of intense and frequent sweep events, which induce slightly enhanced shear stress conditions. In energetic terms, it is observed that the bed-interstices are dominated by the wake production which furnishes enough energy for the bed to be still active. Overall, given the interaction between the shear layer and the sphere downstream, wake interference flow conditions are predominant. Therefore, the measured flow patterns confirm the hypothesis made in Chapter 2 that the third erosive regime can be identified as wake-interference sheltering regime.

A radical change in the flow conditions in the bed interstices is observed, once the bed reaches a stable bed elevation, i.e. for protrusion levels $P > P_{c3}$ (fourth erosive regime). The region of upflow, limited for lower protrusion levels to the lee side of the spheres, expands above the spheres' top, forcing the shear layer above the spheres. A net separation between a region of enhanced shear stresses at the spheres' top and a region of damped shear stresses near the fine-sediment bed is observed. At the fine-sediment bed, shear stress conditions below critical are observed in the lee side of the spheres and above critical in their stoss side, suggesting that, even though the bed is stable, intermittent sediment transport is possible. The quadrant distribution of turbulent events between the lee side of the sphere and the stoss side of the spheres is significantly different. In the lee side, the predominance of vertical velocity fluctuations suggests decreased drag. The lee side is, in fact, dominated by inward interactions and the shear intensity of all quadrant events is below critical. In the stoss side, instead, quasi-isotropic turbulence is observed. The localized downflow region in the stoss side of the sphere might allow still the penetration of sweep events from above. The energy budget in the bed-interstices suggests that the energy transfer is blocked far above the fine-sediment bed, so that complete sheltering conditions are given and sediment transport ceases. The observation that the zero-plane is located at the top of the spheres suggests that the outer flow is effectively disconnected from the region below the top of the spheres, which is dominated, as such, by skimming flow conditions. Therefore,

the fourth erosive regime can be effectively defined as skimming-flow sheltering regime, as proposed in Chapter 2.

The flow pattern just described occupies predominantly the region in the wake of the sphere, while in the region in between the spheres predominant downflow conditions persist also for high protrusion levels. Indeed, the energy transfer towards the fine sediments is strongly attenuated but not as much as in the wake of the spheres. The intensity of the sweep events is higher than in the region behind the spheres but they are characterized by lower frequencies and duration suggesting similar conditions of complete sheltering as in the sphere's lee.

6 Influence of the immobile-roughness density, the fine-sediment size, the Shields parameter and the relative submergence on the fine-sediment erosion

A parameteric study is performed in the following by analysing how the immobile-roughness density, the fine-sediment size, the Shields parameter and the relative submergence influence the local fine sediment erosion. For example, the work by Fang et al. (2017) analysing the flow conditions for varying density of an array of boulders over an immobile flat bed, shows how the shear stress conditions vary significantly with the reduction of the spacing in between roughness elements, leading to reduced shear stress conditions in the interspace of the boulders and enhanced shear stress conditions in the alleys in between. To this regard, the experimental works by Ghilardi et al. (2014b) and McKie et al. (2021) show that the sediment transport rates decrease the more the spacing between boulders decreases. A clear hydro- and morphodynamic characterization of the erosion process as the density of the immobile roughness elements varies, has not yet been performed, though.

As the relative submergence is concerned, Shamloo et al. (2001) and Schlömer et al. (2020) showed that the reduction of the relative submergence of isolated obstacles changes significantly the wake patterns with a possible disappearance of the shear layer for low relative submergences and the strengthening of the horseshoe vortex. How these changes in relative submergence alter the erosion processes and the final erosion depth given similar bed shear stress conditions is still an open question.

6.1 The influence of the Shields parameter θ on the morho- and hydrodynamics

In this Section, the impact of the Shields parameter, i.e. of the shear stress conditions, on the bed morhodynamics and on the flow pattern within the bed interstices is analysed. The analysis is focussed on Exp. 5 ($G\theta l$), Exp. 6 ($G\theta l$), Exp. 1 (R-$G\lambda h$) and Exp. 7 ($G\theta h$), characterized by increasing values of the Shields parameter (see Table 3.1) while the other reference parameters (λ_f, S_r,d_{50}) are kept constant. Exp. 1 (R-$G\lambda h$) analysed in Chapter 5 is used as a reference to characterize the changes in bed topography and flow patterns observed in the other experiments. In the following, the analysis of the bed morphodynamics is conducted only in the central reference pattern of the configuration of spheres with the highest density (see Figure 3.2a) and is focussed on the overall temporal evolution of the protrusion levels at the pattern scale. The analysis of the flow conditions is performed by comparing the PIV measurements performed at the end of the experiments in plane A and in plane B within the reference pattern. The aim is to understand how the final protrusion level correlates with the shear stress conditions within the bed interstices. All informations
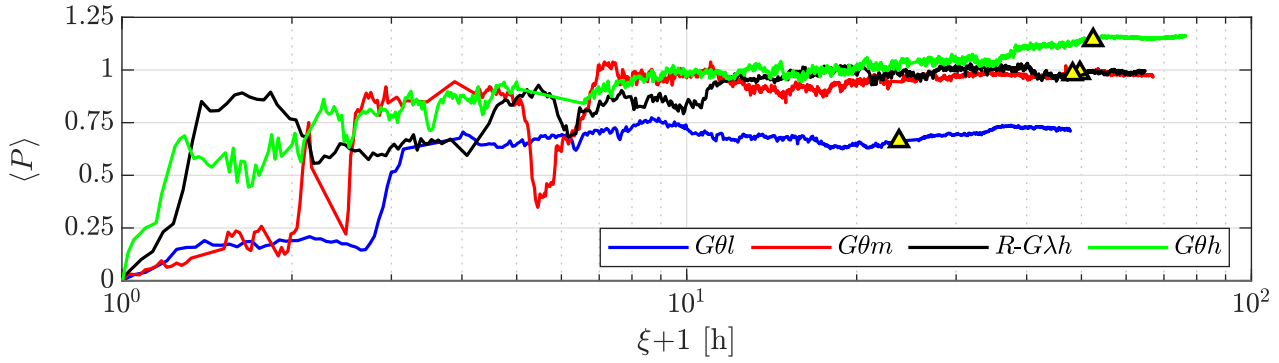
Figure 6.1: Temporal profile of the pattern-averaged protrusion level $\langle P \rangle$ during the Exp. 5 ($G\theta l$), Exp. 6 ($G\theta m$) and Exp. 7 ($G\theta h$) compared to the reference Exp. 1 (R-$G\lambda h$). The yellow triangles identify the times at which the PIV measurements were performed. The ξ-axis is shifted by 1 hour for visualization purposes.

about the acquisition of the stereo-PIV, topographic and sediment-transport data are thoroughly described in Sections 3.4.1.3, 3.4.2.2 and 3.4.3.2.

6.1.1 Bed morphodynamics (θ)

General remarks on the evolution of the bed topography at the reach scale are first given to analyse further on the evolution of the bed topography at the pattern scale. It is observed that at the beginning of Exp. 5 ($G\theta l$), Exp. 6 ($G\theta m$) and Exp. 7 ($G\theta h$), the bed topography is characterized by dunes, as also observed in Exp. 1 (R-$G\lambda h$). The dunes migrate along the flume eventually disappearing after same time in all four experiments. The time at which the dunes disappear is different, though, for the four experiments. At the position of the central reference pattern, the time at which the spheres start to protrude without being covered again by dunes, t_0 is equal to 23.5 hours for Exp. 5 ($G\theta l$), 4 hours for Exp. 6 ($G\theta m$), 3.2 hours for Exp. 1 (R-$G\lambda h$) and 1.7 hours for Exp. 7 ($G\theta h$). t_0 decreases, as such, with increasing Shields parameter, showing that the celerity of the dunes depends on the latter. Once the dunes disappear, a ridge develops at $y/W \simeq$ -0.2 in all four experiments, suggesting that similar secondary flow patterns develop over the bed. The local bed morphodynamics at the pattern scale can be, as such, compared.

The temporal evolution of the protrusion level of the spheres $\langle P \rangle$, spatially averaged within the central reference pattern, is now analysed (for the definition of P see Section 3.5.1). Since the dunes disappear at different times t_0, the $\langle P \rangle$-signal for each experiment is offset by t_0, in order to compare effectively the different profiles. A similar procedure was also applied in Part I in Section 2.3.4. A new time-frame $\xi = t$-t_0 is defined. Figure 6.1 shows the temporal evolution of $\langle P \rangle$ as a function of ξ. Please note, that the time ξ was offset in Figure 6.1 by 1 hour just for visualization purposes. It is observed that the protrusion profiles are characterized by similar qualitative trends. The evolution of the system is faster, though, for increasing values of the Shields parameter. It can be seen, that Exp. 7 ($G\theta h$) with the highest Shields parameter shows the fastest evolution, while Exp. 5 ($G\theta l$) characterized by the lowest Shields parameter the slowest one. A faster evolution for higher Shields parameter was observed similarly in Part I in Section 2.3.4.

Figure 6.1 shows, furthermore, that the protrusion level tends to a constant level over time. The stable final protrusion level appears to increase with increasing Shields parameter, as also observed by Kuhnle et al.

(2016) and by Stradiotti et al. (2020) analysing the erosion of fine sediments from a gravel bed. It is noteworthy, though, that Exp. 6 ($G\theta l$) and Exp. 1 (R-$G\lambda h$) share the same final protrusion levels, even though the Shields parameter in Exp. 1 is higher than in Exp. 6. This can be explained considering that the local shear stress conditions measured within the bed interstices appear to be similar, as will be shown further on.

As compared to the first series of experiments in Part I, where higher Shields parameters were employed, it is observed that the final protrusion levels are equivalent or higher here. It is observed, for example, that for Exp. $G\theta h$, which shares the Shields parameter with Exp. 1a/b, Exp. 4 and Exp. 5a/b in the preliminarey study, the final protrusion level is higher being equal to 1 for the first and 0.8 for the latter. For Exp. $G\theta m$ the final protrusion level is similar to the one observed in Exp. 1a/b, Exp. 4 and Exp. 5a/b even though the Shields parameter is lower. The reason for higher final protrusion levels can be related to the different immobile beds. In the first series of experiments in Part I, a one-layered bed of spheres was used, while here a two-layered one. The first one is characterized by a lower inter-sphere volume for the fluid exchange between surface and subsurface compared to the second one, so that it can be considered more impermeable (Manes et al., 2009). It appears that the difference in hyporeic flow induces changes in the final erosion depth. Cooper et al. (2017) analysing the differences between porous and impermeable beds, found out that the turbulence is more coherent over permeable bed and more efficient in transferring momentum into the bed. This explains why the two-layered bed was characterized by higher erosion than the one-layered bed for the same flow conditions.

In the analysis of the bed morphodynamics at the pattern scale performed both in Part I in Section 2.3.4 and for Exp. 1 in Section 5.2, it was observed that three transitions in bed behaviour take place at three different and approximately constant protrusion levels. The first two transitions were identified on the basis of the local minimum and the local maximum in erosion rates E and the third one by negligible erosion rates corresponding to 0.5% of the erosion rates on a uniform fine-sediment bed E_{P0}. These three transitions in bed behaviour are also observable in the experiments being analysed here. Figures 6.2a-f shows the critical times ξ_{ci}, the critical protrusion levels $\langle P_{ci}\rangle$, the critical erosion rates E_{ci} and the critical concentration of displaced sediments $C_{s,ci}$ corresponding to the three transitions in bed behaviour as a function of the Shields parameter. Only the critical erosion rates for the first and second transition are shown as the critical values for the first transition are known a priori being 0.5% of E_{P0}.

Figure 6.2a shows that ξ_{ci} decreases with increasing Shields parameter, consistent with the trend observed in Figure 2.15a for the experiments performed in Part I. The outlier represented by the transitional time for the third transition ξ_{c3} for Exp. 1 ($R-G\lambda h$) is connected to the particular morphodynamics observed during this experiments caused by a ridge enlargement (for further details see Section 5.2.2).

Figure 6.2b shows that the critical protrusion levels for the first and second transitions, $\langle P_{c1}\rangle$ (squares) and $\langle P_{c2}\rangle$ (triangles), are close to 0.2 and 0.4, respectively, comparable with the values observed in Part I for experimental conditions with higher Shields parameters (see Figure 2.15a). The measured values of P_{c1} correspond to angles of attack α_a comprised between 20° and 30°, consistent with the development of a shear layer as hypothesized in Section 2.3.4 and confirmed by velocity measurements in Chapter 5. The planar densities λ_p corresponding to the measured $\langle P_{c2}\rangle$ are all close to 0.3, showing that the second transition in bed behaviour can be effectively associated to the transition from isolated to wake-interference conditions (Grimmond and Oke, 1999), as the flow measurements in Chapter 5 show and consistent with the results of the first experimental campaign in Section 2.5. In Figure 6.2b, the third transition in erosive regime shows critical protrusion levels $\langle P_{c3}\rangle$ comprised between 0.65 and 0.8. The corresponding planar densities are all
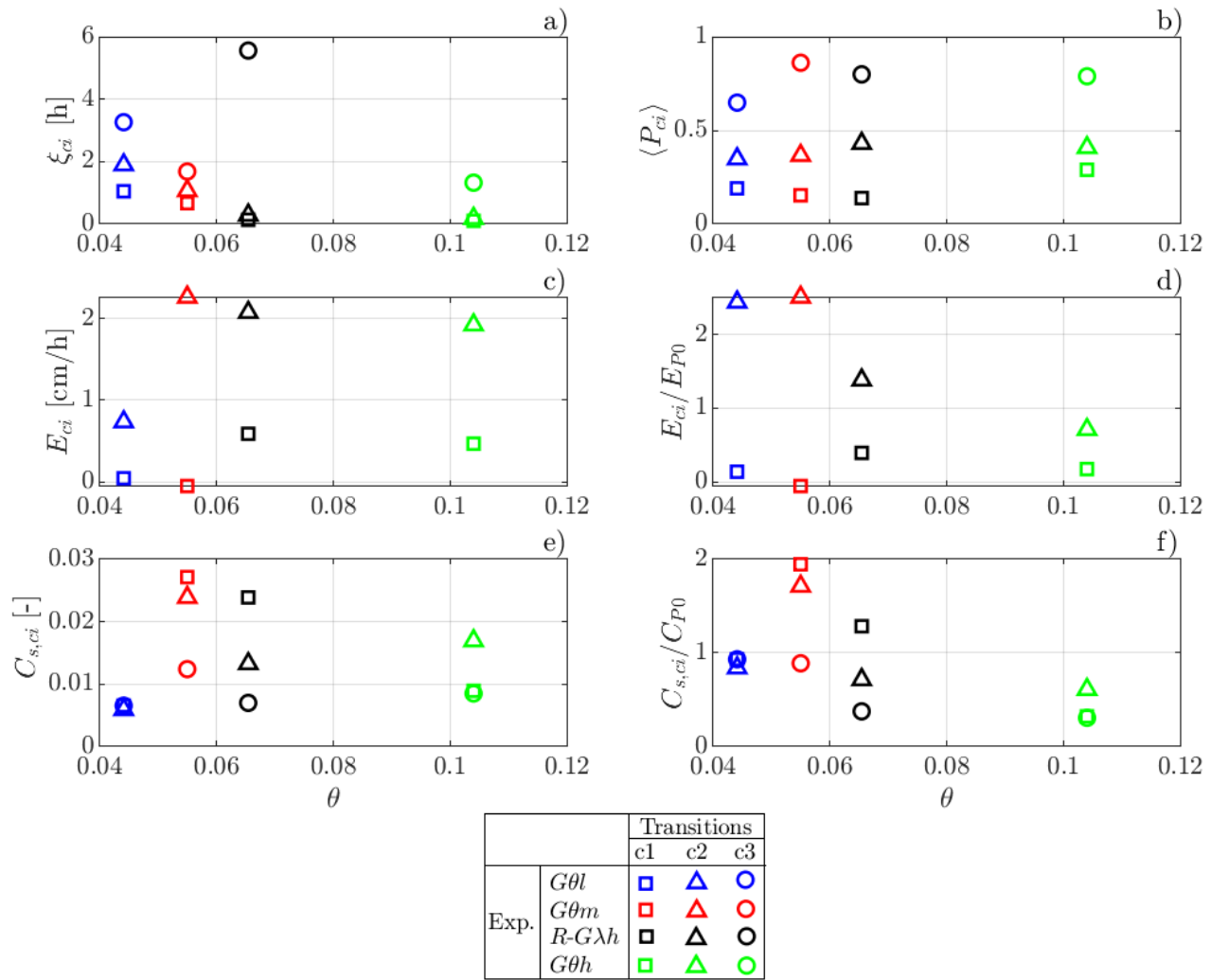
Figure 6.2: Critical values at the three transitions in bed behaviour as a function of the Shields parameter θ: (a) critical time ξ_{ci}, (b) critical protrusion levels $\langle P_{ci} \rangle$, (c) erosion rate at the transition E_{ci} and (d) normalized by the erosion rate for a uniform fine-sediment bed E_{P0}, (e) concentration of displaced sediments at the transition $C_{s,ci}$ and (f) normalized by the concentration of displaced sediments for a uniform bed C_{P0}.

equal to 0.5, showing that the third transition in erosive behaviour is associated also in this case to the transition from wake-interference to skimming flow consistent with the results of the first experimental campaign (see Section 2.5) and of Chapter 5. These results show that the critical angle of attack for the first transition in erosive behaviour and the critical planar densities for the second and third transitions in erosive behaviour are independent of the Shields parameter.

Figure 6.2c shows that a jump in critical erosion rates for $\theta > 0.06$ in the case of E_{c1} (squares) and for $\theta > 0.05$ in the case of E_{c2} (triangles), after which the critical erosion rates appear to remain approximately constant. This behaviour is quite counter-intuitive, as it was expected an increase in erosion rates with increase in the Shields parameter, as the trend in critical erosion rates observed in the Part I suggested (see Figures 2.15e-f). It is observed also that the critical erosion rates for the second transition E_{c2} in Figure 6.2c are much higher than the ones observed in Part I in Figure 2.15e-f for higher Shields parameters as the ones investigated

here. The main difference between the two set of experiments lies in the immobile bed of spheres which is one-layered in the case of the first series of experiments in Part I, while two-layered in this case. Without considering the fine sediments infilling the bed, the one-layered bed can be considered impermeable, while the two-layered permeable (Manes et al., 2009). The hyporeic flow exchange is as such more active in the case of a two-layered bed, suggesting a higher influence on the erosion processes, which would not depend anymore only on the Shield parameter, as for a one-layered bed of spheres. Further analysis is needed to confirm this hypothesis.

Figure 6.2d shows that the ratio between the second transition in erosive behaviour E_{c2} and the erosion rate for a uniform bed E_{P0} decreases with increasing Shields parameter. For $\theta < 0.08$, E_{c2} is higher than E_{P0}, while for $\theta > 0.08$ is lower. An opposite trend was observed, though, in the experimental results in Part I (see Figures 2.15i-l). This opposite behaviour might also be related to the difference in hyporeic flow between the two beds.

The critical erosion rate for the first transition in bed behaviour E_{c1} in Figure 6.2d is always lower than E_{P0} and shows that the first transition in erosive behaviour is associated by consistent damping of the erosion rates compared to a uniform fine sediment bed.

The critical concentration of displaced sediments in Figure 6.2e displays a significant decrease with increasing Shields parameters. The same is also observed for the ratio $C_s/C_{s,P0}$. This behaviour is also counter-intuitive and needs more clarification.

6.1.2 Shear stress distribution in the bed interstices (θ)

In this Section, the shear stress conditions in the bed interstices are analysed at the end of Exp. 5 ($G\theta l$), Exp. 6 ($G\theta l$) and Exp. 7 ($G\theta h$), once the bed is stable. The location of the PIV mieasurements during the experiments is identified in Figure 6.1 with yellow triangles. The aim is to determine whether skimming flow conditions are achieved at this point, as observed in the case of Exp. 1 (R-$G\theta l$) and explain the different final protrusion levels. The flow analysis is similar to the one performed in Section 5.3 Exp. 1 (R-$G\theta l$). First, the local fluid shear stresses $\tau_{xz}|_{local}$ are compared to the reference bed shear stresses acting on a fine-uniform bed τ_{P0} in Figures 6.3b-c, 6.3e-f and 6.3h-i for Exp. 5 ($G\theta l$), Exp. 6 ($G\theta l$) and Exp. 7 ($G\theta h$), respectively. Figures 6.3b, 6.3e and 6.3h show that in plane A for all experiments, a strong shear layer develops at the spheres' top with magnitudes as high as two times the shear stress acting on a fine-sediment bed for all Shields-parameter conditions analysed. In the bed interstices, reduced shear stress conditions are observed with a net separation from the shear layers. A clear drift of the shear layers over the sphere downstream is observed, leading to a region of enhanced shear stress high above the spheres. Similar features were also observed for the shear layers developing at the end of Exp. 1 (R-$G\theta h$), as observed in Figure 5.12d in plane A. They were associated effectively to skimming flow conditions. In plane B, Figures 6.3c, 6.3f and 6.3i show that the shear layers penetrate deeper into the ned interstices as compared to plane A, consistent with the shear layers observed in plane B in Figure 5.12h at the end of Exp. 1 (R-$G\theta h$). In the case of Exp. 5 ($G\theta l$), Figure 6.3c shows that the shear layer reaches the fine-sediment bed which is higher than the one observed in plane A, suggesting that skimming flow conditions are not yet present in plane B. Figure 6.1 shows, indeed, that the bed still evolves after the PIV measurement. In Exp. 6 ($G\theta m$) and Exp. 7 ($G\theta h$), Figures 6.3f anf 6.3i show that the shear layer does not reach the fine-sediment bed. The bed interstices are actually characterized by negative shear stresses in the case of Exp. 7 ($G\theta h$).

In Figures 6.3j and 6.3k the transport stage parameter $\theta_S^x - \theta_c'$ determined at the top of the fine-sediment roughness sublayer is analysed compared to the transport stage parameter for a uniform fine-sediment bed $\theta_{P0}^x - \theta_c'$ (please refer to Section 5.4.1 for the definition of the transport stage parameter). As the bed is stable, the roughness sublayer is considered equal to one d_{50} (see Section 5.3.5). Figure 6.3j, shows that in plane A, complete sheltering is observed in all Experiments, as the transport parameter is below critical conditions of motion. In the case Exp. $G\theta m$ and Exp. $G\theta l$, the highest transport parameters are observed in the stoss side of the spheres as the reference Exp. R-$G\lambda h$, suggesting local intermittent sediment transport. Exp. $G\theta l$ shows instead higher sediment transport parameters in the lee side of the spheres, probably connected to the fact, that the local bed level is nearer to the shear layer as observed in Figure 6.3a.

In plane B, Figure 6.3k shows that in the case of Exp. $G\theta l$, transport parameters are enhanced compared to a uniform fine-sediment bed leading ot the erosion of the bed, as observed previously in Figure 6.1. In the case of Exp. $G\theta m$ the transport parameters are damped compared to uniform fine-sediment bed conditions but still higher than the critical conditions of motion. The profile is similar to the one observed for R-$G\lambda h$. For Exp. $G\theta h$, the sediment transport parameters in plane B are enhanced for x'<0.25, but they are associated with negative shear stress, so that grains are pushed rather upstream than downstream.

In Table 6.1, the boundary layer parameters for the different experiments are listed. It is observed that the shear velocity u_*, determined at the top of the spheres from the linear extrapolation of the total fluid shear stresses τ_{xz} increases with increasing Shields parameter, as expected. It is observed, that even though Exp. $G\theta m$ is characterized by a lower Shields parameter than Exp. R-$G\lambda h$, the shear velocity acting at the top of the spheres is similar. The similar u_* explains why the protrusion levels at the end of Exp. $G\theta m$ and Exp. R-$G\lambda h$ is similar. It is though unclear, why higher shear velocities were observed in Exp. $G\theta m$ than the ones expected on the basis of the depth slope product in Table 3.1. Since higher water levels were observed during the course of the Exp. $G\theta m$ compared to the level of the boat, increased flow acceleration might have been triggered below the boat, increasing the shear stresses.

Table 6.1 shows, furthermore, that the zero-plane is positioned at the top of the spheres or slightly below in all experiments. This confirms that skimming flow conditions were reached at the end of the experiments, when the bed reached a stable bed level. The equivalent roughness length values do not seem to follow any particular trend, in conformity with skimming flow conditions for which the equivalent roughness does not depend any more on the roughness conditions of the bed (Perry et al., 1969; Jiménez, 2004).
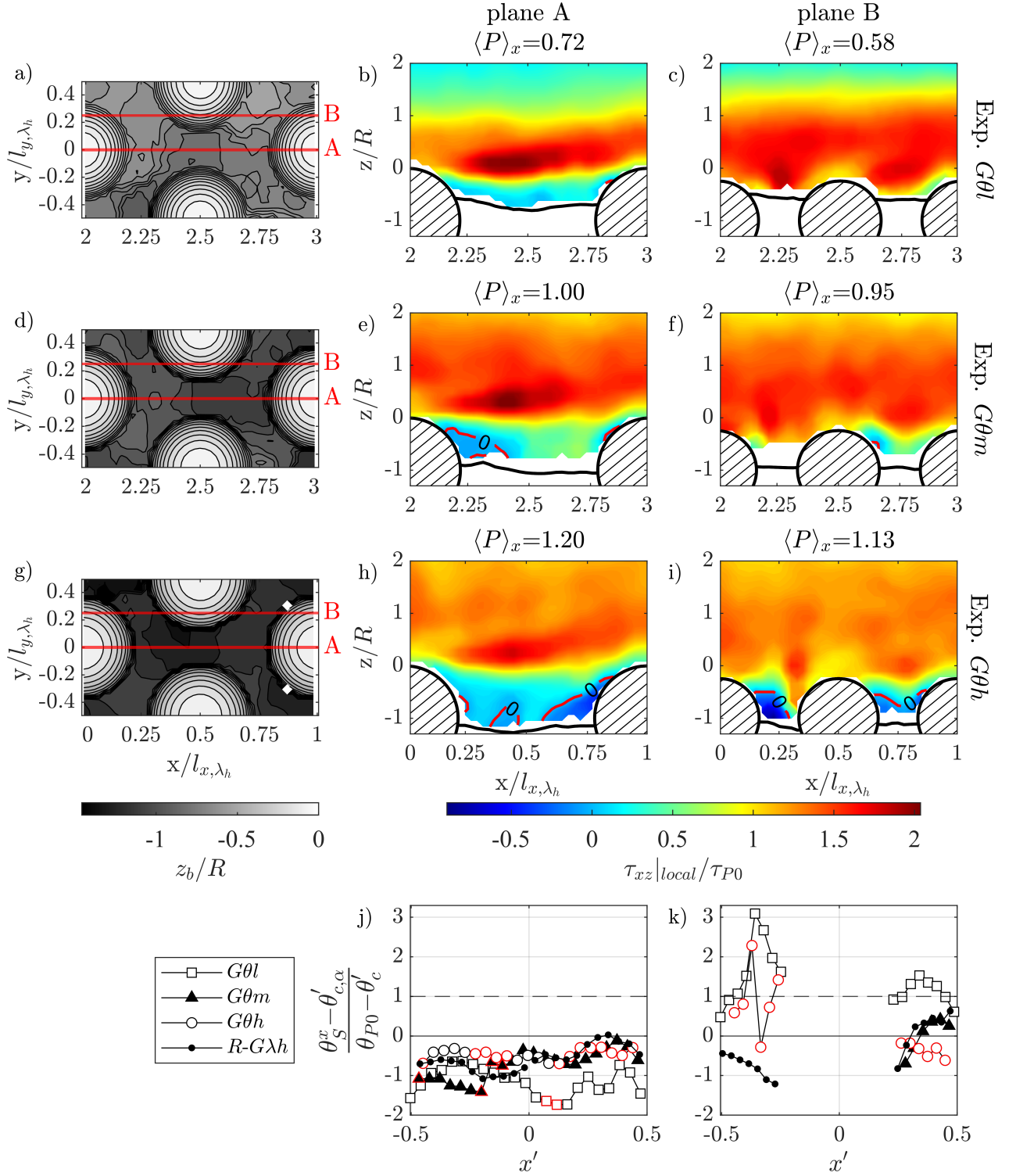
Figure 6.3: (a-i) Bed topography and local fluid shear stress $\tau_{xz}|_{local}$ fields normalized by the bed shear stress acting on a uniform fine-sediment bed τ_{P0} in plane A and plane B at the end of Exp. 5 ($G\theta l$), Exp. 6 ($G\theta m$) and Exp. 7 ($G\theta l$). (j-l) Longitudinal profiles of the fine-sediment transport parameter in streamwise direction θ_S^x-θ_c' determined at the top of the fine-sediment roughness sublayer ($h_{rs}^s = d_{50}$) and normalized by the transport parameter for a uniform bed θ_{P0}-θ_c' for Exp. 5, Exp. 6 and Exp. 7 in comparison with the reference Exp. 1 (R-$G\lambda h$). The red symbols identify negative shear stress conditions. x' is a local coordinate system centred in the pattern and normalized by the distance between the spheres b (see Figure 5.21).

Exp.	plane	θ	$\langle P \rangle$	$\langle P \rangle_x$	$\sigma_{z,G}$	λ_p	λ_f	δ	S_r	u_*	τ_b	k_s	$z_d/\langle k \rangle$
			[-]	[-]	[cm]	[-]	[-]	[cm]	[-]	[cm/s]	[Pa]	[cm]	[-]
R-$G\lambda h$	A	0.065	0.98	0.93	0.37	0.51	0.30	2.9	3.9	2.57	0.81	0.85	0.00
	B	0.065	0.98	1.00	0.37	0.51	0.29	2.7	3.8	2.63	0.85	0.85	0.00
$G\theta l$	A	0.044	0.67	0.72	0.24	0.46	0.19	3.0	5.5	2.35	0.64	0.92	−0.07
	B	0.044	0.66	0.58	0.24	0.46	0.19	2.3	4.5	2.35	0.65	0.94	−0.05
$G\theta m$	A	0.055	0.97	1.00	0.37	0.51	0.28	4.3	5.4	2.57	0.77	1.07	−0.07
	B	0.055	0.99	0.95	0.38	0.52	0.27	4.1	5.4	2.50	0.72	0.87	−0.05
$G\theta h$	A	0.104	1.16	1.20	0.46	0.54	0.34	5.3	5.6	2.73	0.84	1.25	−0.03
	B	0.104	1.16	1.13	0.46	0.54	0.34	5.3	5.6	2.73	0.84	1.04	−0.01
										±0.06	±0.03	±0.01	±0.005

Table 6.1: Roughness and boundary layer parameters for the experiments with variations in Shields parameter for stable bed conditions at the end of the experiments: Shields parameter θ ($= u_{*R^c}^2/(g\Delta d_{50})$), pattern-averaged protrusion level $\langle P \rangle$, streamwise-averaged protrusion level in the PIV plane $\langle P \rangle_x$, standard deviation of bed elevations at the pattern scale $\sigma_{z,G}$, planar density λ_p, frontal density λ_f, boundary layer depth δ, relative submergence of the pattern $S_r = (\delta + \langle P \rangle)/\langle P \rangle$, shear velocity u_* obtained from the linear extrapolation of the total fluid shear stress to the top of the spheres, bed shear stress τ_b, equivalent sand roughness k_s, roughness displacement length z_d normalized by the protrusion height of the spheres $\langle k \rangle$ ($= \langle P \rangle R$).

6.2 The impact of the immobile-roughness density λ_f on the morpho- and hydrdynamics

In this Section, the impact of the roughness density of the first layer of spheres on the bed morhodynamics and on the flow patterns within the bed interstices is analysed. The analysis is focussed on Exp. 1 (R-$G\lambda h$), Exp. 2 (R-$G\lambda m$) and Exp. 3 (R-$G\lambda l$), characterized by decreasing roughness densities of the first layer of spheres. Exp. 1 (R-$G\lambda h$) analysed in Chapter 5 is always used as a reference. The analysis of the bed morphodynamics is performed at the pattern scale within the pattern of spheres in the centre of the channel. The size of the pattern is varied according to the roughness density of the first layer of spheres (see Figure 3.2a-c).

6.2.1 Bed morphodynamics (λ_f)

The evolution of the bed topography at the reach scale is first analysed. Figures 6.4a and 6.4b show the temporal evolution of the protrusion levels $\langle P \rangle_x$ spatially averaged in the streamwise direction over the length of the reference pattern for Exp. R-$G\lambda m$ and Exp. R-$G\lambda l$, respectively. Figures 6.4a and 6.4b show that at the beginning of the experiments, dunes develop, which disappear, within the central reference pattern, after about three hours in Exp. R-$G\lambda m$ with the intermediate roughness density (like in the reference Exp. R-$G\lambda h$) and after 1.2 hours in Exp. R-$G\lambda l$ with the lowest roughness density. This suggests that with decreasing roughness density of the immobile spheres, the dunes travel faster.

Figure 6.4a shows that during Exp. R-$G\lambda m$ a ridge develops at y/W $\simeq$ -0.1 at a similar position as the ridges observed to develop in the reference Exp. R-$G\lambda h$ in Figure 5.1. The ridge is in Exp. R-$G\lambda m$ much larger, though. Furthermore, it appears that the protrusion level in the troughs develops over a much longer
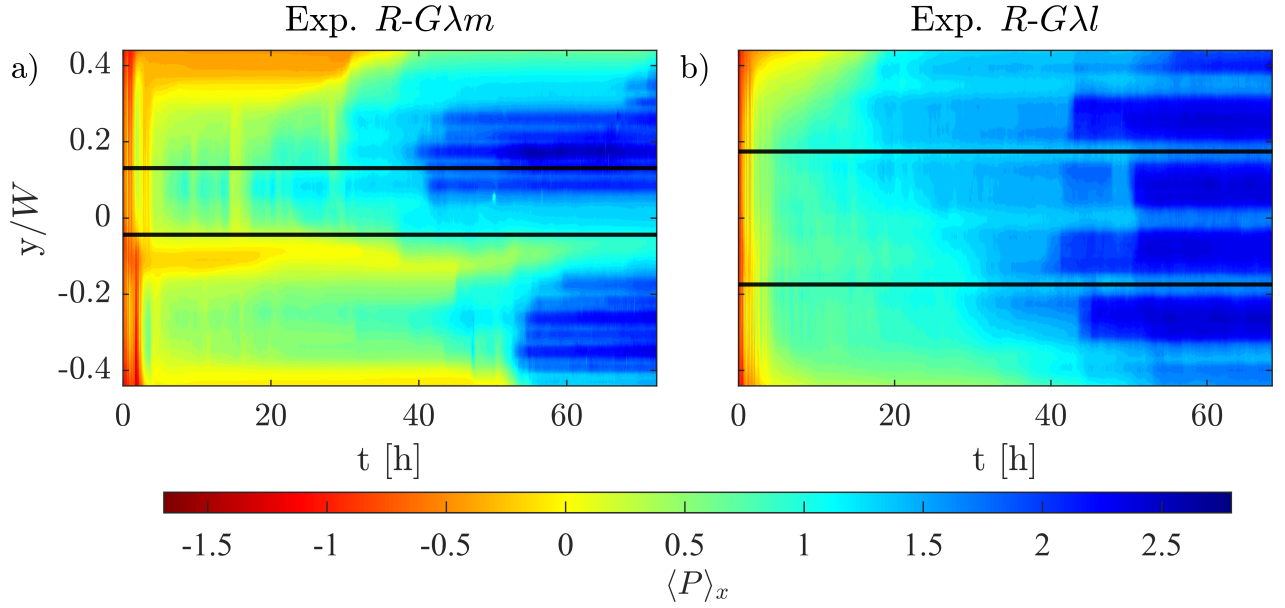
Figure 6.4: Hovmöller diagrams of the longitudinally-averaged protrusion level $\langle P \rangle_x$ as a function of t and y/W for Exp. 2 (R-$G\lambda m$) (a) and Exp. 3 (R-$G\lambda l$) (b). The two continuous lines in the centre of the pattern identify the lateral extension of the reference pattern.

time. At the end of the experiment, a wavy lateral pattern in protrusion levels is observed in the troughs, with a wavelength equal to half the pattern width. This lateral pattern corresponds to the alternation of eroded areas in between the spheres and of higher sediment deposits behind the spheres.

Figure6.4b shows that during Exp. R-$G\lambda l$ with the lowest roughness density, no clear development of a ridge is observed. For t > 35 hours, a similar lateral variation in protrusion levels is observed as in Exp. R-$G\lambda m$ due to the higher sediment deposits behind the spheres.

The morphodynamics at the pattern scale is now analysed on the basis of the protrusion levels $\langle P \rangle$ spatially averaged over the reference pattern. It should be noticed, that in the case of Exp. R-$G\lambda m$ with intermediate density, the spatial average is performed only over half of the pattern located in the bed troughs for 0.08 < y/W< 0.13 since the other half is occupied by the ridge (see Figure 6.4a). Figures 6.5a-c show the temporal evolution of $\langle P \rangle$, of the erosion rates E (= $RC\partial_t\langle P \rangle$) and of the concentration of displaced sediments C_s during Exp. R-$G\lambda h$, Exp. R-$G\lambda m$ and Exp. R-$G\lambda l$. E and C_s are normalized by the erosion rate and concentration of displaced sediments over a uniform bed E_{P0} and C_{P0}, respectively. To compare the experiments, the $\langle P \rangle$-, E- and C_s-signals are offset by the time t_0 for which the spheres protrude without being covered again by dune. The time-frame ξ = t-t_0 is used. Figure 6.4a shows that during Exp. R-$G\lambda m$ and Exp. R-$G\lambda l$ with an intermediate and low roughness density, respectively, $\langle P \rangle$ evolves slower than during the reference Exp. R-$G\lambda h$. It is observed that in the first hours, the evolution of the three profiles is similar. The $\langle P \rangle$-profile of the reference Exp. R-$G\lambda h$ departs from the other two profiles when the critical protrusion level $\langle P_{c1} \rangle$ = 0.15 (see Section 5.2.2) is reached, which triggers enhanced erosion rates. As explained in Chapter 5, this enhancement of the erosion rates is connected to the shear layer impacting the fine-sediments. It is expected that the protruding spheres in Exp. R-$G\lambda m$ and Exp. R-$G\lambda l$ produce also localized enhancement of the shear stress conditions for similar protrusion levels, as the erosive patterns visually observed around the spheres suggested. The density of the spheres is much lower though compared to Exp. R-$G\lambda h$, so that the shear stress enhancement is only significant at a local sphere-scale and not perceivable at the pattern scale.
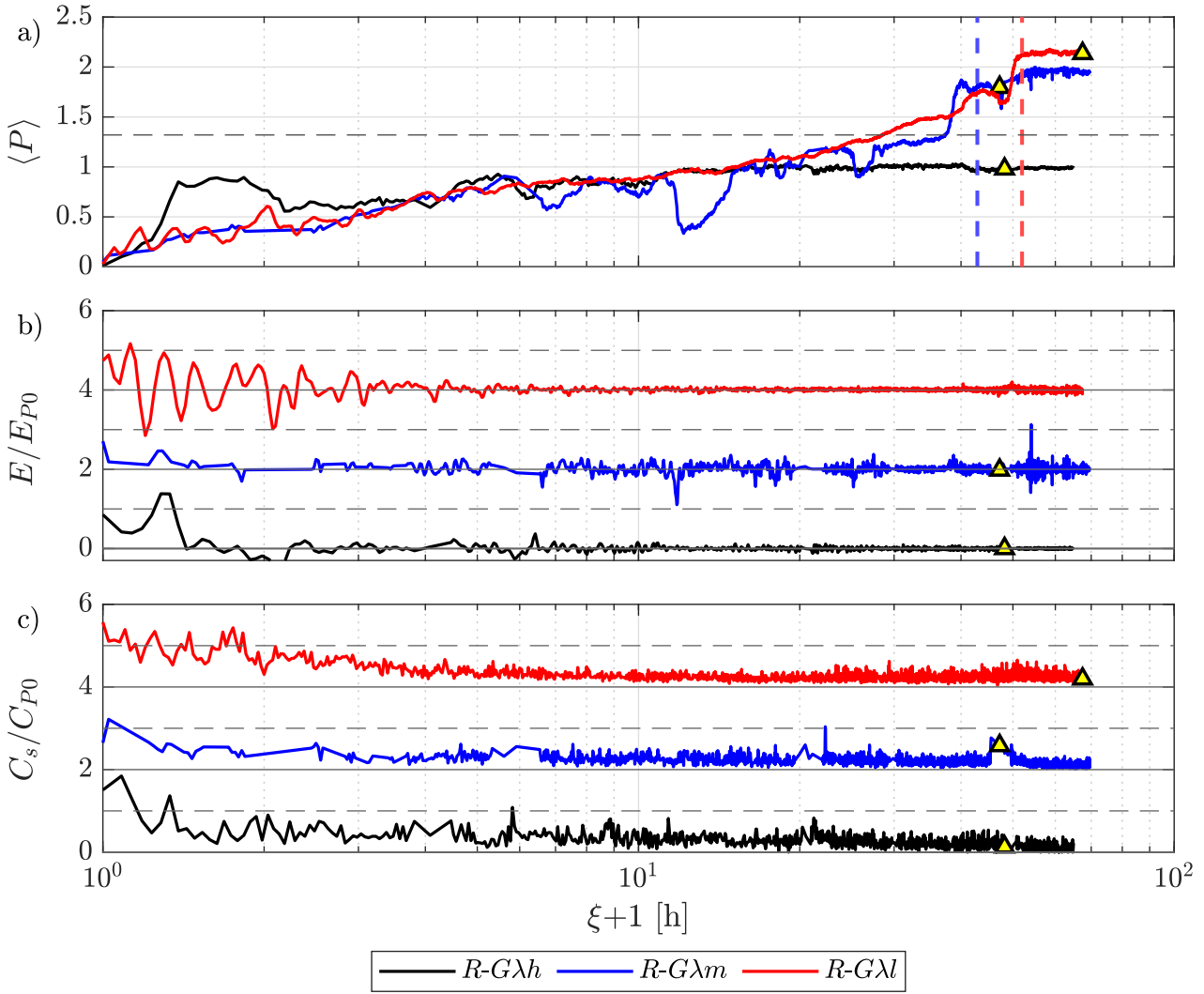
Figure 6.5: Temporal profiles of the pattern-averaged protrusion levels $\langle P \rangle$, of the total erosion rates E_t (b) and of the concentration od displaced sediments C_s during Exp. 2 (R-$G\lambda m$) and 3 (R-$G\lambda l$) compared to the reference Exp. 1 (R-$G\lambda h$). E and C_s are normalized by the erosion rates and the concentration of displaced sediments for a uniform fine-sediment bed, E_{P0} and C_{P0}. The E- and C_s-curves are shifted by 2 units in the vertical direction; the horizontal continuous lines identify $E = C_s = 0$ and the dashed lines $E/E_{P0} = C_s/C_{P0} = 1$. The yellow triangles identify the times at which the PIV measurements were performed. The ξ-axis is shifted by 1 hour for visualization purposes.

Figures 6.5b and 6.5c show, indeed, that the erosion rates E and the concentration of displaced sediments C_s at the beginning of Exp. R-$G\lambda m$ and Exp. R-$G\lambda l$ are as high or even higher than E_{P0} and C_{P0} for uniform fine-sediment beds.

Figure 6.4a shows that while in Exp. R-$G\lambda h$, the bed reaches a final stable bed level $\langle P \rangle \simeq 1$, the first layer of spheres is completely eroded in in Exp. R-$G\lambda m$ and R-$G\lambda l$. It is noteworthy that the the $\langle P \rangle$-profiles of Exp. R-$G\lambda m$ and R-$G\lambda l$ evolve in a similar manner until a protrusion $\langle P \rangle \simeq 1.32$ (i.e. the beginning of the second layer of spheres) is reached, event though the roughness density of the first layer of spheres is different. Further investigations are needed at a scale smaller than the pattern to discern this aspect. As

soon as the second layer of spheres is reached, both $\langle P \rangle$-profiles of Exp. R-$G\lambda m$ and R-$G\lambda l$ show a rapid evolution, followed by a stabilizing trend. These evolution patterns are similar to the ones observed during the reference Exp. R-$G\lambda h$ within the first layer of spheres (see Section 5.2.2), which shares the same high roughness density as the second layer of spheres. It is surmised, as such, that the same transitions in erosive behaviour take place during Exp. R-$G\lambda m$ and Exp. R-$G\lambda l$ when the second layer of spheres is reached. Considering the third transition in erosive behaviour characterized by a transition to negligible erosion rates leading eventually to a stable bed level and identified by the vertical dashed lines in Figure 6.5a, it is observed that even though the transition takes place for $\langle P \rangle \simeq 1.8$ in Exp. R-$G\lambda m$ and for $\langle P \rangle \simeq 2.1$ for Exp. R-$G\lambda l$, the planar density λ_p is equal in both cases to 0.5, as also observed in Section 5.2.2 for the third transition in bed behaviour taking place in reference Exp. R-$G\lambda h$. This shows that at least the third transition in bed behaviour is independent of the roughness density of the bed of spheres and is identified by a critical planar density $\lambda_p \simeq 0.5$.

Exp. R-$G\lambda m$ stabilizes at $\langle P \rangle \simeq 1.85$, while Exp. R-$G\lambda l$ at $\langle P \rangle \simeq 2.1$, consistent with the fact that globally the roughness density of Exp. R-$G\lambda m$ is higher than in Exp. R-$G\lambda l$, resulting in a higher sheltering effect. The planar density reached when the bed is stable, is for both Exp. R-$G\lambda m$ and Exp. R-$G\lambda l$ equal to 0.5, which corresponds to the onset of skimming flow conditions (Grimmond and Oke, 1999).

6.2.2 Shear stress distribution in the bed interstices (λ_f)

In this Section, the shear stress condition within the bed interstices are analysed at the end of Exp. R-$G\lambda m$ and Exp. R-$G\lambda l$, when the spheres reach a stable protrusion level. The results are compared with the shear stress conditions observed at the end of the reference Exp. R-$G\lambda h$ during the fourth PIV run $r4$. The time at which the PIV measurements are performed, is highlighted by a triangle in Figure 6.5a. Figures 6.6a and 6.6b show the bed topographies measured during the PIV measurements in plane A and in plane B for Exp. R-$G\lambda m$ and Exp. R-$G\lambda l$, respectively. Figure 6.6a shows that in Exp. R-$G\lambda m$, areas eroded down to the second layer of spheres are observed in the front and on the sides of the spheres of the first layer in the region not occupied by the ridge ($y/l_{y,\lambda_m} > 0.25$). In their lee side, sediment shadows partially covering the second layer of spheres are present. In the eroded areas, such as in Plane B, small sediment shadows are also present in the lee side of the spheres of the second layer.

Figure 6.6b shows that in Exp. R-$G\lambda l$, the pattern is subdivided in areas characterized by higher bed levels in the lee side of the spheres along plane A and area with lower bed levels in between the spheres of the first layer, essentially below plane B. It appears that the areas of higher erosion depart from the lee side of the spheres in the upper layer prolonging themselves to the sides [1]. Overall, it is noteworthy that plane A in Exp. R-$G\lambda l$ is less eroded than the corresponding plane in Exp. R-$G\lambda m$, while for plane B the opposite is observed.

Figures 6.6c,e and 6.6d,f show the local fluid shear stress field $\tau_{xz}|_{local}$ normalized by the bed shear stress acting on a uniform fine sediment bed τ_{P0} for Exp. R-$G\lambda m$ and Exp. R-$G\lambda l$, respectively. Figure 6.6c shows that in Exp. R-$G\lambda m$, plane A is characterized by the presence of a shear layer developing horizontally

---

[1] Please note that the second layer of spheres is inverted in Exp. R-$G\lambda l$ compared to Exp. R-$G\lambda m$, so that erosion is possible directly below the spheres of the upper layers.
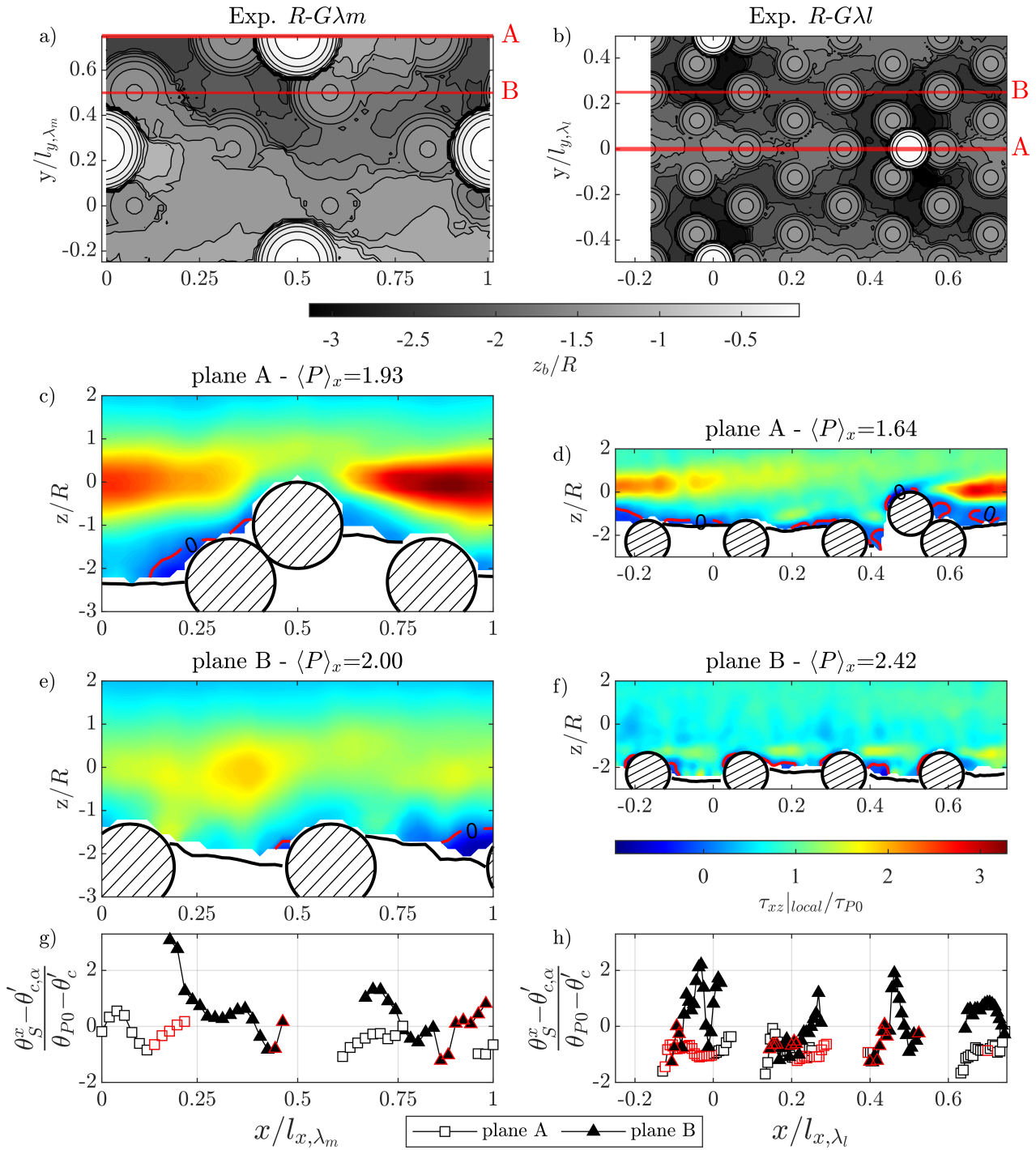
Figure 6.6: (a-f) Bed topographies and local fluid shear stress fields $\tau_{xz}|_{local}$ normalized by the reference bed shear stress on a uniform fine-sediment bed τ_{P0} in plane A and plane B at the end of Exp. R-$G\lambda m$ (left column) and Exp. R-$G\lambda l$ (right column). (g-h) Longitudinal profiles of the fine-sediment transport parameter in streamwise direction θ_S^x-θ_c' determined at the top of the fine-sediment roughness sublayer h_{rs}^s (=d_{50}) and normalized by the transport parameter for a uniform bed θ_{P0}-θ_c' in plane A and B for Exp. R-$G\lambda m$ and Exp. R-$G\lambda l$. The red symbols identify negative shear stress conditions.

and expanding deep into the bed interstices down to z/R = -1. Plane A in Exp. R-$G\lambda l$ (Figure 6.6d) is characterized by an inclined shear layer expanding into the bed interstices down to z/R = -0.3. As a result, plane A in Exp. R-$G\lambda l$ is eroded less than in Exp. R-$G\lambda m$. Compared to the shear layers developing at the spheres' top at the end of the reference Exp. R-$G\lambda h$ (see Figure 5.12d), the shear layer observed here penetrate deeper into the bed interstices and do not merge into a region of higher shear stresses above the spheres. The shear layer collides with the sphere downstream in Exp. R-$G\lambda m$ suggesting wake interference flow conditions for the upper layer of spheres, while in Exp. R-$G\lambda l$ the shear layer does not interact suggesting isolated flow conditions. Nevertheless, the near bed region in plane A for both Exp. R-$G\lambda m$ and Exp. R-$G\lambda l$ is characterized by reduced shear stresses. Figure 6.6d shows that in Exp. R-$G\lambda l$, negative shear stresses dominate near the bed and the shear layer which develops at x/$l_{x,\lambda_l} \simeq 0.2$, does not impact the fine-sediment bed. In the stoss side of the sphere in the top layer, Figures 6.6a and 6.6d show that the bed is eroded much deeper than the average bed level in plane A. In Figure 6.6a, the topographic pattern characterized by increased erosion and developing in the form of a horseshoe around the sphere in the top layer, suggests the development of a horseshoe vortex over time which erodes the bed until negative shear stress conditions are reached as observed deep inside the bed in the stoss side of the sphere of the top layer in Figure 6.6d.

In plane B, Figure 6.6e shows that in Exp. R-$G\lambda m$ a region of enhanced shear stresses is observed at the level z/R = 0, probably the result of the shear layers expanding laterally from the adjacent planes. This appears weaker than the shear layer developing in plane A (Figure 6.6c). In the near-bed region, higher shear stresses are observed in the lee of the spheres as the result of the upper region of increased shear stresses extending down. In the stoss sides, lower shear stress are present, instead. In Figure 6.6f for plane B R-$G\lambda l$ no region of enhanced shear stresses is observed at z/R = 0, suggesting that the shear layers developing in plane A behind the spheres of the upper layer do not extend to plane B. The near-bed region is characterized, though, by the shear layers of the spheres in the second layer. The magnitude of these shear layers is of the order of τ_{P0} and appear to extend down in the stoss side of the spheres. The near-bed region in the lee side is characterized, instead, by negative shear stresses. The development of shear layers when the second layer of spheres is exposed, is probably the cause of the higher erosion observed in plane B for Exp. R-$G\lambda m$ and Exp. R-$G\lambda l$, as compared to Exp. R-$G\lambda h$, where the erosion is limited to the first layer of spheres (see Figure 5.12h).

Figures 6.6g and 6.6h show the transport stage parameters $\theta_s^x - \theta_c'$, as defined in Section 5.4.1, determined at the top of the fine-sediment roughness sublayer ($h_{rs}^s = d_{50}$). Figure 6.6g shows that plane A in Exp. R-$G\lambda m$ is characterized by critical conditions of motion. Plane B shows increased shear stress conditions in the lee side of the spheres probably due to the upper shear layer extending down (see Figure 6.6g). This suggests that the sediment accumulations in the lee side of the spheres in plane B will be eventually eroded. From the protrusion profile for Exp. R-$G\lambda m$ in Figure 6.5a it is observed that the bed still evolves after the PIV measurements confirming the plausibility of the shear stress conditions in the lee sides of the spheres. The stoss sides are, instead, near critical conditions of motion.

Figure 6.6h shows that plane A in Exp. R-$G\lambda l$ is characterized by critical conditions of motion consistent with the stable bed level. In plane B, the bed is characterized by shear stress conditions below critical in the lee side of the spheres of the second layer, while in the stoss side, by enhanced shear stress conditions. Considering that the protrusion levels for Exp. R-$G\lambda l$ in Figure 6.6a are stable and that it was observed visually that no sediment transport took place, it is likely that these local enhanced shear stress areas derive from measurement errors. In Figure 6.6f these enhanced shear stress conditions near the bed are quite localized and

disconnected by a region of lower shear stress from the shear layer. Further analysis of these data is needed. Overall, the results show that the higher erosion depths for decreasing roughness densities are to be ascribed

Exp.	plane	$\langle P \rangle$	$\langle P \rangle_x$	$\sigma_{z,G}$	λ_p	λ_f	δ	S_r	u_*	τ_b	k_s	$z_d/\langle k \rangle$
		[-]	[-]	[cm]	[-]	[-]	[cm]	[-]	[cm/s]	[Pa]	[cm]	[-]
$R\text{-}G\lambda h$	A	0.98	0.93	0.37	0.51	0.30	2.9	3.9	2.57	0.81	0.85	0.00
	B	0.98	1.00	0.37	0.51	0.29	2.7	3.8	2.63	0.85	0.85	0.00
$R\text{-}G\lambda m$	A	1.85	1.93	0.57	0.52	0.29	4.3	3.3	2.72	1.00	1.36	−0.16
	B	1.85	2.00	0.57	0.52	0.29	4.5	3.4	2.4	0.77	1.15	−0.34
$R\text{-}G\lambda l$	A	2.09	1.64	0.48	0.5	0.27	5.2	3.5	2.29	0.70	1.69	−0.20
	B	2.04	2.42	0.49	0.48	0.27	5.1	3.5	2.29	0.64	2.67	−0.50
									±0.06	±0.03	±0.01	±0.005

Table 6.2: Roughness and boundary layer parameters for the experiments with variations in the roughness density of the spheres: pattern scale protrusion level $\langle P \rangle$, streamwise averaged protrusion level in the PIV plane $\langle P \rangle_x$, standard deviation of bed elevations at the pattern scale $\sigma_{z,G}$, planar density λ_p, frontal density λ_f, boundary layer depth δ, relative submergence of the pattern $S_r = (\delta + \langle P \rangle)/\langle P \rangle$, shear velocity u_* obtained from the linear extrapolation of the total fluid shear stress τ_{xz} to the top of the spheres, bed shear stress τ_b, equivalent sand roughness k_s, roughness displacement length z_d normalized by the protrusion height of the spheres $\langle k \rangle \; (= \langle P \rangle R)$.

to a larger vertical extent of the shear layers developing behind the spheres in the upper layer. The final constant bed levels in plane A are to be associated to the fact, that the shear layers do not manage to reach the fine-sediment bed.

In Table 6.2 the boundary layer parameters for all planes analysed are listed for Exp. $R\text{-}G\lambda h$, Exp. $R\text{-}G\lambda m$ and Exp. $R\text{-}G\lambda l$. For both plane A and plane B, it is observed that the the total resistance of bed τ_b decreases with decreasing roughness density consistent with the fact that with decreasing roughness density, the drag extracted by the roughness elements is reduced. The values of k_s increase instead, which is not expected. Further analysis should be performed. The values of the zero-plane position show that while for the reference Exp. $R\text{-}G\lambda h$, z_d is at the top of the spheres, with decreasing roughness, z_d decreases within the bed interstice. The highest decrease is observed for plane B, which is the plane sheltered the least by the spheres of the first layer. These results are consistent with the trend in z_b observed for decreasing roughness densities of arrays of roughness elements (Leonardi, 2010; Placidi and Ganapathisubramani, 2015). It is noteworthy that the fine-sediment bed level is below the top of the second layer of spheres for both Exp. $R\text{-}G\lambda l$ and for Exp. $R\text{-}G\lambda m$, so that the actual relevant roughness density is the one of the second layer of spheres for the definition of the local sheltering conditions. The planar density of the pattern is equal for both the intermediate and low density case by planar densities associated with skimming flow conditions, suggesting that the shear stress patterns observed in the near-bed region, especially for plane A, are effectively connected to a decoupling of the outer flow from the bed interstices. z_b does not reach, in fact, the second layer of sphere as the roughness density of the first layer decreases.

6.3 Influence of relative submergence S_r on the morpho- and hydrodynamics

In this Section, the impact of the relative submergence on the bed morhodynamics and on the flow patterns within the bed interstices is analysed. The analysis is focussed on Exp. 1 (R-$G\lambda h$), Exp. 4 (R-$GS_r h$), characterized by increasing relative submergence. The analysis of the bed morphodynamics is performed at the pattern scale within the pattern of spheres in the centre of the channel (see Figure 3.2a).

6.3.1 Bed morphodynmics (S_r)

Figure 6.7 shows the temporal evolution of the pattern-averaged protrusion level $\langle P \rangle$ for Exp. R-$G\lambda h$ and Exp. R-$GS_r h$. The profiles are offset by the time at which the spheres protrude without being covered again, t_0, equal to 3.3 for Exp. R-$G\lambda h$ and 5.5 hours for Exp. R-$GS_r h$. The time-frame is defined as: ξ = t-t_0. Figure 6.7 shows that the evolution of Exp. R-$GS_r h$ with the higher submergence is slower than Exp. R-$G\lambda h$. Exp. R-$GS_r h$ reaches, though, the same stable protrudion level as Exp. R-$G\lambda h$. It appears that increasing the flow submergence impact the erosion rates of the system, but not the final bed level.

Table 6.3 shows the values of the critical time ξ_{ci}, the critical protrusion levels $\langle P_{ci} \rangle$, the critical erosion rates E_{ci} and the critical concentration of displaced sediments $C_{s,ci}$ for the three transitions in bed behaviour identified in Part I in Chapter 2 and in Chapter 5. The latter two are normalized by the erosion rates and the concentration of displaced sediments for a uniform bed. It is observed that the higher relative submergence increases the time ξ_{ci} at which the transitions take place. The critical protrusion levels P_{ci} at which the three transitions take place remains, instead the same. As also observed for variations in the Shields parameter (Section 6.1.1) and in the roughness density of the spheres (Section 6.2.1), the critical protrusion level for the first transition P_{c1} corresponds also in this case to an angle of attack α_a of approximately 20°, while the second and third critical protrusion levels to planar densities $\lambda_p = 0.3$ and $\lambda_p = 0.5$, respectively. The critical angle of attack for the first transition in bed behaviour and the critical planar densities for the second and third transitions are, as such, independent of the relative submergence.

Overall, the ratio E_{ci}/E_{P0} for the first and second transitions is lower for Exp. R-$GS_r h$ with a higher submergence. Since the first transition is connected to the development of a shear layer at the spheres' top or possibly to a horseshoe vortex too, it is surmised, that with a lower submerged, the shear layer and the
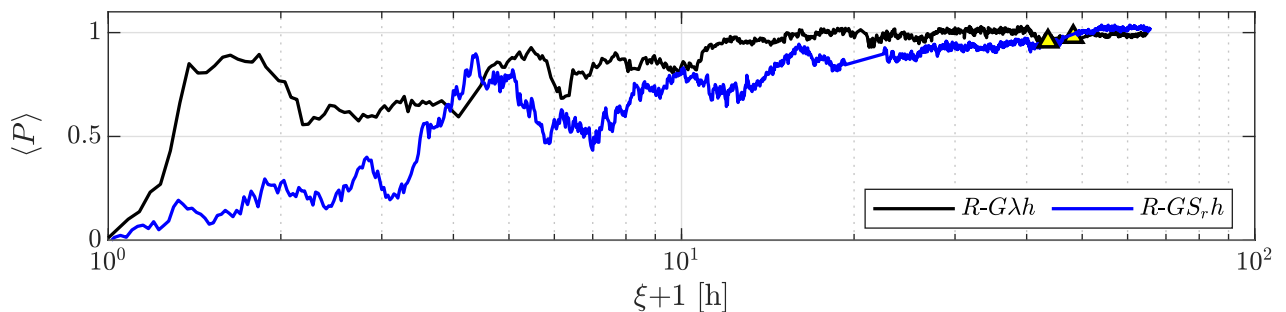

Figure 6.7: Temporal profile of the pattern-averaged protrusion level $\langle P \rangle$ during Exp. 4 (R-$GS_r h$) compared to the reference Exp. 1 (R-$G\lambda h$). The yellow triangles identify the times at which the PIV measurements were performed. The ξ-axis is shifted by 1 hours for visualization purposes.

	1. transition				2. transition				3. transition			
Exp.	ξ_{c1}	$\langle P_{c1} \rangle$	E_{c1}/E_{P0}	$C_{s,c1}/C_{P0}$	ξ_{c2}	$\langle P_{c2} \rangle$	E_{c2}/E_{P0}	$C_{s,c2}/C_{P0}$	ξ_{c3}	$\langle P_{c3} \rangle$	E_{c3}/E_{P0}	$C_{s,c3}/C_{P0}$
R-$G\lambda h$	0.13	0.14	0.39	1.28	0.28	0.43	1.38	0.71	5.57	0.80	0.005	0.37
R-$GS_r h$	2.1	0.20	−0.04	0.36	2.48	0.42	0.61	0.64	12.00	0.79	0.005	0.17

Table 6.3: Critical values at the transitions in erosive behaviour for Exp. 4 (R-$GS_r h$) compared to Exp. 1 (R-$G\lambda h$): critical time ξ_{ci} [t], critical protrusion level $\langle P_{ci} \rangle$, erosion rates and concentration of the displaced sediments at the transitions, E_{ci} and C_{si}, normalized by the erosion rates and the concentration of displaced sediments for a uniform bed, E_{P0} and C_{P0}.

horseshoe vortex are more confined causing an increase in erosion rates. The erosion rates for the second transition in erosion rates E_{c2} are lower than the erosion rates for a uniform bed in the case of a higher submergence. The values of the critical concentration of displaced sediments are also lower for the lower relative submergence, confirming a lower evolution of the system.

6.3.2 Shear stress distribution in the bed intersticescs (S_r)

In this Section, the shear stress condition within the bed interstices are analysed at the end of Exp. R-$GS_r h$, when the spheres reach a stable protrusion level. The results are compared with the shear stress conditions observed at the end of the reference Exp. R-$G\lambda h$ during the fourth PIV run $r4$. The time at which the PIV measurements are performed, is highlighted by a triangle in Figure 6.7. Figure 6.8a shows the bed topography measured during the PIV measurements for Exp. R-$GS_r h$, characterized by a sediment shadow in the lee side of the spheres as in Exp. R-$G\lambda h$. Figures 6.8b-c show the local fluid shear stress $\overline{\tau}_{xz}|_{local}$ normalized by the reference bed shear stress acting on a uniform fine-sediment bed τ_{P0} for plane A and plane B. Figure 6.8a shows that a shear layer develop at the top of the spheres. There is a net separation between the shear layer and the near-bed region characterized by reduced shear stress conditions. In plane B, the shear layer penetrates lower into the bed interstices, but near the near-bed region negative shear stressses are prevalent. Overall the shear-stress pattern are similar to the ones observed in Exp. R-$G\lambda h$ in Figures 5.12d and 5.12h, suggesting that also for Exp. R-$GS_r h$ with a higher relative submergence, the final stable bed level is associated with skimming flow conditions. The hypothesis is supported by the transport-parameter profiles sampled at the level of the fine-sediment roughness sublayer in Figures 6.8f and 6.8f, which show that the shear stress conditions are below critical in the near bed region for Exp. R-$GS_r h$ for both plane A and plane B. This is consistent with the transport parameter profiles observed for Exp. R-$G\lambda h$.

Table 6.4 shows that the shear velocity u_* at the top of the spheres is similar for the low and high submergence case suggesting that the intensity of the coherent structure generated, at least when the bed is stable, is similar. A lower bed shear stress τ_b is observed for Exp. R-$GS_r h$, being mainly related to a higher relative submergence. The zero-plane, being at the top of the spheres for Exp. R-$GS_r h$ confirms that the final stable bed level reached with a higher relative submergence is associated with skimming flow conditions.
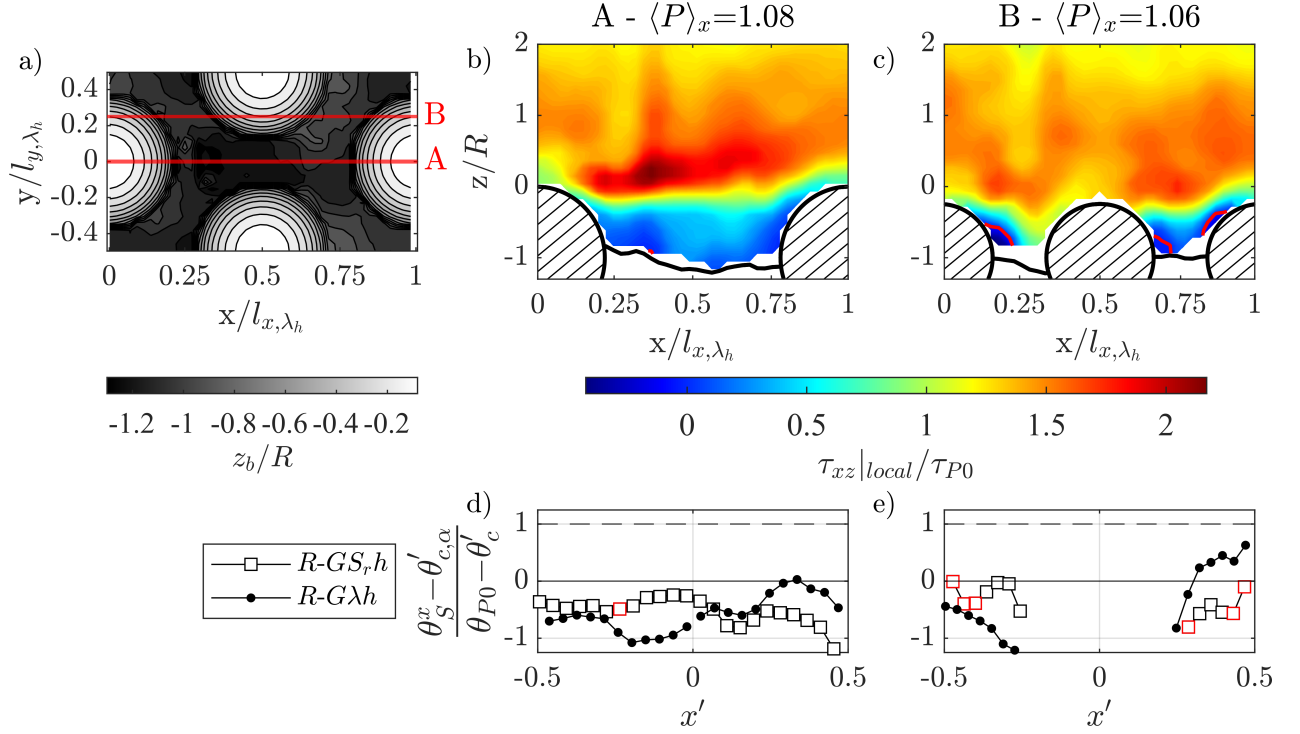
Figure 6.8: (a) Local fluid shear stress field $\tau_{xz}|_{local}$ normalized by the reference bed shear stress acting on a uniform fine-sediment bed τ_{P0} in plane A and plane B at the end of Exp. 8 ($S\theta l$), Exp. 9 ($S\theta m$) and Exp. 10 ($S\theta h$). (g-h) Longitudinal profiles of the fine-sediment transport parameter in streamwise direction θ_S^x-θ_c' determined at the top of the fine-sediment roughness sublayer h_{rs}^s (=d_{50}) and normalized by the transport parameter for a uniform bed θ_{P0}-θ_c' for Exp. 8, Exp. 9, Exp. 10 in comparison with the reference Exp. 1 R-$G\lambda h$. The red symbols identify negative shear stress conditions. x' is a local coordinate system centred in the pattern and normalized by the distance between the spheres b (see Figure 5.21).

Exp.	plane	$\langle P \rangle$	$\langle P \rangle_x$	$\sigma_{z,G}$	λ_p	λ_f	δ	S_r	u_*	τ_b	k_s	$z_d/\langle k \rangle$
		[-]	[-]	[cm]	[-]	[-]	[cm]	[-]	[cm/s]	[Pa]	[cm]	[-]
R-$G\lambda h$	A	0.98	0.93	0.37	0.51	0.30	2.9	3.9	2.57	0.81	0.85	0.00
	B	0.98	1.00	0.37	0.51	0.29	2.7	3.8	2.63	0.85	0.85	0.00
R-$GS_r h$	A	1.05	1.08	0.41	0.52	0.31	6.4	7.1	2.48	0.70	1.02	−0.03
	B	1.08	1.06	0.42	0.51	0.31	6.1	6.6	2.52	0.70	1.08	−0.03
							±0.06	±0.03	±0.01	±0.005

Table 6.4: Roughness and boundary layer parameters for the experiments with variations in relative submergence: pattern scale protrusion level $\langle P \rangle$, streamwise averaged protrusion level in the PIV plane $\langle P \rangle_x$, standard deviation of bed elevations at the pattern scale $\sigma_{z,G}$, planar density λ_p, frontal density λ_f, boundary layer depth δ, relative submergence of the pattern $S_r = (\delta + \langle P \rangle)/\langle P \rangle$, shear velocity u_* obtained from the linear extrapolation of the total fluid shear stress τ_{xz} to the top of the spheres, bed shear stress τ_b, equivalent sand roughness k_s, roughness displacement length z_d normalized by the protrusion height of the spheres $\langle k \rangle$ (= $\langle P \rangle R$).

6.4 Influence of the sediment size d_{50} on the morpho- and hydrodynamics

In this Section, the impact of the size of the sediments on the bed morhodynamics and on the flow patterns within the bed interstices is analysed. The analysis is focussed on Exp. 8 ($S\theta l$), Exp. 9 ($S\theta m$) and Exp. 10 ($S\theta h$), characterized by a smaller median size of the fine-sediments (sand) and by increasing Shields parameter. Exp. 1 (R-$G\lambda h$) The analysis of the bed morphodynamics is performed at the pattern scale within the pattern of spheres in the centre of the channel (see Figure 3.2a).

6.4.1 Bed morphodynamics (d_{50})

For the analysis of the bed morphodynamics only a qualitative overview of the temporal evolution of the bed is given, since the pattern recognition technique applied (described in Section 3.4.2.4) did not allow to obtain accurate bed topographies for high protrusion levels of the spheres. This is connected to the fact, that the sand used does not have a strong texture like the plastic granulate, so that when the correlation box is applied to an image area containing in part a sphere (with the limitation any way that it should not cover more than 20 % of the pattern), the correlation box is shifted in the search of the best match in the second stereo-image towards the sphere, biasing the results. The evolution of the pattern averaged protrusion levels is given in Figure 6.9 for Exp. $S\theta m$ and Exp. $S\theta h$ and for the reference Exp. R-$G\lambda h$. The protrusion levels for Exp. $S\theta m$ and Exp. $S\theta h$ are reliable in the absence of spheres, i.e. for $\langle P \rangle < 0$, while when the spheres protrude, the values of $\langle P \rangle$ are underestimated. For the maximum protrusion levels reached, the underestimation is approximately equal to 0.2-0.4.

Figure 6.9 illustrates only the $\langle P \rangle$-profiles for Exp. $S\theta m$ and Exp. $S\theta h$ compared to the reference Exp. R-$G\lambda h$. Exp. $S\theta l$, not illustrated, shows a similar behaviour. It is observed that the temporal evolution of $\langle P \rangle$ for Exp. $S\theta m$ and Exp. $S\theta h$ is significantly different than the one observed in the reference Exp. R-$G\lambda h$ where plastic granulate was used. The $\langle P \rangle$-profiles for Exp. $S\theta m$ and Exp. $S\theta h$ are characterized by strong oscillation due to the passage of dunes, which persist on the bed for the whole duration of the experiments.
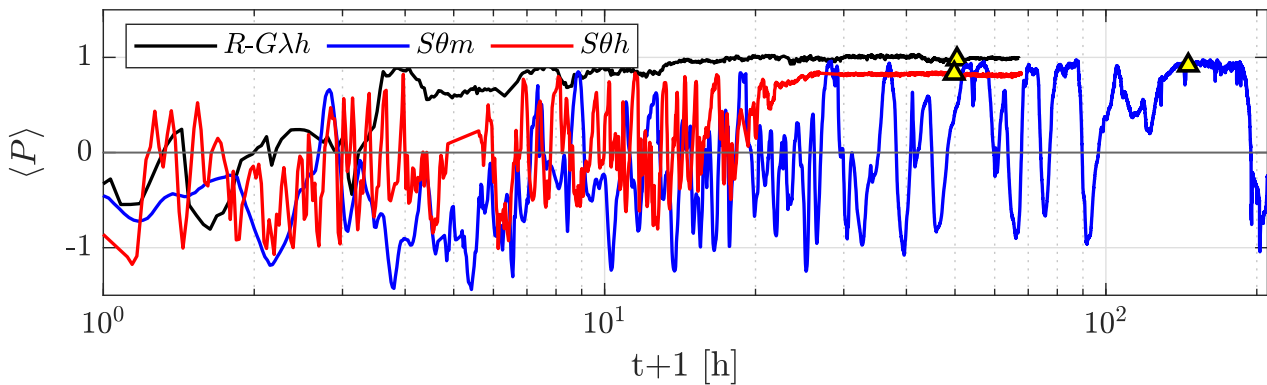

Figure 6.9: Temporal profiles of the pattern-averaged protrusion level $\langle P \rangle$ during the Exp. 9 (S-$G\theta m$) and 10 (S-$G\theta h$) compared to the reference Exp. 1 (R-$G\lambda h$). The yellow triangles identify the times at which the PIV measurements were performed. The t-axis is shifted by 1 hour for visualization purposes.

Only in Exp. $S\theta h$, characterized by the highest Shields parameter, the dunes disappeared at the end of the experiments. Compared to the Reference Exp. $R\text{-}G\lambda h$, where two-dimentional dunes were observed, in the experiments with sand the dunes were completely three-dimensional. It is noteworthy that the dunes occupy approximately the same region above and below the top of the spheres (for example, in the case of Exp. $S\theta m$ approximately 1.2 cm above and 1.2 cm below). Values of the height of the dunes predicted with the empirical formula by (van Rijn, 1984b) for dunes developing over uniform fine-sediment bed, were 50% smaller than the ones observed. The increased dunes' height can be connected to the interaction between the dunes and the spheres. It was visually observed that, when a sphere was uncovered by a dune passing by, a strong horseshoe vortex developed around the sphere supplementing the dune with new material and inducing strong localized erosion. It is hypothesized that the three-dimensionality of the flow field around the dunes sustained this self-enhancing process. This self-enhancing process was not observed for the plastic granulate probably because of the small size of the coherent structures shed within the horseshoe vortex for low levels of protrusion of the spheres compared to the size of the sediments.

6.4.2 Shear stress distribution in the bed interstices (d_{50})

In this Section, the PIV measurement performed at the end of Exp. $S\theta l$, Exp.$S\theta m$ and Exp. $S\theta h$ in plane A and in plane B are analysed and compared to the ones performed at the end of the reference Exp. $R\text{-}G\lambda h$. The PIV measurements were performed during Exp. $S\theta m$ and Exp. $S\theta h$ in the absence of dunes when the protrusion level of the spheres was the highest (see the triangles in Figure 6.9). The PIV measurements during Exp. ($S\theta l$) were performed instead in the stoss side of a dune. The local bed elevation was obtained on the basis of the PIV images so that the geometric features of the fine-sediment bed could be reconstructed, as reported in Table 6.5. It is observed that independently of the Shields parameters, approximately the same bed levels are observed for Exp. $S\theta l$, Exp.$S\theta m$ and Exp. $S\theta h$. Figures 6.10a-f show the local fluid shear stress fields $\tau_{xz}|_{local}$ normalized by the reference bed shear stress acting on a flat, uniform bed τ_{P0} in Exp. $S\theta l$, Exp. $S\theta m$ and Exp. $S\theta h$ for both plane A and plane B. Figures 6.10a and 6.10d show that in Exp. $S\theta l$ a shear layer at an elevation z/$R \simeq 1.5$ is present both in plane A and in plane B. The shear layer at the top of the spheres appears to be significantly attenuated and the fine sediment bed is characterized by negative shear stresses. Figures 6.10b and 6.10e show that in Exp. $S\theta m$, characterized by intermediate Sields parameters, a shear layer develops at the top of the spheres with an intensity equal to about two times τ_{P0}. The near-bed region is characterize by reduced shear stress. In Exp. $S\theta h$, characterized by the highest Shields parameter, the shear layer is stronger and equal to 3 times τ_{P0} (see Figure 5.12c). The bed interstices present a region of predominant negative shear stresses in the lee side and damped shear stress in the stoss side. Overall, the shear stress patterns observed for Exp. $S\theta m$ and $S\theta h$ are comparable to the ones observed in the reference Exp. $R\text{-}G\lambda h$ in Figures 5.12d and 5.12h, characterized by a net separation of the shear layer from the reduced shear stress region in the bed interstices. It is noteworthy that the bed topography in the case of sand is characterized by a sediment deposit in the centre of the pattern (see Figures 5.12b-c), while in the presence of gravel it forms in the lee side of the spheres.

Figures 6.10g-h show the streamwise transport parameter $\theta_s^x - \theta_c'$ measured at the top of the fine-sediment roughness sublayer and normalized by the transport parameter for a uniform fine-sediment bed $\theta_{P0} - \theta_c'$. The fine-sediment roughness sublayer is considered to be equal to one d_{50} also for the sand, under the conditions that the sediments are not moving (see Section 5.3.5). In plane A, Figure 6.10g shows that both in the case
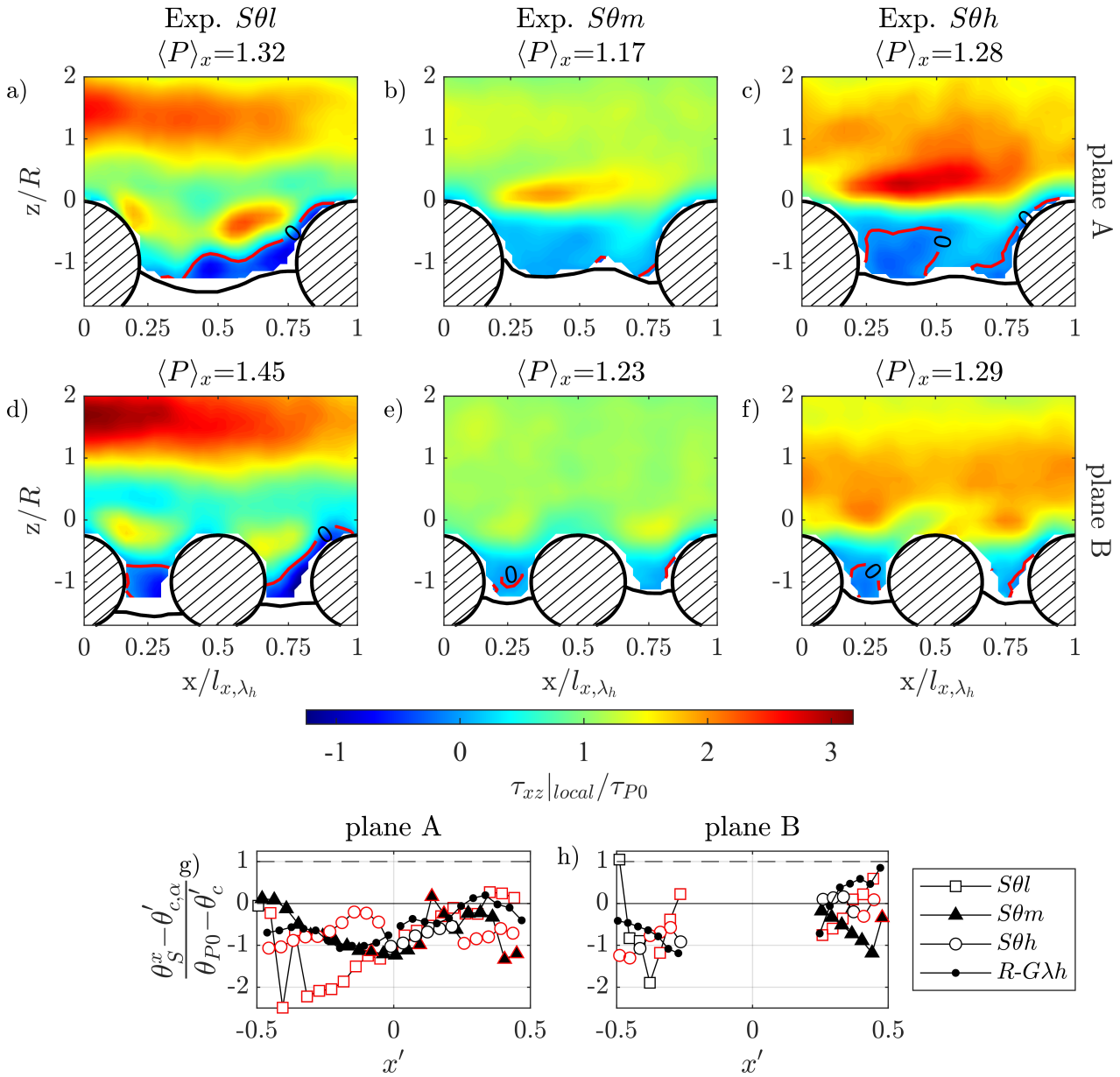
Figure 6.10: (a-f) Local fluid shear stress fields $\tau_{xz}|_{local}$ normalized by the reference bed shear stress acting on a uniform fine-sediment bed τ_{P0} in plane A and plane B at the end of Exp. 8 ($S\theta l$), Exp. 9 ($S\theta m$) and Exp. 10 ($S\theta h$). (g-h) Longitudinal profiles of the fine-sediment transport parameter in streamwise direction θ_S^x-θ_c' determined at the top of the fine-sediment roughness sublayer h_{rs}^s (=d_{50}) and normalized by the transport parameter for a uniform bed θ_{P0}-θ_c' for Exp. 8, Exp. 9, Exp. 10 in comparison with the reference Exp. 1 R-$G\lambda h$. The red symbols identify negative shear stress conditions. x' is a local coordinate system centred in the pattern and normalized by the distance between the spheres b (see Figure 5.21).

of the experiments with sand and in the case of the reference Exp. $R\text{-}G\lambda h$, the shear stress condition are below critical conditions of motion in the lee side of the spheres and at critical conditions of motions in the stoss side, suggesting local intermittent sediment transport. In plane B, 6.10h shows that the shear stress conditions are below or at the critical conditions of motion for all Exp. with sand. As such both planes are stable.

Table 6.5 illustrates the boundary layer parameters for the reference Exp. $R\text{-}G\lambda h$ and the three experiments with sand. First the shear velocity u_* is analysed determined from the extrapolation of the double averaged total fluid shear stress to the top of the spheres (in the case of the dune in Exp. $S\theta l$ u_* is not given due to the presence of the dune's shear layer high above the bed). It is observed that for Exp. $S\theta m$ and $S\theta h$, u_* increases with the Shields parameter. The protrusion levels do not change significantly, though. This suggests that the final protrusion level is not the result of the erosion induced by the coherent structures shed by the shear layer at the spheres' top, but of coherent structures associated with the three-dimensional dunes characterized by stronger magnitudes. In the presence of the dune, Exp. $S\theta l$ shows, in fact, a higher protrusion level, even though the Shields parameter is lower than Exp. $S\theta m$ and $S\theta h$. The Exp. $S\theta m$ and $S\theta h$ are characterized by a zero-plane positioned close to the top of the spheres, which suggest skimming flow conditions as in the case of the reference Experiment $R\text{-}G\lambda h$. The planar density is effectively close to 0.5.

Exp.	plane	θ	$\langle P \rangle$	$\langle P \rangle_x$	$\sigma_{z,G}$	λ_p	λ_f	δ	S_r	u_*	τ_b	k_s	$z_d/\langle k \rangle$
			[-]	[-]	[cm]	[-]	[-]	[cm]	[-]	[cm/s]	[Pa]	[cm]	[-]
$R\text{-}G\lambda h$	A	0.065	0.98	0.93	0.37	0.51	0.30	2.9	2.9	2.57	0.81	0.85	−0.004
	B	0.065	0.98	1.00	0.37	0.51	0.29	2.7	2.8	2.63	0.85	0.85	−0.003
$S\theta l$	A	0.049	1.41	1.32	0.28	0.54	0.41	5.0	4.5				
	B	0.049	1.41	1.45	0.28	0.54	0.41	5.2	4.7				
$S\theta m$	A	0.069	1.21	1.17	0.27	0.51	0.33	5.7	4.7	2.29	0.59	1.61	−0.05
	B	0.069	1.21	1.23	0.27	0.51	0.33	5.7	4.7	2.28	0.59	1.49	−0.07
$S\theta h$	A	0.0106	1.28	1.28	0.28	0.49	0.36	5.2	5.1	2.93	0.99	1.16	−0.05
	B	0.0106	1.28	1.29	0.28	0.49	0.36	5.1	4.9	2.84	0.93	0.95	−0.02
										±0.06	±0.03	±0.01	±0.005

Table 6.5: Roughness and boundary layer parameters for the experiments with sand: pattern scale protrusion level $\langle P \rangle$, streamwise averaged protrusion level in the PIV plane $\langle P \rangle_x$, standard deviation of bed elevations at the pattern scale $\sigma_{z,G}$, planar density λ_p, frontal density λ_f, boundary layer depth δ, relative submergence of the pattern $S_r = (\delta + \langle P \rangle)/\langle P \rangle$, shear velocity u_* obtained from the linear extrapolation of the total fluid shear stress τ_{xz} to the top of the spheres, bed shear stress τ_b, equivalent sand roughness k_s, roughness displacement length z_d normalized by the protrusion height of the spheres $\langle k \rangle$ $(= \langle P \rangle R)$.

6.5 Shear stress partitioning

The shear stress acting on the fine sediments was observed to vary significantly both in space and in time as the result of the increasing protrusion level of the spheres. In order to analyse the sheltering effect of the protruding spheres on the fine sediments, the pattern-averaged fine-sediment shear stress $\langle \tau_s \rangle$ and the local

maximum fine-sediment shear stress $\tau_{s,max}$ are compared to the bed shear stress τ_b in the following. The pattern-averaged fine-sediment shear stress $\langle \tau_s \rangle$ is determined by spatially averaging the fine sediment shear stress in the longitudinal direction τ_s^x obtained at the top of the fine-sediment roughness sublayer in plane A and plane B. τ_b is determined, in first approximation, as spatial average between the values obtained in plane A and in plane B. The measured pattern-averaged and maximum shear-stresses are compared to the prediction based on the shear stress partitioning model by Raupach et al. (1993). The model assumes, that the ratio $\langle \tau_s \rangle / \tau_b$ can be determined on the basis of the frontal density of the protruding roughness elements as follows:

$$\frac{\langle \tau_s \rangle}{\tau_b} = \frac{1}{(1 - \sigma \lambda_f)(1 + \beta_R \lambda_f)} \tag{6.1}$$

where $\sigma = \lambda_p / \lambda_f$ and $\beta_R = C_{d,R} / C_{d,S}$ with $C_{d,R}$ the drag coefficient for an isolated roughness element and $C_{d,S}$ the drag coefficient of the fine-sediment surface in the absence of protruding roughness elements. $C_{d,S}$ is determined on the basis of the PIV measurements over a uniform fine-sediment bed performed in Chapter 4 as $\tau_{P0} = \rho_f C_{d,S} U^2$. For the plastic granulate $C_{d,S} = 0.0045$ and for the sand $C_{d,S} = 0.004$. A value of $C_{d,R} = 0.36$ is used, as suggested by Schmeeckle et al. (2007) who measured the drag forces on spherical particles with different degrees of exposure over a rough bed. The maximum shear stress $\tau_{s,max}$ is predicted by Raupach et al. (1993) by making the empirical assumption that $\tau_{s,max}$ for a certain surface is equal to $\langle \tau_s \rangle$ for a less dense surface composed of the same roughness elements. By introducing a coefficient $m < 1$ for the reduction of the frontal density, $\tau_{s,max}$ is given by:

$$\frac{\tau_{s,max}}{\tau_b} = \frac{1}{(1 - m\sigma \lambda_f)(1 + m\beta_R \lambda_f)} \tag{6.2}$$

Figures 6.11a and 6.11b show the evolution of $\langle \tau_s \rangle$ and $\tau_{s,max}$ with the protrusion level of the immobile spheres. The data are grouped according to the type of fine-sediment used, plastic granulate (G) or sand (S) and to the roughness density of the top layer of spheres, i.e. high (λ_h), intermediate (λ_m) or low (λ_l), as the parameters of the Raupach model depend on these two factors. The lines (coloured like the corresponding dataset) represent the prediction obtained with the Raupach et al. (1993) model. In Figure 6.11b it is distinguished between predictions obtained with $m = 0.05$ (dashed lines) and with $m = 0.2$ (continuous lines).

Figure 6.11a shows that the spatially averaged shear stress $\langle \tau_s \rangle$ acting on the fine-sediments decreases with increasing protrusion level of the spheres $\langle P \rangle$. For protrusion levels higher than 1, $\langle \tau_s \rangle$ is less than 15% of the total bed shear stress. It is observed, that for $\langle P \rangle > 1$, also negative shear stress conditions can act predominantly on the fine-sediments. The Raupach model is observed to deviate significantly from the measured data for protrusion levels $\langle P \rangle < 0.8$ (see the red dataset $G\lambda_h$). For high protrusion levels $\langle P \rangle > 0.8$, there is very good agreement between the model and the measured $\langle \tau_s \rangle$ for the datasets $G\lambda_h$, $G\lambda_m$ and $G\lambda_l$. This result is quite remarkable since the Raupach model was developed, strictly speaking for roughness elements with frontal densities less than 0.1. The data just mentioned are characterized, instead by frontal densities higher than 0.3. In the case of dataset $S\lambda_h$ (black symbols), the Raupach model does manage to predict the negative shear stress conditions. It should be stressed, though, that the spatial average is performed only on two plains, so that, strictly speaking, the measured $\langle \tau_s \rangle$ is not spatially converged.

Figure 6.11b shows that the maximum shear stress $\tau_{s,max}$ is slightly higher than 1 for zero protrusion level, i.e. for the uniform fine-sediment bed. As shown in Figure 4.3b, the shear stress conditions are spatially inhomogeneous in the near bed region due to the presence of the roughness sublayer, so that ratios $\tau_{s,max}/\tau_b$
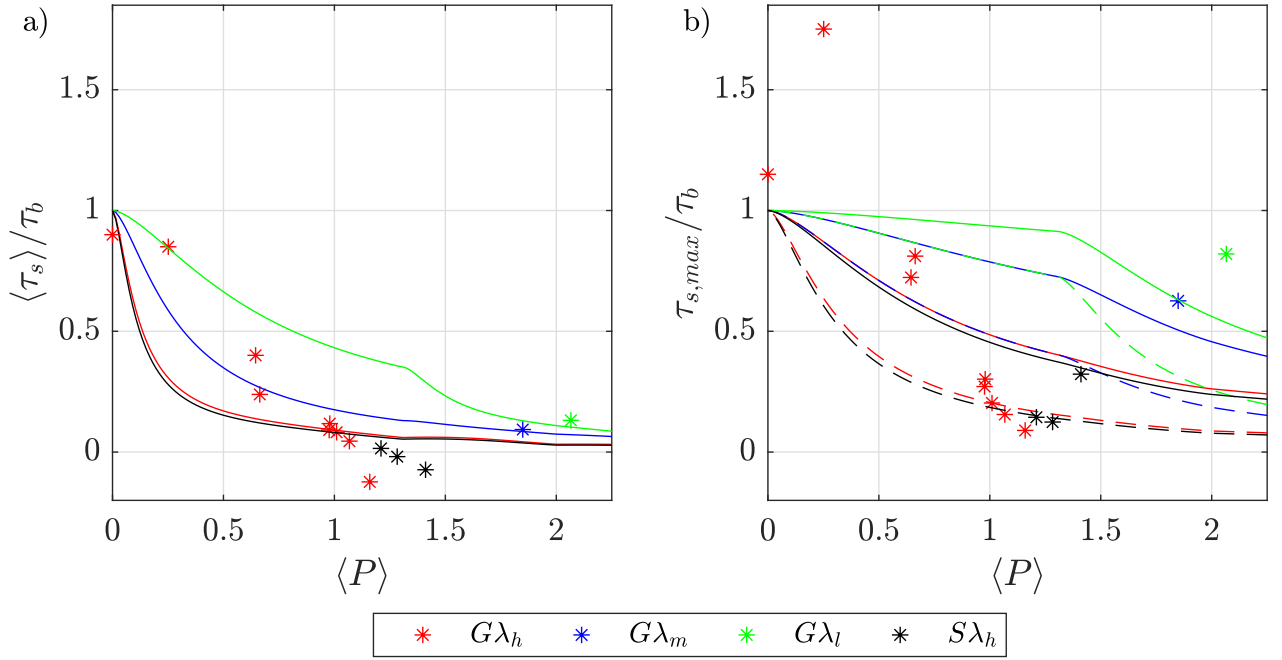
Figure 6.11: Variation of the pattern-averaged shear stress $\langle \tau_s \rangle$ (a) and of the maximum shear stress $\tau_{s,max}$ (b) acting on the fine sediments (measured at the top of the fine-sediment roughness sublayer h_{rs}^s) normalized by the total bed shear stress as a funtion of the pattern averaged protrusion level $\langle P \rangle$. The acronyms in the legend represent experiments performed with gravel (G) or sand (S) and with high (λ_h), medium (λ_m) or low (λ_l) roughness density of the immobile bed of spheres. The continuous lines in (a) correspond to the predictions based on Equation 6.1 by Raupach et al. (1993). The lines in (b) correspond to the prediction based on Equation 6.2 with $m = 0.05$ (continuous line) and $m = 0.2$ (dashed line).

$\neq 1$ are possible. For $\langle P \rangle = 0.25$, $\tau_{s,max}$ reaches a peak equal to 1.7 times the bed shear stress τ_b, confirming enhanced shear stress conditions for protrusion levels higher than the critical protrusion level in erosive behaviour P_{c1} (see Sections 2.3.4 and 5.2.2). For higher protrusion levels, the maximum shear stress decreases below the total bed shear stress, consistent with sheltering conditions. It is observed that $\tau_{s,max}$ increases with a reduction in the roughness density of the configuration of spheres. $\tau_{s,max}$ is only reduced by 20% for protrusion levels $\langle P \rangle > 2$ in the case of the lowest roughness density $G\lambda_l$. In the case of the intermediate roughness density $G\lambda_m$, $\tau_{s,max}$ is reduced by 40 % for $\langle P \rangle \simeq 1.7$, while the highest roughness density is charaterized by reductions up to 90 % for lower protrusion levels $\langle P \rangle \simeq 1$. This trend suggests that lower roughness densities are characterized by significantly reduced sheltering levels as compared to higher roughness densities, even though they might be characterized by similar spatially averaged shear stress conditions as Figure 6.11a shows.

The predictive capability of the Raupach model in the case of the maximum shear stresses is rather poor and highly dependent on the value of m. Figure 6.11b shows that the Raupach model is able to predict the maximum shear stress conditions for $\langle P \rangle > 1$ in the case of the datasets $G\lambda_h$ and $S\lambda_h$ for $m = 0.05$. In all other cases, huge discrepancies are evident for the m values chosen. First of all, the Raupach model cannot predict the shear stress enhancement for low protrusion levels. This is expected as the model was developed for the prediction of sheltering conditions. In the case of the data points for the low and intermediate roughness densities, $G\lambda_l$ and $G\lambda_m$, higher values of m would have given better predictions.

6.6 Clean-out depth

The parametric study performed in this Chapter, has shown that the protrusion level for which the fine-sediment bed becomes stable, varies significantly as a function of the fine-sediments used, of the roughness density of the immobile roughness elements and of the forcing conditions. The aim of this Section is to give an overview of the trends observed and to assess whether the maximum erosion depths observed, i.e. the clean-out depths z_{cd}, can be predicted by applying the model developed by Stradiotti et al. (2020) on the basis of dimensional analysis. The model assumes that the clean out depth of fine sediments from an immobile gravel bed follows the following power law:

$$\frac{z_{cd}}{D_{90}} = -aT_\theta^b \tag{6.3}$$

where D_{90} is the 90th-percentile of the cumulative density function of the grain sizes distribution of the immobile sediment bed fractions and $T_\theta = (\theta - \theta_c)/\theta_c$ [2] is the normalized sediment transport parameter defined on the basis of the shear stress conditions acting at the top of the roughness. The a- and b-coefficients were determined empirically and are equal to $a = 0.32$ and $b = 0.37$. Since here the immobile roughness elements are spheres, D_{90} is set equal to the sphere's diameter D. The normalized sediment transport parameter T_θ is estimated on the basis of the shear velocity obtained by linear extrapolation of the double-averaged total fluid shear stresses to the top of the spheres during the last PIV measurement at the end of the experiments when the highest stable protrusion level is reached. u_* is then spatially averaged over the PIV measurement planes
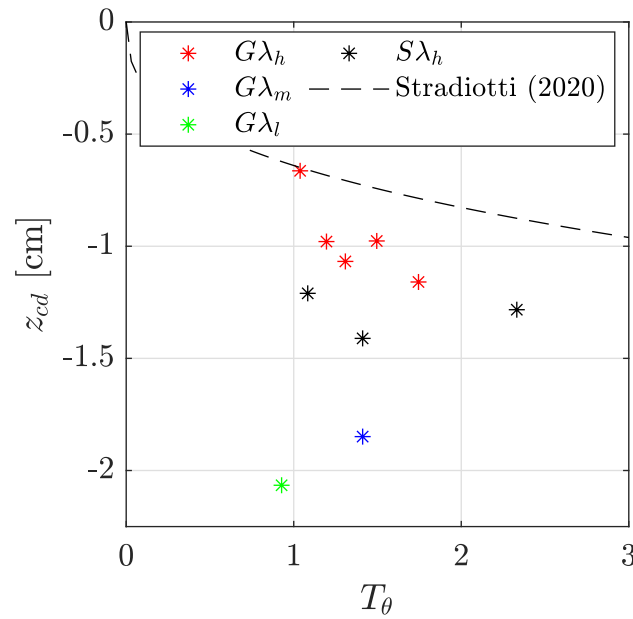

Figure 6.12: Clean-out depth z_{cd} as a function of the normalized transport stage parameter T_θ for the experiments with various combinations of fine sediments (G-gravel and S-sand) and roughness densities of the immbile bed of spheres (λ_h-high, λ_m-medium and low-λ_c. The dashed line represents the prediction of z_{co} based on equation 6.3 by Stradiotti et al. (2020).

---

[2] Please note that θ_c is the critical Shields parameter defined on the basis of the Shields diagram for permanent grain movement (see Section 3.2.2.1).

A and B. The clean-out depth is measured, at the same time, as the spatial average of the bed-elevation within the reference measurement pattern.

Figure 6.12 shows the clean-out depth z_{cd} as a function of T_θ with the data grouped according to the type of fine-sediment used, plastic granulate (G) or sand (S) and to the roughness density of the top layer of spheres, i.e. high (λ_h), intermediate (λ_m) or low (λ_l), as the parameters of the Raupach model depend on these two factors. The dashed line corresponds to the prediction based on the model by Stradiotti.

Figure 6.12 shows that for the experiments performed with plastic granulate and the highest roughness density $G\lambda_h$ the clean-out depth decreases with increasing transport stage parameter T_θ. For similar transport stage parameters the clean out depth obtained with intermediate and low roughness densities $G\lambda_m$ and $G\lambda_l$, is significantly lower and decreases with decreasing roughness density. For the experiments performed with sand $S\lambda_h$ the clean out depth is approximately constant and independent of T_θ, due to the particular interactions between dunes and the immobile spheres (see Section 6.4).

The predictions by Stradiotti et al. (2020) are the closest to the clean out depths of the experiments $G\lambda_h$. The latter are characterized by high roughness densities consistent with the high roughness densities of gravel beds for which the model was tuned. The model breaks completely down in the case variations of the roughness density of the first layer of spheres are considered, as it does not account for the dependency of z_{cd} on the roughness density. A model which takes into account the density of the immobile roughness elements, is the model by Kuhnle et al. (2016) which scales the shear stress acting on the fine sediments with the square root of the roughness geometry function and the shear stress acting at the spheres' top. The model defines the clean-out depth as the bed level for which the level of the roughness geometry function induces a reduction of the shear stress to condition of no sediment movement. The model is difficult to apply when the roughness geometry function is not a monotonic function of the vertical direction, as in this case.

6.7 Conclusions

In this Chapter, a parameteric study was conducted in order to assess how the erosion of fine sediments from an immobile rough bed is influenced by changes in Shields parameter θ, in roughness density of the first layer of immobile spheres λ_f, in relative submergence S_r and in fine-sediment size d_{50}.

Changes in the Shields parameter revealed that the evolution of the bed becomes faster and higher erosion depths associated with a stable bed are reached by the system with increasing θ. Compared to the results in Part I, higher erosion depths were observed for a two-layered immobile sphere's bed compared to a one-layered for similar flow conditions, suggesting an influence of the hyporheic flow conditions on the erosion. For all Shields parameters investigated, three transitions in erosive behaviour were observed equal to the ones observed in Part I. Independently of the Shields parameter, the three transitions in erosive behaviour take place at approximately the same protrusion levels, consistent with the results of the first experimental campaign in Part I. The critical erosion rates and the critical concentration of displaced sediments showed an increasing trend followed by a decreasing one with increasing Shields parameter in contrast with the clear increasing trend observed in the results of the first series of experiments in Part I. Further investigations are needed to explain this difference.

The shear stress patterns within the bed interstices measured when the maximum erosion is reached are independent of the Shields parameter and characterized by a net separation between the shear layer characterized

by higher shear stresses and the near-bed region characterized by damped shear stresses. Critical conditions of motions are effectively observed for all Shields parameters investigated when the bed reaches a stable level, suggesting complete sheltering. The fact that the zero-plane is positioned at the top of the spheres independently of the Shields parameter, when the bed is stable, suggests that skimming flow are necessary to reach complete sheltering.

Variations of the roughness density of the first layer of spheres from sparse to dense show that the bed is eroded down to the second layer of spheres for the sparse and medium roughness densities, while for the dense one the erosion stops within the first layer. The evolution of the system is similar for the sparse and medium roughness density as long as the bed levels remain within the first layer of spheres, suggesting that the protruding spheres do not alter significantly the erosive conditions. Once the second layer of spheres with a dense bed configuration is reached a fast evolution is observed with trends similar to the ones observed for a dense configuration of spheres of the first layer of spheres. Higher erosion depths in the second layer of spheres are observed for the sparse configuration compared to the medium. This suggests that, even though the second layer of spheres is common for both bed configurations, the upper layer with a medium density offers a higher degree of sheltering compared to the sparse one. For the sparse and medium roughness configurations, the erosion depths are quite heterogeneous in the transverse direction with higher local erosion depths observed in the alleys in between the spheres of the upper layer while lower erosion depths are observed at transverse locations in line with the spheres of the upper layer.

Shear stress patterns measured for stable bed conditions in the presence of the maximum erosion revealed that for sparse and medium roughness densities the shear layer behind the spheres spreads more within the bed interstices as compared to dense roughness configurations where the shear layer is displayed above the spheres due to the skimming flow conditions. For the sparse and medium roughness densities investigated rather isolated and wake-interference flow conditions are suggested. The lower protrusion depths behind the spheres in the top layer are connected to preferential negative shear stress conditions at the level of the fine sediments. The higher erosion depths observed in the alleys in between the spheres of the upper layer are associated for the medium density to a high shear stress regions penetrating down to the second layer of spheres and induced by the lateral spreading of the shear layers behind the spheres of the upper layer. For the sparse density, instead, the high local erosion in the alleys is connected to the development of shear layers at the top of the spheres in the second layer. Overall, it was observed that the actual reason for the bed to be stable within the second layer of spheres is that skimming flow conditions take over herein.

Changes in the relative submergence under the same shear stress conditions do not influence the final erosion depth. The evolution of the system is faster, though, for low relative submergences due to an increased vertical confinement of the shear layer. The shear stress patterns in the bed interstices, observed for stable bed conditions, are associated, also in this case, to skimming flow conditions and shear stress conditions below critical act on the fine sediments.

Overall, the analysis of the influence of the Shields parameter, of the roughness density of the spheres and of the relative submergence on the erosive process has shown that the three transitions in erosive behaviour can be associated to the geometric characteristic of the bed and are independent of the three parameters analysed. The first transition is associated to angles of attack of the spheres of approximately 20°-30°, while the second and third transitions to a planar density of the spheres $\lambda_p = 0.3$ and $\lambda_p = 0.5$, respectively.

To analyse the changes in fine-sediment size, experiments with sand with increasing Shields parameter are performed. The system is characterized by the development of three-dimensional dunes persisting on the bed

for the whole duration of the experiments. The dunes stretch both above and below the top of the spheres by the same amount and cause deeper erosion within the bed interstices as compared to a bed composed of sediments of larger size given the same shear stress conditions. The deeper erosion is suggested to be connected to a coupling between the coherent structures shed by the dunes and the horseshoe vortices, enhancing the erosive potential of the latter. Independently of the Shields parameter, the same maximum erosion depth is observed. Flow measurements performed during periods of absence of dunes show, though, that, the intensity of the shear layers increases with the Shields parameter. Since the maximum erosion rates are not connected to the shear layers developing at the spheres' top, they must have been the result of intenser coherent structures arising from the interaction between the dunes and the spheres. The bed interstices are found to be characterized by skimming flow conditions also in this case. The maximum erosion depth reached is higher than the ones which would have set in if the erosion would have been only dominated by the developing shear layer at the spheres' top.

In order to charaterize the overall effect of the spheres on the fine-sediment erosion, the sheltering effect of the spheres is analysed for roughness densities ranging from rough to dense. Overall the average shear stress acting on the fine-sediments reduces with increasing protrusion levels of the spheres reaching just 10 % of the total bed shear stress for bed conditions characterized by stable bed levels. The maximum shear stress acting on the fine-sediments shows a peak for protrusion levels $P \simeq 0.2$ for the densest sphere configuration consistent with enhanced erosion rates. For higher protrusion levels the maximum shear stress decreases. For the sparse and dense roughness configurations the maximum shear stresses are below the total bed shear stress but are higher than the ones characterising the dense roughness configuration for protrusion levels higher than 1. The applicability of the Raupach model is also assessed, showing that it is able to predict the spatially averaged shear stress conditions on the fine-sediments for high level of protrusion. The model is also effective in predicting the maximum shear stresses, given that the appropriate m parameter is given, which is in general not known a priori.

Finally the applicability of the model of Stradiotti for the presiction of the clean-out depth is assessed, showing that the predictive capability of the model is limited. It does not consider relevant factors, such as roughness density of the immobile roughness for the prediction of the clean-out depth.

7 Conclusions

In sediment-supply limited river systems, such as mountain streams, river reaches below dams or gravel-sand transition in low-land rivers, the transport of fine-sediments takes place for most of the flow conditions over an immobile rough bed of coarse grains. Under these circumstances, the prediction of the fine-sediment transport is quite challenging, as the protruding immobile coarse grains either increase or decrease the fine sediment transport rates depending on their protrusion level. However, the level of protrusion for which enhanced erosion or grain sheltering predominate and which are the hydrodynamic processes involved, is still an open question. At a larger bedform scale, the reduced surface availability of fine mobile sediments caused by the protruding immobile grains, leads to the formation of ridges causing transverse heterogeneities in erosive behaviour. Till now, though, the temporal evolution of the ridges and the connected changes in secondary flow intensity has not been described yet. To answer these two open questions, this work has analysed experimentally the hydro- and morphodynamic processes connected to the erosion of fine-sediments from an artificial immobile rough bed of spheres under sediment-supply limited conditions. On the basis of two laboratory campaigns, a top-down approach was implemented analysing first the bed morphodynamics at the bedform scale and then narrowing down the focus to the roughness scale with particular emphasis on changes in the hydrodynamics near the fine-sediment bed, as the fine sediments are eroded. The originality of this work lies in the development of a new experimental setup able to resolve simultaneously for the first time the bed topography, the sediment transport and the flow field, also in the bed interstices in between roughness elements.

Experimental approach

Two laboratory campaigns were performed in a tilting flume, 9m long and 30 cm wide, to analyse the erosion of an initially uniform fine sediment bed covering an immobile coarse bed of spheres (2 cm in diameter) disposed in a staggered symmetric pattern. The first laboratory campaing was primarily designed to analyse the ridge morphodynamics while the second laboratory campaign to investigate the fine-sediment bed morphodynamics and the coupled near bed hydrodynamics at the scale of a characteristic spheres' pattern.
In the first laboratory campaign (discussed in Part I), the fine sediments were modelled with plastic granulate (1.72 mm in size) and the immobile gravel with just one layer of spheres. A total of seven experiments were performed by either varying the aspect ratio $A = [3, 5, 6.5]$ and keeping the Shields parameter constant ($\theta = 0.11$) or vice-versa with $\theta = [0.11, 0.15, 0.18]$ and $A = 5$ (Section 2.2.3). The bed topography was measured continuously during the experiments with a camera positioned above the flume (Section 2.2.4.1), which allowed to determine the protrusion level of each sphere $P = k/R$ (where k is the average protrusion height of a sphere) on the basis of the sphere's exposed planar area. Flow field measurements above the top of the spheres were performed with a side-looking 2D planar PIV system at selected times over two vertical planes positioned both in the centre and in the quarter plane of the channel to analyse the flow over ridges

and troughs (Section 2.2.4.2).

In the second laboratory campaign (discussed in Part II), the immobile bed configuration was improved by adding a second layer of spheres in order to obtain hyporeic flow conditions closer to a permeable bed. A parametric study with a total of 10 experiments was performed by varying two flow parameters (the Shields parameter θ and the relative submergence of the spheres S_r) and two geometric parameters of the bed (the roughness density of the first layer of spheres λ_f and the grain size of the fine-sediments d_{50}) to assess their influence on the erosion of the fine-sediments and on the near-bed hydrodynamics at the pattern-scale (Section 3.2.2). Four Shields parameters θ = [0.045, 0.055, 0.065, 0.11] were investigated to analyse shear stress conditions closer to the critical conditions of motion. By varying the relative submergence S_r = [2.9, 5.4], the influence of the intensity of the coherent structures developing around the protruding spheres on the erosion processes was studied. The values of roughness density λ_f = [0.003, 0.13, 0.53] were chosen so as to investigate different flow regimes from isolated to skimming flow when the spheres protrude from the fine-sediment bed. Besides the plastic granulate, the erosion of fine sand with a diameter of 0.43 mm was also investigated. For the analysis of the morpho- and hydrodynamics at the pattern scale in the second laboratory campaign, a new experimental setup was developed with the aim of measuring simultaneously the bed topography (with a higher resolution compared to the measurements of the first laboratory campaign), the sediment transport rates and the flow field deep in between the protruding spheres and not only above (Chapter 3). The experimental setup was composed of a stereo-PIV system (Section 3.4.1) and a stereo photogrammetric system (Section 3.4.2). A stereo-PIV system composed of two cameras positioned above the flume at a horizontal stereo-angle of 26° and imaging the flow from above at a steep vertical angle of 20° was conceived, to reconstruct the 3D velocity field deep inside the bed interstices of a reference pattern of spheres in the centre of the channel. The stereo-photogrammetric system was installed at the same location with two cameras positioned symmetrically to each other at a stereo angle of 18° above the flume in the centre of the channel. Via the stereo-photogrammetric system, the fine-sediment bed was reconstructed with a resolution of 1 mm. The stereo photogrammetric system was used also for sediment transport measurement by recording a sequence of bed images at a high frequency and by determining the number of displaced grains via image subtraction.

A new stereo PIV setup for flow measurements within the bed interstices

To the knowledge of the author, this work manages for the first time, to measure experimentally the flow field deep inside the canopy of a rough bed filled with sediments. Flow measurements within the canopy are quite challenging as traditional planar-PIV measurements are not feasible due to the restricted optical access and refractive-index matching techniques fail due to inappropriate flow scaling. To overcome these limitations, a stereo-PIV system with steep vertical viewing angles was developed. The two main issues related to a vertical viewing system, i.e. random image distortions due to the surface waves and laser reflections at the bed, were solved by installing a glass plate at the water surface and by seeding the flow with fluorescent particles, respectively. As far as the image distortions induced by the steep vertical viewing angles are concerned, the flow field measured with stereo-PIV system was validated with a planar side-looking PIV system (Appendix Section H.2). The influence of the boundary layer developing along the glass plate on the flow field was also investigated by comparing the same flow with and without the glass plate (Appendix Section H.3).

In the presence of steep vertical viewing angles, it is demonstrated that the stereo-PIV system is able to properly reconstruct the velocity field both above and within the bed interstices. Within the bed interstices, the

analysis via topological principles (Foss, 2004) of the mean in-plane velocity-vector field revealed it to be cinematically correct (Figure H.2). In the bulk flow region, the first, second and third order moments displayed similar trends between the stereo-PIV and planar-PIV measurements with slight discrepancies within the time-convergence error (Figure H.3). The second order moment of the vertical velocities represented the only exception, being overestimated by 20% by the stereo-PIV system. The overestimation of the vertical velocity fluctuations was associated to the strong deformation of the PIV particles induced by the dewarping process during the stereo-PIV processing, which enhances differences in the particle shape between stereo-PIV image frames due to differences in particle intensity, introducing in this manner a bias in the vertical particle displacement. Nevertheless, the instantaneous signals of the vertical velocity fluctuations was synchronous between the planar and the stereo-PIV showing that the turbulent events are well represented by the stereo-PIV, even though they might be slightly overestimated.

The analysis of the boundary layer developing along the surface glass plate highlighted that both the development of the boundary layer thickness and of the displacement thickness can be treated with traditional scaling power laws ($x^{4/5}$) for turbulent boundary layers developing along smooths plates in the form (Figure H.11). A virtual origin needs to be introduced, though, to account for a non-zero boundary layer depth at the upstream leading edge of the surface glass plate. The virtual origin and the proportionality factor of the power law increase and decrease respectively with the water depth super-elevation at the leading edge of the glass plate. The hydraulic conditions at the leading edge of the glass plate influence the boundary layer development in as much as they trigger an early transition to a turbulent boundary layer probably due to Görtler instabilities.

As far as the influence of the boundary layer on the flow field is concerned, the displacement thickness covers only 1% of the water depth, so that the flow acceleration induced by the developing boundary layer along the surface glass plate can be effectively neglected (Figure H.17). Comparison of the flow statistics with and without the surface glass plate show that the shear stress conditions near the bed are the same, since dominated by the shear production induced by the shear layers developing at the top of the spheres.

The morphodynamics of ridges and the evolution of the secondary currents

The morphodynamics of fine-sediment ridges in the presence of immobile roughness elements are analysed during the first measurement campaign discussed in Chapter 2. The presence of ridges is attested for all experiments when the spheres start to protrude from the fine-sediment bed. Initially, the bed is covered by three-dimensional reach-spanning dunes (Figure 2.6) which die out when the protruding spheres reduce the area covered by fine-sediments, limiting the sediment availability in accordance with Kleinhans et al. (2002). The transition between dunes and ridges does not happen abruptly, though, but a superimposition of the two types of bed-forms is observed with ridges developing in the tail of the dunes. While the life-time of the dunes is restricted to a few hours, the ridges shape the bed topography for days even when the fine-sediment bed level is below the top of the spheres (Figure 2.7). As soon as the dunes die out, the erosion takes place preferentially over the troughs than over the ridges. In the troughs, the fine-sediment bed level decreases within a few hours to a stable bed level below the top of the spheres. The ridge decrease, instead, in height over a much longer period of time, eventually reaching the same stable sediment-bed level as the troughs and creating a uniform rough bed (Figures 2.7 and 2.8b). The ridges act as such as continuous sediment sources, slowing down the process of sediment decolmation from clogged gravel beds.

The ridge morphology is characterized by an initial rapid increase of the ridge height and side-slopes and by a decrease of the ridge width (Figure 2.9). The resulting increase in the lateral roughness heterogeneity (given the increasing protrusion height of the spheres in the troughs and the preferential presence of fine-sediments over the ridge) and triangular ridge shape enhances the intensity of the secondary currents as studies on artificial ridges have shown (Wang and Cheng, 2006; Willingham et al., 2014). These cause increased shear stresses in the troughs, leading to a self-enhancing mechanism by which the ridge height is increased again, enhancing in turn the secondary currents. Eventually, the erosion in the trough reduces due to the sheltering effect of the protruding spheres, leading to similar erosion rates between the ridges and troughs. Thus, the ridge height and side-slopes reach a plateau. Once the troughs reach a stable bed level, the ridge height and side-slopes decrease over time. The width of the ridges reaches, instead, a constant value of approximately $20d_{50}$ after the initial decrease (Figure 2.10b).

The lateral position of the ridges meanders in the initial stages of the ridge development, stabilizing after approximately one day, yielding an inter-ridge spacing scaling with 1.3 times the effective water depth H_e (Figure 2.11) in agreement with the transverse ridge wavelength Λ_{Col} derived by Colombini and Parker (1995) as the result of the interaction with secondary currents triggered by an initial bed perturbation. For application purposes, the number of characteristic Λ_{Col}-wavelengths (N_Λ) which fit into the effective width of the channel defines the number of ridges developing on the bed, equal to the integer part of the number of N_Λ - 1 (Table 2.4). It should be underlined that the effective with of the channel results from the reduction of the actual width of the channel by the presence of side-wall accumulations. Thus, the prediction of the number of developing ridges requires an estimate of the width of the side-wall accumulations. For the cases when a non-integer number of wavelengths fit into the effective width of the channel, two cases can be distiguished. If the fractional part is higher than 0.5, a secondary unstable ridge develops which disappears over time. For a remaining fractional part less than 0.5, no additional ridges develop.

The flow measurements performed over the ridges revealed that the intensity of the upflow decreases and the streamwise velocity at the water surface increases (Figure 2.17), as the protrusion level of the spheres over the ridge increases (Figure 2.16), i.e. as the ridge height decreases. The ridges influence the secondary-currents' intensity, not only when they are elevated compared to the surrounding immobile roughness, but also when they are recessed. These changes in the intensity of the secondary flows are related both to topographical and roughness variations. For protrusion levels $P < 0.4$, the intensity of the secondary currents is mainly affected by changes in the ridge's height with the roughness of the ridge remaining almost unaltered. For protrusion levels $P > 0.4$, the opposite is true with changes in the lateral roughness heterogeneity being the predominant factor.

The higher shear stress conditions characterizing the troughs as compared to the ridges cause the higher erosion rates observed over the troughs than over the ridges (Figures 2.14 and 2.17). This difference in shear stress conditions derives from changes in the local vertical structure of the turbulence, as the quadrant analysis applied over the ridges and over the troughs revealed (Section 2.4.1). Indeed, the downflow taking place over the troughs concentrates the most intense sweeps in the near bed region leading to higher shear stresses and, as a result, higher local erosion. Over the ridges, instead, the upflow causes the sweep events with the highest intensity to be displaced higher up into the bulk flow to approximately 20% of the water depth leading to reduced local erosion.

Fine-sediment erosion enhancement and reduction by immobile coarse grains: a hydro and morphodynamic explanation

The impact of the protruding spheres on the fine-sediment erosion at the pattern scale was investigated from a morphodynamic point of view in Chapter 2 and from a hydrodynamic one in Chapter 5 with reference to the configuration of spheres with the highest roughness density $\lambda_f = 0.53$. A uniform fine-sediment bed with no protruding spheres was taken as a reference condition (Chapter 4). The analysis managed to identify, for the first time, how changes in the near-bed shear stress conditions induced by changes in the protrusion level of the spheres affect the erosive behaviour, as the fine sediments are eroded. The analysis of the erosion rates in Sections 2.3.4 and 5.2.2 attests an alternation of erosion reducing (sheltering) and enhancing conditions for increasing protrusion levels of the spheres, yielding four different erosive regimes. Figure 7.1 provides a schematic overview of the four erosive regimes along with the morpho-and hydrodynamic processes involved. An initial decrease in the erosion rates, characterizing the first erosive regime, is observed when the spheres start to protrude from the fine-sediment bed. Once a critical protrusion level $P_{c1} \simeq 0.2$ is reached, the erosion rates are enhanced within the second erosive regime. A local peak in erosion rates is reached at a critical protrusion level $P_{c2} \simeq 0.4$ and can attain values as high as two times the erosion rates over a uniform fine-sediment bed. For higher protrusion levels the erosion rates decrease again within the the third erosive regime. Once the protrusion levels surpass a critical value $P_{c3} \simeq 0.7$, the fourth erosive regime leads to very low erosion rates with the fine-sediment bed tending to a stable level.

The sediment transport rates follow a similar trend as the erosion rates (Section 5.2.2). A temporal lag between the peak in sediment transport rates and the peak in erosion rates is observed, though, suggesting a delay in how the sediment transport rates adapt to changes in the erosion rates.

The hydrodynamic processes responsible for the four erosive regime are investigated in Chapter 5 on the basis of flow-field measurements deep inside the canopy of the protruding spheres, possible thanks to the newly-developed stereo-PIV setup with steep viewing angles. As far as the first erosive regime is concerned, no flow field data are available since the bed evolution was too fast to collect them. Nevertheless, during the first erosive regime ($0 < P < P_{c1}$), the fine-sediment bed is eroded uniformly over the whole spheres' pattern with the absence of obstacle marks (Figure 5.3), such as frontal scours. This suggests the absence of coherent structures, such as horseshoe vortices, shed by the spheres. Therefore, the reduction in erosion rates observed in the first erosive regime, is the result of the increasing drag induced by the spheres as they start to protrude from the bed. The first erosive regime is thus identified as a *drag sheltering regime* (Figure 7.1).

During the second erosive regime ($P_{c1} < P < P_{c2}$), an intense shear layer develops at the top of the spheres (Figures 5.12a and 7.1), extending down into the bed interstices to the level of the fine sediments. The shear stresses near the fine-sediment bed are enhanced compared to a uniform fine-sediment bed (Figure 5.22a) leading to increased erosion rates. The enhancement is due to intense sweep events of high frequency and duration generated within the shear layer (Section 5.4.4) and advected by the dominant downflow towards the fine-sediment bed. As a result, significant turbulent kinetic energy production and transport towards the fine-sediment bed takes place within the bed interstices. Lower local shear stresses observed in the lee side of the spheres compared to the stoss side favours the development of sediment deposits in the lee side (the higher shear stresses in the stoss side of the sphere are probably the result of a developing horseshoe vortex). Since the shear layer is responsible for generating the intense turbulent events in the near-bed region, the second erosive regime is defined as *turbulence-enhancement regime*.
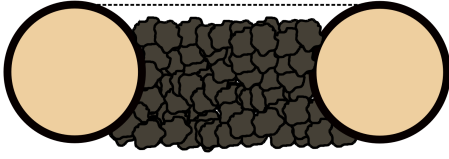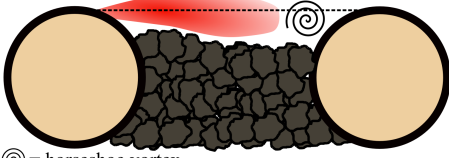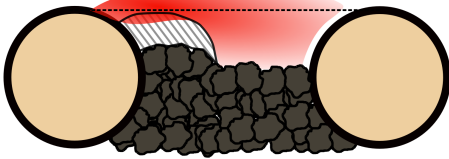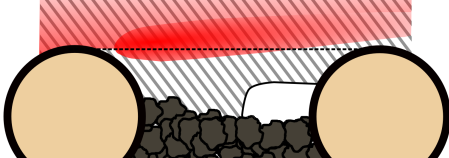
Erosive regimes	Geometric parameters (θ, S_r, λ_f -independant)	Interstitial upflow	Shear layer	Interstitial TKE exchange	Near-bed sweeps
1. drag sheltering	$0 < P < P_{c1}$ $P_{c1} = P(\alpha_a = 20°)$	Absent	Absent		
$P = P_{c1}$			low		high
2. turbulence enhancement ⊚ = horseshoe vortex	$P_{c1} < P < P_{c2}$ $P_{c2} = P(\lambda_p = 0.3)$	Absent	Intensity	active TKE production and transport	$\tau_{s,4}$ – $f_{4,0}$ – $D_{4,0}$
$P = P_{c2}$					
3. wake-interference sheltering	$P_{c2} < P < P_{c3}$ $P_{c3} = P(\lambda_p = 0.5)$	Sphere lee side (vorticity annihilation)	Intensity		
$P = P_{c3}$					
4. skimming-flow sheltering	$P > P_{c3}$ Stable bed	Sphere lee side + sphere top; high	high	Cut-off	low

Figure 7.1: Schematic representation of the erosion regimes with the corresponding range of occurrence based on the critical protrusion levels P_{ci} defined on the basis of the angle of attack α_a and of the planar density λ_p of the immobile roughness elements. The most relevant hydrodynamic processes are described with reference to the extension of the upflow region (identified by a diagonal line pattern), to the intensity and extension od the shear layer (red-shaded region with the intensity proportional to the saturation of the red colour), to the TKE exchange in the bed interstices and to the intensity $\tau_{s,4}$, frequency $f_{4,0}$ and duration $D_{4,0}$ of the sweep events.

In the third erosive regime ($P_{c2} < P < P_{c3}$), upflow conditions develop in the lee side of the spheres due to the presence of a sediment shadow (Figures 5.8f and 7.1), preventing the shear layer to reach the fine-sediment bed. The resulting reduction in erosion rates is, as such, not caused by the development of a recirculation zone behind the spheres as previous studies over immobile rough beds suggested (Raus et al., 2019; Fang et al., 2017; Papanicolaou et al., 2012). The recirculation region is annihilated, in fact, by the upflow in the sphere's lee side. The sheltering region in the sphere's lee is characterized by almost isotropic turbulence (Figure 5.23) and by the reduction of the frequency of the sweep events (Figure 5.27). As a result, the shear stresses are damped compared to a uniform fine-sediment bed (Figure 5.22a). Nevertheless, erosion takes place in the bed interstices, since the shear layer can reach the fine-sediment bed in the stoss side of the spheres, where enhanced shear stress conditions are still present. The interaction of the shear layer with the downstream sphere suggests that the flow is effectively wake interfering. Thus, the third erosive regime is called *wake-interference sheltering regime* (Figure 7.1).

In the fourth erosive regime ($P > P_{c3}$), upflow conditions dominate not only the lee side of the spheres but also the spheres' top (Figures 5.8g-h and 7.1). As a result, the shear layer is forced outside of the bed interstices (Figures 5.12c-d) and is not able to reach the fine-sediment bed anymore leading to very low erosion rates. Since the shear layer does not interact with the sphere positioned downstream, skimming-flow conditions are present. The shear stress conditions at the level of the fine sediments are significantly below the critical conditions of motion in the lee side of the spheres (Figure 5.22a). In the stoss side, critical conditions of motion are present consistent with the intermittent sediment transport visually observed at the end of the experiments. The quasi-negligible erosion rates, leading eventually to a stable bed, are caused by a clear change in the turbulent structure at the level of the bed with inward interactions dominating the sphere's lee side and quasi-isotropic turbulence conditions the stoss side (Figure 5.23). This results in a reduction of the frequency and of the duration of the sweep events in the lee and stoss side of the spheres (Figures 5.27 and 5.28), respectively. The region below the shear layer shows furthermore no kinetic energy production or transport (Figure 5.20), so that the near-bed region is effectively disconnected from the outer flow. Thus, the grain sheltering is the result of skimming flow conditions in the fourth erosive regime, which is given the name *skimming-flow sheltering regime* (Figure 7.1).

The influence of flow and geometric bed parameters on the erosion of fine-sediments from an immobile rough bed

The influence of the Shields parameter, the relative submergence of the spheres and the roughness density of the sphere on the fine-sediment erosion was analysed in Chapter 6 (a preliminary analysis on the influence of the Shields parameter is already given in Chapter 2 in Section 2.3.4). The analysis showed that the three transitions in erosive regimes are independent of these three parameters and can be associated to the geometric characteristics of the bed. More specifically, the critical protrusion level P_{c1} (drag sheltering $\rightarrow$ turbulence enhancement regime) corresponds to an angle of attack α_a of 20°-30° for which the shear layer starts to develop. The second critical protrusion level P_{c2} (turbulence enhancement $\rightarrow$ wake-interference sheltering regime) can be identified by the planar density $\lambda_p \simeq 0.3$ for which the transition between isolated and wake-interference flow is given and the third P_{c3} (wake-interference $\rightarrow$ skimming sheltering regime) by a planar density $\lambda_p \simeq 0.5$, for which the transition between wake-interference and skimming flow takes place.

In this manner, it is possible to define the critical protrusion levels of the roughness elements for a generic immobile rough bed once the bed topography is known. A summary of the thresholds of the bed geometrical parameters for the definition of the four erosive regimes is given in Figure 7.1.

While transitions in erosive behaviour are unaffected by the Shields parameter, the final erosion depth was shown to increase with increasing Shields parameter (Section 5.4.4), while maintaining a constant roughness density of the bed of spheres and a constant fine-sediment size (plastic granulate). The maximum protrusion level reached once the sediment bed level is stable, is always higher or equal to the critical protrusion level for the third transition in erosive behaviour P_{c3}. Skimming flow conditions are always present, in fact, when the system has reached the final stable sediment bed level. The fact that the final protrusion levels are observed for $P \geq P_{c3}$, suggests that the transition from the wake-interference sheltering regime to the skimming flow sheltering regime does not guarantee necessarily critical conditions of motion, even though there is a significant reduction in erosion rates. The skimming flow conditions reached for $P = P_{c3}$ can be considered as such a necessary but not sufficient conditions for the bed to reach a stable bed level. The final bed level is reached when the sediment bed level is so low that the most intense sweep events reach the fine-sediment bed with such a low frequency that critical conditions of motion set in, as the analysis of the frequency of the sweep events in Section 5.4.4 suggests.

The analysis of the influence of the roughness density of the immobile two-layered bed of spheres on the erosion process showed that of the three roughness densities studied (λ_f = [0.53, 0.13, 0.003], which characterize the first layer of spheres; the second layer has always a λ_f = 0.53), the medium and sparse densities lead to the complete erosion of the first layer of spheres (Section 6.2). In these cases, the bed stabilizes in the second layer of spheres. The maximum erosion depth increases with decreasing roughness density. The maximum fine-sediment shear stress measured once the bed has stabilized, increases in fact for decreasing roughness density of the spheres. Thus, the sheltering capability of the spheres in inversely proportional to their roughness density. Indeed, the bed of spheres with sparse and medium roughness density are characterized by isolated and wake-interference flow conditions, respectively, once the first layer of spheres is fully exposed. The flow patterns connected to these two flow regimes are not able to shelter the fine-sediment bed over the whole pattern, so that the fine-sediments are eroded down to the second layer of spheres. The bed stabilizes within the second layer of spheres for both configurations with medium and sparse roughness density, once a planar area $\lambda_p = 0.5$ corresponding to skimming flow conditions is reached. The spheres of the first layer contribute only locally to the fine-sediment sheltering, as higher fine-sediment levels are observed in their lee sides. Overall, for multi-layered beds, the erosion of fine sediments will cease only when a bed layer is reached characterized by a planar density for which skimming flow conditions set in.

Variations in the relative submergence do not change the final erosion depth and the transitions in erosive behaviour, but the evolution of the system is faster for lower relative submergences (Section 6.3). This is probably due to a vertical confinement of the shear layer developing along the top of the spheres, which is pressed towards the fine-sediment bed in the case of low relative submergence.

Variations in the fine-sediment size given a constant roughness density of the spheres showed that in the presence of sand (finer than the otherwise used plastic granulate), the system develops three-dimensional dunes which persist during the whole experiment eroding the bed down to the equator of the first layer of spheres (Section 6.4). The maximum erosion depth does not change with variations in the Shields parameter, as observed for the coarser sediments. The intensity of the shear layer developing at the top of the spheres and responsible for the erosion of the bed, increases in intensity with increasing Shields parameter, though.

This suggests that the final erosion depth is not only controlled by the coherent structures generated by the shear layers, but also by coherent structures arising from the interaction between the dunes and the protruding spheres.

Significance of the study and future work

This work has contributed to the better understanding of the erosion processes of fine-sediments in coarse immobile beds. The results are relevant for both the prediction of the bed morphodynamics under sediment-supply limited conditions and the planning of sediment flushing from dams. As far as the first issue is concerned, this work gives some practical tools on how to predict the number of ridges developing over a rough immobile bed under sediment supply limited conditions. This information can be used to determine the global friction factor of the bed in the presence of fine-sediment ridges on the basis of the work by Zampiron et al. (2020b).

For the planning of sediment flushing operations to remove superficial and interstitial fine-sediments from a gravel beds in dam-regulated rivers, this work provides some guidelines to determine the erosion depth of the fine sediments given the shear stress conditions acting on the bed on the basis of the erosive regimes identified. Once the spheres start to protrude from the fine-sediment bed and the first critical protrusion level P_{c1} (i.e. the threshold for the turbulence-enhancement regime) is reached, a self-cleaning mechanism sets in by which the immobile grains enhance the erosion rates due to the developing shear layers. A minimum clean-out depth can be identified then as the bed level corresponding to the second critical protrusion level P_{c2}, since the ensuing wake-interference sheltering regime leads to a reduction of the erosion rates. A first estimate of the maximum clean-out depth is provided by the protrusion level P_{c3} for the transition between wake-interference and skimming flow conditions P_{c3}, as it represents the threshold for which negligible erosion rates are reached. P_{c3} represents an estimate of the maximum erosion depth on the safe side, as critical conditions of motion are reached for higher protrusion levels.

To this regard, future works should focus on identifying which are the exact hydrodynamic conditions which lead to a stable fine-sediment bed once the critical protrusion level P_{c3} is reached. The result of this work hint to a decrease in frequency and duration of the sweep events at the level of the sediment bed, as the result of the shear layer being pushed out of the bed interstices. The exact mechanism of this damping process is still not clear, though, and could be disclosed by tracking the coherent structures shed by the protruding spheres. As far as the first drag sheltering regime is concerned, this study did not measure the flow conditions in the bed interstices for $P < P_{c1}$, as the bed developed too quickly to capture them. Flow measurements in this range of protrusion levels should be performed in the future to assess whether the initial decrease in erosion rates can be effectively ascribed to the drag induced by the protruding spheres.

This work has highlighted furthermore, that in the presence of fine sand, the final erosion depth does not depend anymore on the Shields parameter. As compared to the coarser plastic granulate for which short-living two-dimentional dunes were observed, the sand displayed the development of long-living highly three-dimentional dunes interacting with the protruding spheres. The superimposition between the coherent structures shed by the dunes and by the spheres might be the cause of the Shields parameter independence of the final erosion depth. In order to explain this behaviour, the coupling between the coherent structures shed by the dunes and by the spheres should be analysed in the future.

Appendices

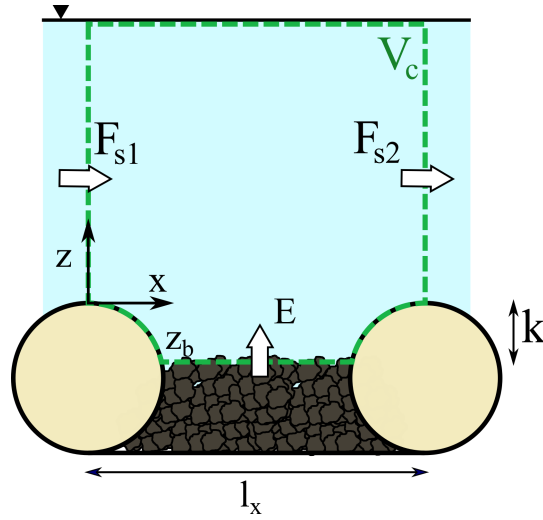# A Derivation of the Exner equation over an immobile rough bed

Figure A.1: Definition of the control volume V_c with sediment fluxes from the bed E and through the vertical surfaces of the control volume F_s

In the presence of immobile roughness elements protruding from the bed, the fine-sediment part of the bed surface changes with protrusion level. To address this, consider the control volume V_c with surface S_c in Figure A.1, spanning one pattern width. The lower surface of the control volume is mobile and follows the variations in the average sediment bed level z_b which moves with a velocity $u_b = \partial_t z$ or equivalently in terms of the average protrusion level P (= $-z_b/R$) with $u_b = -R\partial_t P$. The conservation of the total sediment mass in V_c can be expressed as follows:

$$\frac{dm_s}{dt} = \frac{d}{dt}\int_{V_c}(\rho_s c)dV_c = 0, \tag{A.1}$$

where c represents the concentration of sediments (both suspended or part of the bed matrix). By applying the Reynolds transport theorem, Equation A.1 can be cast in the following form:

$$\int_{V_c}\frac{\partial(\rho_s c)}{\partial t}dV_c + \int_{S_c}(\rho_s c)\vec{u}\cdot d\vec{S}_c = 0, \tag{A.2}$$

where $\vec{u}$ is the advection velocity of the sediments. The first term in Equation A.2 represents the variation of suspended sediments within the control volume, which can be considered negligible in the presence of bed-load. The momentum balance therefore reduces to the second term in Equation A.2, given by the flux

189

of sediments $F_{s,i}$ entering and leaving the control volume and by the flux of sediments E through the fine-sediment bed surface S_b (see Figure A.1). E can be expressed as follows:

$$E = \int_{S_b} (\rho_s C u_b) dS_b \tag{A.3}$$

where C is the concentration of the fine sediments in the bed (solidity) and the fine-sediment bed surface $S_b = A_r - A_p = l_x l_y (1 - \lambda_p)$. Given that all quantities here are pattern-averaged, C and u_b are taken as averages over S_b so that Equation A.3 yields:

$$E = -\rho_s C(1 - \lambda_p) R \frac{\partial P}{\partial t} l_x l_y. \tag{A.4}$$

Similarly, with an average volumetric sediment transport rate $Q_{s,i} = \int_{S_{v,i}} (cu) dS_{v,i}$ through the vertical control surfaces of the control volume $S_{v,i}$, the net streamwise sediment flux $\Delta F_s = F_{s,2} - F_{s,1}$ can be expressed as:

$$\Delta F_s = \rho_s \Delta Q_s \tag{A.5}$$

The conservation of mass, $\Delta F_s + E = 0$, can be then written as

$$\frac{\Delta q_s}{l_x} - C(1 - \lambda_p) R \frac{\partial P}{\partial t} = 0, \tag{A.6}$$

where $q_s = Q_s / l_y$ is the sediment transport rate per unit width. Considering the pattern average as a local quantity, conservation of mass on the pattern scale becomes

$$\frac{\partial q_s}{\partial x} - C(1 - \lambda_p) R \frac{\partial P}{\partial t} = 0, \tag{A.7}$$

where the longitudinal gradient is understood on the pattern scale consistent with the definition of P. The term $1 - \lambda_p$ reflects the reduced availability of sediments due to the presence of of roughness elements. The second term in Equation A.7 represents the total erosion rate from the bed, denoted E_t. This erosion rate does not give an estimate of the sediment transport rate, but of the longitudinal variability of the sediment fluxes through the control volume. As such, the erosion rates are a proxi of whether equilibrium sediment transport conditions are present.

It can be noted that in the absence of protruding immobile roughness elements $\lambda_p = 0$, the Exner equation for a uniform fine sediment bed is retrieved:

$$\frac{\partial q_s}{\partial x} - CR \frac{\partial P}{\partial t} = 0. \tag{A.8}$$

B   Flow conditions at the inlet

In order to assess whether the grids generate a homogenous flow with low turbulence levels at the inlet of the flume, horizontal 2D planar PIV measurements are performed 1.3 m downstream of the grids directly after the inlet ramp over the rough bed with the highest planar density λ_h (see Figure B.1). The flow condition investigated is the same as the one defined for the reference Exp. 1 ($R\text{-}G\lambda h$) in table 3.1. A local, right-hand sided coordinate system [x',y',z'] is used with the origin located in the centre of the channel on top of the first row of spheres. An iDs UI-3060CP-M-GL high speed camera equipped with a Nikkor 24mm lens is positioned in the centre of the channel at a height of 0.9 m above the top of the spheres, perpendicularly to a 4W blue laser positioned 1 m away from the flume side-wall and parallel to the rough bed. A boat is installed at the water surface to avoid distortions due to waves (for more details on the boat see section H.3). Three horizontal PIV planes are investigated at a height z'/H = [0.14, 0.50, 0.75] above the top of the spheres. The highest measurement location is chosen to be below the boundary layer developing along the boat characterized by a maximum boundary layer depth equal to 15% H for the flow conditions investigated (as discussed in section H.3). The field of view is 3 reference pattern lengths l_{x,λ_h} long in streamwise direction and covers the whole width of the channel. At each horizontal plane a total of 5000 burst are recorded over 22 minutes at an image frequency of 143 Hz, in order to ensure statistical convergence of the flow statistics.
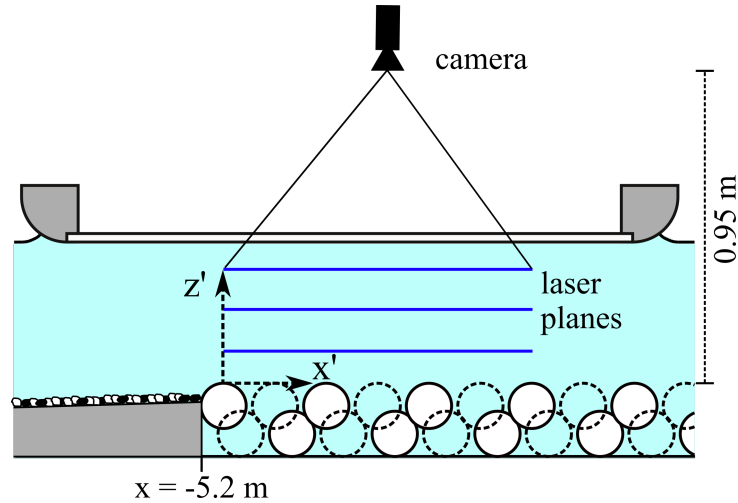

Figure B.1: Longitudinal section in the middle of the channel of the horizontal planar PIV setup.

Figure B.2a shows the transverse profiles of the double-averaged streamwise velocity $\langle \overline{u} \rangle_x$ at the three heights. The lateral variations in streamwise velocity are strongest near the bed (at z'/H = 0.14) due to the high spatial flow heterogeneity induced by presence of the spheres. The transverse u-profiles at z'/H = [0.5, 0.75] overlap showing the presence of an outer-region with a vertically uniform velocity. A reduction in the streamwise

velocity is observed at y/W = -0.05 for all profiles determining a slight lateral asymmetry in the inflow conditions. The origin of this reduction in streamwise velocity along with its asymmetry is not clear. The asymmetry might be related to the pipe system, delivering water to the bottom of the inlet chamber from its right hand side and not symmetrically along the flume centreline. The reduction in streamwise velocity might be related to the presence of secondary currents already developing in the first meters of the flume, as the aspect ratio of the flow is close to 5, i.e. close to the threshold for the development of secondary currents in narrow channels (Nezu and Rodi, 1985).

The transverse profiles of the longitudinally-averaged turbulent intensity profile $\langle\sigma_u\rangle_x = \langle\overline{u'^2}\rangle_x^{0.5}$ in figure B.2b shows that the turbulent intensity is the strongest near the bed at z'/H = 0.14 due to the influence of the roughness sublayer, as observed also for the longitudinal velocity. The values of turbulent intensity of the order of 10-20% of the local double-averaged streamwise velocity $\langle\overline{u}\rangle_x$ are in good agreement with the values observed over gravel beds at similar heights above the bed (Mignot et al., 2009a; Dey and Das, 2012). Further away from the bed the turbulent intensities attain much lower values of the order of 2.5% $\langle\overline{u}\rangle_x$, characterized by lateral homogeneity in the central region of the channel between y$'$/W = -0.35 and y$'$/W = 0.35. No lateral asymmetry in turbulent intensities can be observed in the outer region. The grids effectively ensure homogeneous turbulent conditions over the whole cross-section with turbulent intensities much lower than the ones generated by the rough bed, so that with the further development of the boundary layer the turbulent statistics measured downstream can be considered only a result of the interaction of the flow with the rough bed.
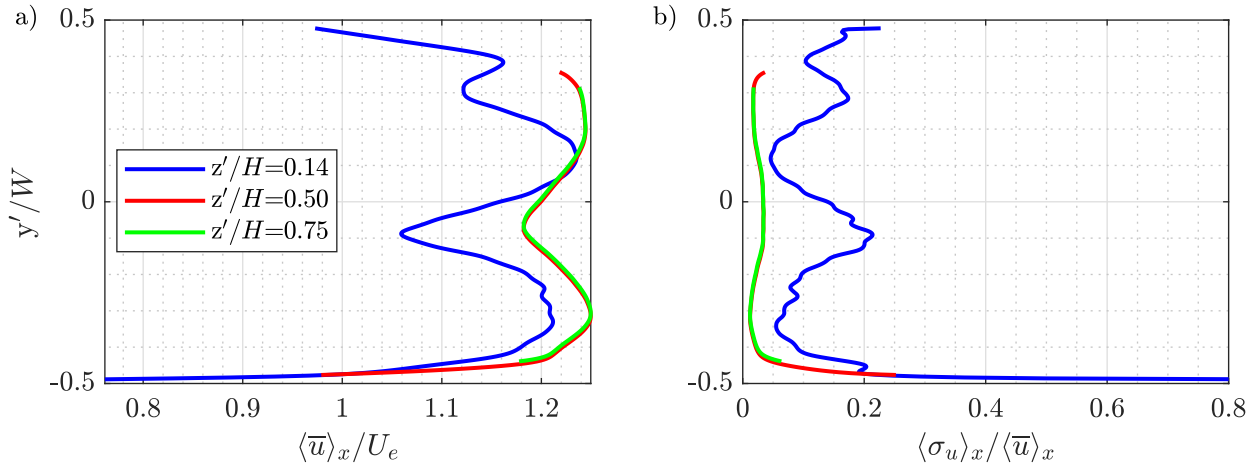

Figure B.2: (a) Transverse profiles of the double-averaged streamwise velocity $\langle\overline{u}\rangle_x$ normalized by the effective velocity $U_e = Q/(WH_e)$ (with $H_e = H + \phi k$ the effective water depth) and (b) of the longitudinally-averaged streamwise turbulent intensities $\langle\sigma_u\rangle_x$ normalized by $\langle\overline{u}\rangle_x$, at three different water depths z/H = [0.14, 0.5, 0.75].

C   Boundary layer development at the inlet and definition of the measurement location

The development of the boundary layer at the beginning of the rough bed of spheres is analysed to establish when the flow can be considered fully developed and define, in this manner, the measurement location. In order to characterize the boundary layer development at the transition between the inlet ramp and the bed of spheres, planar PIV measurements are performed over two vertical planes in the middle (m) at $y'/W = 0$ and in the quarter plane (q) at $y'/W = -0.22$ (see Figure C.1) over the same bed configuration and at the same measurement location of the horizontal PIV measurements described in Appendix B. The planar PIV system consists of a 4W blue diode laser installed 1m above the flume and of a UI-3060CP-M-GL Rev.2 iDS 8-bit high frequency camera, equipped with a 50mm Nikkor lens, positioned perpendicularly to the laser sheet 1m away from the wall. The field of view covers the whole water depth and spans over an area 4 reference patterns long, one pattern length long over the ramp and 3 over the bed of spheres (see insert in Figure C.1). During each PIV measurement in the middle and in the quarter plane, 5000 bursts are recorded at a burst frequency of $4.3 Hz$ (a time interval high enough to obtain statistically independent samples) and at an image frequency of 232 Hz. The flow conditions investigated are the same as the ones of the reference Exp. 1 (R-$G\lambda h$) in table 3.1.

Figure C.2 shows the 2D fields of the time-averaged streamwise velocity $\overline{u}$ and of the local fluid shear stress $\tau_{xz}|_{local}$ (equal to the sum of the Reynolds $\tau_{uw} = -\rho_f \overline{u'w'}$ and of the time-averaged viscous shear stress $\overline{\tau}_{vis} = \rho_f \nu \partial \overline{u}/\partial z$). On the basis of the isovelocity lines in Figures C.2a and C.2c it is observed, that the streamwise velocity first increases in the longitudinal direction over the ramp reaching a peak at $x/l_{x,\lambda_h} \simeq$ 0.5-1 and decreasing again over the bed of spheres. The increase in streamwise velocity is induced by the
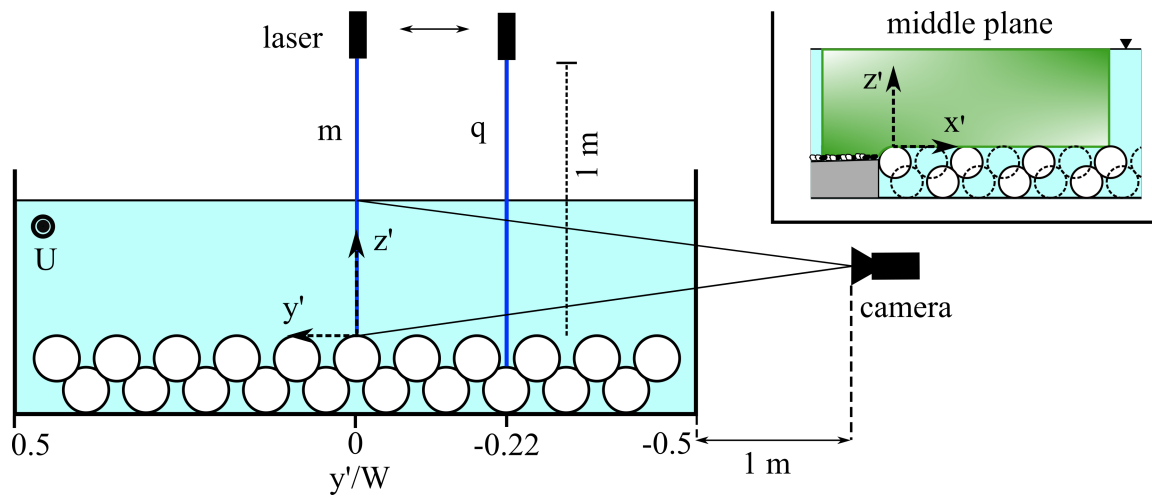

Figure C.1: Cross-sectional plane of the planar PIV setup at the beginning of the bed of spheres. The insert in the up-right corner displays the measurement field in the middle plane.

flow acceleration resulting from the reduction of the water depth along the inclined ramp. The transition from the ramp covered by fine grains to the bed of spheres, i.e. from smoother to rougher bed conditions, determines the subsequent reduction in streamwise velocity. While the outer region of the flow ($z'/H > 0.2$) is characterized by rather homogeneous velocities in the vertical direction, the near bed region is characterized by high velocity gradients due to the presence of two boundary layers: an outer boundary layer (OBL) developing over the ramp and an internal boundary layer (IBL) triggered by the transition from a smoother to a rougher surface. The near bed flow region for $x'/l_{x,\lambda_h} > 0$ is, in fact, characterized by wake-like flow structures shed by the spheres with reduced flow velocities in their lee and flow acceleration above them. In a similar way, figures C.2b and C.2d show that the total fluid shear stress is almost zero in the outer flow region for $z'/H > 0.2$, while in the near bed region over the spheres the flow is characterized by high spatial heterogeneity, characteristic of a roughness sublayer (Raupach et al., 1991; Florens et al., 2013). The stoss side of the spheres is characterized by a strong shear layer which increases in its vertical spatial extent in the downstream direction. The IBL developing over the spheres is the result, in fact, of the interaction and convolution of the wakes shed by the spheres one after the other in the streamwise direction.

In order to determine how fast the shear stress conditions at the level of the spheres develop towards fully-developed boundary layer conditions, the vertical profiles of the local fluid shear stress $\tau_{xz}|_{local}$ are illustrated
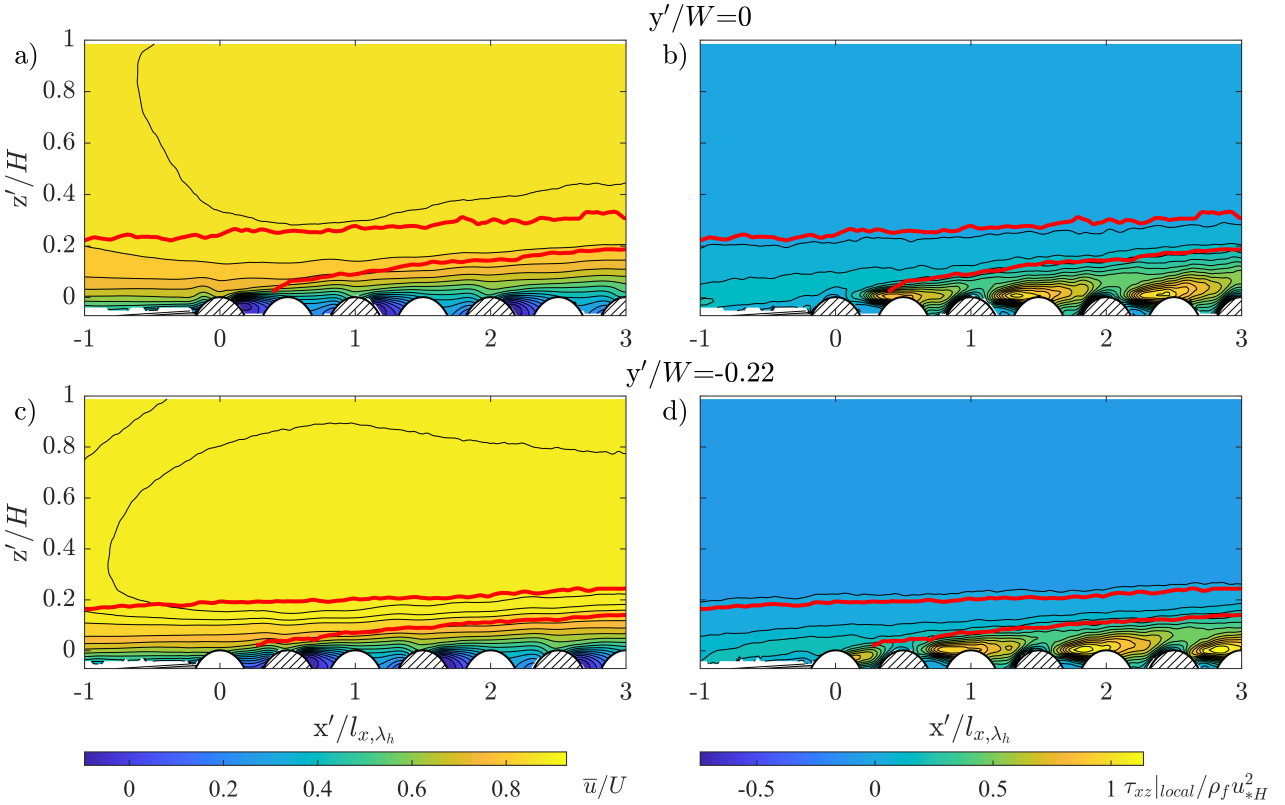

Figure C.2: 2D-fields of the time-averaged streamwise velocity $\overline{u}$, normalized by the bulk velocity U, and of the local fluid shear stress $\tau_{xz}|_{local} = -\rho_f \overline{u'w'} + \rho_f \nu(\partial \overline{u}/\partial z)$, normalized by the shear velocity obtained from the depth-slope product u_{*H}, for the middle plane $y'/W = 0$ (a-b) and for the quarter plane $y'/W = -0.22$ (c-d). The continuous red lines identify the development of the outer and inner boundary layers. The spheres in the laser plane are identified by a diagonal pattern, while the ones in the out-of-plane are white.

in Figures C.3a and C.3b for different x-positions over the ramp and the spheres at $l_{x,\lambda_h}/2$ intervals both for the middle and the quarter plane, respectively. The profiles are normalized by the shear velocity u_{*H} obtained from the depth slope product, as it represents the characteristic shear velocity at the top of the spheres when the boundary layer is fully developed. All profiles overlap in the outer layer showing an almost vertically homogenous region with low or almost zero level of turbulent correlation (i.e. quasi-isotropic turbulence), showing that the outer flow is the result of the grid generated turbulence at the entrance of the channel. In the near bed region the peak in the $\overline{\tau}_{xz}$ vertical profiles is observed at the level of the ramp for $x'/l_{x,\lambda_h} < 0$, while it shifts to a region near the top of the spheres for $x'/l_{x,\lambda_h} \geq 0$ due to the shear layers developing at the spheres' top. The peak in fluid shear stress increases in downstream direction showing a strengthening of the shear layers. For $x'/l_{x,\lambda_h} \geq 0$ the highest peak in shear stress is observed at the top of the spheres in the centre of the patterns (non integer $x'/l_{x,\lambda_h}$ values in Figures C.3a-b), while over the spheres the peak is shifted upwards at $z'/H \simeq 6\%$ and is characterized by a lower magnitude (integer $x'/l_{x,\lambda_h}$ values in Figure C.3b). The peak position and the relative magnitude of the two profiles correspond well to the S-shaped and accelerated shear stress profile class observed in the wake and on top of roughness elements, respectively, in fully developed boundary layers over gravel beds (Mignot et al., 2009a; Dey and Das, 2012), showing that the roughness sublayer quickly adapts to the roughness transition.

The flow adjustment after the roughness transition is analysed on the basis of the longitudinal development of the local shear velocity u_* obtained locally from the extrapolation of the total fluid shear stress $\overline{\tau_{xz}}$ to the top of the spheres, as shown in Figure C.4c for both the middle and quarter plane. The profiles of u_* show a longitudinal wavy variation in phase with the geometry of the pattern of spheres, with the lowest u_* values observed over the spheres (identified by the vertical lines in Figure C.3c) and the highest in the centre of the patterns. The shift in profiles is connected to the fact that in the central plane the first sphere is adjacent to the ramp while in the quarter plane the first sphere is shifted half a pattern downstream. Both in the middle and in the quarter plane, the shear velocity increases in the longitudinal direction, settling down already after 2 roughness patterns around values comprised between 0.9-1.1 u_{*H}, i.e. to shear stress conditions near the bed similar to those characterizing a fully developed boundary layer. As such, the roughness sublayer of the IBL reaches quickly a state of equilibrium after the roughness change. Nevertheless, as pointed out in the wind-tunnel study by Cheng and Castro (2002) on the flow development after a roughness transition from a smooth to a rough bed, the IBL needs at least 40 roughness pattern lengths to develop an inertial sublayer characterized by a log law matching with the underlying surface.

The outer and inner boundary layer depths are defined on the basis of the total fluid shear stress profiles. The OBL-depth is defined as the vertical height where the total fluid shear stress reaches 101% of the constant fluid shear stress in the outer flow (identified by the dashed vertical line in figures C.3a-b). The IBL-depth is defined, instead, visually by identifying the outer edge of the convolution of all wakes shed by the spheres. Figures C.4a and C.4b illustrate the streamwise velocity at the boundary layer depth U_δ and the boundary layer depth δ for both the OBL and the IBL. The streamwise velocity for the OBL follows the same trend discussed in figures C.2a and C.2c with a first acceleration followed by a deceleration. In the case of the IBL, the streamwise velocity is characterized by a steady increase, as the boundary layer occupies regions of higher velocity while developing. The OBL-depth in Figure C.4b covers already 20% of the water depth at the roughness transition ($x'/l_{x,\lambda_h} = -0.22$). The discrepancy in OBL depth between the middle and quarter plane position can be explained by considering that the incoming flow is not perfectly symmetric as shown in Appendix B. The IBL-depths show instead a similar development.
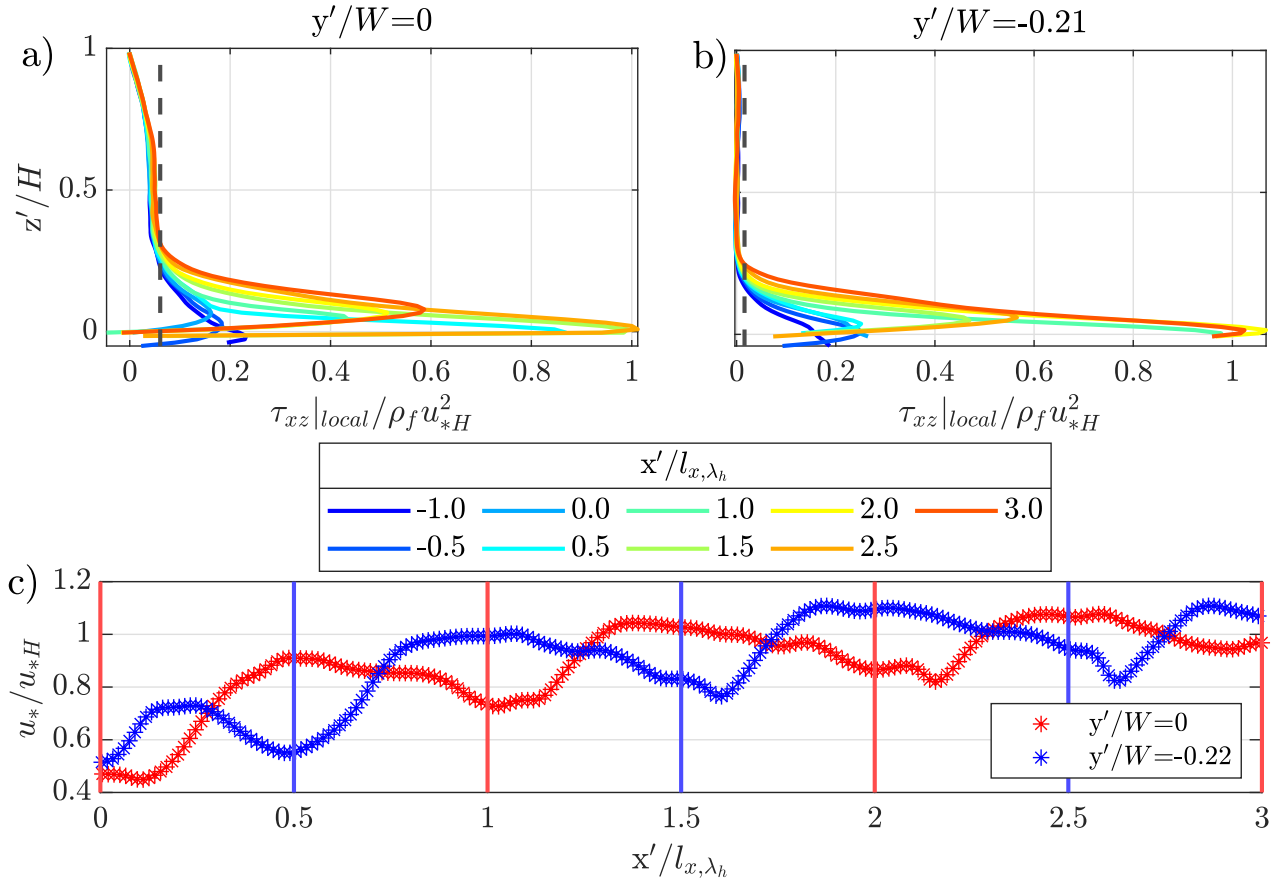
Figure C.3: (a-b) Vertical profile of the local fluid shear stress $\tau_{xz}|_{local}$ at different x positions over the middle and quarter plane, respectively; (c) longitudinal profiles of the local shear velocity u_* in the middle and quarter plane. All plots are normalized by the shear velocity obtained from the depth-slope product u_{*H}. The vertical lines identify the position of the top of the spheres.
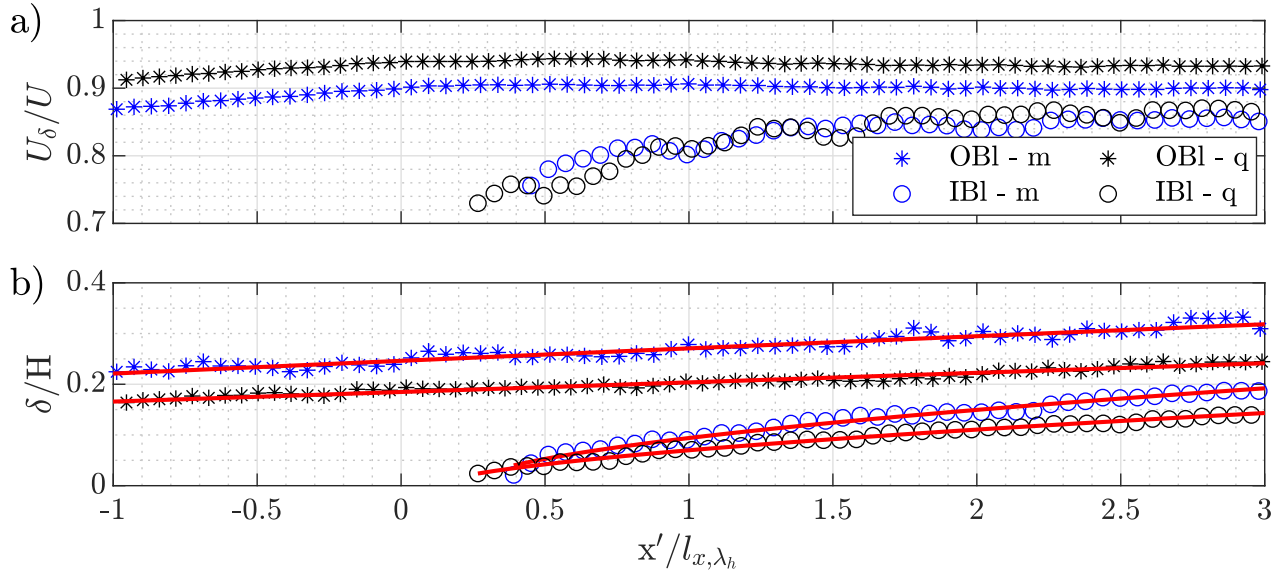

Figure C.4: Longitudinal profiles of the velocity U_δ at the top of the outer and inner boundary layers (a) and of the corresponding boundary layer depths δ (b) in the middle and quarter plane.

Plane	OBL			IBL			
	a	dx	x_{fd}	a	dx	t	x_{fd}
	[-]	[cm]	[cm]	[-]	[cm]	[-]	[-]
m - y/B=0	0.30	-34	251	0.17	-0.5	0.61	320
q - y/B=-0.22	0.39	-35	170	0.27	0	0.56	239

Table C.1: Parameters of the outer (OBL) and inner boundary layer (IBL): proportionality factor a, origin dx, power-law exponent t of equations C.1 and C.2 and downstream distance for fully developed flow conditions x_{fd}.

The evolution of the OBL-depth is fitted with the classical $x^{4/5}$-law for turbulent boundary layer development over rough surfaces (Schlichting and Gersten, 2017):

$$\delta = a(x - dx)Re_{x-dx}^{1/5} \tag{C.1}$$

where a is a fitting coefficient, dx the origin of the OBL and $Re_{x-dx} = (x - dx)U_{bl}/\nu$. Equation C.1 is valid, strictly speaking, only in boundary layers with zero pressure gradient. Nevertheless, given the low inclination of the ramp and that the variations in U_{bl} are less than 5%, equation C.1 is considered a good approximation of the actual boundary layer development. Figure C.4b shows, in fact, good agreement between the OBL thickness and equation C.1. Furthermore, the values of the a coefficient in table C.1 are quite close to the classical value of 0.36 (Schlichting and Gersten, 2017).

In the case of the IBL, there is no consensus in the literature on the most appropriate law to describe its development (Savelyev and Taylor, 2005). Therefore, the evolution of the IBL is fitted to the following power law, as done in other studies (Antonia and Luxton, 1971; Cheng and Castro, 2002):

$$\delta = a(x - dx)^t \tag{C.2}$$

where the coefficient a, the origin dx of the IBL and the power law exponent t are all fitting parameters. The origin dx of the boundary layer is correctly situated over the first row sphere (see table C.1). In table C.1, the values of the power-law exponent t are in the order of 0.6. They are comprised between the value of 0.5, observed by Antonia and Luxton (1971) for the transition from a smooth bed to a two dimensional rib roughness, and the values of 0.8, observed by Pendergrass and Aria (1984) for the transition from a smooth bed to a cubic roughness. Given that the rate of growth of a bluff body wake is of the order of 0.5 (Antonia and Luxton, 1971), the power law exponent of 0.6 can result from the interaction of the wakes shed by the spheres.

In order to determine at which position downstream of the inlet the flow can be considered fully developed, the longitudinal position x_{fd} at which the OBL and the IBL reach the water surface, are defined on the basis of equations C.1 and C.2. x_{fd} defined on the basis of the OBL is relevant for bed conditions at the beginning of the experiments discussed in chapter 3.2, when the spheres are covered by the fine sediments or start to protrude, as there is no relevant change in roughness during the transition from the ramp to the sediment bed. On the other hand, x_{fd} defined on the basis of the IBL is relevant for bed conditions, when the fine sediments are eroded and the spheres protrude significantly from the bed, since there is, as a result, a change of roughness at the transition between the ramp and the rough bed. Table C.1 shows that the OBL

reaches the water surface about 2m downstream of the inlet, while the IBL 3m downstream. These results show that positioning the measurement system 5.8 m downstream of the inlet guarantees fully developed flow conditions.
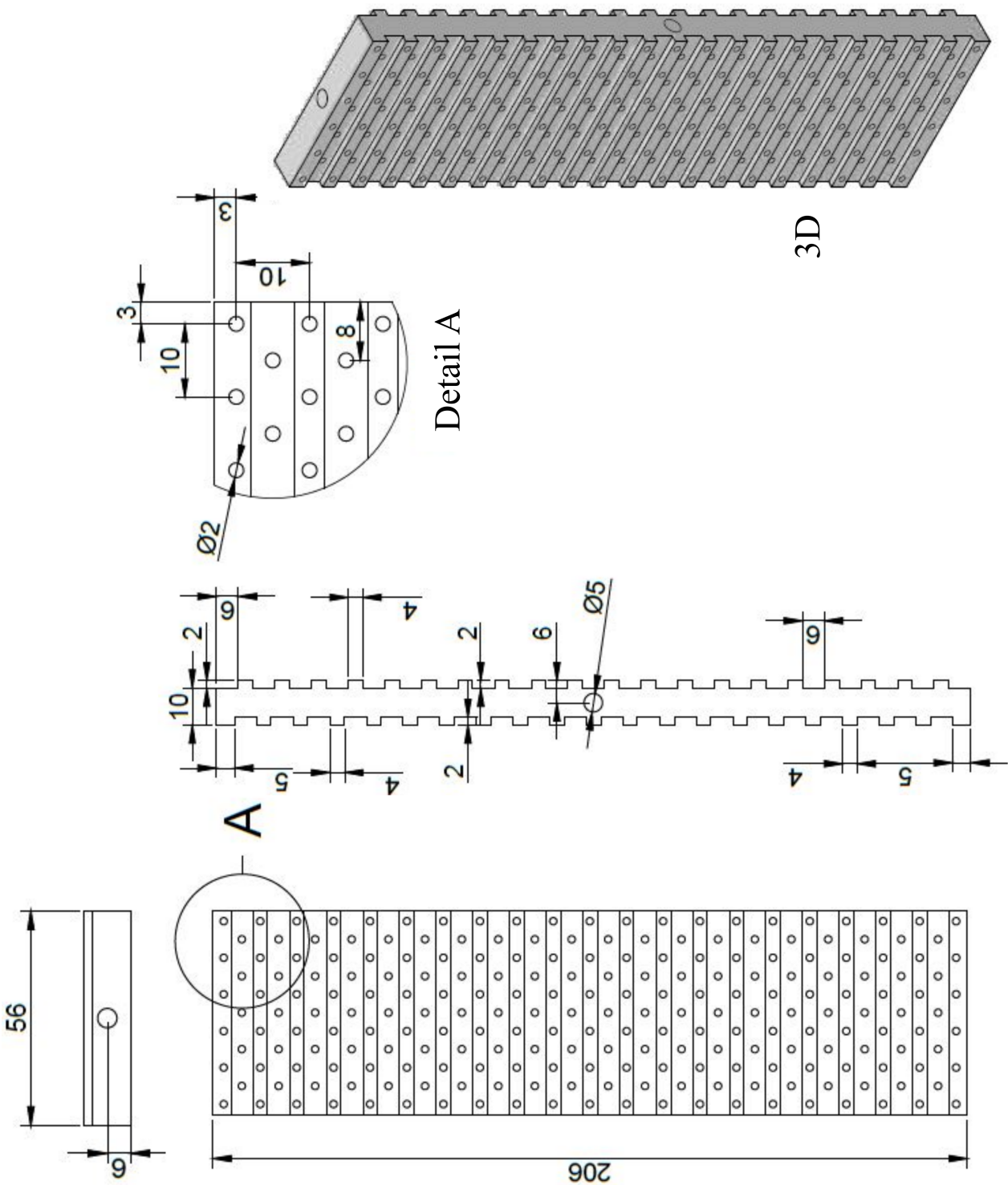
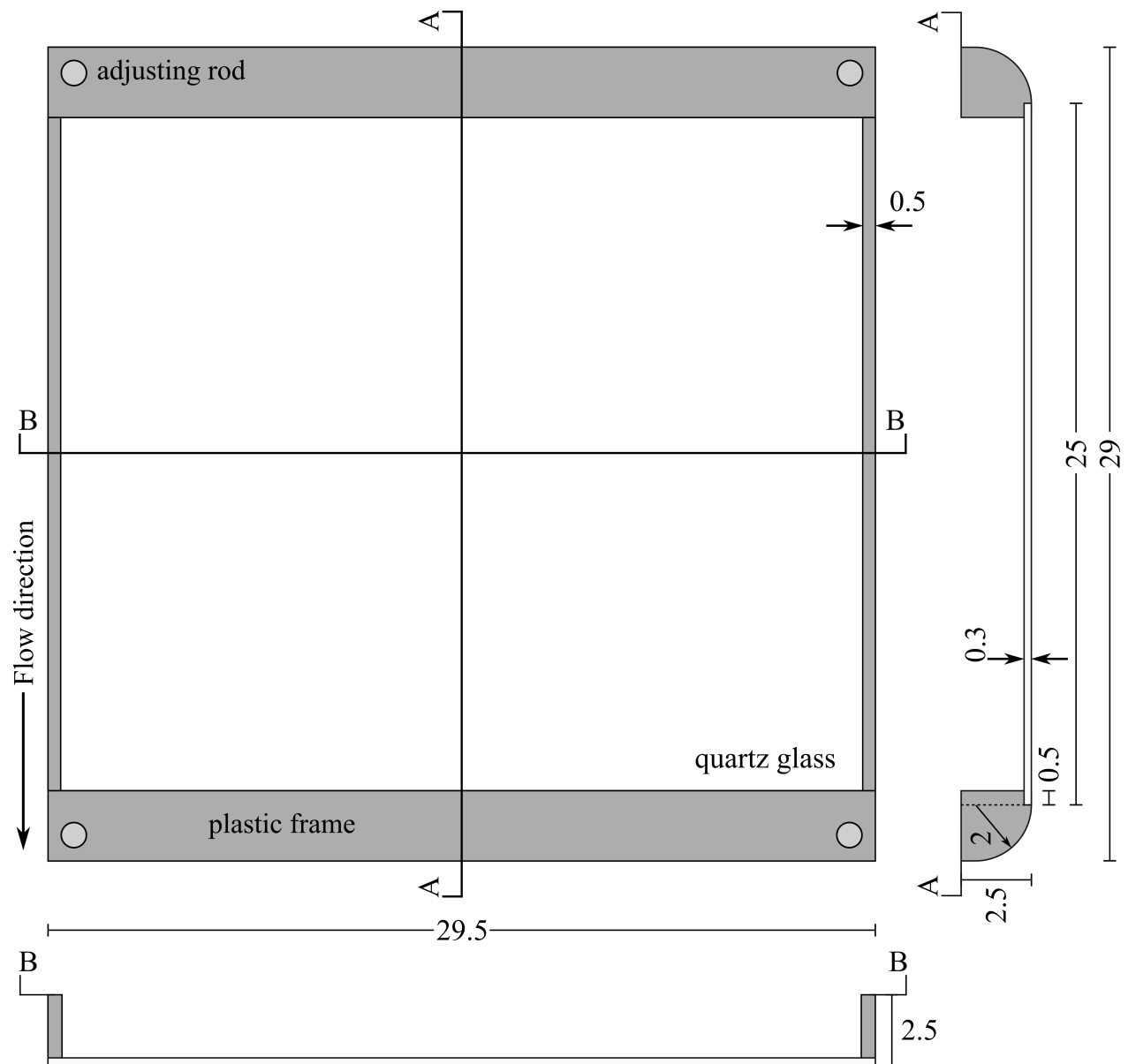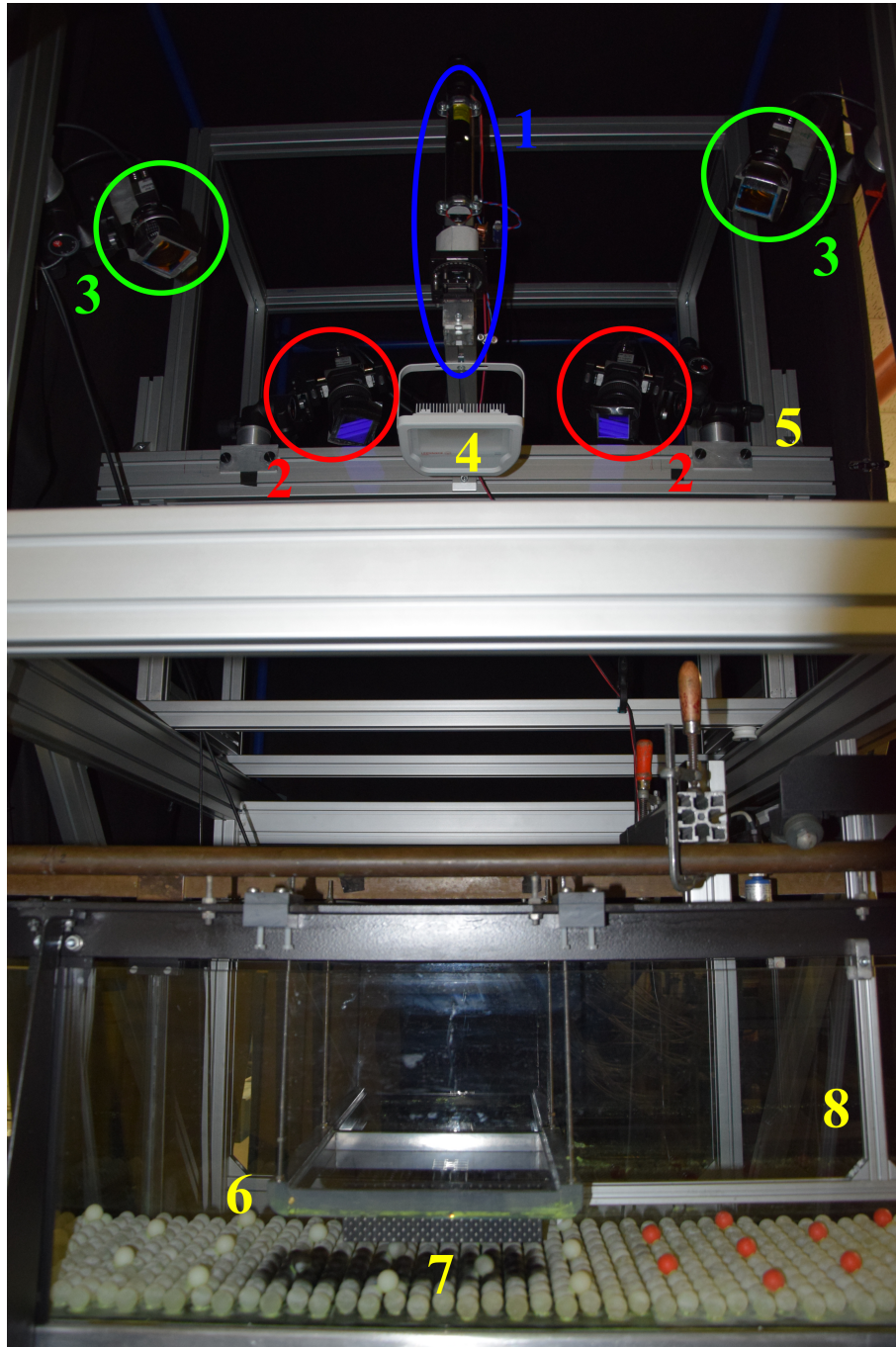# D Technical drawings

Figure D.1: Calibration plate 206×56 mm^2

Figure D.2: Calibration plate 206×106 mm^2

Figure D.3: Top view of the surface glass plate (boat) with two cross-sections AA and BB; the units are cm.

E   Foto of the experimental setup

Figure E.1: Experimental setup: 1. laser; 2. cameras of the stereo PIV system; 3. cameras of the photogrammetric system; 4. LED lamp; 5. movable carriage to translate the sPIV and photogrammetric system in the y-direction; 6. surface boat; 7. Calibration plate; 8. structure to hold the calibration plate.

F   PIV errors and convergence of the flow statistics

PIV measurements are affected both by random and bias errors. Random errors are generally connected to electronic noise of the camera sensors, shot noise, non-linear response of the cameras, but also non-uniform seeding and non-uniform reflection of particles (Huang et al., 1997; Christensen and Adrian, 2002). Random errors have an impact on the instantaneous velocity fields, but their random nature allows to neglect them when working with time-averaged flow statistics. On the other hand, bias errors, stemming for example from misalignments between calibration plate and laser sheet or peak locking, can alter the time-averaged statistics (Christensen, 2004). The peak-locking error is a bias of the particle displacement towards integer values, generally connected to an image particle size smaller than 1 px. In the present case, the fluorescent particles have a dewarped image size of 4-5 pixels, so that the peak locking error can be estimated to be in the order of 0.03 pixels (Raffel et al., 2018) and the turbulent statistics can be considered unbiased. This value of the peak-locking error holds for the in-plane velocity components. For the out-of-plane component, the uncertainty can be estimated in the centre of the measurement field, where it is maximum, in the following way (Lawson and Wu, 1997a):

$$\epsilon_{\Delta z} = \frac{\epsilon_{\Delta x}}{\tan \gamma} \tag{F.1}$$

where γ is the horizontal stereo angle (since the out-of plane component is estimated on the basis of the longitual velocity component as shown in equation 3.5) and $\epsilon_{\Delta x}$ the peak-locking error in streamwise direction. For the present stereo-PIV setup, the error in the out-of plane component is two times the error in the longitudinal direction.

When working with time-averaged flow statistics in turbulent flows, it is important to not only guarantee low-measurement errors, but also to ensure that the number of PIV samples (in this case 4500) is high enough for the flow statistics to be temporally converged. The convergence of the flow statistics is checked for each PIV measurement by analysing the cumulative average of the three velocity component (u, w, v), of the Reynolds shear stresses $-\rho_f \overline{u'w'}$ and of the turbulent intensities $\overline{u'^2}, \overline{v'^2}, \overline{w'^2}$ at three vertical positions in the centre of the measurement area, i.e. in the bed interstices, within the shear layer in the lee side of the sphere and in the bulk flow, as shown in Figure F.1a. An example of the convergence analysis is shown in Figures F.1b-s, where the data are extracted from the third PIV measurement over plane A during Exp. 1. Figures F.1b-s show that in the bulk (z/H = 0.6) and at the level of the bed (z/H = 0.06) at least 3000 samples are needed to reach convergence of the flow statistics. In the bed interstices (z/H = -0.15) a higher number of samples of about 4000 is needed instead.

The time convergence error of the time averaged statistics can be estimated on the basis of their confidence intervals, as shown by Florens (2010). Given a time series of N independent samples of a flow variable ϕ_v,
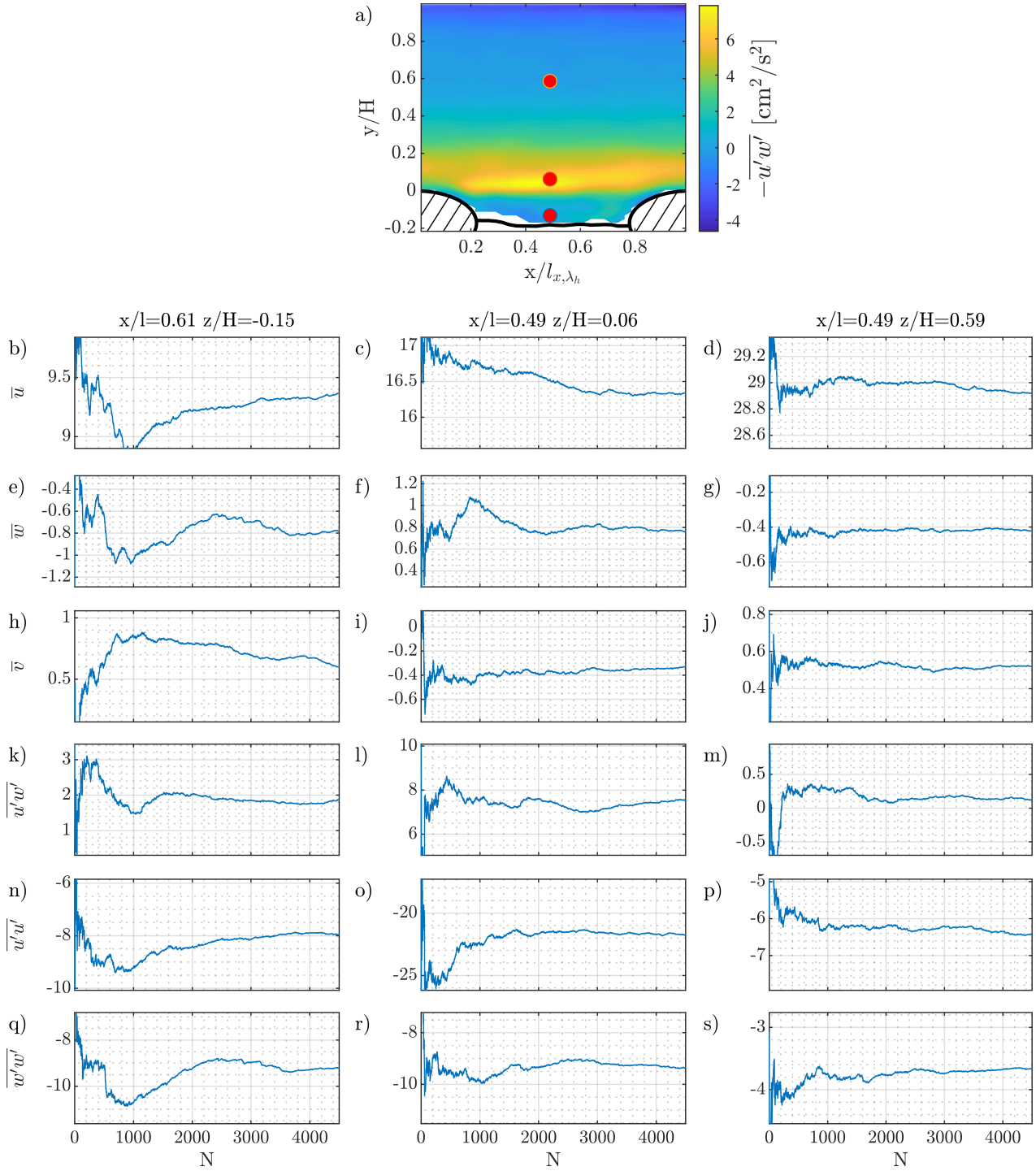
Figure F.1: a) Reynolds shear stress field with the position of the grid points where the time convergence analysis is performed. b)-s) Cumulative time average of the longitudinal, vertical and transverse velocity $\overline{u}$, $\overline{w}$, $\overline{v}$, of the Reynolds shear stresses $-\overline{u'w'}$ and of the streamwise and vertical turbulent intensities $-\overline{u'u'}$, $-\overline{w'w'}$ as a function of the number of samples at the three vertical elevations identified in Figure a).

the time convergence error on the the first-order moment $\overline{\phi_v}$ (i.e. the time average of the velocity signal) can be estimated as follows (Bendat and Piersol, 1986):

$$\epsilon^{\pm}_{\overline{\phi_v}} = \frac{\sqrt{\overline{\phi_v'^2}}t_{N-1,1-\alpha_s/2}}{\sqrt{N}} \tag{F.2}$$

where $t_{N-1,1-\alpha_s/2}$ is the quantile of the t-Student law with N-1 degrees of freedom with a confidence level $\alpha_s = 0.05$. Equation F.2 defines the confidence interval with a 95% probability that the estimated value of the first order moment is equal to its true value. In a similar manner, the convergence error for second order moments $\overline{\phi_v'^2}$ (i.e. turbulent intensities) can be defined in the following way:

$$\epsilon^{+}_{\overline{\phi_v'^2}} = \frac{(N-1)\overline{\phi_v'^2}}{\chi^2_{N-1,1-\alpha_s/2}} - \overline{\phi_v'^2} \tag{F.3}$$

$$\epsilon^{-}_{\overline{\phi_v'^2}} = \overline{\phi_v'^2} - \frac{(N-1)\overline{\phi_v'^2}}{\chi^2_{N-1,\alpha_s/2}} \tag{F.4}$$

where $\chi^2_{N-1,1-\alpha_s/2}$ is the quantile of the χ^2 distribution with N-1 degrees of freedom. Contrary to the first order moments, the error of second order moments are not symmetric around the mean so that the errors on the left (-) and right (+) side of the mean are defined. Since Bendat and Piersol (1986) does not provide an error estimation for the covariances, the following convergence error for $\overline{u'w'}$ is proposed (derived independently from Florens (2010)):

$$\epsilon^{+}_{\overline{u'w'}} = \frac{(N-1)\overline{u'w'}}{\chi^2_{N-1,1-\alpha_s/2}} - \overline{u'w'} \tag{F.5}$$

$$\epsilon^{-}_{\overline{u'w'}} = \overline{u'w'} - \frac{(N-1)\overline{u'w'}}{\chi^2_{N-1,\alpha_s/2}} \tag{F.6}$$

In a similar way, the error for $\overline{u'v'}$ and $\overline{v'w'}$ can be defined. For the errors on the third order moments $M_{ij} = \overline{\tilde{u}^i \tilde{w}^j}$ with $i+j=3$ and $\tilde{u} = u'/(\overline{u'^2})^{0.5}$, Podesta et al. (2009) provides the following relationship for M_{30}:

$$\epsilon^{\pm}_{M_{30}} = \frac{M_{30}}{\sqrt{N}} \left| \frac{\overline{u'^6}}{(\overline{u'^3})^2} - 1 \right|^{1/2} \tag{F.7}$$

Equation F.7 is also valid for M_{03} provided that w' is used instead of u'. Since Podesta et al. (2009) does not provide an error estimate for the mixed third order moments M_{21} and M_{12}, the following relationship is proposed for M_{21} (a similar one can be defined for M_{12}):

$$\epsilon^{\pm}_{M_{21}} = \frac{M_{21}}{\sqrt{N}} \left| \frac{\overline{u'^4 w'^2}}{(\overline{u'^2 w'})^2} - 1 \right|^{1/2} \tag{F.8}$$

Figures F.2a-f illustrate, as an example, the spatially-averaged normalized time-convergence errors for the spatially-averaged velocity components $\langle \overline{u} \rangle_x$, $\langle \overline{v} \rangle_x$ and $\langle \overline{w} \rangle_x$, the streamwise turbulent intensities $\langle \overline{u'u'} \rangle_x$, the Reynolds shear stress $\langle \overline{u'w'} \rangle_x$ and the third order moment $\langle M_{30} \rangle_x$, obtained from the velocity data of the third PIV measurement over plane A in Exp.1 (see Table 3.1 and Chapter 5). Figures F.2a-e show that the errors for the first order statics are the highest near the bed (around 2% of $\langle \overline{u} \rangle_x$) and decrease with the distance from the
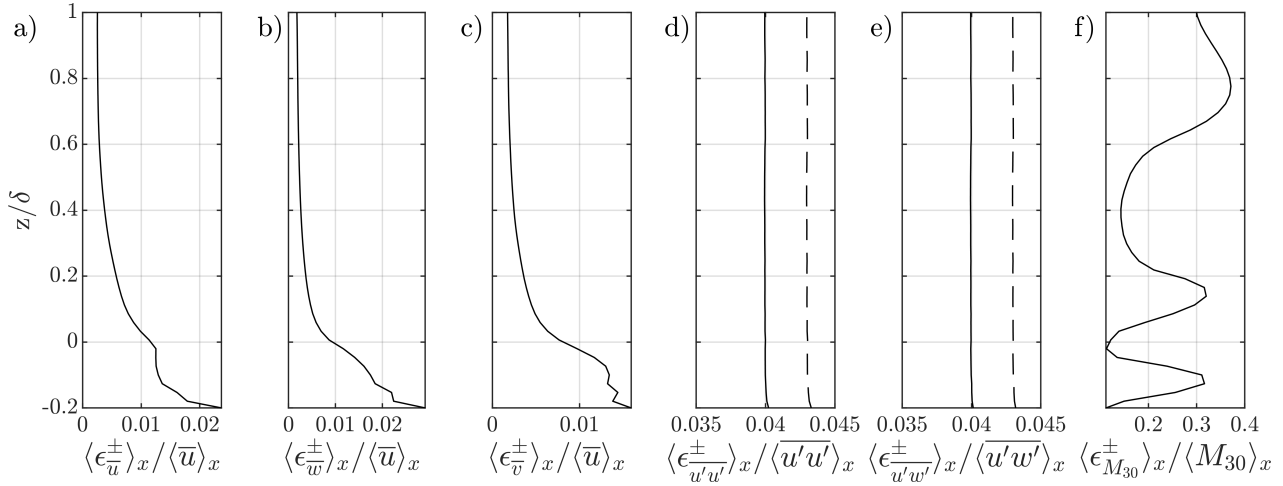
Figure F.2: Spatially-averaged time convergence errors normalized by the spatially-averaged flow statistics. The data are from the third PIV measurement on plane A in Exp. 1. Solid lines define ϵ^- and dashed lines ϵ^+ (superimposed for the first and third order moments).

bed. The relative errors for the second order moments (in Figures F.2d-e) are roughly constant over the whole water depth and equal to 4%. The relative errors for $\langle \overline{u'u'} \rangle_x$ are equal to the relative errors of the Reynolds shear stresses as they depend only on the number of samples (see above). They are representative, as such, also of the relative errors of the vertical and transverse turbulent intensities and of the vertical and transverse Reynolds stresses. Figure F.2f shows that the third order moment is characterized by higher relative errors in the range of 10-20%. Please note, that the 30% relative error peaks are only due to the fact, that M_{30} assumes locally values close to zero. The higher relative error observed for the third order moment, is expected, since the higher the order of the moment, the higher the number of samples needed to reduce the time convergence error.

G   Influence of the spatial resolution on the flow statistics

The aim of this Section is to determine whether the spatial resolution of the stereo-PIV measurements is enough to accurately measure the flow statics and which turbulent length scales are resolved. PIV acts as a local spatial filter, by averaging the displacement of the particles within the correlation window. As a result, bias errors on the velocity measurements can arise, if the displacement of the particles within the correlation window is not homogeneous, such as in the presence of strong velocity gradients (Atkinson et al., 2014). The correlation window size and the grid spacing determine, as such, the accuracy of the PIV measurement and the size of the length scales which can be resolved. For a multipass PIV algorithm, the size of the smallest resolvable length scales lies between the grid size and the correlation window size. Most length scales below the correlation window size are weakened, in fact, by the spatial filtering effect (Aberle et al., 2017).

As discussed in Section 3.4.1.6, the correlation window size used for all stereo-PIV measurements is equal to $36{\times}36$ pixels^2 ($0.22{\times}0.22$ cm^2) with a 50% overlap, corresponding to a grid spacing of 0.11 cm. Unfortunately, it is not possible to apply smaller window sizes to the stereo-PIV data for the analysis on the influence of the spatial resolution, given the quality of the dewarped stereo-PIV images. For this reason, the analysis is performed on the data obtained with the 2D2C planar PIV system, acquired for the validation of the stereo-PIV system (see Section H.2), as it allows to reach higher spatial resolutions. As discussed in Section H.2, the flow statistics obtained with the 2D2C PIV system are similar to the ones obtained with the stereo-PIV system, so that the following results can be translated to the stereo-PIV measurements. The dataset Hl in table H.1 is processed with three different interrogation windows with a 50% overlap: [$0.11{\times}0.11$, $0.22{\times}0.22$, $0.30{\times}0.30$] cm^2 corresponding to [0.5, 1, 1.4] times the size of the interrogation window of the stereo-PIV measurements.

Figure G.1 illustrates the comparison between the longitudinally-averaged first and second order moments obtained with the three different interrogation windows. The first order moments are normalized by the effective velocity, while the second order moments by the shear velocity obtained from the extrapolation of the Reynolds shear stress with the highest spatial resolution (0.11 cm) to the top of the spheres. The streamwise and vertical velocity profiles in Figures G.1a-b match over the whole water depth within the time convergence interval. In Figures G.1c-d, the Reynolds shear stress and the streamwise and vertical normal stresses show, instead, a dependency on the spatial resolution near the top of the spheres and near the boat, i.e. where the velocity gradients are the strongest. With decreasing measurement resolution the turbulent shear and normal stresses are increasingly underestimated. The Reynolds shear stresses show a reduction of 20% between the highest and the lowest spatial resolution. In the case of the vertical normal stresses $\langle \overline{w'^2} \rangle_x$, the underestimation is not only restricted to the regions with the highest velocity gradients, but it extends over the whole water depth.

The influence of the spatial resolution on the estimate of the shear velocity u_* and on the log-law parameters is investigated in the following. The shear velocity is determined by extrapolating the Reynolds shear stress
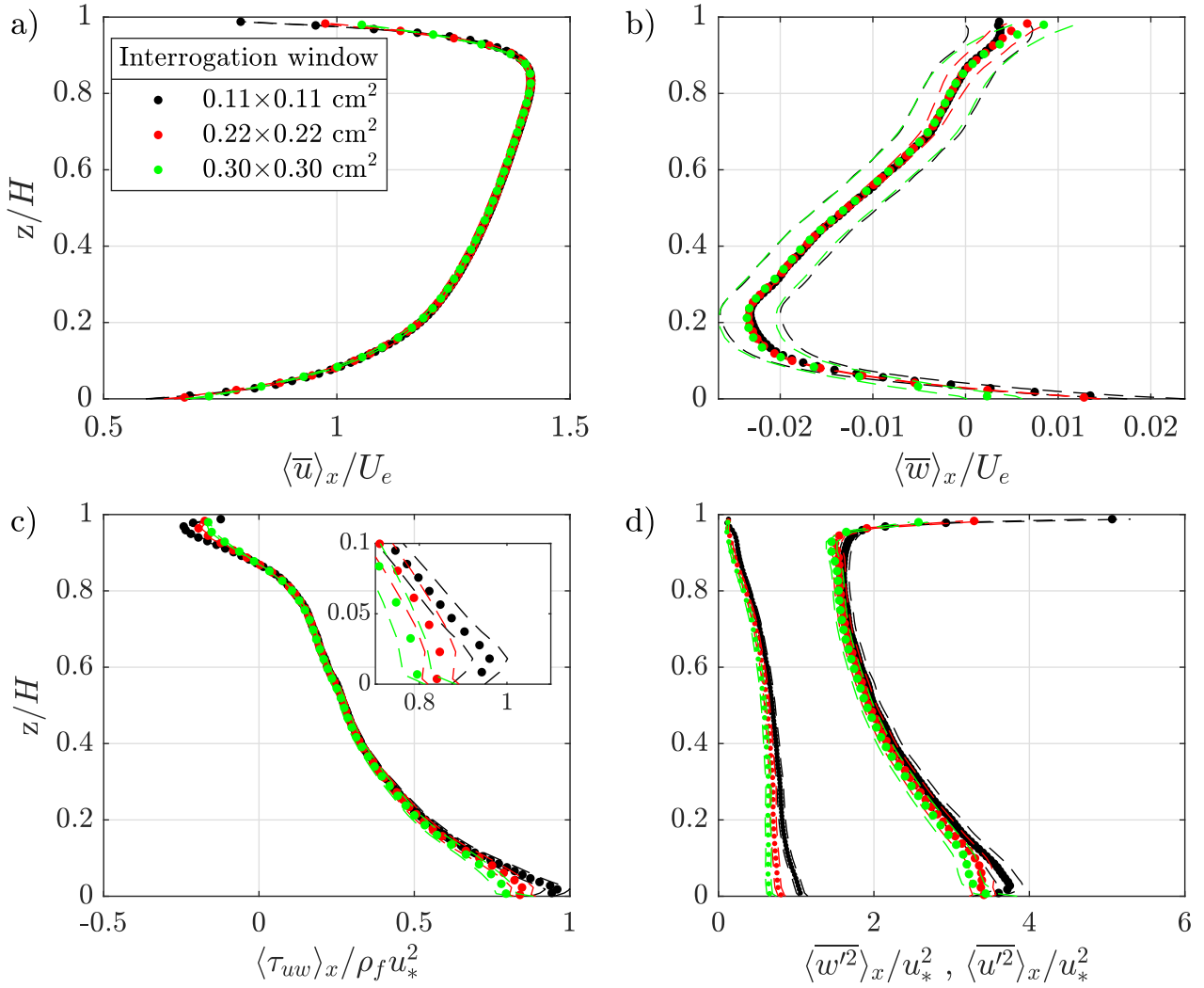
Figure G.1: Vertical profiles of the double-averaged streamwise $\langle \overline{u} \rangle_x$ and vertical $\langle \overline{w} \rangle_x$ velocities (a-b), of the longitudinally-averaged Reynolds shear stresses $\langle \overline{\tau}_{uw} \rangle_x$ (c) and of the longitudinally-averaged vertical $\rho_f \langle \overline{w'^2} \rangle_x$ and streamwise $\rho_f \langle \overline{u'^2} \rangle_x$ normal stresses (d), obtained with three different PIV interrogation window sizes.

profiles to the top of the spheres on the basis of a cubic spline interpolation, as the profiles are not linear (see Figure G.1d). Table G.1 shows that the shear velocity obtained with the highest resolution is in good agreement with the shear velocity obtained from the slope depth product u_{*H} in table H.1. With decreasing spatial resolution, the shear velocity u_* decreases. A difference of 10% is observed between the shear velocities obtained with the highest and the lowest measurement resolution.

In the following, the influence of the spatial resolution on the log-law parameters is investigated. The log law parameters are determined on the basis of the procedure already described in Section H.3.4 by fitting the log law to the double-averaged streamwise velocity profile. Table G.1 shows that for the highest spatial resolution of 0.11 cm, $k_s/D = 0.65$ and $d/D = -0.22$ (where D is the diameter of the spheres), similar to the values observed by Grass et al. (1991) and by Detert and Nikora (2010) over a bed of spheres. However, with decreasing measurement resolution k_s decreases and d increases. Given that the streamwise velocity profiles are slightly affected by the spatial resolution, the reduction in the log law parameters derives from the

Resolution	u_*	k_s	z_d	z_m/H	z_M/H
[cm^2]	[cm/s]	[cm]	[cm]	[-]	[-]
0.11×0.11	2.81 ± 0.06	1.31 ± 0.01	-0.44 ± 0.01	0.085	0.172
0.22×0.22	2.66 ± 0.06	1.04 ± 0.01	-0.38 ± 0.01	0.081	0.177
0.30×0.30	2.58 ± 0.05	0.82 ± 0.01	-0.25 ± 0.01	0.007	0.135

Table G.1: Log law parameters as a function of the measurement resolution (given by the PIV interrogation window size): shear velocity u_* obtained by linearly extrapolating the Reynolds shear stress profile to the top of the spheres, equivalent sand roughness k_s, zero-plane position z_d, start and end point of the logarithmic region, z_m and z_M.

apparent reduction in shear velocity. Table G.1 shows that an apparent reduction of 5% of the shear velocity, moving from the highest to the lowest measurement resolution, causes a reduction of k_s and an increase of d of about 40%. For the range of validity of the log law, the finest and intermediate spatial resolutions show similar intervals, comprised between 0.1-0.2 H in accordance with other investigations on rough beds Detert and Nikora (2010); Raus et al. (2019); Rouzes et al. (2019). For the lowest spatial resolution there is, instead, a shift of the range of validity towards the spheres.

In order to assess, whether the spatial resolution of the stereo-PIV measurements is enough to resolve the characteristic turbulent length scales, the Taylor and the Kolmogorov length scales are estimated on the basis of the 2D2C PIV data with the highest resolution (0.11 cm). The Taylor microscale λ_t represents the characteristic length scale of the inertial subregion, while the Kolmogorov length scale η the size of the smallest turbulent eddies (Pope, 2000). Both scales can be defined through dimensional analysis as follows (Nezu and Nakagawa, 1993):

$$\lambda_t = \sqrt{\frac{15\nu\overline{u'^2}}{\epsilon}} \tag{G.1}$$

$$\eta = \left(\frac{\nu^3}{\epsilon}\right) \tag{G.2}$$

The turbulent energy dissipation ϵ can be estimated on the basis of the macroscale approach (Nezu et al., 1993):

$$\epsilon = K\frac{(\overline{u'^2})^{\frac{3}{2}}}{L_x} \tag{G.3}$$

where the constant K is set to 1.67 following Nezu and Nakagawa (1993) and L_x is the integral length scale in the longitudinal direction. On the basis of Taylor's frozen turbulence hypothesis L_x is estimated on the basis of the integral time scale L_t: $L_x = \overline{u}(x,z)L_t$. The integral time scale is defined as the integral of the normalized autocorrelation function of the streamwise velocity fluctuations:

$$L_t(x,z) = \lim_{T \to \infty} \int_0^T \frac{u'(x,z,t)u'(x,z,t+d\tau)}{\overline{u'^2}}d\tau \tag{G.4}$$

Figure G.2a illustrates the vertical profile of the space averaged Taylor microscale $\langle\lambda_t\rangle_x$. $\langle\lambda_t\rangle_x$ increases with increasing distance from the bed. The smallest eddies in the inertial subrange are observed at the top of the spheres where the turbulent shear layer develops. It is expected that below the top of the spheres the eddy-size increases again since the turbulent production decreases, as measurements conducted over an immobile
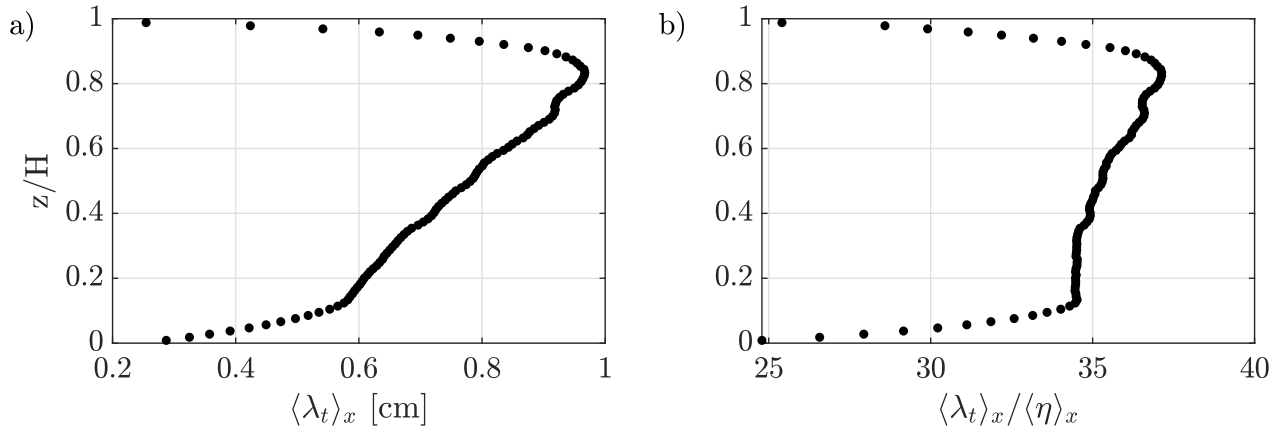
Figure G.2: a) Vertical profile of the longitudinally-averaged Taylor microscale $\langle\lambda_t\rangle_x$; b) vertical profile of the ratio between the longitudinally-averaged Taylor microscale $\langle\lambda_t\rangle_x$ and the longitudinally-averaged Kolmogorov length scale $\langle\eta\rangle_x$

gravel bed by Mignot et al. (2009b) and discussed by Dey et al. (2011c) show. The size of the eddies at the top of the spheres equal to 0.29 mm represents, therefore, the most stringent condition for the measurement resolution. Therefore, the spatial resolution of the stereo-PIV measurements, estimated to be equal to the interrogation window size of 0.22 mm to be on the safe side, is adequate to resolve the Taylor microscale.

Figure G.2b illustrates the ratio between the spatially-averaged Taylor and Kolmogorov microscales. The size of the smallest turbulent eddies relative to the Kolmogorov length scale decreases with the distance from the wall. The smallest Kolgomorov legth scale is also observed near the wall with an eddy size equal to 0.011 cm. As already mentioned, the actual spatial resolution of the stereo-PIV measurements is comprised between the grid spacing (0.11 cm) and the interrogation window size (0.22 cm), equivalent to 10 and 20 Kolmogorov length scales, respectively. According to Moin and Mahesh (1998), most of the energy is dissipated for scales bigger than 15η, so that the stereo-PIV spatial resolution is enough to capture most of the energy dissipation. In summary, the results show that the spatial resolution of the stereo PIV measurements (corresponding to the interrogation window size 0.22×0.22 cm^2) is enough to resolve the first order flow statistics over the whole water depth, while the second order statistics only in the bulk flow. At the level of the top of the spheres the latter are slightly underestimated, as the interrogation window averages out the strong velocity gradients present in the shear layer, resulting in a damping of the turbulent fluctuations. This damping results in an underestimation of 5% of the shear velocity u_*, which causes a decrease of about 20% of the sand roughness and an increase of the roughness displacement length of about 13%. The range of validity of the log-law is instead unaffected. As for the turbulent length scales, the resolution of the stereo-PIV measurements are enough to resolve the Taylor micro scale and most of the turbulent dissipation.

H   Validation of the stereo-PIV system

H.1 Introduction

In this chapter, the stereo-PIV system is validated in regard to two aspects. First, the influence of the steep viewing angles of the stereo-PIV cameras on the reconstruction of the flow field is assessed by comparing the stereo PIV measurements with simultaneous 2D2C PIV measurements. Second, the influence of the surface glass plate (boat) on the bulk flow statistics is investigated by performing 2D2C PIV measurements with and without the presence of the boat.

H.2 Stereo-PIV validation with 2D2C PIV

The stereo-PIV setup is characterized by steep vertical viewing angles which cause a significant deformation of the image in the vertical direction. Since the images are compressed in the vertical direction by a factor of three compared to the longitudinal direction, the vertical resolution is reduced, so that the detection of vertical displacements is potentially more prone to errors. In order to validate the flow field reconstructed with the stereo-PIV system, 2D2C planar PIV measurements are performed simultaneously with stereo-PIV measurements. The flow fields reconstructed with both PIV systems are compared, keeping in mind that 2D2C planar PIV measurements are always affected by perspective errors.

H.2.1 Experimental setup

A set of two experiments is performed over the densest bed configuration λ_h with no fine sediments present with the flow conditions listed in Table H.1, covering both flow depths analysed in the experiments in Table 3.1. Hl corresponds to the flow conditions of experiment 7 ($G\theta h$), while Hh shares the same water depth as experiment 4 (R-GAh) but the same shear stress conditions as experiment 7 ($G\theta h$). These flow conditions, characterized by the highest shear stress investigated in Table 3.1, are selected in order to test the performance of the stereo-PIV system under the most challenging flow conditions, i.e. in the presence of high velocity gradients in the near bed region. In the next Sections, the experimental setup and the results related to experiment Hl are presented, while those related to experiment Hh are illustrated in Appendix I, since the results are similar.

The 2D2C planar PIV system is installed at the same location of the stereo-PIV system, described in Section 3.4.1.2. The 2D2C PIV setup consists of a UI-3060CP-M-GL rev.2 iDS high-frequency camera, equipped with a 50 mm Nikkor lens and with a 475 nm long-pass filter, to filter out reflections at the level of the spheres (as the flow is seeded, also in this case, with fluorescent particles). The camera is installed perpendicularly to the laser sheet at distance of 90 cm from the flume glass wall. The PIV measurements are performed in the

centre of the channel over plane A (see Figure 3.2a). The field of view corresponds to the one shown in figure 3.7b over the second pattern of spheres. For the 2D2C PIV system the field of view covers only the region above to the top of the spheres. The stereo-PIV and the 2D2C PIV systems are triggered simultaneously at a burst frequency of 5 Hz. As the two PIV systems do not share the same resolution, the image frequency is adjusted for each PIV system, to yield a maximum particle displacement of 10 pixels: 400 Hz for the sPIV system and 274 Hz for the 2D2C PIV system in Exp. Hl and 376 Hz and 241 Hz, respectively, in Exp. Hh. The PIV data are processed with the Davis-PIV software 8.4.0 (for more details see Section 3.4.1.6). A final correlation window size of 32×32 pixels and of 24×24 with a 50 % overlap is chosen for the stereo- and the 2D2C PIV system, respectively, to yield the same grid resolution of 1.1×1.1 mm^2 for both PIV systems.

Exp.	H	Q	i	U	U_e	R_h	u_{*R}	u_{*H}	Re	Fr
	[cm]	[l/s]	[%]	[cm/s]	[cm/s]	[cm]	[cm/s]	[cm/s]	[-]	[-]
Hl	5.90	5.0	0.17	28	21	4.2	2.7	3.1	16600	0.37
Hh	10.80	10.4	0.11	32	27	6.3	2.6	3.4	34600	0.31
	±0.05	±0.5	±0.01	±2	±2	±0.1	±0.2	±0.2		

Table H.1: Flow conditions for the comparison of the stereo-PIV with the 2D2C PIV system: water depth above top of the spheres H, flow rate Q, slope s, bulk velocity $U = Q/(WH)$, effective velocity $U_e = Q/(WH_e)$ (with $H_e = H+\phi k$ the effective water depth, $k = 3.3$ cm the thickness of the spheres' bed and $\phi = 0.57$ the bed porosity), hydraulic radius R_h, shear velocity based on the hydraulic radius $u_{*R} = \sqrt{gR_h i}$, shear velocity based on the water depth $u_{*H} = \sqrt{gHi}$, bulk Reynolds number $Re = UH/\nu$, Froude number $Fr = U/\sqrt{gH}$

H.2.2 2D2C and stereo-PIV time-averaged flow fields

In Figure H.1 the time-averaged streamwise and vertical velocities, $\overline{u}$ and $\overline{w}$, and the Reynolds shear stresses τ_{uw} ($= -\rho_f \overline{u'w'}$) obtained with the 2D2C PIV system and with the stereo-PIV system are compared for the Hl case. $\overline{u}$ and $\overline{w}$ are normalized by the effective bulk velocity $U_e = Q/(WH_e)$, where the effective water depth $H_e = H + \phi k$ takes into account the volumetric displacement induced by the spheres (with $\phi(z = -k)$ the bed porosity of the total layer of spheres with thickness $k = 3.3$ cm - see figure 3.1c). τ_{uw} is normalized by the shear velocity obtained from the slope depth product u_{*H}. Figures H.1a-c show that the 2D2C PIV data are able to resolve the flow above the spheres along with a narrow region below the top of the spheres few mm deep. The view in the central part of the bed interstices is impaired by the sphere in the out of plane position. The stereo-PIV system manages, instead, to resolve the flow deep below the spheres' top, down to the bottom layer of spheres (Figures H.1d-f).

The streamwise velocity field $\overline{u}$ obtained from the stereo-PIV in Figure H.1d shows perfect agreement with the one obtained from the 2D2C PIV in Figure H.1a both in the bulk and in the near-bed region. The region of reduced streamwise velocity below the top of the spheres is, in fact, detectable in both velocity fields at the same location.

The vertical velocities obtained from the stereo-PIV in Figure H.1e show similar patterns as the vertical velocity field obtained from the 2D2C PIV in Figure H.1b. Both fields are characterized by a broad region of negative vertical velocities in the bulk flow. A region of positive vertical velocity is observed directly above
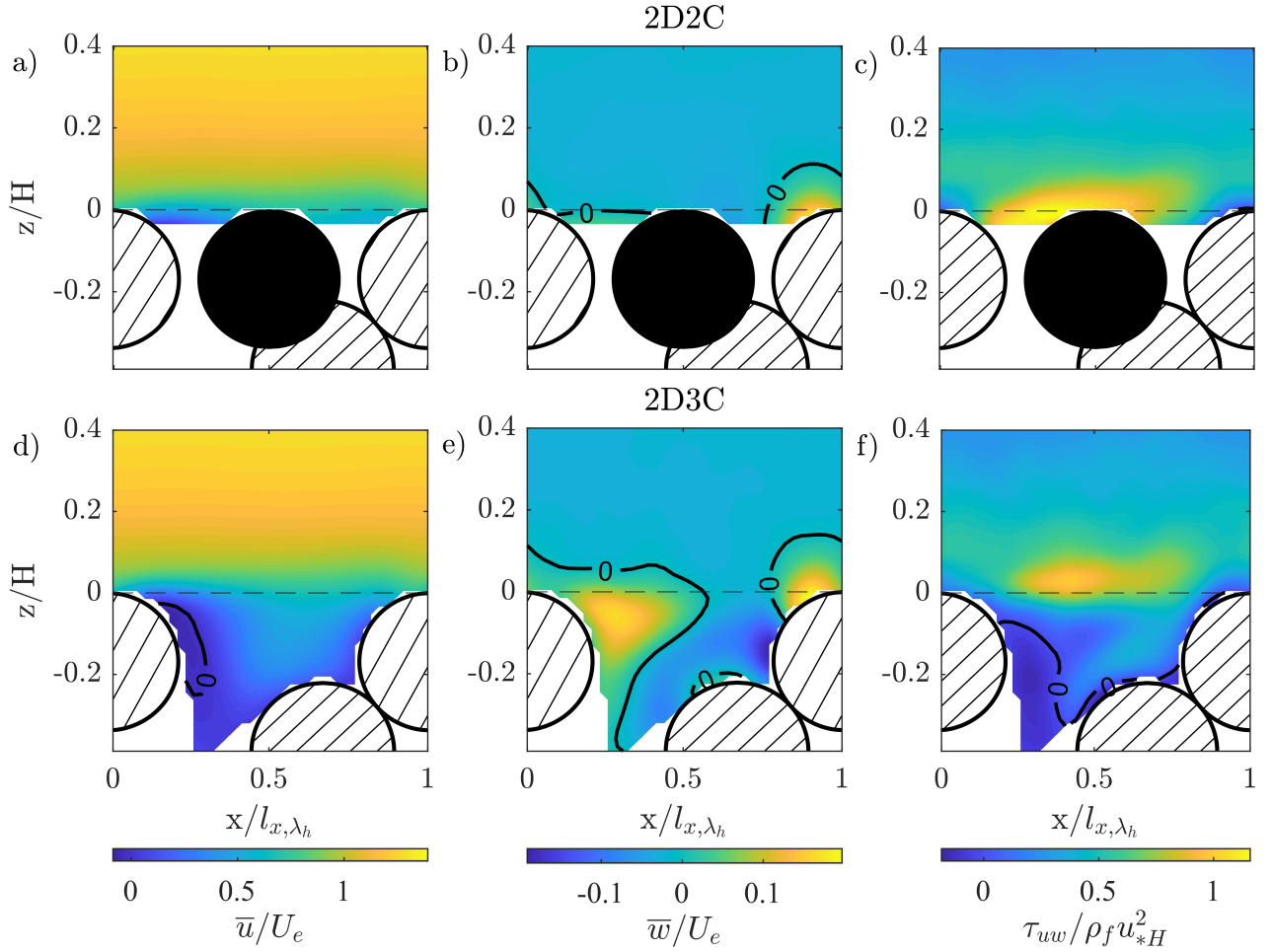
Figure H.1: Time-averaged streamwise and vertical velocity fields, $\overline{u}$ and $\overline{w}$, and Reynolds shear stresses τ_{uw} field for experiment Hl: (a-c) 2D2C PIV measurements, (d-f) 2D3C stereo-PIV measurements.

the spheres (for $0.75 < \mathrm{x}/l_{x,\lambda_h} < 1$) and in their lee side (for $0.1 < \mathrm{x}/l_{x,\lambda_h} < 0.55$). The 2D2C and stereo-PIV show a similar lateral and vertical extension of the region of positive vertical velocity above the spheres. The region of positive vertical velocity in the lee side shows, instead, a slight difference in its vertical extension between the two datasets. In the case of the stereo-PIV data, this region extends above the top of the spheres up to a height of $0.05~H$, while this region is confined under the top of the spheres for the 2D2C data.

As for the Reynolds-shear-stress fields in Figures H.1c,f, the 2D2C and stereo-PIV data show similar patterns, with a region of higher shear stress developing at the top of the spheres, corresponding to the shear layer. The centre of the shear layer is slightly shifted upwards for the stereo-PIV data compared to the 2D2C PIV data. In summary, apart from slight misalignments in the flow field patterns, the stereo-PIV system is able to properly reconstruct the flow field above the spheres.

H.2.3 Topological characterization of the flow field in the bed interstices

The validation of the flow field in the bed interstices is performed on the basis of topological principles for the assessment of the integrity of a measured vector field, following the procedure developed by Foss (2004). The method allows to assess whether a measured flow pattern overlaid to a surface of interest (e.g. a PIV plane)

is cinematically possible, on the basis of the number of critical points present in the surface. A critical point is a topological feature of a flow field, classifiable as node N or saddle S, where the slope of a streamline is indeterminate (Perry et al., 1969). Infinite stream-lines converge in or diverge from a nodal point, while only two stream-lines pass through a saddel point in opposite directions. Given a flow field bound by a three dimensional surface, the Poincarè-Hopf theorem states that the admissible number of nodes and of saddles depends on the experimental Euler characteristic of the surface χ_e (Foss, 2004):

$$\chi_e = \sum N - \sum S \tag{H.1}$$

The topological constraint H.1 can be extended also to the case of a 3D-surface collapsed onto a 2-dimensional plane (Foss et al., 2016):

$$\chi_e = 2\sum N + \sum N' - 2\sum S - \sum S' - \sum OA \tag{H.2}$$

where N' and S' are half nodes and half saddles on the perimeter of the surface and OA are the obtuse angles found along the perimeter. By considering that any surface can be obtained from the continuous deformation of a sphere "through which holes have been punched and to which handles have been attached" (Foss et al., 2016), the Euler characteristic of the surface is given a priori by its formation process (Foss, 2004):

$$\chi_a = \chi_{sphere} - 2\sum Handles - \sum Holes \tag{H.3}$$

where $\chi_{sphere} = 2$. The edges of the surface where the velocity vectors point inward or outward of the surface, identify holes, while edges tangential to the velocity vectors are called seams. Once the holes and the handles as well as the nodes and saddles are identified within the surface of interest, the integrity of the measured flow field is verified if $\chi_e = \chi_a$.

Figure H.2a shows the time averaged velocity vector field in the x-z plane superimposed to the time averaged transverse velocity field in the bed interstices. For the topological characterization of the velocity field the surface of interest is chosen such that it covers the whole region in between the spheres and the flow field above the spheres up to a height of z/H = 0.08. The perimeter lines in red identify seams while the ones in blue holes. The surface is characterized by a total of five holes and no handles, so that χ_a = -3. At the same time, a total of three half saddles S' can be identified in the vector field. Since the surface of interest represents a collapsed sphere, equation H.2 yields χ_e = -3. As such, the integrity of the flow field in between the spheres is verified.

The flow pattern in Figure H.2a does not show the presence of a recirculation region in the lee side of the sphere, as generally expected for flows around submerged spheres (Papanicolaou et al., 2011; Dey et al., 2011a; Liu et al., 2017). It is characterized, instead, by an upwelling region originating below the sphere upstream. It is surmised, that the upwelling flow, being accelerated in the inter-sphere space, leads to vorticity annihilation, which is associated with the convergence of streamlines (Hunt and Eames, 2002; Sau et al., 2003). In a similar way, Neuman and Bédard (2015) observes in the case of a submerged isolated cylinder over an erodible bed that the legs of the horseshoe vortex upwelling from the scour hole in the lee of the cylinder lead to the cancellation of the recirculation region.

The non-zero transverse velocities in Figure H.2a suggest that the laser sheet plane is not perfectly positioned in the symmetry plane of the pattern, but is shifted in the transverse positive direction. On the basis of
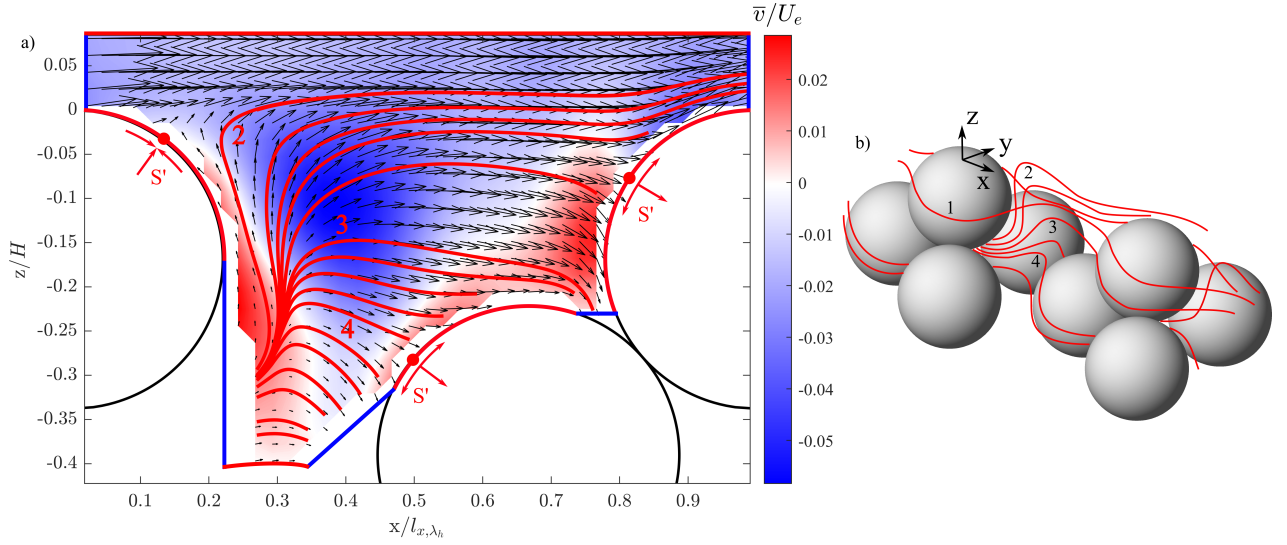
Figure H.2: (a) Time-averaged velocity vector field in the x-z plane superimposed to the time-averaged transverse velocity field $\overline{v}$. The perimeter of the surface for the topological characterization of the vector field is highlighted with the seams in red and the holes in blue. The critical half-saddle points are marked with a red dot. (b) Possible streamline configuration consistent with the flow patterns in Figure a.

the flow field in Figure H.2a, a possible configuration of the streamlines is sketched in Figure H.2b. The corresponding groups of streamlines are identified by the same numbers in Figures H.2a and b. The negative transverse velocity region in the lee side of the sphere upstream in Figure H.2a are probably associated to fluxes deriving from the side of the sphere (streamline 1 in Figure H.2b). The groups of streamlines 2 and 3 in Figures H.2a and H.2b show that part of the upwelling flow reaches the top layer of spheres and is advected above the downstream sphere (group 2) and probably around or below (group 3). The group of upwelling streamlines 4 is deflected, instead, by the downstream bottom sphere into the bottom layer of spheres again.

H.2.4 Double-averaged flow statistics and quadrant analysis

Figure H.3 illustrates the comparison between the longitudinally-averaged vertical profiles of the first, second and third order moments obtained with the 2D2C and the stereo-PIV system. The first order moments, i.e. the double-averaged streamwise and vertical velocities, $\langle \overline{u} \rangle_x$ and $\langle \overline{w} \rangle_x$, are normalized by the effective bulk velocity. The second order moments, i.e. the longitudinally-averaged streamwise, vertical and transverse normal stresses $\rho_f \langle \overline{u'^2} \rangle_x$, $\rho_f \langle \overline{w'^2} \rangle_x$, $\rho_f \langle \overline{v'^2} \rangle_x$ and the longitudinally-averaged Reynolds shear stresses $-\rho_f \langle \overline{u'w'} \rangle_x$ are normalized by the shear velocity $u_{*,2C}$ obtained from the extrapolation of the shear stress profile obtained from the 2D2C PIV system to the top of the spheres (the viscous and form-induced stresses are negligible). For the stereo-PIV data, the longitudinally-averaged turbulent kinetic energy is expressed as $\langle k \rangle_x^{2D3C} = \frac{1}{2}(\langle \overline{u'^2} \rangle_x + \langle \overline{w'^2} \rangle_x + \langle \overline{v'^2} \rangle_x)$, while for the 2D2C system providing only two velocity components, the relationship by Nezu and Nakagawa (1993) is used: $\langle k \rangle_x^{2D2C} = \frac{1}{2} \frac{1}{0.72}(\langle \overline{u'^2} \rangle_x + \langle \overline{w'^2} \rangle_x)$. The set of third order moments, describing the flux of the turbulent normal stresses, is expressed as $M_{i,j} = \langle \hat{u}^i \hat{w}^j \rangle_x$ with $i + j = 3$ and $\hat{u} = u'/(\overline{u'^2})^{0.5}$, $\hat{w} = w'/(\overline{w'^2})^{0.5}$ (Raupach, 1981). For all flow statistics in Figure H.3 the confidence interval based on the time convergence error (see Appendix F) is highlighted as dashed lines.

Figures H.3a and H.3b show that, while the longitudinal velocity profiles of the 2D2C and of the stereo-PIV system are in good agreement, the vertical velocity profiles are affected by some discrepancies. Even though the two vertical velocity profiles share similar trends, the vertical velocities obtained with the stereo-PIV system are characterized by stronger magnitudes compared to the 2D2C PIV system. This difference is particularly evident in the region near the top of the spheres, where the highest turbulent production takes place Mignot et al. (2009a); Dey and Das (2012); Sarkar et al. (2016).

Similar considerations can be drawn also for the second order moments in Figures H.3c-e. As a reference,
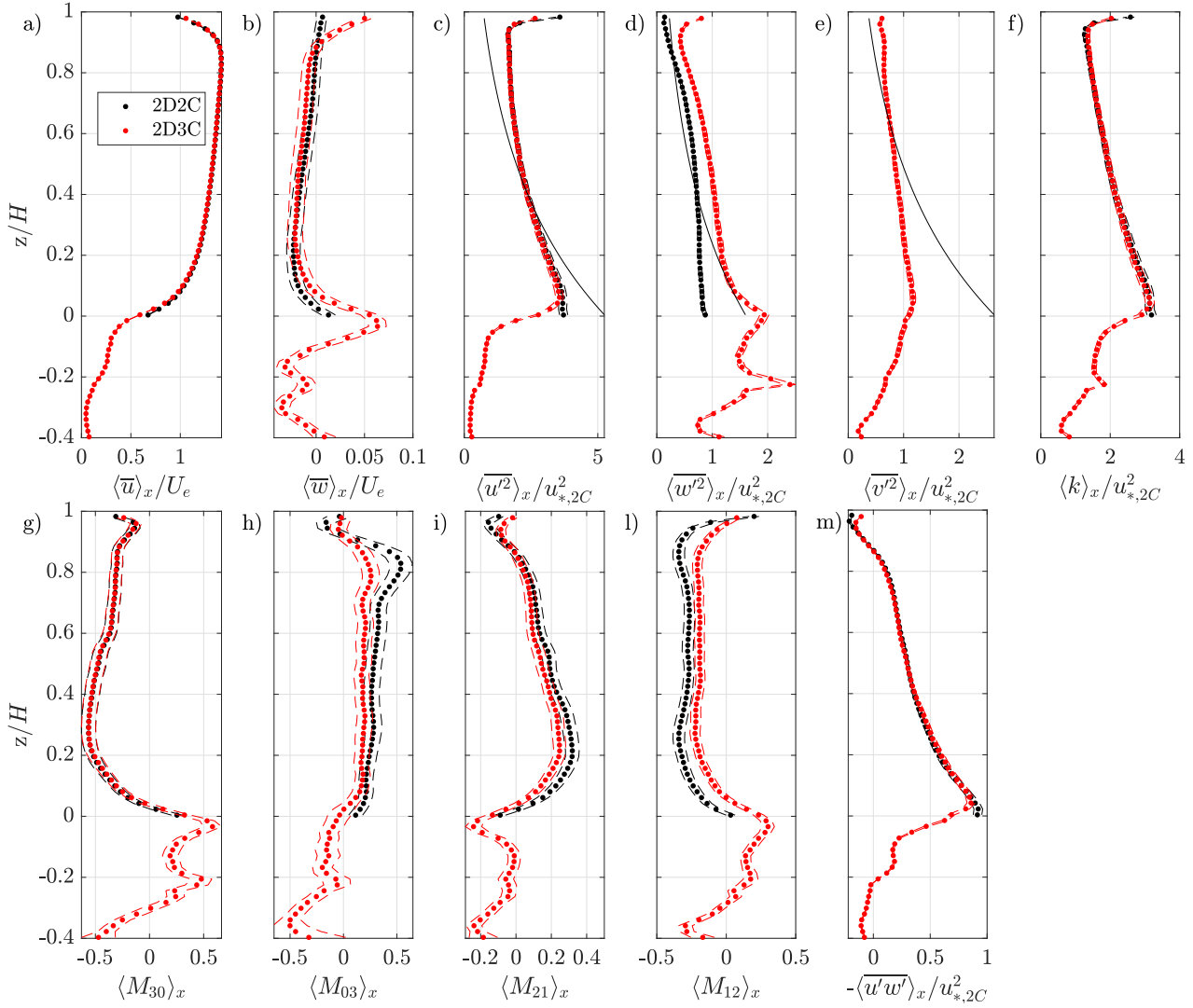

Figure H.3: Comparison of the longitudinally-averaged profiles of the first, second and third order moments obtained with the planar PIV system (2D2C) and the stereo-PIV system (2D3C) for the Hl case: streamwise $\langle \overline{u} \rangle_x$ and vertical $\langle \overline{w} \rangle_x$ velocities (a-b), streamwise $\rho_f \langle \overline{u'^2} \rangle_x$, vertical $\rho_f \langle \overline{w'^2} \rangle_x$ and transverse $\rho_f \langle \overline{v'^2} \rangle_x$ normal stresses (c-e), turbulent kinetic energy $\langle k \rangle_x$ (f), third order moments $\langle M_{i,j} \rangle_x$ (g-l) and Reynolds shear stresses $-\rho_f \langle \overline{u'w'} \rangle_x$ (m). The first order moments are normalized by the effective bulk velocity U_e and the second order moments by the shear velocity $u_{*,2C}$ obtained from the extrapolation of the shear stress profile obtained with the planar PIV system. The exponential laws by Nezu and Nakagawa (1993) for the normal turbulent stresses are plotted as black continuous lines in Figures (c-e).

the exponential fitting laws, determined experimentally by Nezu and Nakagawa (1993), are plotted with continuous black lines. Figure H.3d shows that the streamwise normal stress profiles match over the whole water depth with a slight difference in the normal stress peak, being slightly displaced upwards for the stereo-PIV data. Compared to the exponential law by Nezu and Nakagawa (1993), the experimental data show higher values near the boat and lower values near the bottom. This deviation is a result of the low submergence of the flow (H/k $\simeq$ 3), as pointed out by Rouzes et al. (2019) who observes similar trends for flows with low submergence over an array of cubes. For the high submergence case Hh, presented in Appendix I, the streamwise normal stresses show, instead, exactly the same trend as Nezu and Nakagawa (1993).

In Figure H.3d, the stereo-PIV vertical normal stresses are consistently higher than the 2D2C PIV vertical normal stresses. The normal stresses differ by a factor of 1.4 in the bulk flow, wile this discrepancy reaches a factor of 2 near the top of the spheres and near the boat. The 2D2C PIV data agree well with the exponential law by Nezu and Nakagawa (1993) in the upper part of the flow, while they deviate near the top the spheres. This deviation could be a result of the low submergence of the flow, consistent with the observations by Rouzes et al. (2019).

As for the transverse normal stresses available only through the stereo-PIV system, Figure H.3e shows that they agree well with the exponential law of Nezu and Nakagawa (1993) in the upper part of the flow, deviating, though, in the lower part. Considering that the transverse velocities are determined during the stereo reconstruction through equation 3.5, where only the streamwise particle displacement appears, the transverse normal stress profiles can be considered reliable.

The turbulent kinetic energy profiles in Figure H.3f show a perfect overlap. The same can be also observed for the turbulent kinetic energy profiles obtained for the high submergence case Hh in Appendix I in Figure I.2f. The result is quite surprising as the vertical normal stresses differ between the 2D2C and stereo-PIV.

The third order moments in Figures H.3g-l show that the overlap between 2D2C PIV data and stereo-PIV profiles depends on the relative contribution of the vertical velocity fluctuations to the specific moment. For the skewness of the streamwise velocity $\langle M_{30} \rangle_x$ in Figure H.3g there is perfect agreement between the 2D2C and stereo-PIV profiles. Figure H.3h shows that the $\langle M_{03} \rangle_x$ profiles tend to depart when going towards the surface boat, but are within the measurements uncertainty near the top of the sphere. For the $\langle M_{21} \rangle_x$ moment in Figure H.3i the two profiles are in good agreement within the measurement uncertainty. In the case of the $\langle M_{12} \rangle_x$ moment, the magnitude of the stereo-PIV profile is higher than the 2D2C PIV profile but the two profiles show a similar trend.

The Reynolds shear stress profile in Figure H.3m match over the whole water depth. For the stereo-PIV data the shear stress peak is located slightly higher than the 2D2C PIV data, consistent with the upward shift of the shear layer observed in the time averaged field of the Reynolds shear stresses in Figure H.1f. The extrapolation of the shear stress profiles to the top of the spheres yields similar shear velocity values within the measurement uncertainty: $u_{*,2C} = 2.79 \pm 0.06$ cm/s for the 2D2C PIV data and $u_{*,3C} = 2.75 \pm 0.06$ cm/s for the stereo-PIV data.

The Reynolds shear stresses can be decomposed in the contribution of different turbulent events, resulting from the bursting cycle (Raupach, 1981; Lu and Willmarth, 1973). They can be identified in the $u'w'$-plane as Q1-outward interactions ($u'>0$ & $w'>0$), Q2-ejections ($u'<0$ & $w'>0$), Q3-inward interacitons ($u'<0$ & $w'<0$) and Q4-sweeps ($u'>0$ & $w'<0$). Since Q2/Q4 events have opposite contributions to the Reynolds shear stresses compared to the Q1/Q3 events, the time-averaged Reynolds shear stresses can hide differences in
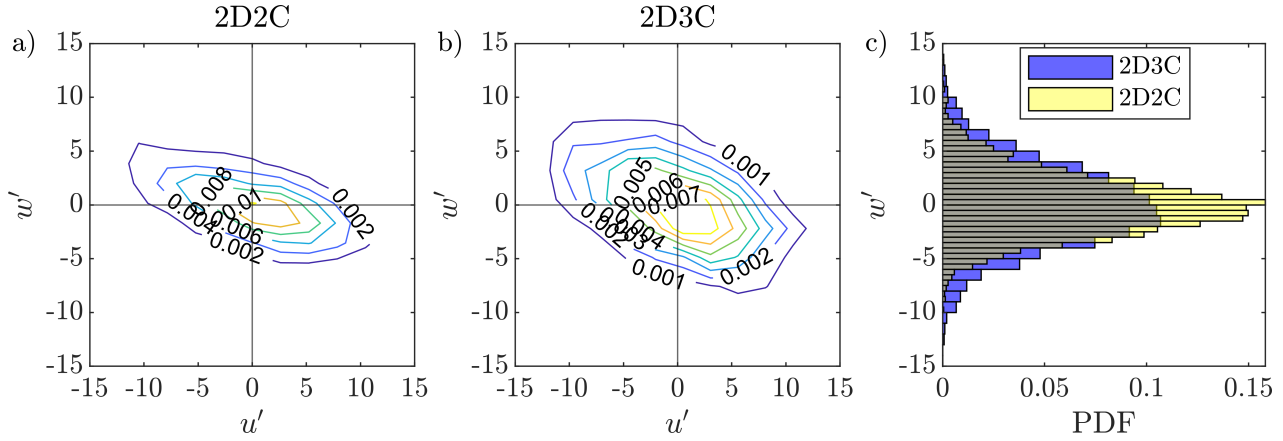
Figure H.4: (a-b) Joint probability density function of the u' and w' fluctuations sampled in the shear layer at z/H = 0.04 and x/l_{x,λ_h} = 0.6 during Exp. Hl for the 2D2C and stereo PIV measurements, respectively; (c) probability density function of the vertical fluctuations w' just mentioned.

the shear stress contributions of different turbulent events between the 2D2C and the stereo-PIV data, deriving from differences in vertical velocities. For this reason, the joint probability density function of the instantaneous streamwise and vertical fluctuations u', w' is analysed locally near the top of the sphere (at x/l_x = 0.6 and z/H = 0.04), where the strongest differences in vertical velocities are observed. Figures H.4a-b show that there is a similar horizontal scatter of streamwise velocities for the 2D2C and stereo-PIV data. The vertical velocity fluctuations show, instead, a higher range of variability for the stereo-PIV data. As a result, the isoprobability contours of the stereo-PIV data are stretched vertically compared to the 2D2C data. The univariate probability density function of the vertical fluctuations in Figure H.4(c) shows that high magnitude w'-fluctuations have a higher probability for the 2D3C data compared to the 2D2C PIV data. The two probability density functions are symmetrically distributed around zero and share a similar shape. The symmetry of the two w'-signals explains why the time integral of the Reynolds shear stresses results in a similar magnitude between the 2D2C and stereo-PIV data.

Quadrant analysis is performed, as in Section 2.4.1, to determine the time and shear stress contribution, T_{i,H_s} and $-\rho_f \overline{u'w'}_{i,H_s}$, of the ith turbulent event within a hyperbolic hole region with Hole size $H_s = 0$. The frequency of each turbulent event f_{i,H_s} is defined, furthermore, as the reciprocal of the average time interval between the single realization of each turbulent event in the velocity signal.

Figures H.5a-c illustrate the longitudinally-averaged vertical profiles of the frequency and of the time and shear stress contributions of the turbulent events for the 2D2C and stereo-PIV data. Figure H.5a shows that the profiles of the time contributions for the 2D2C PIV and stereo-PIV data are in good agreement in the bulk flow region with slight differences. A stronger departure of the stereo-PIV profiles from the 2D2C PIV profiles is observed near the top of the spheres where the contribution of the inward and outwards interactions increases for the stereo-PIV data compared to the 2D2C PIV data, while the contribution of the sweep and ejection events decreases. Nevertheless, both datasets show a change in dominance between ejections and sweep events near the top of the spheres, consistent with observations over rough beds (Raupach, 1981; Dey and Das, 2012; Mignot et al., 2009b).

Figure H.5b shows that the 2D2C and stereo-PIV data are characterized by similar frequency profiles. Just in the case of the outward interactions the stereo-PIV data show higher frequencies than the 2D2C PIV data. The shear stress contribution profiles in Figure H.5c show similar trends for the 2D2C PIV data and the

stereo-PIV data. The shear stress contribution of sweeps and ejection events obtained from the stereo-PIV data is slightly higher compared to the 2D2C data, while the contribution of the outward and inward interactions slightly lower. The highest contribution to the Reynolds shear stresses is provided above the bed by the ejection events, while near the bed the sweeps dominate the momentum transfer, as also observed over gravel beds (Raupach, 1981; Dey and Das, 2012; Mignot et al., 2009b). Even though there are some differences in the magnitude of the shear stress contributions, the overall turbulent behaviour of the flow is properly described by the stereo-PIV data.
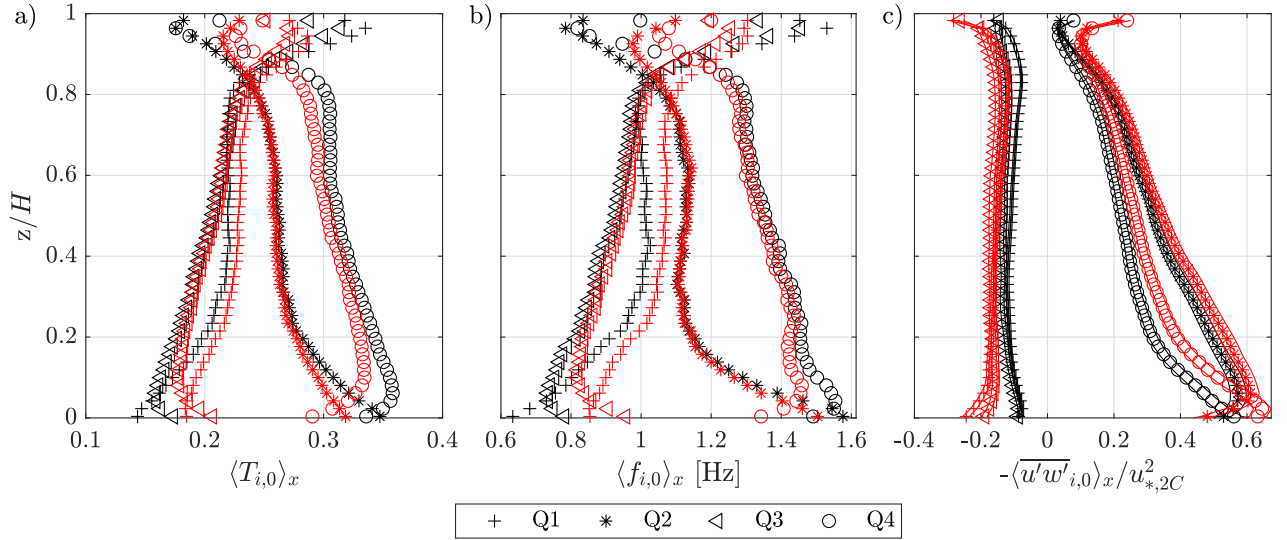

Figure H.5: Longitudinally-averaged time contribution $\langle T_{i,0} \rangle_x$ (a), frequency $\langle f_{i,0} \rangle_x$ (b) and shear stress contribution $-\rho_f \langle \overline{u'w'}_{i,0} \rangle_x$ (c) of the turbulent events for the 2D2C data (black profiles) and the stereo-PIV data (red profiles) for Exp. Hl.

H.2.5 Signal analysis

The comparison of the time averaged flow fields and of the double averaged flow statistics have shown that the stereo-PIV data are characterized by higher values of the vertical velocity compared to the 2D2C PIV data. Since the 2D2C and stereo-PIV images are acquired simultaneously, a direct comparison of the temporal signal of the different flow quantities is possible, in order to determine any temporal lag. Figure H.6 illustrates the comparison of the instantaneous signals of the streamwise u and vertical w velocities, of the streamwise $u'u'$ and vertical $w'w'$ normal stresses and of the Reynolds shear stresses, obtained with the 2D2C and the stereo-PIV system. The analysis is performed at x/l_x = 0.6 over three vertical positions: in the shear layer near the top of the spheres (z/H = 0.04), in the centre of the 2D2C-PIV camera sensor (z/H = 0.23), where the perspective error on the vertical velocities should be zero for the 2D2C PIV system and near the boat z/H = 0.83.

Figures H.6a-c and H.6g-i show that the signals of u and $u'u'$ are in perfect agreement with no phase shift between the two signals. Figures H.6d-f show, furthermore, that the vertical velocity signal of the stereo-PIV data tends to overestimate the 2D2C PIV signal. The two signals are, nevertheless, in phase. In the case of the turbulent intensities in Figures H.6j-l, the stereo-PIV signal is also characterized by higher magnitude
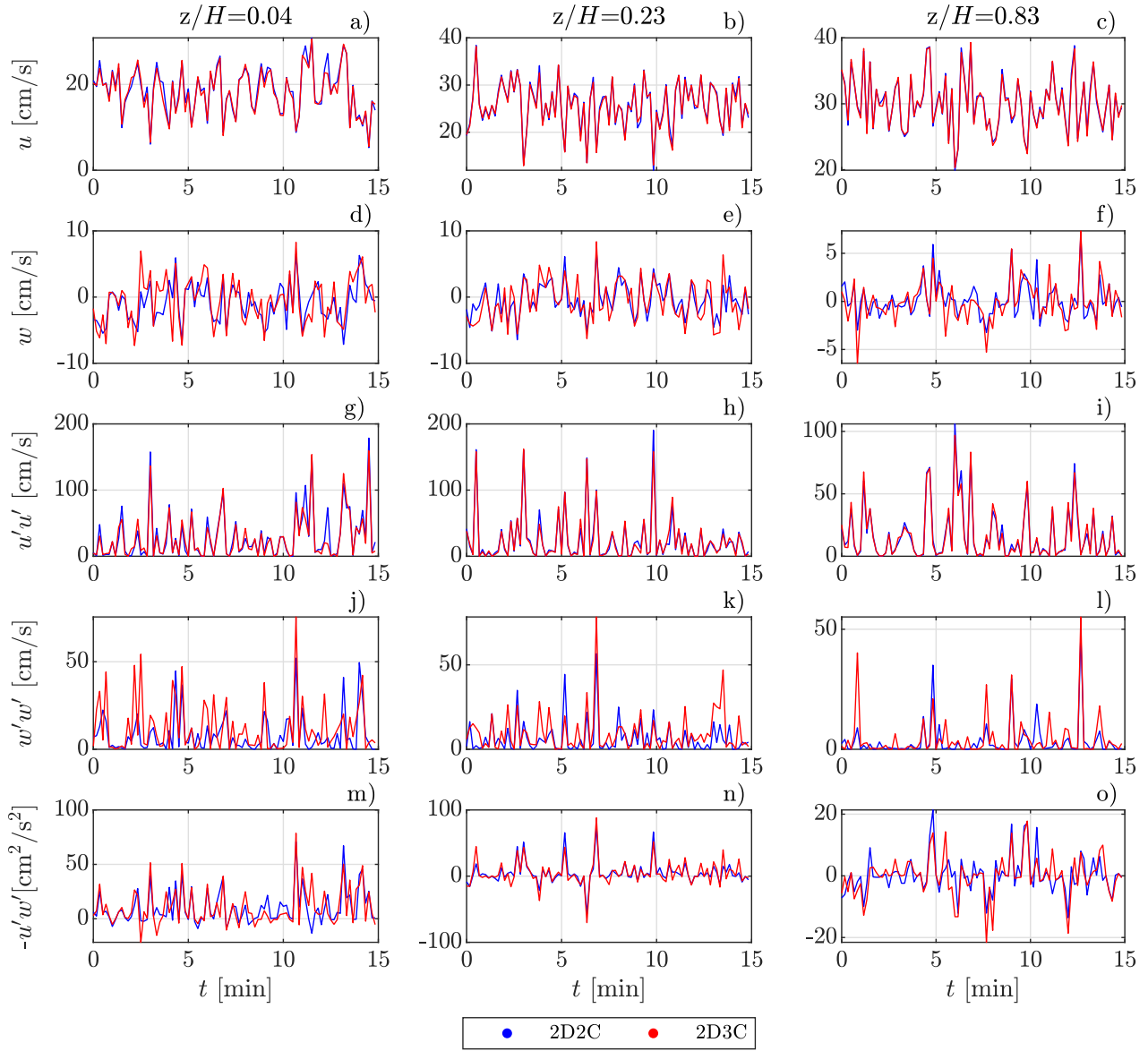
221

Figure H.6: Comparison of the time series of the instantaneous signal of the (a-c) instantaneous streamwise velocity u, (d-f) the vertical velocity w, (g-i) the streamwise normal stresses $u'u'$, (j-l) the vertical normal stresses $w'w'$ and (m-o) the Reynolds shear stresses $-u'w'$, sampled with the 2D2C PIV system and the 2D3C stereo-PIV system at x/l_{x,λ_h} = 0.6 at three different heights in Exp. Hl.

events compared to the 2D2C PIV signal. The most significant difference in the two signals is observed for z/H = 0.04 in Figure H.6j, consistent with the double averaged profiles in Figure H.3(e). The Reynolds shear stresses in Figures H.6m-o show good agreement between the signals, even though the magnitude of the stereo-PIV signal is sometimes higher than the 2D2C PIV signal in agreement with the quadrant analysis performed in Section H.2.4.

Figures H.7a-c illustrate the difference in vertical particle displacement between the stereo- $\Delta z_{[2D3C]}$ and 2D2C PIV data $\Delta z_{[2D2C]}$ for the three vertical velocity signals shown in Figures H.6d-f. The 2D2C velocity signal is first subdivided into hundred bins. For each bin the average difference in vertical displacement between the stereo-PIV and 2D2C PIV vertical velocity signal is computed. Figures H.7a-c show that the
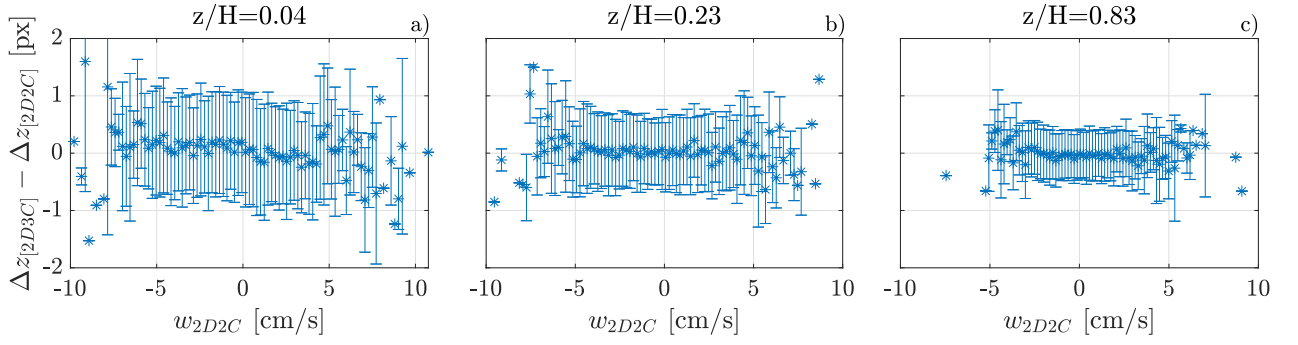
Figure H.7: Difference in vertical particle displacement between the stereo and the 2D2C PIV for the vertical velocity signals sampled at $x/l_{x,\lambda_h}$=0.6 and at three different heights for Exp. Hl. The vertical whiskers represent one standard deviation around the average difference in particle displacement.

difference in vertical particle displacement does not depend on the magnitude of the vertical velocity. Even though the average difference in vertical particle displacement is near zero, the standard deviation range shows that the vertical particle displacements of the stereo-PIV signal tends to over or underestimate the vertical particle displacements of the 2D2C signal up to 1 pixel. It is apparent that this error is random and acts, as such, in the same way as a peak-locking error. Given that the error range is constant, small vertical particle displacements with lower magnitudes will be affected more percent-wise than larger vertical displacements. This leads on average to an overestimation of small vertical particle displacements for the stereo-PIV system which results in a flatter and broader probability density function of the vertical velocities, as shown in Figure H.4c.

A possible reason for the difference in vertical velocities can be related to the fact that, even though the stereo and 2D2C PIV images are recorded simultaneously, the PIV particles recorded by the stereo-PIV system are affected by strong vertical image deformations due to the steep vertical viewing angles during the PIV processing. The seeding particles in the stereo-PIV images are, in fact, compressed by a factor of 3.3 in the vertical direction compared to the homologous particles in the 2D2C PIV images. Visual comparison of the 2D2C PIV images and of the dewarped stereo-PIV images shows that the shape and position of the dewarped seeding particles slightly differs from the homologous 2D2C PIV particles. Image dewarping results in particles of bigger size and higher vertical stretching compared to the undistorted 2D2C PIV particles. Theoretically, if the shape of the dewarped particles does not change between the two frames, the particle displacement should not be affected by the dewarping. Unfortunately, changes in the shape of the dewarped particles in the second frame can be caused by the following factors:

- changes in the intensity of the particles between the first and second frame due to the particles being advected to regions of lower or higher laser power;

- changes in the orientation of the particles modifying their reflection pattern, as the particles are not perfectly spherical;

- differences in the local magnification factor, as the particle is vertically displaced between the first and second frame
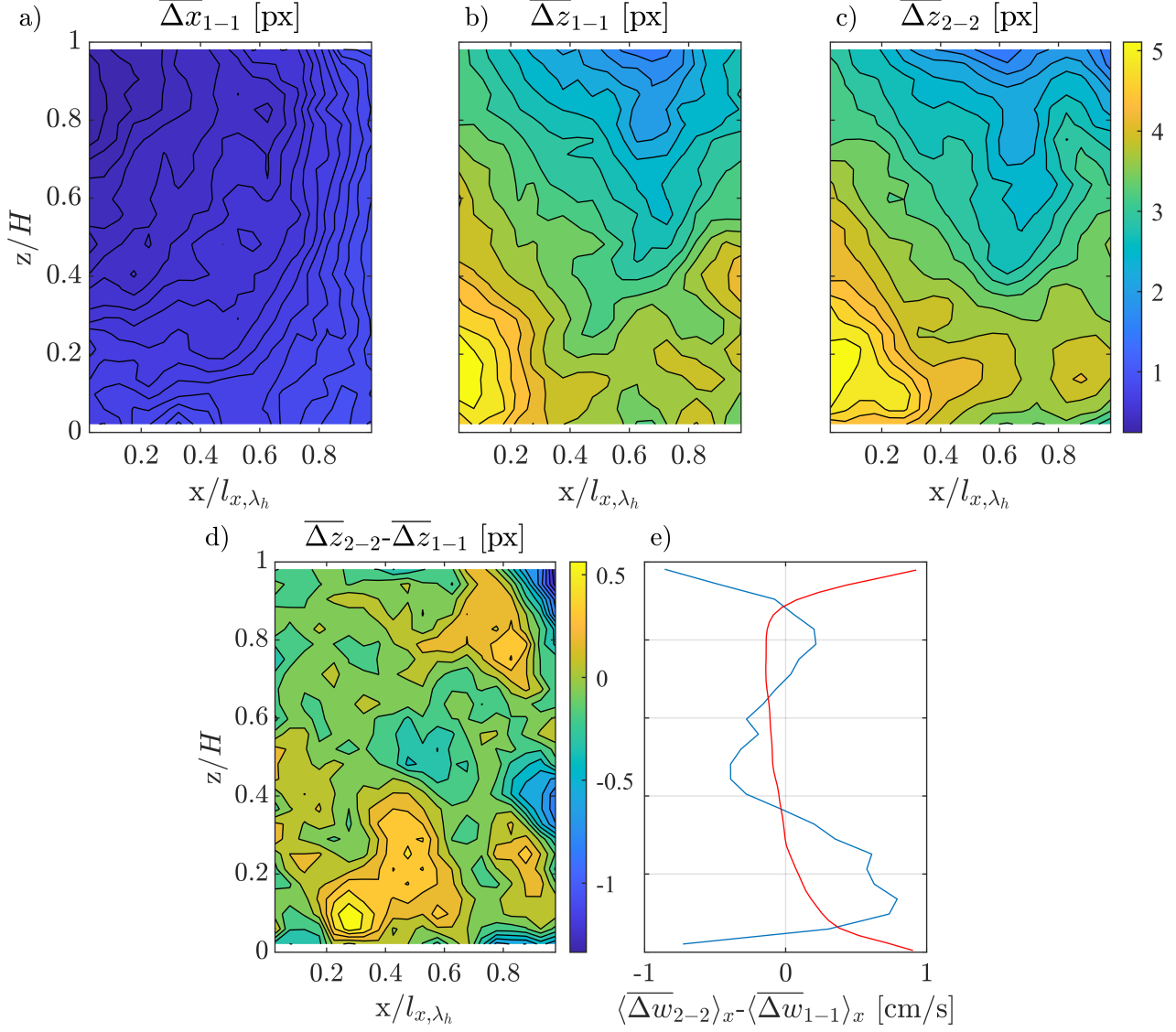
223

Figure H.8: (a) Time-averaged streamwise difference in particle position between the first frames of the 2D2C and stero-PIV bursts $\overline{\Delta x}_{1-1}$; (b-c) Time-averaged vertical difference in particle position between the first and second frames of the 2D2C and stereo-PIV bursts, $\overline{\Delta z}_{1-1}$ and $\overline{\Delta z}_{2-2}$, respectively; (d) difference in vertical particle displacement $\overline{\Delta z}_{2-2}$-$\overline{\Delta z}_{1-1}$; (e) double-averaged difference in vertical velocities between the 2D2C and the stereo PIV measurements obtained from the difference in vertical particle displacement (blue line) and from the difference between the double averaged vertical velocity profiles of the 2D2C and the stero-PIV data of Figure H.3b (red line).

Due to the change in shape of the dewarped particles in the second frame, their centroid is displaced from its actual location, introducing an error on the displacement of the particles.

In order to quantify the difference between the 2D2C PIV images and the dewarped stereo-PIV images along with the influence of the dewarping process on the particle displacements, cross correlation is performed between the first frame of the 2D2C PIV image bursts and the first frame of the dewarped stereo-PIV image bursts, by applying a planar PIV algorithm. The same is done also for the second frames. Since the image frequency within one burst is higher for the stereo-PIV system than for the 2D2C PIV system, the position of the particles in the second frame of the dewarped stereo image bursts is translated in the longitudinal direction by the means of the mean advection velocity, to overlap with the location of the PIV particles in the second frame of the 2D2C PIV images. Figures H.8a-c show the time-averaged difference in streamwise and vertical location of the PIV particles between the first frames, $\overline{\Delta x}_{1-1}$ and $\overline{\Delta z}_{1-1}$, and between the second frames $\overline{\Delta z}_{2-2}$, respectively. Figure H.8a shows that the difference in streamwise particle position between the first image frames $\overline{\Delta x}_{1-1}$ is below 1 pixel (the same is also true for $\overline{\Delta x}_{2-2}$, not shown here). The streamwise velocities are not affected, as such, by the image dewarping. Figures H.6b-c show, instead, that the difference in the vertical particle position for both the first and the second image frames, $\overline{\Delta z}_{1-1}$ and $\overline{\Delta z}_{2-2}$, is the highest near the spheres, with peak values of 5 pixels, and reduces towards the boat. This vertical shift of the position of the dewarped PIV particles accounts for the vertical shift in the position of the shear layer observed in Section H.2.2. The difference in vertical particle displacement between the stereo-PIV and 2D2C PIV measurements is given by the difference between $\overline{\Delta z}_{2-2}$ and $\overline{\Delta z}_{1-1}$. Figure H.8d shows that this difference in vertical particle displacement is of the orders of 0.5-1 pixels. Figure H.8e shows the difference in vertical velocity obtained from the spatial average of the difference in vertical particle displacement shown in Figure H.8d (blue profile) and the difference in the double averaged vertical velocity profiles between the stereo- and the 2D2C PIV system of Figure H.3b. The two profiles are quite similar at least in the bulk with a common trend to underestimate the vertical velocities near the surface and overestimate them near the bed. This suggests that the vertical dewarping of the stereo-PIV images is the main cause for the overestimation of the vertical velocities by the stereo-PIV system. For future measurements, a possible way to minimize the errors deriving from the dewarping could consist in ensuring that the integral of the particle intensities is not altered between the original and the dewarped image. An alternative could consist in calculating the velocity field on the raw images, reconstructing then the velocity field in the world coordinate system on the basis of the camera calibration. In this manner, the image-dewarping step could be avoided.

H.3 The influence of the glass-boat on the flow

The influence of the glass boat used in the stereo-PIV measurements to look through the water surface is investigated in this Section via an experimental approach. The use of surface glass plates to access flow regions which are otherwise not accessible or to reduce the influence of surface waves on the imaging techniques is quite widespread both in PIV (Detert and Nikora, 2010; Cameron et al., 2013; Mohajeri et al., 2015; Nikora et al., 2019) and sediment transport measurement applications (Nelson et al., 1995; Radice et al., 2006; Yager and Schmeeckle, 2013). The size and shape of glass boats varies according to their application from narrow streamlined ones used to stabilize the position of laser sheets passing through the water surface (Hofland and Booij, 2004; Nikora et al., 2019) to wide-area-covering ones for camera recordings of the flow field or of

the sediment transport. For example, Detert and Nikora (2010) used a 10×30 cm^2 glass boat to measure the flow field on a horizontal plane few cm above a gravel bed. In the field of sediment transport, Radice et al. (2006) used a 1 m long, channel-width spanning glass plate to record sediment transport. The glass boats are installed to slightly touch the water surface (Mohajeri et al., 2015; Yager and Schmeeckle, 2013), in order to limit their influence on the flow, since they trigger the development of a boundary layer. However, despite their wide use, only theoretical approaches have been used until now to predict the boundary layer growth under surface glass plates. Cameron et al. (2013) and Mohajeri et al. (2015) applied, for example, traditional formulas for turbulent boundary layer thickness development over an idealized smooth plate (Schlichting and Gersten, 2017).

H.3.1 Experimental setup

A series of experiments is performed to assess to which extent the development of the boundary layer along the boat influences the bulk flow statistics of the fully developed boundary layer over the bed of spheres and whether traditional approaches for the prediction of the boundary layer development apply. The flow field, developing with and without the presence of the boat over the densest bed configuration of spheres λ_h, is investigated for three different flow conditions, by varying the bulk Reynolds number and the water depth (see Table H.2). Two Reynolds numbers $Re = [15000, 30000]$ and two water depths $H = [5.8, 10.8]$ cm are investigated. The names of the experiments in Table H.2 highlight the characteristic flow parameters ($R-$ or $H-$) and their magnitude (l-low and h-high). The flow conditions of the Exp. $RlHl$ and $RhHh$ in Table H.2 correspond to the flow conditions of experiments 1 and 4 in Table 3.1. Exp. $RhHl$ represents a "bridge" experiment with the same water depth as Exp. $RlHl$ and with the same Reynolds number as Exp. $RhHh$. The experiments are performed with a 2D2C planar PIV system, similar to the one used for the stereo-PIV

Exp.	Re	H	Q	U	s	R_h	u_{*H}	u_{*R}	Fr	Δt	f
	[-]	[cm/s]	[l/s]	[cm/s]	[%]	[cm]	[cm/s]	[cm/s]	[-]	[s]	[Hz]
$RlHl$	15000	5.8	4.5	25	0.11	4.18	2.5	2.1	0.34	0.23	200
$RhHl$	30000	5.8	9	51	0.61	4.18	5.9	5.0	0.69	0.12	300
$RhHh$	30000	10.8	9.2	28	0.07	6.28	2.8	2.1	0.28	0.38	200
		±0.05	±0.5	±2.5	±0.01	±0.2	±0.2	±0.2			

Table H.2: Flow parameters: Reynolds number $Re = HU/\nu$, water depth H, flow rate Q, bulk velocity $U = Q/(WH)$, slope s, hydraulic radius R_h, shear velocity based on the water depth $u_{*,H} = \sqrt{gHs}$, shear velocity based on the hydraulic radius $u_{*,R} = \sqrt{gR_h s}$, Froude number $Fr = U/\sqrt{gH}$. PIV measurement parameters: bulk time unit Δt, image frequency f.

validation in Section H.2. The only difference lies in the position of the camera located, in this case, 110 cm away from the glass wall of the flume. The field of view of the camera spans over the whole length of the boat (see the red region in Figure H.9). A local reference system is defined with the origin of the x-axis flush with the leading edge of the glass plate (see Figure H.9). For each experiment in Table H.2 two PIV runs are performed one with and one without boat (referred to wb and nb in the following) with the laser sheet positioned over plane A (see Figure 3.2a). During each PIV run, a total number of bursts equivalent to 5000
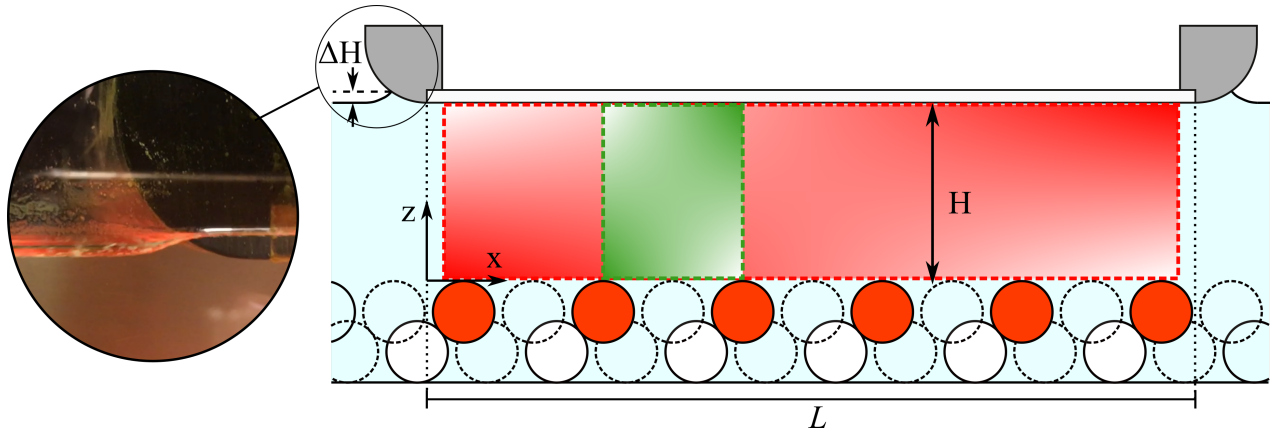
Figure H.9: Longitudinal section of the central PIV plane under the boat. The insert shows a picture of the leading edge of the boat characterized by a local raise in water depth. The red region below the boat corresponds to the measurement area and the green region identifies the area where the flow statistics are spatially averaged in Section H.3.4.

bulk time units are recorded. The bulk time units Δt and the image frequencies f are shown in Table H.2. The PIV images are processed with the Davis-PIV software 8.4.0 with a correlation window size of $12{\times}12$ pixels^2 with a 50% overlap (equivalent to a grid size of $1.5{\times}1.5$ mm^2).

The water depth is monitored with two ultrasonic sensors positioned at the entrance of the flume and before the boat (see Figure 3.5) to assess the flow uniformity. Furthermore, a ruler is positioned at the upstream edge of the boat to measure the influence of the boat on the local water levels. At the beginning of the experiments, uniform flow conditions are first established without the presence of the boat. The boat is then introduced and its elevation adjusted to be flush with the water surface within $\pm$ 0.5 mm.

H.3.2 Water levels and flow field below the boat

This Section is dedicated to the macroscopic characterization of the influence of the boat on the flow. As the insert in Figure H.9 shows, a stagnating surface region of increased water levels develops at the leading edge of the boat. From visual observation, this region extends few cm upstream of the leading edge with the highest water level observed at the boat. The influence of the boat on the water levels upstream is restricted only to this region. The ultrasonic water level measurements upstream of the boat, presented in Table H.3, show that the water levels do not change with or without the presence of the boat. The increase in water levels ΔH at the leading edge of the boat changes between experiments. Table H.3 shows that the highest water level displacement, of about 4 mm, is observed for Exp. $RhHl$, characterized by the highest streamwise velocity at the water surface U_H in the absence of the boat. Exp. $RlHl$ and $RhHh$, characterized by similar surface velocities lower than in Exp. $RlHh$, are characterized by ΔH of about 0.1-0.2 mm. These results suggest an increase in the water surface elevation at the leading edge of the boat with increasing surface velocity of the undisturbed flow, in accordance with the principle of Bernoulli.

The influence of the boat is also apparent in the time-averaged field of the streamwise velocity $\overline{u}$ and in the local fluid shear stress field $\tau_{xz}|_{local}$ (obtained from the sum of the Reynolds shear stress $\tau_{uw} = -\rho_f \overline{u'w'}$ and of the time-averaged viscous shear stress $\overline{\tau}_{vis} = \mu \partial \overline{u}/\partial z$), illustrated in Figures H.10a-d for the Exp. $RlHl$. The $\overline{u}$ and $\overline{\tau}_{xz}|_{local}$ fields for the other two experiments are not illustrated, as they present similar

Exp.	H_{NB} [cm]	H_{WB} [cm]	ΔH [cm]	U_H [cm/s]
$RlHl$	5.83	5.84	0.2	27.3
$RhHl$	5.81	5.84	0.4	56.1
$RhHh$	10.82	10.81	0.1	32.7

Table H.3: Water levels measured by the ultrasonic sensor upstream of the boat without and with the boat, H_{NB} and H_{WB}; increase in the water level ΔH at the leading edge of the boat; surface velocity measured in the absence of the boat U_H.
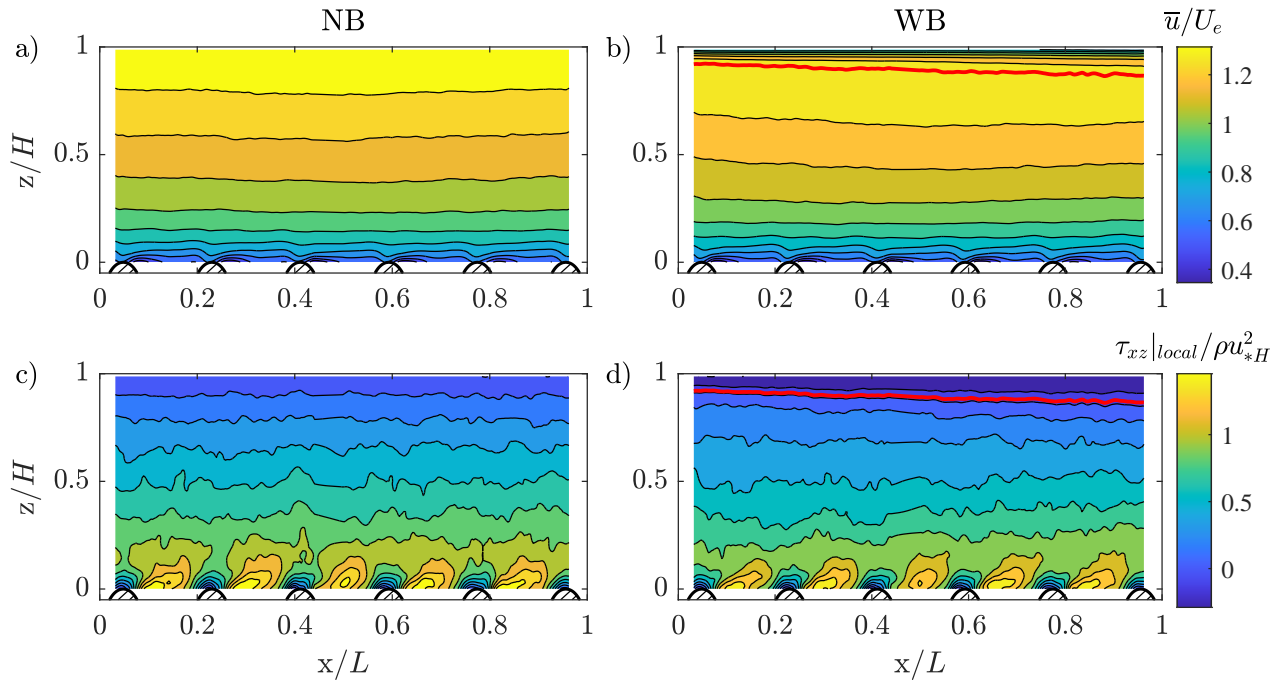

Figure H.10: Time-averaged streamwise velocity fields $\overline{u}$ (a-b) and local fluid shear stress fields $\tau_{xz}|_{local}$ (c-d) for experiment $RlHl$. The plots on the left are data collected with no boat (NB) and on the right with the boat (WB). The red continuous line in plot (b) and (d) highlights the development of the boundary layer thickness and corresponds to the isostress line $\tau_{xz}|_{local} = 0$. The x-axis is normalized by the length of the boat L.

behaviours. In the absence of the boat, Figures H.10a and H.10c show that the bulk flow is uniform in the longitudinal direction, as both the isovels and isostress lines are horizontal. The isovel and isostress lines are disturbed, though, near the top of the spheres by the presence of the roughness sublayer, which causes local flow non-uniformities. Flow acceleration is observed over each pattern on top of the spheres, followed by flow deceleration in their lee (see Figure H.10a). Figure H.10c shows, furthermore, that a shear layer develops in the lee side of each sphere, expanding up to a height of approximately $0.1H$. In the presence of the boat, the development of a surface boundary layer can be identified in Figure H.10b, which displays a region of flow retardation beneath the boat thickening in streamwise direction. Similarly, Figure H.10d shows decreasing negative shear stress values in the upper 80-90% of the flow. Below the boundary layer, the bulk flow region is characterized by streamwise flow non-uniformity, as the isovels and isostress lines are negatively inclined in the streamwise direction, meaning that the flow is being accelerated (see Figure H.10b and H.10d). The development of the boundary layer along the boat seems to not affect significantly the flow in the near bed region, though. Moving towards the bed, Figure H.10b shows that the isovels turn first horizontal and, near the spheres, the characteristic periodic flow disturbances caused by the roughness sublayer appear with similar patterns as observed in the no-boat case. In a similar manner, the shear layer patterns behind the spheres in Figure H.10d present similar shapes and shear stress magnitudes comparable to the no-boat case in Figure H.10c.

H.3.3 The development of the surface boundary layer

The development of the boundary layer along the boat is analysed in this Section on the basis of the boundary-layer thickness and of the displacement thickness. The boundary-layer thickness δ is usually identified by the plane where the velocity $\overline{u}$ reaches 99% of the free-stream velocity U_∞ (Schlichting and Gersten, 2017). In this case, though, the boundary layer developing along the boat is not exposed to a uniform, homogenous outer flow for which U_∞ is constant, but it interacts with the turbulent boundary layer developed above the spheres characterized by a vertically non-homogeneous velocity distribution, deeming the previous definition inapplicable. Two suitable conditions for an alternative definition of the boundary layer thickness can be drawn from Figures H.10b and d. They show that near the edge of the boundary layer $\overline{u}$ reaches a maximum and $\tau_{xz}|_{local}$ crosses the zero shear stress plane. Unfortunately, these two planes do not coincide, as the plane of zero shear stress lies closer to the boat than the plane of maximum velocity (for a visual proof compare the vertical double averaged profiles of $\overline{u}$ and $\tau_{xz}|_{local}$ in Figure H.17). In bottom and surface wall-bounded turbulent channel flows with asymmetric roughness, such as the case of ice-covered rivers or ducts, it was observed, in fact, that the plane of zero shear stress always lies closer to the smooth wall (Parthasarathy and Muste, 1972, 1994; Chen et al., 2015). Chen et al. (2015) proposed to subdivide the two flow regions pertaining to bottom and surface roughness on the basis of the plane of zero shear stress following the hydraulic radius separation theory by Einstein (1942). In a similar manner, the boundary-layer thickness δ is defined, here, as the elevation for which $\tau_{xz}|_{local} = 0$. As a consequence, the maximum in streamwise velocity lies outside of the surface boundary layer. This appears, therefore, as a velocity dip in the boundary layer developing over the sphere, consistent with the accelerated non-uniform flow conditions, observed previously. Studies on non-uniform accelerated open-channel flows have, in fact, observed that the velocity profile is characterized by a velocity dip below the water surface (Kironoto and Graf, 1996; Yang

et al., 2006).

To further characterize the boundary layer, the displacement thickness δ^* is defined as follows:

$$\delta^* = \int_{H}^{H-\delta} \left(1 - \frac{\overline{u}(z)}{U_\delta}\right) dz \tag{H.4}$$

where U_δ is the time-averaged streamwise velocity at the edge of the boundary layer. δ^* quantifies the vertical displacement of the streamlines of the outer flow caused by the drop in velocity within the boundary layer (Schlichting and Gersten, 2017). As such, it has relevant implications on the non-uniformity of the outer flow when the latter is vertically confined (like in the present case), as further discussed in Section H.3.4.

Figures H.11a-b illustrate the development along the boat of δ and δ^* for the three experimental conditions. Both the boundary-layer thickness and the displacement thickness monotonically increase in the streamwise direction for all experiments. Figure H.11a shows that for Exp. $RlHl$ and $RhHl$, characterized by the lower water depth, δ evolves with a similar trend with the boundary-layer thickness of Exp. $RlHl$ slightly higher than the boundary-layer thickness of Exp. $RhHl$. Exp. $RhHh$ is characterized, instead, by a thicker boundary layer, which develops at a faster rate compared to the other two experiments. The insert in Figure H.11a shows that, near the leading edge of the boat, the boundary layer covers 8% of the water depth for Exp. $RlHl$ and $RhHl$ and 5% for Exp. $RhHh$. At the end of the boat, the boundary layer covers, instead, about 15% of the water depth in all three experiments.

Figure H.11b shows that the displacement thickness δ^* for Exp. $RlHl$ with the low bulk Reynolds number is
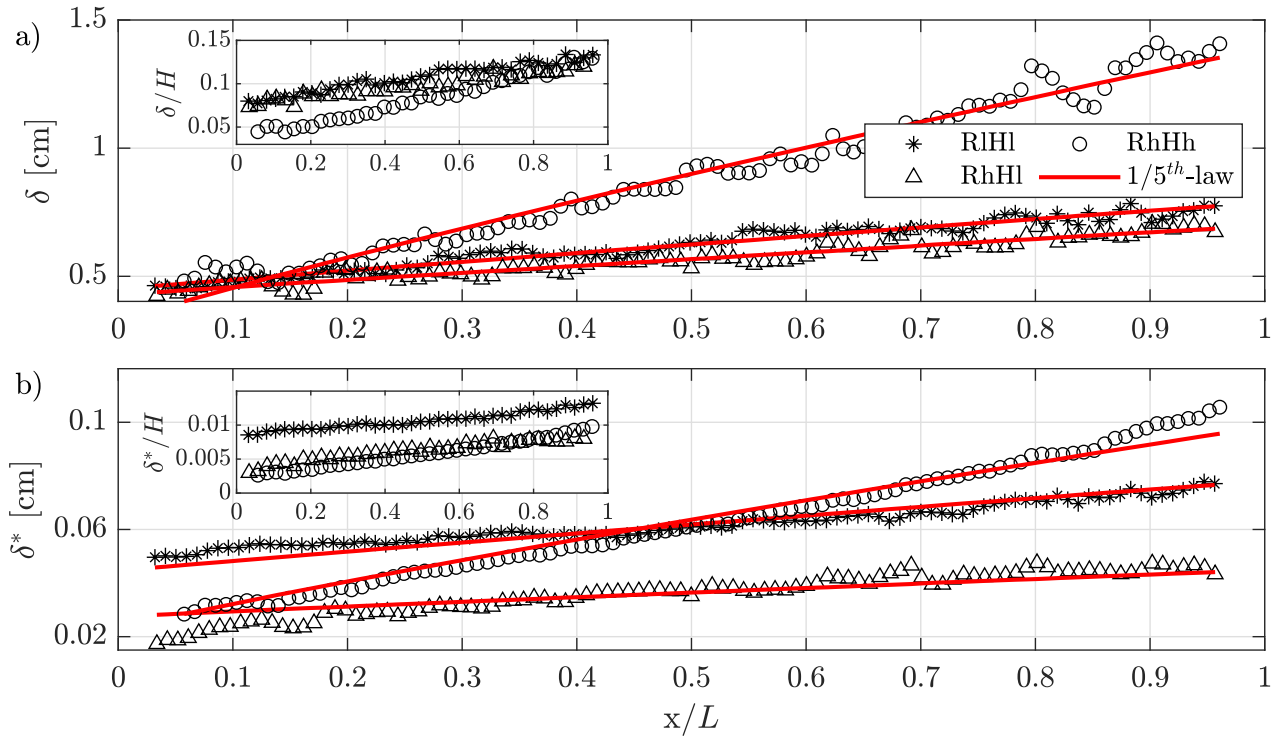

Figure H.11: (a) Longitudinal evolution of the boundary layer thickness δ and (b) of the displacement thickness δ^* along the boat. The red continuous lines are the best fit of equation H.5.

significantly higher than for Exp. $RhHl$ with the higher Reynolds number and same water depth. The growth rate of the two displacement thicknesses is, instead, similar. Exp. $RhHh$ with high bulk Reynolds number

and high water depth displays, also in this case, a faster evolution compared to the other two experiments. The insert in Figure H.11b shows that for Exp. $RlHl$ with the lower bulk Reynolds number the displacement thickness covers 1-1.3% of H, while for the other two experiments with the highest bulk Reynolds number δ^* is limited to 0.5-1% of H. The influence of the boundary layer on the outer flow statistics corresponds, therefore, to a contraction of the flow cross-section of approximately 1%.

Figure H.12 illustrates the evolution of the streamwise velocity at the edge of the boundary layer U_δ normalized by the effective velocity. U_δ shows for Exp. $RlHl$ and $RhHl$ a slight decrease along the boat consistent with the fact that the developing boundary layer expands into the bulk flow region characterized by lower streamwise velocities (see the time-averaged fields of the stramwise velocity in Figure H.10b). Exp. $RhHh$ shows, instead, an almost constant U_δ-profile consistent with the almost constant velocity distribution in the bulk flow region, as shown in Section H.3.4 in the double averaged streamwise velocity profile in Figure H.17k. Overall, U_δ varies by less than 3% between the leading edge and the end of the boat, so that for the purpose of predicting the boundary layer development, it can be considered constant.

The boundary layer development along boats is usually predicted by applying traditional scaling laws for tur-
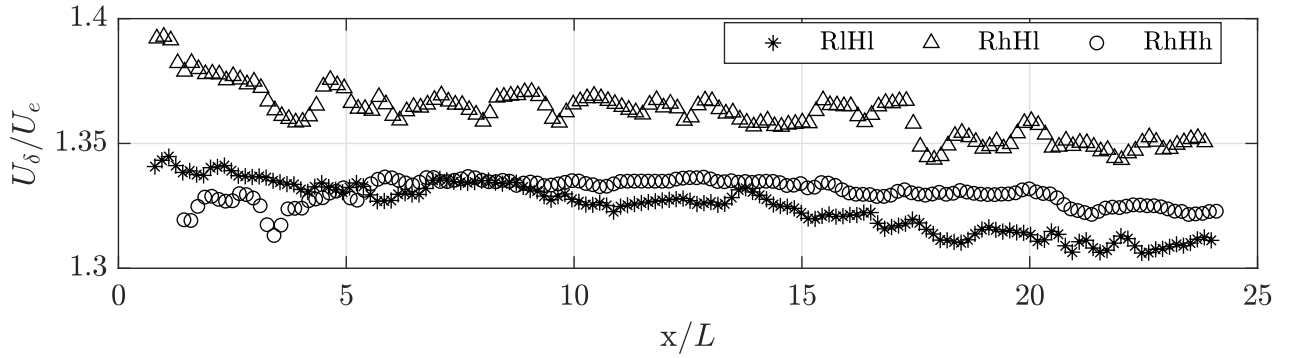

Figure H.12: Longitudinal velocity at the boundary layer normalized by the effective bulk velocity.

bulent boundary layers. Under the hypothesis that the vertical velocity profile of a turbulent boundary layer is self-similar and that it can be approximated with a $1/7^{\text{th}}$ power-law, Schlichting (1936) shows that the development of the boundary layer thickness and the displacement thickness for a turbulent boundary layer is proportional to $x Re_x^{-1/5}$ (where $Re_x = U_\infty x/\nu$). The proportionality constant for the development of δ is equal to 0.37. δ^* follows a similar growth law with a proportionality factor equal to 0.046. Therefore, δ^*/δ = 1/8. In order to assess whether the boundary layer developing along the boat actually grows with $x^{4/5}$, the evolution of boundary-layer thickness is fit as follows:

$$\delta = a_\delta x' Re_{x'}^{-1/5} = a_\delta (x - \Delta x) Re_{x-\Delta x}^{-1/5} \tag{H.5}$$

where a_δ is a proportionality constant, Δx the virtual origin, introduced to account for the fact that the thickness of the boundary layer near the leading edge is non-zero, and $Re_{x'} = U_\delta(x - \Delta x)/\nu$. a_δ and Δx are determined by minimizing the root mean square error between δ and the fitting law H.5. A fitting law similar to H.5 is used also for the displacement thickness, where the proportionality factor $a_{\delta*}$ is used as single fitting parameter, while the virtual origin is taken from the fitting procedure of δ.

Figures H.11a and b show good agreement between the development of δ and δ^* and the fitting laws (red curves). The mean absolute percentage error (MAPE) between the measured and estimated boundary layer

parameters is, in fact, less than 5% for both δ and δ^* (see Table H.4). Only Exp. $RhHh$ shows a MAPE of 9% for the displacement thickness, to be related to the deviation of the fitting law from the measurement evolution of the displacement thickness for x/L<0.2.

Table H.4 lists the parameters of the fitting law H.5 for both δ and δ^*. The virtual origin of the boundary layer is displaced by about 5 cm upstream of the leading edge of the boat for Exp. $RhHh$ and it increases for Exp. $RlHl$ and $RhHl$ to 25 and 30 cm, respectively. In a similar manner, Table H.3 shows that the increase in water water levels ΔH at the leading edge is the lowest for the $RhHh$ case and it increases for the $RlHl$ and $RhHh$ cases. It is surmised, as such, that the virtual origin of the boundary layer increases with increasing superelevation of the water surface at the leading edge.

The proportionality factor for the BL-thickness a_δ in Table H.4 is below the theoretical value of 0.37 for Exp.

Exp.	Δx [cm]	a_δ [-]	$MAPE_\delta$ [%]	$a_{\delta*}$ [-]	$MAPE_{\delta*}$ [%]	$a_\delta/a_{\delta*}$ [-]
$RlHl$	-25.1	0.17	2	0.016	4	10.1
$RhHl$	-30.4	0.16	3	0.01	9	15.6
$RhHh$	-4.9	0.46	4	0.033	4	14.1

Table H.4: Fitting parameters of the boundary layer depth δ and of the displacement thickness δ^*: virtual origin Δx, and proportionality factor in equation H.5 a_δ or $a_{\delta*}$ and mean absolute percentage error of the fit $MAPE$.

$RlHl$ and $RhHl$, while above for Exp. $RhHh$. The proportionality factor for the displacement thickness is, instead, below the theoretical value of 0.046 for all experiments. The ratio $a_\delta/a_{\delta*}$ is, in fact, higher than the theoretical value of 8 and comprised between 10 and 15. As discussed for the virtual origin, the proportionality factor appears also to scale with the water surface superelevation, with decreasing values of a_δ or $a_{\delta*}$ with increasing ΔH.

If the boundary layer depth is normalized by x' and plotted as a function of the Reynolds number $Re_{x'}$, Figures H.13a-b show that the profiles of δ and δ^* do not collapse. The highest $Re_{x'}$ is observed for Exp. $RhHh$ consistent with the fact that δ and δ_* are the lowest. The lower $Re_{x'}$ observed for Exp. $RhHh$, compared to Exp. $RhHl$ explains why, even though the bulk Reynolds number is the same, δ and δ_* are higher for Exp. $RhHh$ than for Exp. $RhHl$. Since $Re_{x'}$ depends on Δx and the latter in turn on ΔH, these results show that independently of the bulk flow Reynolds number or of the water depth, the boundary layer development is affected primarily by the leading edge conditions.

The significance of the hydraulic conditions at the leading edge is highlighted also by the fact that all boundary layers show $Re_{x'}$ below the threshold Reynolds number of 3.5×10^5 - 10^6 for the transition from laminar to turbulent of a boundary layer developing over a flat plate with a sharp leading edge (Schlichting and Gersten, 2017), even though their scaling law is the one characteristic for turbulent boundary layers. Along with the observation that δ and δ^* start with non-zero values at the leading edge, it is surmised that an abrupt transition from laminar to turbulent takes place at the leading edge of the boat. For the development of a boundary layer over a flat plate, the leading edge is, in fact, a site of high receptivity of flow disturbances (such as free stream turbulence), which can lead to boundary layer instabilities and to the abrupt transition to turbulence (Saric et al., 2002). Geometrical features of the leading edge, such as curvature or localized regions with changes in curvature, contribute to the destabilizing process (Hanson et al., 2012). Floryan (1986) shows

that boundary layers developing over convex surface in the presence of a non-monotonic velocity profile are inherently unstable due to the development of Görtler instabilities. This can be the case of the boundary layers analysed, as the leading edge is convex and the velocity distribution reaches a maximum below the boat (i.e. it is not monotonic). The free stream turbulence levels at the water surface, as high as 14% of the streamwise velocity, can also contribute to the destabilization.
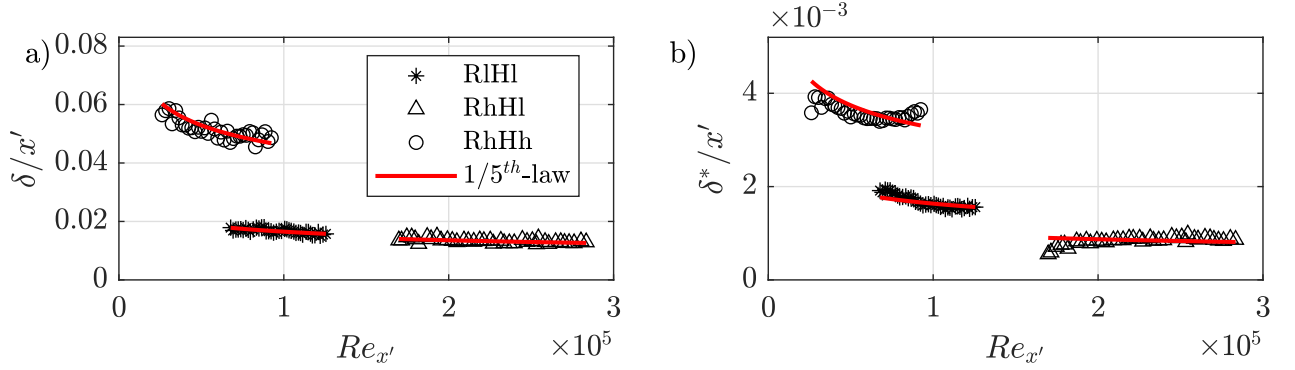

Figure H.13: (a) Longitudinal profiles of the boundary layer depth δ and (b) of the displacement thickness δ^* normalized by x' as a function of the boundary-layer Reynolds number $Re_{x'}$. The red continuous lines are the best fit of equation H.5.

H.3.4 Influence of the boat on the bulk flow statistics

The development of the boundary layer along the boat causes non-uniform bulk flow conditions in the streamwise direction, as discussed in Section H.3.2. In the presence of flow non-uniformities the flow statistics are expected to vary in the streamwise direction. However, if the flow is in equilibrium, the vertical profiles of velocity and turbulent statistics, appropriately normalized, do not depend on the streamwise direction (Rotta, 1962). Mathematically, the self-similarity condition can be expressed for boundary layers as:

$$\frac{\overline{u}}{U_\infty} = f(\eta) \tag{H.6}$$

$$\frac{-\overline{u'w'}}{u_*^2} = g(\eta) \tag{H.7}$$

where $\eta = y/\delta$. For non-uniform open channel flows, Song and Chiew (2001) show that equilibrium conditions are given when the flow equilibrium parameter β, also called non-uniformity parameter, is constant. The β-parameter is defined in the following way:

$$\beta = \frac{gH'}{u_*^2}\left(\frac{dH'}{dx} - i\right) \tag{H.8}$$

where H' is an appropriate vertical length scale of the flow (e.g. the water depth for non-uniform open-channel flows). The parameter β allows to characterize non-uniform flow conditions. $\beta = -1$ identifies uniform flow conditions, $\beta < 1$ flow acceleration and $\beta > 1$ flow deceleration in the streamwise direction. In order to determine the β-parameter according to equation H.8, the vertical length scale H' is defined here

233

as the difference between the water depth H and the displacement thickness δ^* of the boat boundary layer: $H' = H-\delta^*$. The displacement thickness defines how much the outer flow is displaced outwards. As such, its variation in longitudinal direction represents the grade of non-uniformity of the bulk flow. The shear velocity in equation H.8 is estimated by local extrapolation of the vertical local fluid shear stress profile $\tau_{xz}|_{local}$ ($= -\rho_f \overline{u'w'} + \mu \partial\overline{u}/\partial z$) to the top of the spheres. For Exp. $RlHl$ and $RhHl$ a simple linear extrapolation is performed, as the vertical profiles are approximately linear above the roughness sublayer. Since, in experiment $RhHh$ the vertical profiles of τ_{xz} are convex (probably due to the presence of secondary currents), the extrapolation to the top of the spheres is performed through a smoothing spline. Figure H.14 shows that for all experiments the β-parameters are approximately constant, meaning that the flow is in equilibrium. The fluctuations in the β-parameter are connected to the periodicity in the u_*-values, induced by the pattern of spheres. The β-parameters for Exp. $RlHl$ and $RhHl$ with the lower water depth is comprised between -1 and -2, i.e. close to uniform flow conditions. For Exp. $RhHh$ the β-parameter is significantly higher close to -6 in average.

The equilibrium condition is tested, furthermore, by assessing, whether the velocity and shear stress profiles
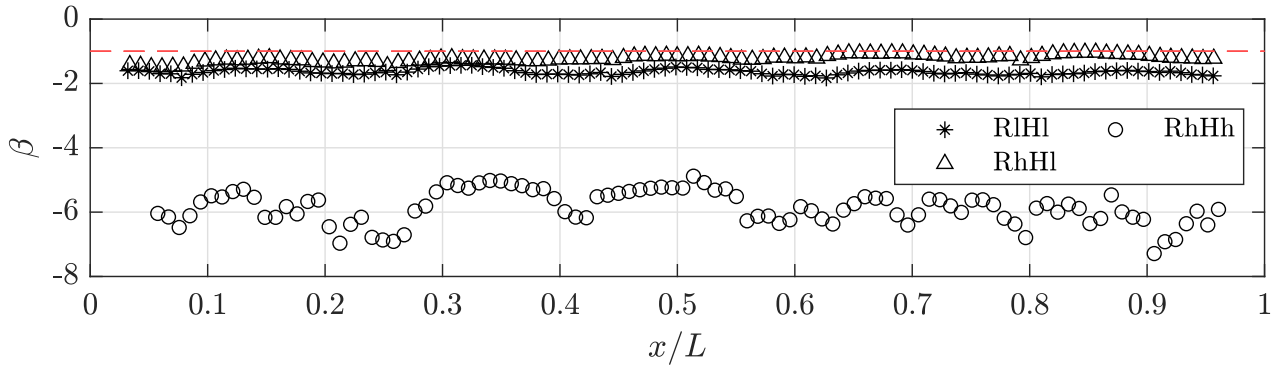

Figure H.14: Longitudinal profile of the non-uniformity parameter β. The horizontal dashed red line represents the condition for uniform flow (β = -1).

are self-similar. Figures H.15a-d illustrate the normalized vertical profiles of the streamwise velocity $\overline{u}$ and of the local fluid shear stress $\tau_{xz}|_{local}$ sampled over the top of the spheres and in the centre of each pattern for Exp. $RlHl$ and $RhHh$. $\overline{u}$ is normalized by the velocity at the top of the boundary layer U_δ and $\tau_{xz}|_{local}$ by the local shear velocity u_*, determined as described previously. z is normalized by H'. Figure H.15a shows that the streamwise velocity profiles for Exp. $RlHl$ present three different regions. For z/H'<0.1 the velocity profiles do not collapse, since the flow near the top of the spheres is characterized by high spatial heterogeneity due to the presence of the roughness sublayer. For 0.1<z/H'<0.25 all velocity profiles collapse. This region corresponds to the one where the log-law holds. For z/H'>0.25 in the outer layer, the velocity profiles show self-similarity starting from the second pattern of spheres (i.e. for x/L>0.23). Similar considerations can be drawn also for the velocity profiles in Figure H.15c for Exp. $RhHh$, with the difference that the region where all profiles collapse is extended up to a height of z/$H' \simeq 0.6$. For z/H'>0.6, instead, the self similarity is not observed, connected probably to the fact, that the velocity profile develops from an S-shaped to a concave-shaped one.

As for the shear stresses, Figures H.15b and d show that the vertical profiles approximately collapse for z/H'>0.15 in Exp. $RlHl$ and z/H'>0.1 in Exp. $RhHh$, respectively. Below, the influence of the roughness sublayer is evident. The peak in shear stress is displaced to the top of the spheres for the profiles extracted
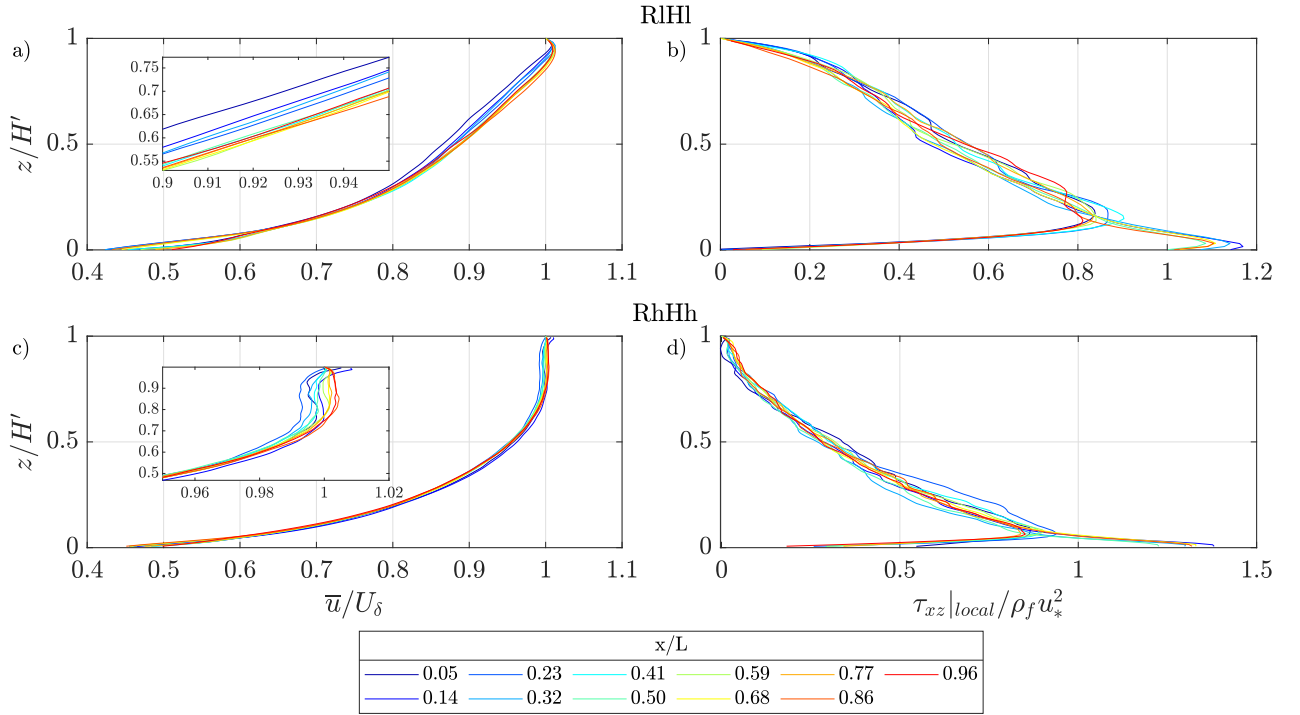
Figure H.15: (a,c) Local streamwise velocity profiles normalized by the streamwise velocity at the boundary layer depth U_δ; (b,d) Local fluid shear stress profiles $\tau_{xz}|_{local}$ normalized by the local shear velocity u_*. The profiles are alternatively extracted over the top of the spheres and in the centre of the patterns. The first profile at x/L = 0.05 is over a sphere, the second one at x/L = 0.14 in the centre of the pattern and so on.

from the centre of the pattern of spheres, where the shear layer develops. These profiles are characterized by total shear stress values higher than the shear velocity extrapolated from the outer layer. The peak of the total shear stress profiles extracted above the top of the sphere is displaced, instead, at a height of z/$H' \simeq$ 0.1-0.15, as the result of the flow acceleration over the spheres. The peak in shear stress is, in this case lower, than the extrapolated local shear velocity.

In the following, the effect of the flow non-uniformity on the bulk flow statistics is analysed by performing a spatial average of the time-averaged flow statistics over the second patter of spheres (i.e. for 0.23 < x/L < 0.41), as it represents the reference pattern for the analysis of the experiments with the highest density of spheres λ_h. As the longitudinal extension of the pattern is limited, the flow can be considered quite homogeneous in the outer layer for the means of spatial averaging, as the increase in boundary-layer depth along the boat over the pattern is negligible. For the broader purpose of this work, in the case of experiments where the bed configurations λ_m and λ_h are analysed (see Table 3.1), the spatial averaging needs to be performed, though, over patterns 2 and 4 times l_{x,λ_h} long, for which the boundary layer depth cannot be considered constant over the whole pattern. Figure H.16 show, nevertheless, that performing the double average of the flow statistics over a pattern one or four l_{x,λ_h} long (representative of the pattern of spheres with the highest and lowest roughness density λ_h and λ_l, respectively) does not significantly influence the vertical profiles of the streamwise and vertical velocities, $\langle \overline{u} \rangle_x$ and $\langle \overline{w} \rangle_x$, of the Reynolds shear stresses $\langle \overline{u'w'} \rangle_x$ and of the normal and vertical turbulent stresses, $\langle \overline{u'u'} \rangle_x$ and $\langle \overline{w'w'} \rangle_x$. In all cases analysed, the difference in the profiles is within the time-convergence error.
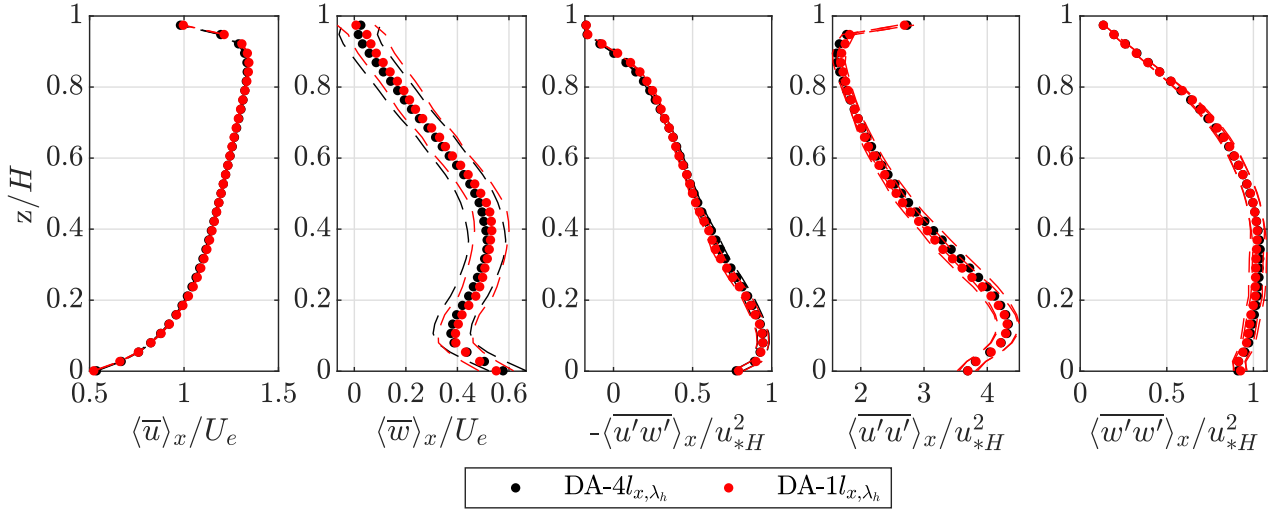
Figure H.16: Comparison of the spatial averaging procedure over a patten of two different lengths, one and four l_{x,λ_h} long, applied to the streamwise and vertical velocities, $\langle \overline{u} \rangle_x$ and $\langle \overline{w} \rangle_x$, to the Reynolds shear stresses $\langle \overline{u'w'} \rangle_x$ and to the normal and vertical turbulent stresses, $\langle \overline{u'u'} \rangle_x$ and $\langle \overline{w'w'} \rangle_x$ for Exp. $RlHl$. The dashed lines represent the time-convergence intervals.

Figures H.17a-k illustrate the comparison between the longitudinally-averaged profiles of the main flow statistics obtained with and without boat for Exp. $RlHl$, $RhHl$ and $RhHh$. The streamwise and vertical velocities $\langle \overline{u} \rangle_x$ and $\langle \overline{w} \rangle_x$ are normalized by the effective bulk velocity, while the Reynolds and normal stresses, $-\rho_f \langle \overline{u'w'} \rangle_x$, $\rho_f \langle \overline{u'u'} \rangle_x$ and $\rho_f \langle \overline{w'w'} \rangle_x$, by the shear velocity $u_{*_{NB}}$ obtained from the extrapolation of the total shear stress profile τ_{xz} of the NB-case to the top of the spheres, in the same manner as described previously for the local shear stress estimate. Figures H.17a,f,k show that the streamwise velocity profiles for the WB-case are characterized by a strong reduction at the level of the boat compared to the no boat case due to the developing boundary layer. In the bulk flow region, the WB-case shows increased streamwise velocities below the boundary layer compared to the NB-case for all three experiments. For accelerated open channel flows, the streamwise velocity profile tends, in fact, to increase compared to a uniform flow, as observed by Kironoto and Graf (1996) and Yang et al. (2006).

Figures H.17b,g,l show that the difference in vertical velocity profiles obtained with and without boat is within the time convergence error (defined in Appendix F). Nevertheless, Figures H.17g and l for Exp. $RhHl$ and $RhHh$ show that the vertical velocity profile of the NB-case is characterized by a shift towards negative values compared to the WB-case. In the case of Exp. $RlHl$ in Figure H.17b this shift is observed only in the upper part of the velocity profile, while for $z/H < 0.6$ the vertical velocity for the WB-case is higher than the NB-case. This discrepancy compared to the other vertical velocity profiles can be ascribed to a slight non-stationarity observed in the data of Exp. $RlHl$. Overall, the shift towards negative values of the vertical velocity is consistent with the experiments by Song and Chiew (2001) on non-uniform open-channel flows, where he observes that flow acceleration in the longitudinal direction causes negative vertical velocities.

Figures H.17c,h,m show the comparison between the longitudinally-averaged Reynolds shear stresses obtained with and without the boat. The non-uniformity caused by the boat results in a damping of the Reynolds shear stresses compared to the NB-case in the bulk flow region, consistent with previous studies on accelerated open-channel flows Kironoto and Graf (1996); Yang and Lee (2007); Yang and Chow (2008). For Exp. $RlHl$ and $RhHh$ with the lowest water depth, the reduction is of the order of 10%, while for Exp. $RhHh$
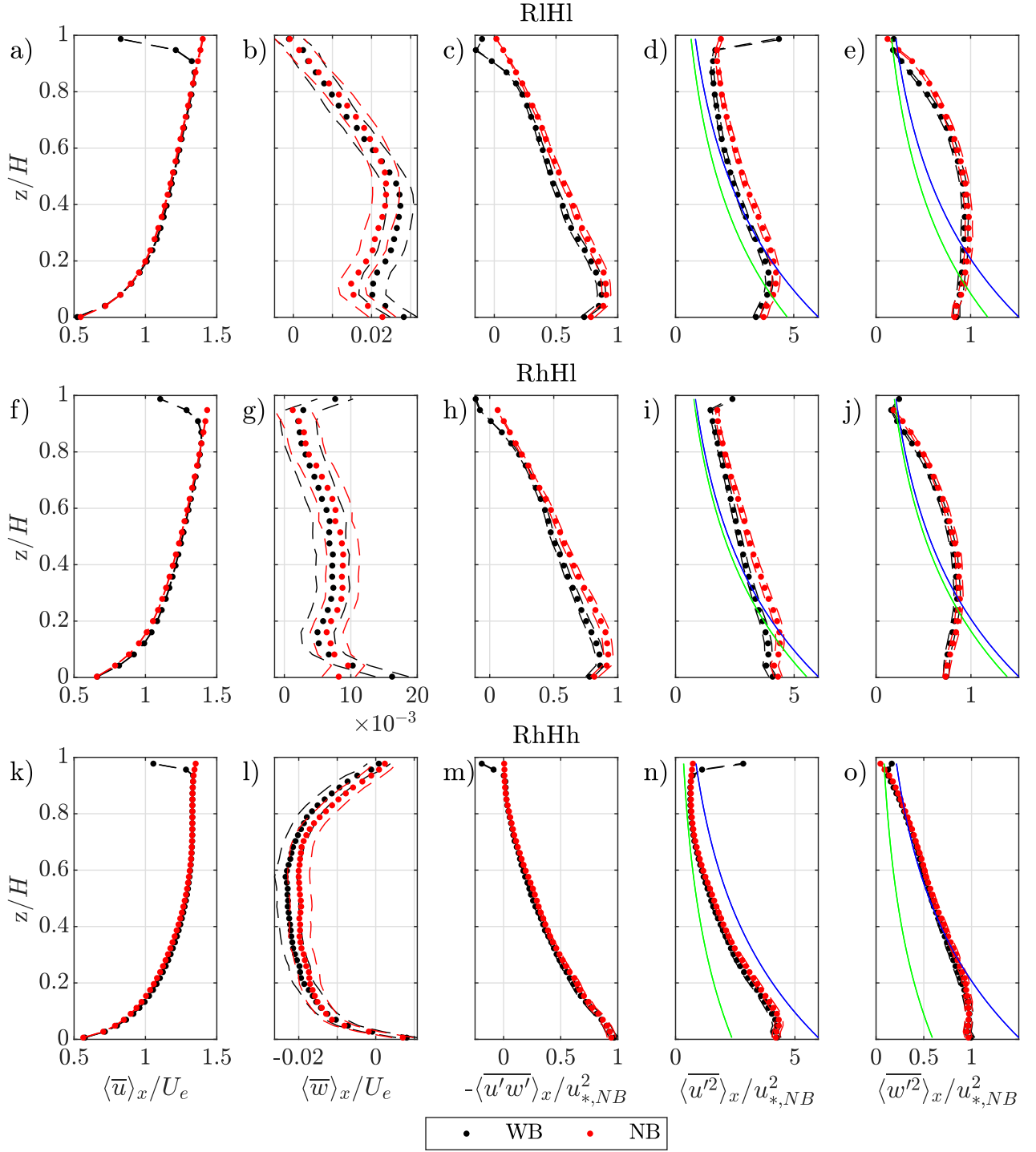
Figure H.17: Comparison of the vertical profiles of the double-averaged streamwise and vertical velocities, $\langle \overline{u} \rangle_x$ and $\langle \overline{w} \rangle_x$, of the longitudinally-averaged Reynolds shear stresses $-\rho_f \langle \overline{u'w'} \rangle_x$ and of the longitudinally-averaged streamwise and vertical normal stresses, $\rho_f \langle \overline{u'u'} \rangle_x$ and $\rho_f \langle \overline{w'w'} \rangle_x$, for the case with ($WB$) and without boat ($NB$) for Exp. $RlHl$, Exp. $RhHl$ and Exp. $RhHh$. The velocities are normalized by the effective bulk velocity U_e and the turbulent stresses by the shear velocity $u_{*,NB}$ obtained from the extrapolation of the total shear stresses τ_{xz} to the top of the spheres for the NB case. The dashed lines represent the time-convergence interval. The blue and green lines represent the exponential laws for the normal stresses by Nezu and Nakagawa (1993) and by Song and Chiew (2001), respectively.

with the highest water depth almost no reduction is observed as the two profiles overlap within the convergence error. This is somewhat contradictory to the fact that experiments $RlHl$ and $RhHl$ are characterized by a lower non-uniformity parameter compared to experiment $RhHh$. These results show that the boundary layer developing along the boat has a higher impact on flows with lower water depth. Near the top of the spheres the Reynolds shear stress profiles for both the WB- and NB-case collapse for all three experiments. The values of shear velocity obtained for the NB and WB boat case are, in fact, the same within the measurement error, as shown in Table H.5.

Figures H.17d,i,n and Figures H.17e,j,o illustrate the vertical profiles of the longitudinally-averaged streamwise and vertical normal stresses, respectively. The presence of the boat causes a reduction both of the streamwise and of the vertical normal stresses. This is consistent with the previous results on non-uniform accelerated open-channel flows where the turbulence levels are damped compared to a uniform flow (Kironoto and Graf, 1996; Song and Chiew, 2001). Like the Reynolds shear stresses, the level of damping is higher for Exp. $RlHl$ and $RhHl$ with the lower water depth compared to Exp. $RhHh$.

Song and Chiew (2001) and Kironoto and Graf (1996) show that the normal stresses in a non-uniform flow can be described through an exponential relationship, similar to the one proposed by Nezu and Nakagawa (1993) for uniform open-channel flows, where the proportionality factors depend on the non-uniformity parameter:

$$\frac{\sqrt{\overline{u'^2}}}{u^*} = D_u(\beta) exp\left(-\frac{z}{H}\right) \tag{H.9}$$

$$\frac{\sqrt{\overline{w'^2}}}{u^*} = D_w(\beta) exp\left(-\frac{z}{H}\right) \tag{H.10}$$

Song and Chiew (2001) proposes the following empirical expressions for D_u and for D_w:

$$D_u = 0.6(0.1\beta^2 + \beta) + 3 \tag{H.11}$$

$$D_w = 0.3(0.1\beta^2 + \beta) + 1.5 \tag{H.12}$$

In Figures H.17d,i,n and Figures H.17e,j,o the exponential laws by Song and Chiew (2001) (green profiles) and by Nezu and Nakagawa (1993) (blue profiles) are compared with the profiles obtained with and without the boat, respectively. Figures H.17d and i show that the streamwise normal stresses for both the WB- and NB-cases deviate from the exponential laws. The deviation is consistent with the one observed by Rouzes et al. (2019) for open channel flows with low relative submergence (H/D<3), as it is the case for Exp. $RlHl$ and $RhHh$. The experimental laws by Song and Chiew (2001) and Nezu and Nakagawa (1993) capture though the reduction in turbulence induced by the flow non-uniformity, as the distance between the two profiles is similar to the distance between the measured streamwise normal stresses profiles. In the case of Exp. $RhHh$ in Figure H.17n the streamwise normal shear stresses for the NB-case are slightly lower than the empirical law by Nezu and Nakagawa (1993), but follow a similar trend. The exponential law by Song and Chiew (2001) is, instead, much lower than the streamwise normal stress profile of the WB-case. This is probably related to the fact that the exponential laws by Song and Chiew (2001) were derived by analysing non-uniforms flows with β-parameters higher than -3.

Similar conclusions can also be drawn for the vertical normal stresses in Figures H.17e,j,o. In Exp. $RlHl$ and $RhHl$ the measured vertical normal stresses have a different concavity compared to the exponential laws. Similar difference in curvature of the normal stresses compared to the exponential laws were also observed

by Rouzes et al. (2019) for low submergence flows. For Exp. $RhHh$ the vertical normal stresses for the NB-case show good agreement with the exponential law by Nezu and Nakagawa (1993), as expected for high submergence flows, while the exponential law by Song and Chiew (2001) is consistently lower than the measured vertical normal stress profile for the WB-case.

The analysis of Figure H.17 has revealed that the presence of the boat causes an increase in the streamwise velocities and a decrease in the vertical velocities. The increase in streamwise velocity can be estimated by taking into account the reduction in cross section induced by the boundary layer, on the basis of the displacement thickness. Per continuity, the streamwise velocity under uniform flow conditions is increased below the boundary layer by a factor:

$$\Delta u = \frac{H}{H - \delta^*} \tag{H.13}$$

when the boat is present. Figures H.18a-b show for Exp. $RhHl$ and $RhHh$ that the double-averaged streamwise velocity profile with no boat $\langle \overline{u}_{NB} \rangle_x$ corrected with the double averaged factor $\langle \Delta u \rangle_x$ agrees with the double averaged streamwise profile measured with the boat $\langle \overline{u}_{WB} \rangle_x$. $\langle \Delta u \rangle_x$ allows to effectively predict the increase in streamwise velocity below the surface boundary layer.

The decrease in vertical velocities can be determined on the basis of the theoretical relationship by Song and Chiew (2001) for the vertical velocity induced by a non-uniform flow:

$$\overline{w}_{nu}(z) = \overline{u}(z) \frac{dH'}{dx} \frac{z}{H'} \tag{H.14}$$

Equation H.14 defines the correction factor for the vertical velocity obtained without boat to determine the increase or decrease in vertical velocity induced by the boat. Figure H.18d shows for Exp. $RhHh$ that the double-averaged vertical velocity without boat $\langle \overline{w}_{NB} \rangle_x$ corrected with $\langle \overline{w}_{nu} \rangle_x$ (dashed red line) agrees well with the double averaged vertical velocity profiles obtained with the boat $\langle \overline{w}_{WB} \rangle_x$ (black line). For Exp. $RhHl$, Figure H.18c shows that there is relative good agreement for z/H > 0.4, while for z/H < 0.4 the corrected profile underestimates the measured double averaged vertical velocity profiles obtained with the boat. The trend of the two profiles is similar, though. It was not possible to compare the vertical velocities for Exp. $RlHl$ as the data are affected by a slight non-stationarity, as mentioned earlier.
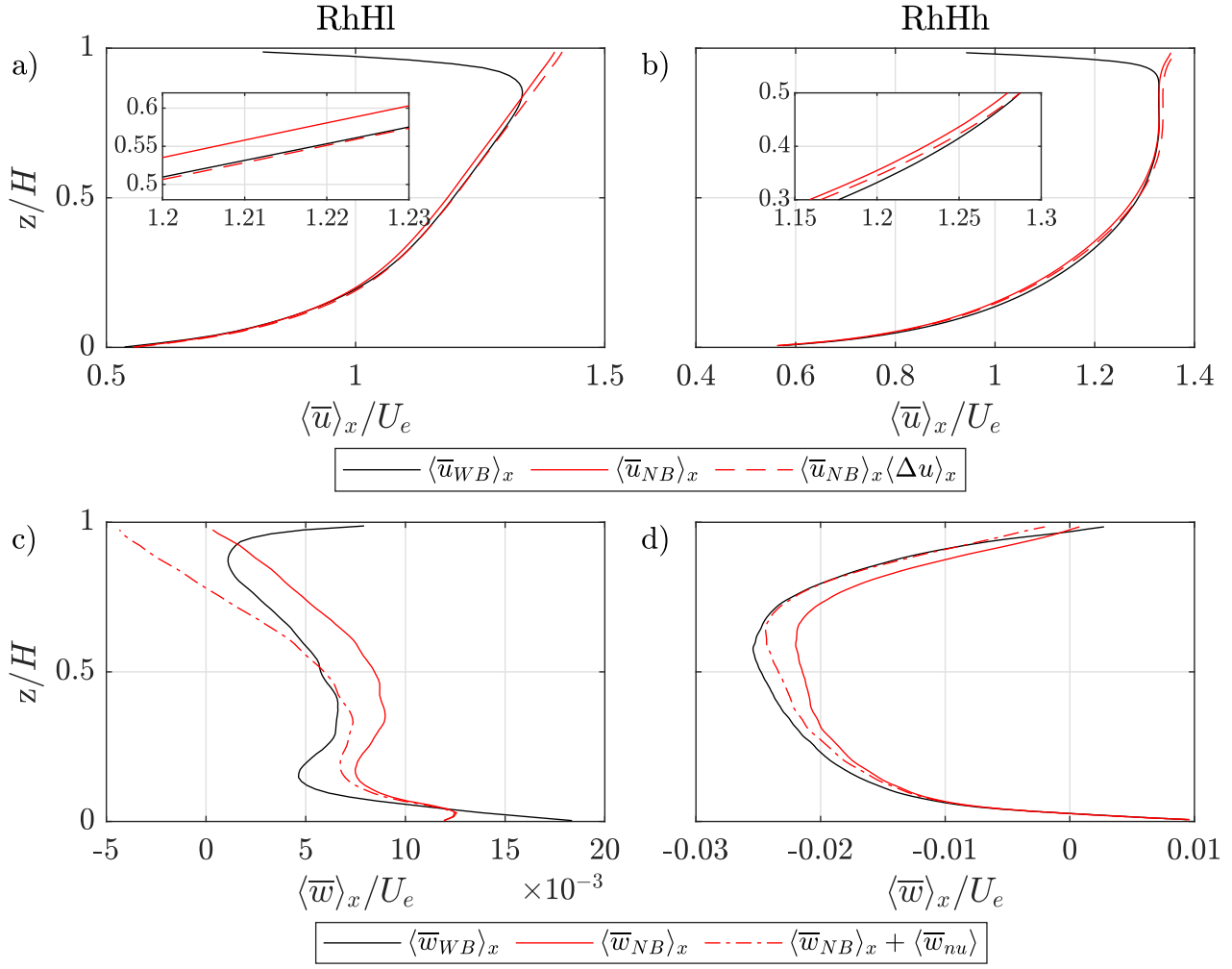
Figure H.18: (a-b) Double-averaged profiles of the streamwise velocities with boat $\langle \overline{u}_{WB} \rangle_x$, without boat $\langle \overline{u}_{NB} \rangle_x$ and the prediction of the increase in streamwise velocity $\langle \overline{u}_{NB} \rangle_x \langle \Delta u \rangle_x$ based on equation H.13; (c-d) Double-averaged profiles of the vertical velocities with boat $\langle \overline{w}_{WB} \rangle_x$, without boat $\langle \overline{w}_{NB} \rangle_x$ and the prediction of the decrease in vertical velocity $\langle \overline{w}_{NB} \rangle_x + \langle \overline{w}_{nu} \rangle_x$ based on equation H.14. The Figures on the left pertain to Exp. $RhHl$ and on the right to Exp. $RhHh$.

H.3.4.1 Log-law characterization

In this Section, the double-averaged streamwise velocity profiles are analysed to determine whether a log-law region can be identified and how the presence of the boat modifies it. The log law is fit to the $\langle \overline{u} \rangle_x$-profile normalized by u_* (the shear velocity obtained from the extrapolation of the total shear stress to the top of the spheres) following the procedure described in Section 4.5.2 to determine the roughness length z_0, the zero-plane position z_d and the equivalent sand roughness k_s.

Table H.5 lists the log law parameters for all experiments distinguishing between NB- and WB-cases. By first comparing the parameters obtained for the NB-case, Table H.5 shows that the equivalent sand roughness k_s is the same for experiments $RlHl$ and $RhHl$ within the measurement error, as they share the same relative submergence (H/D). The equivalent sand roughness for experiment $RhHh$ with a higher relative submergence is, instead, lower. Rouzes et al. (2019) showed conversely, that the equivalent sand roughness increases

with relative submergence. The decrease in equivalent sand roughness with increasing relative submergence is probably related, in this case, to the presence of secondary currents, as evident from the convex shear stress profiles in Figure H.17m. Considering now the influence of the boat on the log-law parameters, Table H.5 shows that the equivalent sand roughness for the WB-cases is lower than the NB-cases. The values of the displacement length z_d do not change significantly and are equal to 20% of the diameter of the spheres, consistent with other experimental studies on rough beds Grass et al. (1991); Detert and Nikora (2010). The range of validity of the log law is similar for the NB- and WB-case and consistent with the range of validity of the log law for for z/H<0.2-0.3 observed in other studies Jiménez (2004); Raupach et al. (1991); Rouzes et al. (2019).

Exp.		$\langle\delta\rangle_x$	u_*	k_s/D	d/D	$z_m/\langle\delta\rangle_x$	$z_M/\langle\delta\rangle_x$
		[cm]	[cm/s]	[-]	[-]	[-]	[-]
RlHl	WB	5.2	2.69 ± 0.05	1.33 ± 0.01	-0.254 ± 0.002	0.12	0.22
	NB	5.8	2.71 ± 0.05	1.37 ± 0.02	-0.250 ± 0.003	0.05	0.17
RhHl	WB	5.3	5.54 ± 0.11	0.99 ± 0.01	-0.200 ± 0.001	0	0.10
	NB	5.8	5.74 ± 0.11	1.35 ± 0.01	-0.253 ± 0.001	0	0.11
RhHh	WB	10.1	2.68 ± 0.05	0.76 ± 0.02	-0.227 ± 0.001	0.15	0.23
	NB	10.8	2.69 ± 0.05	0.83 ± 0.02	-0.212 ± 0.001	0.06	0.27

Table H.5: Log law parameters determined on the basis of the streamwise velocity $\langle\overline{u}\rangle_x$: thickness of the boundary layer above the spheres $\langle\delta\rangle_x$ equal to H' for the WB-case and to H for the NB-case, shear velocity obtained from the extrapolation of the total fluid shear stress $\langle\overline{\tau}_{xz}\rangle_x$ to the top of the spheres u_*, k_s equivalent sand roughness, z_d zero-displacement length, z_m and z_M start and end elevation of the best-fit range of the log-law.

Figure H.19 shows the plot of the double averaged streamwise velocity for all three experimental runs for the NB- and WB-cases with the log-law fit. Quite interestingly the velocity profiles are characterized by a negative wake in the outer layer (the velocity profile is below the log law distribution). Accelerated open-channel flows are characterized by negative wakes (Song and Chiew, 2001; Kironoto and Graf, 1996), but the negative wake observed here cannot be ascribed to the flow non-uniformity induced by the boat, as the velocity profiles with no boat under uniform flow conditions show a similar deviation. For experiment $RhHh$ this deviation can be connected to the presence of secondary currents. Experiment $RhHh$ is characterized, in fact, by strong negative vertical velocities which induces the deviation of the streamwise velocity profile from the theoretical log profile in the outer layer. For experiments $RlHl$ and $RhHl$ no explanation is evident.
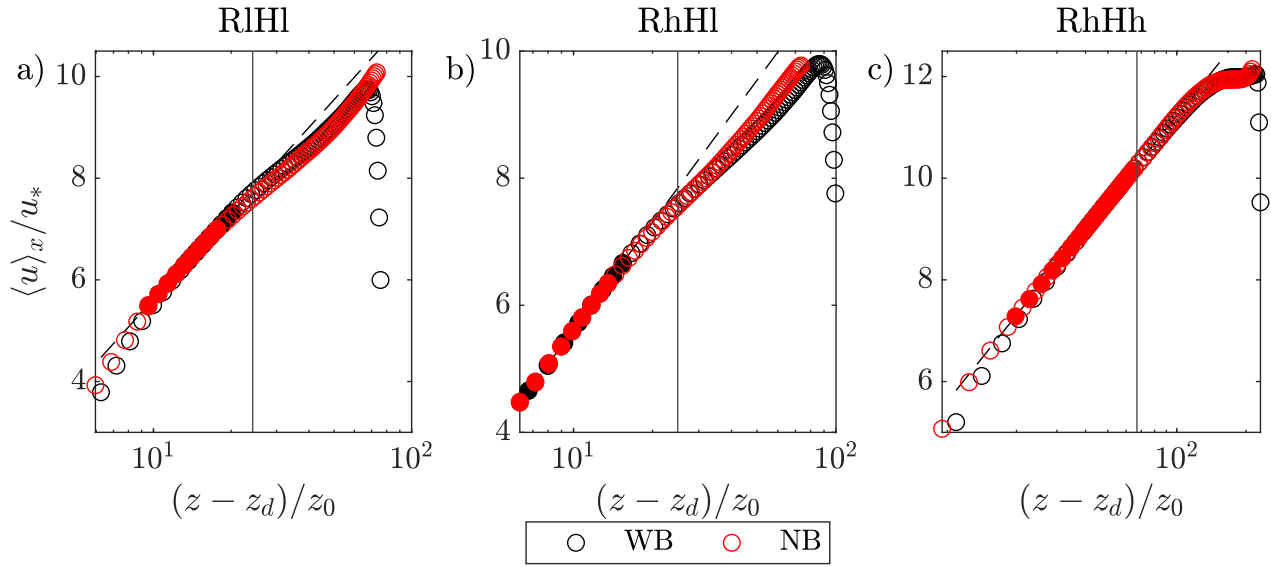
Figure H.19: Log law fit of the double averaged streamwise velocity profiles $\langle \overline{u} \rangle_x$. The filled circles represent the vertical range where the best fit was found.

H.4 Conclusion

The stereo PIV system has been validated with reference to two different aspects: on the one hand, the capability to reconstruct the velocity field given the steep vertical viewing angles of the stereo cameras, necessary to investigate the flow in between the spheres, and, on the other hand, the influence of the boat, which is needed to look through the water surface, on the flow field.

The first issue has been investigated by comparing flow measurements obtained simultaneously with the stereo-PIV system and with a planar 2D2C PIV system for two different flow depths. Since the planar PIV measurements are restricted to the flow region above the top of the spheres, the flow field in between the spheres has been validated by assessing its integrity on the basis of topological principles. The results show perfect agreement between the stereo-PIV and planar PIV data for the streamwise velocity components, both for time-averaged flow fields and for the double averaged vertical profiles ($\langle \overline{u} \rangle_x$, $\langle \overline{u'u'} \rangle_x$, $\langle M_{30} \rangle_x$). The instantaneous signals of the streamwise velocity component and of the streamwise normal stresses overlap, in fact, perfectly. The flow statistics involving the vertical velocity component w show, instead, higher discrepancies in the magnitude between the stereo-PIV and planar PIV measurements, while the spatial patterns of the time-averaged flow fields and the vertical trends of the double averaged profiles are similar. More specifically, the double averaged profiles of the vertical velocity $\langle \overline{w} \rangle_x$, the vertical normal stresses $\langle \overline{w'w'} \rangle_x$ and the third order moments M_{03}, M_{12}, M_{21} obtained with the stereo-PIV system tend to overestimate the corresponding flow statics obtained with the planar PIV. This deviation is comparable with the time-convergence error for the vertical first and third order moments, while the vertical normal stresses deviate by a factor of about 1.4 over the whole water depth, so that care should be taken to interpret them in an absolute sense. The time-averaged field and the double averaged profiles of the Reynolds shear stress are in very good agreement between the stereo and planar PIV system. The quadrant analysis revealed though that the contributions of the turbulent events to the Reynolds shear stresses are slightly overestimated for the stereo-PIV measurements. The time fraction and frequencies of the turbulent events are instead in good agreement. Overall, the analysis

of the instantaneous deviation of the vertical velocity obtained with the stereo-PIV from the vertical velocities obtained with planar PIV shows that the error is random and comparable with the peak locking error. Through direct comparison, via cross correlation, of the position of the PIV particles in the planar PIV image-frames and the dewarped stereo PIV image frames, it was assessed that the deviation in vertical velocities results from the strong deformation of the PIV particles resulting from the dewarping processes. More specifically, due to changes in particle intensity or particle orientation, the shape of the particle changes between image frames within one PIV burst. The dewarping process applied to the stereo-PIV images magnifies these differences causing a shift in the relative position of the particles centroid, resulting in an incorrect definition of the displacement.

The influence of the boat on the flow was investigated via ultrasonic measurements of the water surface and planar PIV measurements of the flow field performed with and without the presence of the boat for three different flow conditions characterized by two different water depths and two bulk Reynolds numbers. The results show that the presence of the boat causes flow stagnation at the leading edge with an increase in water levels limited to a region close to the leading edge. It is shown that the increase in water level depends on the velocity at the water surface for the undisturbed flow in accordance with the Bernoulli principle. The flow field measurements show the development of a boundary layer along the boat, which is found to increase with $x^{4/5}$ as for turbulent boundary layers developing along a smooth plates. A virtual origin needs to be introduced though to account for a non-zero boundary layer depth at the leading edge of the boat. The virtual origin increases with increasing water depth super-elevation at the leading edge. In a similar manner, the proportionality factor for the boundary layer growth law decreases with increasing super-elevation. The development of the boundary layer depends, as such, on the hydraulic conditions at the leading edge, in as much as they trigger the early transition to a turbulent boundary layer for Reynolds numbers lower than the threshold. This is probably connected to Görtler instabilities developing as a result of the local curvature.

The analysis of the flow statistics shows that the boundary layer developing along the boat causes accelerated flow conditions of the bulk flow. The streamwise velocity and turbulent shear stress profiles reach self-similarity one pattern of spheres downstream of the leading edge, though. The comparison of double averaged flow statistics shows that the accelerated flow conditions cause a slight increase in the streamwise velocity profiles and a slight decrease in the vertical velocity profiles. Both effects can be predicted on the basis of the continuity equation and the theoretical relation developed by Song and Chiew (2001) for the prediction of vertical velocities in non-uniform flows, by taking the displacement thickness as relevant length scale to quantify the reduction in cross section induced by the boundary layer. The influence of the boundary layer is felt also on the turbulent statistics with a slight decrease in turbulent shear stress and normal shear stresses in the bulk flow region. The shear stress values near the top of the roughness remain almost unaltered though, as the momentum exchange is dominated there by the shear layers developing in the lee side of the spheres. The analysis of the log law parameters show that the roughness displacement length is not modified by the presence of the boat, while the equivalent sand roughness is underestimated.

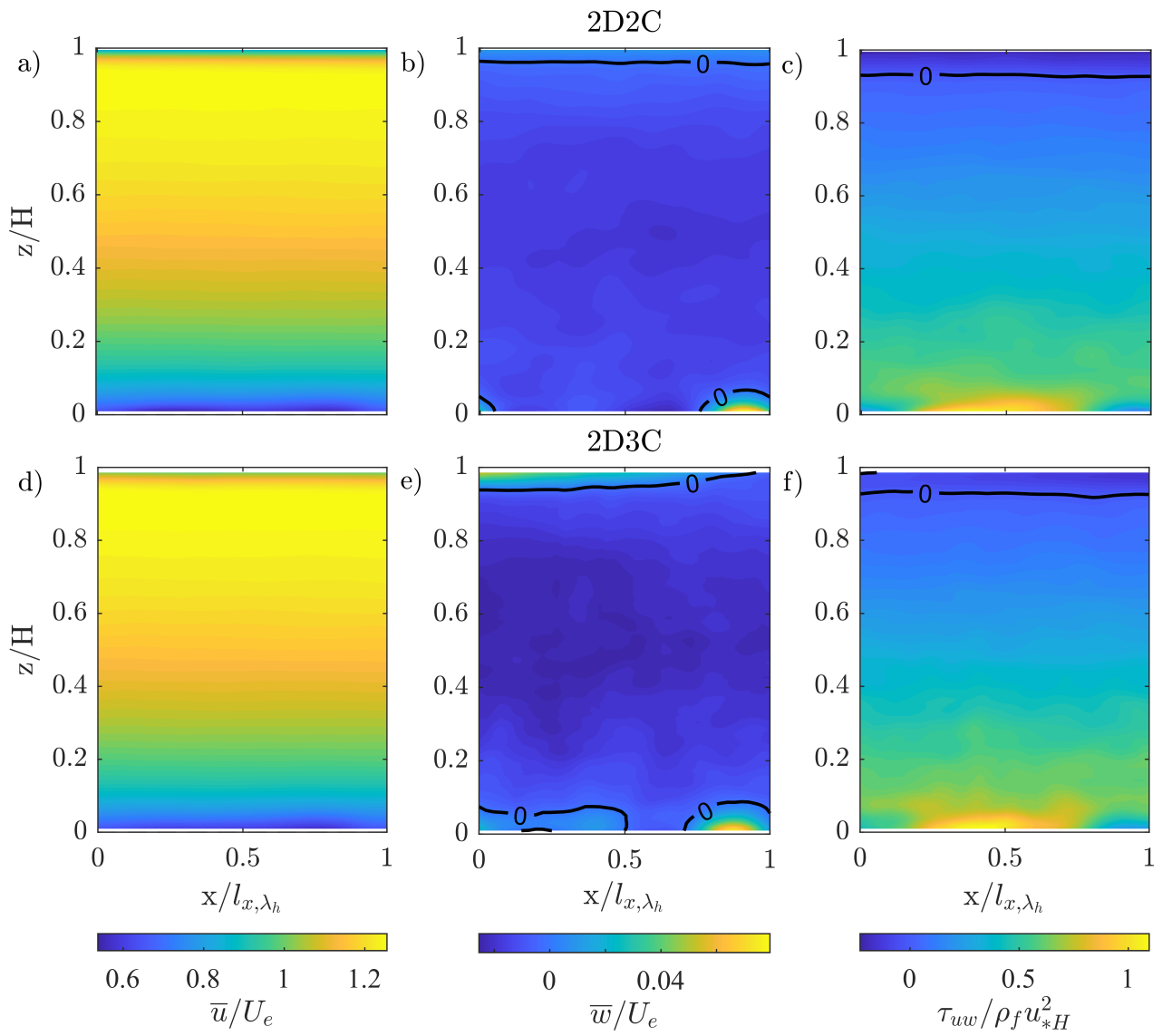# I   Validation of the stereo-PIV system: Case Hh

Figure I.1: Time-averaged streamwise and vertical velocity fields, $\overline{u}$ and $\overline{w}$, and Reynolds shear stress field τ_{uw} for experiment Hh: a)-c) 2D2C PIV measurements, d)-f) 2D3C stereo-PIV measurements. The flow is form left to right.
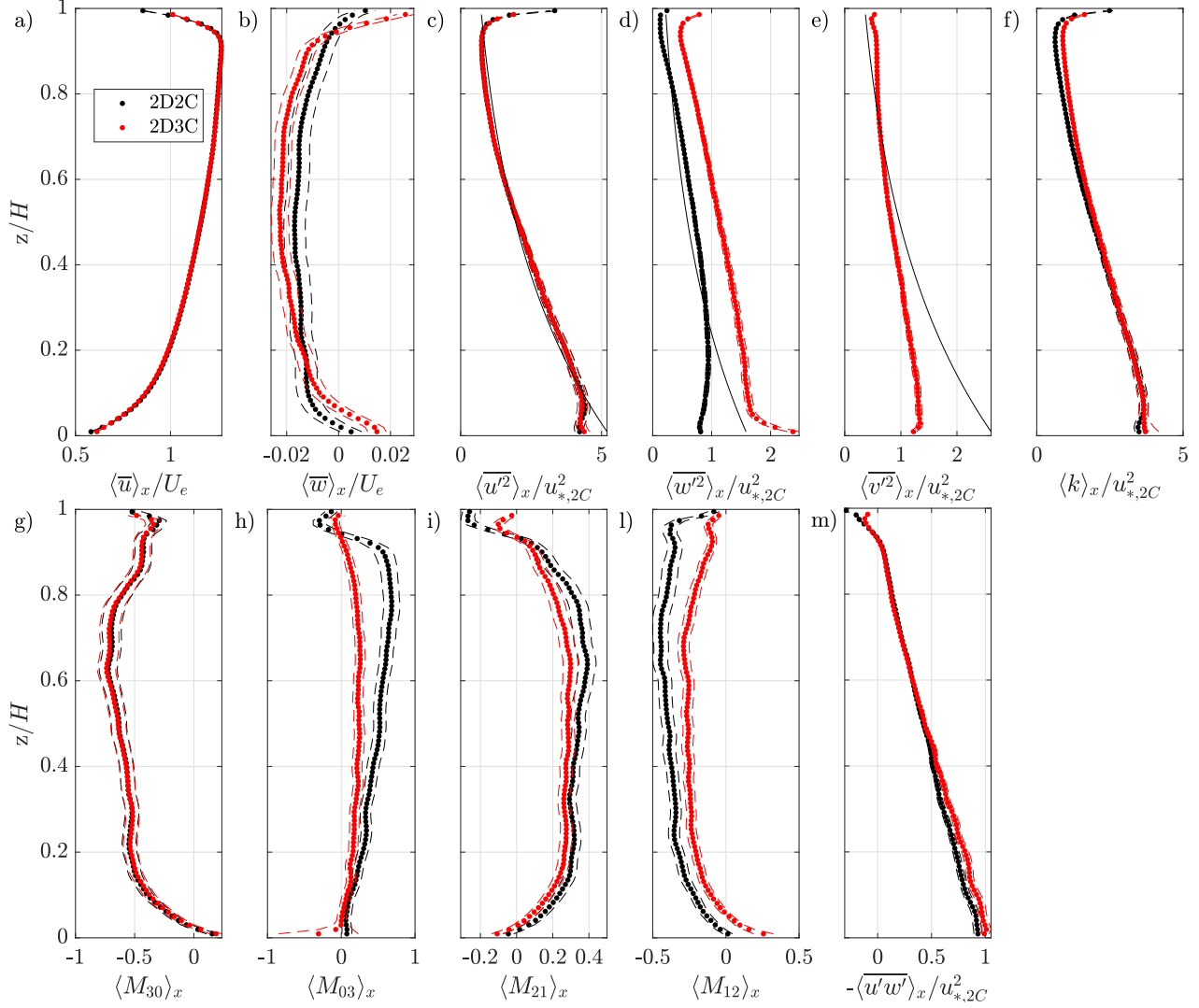
Figure I.2: Comparison of the longitudinally-averaged profiles of the first, second and third order moments obtained with the planar PIV system (2D2C) and the stereo-PIV system (2D3C) for the Hh case: streamwise $\langle \overline{u} \rangle_x$ and vertical $\langle \overline{w} \rangle_x$ velocities (a-b), streamwise $\rho_f \langle \overline{u'^2} \rangle_x$, vertical $\rho_f \langle \overline{w'^2} \rangle_x$ and transverse $\rho_f \langle \overline{v'^2} \rangle_x$ normal stresses (c-e), turbulent kinetic energy $\langle k \rangle_x$ (f), third order moments $\langle M_{i,j} \rangle_x$ (g-l) and Reynolds shear stresses $-\rho_f \langle \overline{u'w'} \rangle_x$ (m). The first order moments are normalized by the effective bulk velocity U_e and the second order moments by the shear velocity $u_{*,2C}$ obtained from the extrapolation of the shear stress profile obtained with the planar PIV system. The exponential laws by Nezu and Nakagawa (1993) for the normal turbulent stresses are plotted as black continuous lines in Figures (c-e).
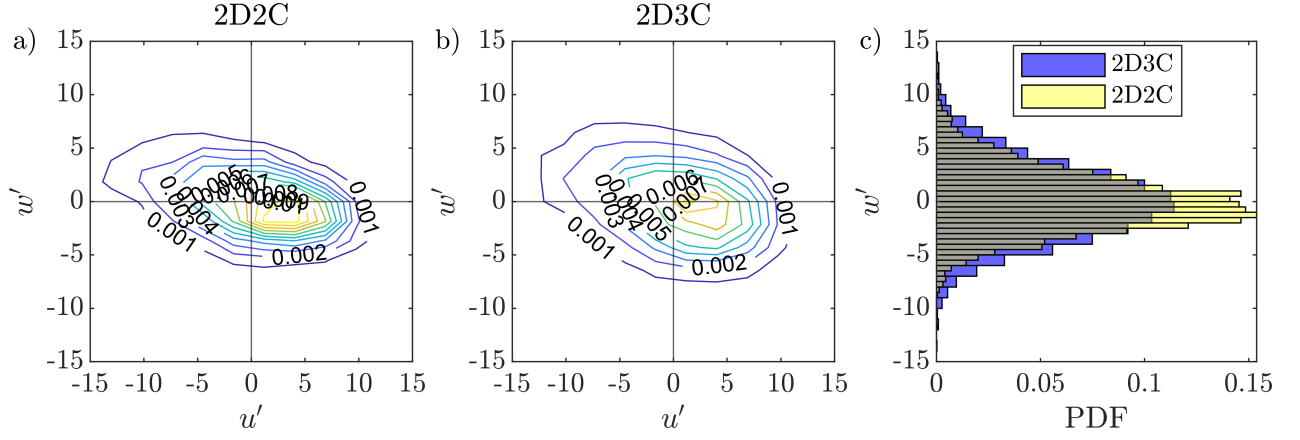
Figure I.3: a)-b) Joint probability density function of the u' and w' fluctuations sampled in the shear layer at z/H = 0.04 and x/l_{x,λ_h} = 0.6 during Exp. Hh for the 2D2C and stereo PIV measurements, respectively. c) probability density function of the vertical fluctuations just mentioned.
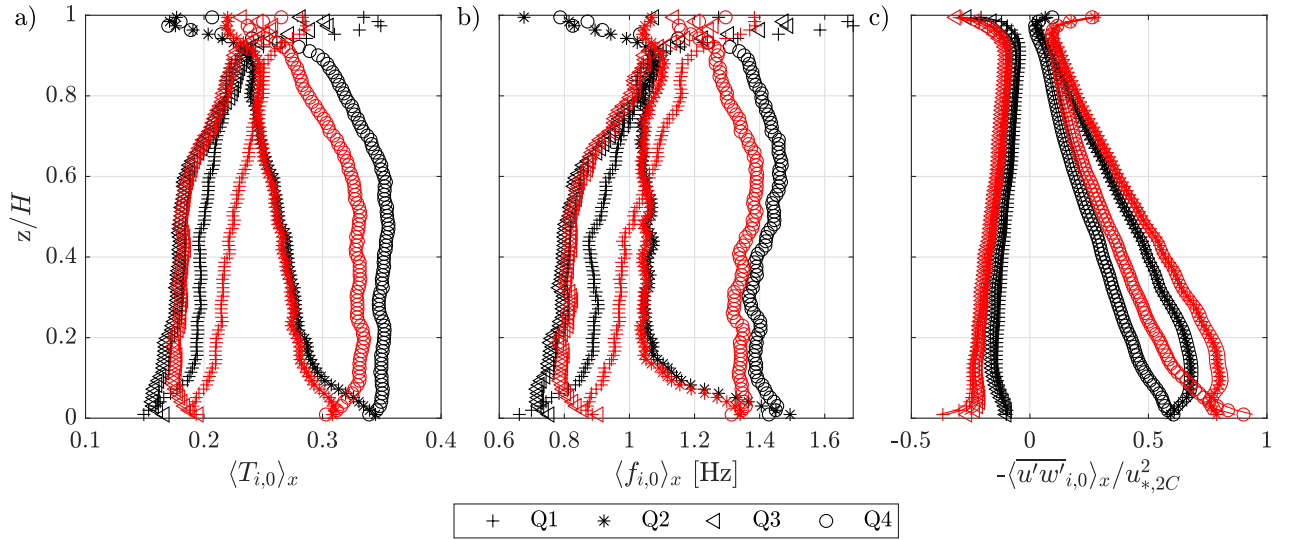

Figure I.4: Longitudinally-averaged time contribution $\langle T_{i,0}\rangle_x$ (a), frequency $\langle f_{i,0}\rangle_x$ (b) and shear stress contribution $-\rho_f\langle\overline{u'w'}_{i,0}\rangle_x$ (c) of the turbulent events for the 2D2C data (black profiles) and the stereo-PIV data (red profiles) for Exp. Hh.
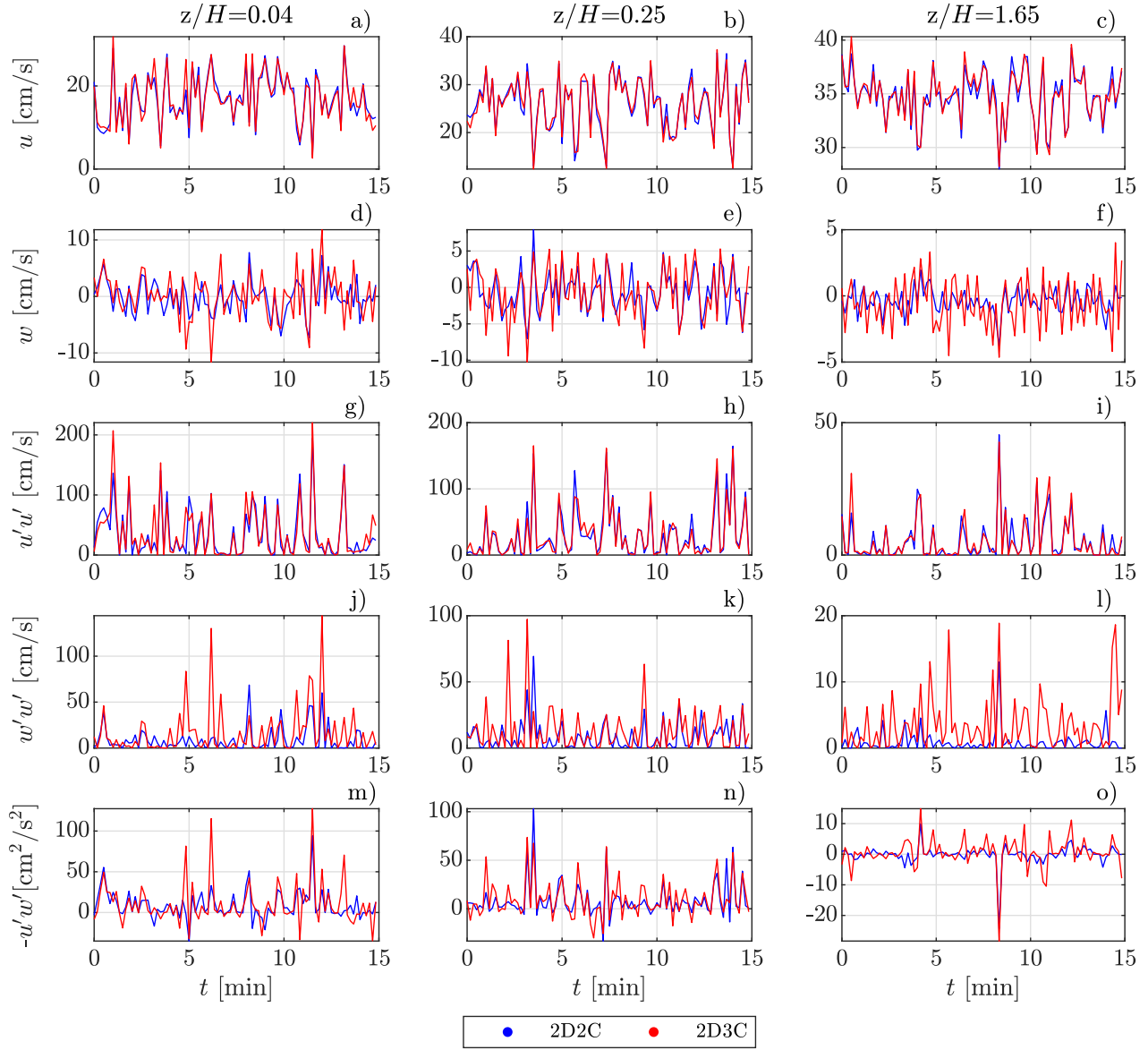
Figure I.5: Comparison of the signal time series of the instantaneous streamwise velocity u (a-c), vertical velocity w (d-f), streamwise normal stresses $u'u'$ (g-i), vertical normal stresses $w'w'$ (j-l) and Reynolds shear stresses $-u'w'$ (m-o), sampled with the 2D2C PIV system and the 2D3C stereo-PIV system at $x/l_{x,\lambda_h}$=0.6 at three different heights during Exp. Hh.
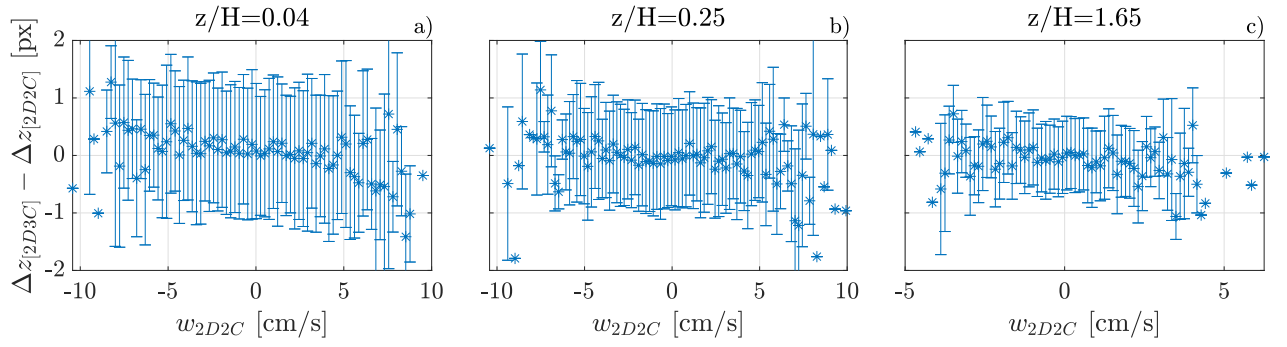
Figure I.6: Difference in vertical particle displacement between the stereo and the 2D2C PIV for the vertical velocity signals sampled at x/l_{x,λ_h}=0.6 and at three different heights for Exp. Hh. The vertical whiskers represent one standard deviation around the average particle displacement.

Bibliography

Aberle, J., Koll, K., and Dittrich, A. (2008). Form induced stresses over rough gravel-beds. *Acta Geophysica*, 56(3):584–600.

Aberle, J. and Nikora, V. (2006). Statistical properties of armored gravel bed surfaces. *Water Resources Research*, 42(W11414).

Aberle, J., Rennie, C., Admiraal, D., and Muste, M. (2017). *Experimental hydraulics: Methods, instruments, data processing and management*. CRC Press (Taylor & Francis Group), Leiden (Netherlands).

Ackermann, F. (1984). Digital image correlation: performance and potential application in photogrammetry. *Photogrammetric Record*, 11(64):429–439.

Akutina, Y. (2015). *Experimental investigation of flow structures in a shallow embayment using 3D-PTV*. PhD thesis, McGill University.

Akutina, Y., Eiff, O., Moulin, F., and Rouzes, M. (2019). Lateral bed-roughness variation in shallow open-channel flow with very low submergence. *Environmental Fluid Mech*, 19:1339–1361.

Albayrak, I. and Lemmin, U. (2011). Secondary currents and corresponding surface velocity patterns in a turbulent open-channel flow over a rough bed. *J. Hydraul. Eng.*, 137(11):1318–1334.

Amir, M. and Castro, I. (2011). Turbulence in rough-wall boundary layers. *Experiments in Fluids*, 51(2):313–326.

Andrews, E. (1984). Downstream effects of flaming gorge reservoir on the green river, colorado and utah. *Geological Society of America Bulletin*, 95:371–378.

Antonia, R. and Luxton, R. (1971). The response of a turbulent boundary layer to an upstanding step change in surface roughness. *J. Basic Eng.*, 93(1):22–32.

Ashworth, P. and Ferguson, R. (1989). Size-selective entrainment of bed load in gravel bed streams. *Water Resources Research*, 25(4):627–634.

Astruc, D., Cazin, S., Cid, E., Eiff, O., Lacaze, L., Robin, P., Toublanc, F., and Cáceres (2012). A stereoscopic method for rapid monitoring of the spatio-temporal evolution of the sand-bed elevation in the swash zone. *Coastal Engineering*, 60:11–20.

Atkinson, C., Buchmann, N., Amili, O., and Soria, J. (2014). On the appropriate filtering of piv measurements of turbulent shear flows. *Exp. Fluids*, 55(1654).

Barzaghi, R., Borghi, A., Brovelli, M., and Sona, G. (2001). A comparison between two methods for outliers detection in dtm data.

Batchelor, G. (1953). *The theory of homogeneous turbulence*. Cambridge University Press.

Bathurst, J. (1985). Flow resistance estimation in mountain rivers. *J. Hydraul. Eng.*, 111(4):625–643.

Bendat, J. and Piersol, A. (1986). *Random Data*. Wiley-Interscience, Canada.

Benetazzo, A. (2006). Measurements of short waves using stereo matched image sequences. *Coastal Engineering*, 53:1013–1032.

Benetazzo, A., Fedele, F., Gallego, G., Shih, P.-C., and Yezzi, A. (2012). Offshore stereo measurements of gravity waves. *Coastal Engineering*, 64:127–138.

Bertin, S. and Friedrich, H. (2019). Effects of sand addition and bed flushing on gravel bed surface microtopography and roughness. *Water Resources Research*, 55:8076–8095.

Bertin, S., Friedrich, H., Delmas, P., and Chan, E. (2013). On the use of close-range digital sterophotogrammetry to measure gravel-bed topography in a laboratory environment. *Proceedings of 2013 IAHR Congress*.

Bertin, S., Friedrich, H., Delmas, P., Chan, P., and Gimel'farb, G. (2015). Digital stereo photogrammetry for grain-scale monitoring of fluvial surfaces: Error evaluation and workflow optimization. *Journal of Photogrammetry and Remote Sensing*, 101:193–208.

Bertin, S., Groom, J., and Friedrich, H. (2017). Isolating roughness scales of gravel-bed patches. *Water Resour. Res.*, 53:6841–6856.

Best, J. (2005). The fluid dynamics of river dunes: A review and future research directions. *Journal of Geophysical Research*, 110.

Bethmann, F. and Luhmann, T. (2011). Least-squares matching with advanced geometric transformation model. *Photogrammetrie-Fernerkundung-Geoinformation*, 2:57–69.

Bouget, J. (2010). Camera calibration toolbox for matlab.

Bouratsis, P., Diplas, P., Dancey, C., and Apsilidis, N. (2013). High-resolution 3-d monitoring of evolving sediment beds. *Water resources Research*, 49:977–992.

Brown, D. (1971). Close-range camera calibration. *Photogrammetric Engineering*, 37(8):855–866.

Bruno, F., Bianco, G., Muzzupappa, M., Barone, S., and Razionale, A. (2011). Experimentation of structured light and stereo vision for underwater 3d reconstruction. *Journal of Photogrammetry and Remote Sensing*, 66:508–518.

Buffington, J., Montgomery, D., and Greenberg, H. (2004). Basin-scale availability of salmonoid spawning gravel as influenced by channel type and hydraulic roughness in mountain catchments. *Can. J. Fish. Aquat. Sci.*, 61:2085–2096.

Cameron, S., Nikora, V., Albayrak, I., Miler, O., Stewart, M., and Siniscalchi, F. (2013). Interactions between aquatic plants and turbulent flow: a field study using stereoscopic piv. *J. Fluid Mech.*, 732:1345–372.

Campbell, L., McEwan, I., Nikora, V., Pokrajac, D., Gallagher, M., and Manes, C. (2005). Bed-load effects on hydrodynamics of rough-bed open-channel flows. *J. Hydraul. Eng.*, 131(7):576–585.

Celik, A., Diplas, P., and Dancey, C. (2013). Instantaneous turbulent forces and impulse on a rough bed: Implications for initiation of bed material movement. *Water Ressources Research*, 49:2213–2227.

Chagot, L., Moulin, F., and Eiff, O. (2020). Towards converged statistics in three-dimensional canopy-dominated flows. *Experiments in Fluids*, 61(24).

Chen, G., Gu, S., Huai, W., and Zhang, Y. (2015). Boundary shear stress in rectangular ice-covered channels. *J. Hydraul. Eng.*, 141(6).

Cheng, H. and Castro, I. (2002). Near-wall flow development after a step change in surface roughness. *Boundary-Layer Meteorology*, 105:411–432.

Cheng, H., Hayden, P., Robins, A., and Castro, I. (2007). Flow over cube arrays of different packing densities. *Journal of Wind Engineering*, 95:715–740.

Chiew, Y. and Parker, G. (1994). Incipient sediment motion on non-horizontal slopes. *J. Hydraul. Res.*, 32:649–660.

Christensen, K. (2004). The influence of peak-locking errors on turbulence statistics computed from piv ensembles. *Experiments in Fluids*, 36:484–497.

Christensen, K. and Adrian, R. (2002). Measurement of instantaneous eulerian acceleration fields by particle image velocimetry: method and accuracy. *Experiments in Fluids*, 33:759–769.

Church, M., McLean, D., and Wolcott, J. (1987). River bed gravels: sampling and analysis. In Thorne, C., Bathurst, J., and Hey, R., editors, *Sediment Transport in Gravel-bed Rivers*, chapter 3, pages 43–88. John Wiley & Sons.

Coleman, S., Nikora, V., McLean, S., and Schicke, E. (2007). Spatially averaged turbulent flow over square ribs. *J. Eng. Mech.*, 133(2):194–204.

Coleman, S. E., Nikora, V. I., and Aberle, J. (2011). Interpretation of alluvial beds through bed-elevation distribution moments. *Water Resources Research*, 47(11).

Collins, A., Walling, D., and Leeks, G. (1997). Fingerprinting the origin of fluvial suspended sediment in larger river basins: combining assessment of spatial provenance and source type. *Geogr. Ann.*, 79(4):239–254.

Colombini, M. and Parker, G. (1995). Longitudinal streaks. *J. Fluid Mech.*, 304:161–183.

Cooper, J., Ockleford, A., Rice, S., and Powell, D. (2017). Does the permeability of gravel river beds affect near-bed hydrodynamics? *Earth Surf. Process. Landforms*, 43:943–955.

Cooper, J. and Tait, S. (2009). Water-worked gravel beds in laboratory flumes - a natural analogue? *Earth Surf. Process. Landforms*, 34:384–397.

Crosa, G., Castelli, E., Gentili, G., and Espa, P. (2010). Effects of suspended sediments from reservoir flushing on fish and macroinvertebrates in an alpine stream. *Aquat. Sci.*, 72:85–95.

Culbertson, J. (1967). Evidence of secondary circulation in an alluvial channel. *U.S. Geol. Survey*, pages D214–D216.

Curran, J. and Waters, K. (2014). The importance of bed sediment sand content for the structure of a static armor layer in a gravel bed river. *J. Geophys. Res.*, 119:1484–1497.

Davies, P. and Nelson, M. (1993). The effect of steep slope logging on fine sediment infiltration into the beds of ephemeral and perennial streams of the dazzler range. *J. Hydrol.*, 150(2-4):481–504.

Davies, T. and Sutherland, A. (1983). Extremal hypothesis for river behaviour. *Water Resources Research*, 19(1):141–148.

de Ruiter, J. (1983). Incipient motion and pick-up of sediment as a function of local variables. Technical Report Report R 657-XI, Delft Hydraulics Laboratory.

de Vries, S., Hill, D., de Schipper, M., and Stive, M. (2011). Remote sensing of surf zone waves using stereo imaging. *Coastal Engineering*, 58:239–250.

Detert, M. and Nikora, V. (2010). Synoptic velocity and pressure fields at the water-sediment interface at streambeds. *J. Fluid. Mech.*, 660:55–86.

Dey, S. (2003). Thershold of sediment motion on combined transverse and longitudinal sloping beds. *Journal of Hydraulic Research*, 41(4):405–415.

Dey, S. (2014). *Fluvial Hydrodynamics*. Springer, Heidelberg.

Dey, S. and Ali, S. (2018). Phenomenological description of scaling laws of sediment transport. In *9th International Conference on Fluvial Hydraulics, River Flow 2018*, volume 40 of *E3S Web of Conferences*. EDP Sciences.

Dey, S. and Das, R. (2012). Gravel-bed hydrodynamica:double-averaging approach. *J. Hyd. Eng.*, 138(8).

Dey, S., Das, R., Gaudio, R., and Bose, S. (2012). Turbulence in mobile-bed streams. *Acta Geophysica*, 60(6):1547–1588.

Dey, S. and Debnath, K. (2001). Sediment pickup on streamwise sloping beds. *J. Irrig. Drain Eng.*, 127(1).

Dey, S. and Raikar, R. (2007). Characteristics of horseshoe vortex in developing scour holes at piers. *J. Hydraul. Eng.*, 133(4):399–413.

Dey, S., Sarkar, S., Bose, S., Tait, S., and Castro-Orgaz, O. (2011a). Wall-wake flows downstream of a sphere placed on a plane rough wall. *J. Hydraul. Eng.*, 137(10):1173–1189.

Dey, S., Sarkar, S., Bose, S. K., Tait, S., and Castro-Orgaz, O. (2011b). Wall-wake flows downstream of a sphere placed on a plane rough wall. *Journal of Hydraulic Engineering*, 137(10):1173–1189.

Dey, S., Sarkar, S., and Solari, L. (2011c). Near-bed turbulence characteristics at the entrainment threshold of sediment beds. *J. Hydraul. Eng.*, 137(9):945–958.

Diplas, P., Dancey, C., Celik, A., Valyrakis, M., Greer, K., and Akar, T. (2008). The role of impulse on the initiation of particle movement under turbulent flow conditions. *Science*, 322:717–720.

Dixen, M., Sumer, B., and Fredsoe, J. (2013). Numerical and experimental investigation of flow and scour around a half-buried sphere. *Coastal Engineering*, 73:84–105.

Dwivedi, A., Melville, B., Raudkivi, A., Shamseldin, A., and Chiew, Y. (2012). Role of turbulence and particle exposure on entrainment of large spherical particles in flows with low relative submergence. *J. Hydraul. Eng.*, 138(512):1022–1030.

Dwivedi, A., Melville, B., and Shamseldin, A. (2010). Hydrodynamic forces generated on a spherical sediment particle during entrainment. *J. Hydraul. Eng.*, 136(10):756–769.

Egiazarov, I. (1956). Calculation of nonuniform sediment concentrations. *J. Hydraul. Div. Am. Soc. Civ. Eng.*, 91(HY4):225–247.

Einstein, H. (1942). Formulas for the transportation of bed load. *Trans. ASCE*, 107(2140):561–577.

Einstein, H. (1950). The bed load function for sediment transport in open channel flows. *United States Department of Agriculture, Technical Bulletin*, 1026.

Engelund, F. and Hansen, E. (1967). *A monograph on sediment transport in alluvial streams*. Teknisk Forlag.

Euler, E., Herget, J., Schlömer, O., and Benito, G. (2017). Hydromorphological processes at submerged solitary boulder obstacles in streams. *Catena*, 157:250–267.

Euler, E., Zemke, J., Rodrigues, S., and Herget, J. (2014). Influence of inclination and permeability of solitary woody riparian plants on local hydraulic and sedimentary processes. *Hydrol. Process.*, 28:1358–1371.

Euler, T. and Herget, J. (2012). Controls on local scour and deposition induced by obstacles in fluvial environments. *Catena*, 91:35–46.

Fang, H., Liu, Y., and Stoesser, T. (2017). Influence of boulder concentration on turbulence and sediment transport in open-channel flow over submerged boulders. *Journal of Geophysical Research: Earth Science*, 122:2392–2410.

Ferguson, R., Prestegaard, K., and Ashworth, P. (1989). Influence of sand on hydraulics and gravel transport in a braided gravel bed river. *Water Resour. Res.*, 25(4):635–643.

Fernandez-Luque, R. (1974). *Erosion and transport of bed-load sediment*. PhD thesis, Delft University of Technology.

Ferré, J. and Giralt, F. (1989). Pattern-recognition analysis of the velocity field in plane turbulent wakes. *J. of Fluid. Mech.*, 198:27–64.

Ferreira, A., Lopes, A., Viegas, D., and Sousa, A. (1995). Experimental and numerical simulation of flow around two-dimensional hills. *J. Wind Eng. Ind. Aerodyn.*, 54:173–181.

Ferreira, R., Franca, M., Leal, J., and Cardoso, A. (2012). Flow over rough mobile beds: Friction factor and vertical distribution of the longitudinal velocity. *Water Resources Research*, 48(W05529).

Fincham, A. and Delerce, G. (2000). Advanced optimization of correlation imaging velocimetry algorithms. *Experiments in fluids*.

Fincham, A. and Spedding, G. (1997). Low cost, high resolution dpiv for measurement of turbulent fluid flow. *Experiments in fluids*, 23:449–462.

Finnigan, J. (2000). Turbulence in plant canopies. *Ann. Rev. Fluid. Mech.*, 32:519–571.

Florens, E. (2010). *Couche limite turbulente dans les écoulements à surface libre: Etude expérimentale d'effets de macro-rugosités*. PhD thesis, University of Toulouse.

Florens, E., Eiff, O., and Moulin, F. (2013). Defining the roughness sublayer and its turbulence statistics. *Exp. Fluids*, 54.

Floryan, J. (1986). Görtler instability of boundary layer over concave and convex walls. *Phys. Fluids*, 29(8):2380–2387.

Foss, J. (2004). Surface selections and topological constraints evaluations for flow field analysis. *Experiments in Fluids*, 37:883–898.

Foss, J., Hedden, M., Barros, J., and Christensen, K. (2016). A topological evaluation procedure to assess the integrity of a piv vector field. *Meas. Sci. Technol.*, 27(094007):9pp.

García, M. (2008). Sediment transport and morphodynamics. In Garcia, M., editor, *Sedimentation engineering, processes, measurements, modeling and practice*, chapter 2, pages 21–146. American Society of Civil Engineering, Reston, VA.

Garcia, D., Orteau, J., and Devy, M. (2000). Accurate calibration of stereovision sensor: comparison of different approaches. *Proceeding of 5th Fall Workshop on Vision, Modeling and Visualization*, 37(8):855–866.

Ghilardi, T., Franca, M., and Schleiss, A. (2014a). Bed load fluctuations in a steep channel. *Water Resour. Res.*, 50:6557–6576.

Ghilardi, T., Franca, M., and Schleiss, A. (2014b). Sediment transport in steep channels with large roughness elements. *River Flow 2014*, 51:5260–5283.

Gibins, C., Vericat, D., and Batalla, R. (2007a). When is stream invertebrate drift catastrophic? the role of hydraulics and sediment transport in initiating drift during flood events. *Freshwater Biology*, 52:2369–2384.

Gibins, C., Vericat, D., Batalla, R., and Gomez, C. (2007b). Shaking and moving: low rates of sediment transport trigger mass drift of stream invertebrates. *Can. J. Fish. Aquat. Sci.*, 64:1–5.

Gibson, S., Abraham, D., Heath, R., and Schoellhamer, D. (2009). Vertical gradational variability of fines deposited in a gravel framework. *Sedimentology*, 56:661–676.

Graf, W. and Pazis, G. (1977). Les phenomenes de deposition et d'erosion dans un canal aluvionaire. *J. Hydraul. Res.*, 15(2).

Graham, D., Reid, I., and Rice, S. (2005). Automated sizing of coarse-grained sediments: image-processing procedures. *Mathematical Geology*, 37(1).

Grams, P. and Wilcock, P. (2007). Equilibrium entrainment of fine sediment over a coarse immobile bed. *Water Resources Research*, 43.

Grams, P. and Wilcock, P. (2014). Transport of fine sediment over a coarse, immobile riverbed. *J. Geophys. Res. Earth Surf.*, 119:188–211.

Grant, G. (2012). The geomorphic response of gravel-bed rivers to dams: perspectives and prospects. In Church, M., Biron, P. M., and Roy, A. G., editors, *Gravel-bed rivers: processes, tools, environments*, chapter 15, pages 165–181. John Wiley & Sons, Chichester, UK.

Grass, A., Stuart, R., Mansour-Tehrani, M., Walker, J. D. A., and Smith, F. T. (1991). Vortical structures and coherent motion in turbulent flow over smooth and rough boundaries. *Philosophical Transactions of the Royal Society of London. Series A: Physical and Engineering Sciences*, 336(1640):36–65.

Griffin, J., Schultz, T., Holman, R., Ukeiley, L., and Cattafesta, L. (2010). Application of multivariate outlier detection to fluid velocity meaasurements. *Exp. Fluids*, 49:305–317.

Grimmond, C. and Oke, T. (1999). Aerodynamic properties of urban areas derived from analysis of surface form. *Journal of applied meteorology*, 38:1262–1292.

Groom, J., Bertin, S., and Friedrich, H. (2018). Evaluation of dem size and grid spacing for fluvial patch-scale roughness parametrization. *Geomorphology*, 320:98–110.

Gruen, A. (1985). Adaptive least square correlation: a powerful image matching technique. *S. Afr. J. of Photogrammetry, Remote Sensing and Cartography*, 14(3):175–187.

Gyr, A. and Müller, A. (1996). *The role of coherent structures in developing bedforms during sediment transport*, pages 227–235. John Wiley & Sons.

Hajimirzaie, S. M., Tsakiris, A., Buchholz, J., and Papanicolaou, A. (2014). Flow characteristics around a wall-mounted spherical obstacle in a thin boundary layer. *Exp. Fluids*, 55(1762).

Hancock, P. E. and Johnson, A. E. (1997). Close spacing of settling chamber screens. *The Aeronautical Journal*, 101(1004):179–183.

Hanna, S. and Britter, R. (2002). *Wind flow and vapour cloud dispersion at industrial and urban sites*. Am. Inst. Chem. Eng., New York.

Hanson, R. E., Buckley, H., and Lavoie, P. (2012). Aerodynamic optimization of the flat-plate leading edge for experimental studies of laminar and transitional boundary layers. *Exp. Fluids*, 53:863–871.

Hardy, R., Best, J., Lane, S., and Carbonneau, P. (2010). Coherent flow structures in a depth-limited flow over a gravel surface: The influence of surface roughness. *J. Geophys. Res.*, 115.

Hassan, M. and Reid, I. (1990). The influence of microform bed roughness elements on flow and sediment transport in gravel bed rivers. *Earth Surface Processes and Landforms*, 15:739–750.

Heikkilä, J. and Silvén, O. (1997). A four-step camera calibration procedure with implicit image correction. *Proceedings of IEEE Computer Society Conference on Computer Vision and Pattern Recognition*, pages 1106–1112.

Hofland, B., Battjes, J., and Booij, R. (2005). Measurement of fluctuating pressures on coarse bed material. *J. Hydraul. Eng.*, 131(9):770–781.

Hofland, B. and Booij, R. (2004). Measuring the flow structures that initiate stone movement. In Greco, C. . D. M., editor, *River Flow 2004*, London. Taylor & Francis Group.

Hovmöller, E. (1949). The trough-and-ridge diagram. *Tellus*, 1(2):62–66.

Huang, H., Dabiri, D., and Gharib, M. (1997). On errors of digital particle image velocimetry. *Experiments in Fluids*, 8:1427–1440.

Hubert, M. and Vandervieren, E. (2008). An adjusted boxplot for skewed distributions. *Comput. Stat. Data Anal.*, 52:5186–5201.

Hunt, J. and Eames, I. (2002). The disappearance of laminar and turbulent wakes in complex flows. *J. Fluid Mech.*, 457:111–132.

Hurther, D., Lemmin, U., and Terray, E. (2007). Turbulent transport in the outer region of rough-wall open-channel flows: the contribution of large coherent shear stress structures (lc3s). *J. Fluid Mech.*, 574:465–493.

Hwang, H. and Lee, J. (2018). Secondary flows in turbulent boundary layers over longitudinal surface roughness. *Phys. Rev. Fluids*, 3(014608).

Ikeda, S. (1981). Self formed straight channels in sandy beds. *J. Hydr. Div., ASCE*, 107:389–406.

Jähne, B. (2012). *Digitale Bildverarbeitung und Gewinnung*. Springer, Berlin, 7th edition.

Jiménez, J. (2004). Turbulent flows over rough walls. *Annu. Rev. Fluid Mech.*, 36:173–196.

Karcz, I. (1973). Reflections on the origin of small-scale longitudinal streambed scours. *Proc. of 4th Ann. Geomorphology Symposia Series*, pages 51–58.

Kim, T., Blois, G., Best, J., and Christensen, K. (2020). Piv measurements of turbulent flow overlying large, cubic and hexagonally-packed hemisphere arrays. *Journal of Hydraulic Research*, 2:363–383.

Kironoto, B. and Graf, W. (1996). Turbulence characteristics in rough non-uniform open-channel flow. *Proc. Inst. Civ. Engrs. Wat., Marit. Energy*, 112:336–348.

Kleinhans, M., Wilbers, A., De Swaaf, A., and VAN DEN BERG, J. (2002). Sediment supply-limited bedforms in sand-gravel bed rivers. *Journal of Sedimentary Research*, 72(5):629–640.

Kondolf, G. and Wilcock, P. (1996). The flushing flow problem: Defining and evaluating objectives. *Water Resources Research*, 32(8):2589–2599.

Kondolf, G. and Wolman, M. (1993). The size of salmonoid spawning gravel. *Water Resources Research*, 29(7):2275–2285.

Kuhnle, R. (2012). Fractional transport rates of bedload on goodwin creek. In P., B., Hey, R., and Thorne, C., editors, *Dynamics of Gravel-bed Rivers*, page 141–155. John Wiley, Chichester, UK.

Kuhnle, R., Wren, D., and Langendoen, E. (2016). Erosion of sand from a gravel bed. *J. Hydraul. Eng.*, 142(2):1–8.

Kuhnle, R., Wren, D., Langendoen, E., and Rigby, J. (2013). Sand transport over an immobile gravel substrate. *J. Hydraul. Eng.*, 139(2):167–176.

Lacey, R. and Rennie, C. (2012). Laboratory investigation of turbulent flow structure around a bed-mounted cube at multiple flow stages. *J. Hydraul. Eng.*, 138(1):71–84.

Lajeunesse, E., Malverti, L., and Charru, F. (2010). Bed load transport in turbulent flow at the grain scale: Experiments and modeling. *Journal of Geophysical Research*, 7115(F04001).

Lancaster, J., Hildrew, A., and Townstead, C. (1991). Invertebrate predation on patchy and mobile prey in streams. *J. Animal Ecol.*, 60:625–641.

Lawson, N. and Wu, J. (1997a). Three-dimensional particle image velocimetry: error analysis of stereoscopic tecniques. *Meas. Sci. Technol.*, 8:894–900.

Lawson, N. and Wu, J. (1997b). Three-dimensional particle image velocimetry: experimental error analysis of a digital angular stereoscopic system. *Meas. Sci. Technol.*, 8:1455–1464.

Lenzi, M. (2004). Displacement and transport of marked pebbles, cobbles and boulders in a steep mountain stream. *Hydrol. Process.*, 18:1899–1914.

Leonardi, S. Castro, I. (2010). Channel flow over large cube roughness: a direct numerical simulation study. *J. Fluid Mech.*, 651:519–539.

Leonardi, S., Orlandi, P., Smalley, R., Djendi, L., and Antonia, R. (2003). Direct numerical simulation of turbulent channel flow with transveerse square bars on one wall. *J. Fluid Mech.*, 491:229–238.

Lisle, T. (1995). Particle size variations between bed load and bed material in natural gravel bed streams. *Water Resour. Res.*, 31(4):1107–1118.

Liu, Y., Stoesser, T., Fang, H., Papanicolaou, A., and Tsakiris, A. (2017). Turbulent flow over an array of boulders placed on a rough, pemeable bed. *Computers and Fluids*, 158:120–132.

Liu, Z., Hu, Y., and Wang, W. (2019). Large eddy simulations of the flow field over simplified hills with different roughness conditions, slopes and hill shapes: a systematical study. *Energies*, 12(3413).

Lu, S. and Willmarth, W. (1973). Measurements of the structure of the reynolds stress in a turbulent boundary layer. *J. Fluid Mech.*, 60(3):481–511.

Luhnmann, T., Robson, S., Kyle, S., and Boehm, J. (2014). *Close-Range Photogrammetry and 3D Imaging*. deGruyter, Berlin, 2nd edition.

Ma, Y., Soatto, S., Kosecka, J., and Shankar Sastry, S. (2004). *An invitation to 3-D Vision: From Images to Geometric Models*. Springer-Verlag, New York.

MacDonald, M., Chan, L., Chung, D., Hutchins, N., and Ooi, A. (2016). Turbulent flow over transitionally rough surfaces with varying roughness densities. *J. Fluid Mech.*, 804:130–161.

MacDonald, R., Griffiths, R., and Hall, D. (1998). An improved method for the estimation of surfacec roughness of obstacle arrays. *Atmomspheric Environment*, 32(11):1857–1864.

Manes, C., Pokrajac, D., McEvan, I., and Nikora, V. (2009). Turbulence structure of open channel flows over permeable and impermeable beds: A comparative study. *Physics of Fluids*, 21(8125109).

Manes, C., Pokrajac, D., and McEwan, I. (2007). Double-averaged open-channel flows with small relative submergence. *J. Hydraul. Eng.*, 133(8):896–904.

McKenna Neuman, C. and Nickling, W. (1995). Aeolian sediment flux decay: non-lineaer behaviour on developing deflation lag surfaces. *Earth Surf. Processes Landforms*, 20:423–435.

McKenna Neuman, C., Sanderson, R. S., and Sutton, S. (2013). Vortex shedding and porphodynamics response of bed surfaces containing non-erodible roughness elements. *Geomorphology*, 198:45–56.

McKie, C., Juez, C., Plumb, B., Annable, W., and Franca, M. (2021). How large immobile sediments in gravel bed rivers impact sediment transport and bed morphology. *J. Hydraul. Eng.*, 147(2).

McLean, S. (1981). The role of non-uniform roughness in the formation of sand ribbons. *Marine Geology*, 42:49–74.

McLean, S., Wolfe, S., and Nelson, J. (1999). Spatially averaged flow over a wavy boundary revisited. *Journal of Geophisical Research*, 104(C7):743–753.

McLelland, S. (2013). Coherent secondarz flows over a water-worked rough bed in a straight channel. *Coherent Flow Structures at Earthßs Surface*, pages 275–288.

McLelland, S., Ashwoth, P., Best, J., and Livesey, J. (1999). Turbulence and secondary flow over sediment stripes in weakly bimodal bed material. *J. Hydraul. Eng.*, 125(5):463–473.

Medjnoun, T., Vanderwel, C., and Ganapathisubramani, B. (2020). Effects of heterogeneous surface geometry on secondary flows in turbulent boundary layers. *J. Fluid Mech.*, 886(A31).

Meyer-Peter, E. and Müller (1948). Formulas for bed-load transport. *Proc. 2nd Meeting IAHSR*, pages 1–26.

Mignot, E., Barthelemy, E., and Hurther, D. (2009a). Double-averaging analysis and local flow characterization of near-bed turbulence in gravel-bed channel flows. *J. Fluid. Mech.*, 618:279–303.

Mignot, E. and Hurther, D. (2008). Turbulent kinetic energy budget in a gravel-bed channel flow. *Acta Geophysica*, 56(3):601–613.

Mignot, E., Hurther, D., and Barthelemy, E. (2009b). On the structure of shear stress and turbulent kinetic energy flux across the roughness layer of a gravel-bed channel flow. *J. of Fluid Mech.*, 638:423–452.

Mohajeri, S., Grizzi, S., Righetti, M., Romano, G., and Nikora, V. (2015). The structure of gravel-bed flow with intermediate submergence: a laboratory study. *Water Resourc. Res.*, 51.

Mohta, J., Wallbrink, P., Hairsine, P., and Grayson, R. (2003). Determining the sources of suspended sediment in a forested catchment in southeastern australia. *Water Resour. Res.*, 39(3).

Moin, P. and Mahesh, K. (1998). Direct numerical simulation: a tool in turbulence research. *Ann. Rev. Fluid Mech.*, 30:539–578.

Monin, A. and Yaglom, A. (1975). *Statistical fluid mechanics: mechanics of turbulence*, volume 2. MIT press, Boston.

Montgomery, D. and Buffington, J. (1993). Channel classification, prediction of channel response and assessment of channel condition. *Rep. THW-SH19-93-002*.

Morris, H. (1955). Flow in rough conduits. *Transactions of the American Society of Civil Engineers*, 120(1):373–398.

Muzzammil, M. and Gangadhariah, T. (2003). The mean characteristics of horseshoe vortex at a cylindrical pier. *J. Hydraul. Res.*, 41(3):285–297.

Nakagawa, H. and Tsujimoto, T. (1980). Sand bed instability due to bed-load motion. *Journal of the Hydraulic Division*, 106(HY12).

Naot, D. (1984). Respponse of channel flow to roughness heterogeneity. *J. Hydraul. Eng.*, 110(11).

Neill, C. and Yalin, M. (1969). Quantitative definition of beginning of bed movement. *J. Hydraul. Div. Am. Soc. Civ. Eng.*, 95:585–588.

Nelson, J., McLean, R., and Drake, T. (1995). Role of near-bed turbulence structure in bed load transport and bed form mechanics. *Water Resources Research*, 31(8):2071–2086.

Nelson, R., John, R., and Greenberg, W. (1989). Regulated flushing in a gravel-bed river for channel habitat maintenance: A trinity river fisheries case study. *Environ. Manag.*, 11(4):479–493.

Neuman, C. and Bédard (2015). A wind tunnel study of flow structure adjustment on deformable sand beds containing a surface-mounted obstacle. *J. Geophys. Res. Earth Surf.*, 120:1824–1840.

Nezu, I. (2005). Open-channel flow turbulence and its research prospect in the 21st century. *J. Hydraul. Eng.*, 131(4):229–246.

Nezu, I. and Nakagawa, H. (1984). Cellular secondary currents in straight conduit. *J. Hydraul. Eng.*, 110(2):173–193.

Nezu, I. and Nakagawa, H. (1989). Self forming mechanism of longitudinal sand ridges and troughs in fluvial open-channel flows. *Proc. of 23rd IAHR Congress*, pages B65–B72.

Nezu, I. and Nakagawa, H. (1993). *Turbulence in Open-Channel Flows*. IAHR.

Nezu, I., Nakagawa, H., and Kawashima, N. (1988). Cellular secondary currents and sand ribbons in fluvial channel flows. *Proc. of 6th Congress of Asian and Pacific Regional Division, IAHR*, II-1:51–58.

Nezu, I. and Rodi, W. (1985). Experimental study on secondary currents in open channel flow. *Proc. of 21st IAHR Congress*, pages 115–119.

Nezu, I. and Sanjou, M. (2008). Turbulence structure and coherent motion in vegetated canopy open-channel flows. *Journal of Hydro-environment Research*, 2:62–90.

Nezu, I., Tominaga, A., and Nakagawa, H. (1993). Field measurements of secondary currents in straight rivers. *J. Hydraul. Eng.*, 119:598–614.

Nickling, W. and McKenna Neumann, C. (1995). Development of deflation lag surfaces. *Sedimentology*, 42:403–414.

Nikora, V., Goring, D., and Biggs, B. (1998). Silverstream eco-hydraulics flume: hydraulic design and tests. *New Zealand Journal of Marine and Freshwater Research*, 32:607–620.

Nikora, V., Goring, D., McEwan, I., and Griffiths, G. (2001). Spatially averaged open-channel flow over rough bed. *J. Hydraul. Eng.*, 127:123–133.

Nikora, V., Habersack, H., Huber, T., and McEwan, I. (2002a). On the bed particle diffusion in gravel bed flows under weak bed load transport. *Water Resour. Res.*, 38(1081).

Nikora, V., Koll, K., McEwan, I., McLean, S., and Dittrich, A. (2004). Velocity distribution in the roughness layer of rough-bed flows. *J. Hydraul. Eng.*, 130(10):1036–1042.

Nikora, V., Koll, K., McLean, S., Dittrich, A., and Aberle, J. (2002b). Zero-plane displacement for rough-bed open-channel flows. *River Flow*.

Nikora, V., McEwan, E., McLean, S., Coleman, S., Pokrajac, D., and Walters, R. (2007). Double-averaging concept for rough-bed open-channel and overland flows: Theoretical background. *J. Hydraul. Eng.*, 133(8).

Nikora, V., Stoesser, T., Cameron, S., Stewart, M., Papadopoulos, K., Ouro, P., McSherry, R., Zampiron, A., Marusic, I., and Falconer, R. (2019). Friction factor decomposition for rough-wall flows: theoretical background and application to open-channel flows. *Journal of Fluid Mechanics*, 872:626–664.

Nikuradse, J. (1933). *Strömungsgesetze in rauhen Rohren. Forschungsheft 361*. VDI-Verlag, Berlin.

Niño, Y. and Garcia, M. (1996). Experiments on particle-turbulence interactions in the near-wall region of an open channel flow: implications for sediment transport. *J. Fluid Mech.*, 326:285–319.

Okamoto, T., Yagita, M., and Kataoka, S. (1977). Flow past cone placed on flat plate. *Bulletin of the Japan Society of Mechanical Engineers*, 20(141):329–336.

Otsu, N. (1979). A threshold selection method form gray-level histograms. *IEEE Transactions on Systems, Man and Cybernetics*, 9(1).

Papanicolaou, A., Dermisis, D., and Elhakeem, M. (2011). Investigating the role of clasts on the movement of sand in gravel bed rivers. *J. Hydraul. Eng.*, 137(9):871–883.

Papanicolaou, A., Kramer, C., Tsakiris, A., Stoesser, T., Bomminayuni, S., and Chen, Z. (2012). Effects of a fully submerged boulder within a boulder array on the mean and turbulent flow fields: Implications to bedload transport. *Acta Geophysica*, 60(6):1502–1546.

Parker, G. (1991). Selective sorting and abrasion of river gravel. i: Theory. *J. Hydraul. Eng.*, 117(2):131–147.

Parker, G. (2008). Transport of gravel and sediment mixtures. In Garcia, M., editor, *Sedimentation engineering, processes, measurements, modeling and practice*, chapter 3, pages 165–251. American Society of Civil Engineering, Reston, VA.

Parker, G. and Klingeman, P. (1982). On why gravel bed streams are paved. *Water Resour. Res.*, 18(5):1409–1423.

Parker, G., Klingeman, P., and McLean, D. (1982). Bedload and size distribution in paved gravel-bed streams. *J. of Hydr. Div.*, 108(4):544–571.

Parker, G. and Toro-Escobar, C. (2002). Equal mobility of gravel in streams: The remains of the day. *Water Resour. Res.*, 38(11).

Parthasarathy, R. and Muste, M. (1972). Fully developed asymmetric flow in a plane channel. *J. Fluid Mech.*, 51(2):301–335.

Parthasarathy, R. and Muste, M. (1994). Velocity measurements in asymmetric turbulent channel flows. *J. Hydraul. Eng.*, 120(9):1000–1020.

Pattenden, R., Turnock, S., and Zhang, X. (2005). Measurements of the flow ocer low-aspect-ratio cylinder mounted on a ground plane. *Experiments in Fluids*, 39:10–21.

Pendergrass, W. and Aria, S. (1984). Dispersion in neutral boundary layer over a step change in surface roughness - i. mean flow and trubulence structure. *Atmos. Environ.*, 18:1267–1279.

Penna, N., Padhi, E., Dey, S., and Gaudio, R. (2021). Statistical characterization of unworked and water-worked gravel-bed roughness structures. *Journal of Hydraulic Research*, 59(3):420–436.

Perret, E., Berni, C., and Camenen, B. (2020). How does the bed surface impact low-magnitude bedload transport rates over gravel-bed rivers? *Earth Surf. Process. Landforms*, 45:1181–1197.

Perry, A., Schofield, W., and Joubert, P. (1969). Rough wall turbulent boundary layers. *J. Fluid Mech.*, 37:383–413.

Placidi, M. and Ganapathisubramani, B. (2015). Effects of frontal and plan solidities on aerodynamic parameters and the roughness sublayer in tubulent boundary layers. *J. Fluid. Mech.*, 782:541–566.

Podesta, J. J., Forman, M. A., Smith, C. W., Elton, D. C., Malécot, Y., and Gagne, Y. (2009). Accurate estimation of third-order moments from turbulence measurements. *Nonlinear Processes in Geophysics*, 16(1):99–110.

Poggi, D., Katul, G., and Albertson, J. (2004). A note on the contribution of dispersive fluxes to momentum transfer within canopies. *Boundary-Layer Meteorology*, 111:615–621.

Pokrajac, D., Finnigan, J., Manes, C., McEwan, I., and Nikora, V. (2006). On the definition of the shear velocity in rough bed open channel flows. In Ferreira, Alves, L. . C., editor, *River Flow 2006*, London. Taylor & Francis Group.

Pope, S. (2000). *Turbulent Flows*. Cambridge University Press.

Powell, D. (1998). Patterns and processes of sediment sorting in gravel-bed rivers. *Progress in Physical Geography*, 22(1):1–32.

Powell, D., Ockelford, A., Rice, S., Hillier, J., Nguyen, T., Reid, I., Tate, N., and Ackerley, D. (2016). Structural properties of mobile armors formed at different flow strengths in gravel-bed rivers. *J. Geophys. Res. Earth Surf.*, 121:1494–1515.

Powell, D., Reid, I., and Laronne, J. (2001). Evolution of bed load grain size distribution with increasing flow strength and the effect of flow duration on the caliber of bed load sediment yield in ephemeral gravel bed rivers. *Water Resources Research*, 37(5):1463–1474.

Prasad, A. (2000). Stereoscopic particle image velocimetry. *Experiments in Fluids*, 29:103–116.

Pretty, J. and Hildrew, A.G.and Trimmer, M. (2006). Nutrient dynamics in relation to surface–subsurface hydrological exchange in a groundwater fed chalk stream. *J. Hydrol.*, 330:84–100.

Radice, A., Malavasi, S., and Ballio, F. (2006). Solid transport measurements through image processing. *Exp Fluids*, 41:721–734.

Radice, A., Nikora, V., Campagnol, J., and Ballio, F. (2013). Active interactions between turbulence and bed load: Conceptual picture and experimental evidence. *Water Resources Research*, 49(1):90–99.

Raffel, M., Willert, C., Scarano, F., Kaehler, C., Werely, S., and Kompenhans, J. (2018). *Particle image velocimetry: a practical guide*. Springer, 3rd edition.

Raupach, M. (1981). Conditional statistics of reynolds stress in rough-wall and smooth wall turbulent boundary layers. *Journal of Fluid Mechanics*, 108:363–381.

Raupach, M. (1992). Drag and drag partition on rough surfaces. *Boundary Layer Meteorology*, 60:375–395.

Raupach, M., Finnigan, J., and Brunet, Y. (1996). Coherent eddies and turbulence in vegetation canopies: the mixing-layer analogy. *Boundary-Layer Meteorology*, 78:351–382.

Raupach, M., Gillette, D., and Leys, J. (1993). The effect of roughness elements on wind erosion threshold. *Journal of Geophysical Research*, 98:3023–3029.

Raupach, M. and Shaw, R. (1982). Averaging procedures for flows over vegetated canopies. *Boundary-Layer Meteorology*, 22:79–90.

Raupach, M. and Thom, A. (1981). Turbulence in and above plant canopies. *Ann. Rev. Fluid Mech.*, 13:97–129.

Raupach, M., Thom, A., and Edwards, I. (1980). A wind-tunnel study of turbulent flow close to regularly arrayed rough surfaces. *Boundary-Layer Meteorology*, 18:373–397.

Raupach, R., Antonia, R., and Rajagopalan, S. (1991). Rough-wall turbulent boundary layers. *Appl. Mech. Rev.*, 44(1).

Raus, D. (2019). *Transport sédimentaire sur rugosités immobiles: De l'hydrodynamique locale à la morphodynamique*. PhD thesis, University of Toulouse.

Raus, D., Moulin, F., and Eiff, O. (2019). The impact of coarse-grain protrusion on near bed hydrodynamics. *Journal of Geophysical Research: Earth Surface*, 124.

Remondino, F., Spera, M., Nocerino, E., Menna, F., and Nex, F. (2013). Dense image matching: comparison and analyses. *Proceedings of the 2013 digital heritage international congress*, 1:47–54.

Rickenmann, D. (2001). Comparison of bed load transport in torrents and gravel bed streams. *Water Resour. Res.*, 37(12):3295–3305.

Rickenmann, D. and Recking, A. (2011). Evaluation of flow resistance in gravel-bed rivers through a large field data set. *Water Resour. Res.*, 47.

Rijn, L. (1993). *Principles of sediment transport in rivers, estuaries and coastal seas*. Aqua Publications, Amsterdam.

Rotta, J. (1962). Turbulent boundary layers in incompressible flow. *Progress in Aerospace Sciences*, 2.

Rousseau, G. and Ancey, C. (2020). Scanning piv of turbulent flows over and through rough porous beds using refractive index matching. *Experiments in Fluids*, 61(172).

Rouzes, M., Moulin, F., Florens, E., and Eiff, O. (2019). Low relative-submergence effects in a rough-bed open-channel flow. *Journal of Hydraulic Research*, 57(2):139–166.

Ryan, S., Porth, L., and Troendle, C. (2002). Defining phases of bedload transport using piecewise regression. *Earth Surf. Process. Landforms*, 27:971–990.

Sambrook Smith, G. and Nicholas, A. (2005). Effect on flow structure of sand deposition on a gravel bed: Results from a two-dimensional flume experiment. *Water Resour. Res.*, 41.

Saric, W., Reed, H., and Kerschen, E. (2002). Boundary-layer receptivity of freestream disturbances. *Annu. Rev. Fluid Mech.*, 34:291–319.

Sarkar, S. and Dey, S. (2010). Double-averaging turbulence characteristics in flows over a gravel bed. *J. Hydraul. Res.*, 48(6):801–809.

Sarkar, S. and Dey, S. (2020). Self-preserving characteristics in wall-wake flow downstream of an isolated bedform. *Environmental Fluid Mechanics*, 20:1119–1139.

Sarkar, S., Papanicolaou, A., and Dey, S. (2016). Turbulence in a gravel-bed stream with an array of large gravel obstacles. *J. Hydraul. Eng.*, 142(11).

Sau, A., Hwang, R., Sheu, T., and Yang, W. (2003). Interaction of trailing vortices in the wake of a wall-mounted rectangular cylinder. *Physical Review*, 68(056303).

Savelyev, S. and Taylor, P. (2005). Internal boundary layers: I. height formulae for neutral and diabatic flows. *Boundary-Layer Meteorology*, 115:1–25.

Scherer, M., Uhlmann, M., Kidanemariam, A., and Krayer, M. (2022). On the role of turbulent large-scale streaks in generating sediment ridges. *J. Fluid Mech.*, 930(A11).

Schlichting, H. (1936). Experimental investigation of the problem of surface roughness. *Ing.-Arch.*, 7:1–34.

Schlichting, H. and Gersten, K. (2017). *Boundary-Layer Theory*. Springer, 9th edition.

Schlömer, O., Herget, J., and Euler, T. (2020). Boundary condition control of fluvial obstacle mark formation - framework from a geoscientific perspective. *Eart Surf. Process. Landofrms*, pages 189–206.

Schmeeckle, M., Nelson, J., and Shreve, R. (2007). Forces on stationary particles in near-bed turbulent flows. *J. Geophys. Res.*, 112.

Schneider, J., Rickenmann, D., Turowski, J., Bunte, K., and Kirchner, J. (2015). Applicability of bed load transport models for mixed-size sediments in steep streams considering macro-roughness. *Water Resour. Res.*, 51:5260–5283.

Sechet, P. and Guennec, B. (2000). Bursting phenomenon and incipient motion of solid particles in bed-load transport. *Journal of Hydraulic Research*, 37(5):683–696.

Shamloo, H., Rajaratnam, N., and Katopodis, C. (2001). Hydraulics of simple habitat structures. *Journal of Hydraulic Research*, 39(4):351–366.

Shields, A. (1936). Anwendung der aehnlichkeitsmechanik und der turbulenzforschung auf die geschiebebewegung. *Mitteilungen der Preussischen Versuchsanstalt für Wasserbau und Schiffbau*, 26.

Smart, G., Aberle, J., Duncan, M., and Walsh, J. (2004). Measruement and analysis of alluvial bed roughness. *Journal of Hydraulic Research*, 42(3):227–237.

Smart, M., Duncan, M., and Walsh, J. (2002). Relative rough flow resistance equations. *J. Hydraul. Eng.*, 128(6):568–578.

Smith, J. and McLean, S. (1977). Spatially averaged flow over a wavy surface. *Journal of geophysical research*, 82(12):1735–1746.

Song, T. and Chiew, Y. (2001). Turbulence measurements in nonuniform open-channel flow using acoustic doppler velocimeter (adv). *J. Eng. Mech.*, 127(3):219–232.

Stradiotti, G., Righetti, M., Tarekegn, T., Wharton, G., and Toffolon, M. (2020). New conceptual framework for the erosion of fine sediment from a gravel matrix based on experimental analysis. *J. Hydraul. Eng.*, 146(9).

Stroh, A., Schaefer, K., Frohnapfel, B., and Forooghi (2020). Rearrangement of secondary flow over spanwise heterogeneous roughness. *J. Fluid. Mech.*, 885.

Strom, K. and Papanicolaou, A. (2007). Adv measurements around a cluster microform in a shallow mountain stream. *J. Hydraul. Eng.*, 133(12):1379–1389.

Sutton, S. and McKenna Neuman, C. (2008a). Sediment entrainment to the lee of roughness elements: Effects of vortical structures. *J. Geophys. Res.*, 113.

Sutton, S. and McKenna Neuman, C. (2008b). Variation in bed level shear stress on surfaces sheltered by nonerodible roughness elements. *J. Geophys. Res.*, 113.

Terwisscha van Scheltinga, R., Friedrich, H., and Coco, G. (2018). A piv-based method to measure spatial gradients in bedload transport over a dune. In *9th International Conference on Fluvial Hydraulics, River Flow 2018*, volume 40 of *E3S Web of Conferences*. EDP Sciences.

Tropea, C., Foss, J., and Yarin, A. (2007). *Handbook of experimental fluid mechanics*. Springer.

Tsai, R. (1986). An efficient and accurate camera calibration technique for 3d machine vision. *Proceedings of the IEEE conference on computer vision and pattern recognition*, pages 364–374.

Tuijnder, A. and Ribberink, J. (2009). An experimental study into the geometry of supply-limited dunes. *Sedimentology*, 56:1713–1727.

Tuijnder, A. and Ribberink, J. (2012). Experimental observation and modelling of roughness variation due to supply-limited sediment transport in uni-directional flow. *Journal of Hydraulic Research*, 50(5):506–520.

Valyrakis, M., Diplas, P., Dancey, C., Greer, K., and Celik, A. (2010). Role of instantaneous force magnitude and duration on particle entrainment. *J. Geophys. Res.*, 115.

van Rijn, L. (1984a). Sediment pick-up functions. *J. Hydraul. Eng.*, 110(510):1494–1502.

van Rijn, L. (1984b). Sediment transport, part iii: Bedforms and alluvial roughness. *J. Hydraul. Eng.*, 110(12):1733–1754.

Vanderwel, C. and Ganapathisubramani, B. (2015). Effects of spanwise spacing on large-scale secondary flows in rough-wall turbulent boundary layers. *J. Fluid Mech.*, pages 1–12.

Vanderwel, C., Stroh, A., Kriegseis, J., Frohnapfel, B., and Ganapathisubramani, B. (2017). The instantaneous structure of secondarz flows in turbulent boundary layers. *J. Fluid Mech.*, 26(025111).

Vanoni, V. A. (1964). Measurements of critical shear stress for entraining fine sediments in a boundary layer. *W. M. Keck Laboratory of Hydraulics and Water Resources Report*, 7.

Venditti, J., Nittrouer, J., Allison, M., Humphries, R., and Church, M. (2019). Supply-limited bedform patterns and scaling downstream of a gravel-sand transition. *Sedimentology*, 66:2538–2556.

Vericat, D., R.J., B., and Gibbins, C. (2008). Sediment entrainment and depletion from patches of fine material in a gravel-bed river. *Water Resour. Res.*, 44.

Voermans, J., Ghisalberti, M., and Ivey, G. (2017). The variation of flow and turbulence across the sediment-water interface. *J. Fluid. Mech.*, 824:413–417.

Wang, J., Dong, Z., Chen, C., and Xia, Z. (1993). The effects of bed roughness on the distribution of turbulent intensities in open-channel flow. *Journal of Hydraulic Research*, 31(1):89–98.

Wang, Z. and Cheng, N. (2006). Time-mean structure of secondary flow in open with longitudinal bedforms. *Advances in Water Resources*, pages 1634–1649.

Wang, Z.-Q. and Cheng, N.-S. (2005). Secondary flows over artificial bed strips. *Advances in water Resources*, 28:441–450.

Wangsawijaya, D. D., Baidya, R., Chung, D., Marusic, I., and Hutchins, N. (2020). The effect of spanwise wavelength of surface heterogeneity on turbulent secondary flows. *Journal of Fluid Mechanics*, 894:A7.

Westerweel, J. and Scarano, F. (2005). Universal outlier detection for piv data. *Exp. Fluids*, 39(5):1096–1100.

Wharton, G., Mohajeri, S., and Righetti, M. (2017). The pernicious problem of streambed colmation, a multi-disciplinary reflection on the mechanics, causes, impacts and management challenges. *WIREs Water*, e1231:1–17.

Wieneke, B. (2005). Stereo-piv using self-calibration on particle images. *Experiments in Fluids*, 39:267–280.

Wieneke, B. and Pfeiffer, K. (2010). Adaptive piv with variable interrogation window size and shape. *15th Int. Symp. on Applications of Laser Techniques to Fluid Mechanics (Lisbon)*.

Wilcock, P. and Kenworthy, S. (2002). A two-fraction model for the transport of sand/gravel mixtures. *Water Resources Research*, 38(10).

Wilcock, P., Kenworthy, S., and Crowe, J. (2001). Experimental study of the transport of mixed sand and gravel. *Water Resources Research*, 37(12):3349–3358.

Wilcock, P., Kondolf, G., Matthews, W., and Barta, A. (1996b). Specification of sediment maintenance flows for a large gravel-bed river. *Water Resources Research*, 32(9):2911–2921.

Wilcock, P. and McArdell, B. (1993). Surface-based fractional transport rates: mobilization thresholds and partial transport of a sand-gravel sediment. *Water Resources Research*, 29(4):1297–1312.

Wilcock, P. and McArdell, B. (1997). Partial transport of a sand/gravel sediment. *Water Resources Research*, 33(1):235–245.

Willingham, D., Anderson, W., Christensen, K., and Barros, J. (2014). Turbulent boundary layer flow over transverse aerodynamic roughness transitions: Induced mixing and flow characterization. *Phys. Fluids*, 26(025111).

Wittenberg, L. (2002). Structural patterns in coarse gravel river beds: typology, survey and assessment of the roles of grain size and river regime. *Geogr. Annal*, 84A(1).

Wolman, M. and Brush, L. (1961). Factors controlling the size and shape of stream channels in coarse noncohesive sands. *Geol. Sur. Prof. Paper*, 282-G:183–210.

Wren, D. and Kuhnle, R. (2014). Turbulent flow and sand transport over a cobble bed in a laboratory flume. *J. Hydraul. Eng.*, 140(4):1–12.

Wren, D., Langendoen, E., and Kuhnle, R. (2011). Effects of sand addition on turbulent flow over an immobile gravel bed. *J. Geophys. Res.*, 116.

Wu, W. and Wang, S. (1999). Movable bed roughness in alluvial rivers. *J. Hydraul. Eng.*, 125(12):1309–1312.

Yager, E., Dietrich, W., Kirchner, J., and McArdell, B. (2012). Prediction of sediment transport in step-pool channels. *Water Resources Research*, 48:1–20.

Yager, E., Kirchner, J., and Dietrich, W. (2007). Calculating bed load transport in steep boulder bed channels. *Water Resour. Res.*, 43.

Yager, E. and Schmeeckle, W. (2013). The influence of vegetation on turbulence and bed load transport. *J. Geophy. Res. Earth Surf.*, 118:1585–1601.

Yang, C. (1984). Unit stream power equation for gravel. *J. Hydraul. Eng.*, 110:1783–1797.

Yang, S. and Chow, A. (2008). Turbulence structures in non-uniform flows. *Advances in Water Resources*, 31(10):1344–1351.

Yang, S. and Lee, J. (2007). Reynolds shear stress distributions ina gradually varied flow in a roughnes channel. *J. Hydraul. Res.*, 45(4):462–471.

Yang, S., Xu, W., and Yu, G. (2006). Velocity distribution in a gradually accelerated free surface flow. *Advances in Water Resources*, 29:1969–1980.

Yuan, J. and Piomelli, U. (2014). Roughness effects on the reynolds stress budgets in near-wall turbulence. *J. Fluid Mech.*, 760.

Zampiron, A., Cameron, S., and V., N. (2020a). Secondary currents and very-large-scale motions inopen-channel flow over streamwise ridges. *J. Fluid Mech.*, pages 1–25.

Zampiron, A., V., N., Cameron, S., Patella, W., I., V., and Stewart, M. (2020b). Effects of streamwise ridges on hydraulic resistance in open-channel flows. *J. Hydraul. Eng.*, 146(1).

Zhang, Z. (1999). Flexible camera calibration by viewing a plane from unknown orientations. *Proceedings of the 7th International Conference on Computer Vision*, pages 666–673.

Zhu, W., van Hout, R., and Katz, J. (2007). On the flow structure and turbulence during sweep and ejection events in a wind tunnel model canopy. *Boundary-Layer Meteorology*, 124:205–233.